IAHR 2017

37th IAHR WORLD CONGRESS

13-18 August, 2017

Kuala Lumpur, Malaysia

Supported by Spain Water and IWHR, China

THEME 2: FLOOD MANAGEMENT

Editor: Ngai Weng Chan

IAHR 2017

37th IAHR WORLD CONGRESS

13-18 August, 2017

Kuala Lumpur, Malaysia

Supported by Spain Water and IWHR, China

FLOOD RISK ASSESSMENT

OUTBURST FLOODS TRIGGERED BY IMPULSE WAVES INSIGHTS FROM HYDRAULIC EXPERIMENTATION

FREDERIC M. EVERS(1), PIERRE-JACQUES FRANK(2) & WILLI H. HAGER(3)

(1,3) ETH Zurich, Laboratory of Hydraulics, Hydrology and Glaciology (VAW), Zurich, Switzerland,
evers@vaw.baug.ethz.ch; hager@vaw.baug.ethz.ch
(2) Axpo Power AG, Baden, Switzerland, (formerly VAW, ETH Zurich),
pierre.frank@axpo.com

ABSTRACT

Outburst floods represent a serious hazard in mountainous regions. A major trigger for these events are impulse waves generated by mass wasting into the water bodies including artificial reservoirs for hydropower generation, lakes impounded by a landslide dam, or moraine dammed proglacial lakes. After a short propagation distance, these impulse waves overtop the dam and erode its top. If the erosion is substantial enough, a dam breach is initiated. The stages leading to an outburst flood were represented by three different hydraulic model setups: impulse wave generation and spatial propagation in a wave basin, wave overtopping in a 2D wave channel, and spatial dam breach in a 1 m wide flume. Selected experiments are presented and the characteristic hydraulic features as well as governing parameters are discussed. The results support an improved hazard assessment and are useful to further develop existing numerical schemes.

Keywords: Dam breach; hydraulic experimentation; impulse wave; outburst flood; wave overtopping.

1 INTRODUCTION

Outburst floods are characterized by a sudden water release from a standing water body to downstream regions with a lower geodetic elevation. Potential water bodies include artificial reservoirs for hydropower generation, lakes impounded by a landslide dam, or moraine dammed proglacial lakes. Water masses over-topping the dam crest are a major load for the downstream dam face which eventually causes a complete failure of the structure due to erosion. The transport of water mass over the dam structure is initiated either by a water level rise exceeding the dam crest elevation or by wave impact. While the former process is gradual and allows for monitoring and a temporal estimation of the instant of overtopping, the latter is subjected to larger uncertainty. Impulse waves generated by substantial mass wasting into the water body pose a particular threat to the stability of embankment dams, even under conditions of a sufficient freeboard to withstand the load of wind waves.

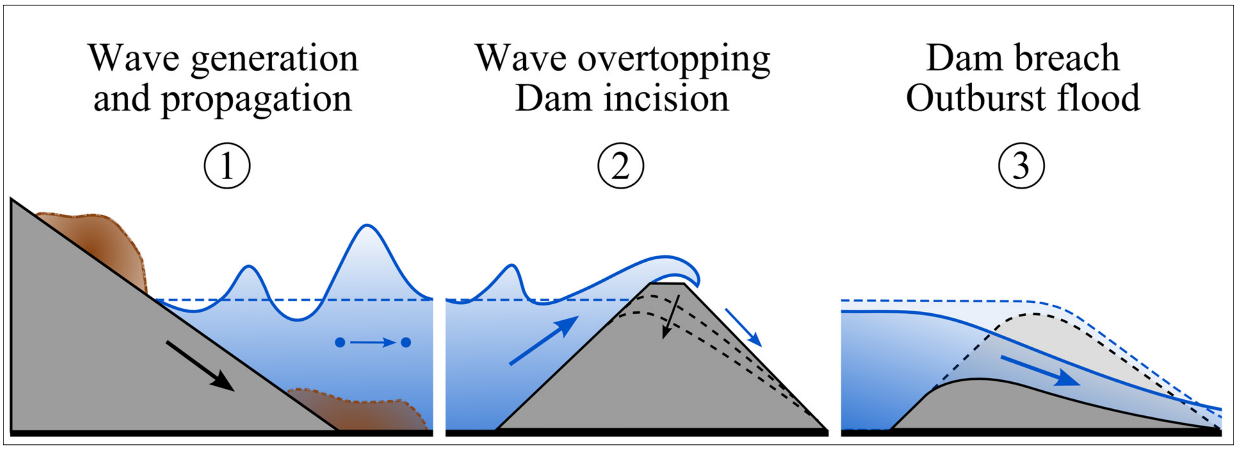

Figure 1. Three stages of outburst flood event triggered by impulse waves.

From a hydraulician's point of view, the chain of events leading to an impulse wave triggered outburst flood is divided into three significant stages (Fig. 1): (1) Mass wasting event such as a rockslide or an ice avalanche generating an impulse wave as a function of the governing sliding mass parameters including slide velocity, slide mass, and slide thickness. A wave train propagates radially from the impact location across the water body. During propagation, the wave characteristics (e.g. wave height, wave length) are subjected to transformation due to wave decay and shoaling effects. (2) Impulse waves overtop the dam structure, thereby eroding its top and forming an incision. The overtopping volume itself might already create severe downstream flooding. If the dam crest is eroded enough, a self-increasing spatial dam breach is induced as stage (3). Depending on the dam geometry, its material, and the shape of the upstream water body, the released outburst flood features a characteristic hydrograph.

Westoby et al. (2014) classifies impulse wave generation by landslides or avalanches as a major triggering mechanism for outburst floods from moraine-dammed lakes. Investigations retracing past events and hazard assessment on possible occurrences in the future back up this statement (e.g. Klimeš et al., 2016; Clague and Evans, 2000). While numerical approaches are the method of choice for flood modelling in complex topographies of the valley downstream, the breach initiation and formation processes, which act as upper boundary condition in numerical models, lack adequate integration (Westoby et al., 2014). To overcome these limitations, the application of physical models provides a better understanding of the underlying processes and means for quantitative estimations. Awal et al. (2010) accomodates wave profiles, dam shape evolution profiles and outflow hydrographs for an integrative experimental setup and described the effect of selected parameters on the overall outburst flood process. Balmforth et al. (2009, 2008) focused on the wave overtopping and incision stage, and present experiments as a starting point for the development of a numerical approach. However, these studies provide a primarily qualitative analysis but overlook possible scale effects.

Three self-contained experimental setups were installed and operated with the objective of gaining detailed insight into the underlying physics of the stages shown in Figure 1. Impulse wave and dam breach tests are conducted in 3D setups, while 2D channel is employed for wave overtopping tests. Given the complex hydraulic processes involving multi-phase flow and spatial test configurations, the requirements regarding measurement techniques are demanding. The following sections present the respective setups and provide descriptions of relevant hydraulic features for selected experiments as well as their main governing parameters.

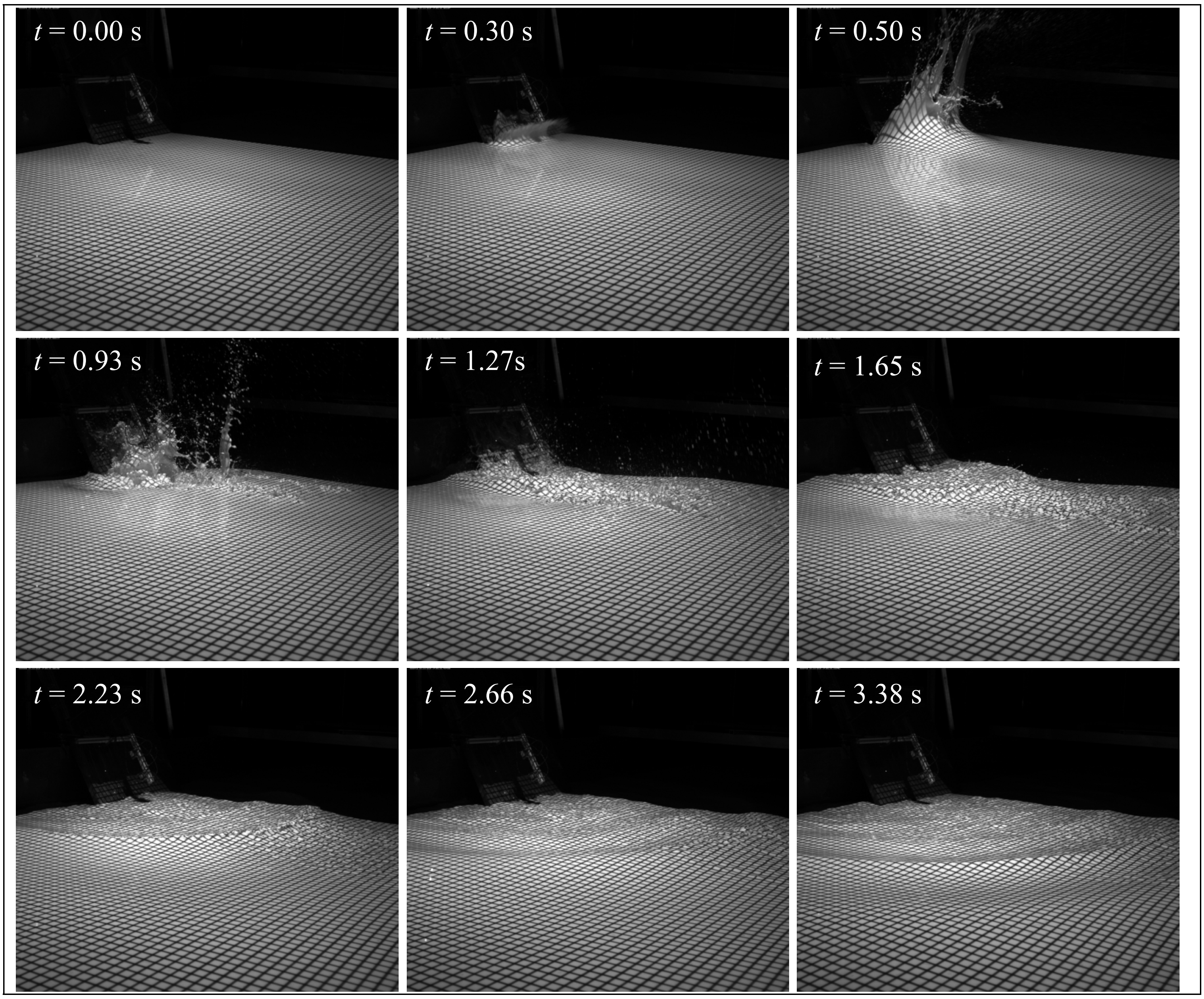

Figure 2. Photo sequences of an impulse wave experiment with spatial wave propagation.

2 IMPULSE WAVES

The stage of impulse wave generation and spatial propagation was modeled in an 8 m by 4.5 m wave basin. A deformable mesh-packed granular slide on an inclined plane was used for wave generation whereas a videometric measurement system was employed for tracking a grid projection on an opaque water surface as shown in Figure 2 (Evers and Hager 2016). When compared with conventional wave gauges, this approach allows for a high spatial resolution with up to 6,000 measurement positions at an acquisition rate of 24 Hz in a measuring field of approximately 14 m^2 (Evers and Hager, 2017).

Figure 2 shows a photo sequences of an experimental run for a slide with impact velocity V_s = 4.55 m/s, mass m_s = 20 kg, slide thickness s = 0.12 m, slide width b = 0.5 m, and impact angle α = 60° at a still water depth h = 0.3 m. At time t = 0 s, the grid projection on the water surface is undisturbed. The sliding mass impacts the water body at t = 0.3 s creating a splash that has developed its maximum extent at t = 0.5 s. Later, the impact crater collapses as shown at t = 0.93 s. The collapse leads to wave run-up at the sliding plane (t = 1.27 s). Simultaneously, the first wave detaches from the impact location featuring a long crest. At t = 1.65 s, the first crest was followed by a wave trough and a second wave crest was generated. A steeper second wave crest was fully developed at t = 2.23 s with spilling features noted at its crest line. At t = 2.66 s, these spilling features have dissipated and a third wave crest had developed. The last photo at t = 2.66 s shows succeeding waves of the wave train generated by the slide impact. Note that the length of the first wave was substantially longer than these succeeding.

Evers and Hager (2016) state that the height of the first wave was mainly governed by the same parameters as in 2D experiments; namely slide impact velocity V_s, slide mass m_s, slide thickness s, and slide impact angle α as well as the still water depth h. The slide width b was identified as an additional governing parameter in spatial environments by Evers and Hager (2017). Only waves outgoing from the slide impact location were analyzed. However, a water body prone to create outburst floods was confined by a dam or a shoreline with expansive slopes. Outgoing waves are reflected, creating an irregular wave pattern with wave superposition or potentially a seiche. These processes cannot be experimentally accounted for in a general setup. To quantify the wave load for wave run-up or overtopping along the shore, an estimation of the decay rate of a wave envelope consisting of multiple impulse waves is required. The envelope's initial maximum wave at impact can be determined from experiments.

3 WAVE OVERTOPPING

The erosional processes of impulse wave overtopping were analyzed in a 2D wave channel. Solitary waves were generated with a piston-type wave maker and the overtopping process at a granular dam of uniform grain size was captured with a high-speed camera. A drainage system was installed at the downstream dam toe to avoid seepage flow. A detailed description of the experimental setup was provided Huber et al. (2017).

Figure 3 shows an experimental run with dam height w = 0.2 m, dam face slope β = 26.57°, crest width b_K = 0.02 m, grain size d_{50} = 1.23 mm, freeboard f = 0.02 m, and solitary wave height H = 0.11 m at a still water depth H = 0.18 m. The water surface was undisturbed and the freeboard intact at t = 0 s. At t = 0.9 s, the solitary wave had reached the dam crest and the overtopping process was initiated. The maximum overtopping depth d_0 was attained at t = 1.12 s and sediment transport occurs both on the upstream side and on top of the dam. At t = 1.22 s the overtopping water mass had reached the dam toe and the downstream portion of the dam was covered with a maximum water column. The water column above the dam crest had substantially dropped and a constant flow depth at the downstream side had formed at t = 1.3 s. In addition, air entrainment from the dam body into the water column was observed. At t = 1.6 s the flow depth above the dam crest continues to drop and the flow on the downstream dam portion becomes highly turbulent. Only a slight flow depth remains at t = 2 s, while water was infiltrating the dam body. The overtopping process was completed at t = 2.42 s along with a freeboard reduction to 50% of its initial extent.

The eroded crest depth h_e was defined by Huber et al. (2017) as the vertical distance between the initial dam crest and the highest dam elevation after a test. It was mainly governed by the freeboard, followed by wave height and dam shape. No effect of the grain size was found for the investigated range between 1.23 mm and 2.68 mm, including mixtures. Another important quantity is the overtopping volume $\forall$. If the dam crest withstands wave loading and the entire structure was not subject to failure, small overtopping volumes can already create severe downstream flooding. Compared to rigid structures, overtopping volumes at granular dams are only slightly lower. As described in the previous section, not only solitary impulse waves will be generated by a landslide or avalanche, but also a wave train with multiple impulse waves including wave reflections impacting the granular dam. Although the impulse wave envelope at impact was subjected to decay, repeated overtopping can erode the dam crest so strong, that its maximum elevation lies beneath the still water level and a constant outflow was initiated. Therefore, the vulnerability of a dam section to become the initial incision for a dam breach is affected by its distance to the slide impact location as well as its freeboard and geometry. It should also be borne in mind that the above-described research applies exclusively to 2D dam overtopping, so that additional 3D effects need to be carefully considered using detailed laboratory experimentation if the failure of the dam structure poses severe risks in the tailwater valley.

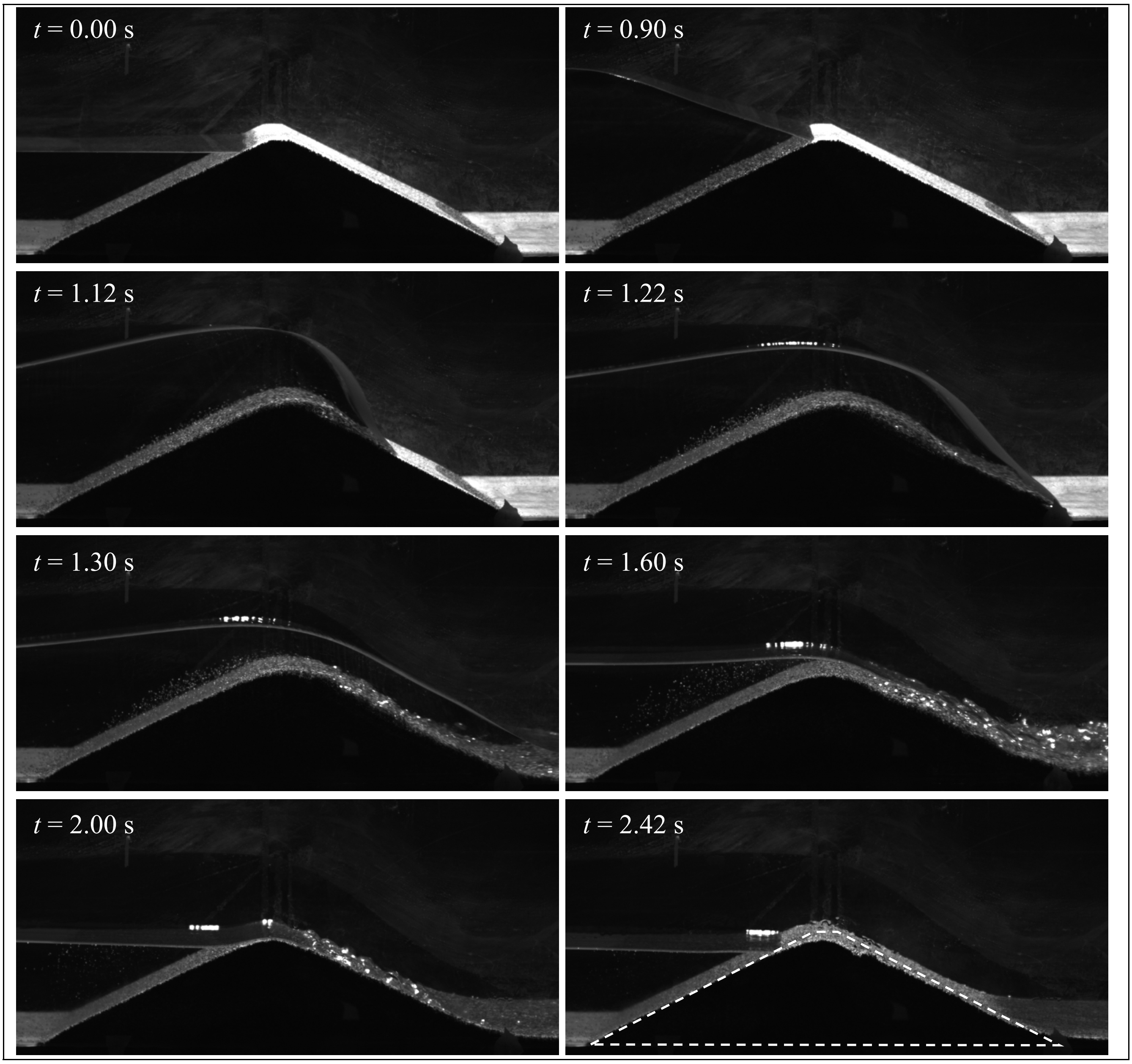

Figure 3. Photo sequences of a solitary wave overtopping experiment at a granular dam.

4 DAM BREACH

The dam breach experiments were conducted in a 1 m wide and 11.9 m long flume. A videometric measurement system was employed for tracking the spatial and temporal evolutions of the breach geometry during a test, taking into account the refraction effects in the submerged breach portions due to the change of the refractive index between air and water (Frank and Hager, 2015). Figure 4 shows the grid projection onto the dam surface of the half-model test. The direction of view is from down- to upstream with the pilot channel at the glass wall on the right, necessary to initiate the spatial breach and representing an incision created by wave overtopping. To simulate the discharge characteristics for different reservoir sizes and shapes, a controller-based pump regulation scheme was applied to add a simulated reservoir volume to the physical reservoir of the laboratory channel (Frank, 2016).

Figure 4 shows a dam breach experiment of dam height w = 0.3 m, dam length b = 1 m and reservoir water surface area A_R = 33.4 m^2. At time t = 0 s, the granular dam was intact and water flows through the pilot channel. The initial small breach discharge mixes with the eroded sediment, so that the water-sediment mix flows slowly and deposits on the downstream dam face up to t = 15 s. The initial main vertical incision has extended to the downstream dam toe at t = 21 s and water continuously runs through the small channel of approximately constant width. At t = 34 s, increased side erosion leads to the characteristic that is so-called hourglass shape of the dam breach channel, while at the same time the base of the breach channel was still eroded vertically. Surface waves form in the downstream reach of the breach channel, inhibiting a clear view of the projected grid and impeding the capturing of the submerged breach shapes, as described by Frank and Hager (2015). For $t > 34$ s, the breach channel widens, the reservoir water level drops and the breach discharge increases up to $t = 200$ s before reducing to zero at $t = 647$ s.

Frank (2016) conducted 45 laboratory tests with dams built of non-cohesive sediment. It was found that the peak breach discharge was mainly governed by the parameters maximum headwater level h_M, reservoir water surface area A_R, cross-sectional dam area A_D, and inflow discharge Q_o if the drainage discharge is assumed to be negligible. The results indicate that A_R represents a more practical parameter to describe peak breach discharge as compared with the often-used reservoir volume. In addition, A_R was directly extracted from ortho-images so that no information of the reservoir bathymetry was needed for estimating the peak discharge. A satisfactory fit with peak breach discharge data of historical dam failures was obtained by introducing a fit parameter for the higher erosion resistance of prototype dike material. The results of Frank (2016) also included data on the spatial breach topographies as well as the breach hydrographs and this allows for a quantification of erosion rates. Given that outburst floods commonly evolve into debris flows (Westoby et al., 2014), these two quantities are relevant as the upper boundary condition in numerical simulations modelling downstream of flood propagation.

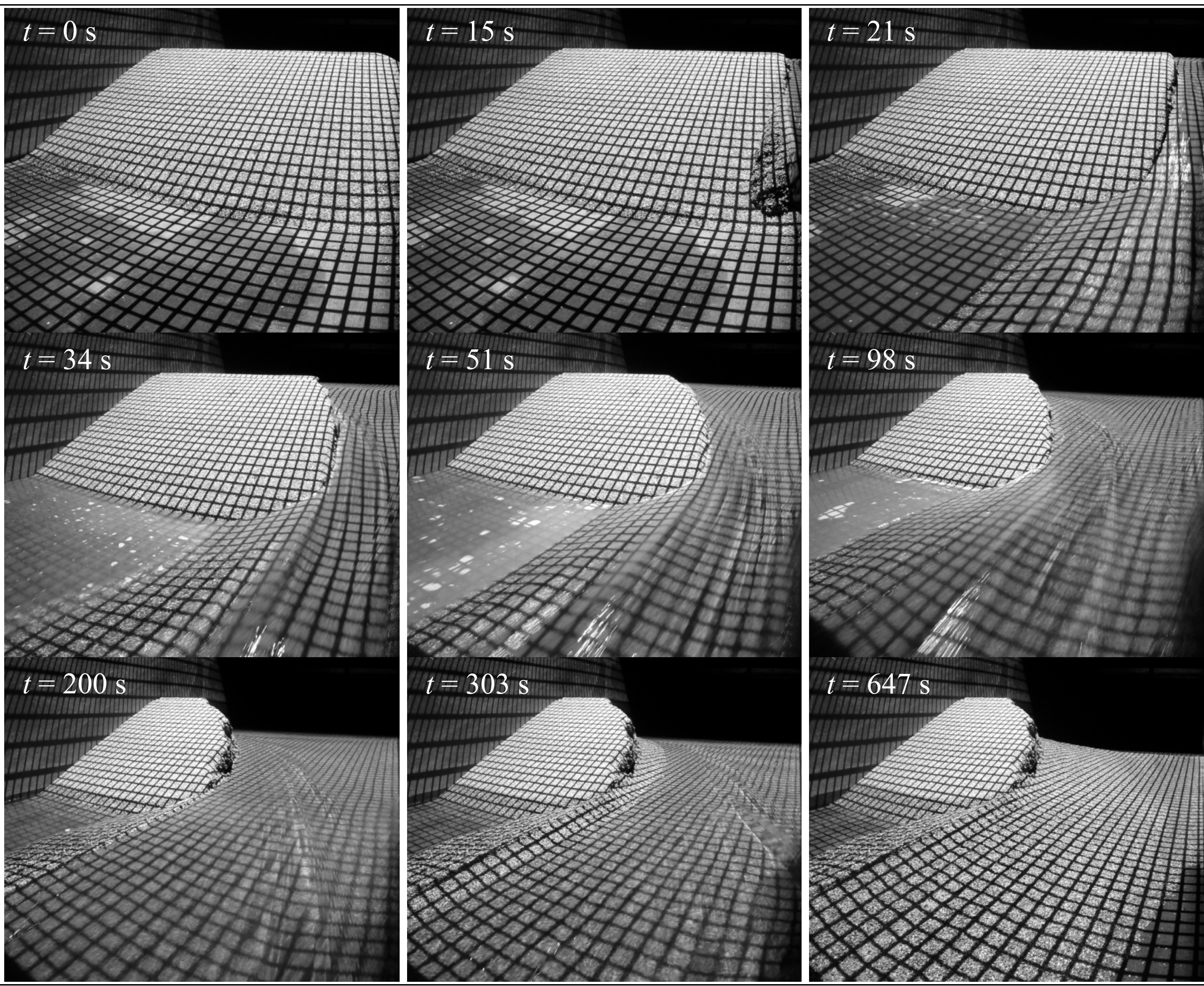

Figure 4. Photo sequences of dam breach experiment with a simulated reservoir volume.

5 CONCLUSIONS

Mass wasting into dammed water bodies is a major triggering mechanism for outburst floods. Related events have occurred in the past and pose a major future hazard in mountainous regions. The hydraulic features of the triggering processes were analyzed for three selected experimental setups. These setups represent the three stages of such an event, including impulse wave generation and propagation, wave overtopping and dam incision coupled with a dam breach that has a characteristic hydrograph as the source for the outburst flood. Key hydraulic features were presented and discussed with photo sequences of selected experimental runs. To obtain quality measurement data of high spatial density and acquisition rate, a novel videometric measurement technique with versatile capabilities is applied. Although outburst flood events are simulated by means of numerical models, the physical principles of the triggering processes are still lacking detailed understanding and are a source of substantial uncertainties. The experimental data are crucial to develop integrated numerical schemes covering all stages of an outburst flood event, offering the potential to \ model prototype settings including downstream reaches. In addition, model tests provide the basis for generally applicable equations serving for an overall hazard assessment as well as a prediction of hydrographs as the input parameter for numerical simulations of the tailwater flood impact.

ACKNOWLEDGMENTS

The Swiss National Science Foundation supported the first (Project No 200021-143657) and the second authors (Project No 200021-140310). Laura E. Huber is acknowledged for having conducted and analyzed the wave overtopping experiments.

REFERENCES

Awal, R., Nakagawa, H., Fujita, M., Kawaike, K., Baba, Y. & Zhang, H. (2010). Experimental Study on Glacial Lake Outburst Floods Due to Waves Overtopping and Erosion of Moraine Dam. *Annuals of Disaster Prev. Res. Inst.*, No. 53 B, Kyoto University, Kyoto.

Balmforth, N.J., von Hardenberg, J., Provenzale, A. & Zammett, R. (2008). Dam Breaking by Wave-Induced Erosional Incision. *Journal of Geophysical Research,* 113(1), 1-12.

Balmforth, N.J., von Hardenberg, J. & Zammett, R.J. (2009). Dam-Breaking Seiches. *Journal of Fluid Mechanics*, 628, 1-21.

Clague, J.J. & Evans, S.G. (2000). A Review of Catastrophic Drainage of Moraine-Dammed Lakes in British Columbia. *Quaternary Science Reviews*, 19(17-18), 1763-1783.

Evers, F.M. & Hager, W.H. (2016). Spatial Impulse Waves: Wave Height Decay Experiments at Laboratory Scale. *Landslides*, 13(6), 1395-1403.

Evers, F.M. & Hager, W.H. (2017). Generation and Spatial Propagation of Landslide Generated Impulse Waves. *Coastal Engineering Proceedings*, 1(35), 13.

Frank, P.-J. (2016). Hydraulics of Spatial Dike Breaches, *Doctoral Thesis.* ETH Zurich, Switzerland.

Frank, P.-J. & Hager, W.H. (2015). Spatial Dike Breach: Sediment Surface Topography using Photogrammetry. *Proceedings of 36th IAHR World Congress*, The Hague, the Netherlands, 1613-1622.

Huber L.E., Evers F.M. & Hager W.H. (2017). Solitary Wave Overtopping at Granular Dams. *Journal of Hydraulic Research* (submitted).

Klimeš, J., Novotný, J., Novotná, I., de Urries, B.J., Vilímek, V., Emmer, A., Strozzi, T., Kusák, M., Rapre, A.C., Hartvich, F. & Frey, H. (2016). Landslides in Moraines as Triggers of Glacial Lake Outburst Floods: Example from Palcacocha Lake (Cordillera Blanca, Peru). *Landslides*, 13(6), 1461-1477.

Westoby, M.J., Glasser, N.F., Brasington, J., Hambrey, M.J., Quincey D.J. & Reynolds, J.M. (2014). Modelling Outburst Floods from Moraine-Dammed Glacial Lakes. *Earth-Science Review*, 134, 137-159.

EXTREME FLOOD FLOW IN AN INCREASINGLY URBANIZED FLOODPLAIN: AN EXPERIMENTAL APPROACH

SEBASTIÁN GUILLÉN-LUDEÑA(1), DIEGO LOPEZ(2), NICOLAS RIVIERE(3) & EMMANUEL MIGNOT(4)

(1,2,3,4) Univ-Lyon, INSA Lyon, LMFA, Villeurbanne, France
sebastian.guillen-ludena@insa-lyon.fr, diego.lopez@insa-lyon.fr, nicolas.riviere@insa-lyon.fr, emmanuel.mignot@insa-lyon.fr

ABSTRACT

During extreme flood events, the land occupation in floodplains becomes a major issue as it highly influences the flow resistance and the hydrodynamic processes. The present work aims at identifying the land occupation (number of emerging obstacles) increment on the evolution of the relative magnitude of resistance forces acting on the flow. The resistance forces are those corresponding to the bed friction and to the drag induced by the obstacles. Firstly, we characterize the transition from a flow governed mostly by bed-friction forces to a flow governed mostly by drag forces. Secondly, we quantify the evolution of the bed friction and obstacle drag resistance coefficients as the number of obstacles increases.

Keywords: Bed friction; drag force; flood plain; friction coefficient; laboratory experiments.

1 INTRODUCTION

In France, the potential adverse impacts related to flood events have increased during the last 30 years (according to the Centre for Research on the Epidemiology of Disasters) because of the increasing human settlements over the floodplains. Recent studies on global flood risk (Hirabayashi et al., 2013) has demonstrated that, on a global scale, the number of people exposed to floods with a return period is higher compared to prvious 100-year and is expected to increase, irrespective of the climate models and scenarios. In this context, the assessment of the existing modeling practices for river floods with T > 100-year becomes a major issue. It is also a major issue in the context of the application of the European Flood Directive (EU, 2007) on the assessment and management of flood risks, notably to build the flood hazard maps in the areas with potential significant flood risks and to complete the flood risk management plans.

Extreme floods are dangerous by nature and rarely characterized because the lack of field data. Flood marks are scarce, velocity measurements are non-existent, and the available stage-discharge relationships are not reliable at this range (Lang et al., 2010). Furthermore, it is usually considered that above T ~ 1000-year all the floodplains are inundated, flood protection systems are surpassed with negligible effects on the flow so that the flow processes and the flow resistance in the floodplain are mostly controlled by the degree of land occupation.

The present study focuses on complex land occupations with interspersed types of hydraulic roughness on emerging square obstacles representing buildings (industries, supermarkets *etc.*), and bottom roughness (representing low vegetation or any type of rough bottom cover). For a floodplain without any macro-roughness or large scale obstacle (low land occupation), the flow resistance is mostly governed by the bottom friction, and such flow configuration can be efficiently described by means of classical formulation such as that by Manning-Strickler (in case of a fully rough flow) or that by Colebrook-White. In contrast, for a floodplain widely occupied by emerging obstacles or buildings (high land occupation), the flow resistance is mostly driven by the total drag force caused by the obstacles. In this case, information on the drag force exerted by the emerging obstacles is required to describe the flow with a 1D formulation. In an intermediate configuration, in which both the spatial density of obstacles and the bed friction highly contribute to the flow resistance, a 1D description of the flow becomes challenging.

To better understand the flow resistance of these intermediate configurations, the present work aims at evaluating, the increases in spatial density of obstacle, the individual contribution of the bed friction and that of the drag induced by emergent obstacles to the overall flow resistance. Existing studies carried out in smooth beds corroborate the influence of the obstacles spatial density on both drag and bed-friction forces and thus on the overall flow resistance (Herbich and Shulits, 1964; Nepf, 1999; Tanino and Nepf, 2008). In addition, Tanino and Nepf (2008) estimated that, for smooth beds, bed friction forces represent about 13% of the overall flow resistance, though they point out that in rough beds such as natural floodplains, the contribution of bed friction to the overall flow resistance should increase. This study goes beyond the aforementioned studies by presenting an experimental set-up with a rough bed and direct measurements of the drag force acting on the obstacles.

2 EXPERIMENTAL SET-UP

2.1 Experimental facility and parameters

The experiments were carried out in a B=1.20 m wide and 8 m long rectangular laboratory flume with a fixed slope S_0=0.18%. The bottom of the flume was covered with an artificial grass layer, on which the emergent obstacles were placed (Fig. 1). The obstacles consist of prismatic bricks of square base section (edge ℓ), and remain emergent in all cases. In this work, it was decided to consider only regular grids of aligned obstacles as shown in Figures 1 and 2. Only uniform flows were considered, and the uniform flow depth was set with the help of an adjustable tailgate located at the downstream end of the flume.

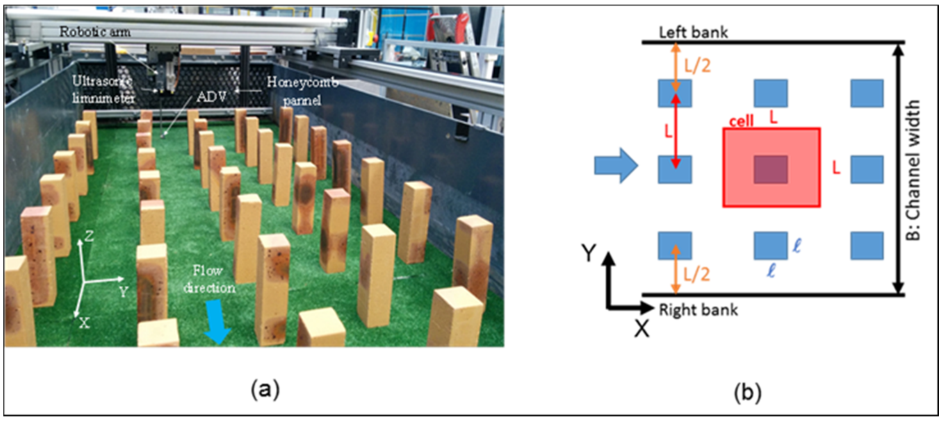

Figure 1. a) Upstream view of the experimental flume, and b) Schematic plan view of the obstacle distribution.

Dimensional analysis yielded 6 non-dimensional parameters characterizing this problem:

$$(B/\ell,\ \varepsilon/\ell,\ \lambda,\ D/\ell,\ Re_\ell,\ Fr) \qquad [1]$$

where B is the channel width, ℓ = 0.054 m the horizontal dimension (width and length) of the obstacles, D the flow depth, λ the obstacle spatial density defined as $\lambda = D\ell/L^2$, ε the bed roughness (ε~7 mm), L the distance between the centers of two consecutive obstacles in both horizontal directions (see Figure 1), and Re_ℓ and Fr are the Reynolds number (based on the obstacles dimension, the edge ℓ) and Froude number respectively. In this study, only fully turbulent flows with low Froude number were considered so that the impact of Re_ℓ and Fr on the flow can be discarded. Moreover, B, ℓ and ε were constant so that the list of characteristic parameters finally reduces to:

$$(\lambda,\ D/\ell) \qquad [2]$$

with λ the obstacle spatial density and D/ℓ the relative shallowness. A total of 50 experiments are performed with $0.0016<\lambda<0.45$ and $0.8<D/\ell<3$.

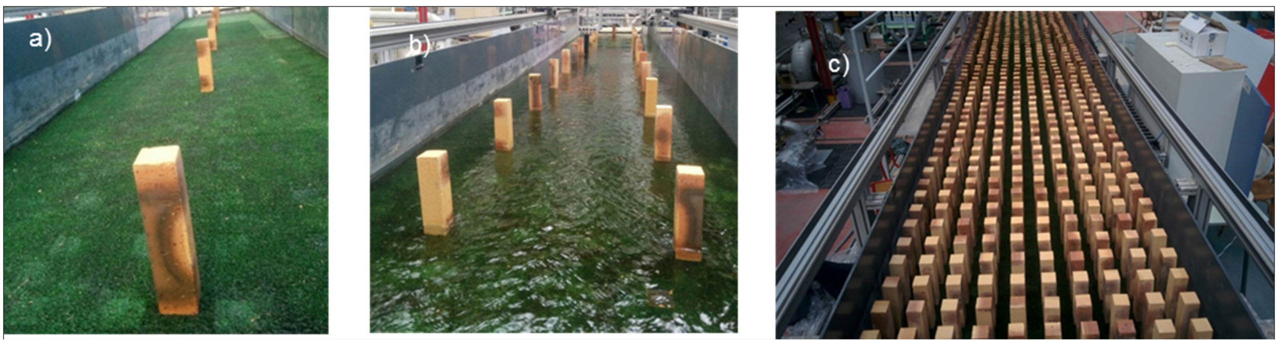

Figure 2. Perspective of the flume with different configurations, in which the spatial density of obstacles (λ) increases from a) to c).

2.2 Experimental strategy

Under uniform flow conditions and assuming local periodicity in streamwise and transverse directions, the streamwise momentum balance applied to the water volume within a cell (red filled square on Figure 1) will simply yield

$$W = F_d + F_b \qquad [3]$$

where W is the streamwise projection of the water weight in the cell, balanced by the drag force on the obstacle located at the center of the cell (F_d) and the bed friction force within the cell (F_b). For given values of the two non-dimensional parameters from Eq.2, the water weight reads:

$$W = \rho g S_0 D\left(L^2 - \ell^2\right) \qquad [4]$$

The experimental strategy in measuring the drag force that the flow exerts on the obstacle located at the middle of the cell can be seen Figure 1. Then, the bed-friction force acting on this cell is obtained using Eq. 3.

2.3 Experimental methods

This study involves two types of measurement that were described in this section. First, velocity fields were measured for a given flow configuration, in order to verify the symmetry and periodicity of the flow and therefore the validity of Eq. 3. In second step we measure the drag force applied on a brick with a novel hydrodynamic balance.

2.3.1 Measurement of the velocity field

The velocity field is measured using a Vectrino+ Nortek side-looking ADV (Acoustic Doppler Velocimeter) mounted on an automatic displacement system and connected to a PC with and acquisition software. This system allows measuring the two horizontal velocity components u, v along the streamwise (X) and transverse (Y) directions respectively. Micro-bubbles were added to the water in the upstream tank to improve the acoustic backscattering. Measurements were performed during 4 minutes at a sampling frequency equal to 50 Hz.

The data presented here were measured for one selected flow configuration, with λ=0.04 and D/ℓ=0.8, at the elevation Z/D=0.4. Figure 3 shows two transverse profiles of mean streamwise velocity at the upstream edge (red line) and downstream edge (black line) of two consecutive cells (along the transverse direction). Both profiles show a good agreement with each other and they were fairly repeated in both cells. Consequently, it was assumed here that measuring the flow and force characteristics in any cell (away from the lateral walls) should be the representative of the flow at large scale.

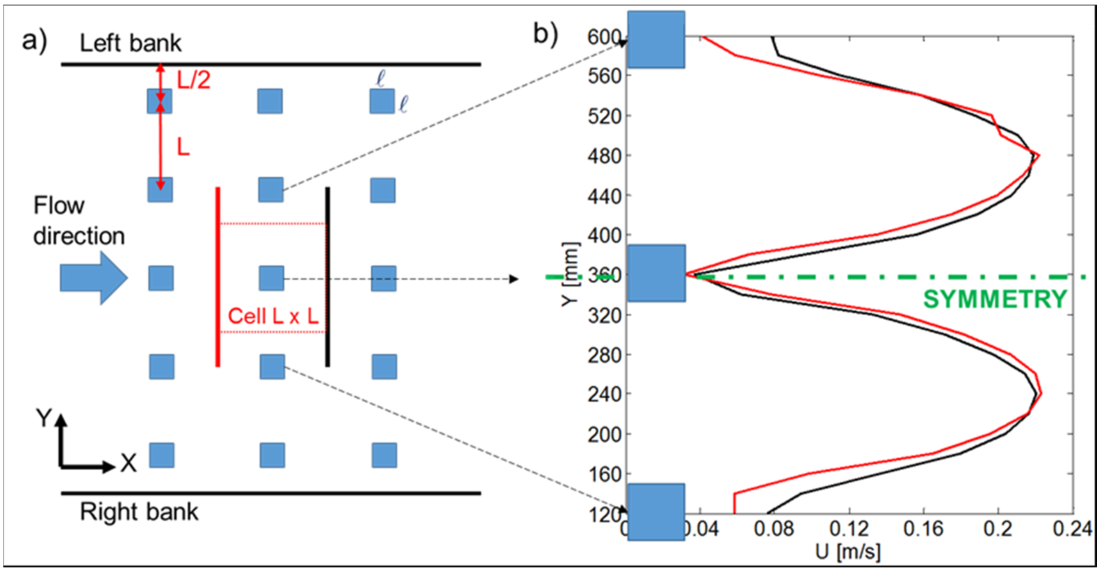

Figure 3. Mean streamwise velocity measured along two transversal profiles, at the upstream and downstream edges of a cell. a) Schematic plan view of the flume with the position of the transversal profiles (red and black solid lines). b) Profiles of the streamwise velocity at the upstream (red line) and downstream (black line) edges of the cell.

2.3.2 Drag force measurement

The drag force (F_d) acting on the selected obstacle was measured with a dedicated hydrodynamic balance represented in Figure 4. The balance consists of a PVC-obstacle attached to a vertical bar, which in turns was attached to two horizontal level arms. The force exerted by the flow on the obstacle (drag) was transmitted to the digital scale (f_1 and f_2 on the sketch) by means of a torque around the rotation axis (black circle in the sketch). Since the application point of the drag force was unknown, two measurements were performed, one for each level arm. With these measurements, the drag force (F_d) and the application point were obtained as:

$$F_d=\frac{a}{b}(f_1\text{-}f_2) \quad [5]$$

$$A=\frac{f_1 b}{f_1\text{-}f_2} \quad [6]$$

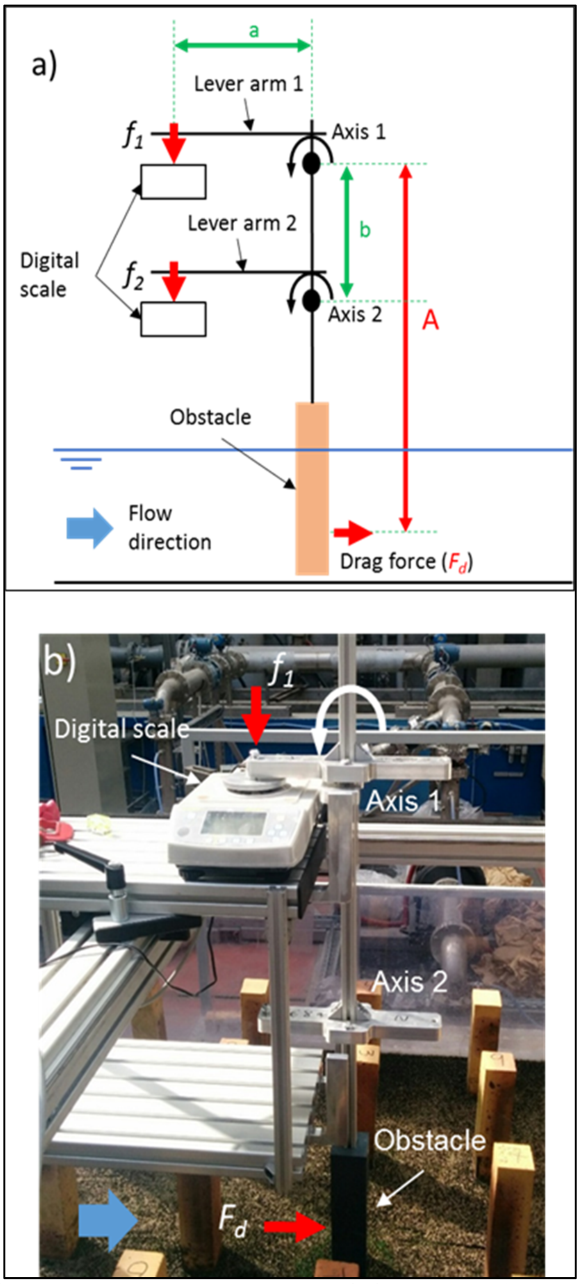

Figure 4. a) Sketch of the hydrodynamic balance. b) Overview of the hydrodynamic balance.

3 RESULTS

3.1 Flow pattern

Figure 5 shows the streamwise and transverse flow patterns, measured for λ=0.04 and *D/ℓ*=0.8 at *Z/D*=0.15. Two typical flow features were observed around an obstacle: i) a low streamwise velocity region just in front of the obstacle as the flow must slow down to finally stop at the obstacle upstream façade; ii) a second low streamwise velocity downstream from the obstacle in the wake region. Oppositely, maximum streamwise velocities were measured on the sides of the obstacles, at mid-distance from the neighboring

  ISSN 1562-6865 (Online) - ISSN 1063-7710 (Print)

obstacle (Y=240mm and Y=480mm). Moreover, the transverse velocity graph (Figure 5, bottom) reveals that the flow escapes from the centerline upstream of obstacle and goes back towards the centerline downstream from the obstacle in the corresponding wake. Note that measurements were only performed in the bottom-left half-cell (bright colors) and are repeated 3 times (dull colors) for clarity.

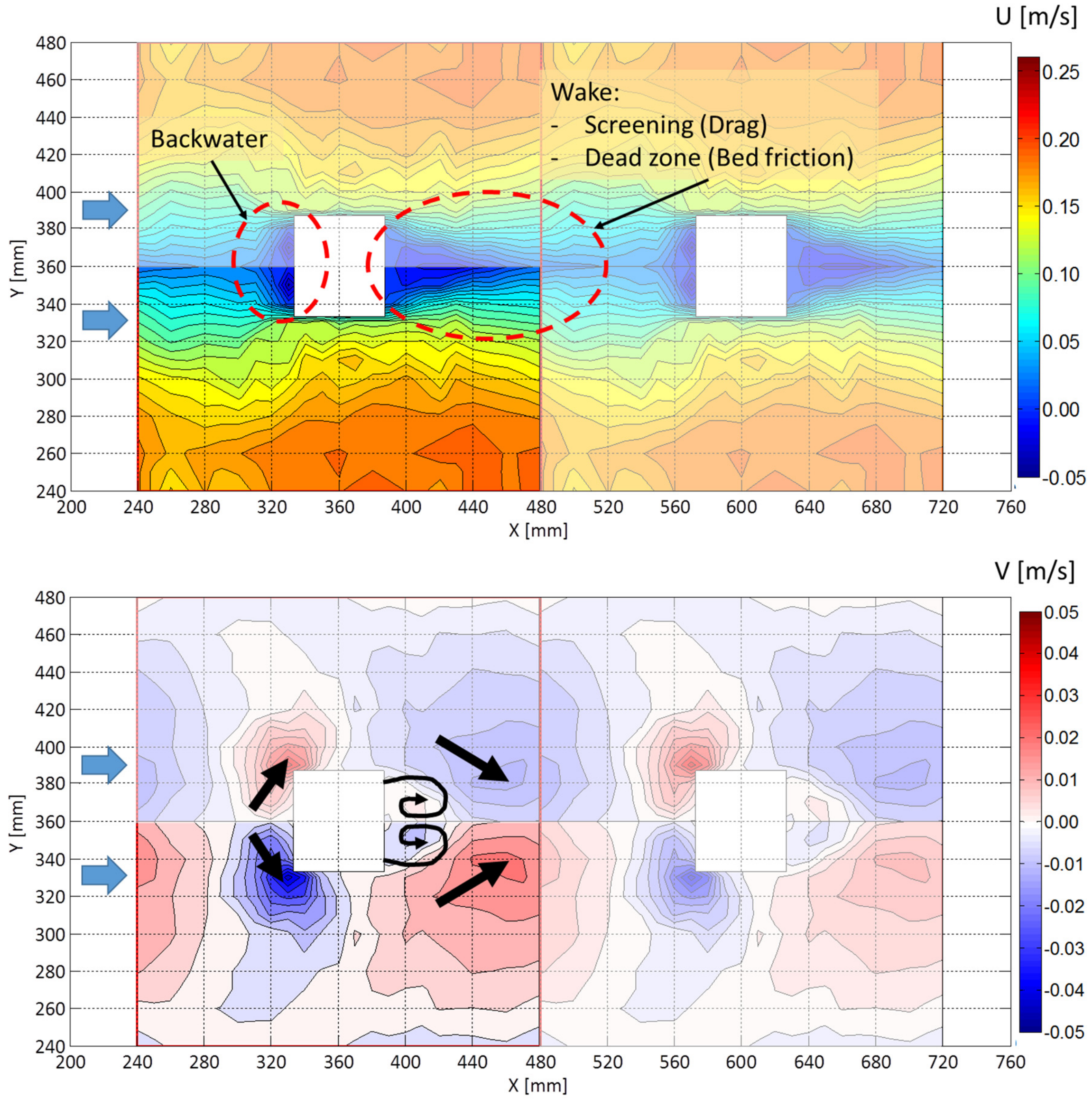

Figure 5. Mean streamwise (U, top) and transverse (V, bottom) velocity distribution for one flow configuration, at one measured elevation (λ=0.04, D/ℓ=0.8, Z/D=0.15). Measurements were only performed in the bottom-left half-cell (bright colors) and are repeated 3 times (dull colors) for better clarity.

3.2 Forces

Figure 6 plots the measured drag (red) and estimated bed friction forces from Eq.3 (normalized by the corresponding weight force) for all measured configurations as a function for the obstacle spatial density λ, including all values of relative shallowness D/ℓ. As expected, for small obstacle densities λ the bed friction force (blue circles) dominates while for high obstacle densities, the drag force (red triangles) dominates. The equal contribution of both forces is obtained for a density λ~0.02 (about 15% surface occupations for a depth comparable to the obstacle size). Figure 6 reveals that the spatial density λ was the most influent parameter regarding the force ratio. Nevertheless, the scattering shows a non-negligible impact of the relative shallowness D/ℓ (in the range of the tested magnitudes).

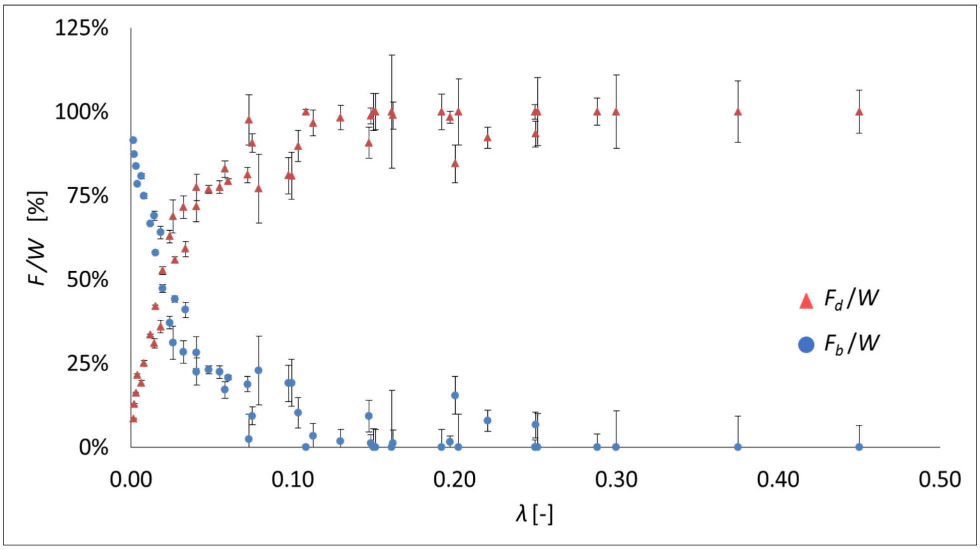

Figure 6. Relative drag and bed friction forces as a function of the obstacle spatial density.

These forces can be written as a function of the drag and friction coefficients C_d and C_b respectively:

$$F_d=\frac{1}{2}\rho C_d U^2 Dl \qquad F_b=\frac{1}{2}\rho C_b U^2\left(L^2-l^2\right) \qquad [7]$$

Now, using Eq.4 and 7, Eq. 3 reads:

$$U=\frac{Q}{BD}=\sqrt{\frac{\left(1-l^2/L^2\right)}{R_d+R_b}}\sqrt{2gDS_0} \qquad [8]$$

where the drag and bottom non-dimensional resistance coefficients respectively read as $R_d=C_d\lambda$ and $R_b=C_b(1-\ell^2/L^2)$. Note that without any obstacle, Eq.8 simplifies in the following well-known uniform of flow relation ($[2g/C_b]^{1/2}$ being the Chézy coefficient):

$$U=\sqrt{\frac{2gDS_0}{C_b}} \qquad [9]$$

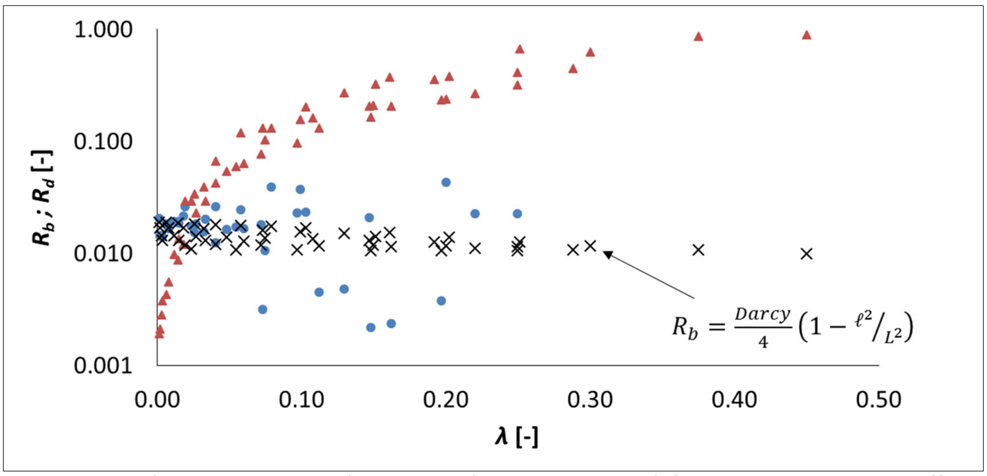

Figure 7. Drag (R_d, red triangles) and bed (R_b, blue circles) friction resistance coefficients as a function of the obstacle spatial density.

Figure 7 then plots, in logarithmic scale, the evolution of these two terms: the drag (R_b, red triangles) and bed-friction (R_d, blue circles) resistance coefficients as a function of the obstacle spatial densityλ. It appears that R_d increases with λ while R_b was hardly affected. Additionally the black crosses correspond to an estimation of R_b using the Darcy-Weisbach friction coefficient for estimating $C_b/4$, which is the friction coefficient that would be obtained with similar water depth and velocity but without any obstacle. Agreement between the measured (blue symbols) and estimated (black symbols) resistance coefficients reveals that the impact of the obstacles (and consecutive wake, flow acceleration, *etc.*) on the bottom friction remains negligible in the present flow configurations. The scattering observed for the values of R_b can be explained by the accuracy of the method. For $\lambda > 0.05$ the measured values of the drag force (F_d) are near those of the streamwise component of the weight (W), which results in low values of the bed-friction force (F_b). Consequently, these low values of F_b are of the same order of magnitude as the error of the measurements.

4 CONCLUSIONS

As a floodplain becomes flooded, the flow interacts with all roughness elements located within the floodplain, including bottom roughness (grass, bushes, *etc.*) and emerging buildings (industries, supermarkets, etc.). The present work is aimed at investigating the flow characteristics of such floodplain using an experimental approach in simplified configurations. The main objective is to estimate the relative contribution to flow resistance due to bed friction and to emergent obstacles. We showed that, while bed friction dominates at very low obstacle density ($\lambda < 0.01$), the obstacle-induced resistance, quickly takes over as the land occupation increases. We ended up with a modified uniform flow equation that relates the mean flow velocity to the water depth, the slope, the obstacle dimensions, spacing and finally the drag and friction resistance coefficients. We showed that the bed friction coefficient remains in fair agreement with the well-known Darcy-Weisbach friction coefficient, regardless of the obstacle density.

ACKNOWLEDGMENTS

This project is funded by the French ANR: FLOWRES project (grant ANR-14-CE03-0010). Authors are grateful to C. Marmounier for his participation to the building and design of the hydrodynamic balance.

REFERENCES

EU. (2007). Directive 2007/60/EC of the European Parliament and of the Council of 23 October 2007 on the Assessment and Management of Flood Risks. *Official Journal of the European Union*, L288, 27-34.

Herbich, J.B. & Shulits, S. (1964). Large Scale Roughness in Open-Channel Flow. Proceedings of the American Society of Civil Engineers. *Journal of the Hydraulics Division*, 203-230.

Hirabayashi, Y., Mahendran, R., Koirala, S., Konoshima, L., Yamazaki, D., Watanabe, S., Kim, H. & Kanae, S. (2013). Global Flood Risk under Climate Change. *Nature Climate Change*, 3(9), 816-821.

Lang, M., Pobanz, K., Renard, B., Renouf, E. & Sauquet, E. (2010). Extrapolation of Rating Curves by Hydraulic Modelling, with Application to Flood Frequency Analysis. *Hydrological Sciences Journal*, 55(6), 883-898.

Nepf, H.M. (1999). Drag, Turbulence, and Diffusion in Flow through Emergent Vegetation. *Water Resources Research*, 35(2), 479-489.

Tanino, Y. & Nepf, HM. (2008). Laboratory Investigation of Mean Drag in a Random Array of Rigid, Emergent Cylinders. *Journal of Hydraulic Engineering*, 134, 34-41.

LARGE WOOD ACCUMULATION PROBABILITY AT A SINGLE BRIDGE PIER

ISABELLA SCHALKO[(1)]

[(1)] Laboratory of Hydraulics, Hydrology and Glaciology (VAW), ETH Zurich, Zurich, Switzerland
schalko@vaw.baug.ethz.ch

ABSTRACT

During flood events, transported large wood (LW) can accumulate at river infrastructures, reduce the flow cross-section, lead to backwater rise and eventually to flooding of the adjacent area. In addition, LW accumulations can damage the river infrastructure itself. To predict the risk of LW accumulations, the estimation of the accumulation probability is essential, especially for an integrated flood hazard assessment. Previous studies on LW accumulation probability focused mainly on the influence of a bridge deck or on the effect of bridge pier shapes. The results are partially contradictory, and the existing design equations for LW accumulation probabilities are only available for bridge decks. Therefore, a series of flume experiments was conducted to analyze the LW accumulation probability as a function of (1) the approach flow conditions, (2) the bridge pier roughness, and (3) the LW characteristics, involving various log lengths, LW with and without branches, and uncongested versus congested LW transport. The LW accumulation probability increases with increasing log length, decreasing approach flow velocity, and for congested LW transport. The approach flow Froude number, the water depth, the bridge pier roughness, and the availability of branches had a negligible effect on the accumulation probability. The results for uncongested LW transport were summarized in a novel design equation to estimate the accumulation probability at a single bridge pier and to identify critical bridge cross-sections prior to a flood event. To upscale the experimental results, and to improve the general process understanding, innovative prototype tests will be conducted in spring 2017.

Keywords: Accumulation probability; Flood protection; Flood risk assessment; Large wood (LW); River engineering.

1 INTRODUCTION

Large wood (LW), herein defined as single logs with a diameter $d_L \geq 0.1$ m and a length $L_L \geq 1.0$ m (Keller and Swanson, 1979; Wohl and Jaeger, 2009; Ruiz-Villanueva *et al.*, 2016a), is a beneficial part of river ecosystems. LW can originate from various sources, including hillslopes, timber wood storages, and the fluvial corridor. Single logs and LW accumulations enhance the diversity of morphological structures, species, and flow conditions (Figure 1a). The connectivity between the channel and the floodplain, or between water, sediments, and nutrients highly improves due to LW in rivers (Wohl *et al.*, 2016). During flood events, LW can be mobilized and transported, possibly resulting in accumulations at river infrastructures like bridges or weirs (Figure 1b). Due to such LW accumulations, the flow cross-section reduces, leading to backwater rise. This may result in flooding of the adjacent area, thereby intensifying the flood hazard. The interaction between LW and sediment transport is relevant for the accumulation process and its consequences. On the one hand, LW accumulations can increase sediment deposition, whereas on the other hand, they can cause local scour at bridge piers, inducing structural damages or even failure. The estimation of the accumulation probability is therefore crucial for an integrated flood hazard assessment, as it directly affects the damage potential. The present study focuses on quantifying the LW accumulation probability at a single bridge pier for various approach flow conditions, bridge pier and LW characteristics.

Figure 1. LW accumulation at (a) the River Thur, Switzerland, and (b) a bridge pier in Tyrol, Austria.

  / ISSN 1562-6865 (Online) - ISSN 1063-7710 (Print)

2 LITERATURE REVIEW

The LW accumulation probability p is mainly affected by the orientation of transported logs, the type of transport, and the LW characteristics (i.e. LW dimensions, logs with and without branches). As stated by Braudrick and Grant (2001), the orientation of transported logs relative to the flow is influenced by the transversal velocity distribution within a channel, usually with the largest flow velocity located in the channel centerline. Logs transported parallel to the flow experience an equal flow velocity over their entire length, leading to a steady transport state. In contrast, a rotational force is exerted on non-parallel oriented logs, as the flow velocities at both log ends are unequal. For large transport distances, the logs therefore tend to orientate parallel to the flow and are transported along the channel thalweg. Braudrick *et al.* (1997) conducted flume experiments on log deposition processes for approach flow depths h_o = 0.15…0.30 m, and log lengths L_L = 0.20 m and 0.40 m. For single LW transport, they observed log deposited mainly in the shallowest areas and orientated non-parallel to the flow. Therefore, both transport orientations for LW occur in channels: parallel and non-parallel to the flow.

Two types of LW transport can be defined in rivers: uncongested and congested (Braudrick *et al.*, 1997). For uncongested LW transport, single logs move independently without contact. In contrast, congested LW transport represents a single mass movement of logs, e.g. as a LW carpet. The transport types are related to the dimensionless input rate, i.e. the ratio of the volumetric log input rate to the approach flow discharge Q_{LW}/Q_o. For increasing Q_{LW}/Q_o, congested LW transport is predominant and characteristic for low-order streams. The different observed transport mechanisms are rolling, sliding, and floating (Haga *et al.* 2002).

LW accumulation bodies are initiated and stabilized by a long piece of wood, the so-called “key member” or “key log” (Nakamura and Swanson, 1994). According to Manners *et al.* (2007), an accumulation consists of approximately 45% of key logs, 25% of LW, 15% of logs with d_L = 0.01…0.1 m, and 15% fine material (e.g. branches, leaves, and soil). Therefore, longer logs play a decisive role for the accumulation probability.

Bezzola *et al.* (2002) conducted flume experiments on the LW accumulation probability p_D at a bridge deck (subscript D). The bridge deck geometry was kept constant, while the flume was adjusted to model rectangular and various trapezoidal cross-sections. The approach flow conditions were defined by the approach flow Froude number F_o = 0.3…1.1, and the ratio of the approach flow depth to the bridge clearance height h_o/H_B = 0.5…1.0. The model LW consisted of logs and rootstocks, and was transported both in an uncongested and congested manner. The experiments were repeated three times. Based on their results, p_D is mainly a function of the LW dimensions (length and diameter) in combination with the cross-sectional geometry, whereas the approach flow conditions (h_o/H_B, F_o) are of minor effect. The maximal $p_{D,\max} \approx$ 80...100% was observed for congested LW transport including rootstocks in trapezoidal cross-sections, compared to $p_{D,\max}$ = 30% for a rectangular cross-section. In the case of single rootstocks, $p_{D,\max} \approx$ 50...70% for trapezoidal cross-sections, compared to $p_{D,\max}$ = 25% for a rectangular cross-section. The minimal probability $p_{D,\min} \approx$ 0...20% was observed for uncongested logs. The results for uncongested transport were combined in design equations.

The effect of different bridge deck types on p_D for uncongested transport was studied by Schmocker and Hager (2011) for approach flow conditions h_o/H_B = 0.9, 1.0, 1.07 and F_o = 0.3…1.2, and model LW consisting of single logs and rootstocks. One test run consisted of N = 8 repetitions. Increasing accumulation probability was observed for increasing log dimensions, decreasing F_o, and decreasing freeboard $(1–(h_o/H_B))$. Given a plain bridge deck without railings, for single logs, and for h_o/H_B = 0.9, p_D was always zero, whereas p_D = 30...100% for h_o/H_B = 1.07. Bridge decks with a truss or railings resulted in higher p_D. Design equations for p_D were defined for single logs and single rootstocks.

The LW accumulation probability at bridge decks including a circular bridge pier was investigated by Gschnitzer *et al.* (2013). Similar to previous studies, their findings indicate an increasing p_D for increasing log length, congested transport, logs with branches, and increasing h_o. The results of Gschnitzer *et al.* (2013) were not summarized in a design equation.

The LW accumulation probability p_P at a single bridge pier (subscript P) was tested by Lyn *et al.* (2003) for various approach flow conditions (h_o, F_o, and approach flow velocity v_o). The model LW consisted of logs with and without branches. Within one test run, 70 single logs were inserted 6 m upstream of the bridge pier in random orientation. The tests were repeated 50 times to improve statistical significance. In contrast to Schmocker and Hager (2011), no governing effect of F_o was found, but p_P increased with decreasing v_o and h_o. If more than six logs with branches accumulated, the branches improved the interrelation between the single logs, thereby increasing the accumulation stability. These accumulations, therefore, attached better to bridge piers, resulting in higher p_P compared to accumulations of logs without branches, which tend to resolve.

De Cicco *et al.* (2016) studied the influence of different bridge pier shapes on p_P. Flume experiments were conducted for uniform logs, steady flow conditions (F_o = 0.3 and 0.5), congested LW transport, and a fixed channel bed. To model congested LW transport, 25 logs with various lengths were inserted randomly ~3 m upstream of the bridge pier. The tests were repeated ten times. The results are contrary to previous studies, as p_P increased with increasing F_o for all tested pier shapes. For F_o = 0.5, the maximum $p_{P,\max}$ = 90%

was observed for a squared pier. In contrast, a trapezoidal pier exhibited $p_{P,\max}$ = 40% for F_o= 0.3. Given an ogival pier, p_P was zero for all tested F_o.

3 OBJECTIVES

The knowledge on LW accumulation probability is still limited and the results are partially contradictory (Table 1). In addition, the required test repetitions *N* to obtain statistically significant accumulation probabilities *p* were defined from *N* = 3…50. The existing design equations for *p* are only valid for bridge decks. Systematic studies on the accumulation probability at bridge piers p_P exist, however, the results are not parameterized. Given the hazard potential of transported LW during flood events, further research on the accumulation process is required. This study is part of the interdisciplinary research project *WoodFlow* on LW management in rivers – a practice oriented research project in Switzerland (Ruiz-Villanueva *et al.*, 2016b). The main objectives of this study are to analyze the LW accumulation probability as a function of (1) the approach flow conditions, (2) the bridge pier roughness, and (3) the LW characteristics, involving various log lengths, LW with and without branches, and uncongested versus congested LW transport. A novel design equation is presented to assess the accumulation probability p_P for uncongested LW transport.

Table 1. Governing parameters on LW accumulation probability determined in past studies.

Type	*Reference*	Approach flow Froude number F_o	Approach flow depth h_o	Approach flow velocity v_o	LW dimensions	LW with branches	Congested LW transport	Cross-section / pier geometry	Number of repetitions *N*
Bridge deck	Bezzola *et al.*, 2002				X		X	X	3
	Schmocker and Hager, 2011	X	X		X				8
Bridge pier	Gschnitzer *et al.*, 2013		X		X	X	X		8
	Lyn *et al.*, 2003		X	X		X	X		50
	De Cicco *et al.*, 2016	X						X	10

4 EXPERIMENTAL SETUP

The experiments were conducted in a 10.7 m long, 1.0 m wide, and 0.8 m deep tilting flume at the Laboratory of Hydraulics, Hydrology and Glaciology (VAW) of ETH Zurich (Figure 2a). The 2.0 m long intake is equipped with a flow straightener to generate undisturbed inflow. The channel has a fixed bed ($k_{St\_Prototype}$ ≈ 30 $m^{1/3}$/s) and side walls made of glass and PVC. The inflow discharge Q_o was measured with an electromagnetic flow meter and regulated with a valve to a maximum of 265 l/s. The channel slope can be varied between $0 \le S_o \le 15\%$. The approach flow conditions (subscript *o*) were regulated by adapting the S_o, Q_o, and a downstream flap gate. They are characterized by h_o, $v_o = Q_o/(Bh_o)$, and $\mathsf{F}_o = v_o/(gh_o)^{1/2}$, with B = channel width, and g = gravitational acceleration (Figure 2b). An Ultrasonic Distance Sensor (UDS) was used to measure h_o with an accuracy of ±1 mm. To avoid viscosity and surface tension effects, Reynolds number $\mathsf{R} = v_o \cdot 4R_h/\nu > 10^4$ (Hughes, 2005) and $h_o \ge 0.05$ m (Heller, 2011) were selected, respectively, where $R_h = Bh_o/(B+2h_o)$ = hydraulic radius, and ν = kinematic viscosity of water. The flow is in the rough turbulent regime for $\mathsf{R} > 10^4$; therefore, the viscous force is independent of R (Hughes, 2005). The tests were performed according to Froude similitude with a model scale of $\lambda \approx 20$. A single circular bridge pier with a diameter d_P = 0.05 m was placed 5 m downstream of the inlet in the channel centerline. For the majority of the experiments, the material of the bridge pier was aluminum (i.e. smooth bridge pier). F_o varied between 0.2, 0.5, 0.8, and 1.2 to model common flow conditions during flood events ranging from subcritical to over-transcritical flow. For a selected range of approach flow conditions, the effects of a rough bridge pier, LW with branches, and congested LW transport on p_P were tested.

4.1 Model large wood

The model LW consisted of natural wood logs with and without branches. The log lengths varied between L_L = 0.10 m, 0.20 m, and 0.40 m, corresponding to ratios d_P/L_L = 0.50, 0.25, and 0.125. The log diameter d_L = 0.015 m was kept constant and the branches were 0.04…0.05 m long and 0.004 m thick. Two different types of logs with branches were used for the experiments: The "2D" type corresponds to logs with alternate branches on two sides, whereas the "3D" type has alternate branches on four sides (Figure 2c). The model LW was not watered and always fully floating during tests. Hence, the transported logs did not interact with the channel bed. The tensile strength and the elasticity of the model LW were overestimated due to the usage of natural wood. In nature, transported logs may break when hitting the bridge pier, thereby decreasing the accumulation probability. This was not observed during the experiments.

  / ISSN 1562-6865 (Online) - ISSN 1063-7710 (Print)

4.2 Test program and procedure

The LW accumulation probability was examined within five test series (Table 2). To model the worst-case scenario of p_P, all logs were added non-parallel to the flow 1 m upstream of the bridge pier. Given the experimental randomness, the required repetitions to obtain statistically significant accumulation probabilities were studied in test A1. The reproducibility was evaluated by repeating four tests twice (A2-A9). Test series B studied the effects of the approach flow conditions and L_L on p_P (B1-B38). Various combinations of v_o and h_o were investigated for each value of F_o = 0.2, 0.5, 0.8, and 1.2. For subcritical flow (B1-B35), L_L was varied to 0.10 m, 0.20 m, and 0.40 m, whereas for over-transcritical flow (B36-B38), L_L was kept constant to 0.20 m. In test series C-E, the experiments were conducted for selected approach flow conditions. The bridge pier roughness was increased to model concrete material (i.e. rough bridge pier), with an equivalent sand roughness of $k_{s\_Prototype} \approx 3$ mm (C1-C4). The effect of branches was studied using two different types of logs with branches (D1-D7). Test series E focused on the impact of congested LW transport on p_P (E1-E11). For these experiments, a bulk of 3 or 5 logs was added simultaneously to the flow 1 m upstream of the bridge pier. The test program comprises of a total of 3,160 individual test runs and 4,360 added logs.

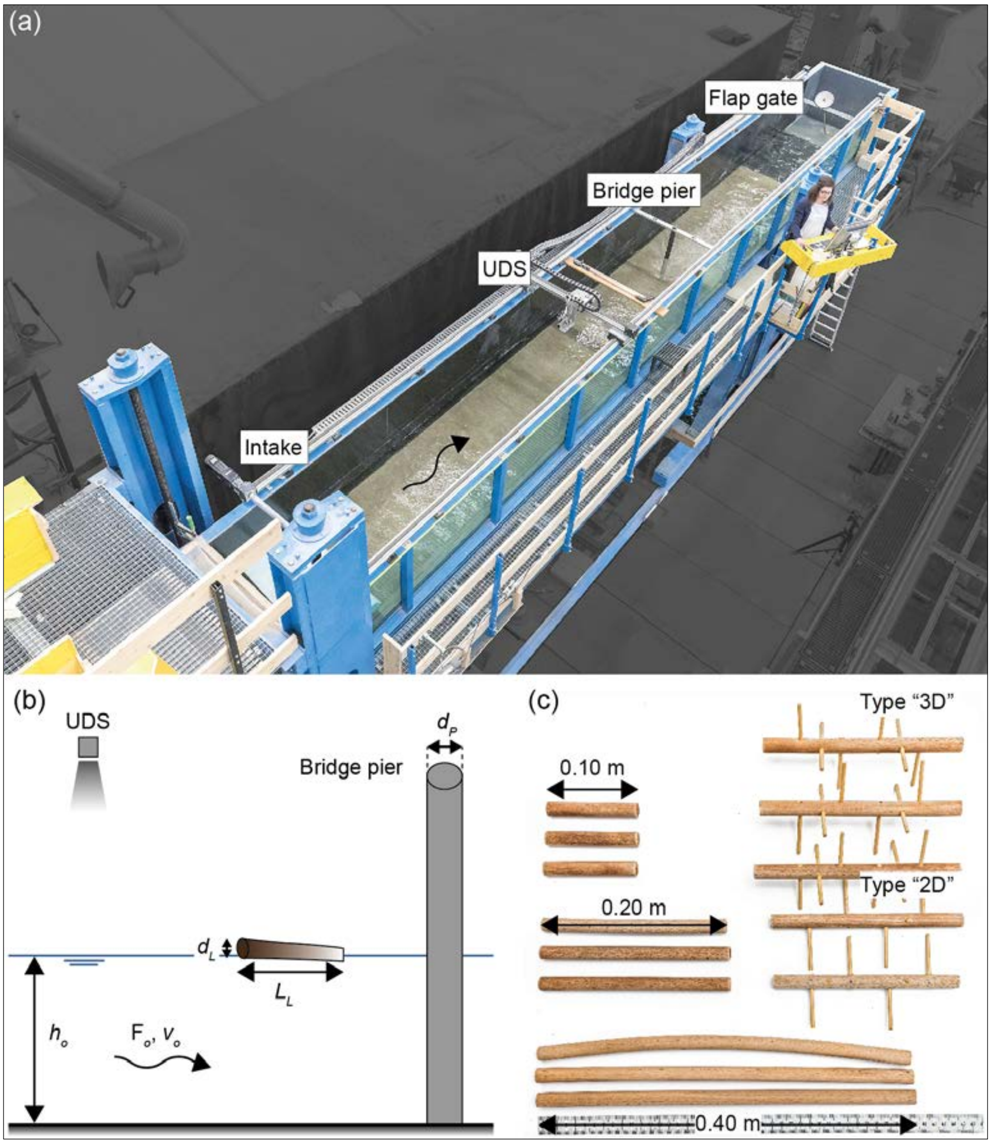

Figure 2. (a) VAW model flume, (b) experimental setup with notation, and (c) model LW.

5 EXPERIMENTAL RESULTS AND DISCUSSION

5.1 Test repetitions and reproducibility

To obtain statistically significant results for the LW accumulation probability p, the required number of test repetitions N is essential. In previous studies, N was defined in a wide range (N = 3…50, Table 1), without quantifying the standard deviation σ of p. For the current study, the required N_{req} was investigated in test run

A1 (Table 2). A single log with L_L = 0.20 m was inserted into the flume N = 300 times for F_o = 0.2, h_o = 0.15 m, and v_o = 0.24 m/s. Figure 3a shows p_P and the corresponding σ as a function of N. The standard deviation σ increases to a maximum of $\sigma \approx 0.20$ for N = 6, and decreases to σ = 0.05 for N = 300. The accumulation probability p_P depends on the corresponding N and varied between 0% and 50%, converging to p_P = 34% for N = 300. To guarantee statistically significant results, a maximum standard deviation of σ = 0.10 was defined. This results in test repetitions of N = 40, which is just reasonable regarding test effort. Selected tests were repeated N = 60, if $\sigma \geq 0.10$ for N = 40. The test reproducibility was investigated with various L_L for four approach flow conditions (A2-A9). In Figure 3b, p_P is plotted as a function of N for tests A6-A7, and B26. All three tests converged to a final value $p_P \approx 25\%$ with σ = 1%. Test reproducibility was consequently confirmed. Note that if N is selected to $N \leq 20$, a value used in previous studies, the accumulation probability would range between 0% and 67%.

Table 2. Test program.

Tests	Tested effect	F_o [-]	h_o [m]	v_o [m/s]	R [-]	L_L [m]	Type of LW (Fig. 2c)	N [-]	Pier type
A1	N_{req}	0.2	0.15	0.24	85,310	0.20	Regular (Reg.)	300	s
A2-3		0.2	0.05	0.14	19,830	0.10		40	
A4-5	Reproducibility	0.5	0.05	0.35	48,618	0.20	Reg.	40	s
A6-7		0.8	0.05	0.55	77,601	0.40		40	
A8-9		0.2	0.20	0.28	120,525	0.20		40	
B1-3			0.05	0.14	19,830	0.10, 0.20, 0.40		40	
B4-6		0.2	0.10	0.20	50,310	0.10, 0.20, 0.40		40	
B7-8			0.15	0.24	85,310	0.10, 0.20[a], 0.40		40	
B9-11			0.20	0.28	120,525	0.10, 0.20, 0.40		40	
B12-14			0.05	0.35	48,618	0.10, 0.20, 0.40		40	
B15-17		0.5	0.10	0.48	125,543	0.10, 0.20, 0.40		40	
B18-20	Approach flow conditions and log lengths		0.15	0.60	211,826	0.10, 0.20, 0.40		40	
B21-23			0.20	0.69	302,745	0.10, 0.20, 0.40	Reg.	40	s
B24-26			0.05	0.55	77,601	0.10, 0.20, 0.40		40	
B27-29		0.8	0.10	0.80	200,541	0.10, 0.20, 0.40		40	
B30-32			0.15	0.96	339,991	0.10, 0.20, 0.40		40	
B33-35			0.20	1.10	302,745	0.10, 0.20, 0.40		40	
B36			0.05	0.84	116,519			40	
B37		1.2	0.10	1.19	300,566	0.20		40	
B38			0.15	1.46	512,364			20[b]	
C1			0.05	0.35	48,618			40	
C2	Pier roughness	0.5	0.10	0.48	125,543	0.20	Reg.	40	r
C3			0.15	0.60	211,826			40	
C4			0.20	0.69	302,745			40	
D1			0.05	0.35	48,618		2D	60	
D2-3	Branches	0.5	0.10	0.48	125,543	0.20		60	s
D4-5			0.15	0.60	211,826		2D, 3D	60	
D6-7			0.20	0.69	302,745			60	
E1-2			0.05	0.35	48,618		3xReg., 5xReg.	40	
E3-5	Congested LW transport	0.5	0.10	0.48	125,543	0.20		40	s
E6-8			0.15	0.60	211,826		3xReg., 5xReg., 3x3D	40	
E9-11			0.20	0.69	302,745			40	

Note: R = Reynolds number ≈ 19,800…512,400 > 10^4,
N_{req} = required repetitions,
s = smooth bridge pier,
r = rough bridge pier,
[a]… corresponds to Test A1, and
[b]… test run stopped after N = 20, as p = 0% for N = 1…20.

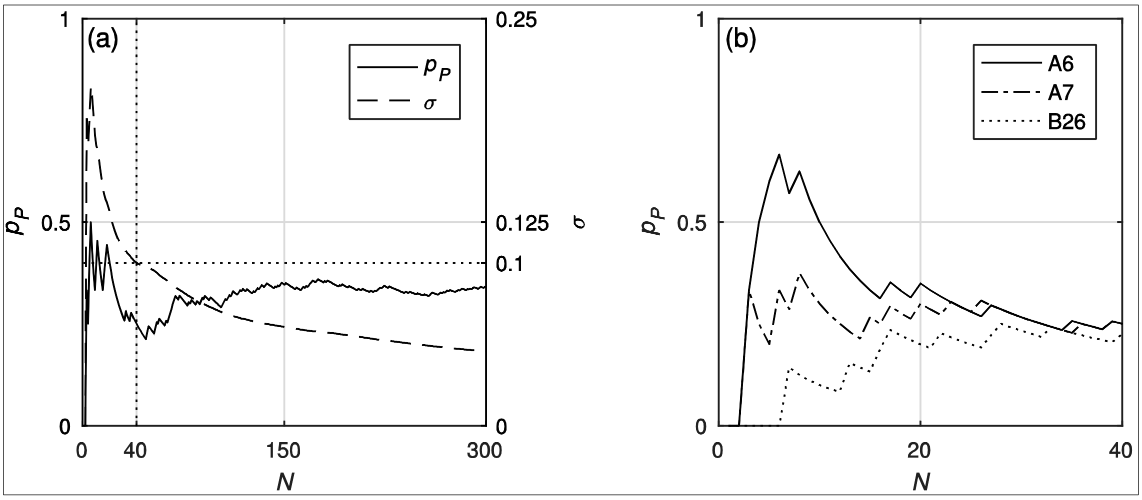

Figure 3. Test results of (a) p_P and σ as a function of N for test A1, (b) p_P as a function of N for reproducibility tests A6, A7, and B26.

5.2 Approach flow conditions and log length

Figure 4a shows p_P as a function of v_o for all tested L_L, and F_o = 0.2 = const. (B1-B11, A1). The accumulation probability for v_o = 0.14 m/s was p_P = 22% (L_L = 0.10 m), 43% (L_L = 0.20 m), and 65% (L_L = 0.40 m), demonstrating a governing effect of the log length. A longer log is more probable to contact the bridge pier compared to shorter logs, resulting in higher p_P for increasing L_L (Figure 5).

For constant F_o, p_P was decreasing with increasing v_o for all tested L_L (Figure 4a). The tests B12-B38, corresponding to constant F_o = 0.5, 0.8, and 1.2, confirmed this trend. For small v_o, logs tended to accumulate as soon as any of their parts touch the bridge pier. In contrast, logs transported with high v_o may touch the bridge pier, but resolve due to the increased turbulence, waves, and impact force. Based on test series B, the LW accumulation probability is $p_P \leq$ 15% for a threshold value of $v_o \geq$ 0.80 m/s.

In Figure 4b, p_P is plotted versus h_o, for L_L = 0.10 m, 0.20 m, and 0.40 m, and $v_o \approx$ 0.30 m/s (A1, B7-B14). The accumulation probability p_P was constant for various h_o. If logs are transported fully floating, they do not interact with the channel bottom. Hence, the effect of h_o on p_P is negligible for a given velocity and log length. As described above, a major effect of the log length on p_P is observed.

In summary, the accumulation probability increases with increasing log length and decreasing approach flow velocity, whereas no effect of the approach flow depth was observed. A constant approach flow Froude number resulted in a large range of accumulation probabilities for a given log length (p_P = 20…43% for L_L = 0.20 m; Figure 4a). Consequently, no governing effect of the approach flow Froude number on the accumulation probability can be concluded, and the approach flow velocity must be used as the decisive parameter for the design equation (Section 5.4).

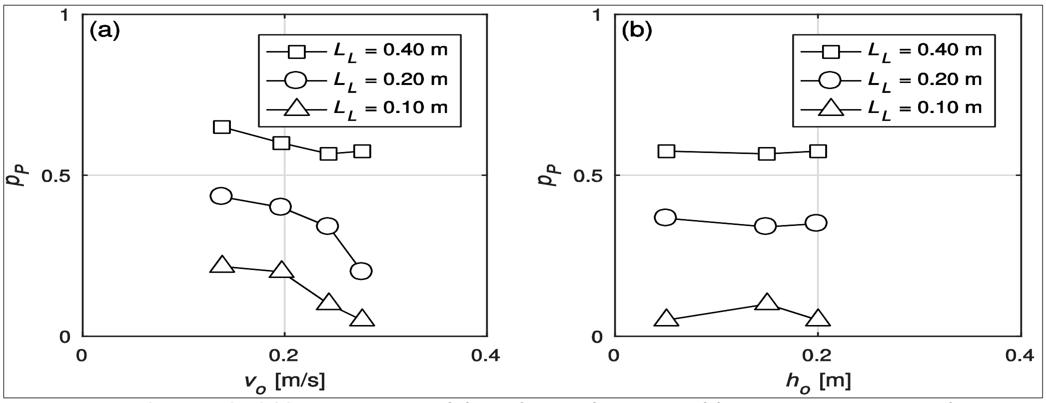

Figure 4. Accumulation probability p_P versus (a) v_o for various L_L with F_o = 0.2 = const. (B1-B11, A1), and (b) h_o for various L_L with $v_o \approx$ 0.30 m/s (A1, B7-B14).

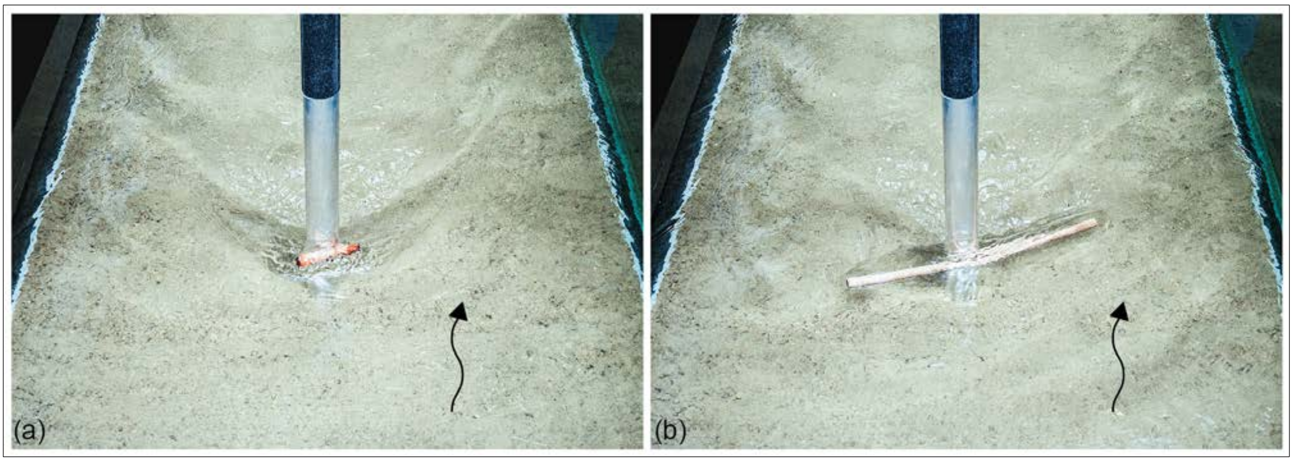

Figure 5. Plan view of LW accumulation with (a) L_L = 0.10 m (Test B18), and (b) L_L = 0.40 m (Test B20).

5.3 Bridge pier roughness and LW characteristics

In Figure 6a-c, p_P is plotted versus v_o for L_L = 0.20 m, and F_o = 0.5 = const. Similar to Figure 4a, p_P was decreasing with increasing v_o for constant F_o, and for all tested bridge pier and LW characteristics. Therefore, a governing effect of v_o on p_P can be deduced, whereas various p_P result for the same F_o.

The effect of a smooth versus a rough bridge pier on p_P is shown in Figure 6a (Test series B vs. C1-C4). For all tested v_o, p_P was slightly higher for the rough bridge pier. However, the difference between smooth and rough pier was 5...10%, and consequently within the range of test reproducibility. Therefore, the tested bridge pier roughness in the present model has no governing effect on p_P.

The influence of uncongested LW with and without branches on p_P is shown in Figure 6b. Regular logs are compared with the two log types with branches (2D and 3D; Test series B vs. D1-D7). No experiments with alternate branches of the type 3D were conducted for v_o < 0.50 m/s (h_o < 0.10 m), since the branches touched the channel bed and were not fully floating. For v_o = 0.50…0.60 m/s, p_P was 5% to 10% higher for LW with branches (2D and 3D) compared to regular logs, whereas p_P was 5% lower for v_o = 0.35 m/s. Again, the differences were within the range of test reproducibility. Similar to the findings of Lyn *et al.* (2003), the effect of branches on p_P is negligible for uncongested LW transport.

Figure 6c compares p_P of uncongested with congested LW transport for the addition of 3 or 5 regular logs, as well as for 3 logs with 3D branches (Test series B vs. E1-E11). For all v_o, p_P was 15% to 40% higher for congested LW transport compared to uncongested. Due to the branches, the interrelations between the single logs improve, leading to an increased stability of the accumulation body, as described in Section 2 (Figure 7). Therefore, the 3 logs with 3D branches result in the highest p_P for all v_o.

In summary, the accumulation probability increases with congested LW transport, whereas only a minor effect of the bridge pier roughness and LW branches for uncongested LW transport was observed.

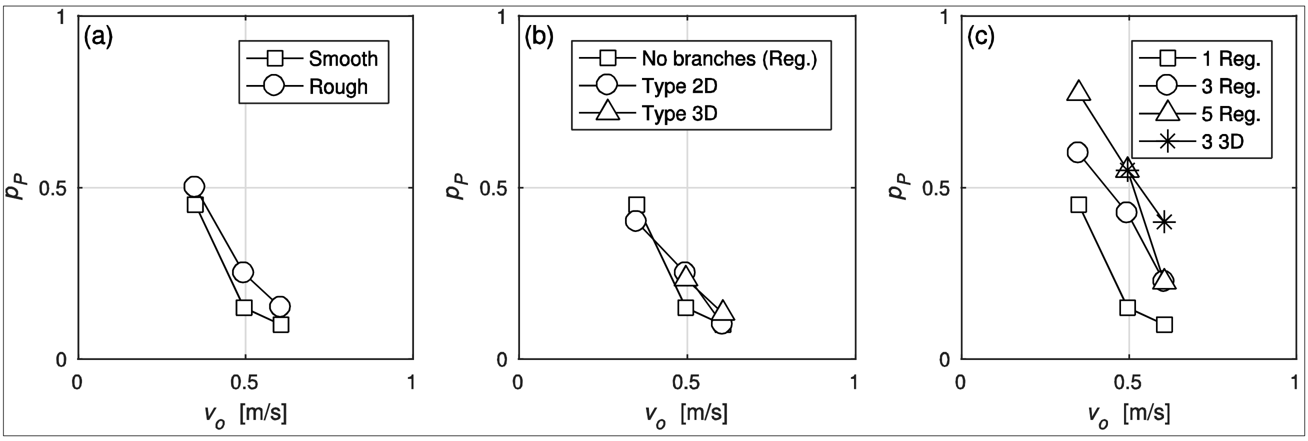

Figure 6. Accumulation probability p_P versus v_o, for (a) smooth versus rough bridge pier (Test series B vs. C1-C4), (b) logs with versus without branches (Test series B vs. D1-D7), and (c) uncongested versus congested LW transport (Test series B vs. E1-E11).

Figure 7. (a) Side view of LW accumulation with a rough bridge pier (Test C3), and (b) plan view of LW accumulation for congested logs with 3D branches (Test E8).

5.4 Normalized accumulation probability for uncongested LW transport

The two governing parameters for p_P of uncongested LW transport were identified as v_o and L_L, or the ratio d_P/L_L, respectively. In addition, these parameters were confirmed with a dimensional analysis. The p_P can therefore be described by the normalized LW accumulation probability parameter

$$LW_P = \left(\frac{v_o^{\,2}}{2gL_L}\right)^{0.60}\left(\frac{d_P}{L_L}\right)^{0.75}. \qquad [1]$$

According to Eq. [1], L_L exhibits the largest effect on p_P, with an exponent of −1.35, followed by v_o with an exponent of 1.20. For the present test range (Test series A and B, Table 2), the LW accumulation probability for single logs at a single bridge pier can be described by the following relationship for $0 \le LW_P \le 0.45$ ($R^2 = 0.81$):

$$p_P = e^{-36\,LW_P}. \qquad [2]$$

Figure 8 shows p_P as a function of LW_p for uncongested LW transport, and Eq. [2]. The Root Mean Squared Error (RMSE) of Eq. [2] is 0.09. As the experimental setup represents a worst-case scenario for p_P (non-parallel log placement directly upstream of bridge pier), the application of Eq. [2] is considered a conservative estimation. The maximum accumulation probability $p_{P,\max} = 65\%$ results for $v_o = 0.14$ m/s, $L_L = 0.40$ m, and $LW_P = 0.006$. For $v_o \ge 1.0$ and $LW_P \ge 0.125$, p_P tends to zero.

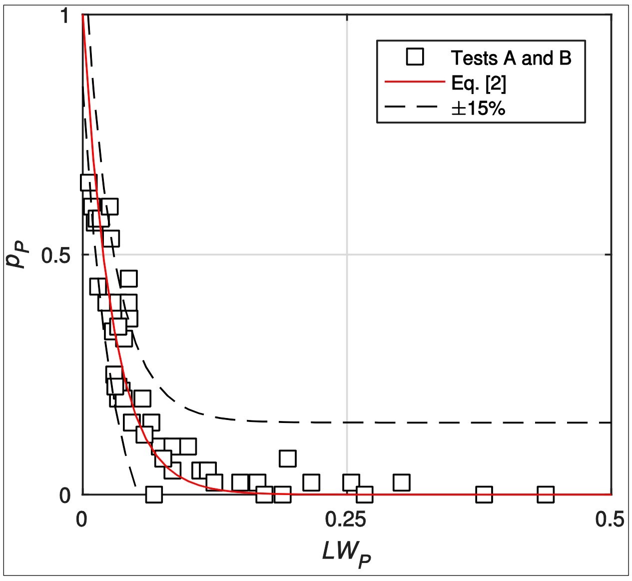

Figure 8. Normalized LW accumulation probability at a single bridge pier for Test series A and B, Eq. [2] (red line), and ±15% (– – line).

6 CONCLUSIONS

A series of flume experiments were conducted to evaluate the LW accumulation probability at a single bridge pier. The physical experiments involved flow conditions typical for flood events, various LW and bridge pier characteristics, and uncongested versus congested LW transport. As a first step, the required number of repetitions to obtain statistically significant accumulation probabilities was defined to $N \geq 40$. Test reproducibility was successfully demonstrated for various flow conditions.

The LW accumulation probability increased with increasing log length, decreasing approach flow velocity, and for congested LW transport. The approach flow Froude number and flow depth generally had a negligible effect on the accumulation probability. For uncongested LW transport, the bridge pier roughness and logs with branches indicated a minor effect on the accumulation probability. The results for uncongested LW transport were summarized in a novel design equation to estimate the accumulation probability at a single bridge pier. Hence, the results of this study are a first relevant step to improve the hazard evaluation of a catchment area. The estimation of the LW accumulation probability is essential for the identification of critical bridge cross-sections prior to a flood event. In addition, the physical experiments on LW accumulation probability with a single bridge pier can be useful to validate numerical models (e.g. Ruiz-Villanueva *et al.*, 2014). As a next step, experiments will be conducted to investigate the effect of multiple bridge piers and a moveable river bed on the LW accumulation probability.

7 OUTLOOK: FIELD TESTS

To validate the experimental results and to ensure their applicability under prototype conditions, field tests (subscript F) will be conducted in cooperation with the Zurich Office of Waste, Water, Energy, and Air (WWEA) in spring 2017. The objective is to compare the results of the field tests with the scale model tests on accumulation probability for uncongested LW transport at a single bridge pier. According to the hydrological estimations, adequate approach flow conditions are expected between April and May 2017. Based on the required cross-section and approach flow conditions, the River Glatt in Zurich, Switzerland, was selected as a suitable location (Figure 9). During these field tests, 60-80 logs with L_L = 3…5 m and d_L = 0.15…0.20 m will be added ≈20 m upstream of the circular bridge pier ($d_{P,F} \approx$ 1.0…1.5 m) non-parallel to the flow. The approach flow conditions vary between $v_{F,\max} \approx$ 1.3…1.5 m/s, and $h_{F,\max} \approx$ 1.0…1.5 m. The surface flow field will be measured using airborne velocimetry. The logs will be removed from the river ≈250 m downstream of the bridge pier with an excavator. Given the limited numbers of investigations on LW accumulation probability at a bridge pier, these field tests are essential to improve the general process understanding. The field experiments will improve the current design equation and give insights on possible scale or model effects.

Figure 9. (a) Plan and (b) side view of the field test site at the River Glatt in Zurich (Switzerland) to study LW accumulation probability at a single bridge pier.

ACKNOWLEDGMENTS

The author was financially supported by the Swiss Federal Office for the Environment (FOEN) within the WoodFlow project, grant 15.0018.PJ / O192-0202. Special thanks go to Dr. L. Schmocker, Dr. V. Weitbrecht, and Prof. Dr. R.M. Boes for the valuable comments and continuous support.

REFERENCES

Bezzola, G.R., Gantenbein, S., Hollenstein, R. & Minor, H.-E. (2002). Verklausung von Brückenquerschnitten (Blocking of Bridge Cross-Sections). *Proceeding International Symposium "Moderne Methoden und Konzepte im Wasserbau",* VAW-Report 175, Ed. H.E. Minor, ETH Zurich, Switzerland, 87-97. (In German).

Braudrick, C.A., Grant, G.E., Ishikawa, Y. & Ikeda, H. (1997). Dynamics of Wood Transport in Streams: A Flume Experiment. *Earth Surf. Process. Landforms*, 22(7), 669-683.

Braudrick, C.A. & Grant, G.E. (2001). Transport and Deposition of Large Woody Debris in Streams: A Flume Experiment. *Geomorphology*, 41(4), 263-283.

De Cicco, P.N., Paris, E. & Solari, L. (2016). Wood Accumulation at Bridges: Laboratory Experiments on the Effect of Pier Shape. *Proceeding of 8th River Flow Congress, Constantinescu, Garcia & Hanes (Eds.)*, St. Louis, USA, 2341-2345.

Gschnitzer, T., Gems, B., Aufleger, M., Mazzorana, B. & Comiti, F. (2013). Physical Scale Model Test on Bridge Clogging. *Proceeding of 35th IAHR World Congress,* Chengdu, Beijing.

Haga, H., Kumagai, T., Otsuki, K. & Ogawa, S. (2002). Transport and Retention of Coarse Woody Debris in Mountain Streams: An in Situ Field Experiment of Log Transport and a Field Survey of Coarse Woody Debris Distribution. *Water Resources Research*, 38(8), 1029-1044.

Heller, V. (2011). Scale Effects in Physical Hydraulic Engineering Models. *Journal of Hydraulic Research*, 49(3), 293-306.

Hughes, S.A. (2005). *Physical Models and Laboratory Techniques in Coastal Engineering*. Advanced series on ocean engineering 7, World Scientific, Singapore, 1-568.

Keller, E.A. & Swanson, F.J. (1979). Effects of Large Organic Material on Channel Form and Fluvial Processes. *Earth Surface Processes Landforms*, 4(4), 361-380.

Lyn, D.A., Cooper, T., Yi, Y.K., Sinha, R. & Rao, A.R. (2003). *Debris Accumulation at Bridge Crossings: Laboratory and Field Studies*. Report No.: FHWA/IN/JTRP-2003/10, Joint Transportation Research Program, Purdue University, West Lafayette, IN, USA, 48.

Manners, R.B., Doyle, M.W. & Small M.J. (2007). Structure and Hydraulics of Natural Woody Debris Jams. *Water Resources Research*, 43(6), 1-17.

Nakamura, F. & Swanson, F.J. (1994). Distribution of Coarse Woody Debris in a Mountain Stream, Western Cascade Range, Oregon. *Canadian Journal 0f Forest Research*, 24(12), 2395-2403.

Ruiz-Villanueva, V., Bladé-Castellet, E., Sánchez-Juny, M., Díez-Herrero, A. & Bodoque, J.M. (2014). Two-Dimensional Numerical Modeling of Wood Transport. *Journal of Hydroinformatics*, 16(5), 1077-1096.

Ruiz-Villanueva, V., Piégay, H., Gurnell, A., Marston, R.A. & Stoffel, M. (2016a). Recent Advances Quantifying the Large Wood Dynamics in River Basins: New Methods and Remaining Challenges. *Review of Geophysics*, 54(3), 611-652.

Ruiz-Villanueva, V., Badoux, A., Boes, R.M., Rickenmann, D., Rickli, C., Schalko, I., Schmocker, L., Schwarz, M., Steeb, N., Stoffel, M. & Weitbrecht, V. (2016b). Large Wood Research in Swiss Watercourses. *Proceeding of 8th River Flow Congress*, Constantinescu, Garcia & Hanes (Eds.), St. Louis, USA, 2307-2312.

Schmocker, L. & Hager, W.H. (2011). Probability of Drift Blockage at Bridge Decks. *Journal of Hydraulic Engineering*, 137(4), 480-492.

Wohl, E. & Jaeger, K. (2009). A Conceptual Model for the Longitudinal Distribution of Wood in Mountain Streams. *Earth Surf. Process. Landforms*, 34(3), 329-344.

Wohl, E., Bledsoe, B.P., Fausch, K.D., Kramer, N., Bestgen, K.R. & Gooseff, M.N. (2016). Management of Large Wood in Streams: An Overview and Proposed Framework for Hazard Evaluation. *Journal of the American Water Resources Association (JAWRA)*, 52(2), 315-335.

Proceedings of the 37th IAHR World Congress
August 13 – 18, 2017, Kuala Lumpur, Malaysia

A FLOOD ANALYSIS MODEL FOR RIVERS IN LOW-LAYING AREAS THAT INTEGRATES INLAND WATER AND BACK WATER

TAKEHIRO OKI(1) & MAKOTO NAKATSUGAWA(2)

(1) Research Department, Hokuden General Design & Consulting Co., Inc, Sapporo, Japan
oki-take@hokuss.co.jp
(2) College of Environmental Technology, Muroran Institute of Technology, Muroran, Japan
mnakatsu@mmm.muroran-it.ac.jp

ABSTRACT

The catchment basin of the Chitose River in the Ishikari River system, which is the basin under study, is on Japan's northern island of Hokkaido. Several typhoons approach the area in summer and fall, and these frequently cause damage from river flooding. A heavy rainfall occurred around Lake Shikotsu, at the upper reaches of the Chitose River, in September 2014. At the time of this heavy rainfall, an unprecedented evacuation advisory was issued to about 0.9 million of the citizens of Sapporo. After the September 2014 flood, the authors concluded that real-time flooding and inundation predictions for localized rainfall and the largest-scale torrential rainfall, evacuation, and preparedness for operation of river management facilities (dams, retarding ponds, and drainage pump stations) were the most pressing needs for the administration and citizens. This study aims to serve as basic research for clarifying the influence of climate change and heavy rainfall, toward proposing a flood analysis model that is able to reproduce the large-scale inundation damages of the past and verifying the reproducibility of that model.

Keywords: iRIC SRM; back water; landside water; unsteady flow; flood analysis.

1 INTRODUCTION

Extreme weather phenomena such as unusually high temperatures and heavy precipitation events have been increasing in recent years. Local downpours caused by linear rain bands have resulted in landslide disasters and embankment collapses. Since rainfall intensity is expected to increase due to global warming (IPCC, 2013), experts note the need for measures to adapt to extreme weather events.

In this study, the basin of the Chitose River (Figure 1), a tributary of the Ishikari River, is used as an example for simulation. In the area around Lake Shikotsu, which is at the upper reaches of the Chitose River, a linear rain band caused heavy rain in September 2014 and an evacuation advisory was issued to 0.9 million Sapporo citizens (Hokkaido Regional Development Bureau, 2014). That event made the authors of this paper consider it urgently necessary to be able to forecast flooding and inundation on a real-time basis during localized torrential rain and extraordinarily heavy rain so that the administration and citizens are well-prepared for evacuation and so that river management facilities can be properly operated. A study by Saeki et al. (2013) regarding similar issues forecast inundation due to large-scale flooding of the Ishikari River. Based on the forecast, these authors pointed out the need for the local authorities to understand the consequences of inundation due to interior runoff or flooding that is larger in scale than flooding against which safety measures are secured. The National Institute for Land and Infrastructure Management (NILIM) developed the NILIM model (Nakamura et al., 2004), an inundation forecasting model that takes sewerage pipes and pumps into account in simulating complex hydraulic phenomena. This model has helped to reduce damage caused by inundation due to interior runoff in urban areas.

The study reported below is characterized by a flood analysis model that the authors developed by integrating inundation due to interior runoff and river flooding in large river basins in low-lying areas. This model takes into consideration overflows of tributaries and navigable/drainage canals caused by backwater effects as well as the operation of sluices and drainage pump stations.

In developing the flood analysis model, the following river characteristics were taken into account.

(a) The Chitose River is a gently sloping river that flows through low-lying areas. As shown in Figure 1, three tributaries (the Wattsu, Old Yubari and Shimamatsu tributaries) flow into the Chitose River at a 3.0-km section at the river's middle reaches. The differences in ground elevation between the river and its tributaries are not easily determined in this section. Thus, a lumped runoff model was used for runoff analysis. Data on the basin area were divided and expressed in units of 10^1-10^2 km^2. These data and the average rainfall over the entire basin area were input into a one-cascade storage routing model in order to calculate the runoff volume of each river/tributary/canal.

  / ISSN 1562-6865 (Online) - ISSN 1063-7710 (Print)

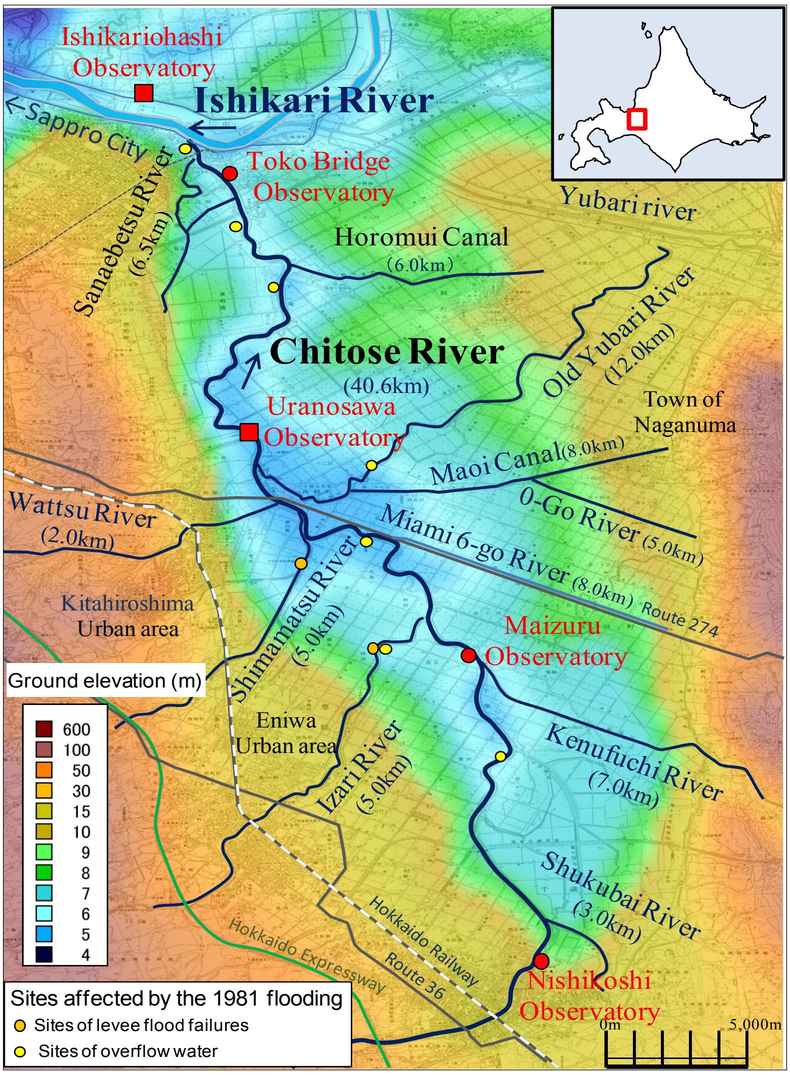

Figure 1. Topographic map of the Chitose River Basin.

(b) The Chitose River is affected for an extended time by backwater from the Ishikari River. The backwater eventually affects tributaries of the Chitose River and navigable/drainage canals connected to those tributaries. For this reason, the authors developed a flood analysis model in which inundation due to interior runoff and river flooding are integrated by taking into consideration levee failures and overflows of tributaries caused by backwater effects. The flood analysis model was verified by simulating a major flood that took place on the Ishikari River in 1981. Figure 2 is a photo showing the 1981 August flood. The downstream water level of the main stream of Ishikari River rose and its backwater caused the water levels of the Chitose and its tributaries to rise, which in turn caused flooding.

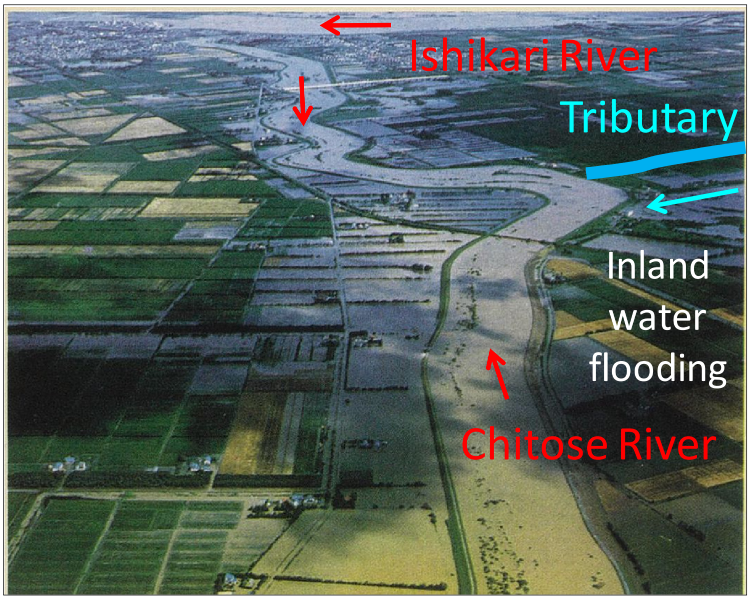

Figure 2. The flood of August 1981.
(Source: The Base of Development and Flood Control of Hokkaido, 1992,
The Ishikari River Development Foundation).

2 THE RESEARCHED BASIN

2.1 The river basin under study

The Chitose River, which flows from Lake Shikotsu, is a tributary of the Ishikari River. Having a channel length of 108 km and a basin area of 1,244 km^2, the Chitose River is as large as a Class A river system. Class A rivers are large major rivers that are administered by the national government. There are four cities (Ebetsu, Chitose, Eniwa and Kitahiroshima) and two towns (Naganuma and Namporo) in the river basin, and these municipalities have a combined population of 367,000. Key industries in this area include rice farming, upland cropping and food processing. Parts of New Chitose Airport are in the basin area. The Hokkaido Expressway, Route 36 and Route 274, which are the three important routes for transporting cargo from New Chitose Airport and Tomakomai Port, pass through the basin area. Route 274, connecting the City of Sapporo to eastern Hokkaido, runs close to the Chitose River and crosses the river at one point. Flooding in the river basin can disrupt the supply of goods via Route 274.

2.2 Flooding damage and factors

The Chitose River basin has a higher mean annual precipitation (about 1,500 mm/year) than the Ishikari River basin (1,300 mm/year). In August 1981, a stationary front over the central part of Hokkaido and Typhoon No. 12 caused heavy rain that continued from August 3 through 6, and massive flooding occurred. The estimated discharge based on data recorded at the Uranosawa observation site was 1200 m^3/s. Rainfall in the Chitose River basin exceeded 330 mm in three days, making it the heaviest rainfall on record at that time. The water level of the Chitose River rose above the design high-water level, and 192 km^2 of land was inundated and 2,700 houses were flooded.

3 METHODS

3.1 Analysis model

We adopted a flood analysis model that integrates inundation due to interior runoff and river flooding. The model combines three slightly modified existing models (Figure 3). The first model is a one-cascade storage routing model developed by K. Hoshi (2007). It is a rainfall-runoff model that calculates river water levels and flooding areas from runoff estimated from the rainfall. The calculated runoff is the input to calculate the water level of each tributary by giving it to the upstream end of each tributary using the second model, a 1-D unsteady flow calculation model. When the estimated water level exceeds the bank height, flooding occurs and the third model, a 2-D planar unsteady flow model, outputs the flooded area. The estimations of river water level and the flooded area are calculated by these two models developed by the Public Research Institute of Japan.

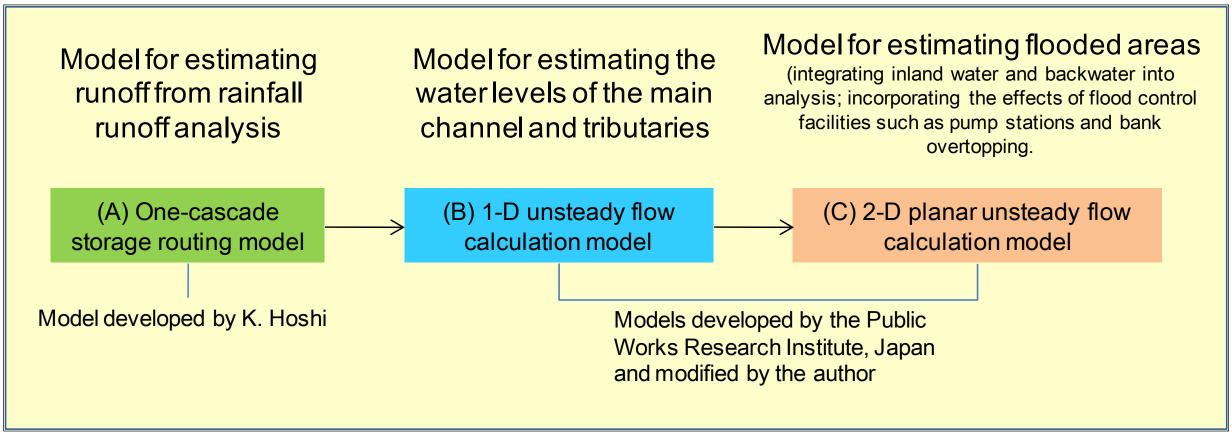

Figure 3. Schematic of the flood analysis model.(runoff analysis + flood routing analysis).

The details of application of these three models are shown in Figure 4. In the first model, runoff analysis was conducted for the area of basin shown "A" or in green in Figure 4. Runoff of the Chitose River and its tributaries was calculated by using a one-cascade storage routing model. In the second model, flood routing in the Chitose River was analyzed by calculating the 1-D unsteady flow for the area shown as "B" or in blue in Figure 4. Flood routing was analyzed for six major tributaries (the Old Yubari, Wattsu, Shimamatsu, Izari, Kembuchi, and Shukubai), other tributaries, and navigable/drainage canals. In this model, the backwater effects of the Chitose River were assumed to be transmitted to these tributaries and canals. In the third model, flood analysis was conducted by calculating 2-D planar unsteady flow for the area shown in "C" or salmon pink in Figure 4. In the flood analysis model, levee failures, as well as overflows of the Chitose River, tributaries and navigable/drainage canals were taken into consideration for the purpose of integrating inundation due to interior runoff and river flooding in low-lying areas. The model also takes into account of major drainage pump stations and road embankments in the floodplain. Considering the future application of the analysis model to the real-time estimation of flooding, we tried to simplify the calculations because calculation speed is important. In future, we plan to propose applications of the model to the comprehensive flood control of a river system, including the operation of dam reservoirs, retarding basins, pump stations and as such, and to develop an evacuation support system to contribute to disaster mitigation.

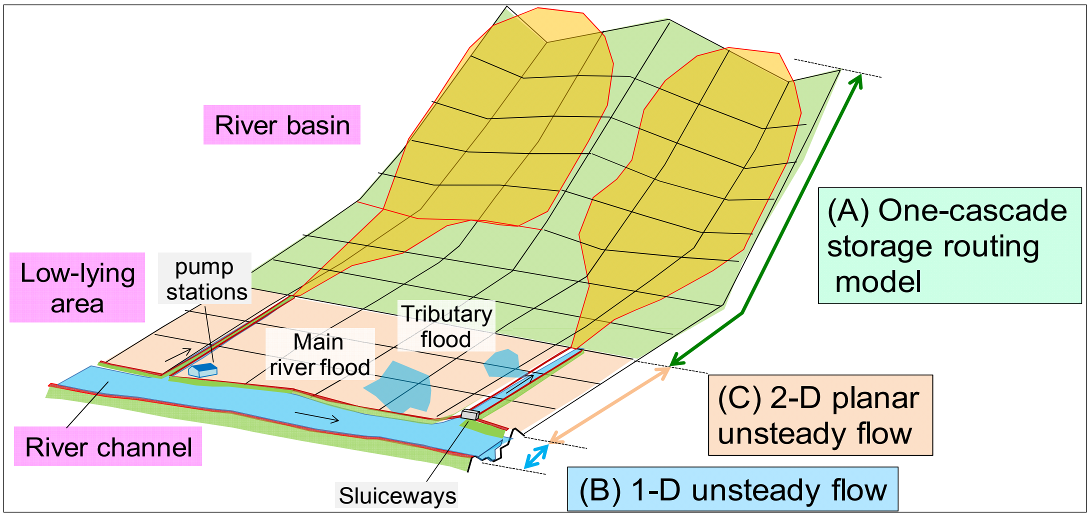

Figure 4. Flood model integrating inundation due to interior runoff and river flooding.

(a) Runoff analysis

Runoff analysis was conducted by using a one-cascade storage routing model that takes into account the loss mechanisms shown in Equation [1] (Figure 5). This model was developed by Hoshi (2007) of the Research Institute, Foundation of Hokkaido River Disaster Prevention Research Center (2004) (now the River Center of Hokkaido). The model, which is used as a solver called the Storage Routing Model (SRM), was incorporated into iRIC simulation software by Nakatsugawa and Usutani (2014) in order to make it easier for many researchers to use when analyzing river flow, sediment transport and riverbed variation. The model parameters k_{11}, k_{12}, k_{13} and λ, shown in a dotted line frame in Equations [1] and [2], are defined as optimum parameters as shown by Equation [3]. These optimum parameters were calculated by Hoshi, et al. by analyzing 72 floods in the Ishikari River System.

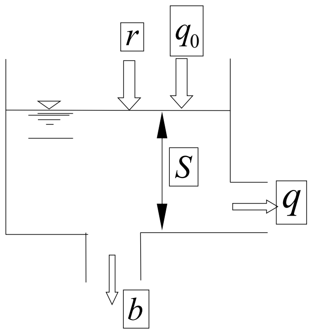

Figure 5. One-cascade storage routing model

$$\begin{cases} S = k_{11} q^{p_1} + k_{12} \dfrac{d}{dt}(q^{P_2}) \\ \dfrac{dS}{dt} = r - q - b + q_0 \\ q_0 = q_B exp(-\lambda\, t)\ ,\ b = k_{13} q \end{cases} \tag{1}$$

$$\begin{cases} k_{11} = c_{11}\ A^{0.24} \\ k_{12} = c_{12}\ k_{11}^2 (\bar{r})^{-0.2648} \\ k_{13} = c_{13} - 1 \end{cases} \tag{2}$$

$$\begin{cases} c_{11} = 11.193\ ,\ c_{12} = 0.144,\ c_{13} = 1.848 \\ \lambda = 0.025 \end{cases} \tag{3}$$

In the equations above:
S: storage height (mm), t: time (h), r: observed rainfall (mm/h), q: calculated height of runoff (mm/h), b: loss of height (mm/h), q_o: height of base runoff (mm/h), q_B: initial height of runoff (mm/h), λ: attenuation coefficient, A: basin area (km^2), $\bar{r}$: mean rainfall intensity (mm/h), k_{11} & k_{12}: storage coefficients, k_{13}: loss coefficient, p_1 & p_2: storage index (p_1=0.6, p_2=0.4648), c_{11}, c_{12} and c_{13}: model parameters

The Figure 6 shows estimated discharge of each tributary of the Chitose River from rainfall using the one-cascade storage routing model. For the Chitose River, the observed value by the discharge gauge at upstream end is shown. These data are the input data to calculate river water levels and areas of inundation. Each data set is to be inputted to the model at each salmon-pink triangle in Figure 7 for flood routing calculation. Here, Figure 7 shows a distribution diagram of the models.

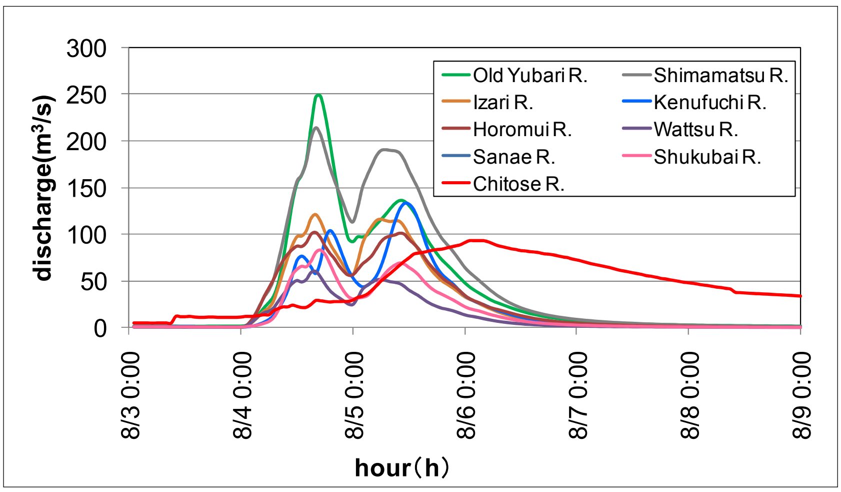

Figure 6. Discharge estimated by the model.

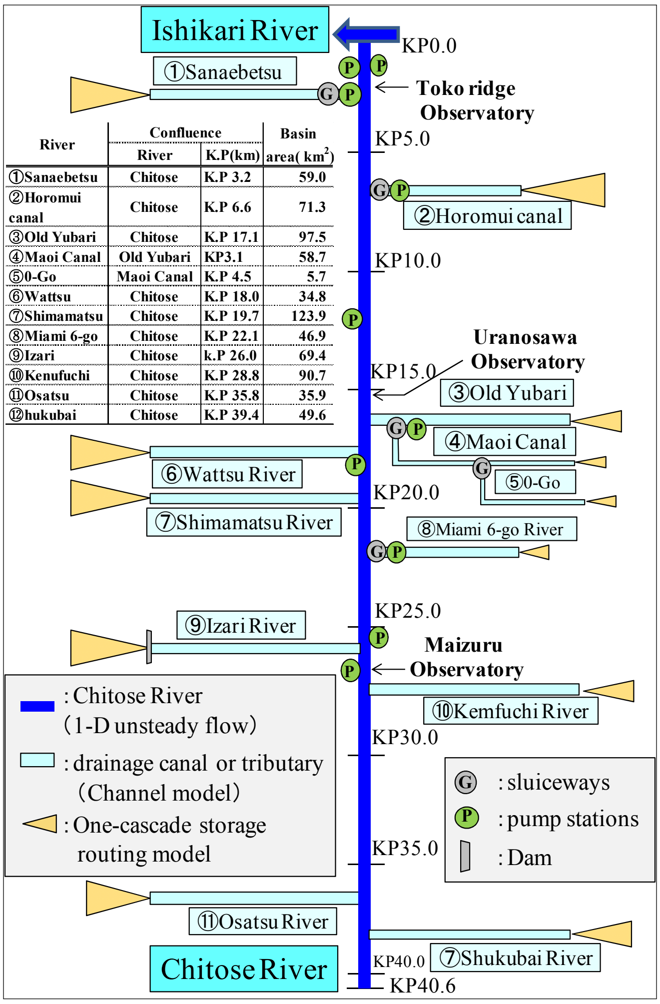

River	Confluence River	Confluence K.P(km)	Basin area(km²)
①Sanaebetsu	Chitose	K.P 3.2	59.0
②Horomui canal	Chitose	K.P 6.6	71.3
③Old Yubari	Chitose	K.P 17.1	97.5
④Maoi Canal	Old Yubari	KP3.1	58.7
⑤0-Go	Maoi Canal	K.P 4.5	5.7
⑥Wattsu	Chitose	K.P 18.0	34.8
⑦Shimamatsu	Chitose	K.P 19.7	123.9
⑧Miami 6-go	Chitose	K.P 22.1	46.9
⑨Izari	Chitose	k.P 26.0	69.4
⑩Kenufuchi	Chitose	K.P 28.8	90.7
⑪Osatsu	Chitose	K.P 35.8	35.9
⑫hukubai	Chitose	K.P 39.4	49.6

Figure 7. Distribution diagram of the models.
(runoff analysis + flood routing analysis).

(b) Flood routing

For flood routing and flood analysis, the authors used a planar two-dimensional flood analysis system developed by Computer Science Co., Ltd. Flood routing in the Chitose River was analyzed by calculating 1-D unsteady flow as shown in Equation [4]. The height of river water was vertically divided into 20 segments, and the cross-sectional properties of each segment (water height (H), sectional area (A), width of water surface (B), and hydraulic radius (R)) were used for calculation. Flood routing in tributaries (which the authors refer to below as "channel models") was also analyzed by calculating 1-D unsteady flow (Figure 8). A cross-section was used for the analysis of the channel models (Figure 8). The elevation of the deepest riverbed surface in the channel model was used for calculating the cross-sectional area of the channel below the top surface of a levee. The width of the channel with a rectangular cross-section was calculated on the basis of the calculated cross-sectional area of the channel. The flow rate at Nishikoshi (KP 40.6) was used as the flow rate at the upstream edge of the Chitose River. Runoff analysis results were used as the flow rates of tributaries and canals.

$$\begin{cases} \dfrac{\partial A}{\partial t} + \dfrac{\partial Q}{\partial x} = q \\ \dfrac{1}{g}\dfrac{\partial u}{\partial t} + \dfrac{\partial}{\partial x}\left(\dfrac{u^2}{g} + h\cos\theta\right) = I_o - I_f \\ I_o = \sin\theta \quad , \quad I_f = n^2u^2 / R^{4/3} \end{cases} \qquad [4]$$

In Equation [4] above:
A: river cross-sectional area (m^2), *Q*: flow rate (m^3/s), *q*: lateral inflow rate per unit width (m^2/s), *t*: time (sec), *g*: gravitational acceleration (m/s^2), *x*: distance along the flow path (m), *u*: flow velocity (m/s), *h*: water height (m), I_o = sinθ: channel gradient, *θ*: angle of channel slope, I_f: friction slope, *n*: Manning's roughness coefficient, *R*: hydraulic radius (m)

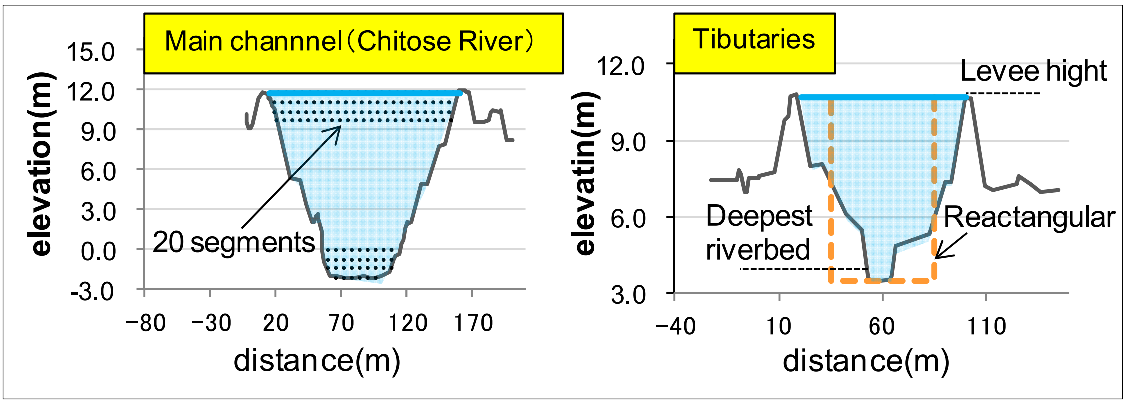

Figure 8. Cross-section of the main channel and tributaries.

(c) Flood analysis

Flood analysis was conducted by using Equation [5] for calculating 2-D planar unsteady flow. The topographic data used for analysis was based on digital national land information with a grid cell size of 250 m. The ground elevations along levees were corrected on the basis of Fundamental Geospatial Data with a grid cell size of 5 m and on the basis of cross-sectional survey data because the flood volume is underestimated when the ground elevations in digital national land information are higher than the actual elevations. To analyze water in the river channel and the flood plain in an integrated manner, the volume of overflow water (i.e., water running off into the flood plain) was calculated by using Homma's overflow formula when the simulated water level of unsteady flow in the Chitose River, which was calculated every 200 m along the river, was higher than the levee height. The calculated volume of overflow water was added to the water volume in the floodplain. The widths of overflows and levee breaches were determined by referring to available materials and photos.

Regarding the 1981 flood, it was reported that overflows took place but no levee failed on the Chitose River, and that there were overflows and levee failures in tributaries. Thus, verification of the flood analysis model was conducted by focusing on the water levels in the river channel and the inundated areas.

$$\begin{cases} \dfrac{\partial H}{\partial t}+\dfrac{\partial M}{\partial x}+\dfrac{\partial N}{\partial y}=0 \\ \dfrac{\partial M}{\partial t}+\dfrac{\partial}{\partial x}(uM)+\dfrac{\partial}{\partial y}(vM)=-gh\dfrac{\partial H}{\partial x}-\dfrac{1}{\rho}\tau_{bx} \\ \dfrac{\partial N}{\partial t}+\dfrac{\partial}{\partial x}(uN)+\dfrac{\partial}{\partial y}(vN)=-gh\dfrac{\partial H}{\partial y}-\dfrac{1}{\rho}\tau_{by} \end{cases} \qquad [5]$$

In Equation [5] above:
H: water level (m), *h*: water height (m), *M*: flux in the x-direction (m^2/s), *N*: flux in the y-direction (m^2/s), *u*: flow velocity in the x-direction (m/s), *v*: flow velocity in the y-direction (m/s), *ρ*: density of water (kg/m^3), τ_{bx} & τ_{by}: shear force in the x- and y- directions (N/m^2), *g*: gravitational acceleration (m/s^2)

Figure 10 shows the drainage pump stations taken into account in the flood analysis. These pump stations existed when the 1981 flood took place. It was assumed that pump drainage was started or stopped depending on the inundation height in each grid cell and that pump stations were operated at full capacity. In the flood analysis model, inundation due to interior runoff (i.e., flooding of tributaries) takes place when the water level in the Chitose River is higher than the water level in the tributaries and thus these tributaries are subject to backwater effects, and overflow take place when the height of the backwater exceeds the levee height.

Drainage pump station	Year of completion	Location		Full drainage capacity	Operation started Water level	Operation stopped Water level
		Drais into	km	(m^3/s)	(m)	(m)
Kamiebetsu	1971	Chitose River	2.6 Left	16.0	6.36	5.86
Ebetsubuto	1971	Chitose River	3.6 Right	4.26	6.15	5.30
Tomambetsu	1972	Chitose River	12.3 Left	16.0	6.70	5.60
Nakanosawa	1965	Chitose River	18.0 Left	4.33	4.15	4.15
Minami 9-go River	1968	Chitose River	25.4 Right	13.0	4.80	4.30
Maoi Canal	1968	Old Yubari	3.2 Left	40.0	4.30	3.80

Figure 10. Drainage pump stations taken into account in the flood analysis model.

4 RESULTS & DISCUSSION

4.1 Simulation results of water levels in the river channel

A longitudinal profile of the maximum water levels in the Chitose River is shown in Figure 9. Figure 9 shows the observed and estimated water levels at three observation sites (Toko Bridge, Uranosawa and Maizuru). The estimated water levels closely reproduced the observed values. The error, or the difference between estimated and observed water level, was about 1 to 15 cm.

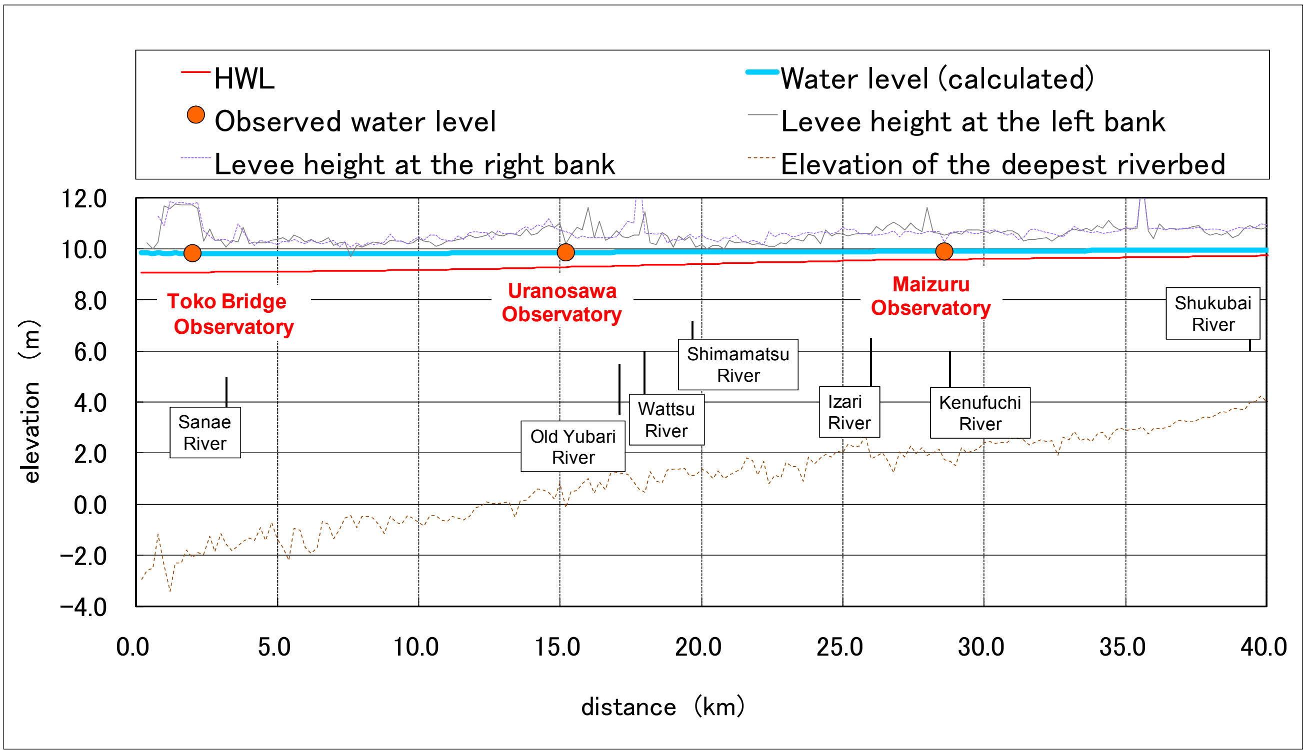

Figure 9. Longitudinal profile of the maximum water levels during the 1981 flood.

4.2 Simulation results for water levels in the floodplain

Water levels at the three water level observation stations (Toko Bridge, Uranosawa, and Maizuru) were satisfactorily simulated. Differences between the observed values and calculated values were within a range of 1 cm to 15 cm. Figure 11 shows the simulation result of the time series variation in water level. The time series variation at each of the three observation stations was accurately simulated.

Simulation results for the 1981 flood are shown in Figure 12. The observed value of the inundated area was 192 km^2, while the corresponding calculated value was 209 km^2. Thus the flood analysis model simulated the inundated area accurately. Although no data on the depth of inundation in the floodplain were available, and thus, the inundation depth was estimated on the basis of photos, the flood analysis model also simulated the depth of inundation satisfactorily.

By building this model, we have been able to develop a water level estimation tool that supports the development of a comprehensive method for controlling a river system. Such control includes the operations of flood control facilities such as dam reservoirs, retarding basins and pump stations. Also the model can be used to develop an estimation tool for evacuation and flood-fighting.

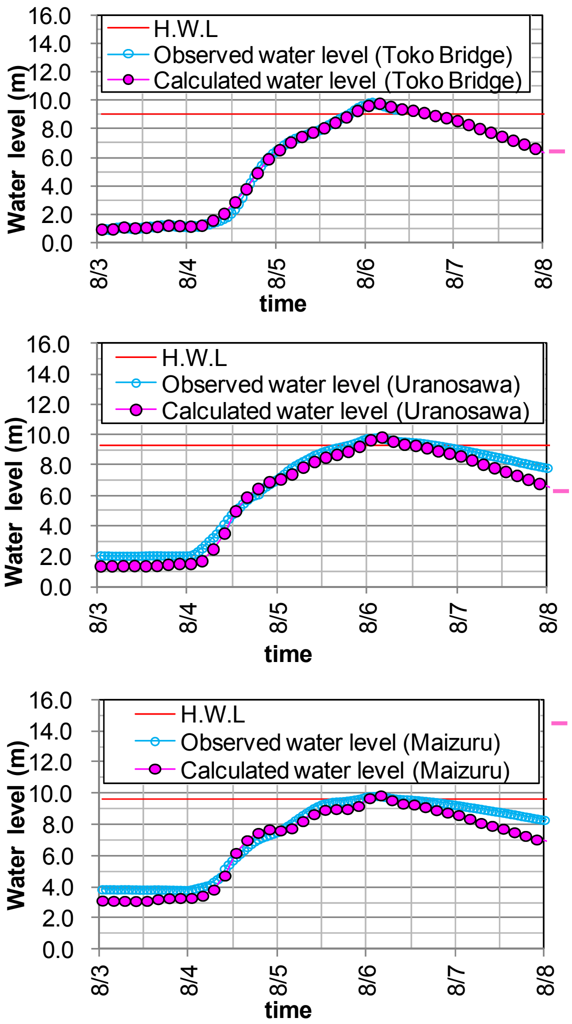

Figure 11. Time series variation in water level during the 1981 flood.

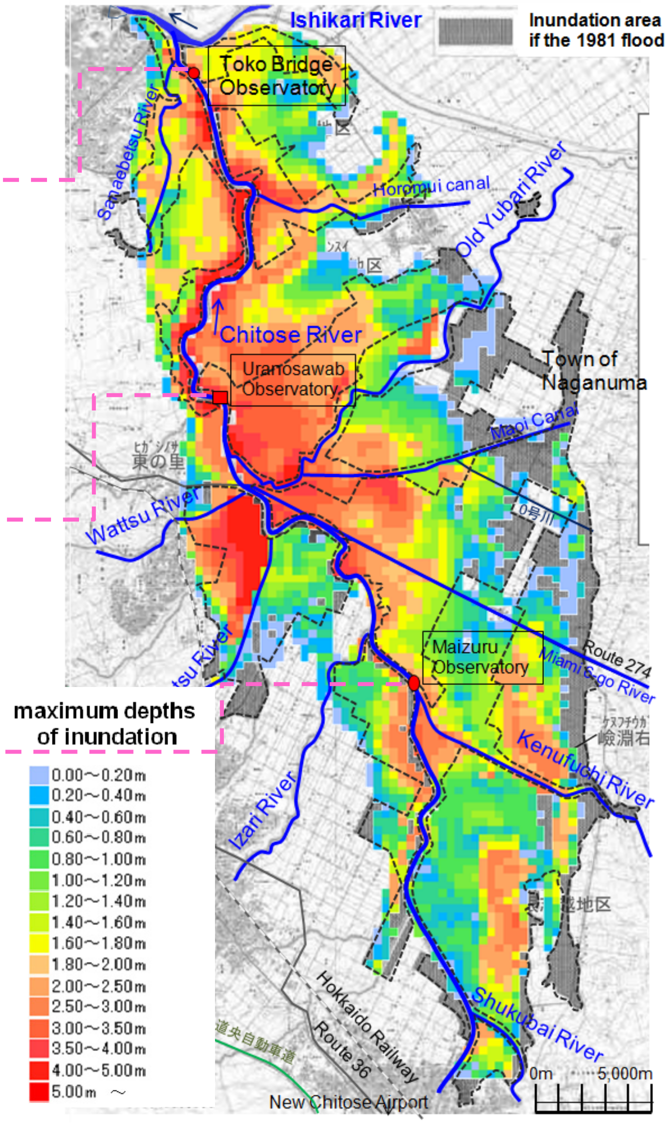

Figure 12. Simulation results for maximum depths of inundation in the floodplain during the 1981 flood.

5 CONCLUSION

The results of this study are summarized as follows.

1. The flood analysis model integrating inundation due to interior runoff and river flooding accurately reproduced flooding and inundation (i.e., water levels in the river channel and inundated areas) in low-lying areas.
2. In the analysis conducted in this study, flooding that continued for 6 days was simulated in 40 minutes by using a commercially available PC with a CPU speed of 3.4 GHz. Simulation in such a short time is possible because the flood analysis model is not very complex. This model is useful for real-time flood and inundation forecasting, as well as for field work.
3. In the future, the analysis model will be used for proposing the comprehensive operation of river management facilities including dams and retarding ponds by taking global warming and localized torrential rainfall into account. The analysis model will be further developed for supporting flood control and evacuation so that it will help prevent and mitigate disasters.

ACKNOWLEDGEMENTS

This research was supported by the Social Implementation Program on Climate Change Adaptation Technology (SI-CAT) of MEXT. The authors wish to express our great appreciation for the assistance rendered by the River Management Division of the Sapporo Development and Construction Department, Hokkaido Regional Development Bureau (2014), in providing various data.

REFERENCES

Hoshi, K. (2007). *Comprehensive Flood Estimation System of a River System*, Foundation of Hokkaido River Disaster Prevention Research Center.

IPCC (2013). *Summary for Policymarks, In Climate Change 2013: The Physical Science Basis*. Cambridge University Press, 1-1522.

Nakamura, T., Sasaki, Y. & Mizukusa, K. (2004). *A Guideline of Application for Flood Analysis Models in the Urban Areas (Draft)*, Technical Note of National Institute for Land and Infrastructure Management, No. 202.

Nakatsugawa, M., Usutani, T. & Nishihara, T. (2014). iRIC SRM Retrieved from :http://i-ric.org/ja/ on January 2017

Hokkaido Regional Development Bureau (2014*). Heavy Rainfall Disaster in Lake Shikotsu Area - Record on the Damage to and Restoration of National Highways*, Sapporo Development and Construction Department. Japan.

Saeki, Y., Suzuki,E. & Yamaguchi, M. (2013). Flood Characteristics in the Ishikari River. *Journal of Japan Society of Civil Engineers*, Ser. B1, 69(4), 1615-1620. (In Japanese).

The Ishikari River Development Foundation (1992). *The Base of Development and Flood Control of Hokkaido*, Ishikari River Development Foundation (In Japanese).

Proceedings of the 37th IAHR World Congress
August 13 – 18, 2017, Kuala Lumpur, Malaysia

A PHYSICALLY-BASED GLOBAL FLOOD HAZARD MAP

YASIR KAHEIL[1], LORENZO BEGNUDELLI[2], JEFF MCCOLLUM[3] & ZHAO LIU[4]

[1,2,3,4]Center for Property Risk Solutions, FM Global, Research Division, 1151 Boston-Providence Turnpike, Norwood, MA 02062, USA.
Yasir.Kaheil@fmglobal.com

ABSTRACT

We employed a physically-based hydrologic model to simulate river discharge, and a 2D hydrodynamic model to simulate inundation. The hydrologic Hillslope River Routing (HRR) model was used to account for runoff by mainly using the Green-Ampt infiltration model, calibrated against observed streamflow data from publicly-available and proprietary datasets. For inundation, a 2D finite-volume model with wetting/drying was implemented. The approach consisted of simulating flood along the river network by forcing the hydraulic model with the simulated hydrographs by HRR scaled up so that the peaks correspond to certain return levels, e.g. 100-year discharges. The model was implemented in a parallel computing environment, and was distributed such that each available processor would take the next simulation. Given an approximate a-priori criterion, the simulations were ordered from most- to least-demanding, to ensure that all processors were terminated nearly simultaneously. Upon completion of all simulations, the maximum-depth envelope was applied to represent the final map. The model was applied globally, with maps shown at different return periods. These maps, which are currently available at 3 arc-sec (~90 m) resolution, can also be made available at higher resolutions by using higher resolution input elevation data.

Keywords: Flood hazard; inundation; natural catastrophe; risk management.

1 GENERAL DESCRIPTION

In this work, we describe the development of the physically-based Global Flood Modeling System (GFMS). The first version of the Global Flood Map (GFM), a product of GFMS is now complete for both the 100-year and 500-year return periods. GFMS includes a hydrologic model based on Hillslope River Routing (HRR) (Beighley et al., 2011), and a two-dimensional finite volume hydraulic model. Figure 1-4 show different views of the GFM overlaying OpenStreetMap (OpenStreetMap contributors, 2016).

The hydrologic model performs the streamflow accounting, taking into consideration a multitude of global datasets, e.g., digital elevations (DEM), precipitation, soil type, and land cover. These global datasets are available at different resolutions. Namely, the rainfall data, which come from CFSR (Saha et al., 2010), are available at 38 km resolution for 31 years, the Re-gridded Harmonized World Soil Database (HWS) (Wieder et al. 2014) is available at 30 arc-sec (roughly 900 m), the GlobCover (Bontemps et al. 2009) land cover dataset is available at 300 m, and SRTM (USGS, 2004) for digital elevation data are available at 3 arc-sec (90 m roughly). HRR is a catchment-based hydrologic model. The size of the catchment can, in theory, be arbitrary. In practice, however, it is usually chosen to reflect the level of accuracy in the input datasets, as well as the level of detail required in the output. With that in mind, the target catchment size for the Global Flood Model was chosen to be 10,000 DEM gridcells; with each gridcell being 3 arc-sec (~90 m), the average catchment size was about 100 km^2. This implies that rivers (or streams) with drainage areas less than that value may not be modeled in the current GFM version. Similar to the work presented in Dottori et al. (2016). in discussing flood hazard mapping using the Global Flood Awareness System (GloFAS), this work is also physically-based. However, the resolution of the first version of GFM is ten times higher than what was discussed in Dottori et al.(2016).

The hydraulic model used as part of the GFMS is two-dimensional (2D), therefore the “river” is not modeled as a sequence of cross sections, but the modeled area is discretized as a grid of 90 m rectangular cells. The model computes the amount of water flowing from each cell to/from the neighboring ones as time advances, and therefore simulates how water flows in the modeled area.

In the GFMS, source points (i.e., sources of water) are placed along the rivers to simulate the excess of water that cannot be contained within-bank, and overflows towards the floodplain. For each source point, the inflow hydrograph is the stream maximum peak for the desired return period (i.e., 100-year or 500-year). This is obtained by scaling up the maximum event during the modeled record (31 years) according to the return period, and the location of the source point within the catchment. For example, in a headwater (or most upstream) river, several points are placed along the river, with one exactly at its catchment outlet. A distribution is fitted to the annual maxima to obtain the 100-year and 500-year streamflows. At the most upstream point in that river, the maximum peak of the outlet time series is scaled by the Q_{100} or Q_{500} value (at the outlet) multiplied by the ratio between the drainage area upstream of that most upstream point, and the total catchment area.

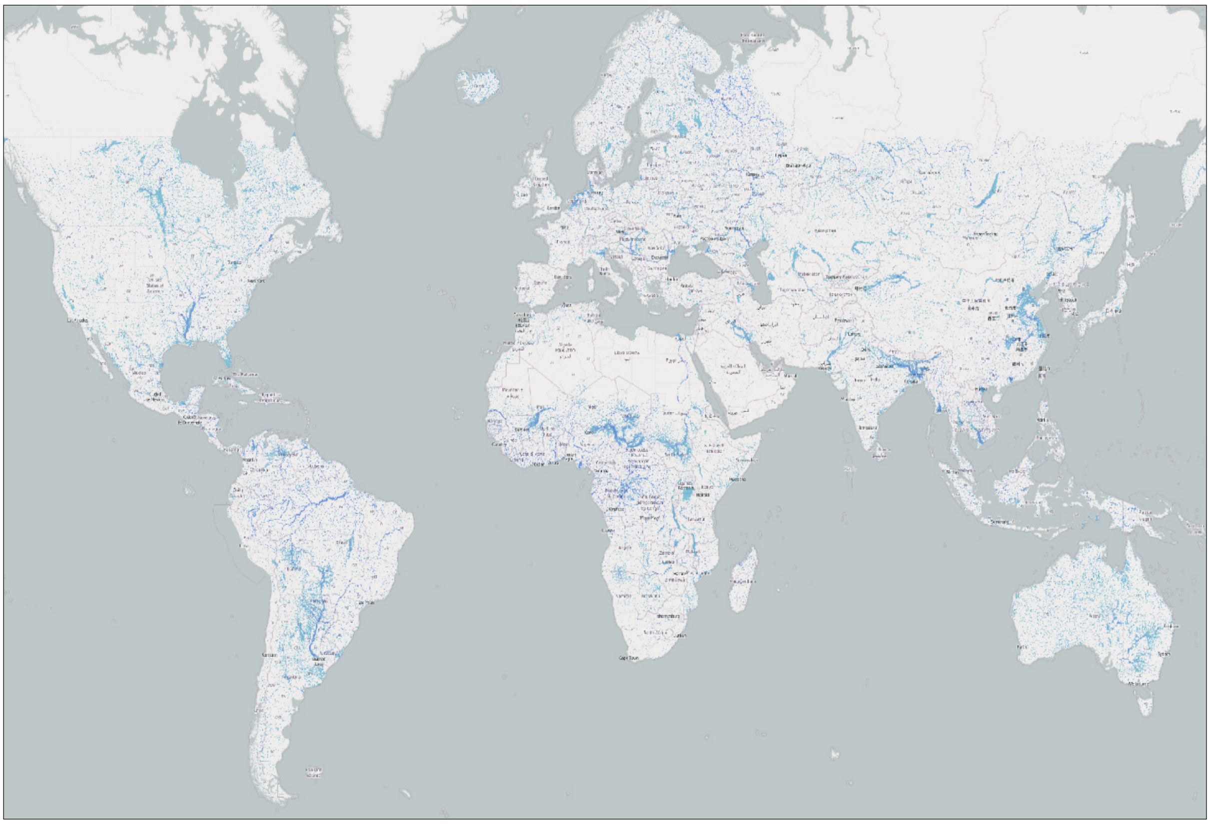

Figure 1. The 100-year Global Flood Map (GFM) overlaying OpenStreetMap

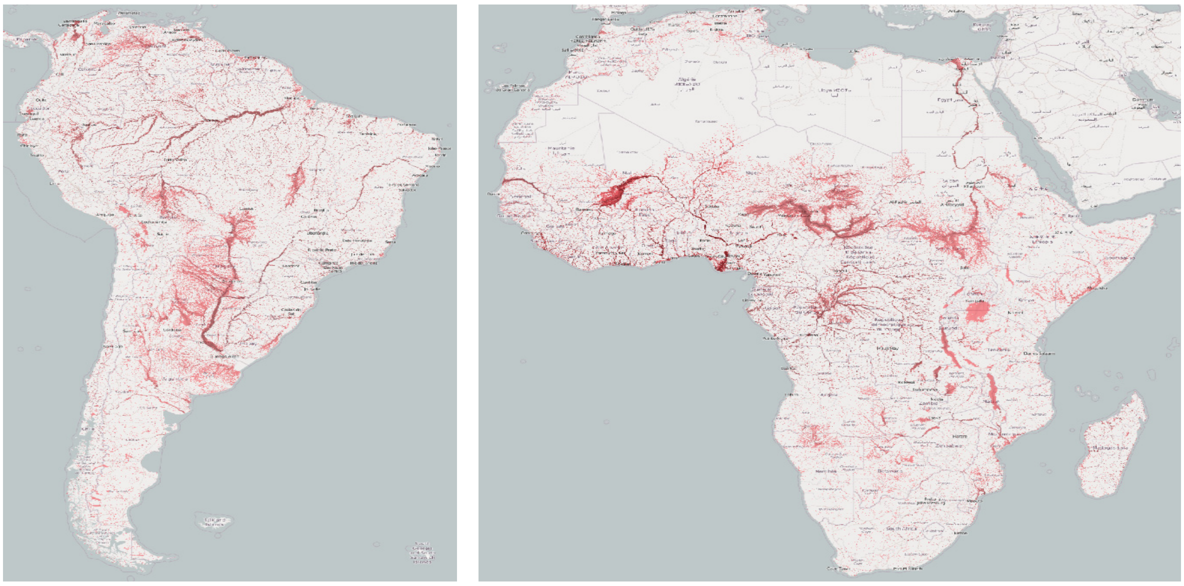

Figure 2. The Global Flood Map (GFM) 500 –year showing South America (left) and Africa (right).

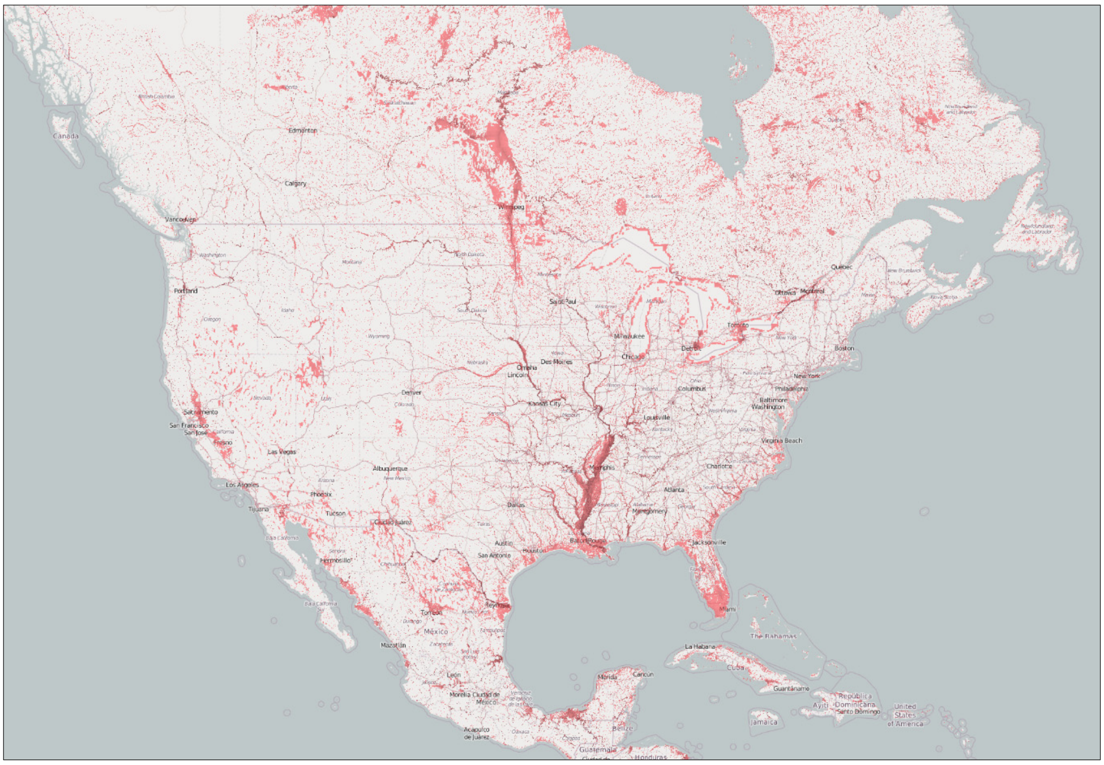

Figure 3. The 500- year Global Flood Map (GFM) showing most of North America.

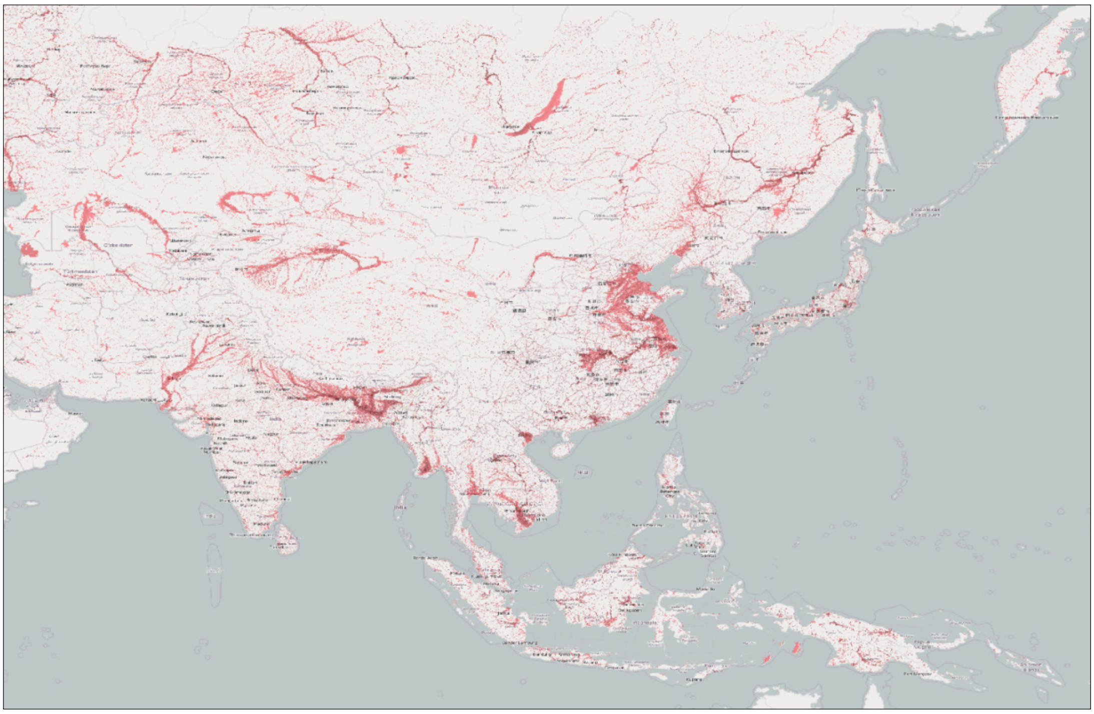

Figure 4. The 500- year Global Flood Map (GFM) showing most of Asia.

2 IMPLEMENTATION

The two main components of the GFMS are the hydrologic model (HRR) and the hydraulic model. Figure 5 shows the general steps of the GFMS. These steps will be discussed in the next few subsections, namely: input data processing, HRR brief description, HRR calibration and parameter transfer, HRR operational mode and output post-processing, a brief description of the hydraulic model, and finally map preparation.

2.1 Input data and preprocessing

Since HRR is a catchment-based hydrologic model, all input datasets have to be averaged to the catchments. However, it is imperative that we first create our catchments and river network. Utilizing HydroSHEDS (Lehner et al., 2008) global flow direction layer (available at 3”), catchments and streams were

  / ISSN 1562-6865 (Online) - ISSN 1063-7710 (Print)

generated around the world. For data management purposes, we divided the world into 65 zones: 11 in Africa, 19 in Asia, 2 in Australia, 10 in Europe, 8 in North America (excluding the US), 8 in South America, and finally 7 in the US. Each zone cannot cross river basins, but can contain multiple river basins.

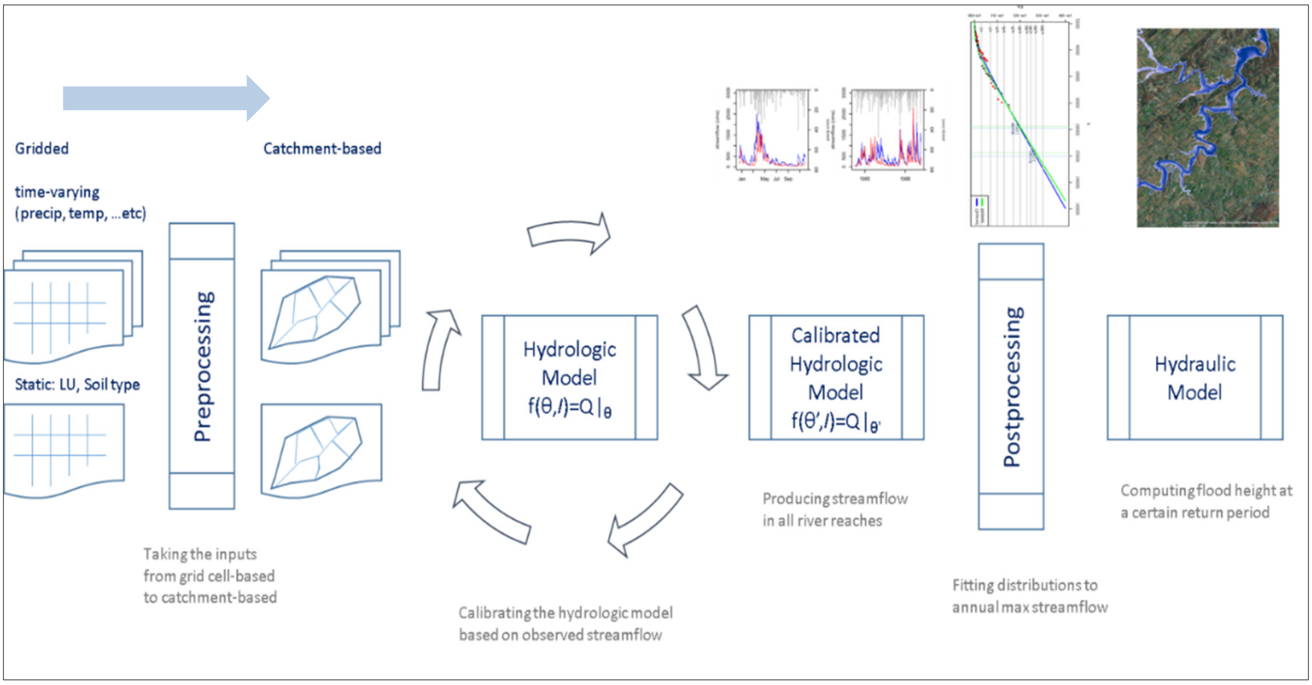

Figure 5. A schematic showing the general steps of the global flood modeling system.

Once our catchments had been created globally, all gridded input datasets such as precipitation, snowmelt, evapotranspiration, soil properties, and land cover properties had to all be averaged to the catchments. We followed an area weighted averaging scheme illustrated in Figure 6. We limited the number of grid cells averaged to one catchment to four. The input data processing step created all the input files required to run HRR. These input files ranged from catchment and channel properties (planes and channels files), and forcing data such as precipitation, snowmelt, and evapotranspiration. Note that the river network information (information pertaining to channel routing, i.e., which river drains to which) was contained in the channels file.

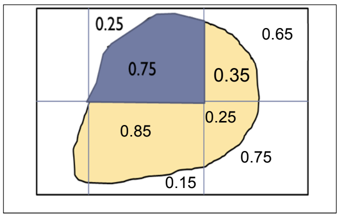

$$P_{c1,t} = \sum_{i=1}^{4} w_i p_{i,t}, \quad w_i = \frac{w'_i}{\sum_{i=1}^{4} w'_i} \qquad [1]$$

Figure 6. Area-weighted averaging scheme.

2.2 HRR

The input variables were used in the HRR equations to model water movement. The Green-Ampt model (Green and Ampt, 1911) was used to estimate the relative distribution of input precipitation infiltrating into the soil vs. flowing over the surface. Surface and subsurface runoff down the hillslopes into the channel were modeled using the kinematic wave approximation (Li et al., 1975). Channel flow was modeled using the Muskingum-Cunge method (Cunge, 1969).

2.2.1 Gauge selection, model calibration, and parameter transfer

As a model, HRR tries to capture the major processes affecting surface water in the context of flooding, i.e., it focuses more on accurate accounting of peak flows. As we previously mentioned, HRR is forced with global datasets, whose accuracy tends to vary from one area to another depending on observed data availability among other factors. Inaccuracies in the data as well as less important processes that are not included in the model are together compensated for by the process of parameter calibration. HRR has three parameters that are actually multipliers of global variables, namely: hydraulic conductivity (k), soil depth (D), and surface roughness (ρ). These multiplier parameters are bound to ranges such that the associated variables assume realistic values. The calibration process changes the parameter values until a reasonable agreement is reached between observed discharge from a gauge and HRR's output at the location of that gauge. The gauge information comes from many sources, e.g., USGS (USGS, 2015).

The HRR calibration gauges were chosen such that the upstream has little to no water management structures. Based on the hydrograph of each gauge alone, a simple classification model using Support Vectors Machines (SVMs) (Vapnik, 1998) utilizes both the lag-1 autocorrelation and the slope of the flow duration curve between the 75^{th} and the 25^{th} quantiles as inputs to classify whether the gauge is "natural".

The calibration algorithm was invoked with the R stats package function "optim" (R Core Team, 2014). It first set the parameter values to the midpoint of their respective range, and invoked the model for all catchments upstream of the gauge. The model outputted the streamflow at the location of the gauge. The root mean square error (RMSE) was computed between the observed discharge and the HRR output at the gauge. We added to that the absolute difference between the top 5 peaks on record and what HRR computed at those time steps. Together these two components made the objective function (OF) of the calibration algorithm. Following the gradient descent approach, the algorithm found the parameter set that minimized the OF within the parameter's range of permissible values.

The outcome of the model calibration process was the different parameter sets (sets of three values for the three model parameters) for each gauge with upstream area deemed "natural." The next step was to use these parameter sets in areas that are heavily managed and/or there was no gauge present. The process of parameter transfer hinges on the concept of catchment similarity.

In GFMS, the parameter transfer process started from identifying the dominant hydrological processes globally. Then, four indices (climate zone from IPCC (IPCC, 2006), land cover type (LC), soil type (ST), and wetness index (WI)) were used to reflect the importance of that process and ultimately to match an ungauged basin to a calibrated gauged one. From literature review, a global shapefile has been compiled that identifies the dominant hydrological processes and assigns weights (that add up to one) to the four indices in order to reflect the dominant hydrological process in a region. For example, if the dominant hydrological process is snowmelt, IPCC and WI get higher weights than LC and ST. Using these indices, each uncalibrated basin gets matched with a calibrated one. The parameter set associated with the calibrated basin that makes the minimum distance gets assigned to the uncalibrated basin.

2.2.2 HRR operational mode and output post-processing

Once the model was equipped with a parameter set, it was ready to run in the operational mode, meaning for the entire length of the precipitation record, generating streamflow data at the outlet of every catchment around the world. Post-processing was aimed at generating the forcing data to the 2D hydraulic model. From the discharge time series, annual maxima were generated. We also kept track of the largest peak on record. At the outlet of each catchment globally, a Gumbel distribution was fitted automatically to the annual maxima using the L-moments method. The 100-year and 500-year return levels can then be obtained from the inverse CDF at exceedance probabilities 0.01, and 0.002, respectively. The Q100, and Q500 "events" were assumed to follow the same hydrograph as the largest peak on record.

Multiple points were generated along the rivers everywhere in the world at the spacing of ~ 200 m. Using the flow accumulation layer, Q100 and Q500 hydrographs were scaled for each point depending on the cumulative area upstream of the point vis-à-vis the cumulative area at the outlet of the catchment. Once this step was accomplished, every point at ~200 m separation distance along every river as well as catchment outlets had two discharge hydrographs assigned to it at the 100- and 500-year levels.

2.3 2D hydraulic model description

The 2D hydraulic model simulates the propagation over the floodplains of the excess water that cannot be contained within-bank. The flow points described in the section on post-processing of HRR output are grouped, river by river worldwide, in sets of 10. For each set of 10 points, an individual 2D model simulation is run.

The model was based on the *Shallow Water Equations*, a set of relationships widely used for a large range of environmental flows, which are obtained by averaging the 3D Navier-Stokes equations over the water depth. These equations were numerically solved using a grid of rectangular cells. At each time step, the model computes the exchanges, or *fluxes*, of water mass and momentum between the cells, and updates the solution in all cells. Since all computations are based on the cells, treated as control volumes, the numerical method is called *finite-volume*.

In the GFMS, the hydraulic model discretized the computational domain in rectangular cells of ~90 m size, corresponding to the cell size of SRTM. Since the computational domain was much larger than the distance between the inflow points used for the individual simulations, there was a great amount of overlapping between the domains (and in most cases the flooded areas) of the simulations for the points along each river. This was to ensure that, when the maximum depth envelope is obtained from all simulations, the final result is as continuous and seamless as possible, and no gaps are left between the model outputs for consecutive points along the rivers. The process to obtain the final 100-year and 500-year flood maps is represented by the sketch shown in Figure 7. The hydraulic model was run for all points along the river

  / ISSN 1562-6865 (Online) - ISSN 1063-7710 (Print)

network (A, B in Figure 7) using, for each point, the 6-day hydrograph computed from the operational run of HRR. Then, all output was combined by taking, for each cell, the maximum water depth resulting from all simulations.

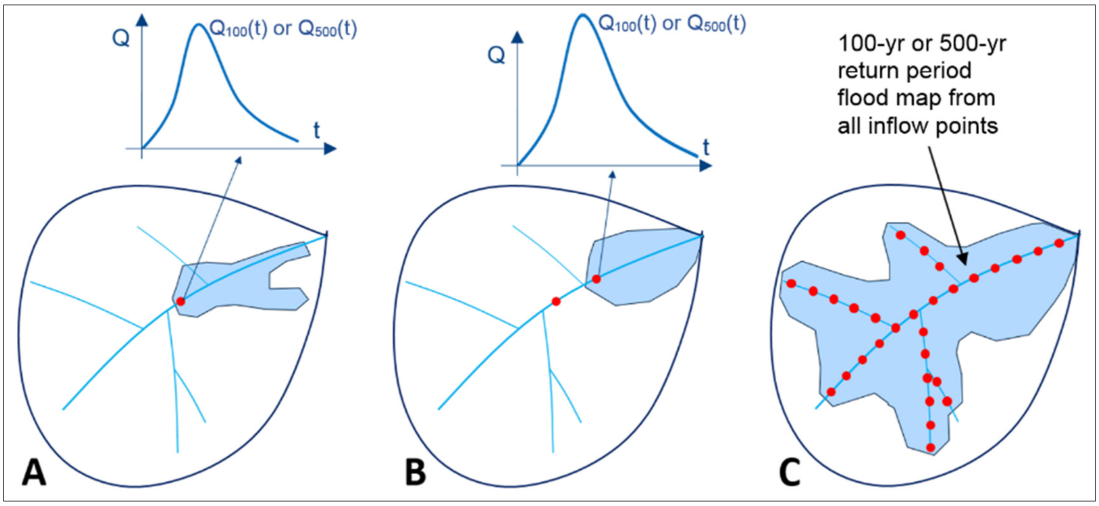

Figure 7. Sketch representing the hydraulic modeling process to obtain the final 100-year and 500-year flood maps.

3 CONCLUSIONS

The first version of the Global Flood Map (GFM), a product of GFMS, is now available at the 100-year and 500-year return periods. GFMS includes a hydrologic model based on Hillslope River Routing (HRR), and a two-dimensional finite volume hydraulic model. The hydrologic model performs the streamflow accounting, taking into consideration a multitude of global datasets. HRR is a catchment-based hydrologic model, meaning that the world is divided into hydrologic catchments. The hydraulic model used as part of the GFMS is two-dimensional (2D). The model computes the amount of water flowing from each cell to/from the neighboring ones as time advances, and therefore simulates how water flows in the modeled area. The first version of the output flood maps is available at a 3 arc-sec, ~90 m resolution globally, at the 100-, and 500-year return periods. Higher resolution maps are in progress (Geoscience Australia, 2015; USGS, 2002; National Land Survey of Finland, 2016).

REFERENCES

Beighley, R. E., Ray, R. L., He, Y., Lee, H., Schaller, L., Andreadis, K. M. & Shum, C. K. (2011). Comparing Satellite Derived Precipitation Datasets using the Hillslope River Routing (HRR) Model in the Congo River Basin. *Hydrological Processes*, 25(20), 3216-3229.

Bontemps, S., Defourny, P., Van Bogaert, E., Olivier, A. & Vasileios, K. (2009). GLOBCOVER 2009 – Product Description Manual. Distributed by ESA, 1-53.

Cunge, J. A., (1969). On the Subject of a Flood Propagation Method (Muskingum Method). *Journal of Hydraulics Research*, 7(2), 205-230.

Geoscience Australia (2015). *Digital Elevation Model (DEM) 25 Metre Grid of Australia derived from LiDAR*, GA: Canberra, ACT, Australia

Green, W. H. & G.A. Ampt, (1911). Studies on Soil Physics. *The Journal of Agricultural Science*, 4(1), 1-24.

Global Climatic Zone dataset from the Intergovernmental Panel on Climate Change (IPCC) IPCC (2006). *Downloaded from the European Soil Data Centre (ESDAC)'s Renewable Energy Directive*, European Commission, Joint Research Centre.

Dottori, F., Salamon, P., Bianchi, A., Alfieri, L., Hirpa, F.A. & Feyen, L., (2016). Development and Evaluation of a Framework for Global Flood Hazard Mapping. *Advances in Water Resources*, 94, 87-102.

Lehner, B., Verdin, K. & Jarvis, A. (2008). New Global Hydrography Derived from Spaceborne Elevation Data. *Eos, Transactions, AGU*, 89(10), 93-94.

Li, R.-M., Simons, D. & Stevens, M. A., (1975). Nonlinear Kinematic Wave Approximation for Water Routing. *Water Resources Research*, 11(2), 245-252.

National Land Survey of Finland. Retrieved in February 2016.

OpenStreetMap contributors. E.T. Seton Park (Map). Open Street Map. Retrieved 5 February 2016.

R Core Team (2014). R: *A Language and Environment for Statistical Computing. R Foundation for Statistical Computing*, Vienna, Austria. URL <http://www.R-project.org/>.

Saha, S., Moorthi, S., Pan, H.L., Wu, X., Wang, J., Nadiga, S., Tripp, P., Kistler, R., Woollen, J., Behringer, D. & Liu, H., (2010). The NCEP Climate Forecast System Reanalysis. *Bulletin of the American Meteorological Society*, 91(8), 1015-1057.

U.S Geological Survey, (2002). National Elevation Dataset. Retrieved in 2015

U.S. Geological Survey, (2015). National Water Information System data available on the World Wide Web (USGS Water Data for the Nation), at URL <http://waterdata.usgs.gov/nwis/>, accessed [January 10, 2015].

USGS (2004). *Shuttle Radar Topography Mission, all 3 Arc Second scenes, Filled Finished-B 2.0, Global Land Cover Facility*, University of Maryland, College Park, Maryland, February 2000.

Vapnik, V. (1998). *Statistical Learning Theory*. Springer Science & Business Media, 1-188.

Wieder, W.R., Boehnert, J., Bonan, G.B. & Langseth, M., (2014*). Regridded Harmonized World Soil Database V1. 2. Data Set*. Available on-line [http://daac. ornl. go v] from Oak Ridge National Laboratory Distributed Active Archive Center, Oak Ridge, Tennessee, USA.

ASSESSMENT OF SPECIAL FLOOD RISK USING DISTRIBUTED HYDROLOGICAL MODEL IN LAOS

SENGPHRACHANH PHRAKONKHAM(1), SO KAZAMA(2) & DAISUKE KOMORI (3

(1) Graduate School of Environmental Studies, Tohoku University, Sendai, Miyagi, Japan
phrakonkham.sengphrachanh.t7@dc.tohoku.ac.jp
(2) Department of Civil and Environmental Engineering, Tohoku University, Sendai, Miyagi, Japan
so.kazama.d3@tohoku.ac.jp; idham.moe@gmail.com
(3) Graduate School of Environmental Studies, Toyama Prefectural University, Imizu , Toyama, Japan
daisuke.komori.e8@tohoku.ac.jp

ABSTRACT

Flood is a common hazard among all natural disaster and it causes the most problems. It is impossible to avoid risks of floods and prevent their occurrence. However, it is possible to work on the reduction of their effects and reduce the losses which they may cause. In order to understand the magnitude of floods as well as the contingency of planning and management decision, river modeling and flood hazard mapping have become more in demand for decision makers to understand the situation. This study is aimed to develop map flood risk by superimposing 4 hazard maps such flood hazard maps and probability of landslide hazard map. Flood hazard maps will be separated in to 3 scenarios which flood hazard map from 100 years return period of peak rain fall, land use change and climate change. The results show that risk of flooding is high around central area and southern part of Laos. . Following it, the flood risk map was compared with records of historical flood events to confirm the valid results.

Keywords: Rainfall; risk map; climate change; land use; forest.

1 INTRODUCTION

The Laos PDR has experienced a range of floods of different magnitudes and duration. Particularly in three consecutive years of 1994, 1995 and 1996, the flood was large and disastrous. Currently Laos is in the stage of development in both economic and social strate and this is another reason it is the impacting resettled communities and people living on the downstream of the dams (Bakker, 1990). A lot researches has been done about the resettlement area both in present and past (Baird and Shoemaker, 2007) but nobody has understood about the safety of the area against the natural hazard yet. This is mainly to create an easy to read and understand,maps which accommodate the identification of risk areas from flooding and also helps prioritize mitigation and response efforts (Bapulu et al., 2005). Flood hazard maps area can be designed to increase awareness of the likelihood of flooding among the public, local authorities and other organisation. The map also can be used as a tool to encourage local people who are living and working in flood-prone areas to understand and realize more about the flood risk in those area and can take appropriate action.

Many studies has been attempted to estimate the risk for different hazards (debris, flood) on various zone by the use of GIS as a powerful tool to integrate and analyse data from different sources. This flood risk mapping was provided for different scenarios of urban growth. Zerger (2002) reported that relative important was introduced as the input parameters, underlining the necessity to connect spatial analysis to help in decision making. In Schumann et al. (2000) a GIS-based methodology for rainfall-runoff modelling was developed, while Liu et al. (2003) connect several parameters in their rainfall-runoff model (slope, land use, soil type etc.) in order to estimate the spatial distribution of runoff and the average flow time in river basins. Their aim was to provide insight on river basin hydrological processes as a support of the flood risk management. Van Der Veen and Logtmeijer. (2005) stated flood vulnerability was liked inconjunction to the importantance of economic information om 28 sectors with the borderline datas of simulation flood events. Forte et al. (2005) said that they expanded an earlier work (Liu et al., 2003) and divided study area into prone zone of different flood rick by super-imposing the GIS layers of both geological and hydrological information. They also combined informations on the study area and information of historical events. Similarly, Dewan et al. (2007) developed flood hazard maps, by processing data of the historical major flood event of 1998 by considering the interactive effect of land cover, elevation and geomorphology.

It should be noted that flooding is inevitable and avoidance of it is impossible. Thus the assessment and management of future floods can be achieved through proper analysis. Identification of prone areas to floods or preparation of susceptibility map of flooding is an important tool to mitigate future flood damage. Therefore, by identifying location with low to high susceptibility of flooding, suitable areas for developmental activities could be recognized. Thus we combined 4 hazard maps namely, flood water depth, probability of landslide, land use impact to flood hazard map with climate change impact hazard map to create a flood risk map.

2 STUDY AREA AND DATA DECRIPTION

The Laos PDR, or Laos, is situated in the middle of South East Asia. The country is landlocked, so it has no direct access to the sea and has common borders with China, Vietnam, Cambodia, Thailand and Myanmar. The country is located in the Center of the Indochinese peninsula, located between Longitude 100 to 108 degree East and latitude 14 to 23 degree North (Figure 1). The total area of Laos is 236,800 km^2 with Mekong river flowing through almost 1,900 km of Laos territory from the North to the south and it forms a natural border with Thailand for over 800 km.

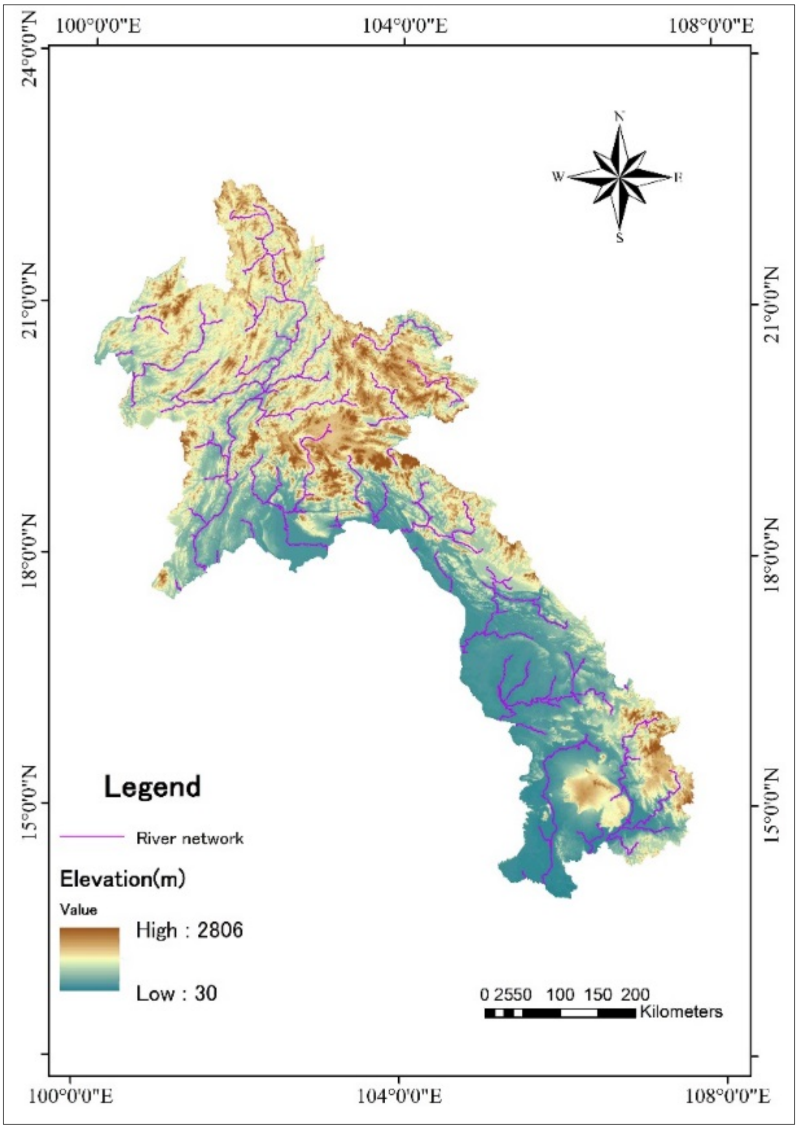

Figure 1. Study area map.

The land in Laos is classified as the forest (65.2 %), vegetation or agriculture area (33.8%) with water body and bare land (1%). Most of the agriculture area is paddy field. The soil data were based on the Harmonized World Soil Database (HWSD 2012), where the HWSD is a 30 arc-second raster database with over 16000 different soil mapping units that combines existing regional and national updates of soil information worldwide. Original soil type data were based on the Soil Unit (SU) Global. In this study the units were converted from SU global code to the soil texture class. Soil type's data play an important role in the infiltration factor of hydrological distribution.

To simulate hydrological distributed models, a hydrological and meteorological dataset from Mekong River Commission were used in this study. The daily meteorological data at 40 stations from 1970 – 2000 is used for rainfall-runoff simulation and it is also used in calibration and validation process of the distributed hydrological model. The parameters are precipitation, soil types and elevation. In addition for the rainfall data, daily maximum data is selected to analyze the rainfall intensity for 100 years return period. The rainfall intensity for many return periods was calculated by using Log Pearson Type III of maximum rainfall data for each year on every stations and it is listed in Table 1.

Table 1. 100 years return period rainfall.

St_id	S_Long	St_Lat	100 y	St_id	St_Longt	St_Lat	100 y
140501	14.1	105.8	220.0	170207	17.9	102.6	198.9
140504	14.3	105.9	160.0	170404	17.4	104.8	409.7
140505	14.8	106.0	291.0	170501	17.8	105.1	275.6
140506	14.7	105.8	187.3	180203	18.0	103.0	233.3
140507	14.9	105.9	272.0	180205	18.6	102.3	198.1
140705	14.5	106.8	310.3	180206	18.4	102.4	309.4
150504	15.1	105.8	200.1	180207	18.9	102.5	223.0
150506	15.6	105.8	193.2	180213	18.2	102.6	207.6
150508	15.4	105.8	225.4	180303	18.4	103.6	370.3
150602	15.7	106.4	234.9	180306	18.4	103.2	287.5
150607	15.2	106.4	234.3	180307	18.6	103.7	231.6
160405	16.6	104.8	188.6	180308	18.5	103.7	396.1
160504	16.0	105.8	202.2	180501	18.3	102.7	323.8
160505	16.4	105.2	223.9	190101	19.7	101.9	128.0
160507	16.2	105.3	145.1	190103	19.2	101.4	149.1
160508	16.0	105.5	301.5	190205	19.8	102.2	149.9
160601	16.0	106.2	183.9	190301	18.9	102.8	184.6
160602	15.2	105.9	252.7	190302	19.3	103.4	155.0
160603	16.7	106.5	233.7	200101	20.9	101.4	111.6
170203	18.0	102.5	167.7	200204	20.7	102.0	167.9

The Digital Elevation Map (DEM) with a 100 m x 100 m in the original spatial resolution that is used in this study are obtained from National University of Laos. DEM acts as a principal source to extract topographic factors and is considered to be one of the most important data which has been used in various research works.

3 METHODOLOGY

In this paper, the methodology consists of two parts which is distribution of hydrological model and landslide probability analysis.

3.1 Hydrological model

In this study a distribution hydrological model developed by Kashiwa et al (2010) was used under the structure proposed by Kazama et al. (2004). The model includes a direct flow and base flow model and it is used to estimate the river flow. Direct flow was calculated using Kinematic wave concepts, which pursues meteoric water runoff using a momentum equation and a continuity equation.

$$\frac{\partial A}{\partial t}+\frac{\partial Q}{\partial x}=(r_e)B \qquad [1]$$

Continuity equation

$$\frac{\Delta h*B}{\Delta t}+\frac{Q_{out}-Q_{in}}{\Delta x}=(r_e)B \qquad [2]$$

$$\Delta h=\frac{\Delta t}{B\Delta x}(Q_{in}-Q_{out})+(r_e)\Delta t \qquad [3]$$

Where, Δh is variation of depth (m), Δt is time interval of flow direction (d), Q is flow rate (m3/d), re is precipitation (m/d), and B is width of flow path (m).

Manning equation

$$Q=\frac{1}{n}B\Delta h^{\frac{5}{3}}I^{\frac{1}{2}} \qquad [4]$$

Where, Q is flow rate (m^3/d), Δh is water depth (m), B is mesh width (m), I is gradient and n is the Manning roughness coefficient (d/ [$m^{1/3}$]).

Infiltration equation

$$R_{in}= K_a*h \qquad [5]$$

Where, Where R_{in} is the amount of infiltration (m/d), k_a is the infiltration coefficient (d^{-1}) and h is water depth (m)

Storage function method

$$s = kq^p \quad [6]$$

$$q = \left(\frac{s}{k}\right)^{\frac{1}{p}} \quad [7]$$

Where, s is apparent storage level (m) q outflow level of base flow (m/s), k (s) and p are constant.

3.2 Possibility of landslide

Landslide is one of the most dangerous natural hazard and it can cause a lot of damage to affected areas. To evaluate the distribution of landslide hazard over Laos, this study uses a probabilistic model based on multiple logistic regression analysis. This model concerns several significant physical parameters such as hydraulic parameters and geographical parameter. Among those parameters, hydrological parameter (hydraulic gradient) is the most significant factor in the occurrence of landslides. Therefore, hydraulic gradient was used as main hydraulic parameter; dynamic factor which includes the effect of 100 years return period of rainfall (Kawagoe et al., 2010; Ono et al., 2011).

Landslide probability analysis

$$p = \frac{1}{1+\exp\left[-\left(\beta_0+\beta_h{*}hydro{*}\beta_r{*}relief\right)\right]} \quad [8]$$

Where, P the event probability of landslide, β_0 is intercept, β_h is the coefficient of hydraulic gradient, β_r is the coefficient of relative relief, hydro is hydraulic gradient, and relief is relative relief.

4 RESULTS AND DISCUSSION

4.1 Flood hazard map

Distribution hydrological model is used to simulate flood hazard map over the entire area of Laos, which we take into account for every grid cell of highest water depth that is determined during the simulation. The simulation consist of contributing factors of 100 years return period rainfall, land types, soil hydrologic characteristics and elevation. In order to superimpose the hazard map, we developed risk index as a parameter, by adopting it from the relationship between velocity and flood depth as shows in Table 2.

Table 2. Flood hazard categories between velocity and depths.

Velocity (m/s)	**depth of flooding (m)**											
	0.05	0.1	0.2	0.3	0.4	0.5	0.6	0.8	1	1.5	2	2.5
0												
0.1												
0.25												
0.5												
1												
1.5												
2												
2.5												
3												
3.5												
4												
4.5												
5												

Remark
small risk medium risk intermediate risk high risk

However, in this study we considered every grid's depth in the map, so we assumed velocity to be the lowest value so that we can transform the depths into new index parameter as a scale from zero to one. The scale at zero is described to be low risk and up to one is high risk as shows in Figure. 2. According to the

  / ISSN 1562-6865 (Online) - ISSN 1063-7710 (Print)

results, potential of flood hazard areas are not only area that is near the river grid but other area also have potential risk to be flooded due to heavy rainfall (Figure. 3).

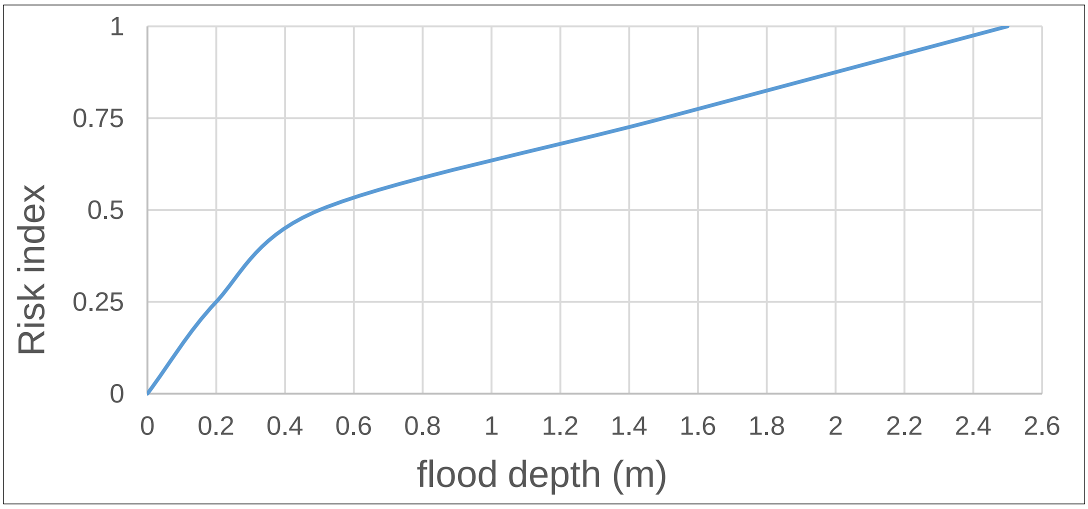

Figure 2. Flood depth and risk index relationship.

4.2 Probability of landslide.

The results of probability model which was based on rainfall induced infiltration condition, geographical conditions and geological formations of the area are described Figure 4. According to records of landslide activity in Laos's, it can be deduced that landslide phenomenon events is closely related to the probability of exceeding values of rainfall.

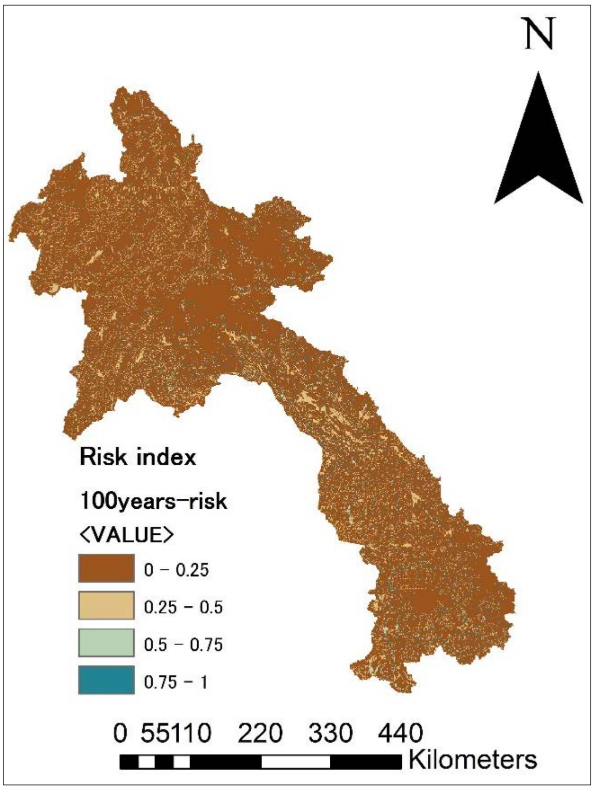

Figure 3. Flood risk map

Figure 4. Probability of landslide map.

4.3 Land use impact to flood

According to Wan and Yang (2007), it can be concluded that land use which is changed by the human activity such as deforestation and cultivation of crops is one of the major drivers in an increased frequency of flooding incidents. At small spatial scales (<$2km^2$) deforestation has been reported to have strong correlation with increase in flooding (Bosch and Hewlett, 1982). However, in the larger catchments it has been reported no significant change in flooding pattern occurred with deforestation (Beschta et al., 2000).

4.3.1 Land use change's data

In order to assess the impact of different land use scenario on the flood hazard was included in the map according to the study area, Reduced forest and increased cropland effects is investigated as well to get a better understanding on flood hazard. The reduction of forest is set to be the worst scenario as all the forest area could be turned to be cropland. According to Ceballos et al. (2003), Choung (2008), their studies show that the suitable geo-environmental factors for crop field is slope angle. Their studies shows that the slope around 6-12 percent will increase the growth of vegetation and in this scenario it was design for the forest area with below slope angle of 12 percent to be changed to cropland and other forest area that higher than 12 percent were set to remain. This is understood to increase the risk of flooding it the area of deforestation.

4.3.2 Results

From the results it shows varying change in flood hazard map distribution as shown in Figure 5. The characteristic of flood hazard had impacts from the land use change as the low risk area (0- 0.25 risk index) were decreased around 21.2 percent, medium risk area (0.25-0.5 risk index) were decreased around 16.6 percent, intermediate risk area (0.5-0.75 risk index) were increase around 7.8 percent and high risk area (0.75-1.0 risk index) were increased to16.8 percent as shows in Table 3.

If we consider the effect of overall land use change to flood hazard map, the overall impact of hazard map was increased significantly. This is because, forest area can slowdown rainfall-runoff and without it all the rainfall-runoff water directly go from the upstream to the downstream without any storage or slowdown factor, Therefore, the risk area in downstream are expanded and some areas has lower water depths and if heavy rainfall were to increase,this can lead to increase of the risk. However there are several non-low responsive area with it where no change was recorded in flood hazard as to land use change.

Table 3. Characteristic of flood hazard change.

Risk parameter	Scenario (km)	Observe (km)	Percent (%)
0-0.25 (low risk)	76882	97550	-21.2
0.25-0.5 (medium risk)	13561	16255	-16.6
0.5-0.75 (intermediate risk)	8507	7889	7.8
0.75-1 (high risk)	8013	6860	16.8

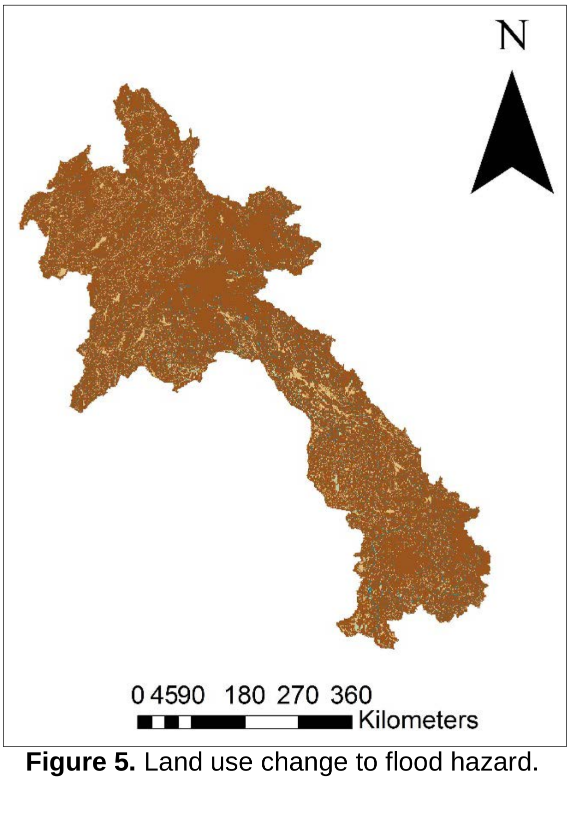

Figure 5. Land use change to flood hazard.

4.4 Climate change impact to flood

Climate change is expected to increase both in magnitude and frequency which leads to extreme precipitation events and give rise to higher river floodings. Several studies have shown that climate has been a contributing factor to flood risk because of raise in the precipitation amount compared to relative average annual rainfall (Hirabayashi et al., 2008). Therefore the basin scale assessment of climate change impacts on flood plays an important role in formulation and evaluation of adaptation and mitigation strategies for flood risk management. In this study we will estimate the impact of climate change to flood hazard map by comparing 2 hazard map of 50 years and 100 years rainfall return period and the objectives are to find the sensitive area from intense rainfall.

According to the result (Figure. 6) shown, the percentage of increase in water depth from 50 years to 100 years flood hazards is lower than 25 percent with only few areas being very sensitive to the climate change. These areas shows the high percentage increase of water depth, which lead to increase of flood risk and it need to taken into consideration for flood management plan or to apply for counter measurements. However, it should be noted that other areas may shows low percentage of increase in water depth because of the difference of heavy rainfall and water depth from 50 years and 100 years are already high and did not change that much in between the periods of these two maps. Hence, this map was illustrated only from low to mid-range or mid to high-range risk of water depth. In addition, southern part of Laos have a lot of areas that are sensitive to the climate change, these area have to be put in areas that require urgent attention.

Figure 6. Climate change impact on flood.

5.5 Integrate Flood Hazard in Laos

The proposed methodology linearly combines the selected hazard maps with taking into account the risk parameter. This involves superimposing the hazard maps with mean value of parameter weights. Eventually, the flood hazard map is created (Figure 7), defining 4 classes of flood vulnerability (low, medium, intermediate and high risk). Classification is based on the inherent information derived from linearly combined data. However, the flood risk map as shown in Figure 8 was prepared by comparing maximum values of each grid among 4 hazard maps. The target of this map is to illustrate the susceptibility area of flood, since Figure 7 could describe the average of overall susceptible areas.

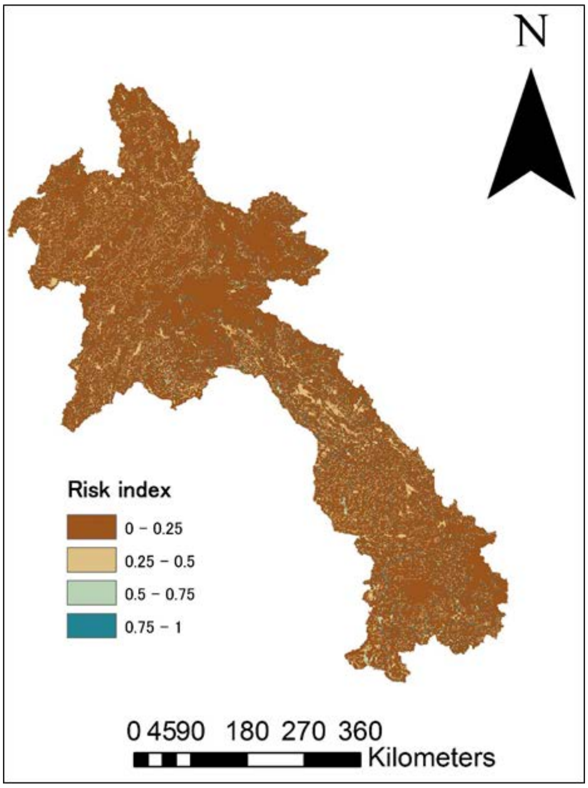

Figure 7. Flood risk map.

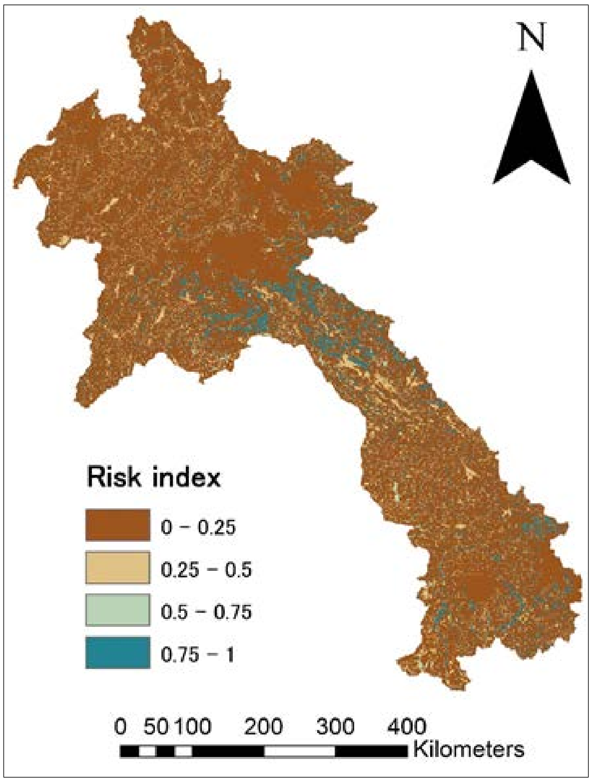

Figure 8. Maximum value of risk index from each grid.

The proposed methodology for the estimation of flood hazard areas can be a useful tool for the mitigation of the devastating impact of floods. The comparison between Figures 7 and 8 has revealed valuable information for the influence and the weight of each parameter in assessing the flood hazard areas. We classify the flood risk index into 4 levels (low risk, medium risk, intermediate risk and high risk). The area with high or intermediate risk level mainly concentrates on the river and flood plains which are designed to draw off and store floodwater. The region in intermediate and medium risk level is mainly located on the central part and southern part. The northern area has medium and low risk, which indicates the place is seldom affected by flood. Thus these methods may appear to be reliable if an additional tool is needed. According to hydrological simulations under different flood scenarios it also can be a valuable tool, especially in areas where such data are available. An additional contribution of this flood simulation models is that a direct estimation of the role of various criteria in a flood event can be tabulated. The main advantage of the proposed flood risk index method is its ability to provide overall assessment on flood hazard areas.

5 CONCLUSIONS

This study was developed by incorporating flood risk index of integrated 4 flood hazards.The map has the ability to show the sensitive area from different kind of hazard, which is a significant information to flood risk management in designing important models such as infrastructure, industrial area or to make countermeasure plans. However, we still have many factors that we did not include in this study for example population density. It is better for further study to be done to compare the output result with other methodology. This is to ensure a more detailed discussion about the accuracy of the model and also to determine land use change according climate scenario.

ACKNOWLEDGEMENTS

This research was partially supported by the Ministry of Education, Science, Sports and Culture, Grant-in-Aid for Scientific Research (B), 2015-2017 (15H05218, So Kazama). The Environment Research and Technology Development Fund (S-14) of the Ministry of the Environment, Japan. Advancing Co-design of Integrated Strategies with Adaptation to Climate Change (ADAP-T) of JST/JICA, SATREPS.

REFERENCES

Baird. & Shoemaker. (2007). Unsettling Experiences: Internal Resettlement and International Aid Agencies in Laos. *Development and Change*, 38, 865–888.

Bakker, E.J. (1990). *Demand for Rainfall Insurance in the Semi - Arid Tropics of India,* Resource Management Program Economics Group, Progress Report – 101. International Crops Research Institute for the Semi - Arid Tropics. Patancheru P.O. Andhra Pradesh 502324. India.

Bapalu, G. V. & Sinha, R. (2005). GIS in flood hazard mapping: A case study of Kosi River Basin, India. *GIS Development Weekly*, 1(13), 1-3.

Beschta, R.L., Pyles, M.R., Skaugset, A.E. & Surfleet, C.G. (2000). Peak Flow Responses to Forest Practices in the Western Cascades of Oregon, USA, *Journal of Hydrology,* 233, 102-120.

Bosch, J.M & Hewlett, J.D. (1982). A review of Catchment Experiment to Determine the Effect of Vegetation Changes on Water Yield and Evapotranspiration, *Journal of hydrology,* 55, 3-23.

Dewan., Sanjeev., Shi., Charles., Gurbaxani. & Vijay, (2007). Investigating The Risk–Return Relationship of Information Technology Investment: Firm-Level Empirical Analysis. *Management Science*, 53(2), 1829-1842.

Hirabayashi, Y., Kanae, S., Emori, S., Oki, T. & Kimoto M. (2008). Global Projections of Changing Risks of Floods and Droughts in a Changing Climate. *Hydrological Sciences Journal*, 53(4), 754-772.

Kashiwa, S., Asaoka, Y., Akira. & Kazama. (2010). Flood Analysis Modeling of Snow Melting and Estimation, *Proceedings of the Rivers Technology*, 16, 289-294.

Kawagoe, S., Kazama, S. & Sarukkalige, P.R. (2010). Probabilistic Modelling of Rainfall Induced Landslide Hazard Assessment, *Hydrology and Earth System Sciences,* 14, 1047–1061.

Kazama, So., Hyejin, K. & Sawamoto M. (2004). Uncertainty of Morphological Data for Rainfall -Runoff Simulation. *Proceedings of the International Conference on sustainable Water Resources Management in the Changing Environment of the Monsoon Region*, 1, 400-406.

Liu, Q.X., Jindra, M., Ueda, H., Hiromi, Y. & Hirose, S., (2003). Drosophila MBF1 is A Co-Activator for Tracheae Defective and Contributes to the Formation of Tracheal and Nervous Systems. *Development,* 130(4), 719-728.

Ono, K., Akimoto, T., Gunawardhana, L.N., Kazama, S. & Kawagoe, S. (2011). Distributed Specific Sediment Yield Estimations in Japan Attributed to Extreme-Rainfall-Induced Slope Failures under a Changing Climate. *Hydrology and Earth System Sciences,* 15, 197–207.

Schumann, A.H. & Geyer, J. (2000). GIS-Based Ways for Considering Spatial Heterogeneity of Catchment Characteristics. Physics and Chemistry of the Earth, Part B: Hydrology, *Oceans and Atmosphere*, 25, 691-694.

Veen, A.V.D. & Logtmeijer, C. (2005). Economic Hotspots: Visualizing Vulnerability to Flooding Hazards. *Natural Hazards*, 36(65).

Wan, R. & Yang, G. (2007). Influence of Land Use/Cover Change on Storm Runoff—A Case Study of Xitiaoxi River Basin in Upstream of Taihu Lake Watershed. *Chinese Geographical Science*, 17, 349-356.

Zerger, A. (2002). Examining GIS Decision Utility for Natural Hazard Risk Modelling. *Environmental Modelling & Software*, 17, 287–294.

Proceedings of the 37th IAHR World Congress
August 13 – 18, 2017, Kuala Lumpur, Malaysia

DAM FLOOD RISK ASSESSMENT BASED ON SET PAIR ANALYSIS- VARIABLE FUZZY SETS (SPA-VFS) MODEL

YU CHEN[(1)] & PENG ZHI LIN[(2)]

[(1,2)] State Key Laboratory of Hydraulics and Mountain River Engineering,
Sichuan University, Chengdu, China
rainchen393@hotmail.com; cvelinpz@126.com

ABSTRACT

Flood is considered to be one of the most widely distributed natural disasters to life and property in the world. In recent decades, continuously increasing flood damages and losses remain at high level. Dam break caused by flood is an important dam safety problem. Therefore, dam flood risk assessment is an essential analytical step in reducing dam-break flood damages and losses. Efforts to reduce the flood risk require appropriate dam flood risk assessment method. The flood risk can be expressed as a function and a product of hazard and vulnerability. There is no unique assessment procedure for flood disaster. Thus, the comprehensive risk assessment that takes into account the hazard and vulnerability is gaining more and more attention in the field of flood risk management. On the basis stated, this paper proposes a comprehensive risk assessment way based on set pair analysis (SPA) and variable fuzzy sets (VFS) theory (namely SPA-VFS for short) to assess the dam flood risk. The practical application demonstrates that the flood disaster risk assessment model based on SPA-VFS is visual, simple and general, and its result is reasonable and its computation precision is high. Thus, it has bright prospects of application for comprehensive flood risk assessment, and moreover has potential to be applicable to comprehensive risk assessment of other natural disasters.

Keywords: SPA; VFS; flood risk assessment; dam.

1 INTRODUCTION

The dam break caused by flood often brings catastrophic damages and enormous impacts to human, society, economy and environment which have become a world-wide problem. Therefore, the dam flood risk is highly important for dam safety management authorities. The increasing flood occurrence necessitates the development of dam flood risk assessment. The purpose of dam flood risk assessment is helpful in obtaining accurate risk grades, which is a reasonable basis of strengthening implementation for decision makers.

Numerous risk assessment methods have been developed, include the mathematical statistic analysis method, the uncertainty method, the decision-making analysis method, and so on (Jiang et al., 2009). In recent years, more and more researchers pay attention to the uncertainty method, such as SPA method, VFS method and etc. In this study, we establish a conceptual framework of dam flood disaster risk assessment indicator system and use the improved SPA-VFS model to get access to the flood risk grades of the studded dams.

2 METHODOLOGY

Before we carry out the dam flood risk assessment based on SPA-VFS model, a simple overview on SPA and VFS is necessary.

2.1 SPA

The basic idea of SPA is to analyze the features of a set pair and to set up a connection degree formula of these two sets including identity degree, discrepancy degree and contrary degree under certain circumstances, which can be given as follows:

$$\mu_{(A-B)} = a + bi + cj \qquad [1]$$

where $\mu_{(A-B)}$ is the connection degree of the set pair; $a+b+c=1$, and a,b,c represent the degrees of identity, discrepancy and contrary, respectively. i Is the coefficient of and its range b and its range is $[0,1]$. j Is the coefficient of and its range is $[-1,0)$, and it shows the opposite instance to a. This is the general connection degree, which is also called three-element connection degree (Zou et al., 2013; Guo et al., 2014). And the five-element connection degree can be achieved according to the develop ability principle of original connection degree as follows:

$$\mu_{(A-B)} = a + bi + cj = a + b_1 i_1 + b_2 i_2 + b_3 i_3 + cj \quad [2]$$

where b_1, b_2, b_3 are the components of discrepancy degree, denoted as the different grades of discrepancy degree, such as mild discrepancy, discrepancy and severe discrepancy, respectively; $a + b_1 + b_2 + b_3 + c = 1$, i_1, i_2, i_3 are the uncertainty component coefficients of discrepancy degree and $i_1, i_2, i_3 \in [-1, 1]$; $j = -1$.

2.2 VFS

VFS theory is a new way to ascertain the membership degree and function of a fuzzy subset in the domain of interest. Let the number of sample sets be denoted by n, then

$$X = \{x_1, x_2, \ldots, x_n\} \quad [3]$$

where x is the sample set.

The indicator eigen value of the sample j can be expressed as

$$x_j = \{x_{1j}, x_{2j}, \ldots, x_{mj}\} \quad [4]$$

where m is the number of indicators.

Then the sample set can be expressed as

$$X = (x_{ij}) \quad [5]$$

where x_{ij} is the eigen value of the indicator i of the sample j; $i = 1, 2, \ldots, m$; $j = 1, 2, \ldots, n$.

In order to define VFS, let a fuzzy subset A in the domain is of interest (Wang et al., 2014). In continuum on the number axis, a number $\mu_A(A)$, $\forall u \in U$, is named as the relative membership degree of u to A with attraction. Consider X_0 as interval $[a, b]$ of attraction domain of V on the number axis, which means $0 < D_A(u) \le 1$, then, X is a certain interval $[c, d]$ including $X_0 (X_0 \subset X)$.

2.3 SPA-VFS

VFS theory, a convenient tool for processing random, fuzzy and multi-indicator problems, had been used in the field of risk evaluation. It can express the nonlinear relationship between evaluation indicators and risk grades, but cannot solve the information duplication problem caused by related assessment indicators, thus many other theories were combined for various improvements. SPA, a system theory using a connection number to process the uncertainty caused by fuzzy, random and incomplete information uniformly, was used in this paper to calculate the relative membership degree.

The VFS and its calculation were based on the membership function. Thus, on how to determine the membership function was one of the important questions of VFS theory. The membership function reflects how people consider a fuzzy problem. The idea of SPA is that it provides a new establish membership function, and construct the SPA based VFS theory which was called SPA-VFS method in this paper (Zhou, 2010).

The steps of SPA-VFS method are as follows:

(1) Determine the dam flood risk assessment indicators and assessment standards. The sets of indicators and standards are looked as a set-pair. The connection degree between the two sets can be used to evaluate the grades of the assessing values. The assessment sample matrix is $X = (x_{ij})_{n \times m}$, $i = 1, 2, \ldots, n; j = 1, 2, \ldots, m$ and standard matrix $S = (s_{jk})_{m \times k}$, $j = 1, 2, \ldots, m; k = 1, 2, \ldots, K$, where n, m, K are the total number of samples, assessment indicators and assessment grades, respectively. And x_{ij} is the eigen value of indicator j of the sample x_i, s_{jk} is the standard of indicator j for the grade k.

(2) Calculate the weights of the indicators $w = (w_j)$, $j = 1, 2, \ldots, m$ based on analytic hierarchy process (AHP), where w_j is the weight of indicator j, and obviously $\sum_{j=1}^{m} w_j = 1, 0 \le w_j \le 1, j = 1, 2, \ldots, m$. More details about AHP can be seen in (Pedcris and Masahiko, 2013).

(3) Calculate the single indicator connection degree and synthetic connection degree based on SPA. The basic principle of SPA-VFS is that, using connection degree of SPA between the sample indicator x_{ij} (the indicator j of the sample x_i) and the assessment grade k to construct the relative difference function of VFS. Thus, to simplify the computational procedure of VFS as well as to improve the reliability of quantitative results, the quantitative analysis can be expressed as the synthetic connection degree μ_{ijk} for the set pair, and μ_{ijk} can be calculated as follows:

$$\mu_{ijk}=\begin{cases}1-2\cdot\left|\dfrac{s_{j(k-1)}-x_{ij}}{s_{j(k-1)}-s_{j(k-2)}}\right|, & \text{if } x_{ij} \text{ locates in the adjacent } k-1 \text{ grade}\\ 1, & \text{if } x_{ij} \text{ locates in the adjacent } k \text{ grade}\\ 1-2\cdot\left|\dfrac{x_{ij}-s_{jk}}{s_{j(k+1)}-s_{jk}}\right|, & \text{if } x_{ij} \text{ locates in the adjacent } k+1 \text{ grade}\\ -1, & \text{if } x_{ij} \text{ locates in the other intensity grades}\end{cases} \qquad [6]$$

where μ_{ijk} is the single indicator connection degree that represents the correlation between the set pair x_{ij} and grade k. After the calculations of Eq. (6), we get access to the synthetic connection of degree μ_{ik}:

$$u_{ik(\text{synthetic})}=\sum_{j=1}^{m} w_j\cdot u_{ijk} \quad 1\le i\le n, 1\le k\le K \qquad [7]$$

where $u_{ik(\text{synthetic})}\in[-1,1]$. And the more indicators x_{ij} differs from the grade k, the closer for value μ_{ik} to become -1, and then it becomes more impossible for the indicator x_{ij} to belongs to the grade k and vice versa. So it is a type of relative membership degree of the VFS (Guo et al., 2014).

(4) Determine the relative membership degree based on VFS. Based on VFS and μ_{ik} obtained from Eq. (7), the corresponding relative membership degree μ_{ik} between the indicator x_{ij} and grade k can be calculated as:

$$u_{ik}=0.5+0.5\cdot u_{ik(\text{synthetic})} \quad 1\le i\le n, 1\le k\le K \qquad [8]$$

(5) Assess the samples. According to the rank feature value method (Chen and Guo, 2006), the assessment grade feature value H_i can be calculated as:

$$u'_{ik}=u_{ik}/\sum_{k=1}^{K}u_{ik}, \quad k=1,2,\ldots,K \qquad [9]$$

$$H_i=\sum_{k=1}^{K}k\cdot u'_{ik} \qquad [10]$$

The flood risk grades are divided into five grades of very low (I), low (II), moderate (III), high (IV) and extreme (V). Based on the calculation results of Eq. (10), we can assign the qualitative grades to each dam according to the following rule (Guo, 2006):

$$\begin{cases} 1.0 \le H \le 1.5, & \text{risk grade=I} \\ 1.5 < H \le 2.5, & \text{risk grade=II} \\ 2.5 < H \le 3.5, & \text{risk grade=III} \\ 3.5 < H \le 4.5, & \text{risk grade=IV} \\ 4.5 < H \le 5.0, & \text{risk grade=V} \end{cases} \quad [11]$$

3 CASE STUDY

To test the usability of the proposed model, the Dadu river basin in China was taken as the study area, and the dams as the basic assessment units. Based on the disaster system theory and the consideration of engineering properties of the dam and natural properties of the flood disaster, three hazard indicators are selected, and they were reservoir capacity (C1), dam height (C2) and dam age (C3). We also selected three vulnerability indicators, including population density (C4), GDP density (C5), and predicted damage (C6). C6 was a qualitative expression, and in the calculation process, we use the highest water level of reservoir (HWL) to describe it.

Busigou, Shuangjiangkou, Luding, Dagangshan, Longtoushi, Pubugou dams in Dadu river basin were chosen as examples. According to the historical information, statistical yearbook and expert judgments, the necessary assessment indicator data were collected. Meanwhile, the assessment standards for indicators were shown in Table 1.

Table 1. Standards for flood risk assessment of dams considered for this study.

Risk indicators	1(Very Low)	2 (Low)	3(Moderate)	4 (High)	5(Extreme)
reservoir capacity ($10^6 m^3$)	<1	1-10	10-100	100-1000	>1000
dam height (m)	<15	15-70	70-166	166-300	>300
dam age (a)	<5	5-45	45-85	85-115	>115
population density (population/km^2)	<10	10-100	100-250	250-500	>500
GDP density (billion yuan/ km^2)	<10	10-40	40-80	80-100	>100
predicted damage (highest water level of reservoir (m))[a]	<UL	UL-DFL	DFL-CFL	CFL-DH	>DH

a UL-Upper water level for flood control; DFL-Design flood level; CFL-Checked flood level; DH-Dam height.

The indicator weights are reasonably determined as follows:

$$w_1 = (0.190,\ 0.111, 0.032, 0.059, 0.130, 0.478) \quad [12]$$

Eqs. (6)-(11) were used step by step to complete the comprehensive dam flood risk assessment. For saving space, only the assessment process of Pubugou dam was shown as follows, and its single indicator connection degree denoted by μ_{single} was calculated as:

$$\mu_{\text{single}} = \begin{bmatrix} -1 & 0.024 & 1 & -0.024 & -1 \\ -1 & -1 & 0.791 & 1 & -0.791 \\ 0.85 & 1 & -0.85 & -1 & -1 \\ -0.161 & 1 & 0.161 & -1 & -1 \\ -0.05 & 1 & 0.05 & -1 & -1 \\ -1 & -1 & 0.919 & 1 & -0.919 \end{bmatrix} \quad [13]$$

And its synthetic connection degree denoted by $\mu_{\text{synthetic}}$ was calculated as:

$$\mu_{\text{synthetic}} = (-0.768, -0.363, 0.706, 0.363, -0.938) \quad [14]$$

Then we get its relative membership degree denoted by μ_1 as:

$$\mu_1 = (0.116, 0.3185, 0.853, 0.6815, 0.031) \quad [15]$$

And get the normalized synthetic relative membership degree μ_1' as:

$$\mu_1' = (0.058, 0.159, 0.427, 0.341, 0.015) \quad [16]$$

And the assessment grade feature value H_1 for Pubugou dam were calculated as:

$$H_1 = \sum_{k=1}^{5} k \cdot \mu_k' = 0.058\times1 + 0.159\times2 + 0.427\times3 + 0.341\times4 + 0.015\times5 = 3.096 \quad [17]$$

Finally, by comparing the value of H_1 and Eq. (11), we can rank the flood risk grade of Pubugou dam as III. And the flood risk assessment results of other dams are shown in Table 2.

Table 2. Results of the flood risk grades of 6 dams.

Dam	Busigou	Shuangjiangkou	Luding	Dagangshan	Longtoushi	Pubugou
Risk grade	II	II	III	III	III	III

4 CONCLUSIONS

In accordance with the principle of flood disaster risk, 6 risk evaluation indicators are selected under the consideration of the key elements such as the dangers of hazard factors and vulnerability of disaster-bearing bodies. Then the weights of all the risk factors are determined based on AHP. Furthermore, the quantitative analysis is made on the risk factors with the SPA-VFS model, which can determine the relative membership degree function of VFS by using SPA. Through the relevant calculation, the flood risk feature values and risk grades of each dam can be obtained. The results indicate that the SPA-VFS method is easy, reasonable and operative for dam flood risk assessment. The total dam flood risk indicator represents a useful indicator which allows for the ranking of “dams more at risk” than others, but it is, of course, highly dependent on receptor-related risk analysis and the weighting process. The results obtained in this study specifically offer new insights and possibility to carry out an efficient way for flood disaster prevention and mitigation. It also provides scientific reference in flood risk management for Dadu River Baisn.

ACKNOWLEDGMENTS

The research reported herein is funded by National Science Foundation of China (Grant No. 41501554), National Grand Fundamental Research 973 Program of China (Grant No. 2013CB036401) and British Council GII.

REFERENCES

Chen, S.Y. & Guo, Y. (2006). Variable Fuzzy Sets and its Application in Comprehensive Risk Evaluation for Flood-Control Engineering System. *Fuzzy Optimization and Decision Making*, 5(2), 153-162.

Guo, E.L., Zhang, J.Q., Ren, X.H., Zhang, Q. & Sun, Z.Y. (2014). Integrated Risk Assessment of Flood Disaster based on Improved Set Pair Analysis and the Variable Fuzzy Set Theory in Central Liaoning Province, China. *Natural Hazards*, 74(2), 947-965.

Guo, Y. (2006). Research on Application of Engineering Fuzzy Sets Theory in Water Resources and Flood Control System, *Ph.D thesis*. Dalian University of Technology.

Jiang, W.G., Deng, L., Chen, L.Y, Wu, J.J. & Li, J. (2009). Risk Assessment and Validation of Flood Disaster based on Fuzzy Mathematics. *Progress in Natural Science*, 19(10), 1419-1425.

Pedcris, M.O. & Masahiko, F. (2013). A Localized Disaster-Resilience Index to Assess Coastal Communities based on an Analytic Hierarchy Process (AHP). *International Journal of Disaster Risk Reduction*, 3(1), 62-75.

Wang, Y.K., Sheng, D., Wang, D., Ma, H.Q., Wu, J.C. & Xu, F. (2014). Variable Fuzzy Set Theory to Assess Water Quality of the Meiliang Bay in Taihu Lake Basin. *Water Resources Management*, 28(3), 867-880.

Zhou, J.F. (2010). SPA–Fuzzy Method based Real-Time Risk Assessment for Major Hazard Installations Storing Flammable Gas. *Safety Science*, 48(6), 819-822.

Zou, Q., Zhou, J.Z., Zhou, C., Song, L.X. & Guo, J. (2013). Comprehensive Flood Risk Assessment based on Set Pair Analysis-Variable Fuzzy Sets Model. *Stochastic Environmental Research and Risk Assessment*, 27(2), 525-546.

EVALUATION ON THE PHYSICO-CHEMICAL AND BACTERIOLOGICAL CONTAMINATION OF THE FLOOD WATER AFTER THE HEAVILY FLOOD INCIDENCE AT THE PAHANG RIVER, MALAYSIA

KAH YEE LIM[1], NOR AZAZI ZAKARIA[2] & KENG YUEN FOO[3]

[1,2,3] River Engineering and Urban Drainage Research Centre (REDAC), Penang, Malaysia.
limkahyee92@gmail.com; redac01@usm.my; k.y.foo@usm.my

ABSTRACT

Floods are the most significant disasters which have brought miseries to the life of thousands of Malaysians, and inflicted damages worth several millions of ringgit a year. The severe flood incidence in 2014 had submerged nearly half of the country in water for one month. During this period, the quality of the river water has deteriorated significantly, with elevated levels of fecal indicators and microbial pathogens in the flood water. In this work, the hydrologic sampling has been conducted according to the United States Environmental Protection Agency (USEPA) standard protocol along the Pahang River. Water quality parameters, including the pH and dissolved oxygen (DO) are measured in-situ, while the analytical determination of biological oxygen demand (BOD_5), chemical oxygen demand (COD), ammonical-nitrogen (NH_3-N) and total suspended solids (TSS) are determined according to the ex-situ standard methods. Results show that the pH, DO, BOD_5, COD, TSS and NH_3-N were ranged between 5.02-5.52, 3.15-4.48 mg/L, 1.00-31.00 mg/L, 4.00-125.00 mg/L, 3.50-37.75 mg/L and 0.91-2.11 mg/L, respectively. According to Interim National Water Quality Standard (INWQS) proposed by the Department of Environment (DOE), the major part of the river was categorized as class V, derived as highly polluted. The collected water samples detected high level of heavy metals content, in the descending order of: $Fe^{3+}>Zn^{2+}>Cr^{3+}>Pb^{2+}>Ni^{2+}>Cu^{2+}>Cd^{2+}$. Water supplies in the flood-prone regions were contaminated with low levels of *Escherichia coli*, *Salmonella typhimurium* and *Shigella flexneri*, ranging from ≤ 50 cfu/100 mL to 96 x 10^3 cfu/100mL. The available findings indicated that the Pahang River basin has been drastically altered by the flood events to which it places a pressing pressure on the morbidity, mortality, social and economical disruption, and establishment of better health-care facilities.

Keywords: Bacteriological parameter; flood; heavy metal; water-borne disease; water quality.

1 INTRODUCTION

Flood, defined as a body of water rising, swelling and overflowing onto low-lying lands, to overtop the levels of natural or artificial banks in river system by prolonged periods of rainfall, snowmelt, and short periods of intense rainfall and is by far the most critical natural disaster to impact Malaysia (McMichael et al., 2006). The worst flood event in 2014 is the most significant hazard in Malaysia for the last 50 years. It had devastated the East Coast states of Kelantan, Terengganu and Pahang, and affected nearly 200,000 of victims, with the infrastructure damages of RM 9.24 billion, 24 reported deaths while 8 are still missing (Akasah and Doraisamy, 2015).

These detrimental damages could be summarized into three major categories: hydraulic and hydrological alteration, chemical and morphological changes of the river system, and the great danger of floods has possible health implications of a large-scale contamination of water supply for human consumption (Chaturongkasumrit et al., 2013), leading to the widespread of communicable diseases. The seasonal changes of the dynamic equilibrium of hydrological system, especially by the introduction of industrial and municipal hazardous pollutants from farms, factories or residential areas would induce irreversible effects on the water quality as well (Dike et al., 2004).

Similarly, seasonal flood may provide suitable medium for the transmission of a wide variety of heterotrophic microorganisms. The urban flood water was found to be faecally contaminated, demonstrated by the elevated concentrations of fecal indicating bacteria (Eregno et al., 2016). As the river water comes ashore, the available water sources could become submerged, and potentially contaminated by the biological pollutants, including human and livestock manure, physical oand chemical toxicants. If these water containing disease-causing microorganisms is ingested, it may develop life-threatening health problems to the affected populations. These enteric pathogens accounts for a vast majority of the gastrointestinal illnesses at global level, and predominantly transmitted via the fecal-oral route (Ashbolt, 2004).

Collectively, the above alterations have raised aesthetic concern among the scientific community. This current study presents a snapshot of the physical, chemical and microbiological characteristics of the Pahang River water immediately following the 2014 heavy flood events in Malaysia. The focus of the initial effort was to compile a complete dataset of chemical and microbial constituents that encompassed the biological oxygen demand (BOD_5), chemical oxygen demand (COD), total suspended solids (TSS), ammonical-nitrogen (NH_3-N), dissolved oxygen (DO) and pH, as well as the likelihood and magnitude of microbial contamination across the flood water column along the Pahang River basin is taken into account.

2 METHODOLOGY

2.1 Site description and sampling scheme

Pahang River located at the eastern part of Peninsular Malaysia, between the latitude of N 2° 48' 45" and N 3° 40' 24" and between the longitude of E 101° 16' 31" and E 103° 29' 34", is the longest river in Malaysia, with the maximum length and breadth catchment of 459 km and 236 km, respectively. It is the major artery of the Pahang River basin, responsible for draining the water from this basin into the South China Sea (Sulaiman et al., 2010). Pahang River has a humid tropical climate, with the constant temperature of 25-27 ºC and an annual rainfall of 2,170 mm.

Figure 1. The study areas along Pahang River.

It is one of the most heavily flood affected area in Malaysia, and the most severe flood incidence took place in 2014. The sampling scheme is designed to cover a wide range of determinates of key sites, which reasonably represent the physicochemical and biological qualities of the Pahang River basin. Water samples were collected from accessible areas in industrial and residential areas located of Pekan, Kampung Pulau Keladi, Palok Hinai, Chenor and Temerloh, Pahang that were heavily destroyed (Figure 1).

Water samples were collected at each sampling site in sterilized high-density polyethylene (HDPE) bottles, previously cleaned by soaking in 10% of concentrated nitric acid (HNO_3) and rinsed in ultrapure water, by dipping each sample bottle at approximately 15 cm below the water surface, projecting the mouth of the container against the direction of flow. The samples were stored in an insulated box containing ice, and transported to the laboratory for immediate analysis.

2.2 Physicochemical and heavy metals measurements

The physicochemical parameters were assessed in according to the laboratory standard procedures (American Public Health Association, 1998). Hydrological parameters, including pH and dissolved oxygen (DO) were measured using a pH meter and YSI 556 MPS multi-probe system, respectively. The multi-probe meter and pH meter were calibrated before field sampling. Chemical analysis was performed according to the Standard Method of Water and Wastewater. The analytical determination of biological oxygen demand (BOD_5), chemical oxygen demand (COD), ammonical-nitrogen (NH_3-N) and total suspended solids (TSS) were determined according to the Luminescence measurement, Closed Reflux Colorimetric, Salicylate and Gravimetric standard methods, respectively, by using a spectrophotometer (HACH DR3900). All measurements were undertaken in triplicates. The water quality Standard for Malaysia (INWQS) is given as:

$$WQI = 0.22SIDO + 0.19SIBOD_5 + 0.16SICOD + 0.16SISS + 0.15SIAN + 0.12SIpH \quad [1]$$

Where:
WQI = Water Quality Index
SIDO = Sub-index DO
$SIBOD_5$ = Sub-index BOD_5
SICOD = Sub-index COD
SIAN = Sub-index AN
SISS = Sub-index TSS
SIpH = Sub-index pH

Sub-Index for DO (in % saturation):

SIDO = 0	For DO < 8	[2.1a]
= 100	For DO > 92	[2.1b]
= $-0.395 + 0.030DO^2 - 0.00020DO^3$	For 8 < DO < 92	[2.1c]

Sub-index for BOD_5:

$SIBOD_5 = 100.4 - 4.23BOD_5$	For $BOD_5 < 5$	[2.2a]
$= 108e^{-0.055BOD} - 0.1BOD_5$	For $BOD_5 > 5$	[2.2b]

Sub-index for COD:

$SICOD = -1.33COD + 99.1$	For COD < 20	[2.3a]
$= 103e^{-0.0157COD} - 0.04COD$	For COD > 20	[2.3b]

Sub-index for AN:

$SIAN = 100.5 - 105AN$	For AN < 0.3	[2.4a]
$= 94e^{-0.573AN} - 5\left\vert [AN - 2] \right\vert$	For 0.3 < AN < 4	[2.4b]
= 0	For AN > 4	[2.4c]

Sub-index for TSS:

$SISS = 97.5e^{-0.00676SS} + 0.05TSS$	For TSS < 100	[2.5a]
$= 71e^{-0.0016SS} - 0.015TSS$	For 100 < TSS < 1000	[2.5b]
= 0	For TSS > 1000	[2.5c]

Sub-index for pH:

$SIpH = 17.2 - 17.2pH + 5.02pH^2$	For pH < 5.5	[2.6a]
$= -242 + 95.5pH - 6.67pH^2$	For 5.5 < pH < 7	[2.6b]
$= -181 + 82.4pH - 6.05pH^2$	For 7 < pH < 8.75	[2.6c]
$= 536 - 77.0pH + 2.76pH^2$	For pH > 8.75	[2.6d]

The collected water samples were preserved by acidifying to pH < 2.0 with ultrapure nitric acid within 6 hours of collection to avoid microbial degradation of heavy metals. The heavy metals content was analysed according to the United States Environmental Protection Agency standard methods 200.8 and 6020, using an Inductively Coupled Plasma-Mass Spectrometry (ICP-MS).

2.3 Bacteriological detection

Water samples were analysed for the target presumptive bacterial pathogens using internationally accepted techniques and principles (Rompré et al., 2002). The collected samples were filtered through a 0.45 μm pore size membrane filter to remove insoluble particulate matter. A 0.2 μm membrane filter was applied for the collection of bacterial cells in the samples. It was aseptically transferred to Petri dishes containing the appropriate selective media, and incubated for 24 hours at 37°C. The bacteria were pelleted by centrifugation at 5000 × g for 15 min, re-suspended in 700 μL of 30% (v/v) glycerol in sterile distilled water, and stored at −80°C. Deoxyribonucleic acid (DNA) was extracted from each bacterial suspension after pelleting by centrifugation at 5000 x g for 15 min using a NucleoSpin® Tissue DNA extraction kit (Macherey-Nagel, Germany) according to manufacturer's protocol. The extracted DNA was used as the DNA template for further Polymerase Chain Reaction (PCR)-based analysis. The targeted genes were amplified by Polymerase Chain Reaction (PCR) using AmpliTaq polymerase. Electrophoresis of the amplified samples was performed in a 2.5% agarose gel followed by the examination using a UV trans-illuminator.

3 RESULTS AND DISCUSSIONS

3.1 Physicochemical and heavy metals measurement

The alterations of the physicochemical parameters in term of BOD_5, COD, DO, TSS, NH_3-N, pH and WQI of the river water after the heavily flood incidence are summarized in Table 1.

Table 1. The alterations of the physicochemical parameters of the Pahang River water.

Water quality parameters	Units	Flood incidence 2014	
		Before	After
Ph	-	7.22-7.62	5.02-5.52
Dissolved Oxygen (DO)	mg/L	6.10-6.93	3.15-4.48
Chemical Oxygen Demand (COD)	mg/L	10.12-13.30	4.00-125.00
Biochemical Oxygen Demand (BOD_5)	mg/L	1.13-1.97	1.00-31.00
Total Suspended Solids (TSS)	mg/L	0.00-0.30	3.50-37.75
Ammonical-Nitrogen (NH_3-N)	mg/L	0.11-0.19	0.91-2.11
Water Quality Index (WQI)		71.17	28.30
Class		III	V

BOD_5 and COD are two different parameters measuring the oxygen content of water to the recipients (Belhaj et al., 2015). BOD_5 is a viable tool to quantify the amount of dissolved oxygen required for the microorganisms to carry out biological decomposition of the organic matters in the water under an aerobic manner over a five-day periods (Juahir et al., 2011; Liu and Mattiasson, 2002). The variation of BOD_5 is dependable on the dynamic of aquatic life present in the river. In the present study, the concentration of BOD_5 in the water before the flood event was ranged within 1.13-1.97 mg/L, and it had raised significantly to 1.00-31.00 mg/L after the flood incidence, which was far higher than the World Health Organization (WHO) limit (10 mg/L).

The high value of the BOD_5 reading was mainly ascribed to the different anthropogenic pollutants, generated from domestic, commercial, industrial and agricultural activities, that had flushed excessive biological loadings into the nearby watercourse, resulting in the greater BOD_5 values (Mallin, 2000). Moreover, the sanitation systems at the local villages and runoff channels that were submerged during the flood event had contributed a significant impact to the dynamic of organic degradation process. Similar results were reported in Piedmont, United States which indicated that the BOD_5 value was drastically increased due to the submersion of 24 municipal treatment plants by flood water after the Hurricane Floyd in 1999 (Mallin et al., 2002). In Kaoping River, Taiwan has received a huge accumulation of organic pollutants from hog farms and domestic wastewater, resulting in the deterioration of water quality after the Typhoon Morakot in 2009 (Kuo et al., 2013).

Conversely, COD is the measurement of the oxidizable organic matters that is susceptible to oxidation by a strong chemical oxidant (Gandaseca et al., 2011). The measurement applies chromate as the oxidizing agent to degrade organic matters for the release of carbon dioxide into water (APHA, 1998). The COD content showed an upward trend, with a increase from 10.12-13.30 mg/L to 4.00-125.00 mg/L. The deterioration might be ascribed to the different sources of contamination by a wide range of chemical and organic fertilizers from the lowland of agricultural areas along the river (Eisakhani and Malakahmad, 2009). According to Gao et al. (2015), the COD concentration at Pu River, China reached to a high level of 100 mg/L during the flood period in 2013, which was due to agricultural non-point source pollution at a higher rainfall rate. The recorded COD levels at Pahang River and Pu River were far above from the INWQS threshold limit (50 mg/L), which is unfit for any diversity of aquatic life and ecosystems.

DO is one of the most important indicators of the ecological water health over a wide range of spatial and temporal scales. It is also a representative variable to measure the quantity of oxygen gas freely available in the surface water. It is primarily dependent of the water temperature, changing of hydro-meteorological conditions, and the intensity of the biological processes such as photosynthesis, respiration and decomposition of organic matters (Rajwa-Kuligiewicz et al., 2015). The DO levels before the flood disaster ranged between 6.10-6.93 mg/L, derived as “Class II”, and it fell under “Class III” (3.15-4.48 mg/L), which was derived as ‘Slightly Polluted” after the flood incidence (Table 2). According to Kataria et al. (2006) and Rani et al. (2004), the depletion of dissolve oxygen was due to the rising of microbial activity in the water source, and was also associated closely with the lower shellfish productions, and massive deaths of phytoplankton and zooplankton coupled with anaerobic decomposition of settled organic matters, and loss of habitat (Diaz and Rosenberg, 2008; Sidek et al., 2016a). A similar depletion of DO was found after the large-scale of flooding at Malak River, India (Sardar et al., 2010), Minjiang River, China (Pardue et al., 2005), and Little River Basin, Louisiana (Foo, 2015).

Table 2. The classification of water quality index according to Interim National Water Quality Standard (INWQS).

Parameters	Class				
(mg/L)	I	II	III	IV	V
pH	>7	6-7	5-6	5	<5
DO	>7	5-7	3-5	1-3	<1
BOD_5	<1	1-3	3-6	6-12	>12
COD	<10	10-25	25-50	50-100	>100
TSS	<25	25-50	50-150	150-300	>300
NH_3-N	<0.1	0.1-0.3	0.3-0.9	0.9-2.7	>2.7
WQI	>92.7	76.5-92.7	51.9-76.6	31.0-51.9	<31.0
Status	Clean	Slightly Polluted		Polluted	

Total suspended solids (TSS) were refered to small solid particles or impurities, which remain in the water suspension, typically in the size range of 0.1-10 mm (Sidek et al., 2016a). The TSS concentration showed a dramatic increase from 0.00-0.30 mg/L to 3.50-37.75 mg/L after the flood event. An average TSS concentration of 25 mg/L was known to be an indicator of unimpaired water quality, and 50 mg/L of TSS has the potential to affect the fish gill function and the penetration of light (Sidek et al., 2016b). The high amount of TSS could be related to minerals and soil being transported from the nearby landscape, and contributed by the dredging activities after a series of heavy rainstorm (Gandaseca et al., 2011; Nyanti et al., 2012). The observed TSS value had exceeded the INWQS recommended maximum threshold levels for TSS of 25 mg/L to support aquatic life in freshwater ecosystems (DOE, 1994).

In surface water, nitrogen could exist in many forms, including organic nitrogen, ammonia nitrogen, nitrite and nitrate nitrogen, with ammonical-nitrogen (NH_3-N) being the major form. The NH_3-N level along the Pahang River lied between 0.11-0.19 mg/L, which was derived as “Clean” according to the INWQS classification, and it had degraded into Class IV, which is derived as “Polluted”, with the range between 0.91-2.11 mg/L after the flood event. Typically, the natural water content of ammonical-nitrogen should be lesser than 0.1 mg/L for potable, industrial and agricultural applications. The detected concentrations of NH_3-N in Pahang River after flood incidence was well above the maximum permissible limit permitted by WHO (2011), and it serves as a concerned indication of the heavily nitrogenous inputs from the livestock farming, domestic sewage, industrial waste, and fertilizer runoffs, which had been washed into the river by high flowing rate of flood water (Al-badaii et al., 2012). This phenomenon was closely related to the rapid conversion of the oxides form of nitrogen compounds induced by the non-point source pollution from the surrounding area, and the fish-raising activities (Li et al., 2007).

pH plays a crucial role to enable normal biological and chemical processes, including photosynthesis and respiratory activities within the river systems (Patel, 2016). The flood water collected in Pahang River showed a destructive impact on the solution pH, from 7.22-7.62 to 5.02-5.52 after flood incidence. The pH values obtained after flood tragedy was slightly acidic than the suggested range proposed by National Water Standard for Malaysia (7.0-8.5) and WHO (6.5-8.5). The low pH value could be due to the accumulation of organic matters in flood water, and high decomposition activities of biotic and abiotic factors from the direct input of uric acid which increases the acidity of the river water (Özsoy and Örnektekin, 2009). The lowest pH value was recorded at the plantation areas consequence of the release of acid-forming substances, including sulphate, phosphate, and nitrates that were flushed by the huge flow of flood water into the river basin to significantly disturb the water pH (William and Booman, 2012).

Water Quality Index (WQI) serves as the basis for environmental assessment of water source in relation to the pollution loads, and designation of 5 classes of beneficial uses is provided by the Interim National Water Quality Standards for Malaysia (INWQS) (Foo, 2015). It combines the measurement of several water quality variables in such a way to produce a single score to represent the quality impairments or suitability of uses (Table 3). The water quality index of DOE was computed to establish the water quality status of the Pahang River. The values of WQI of the Pahang River was 71.17 (slight polluted), and it turned into Class V, derived as ‘very polluted’ after the flood event. The poor water quality in the flood water was resulted from the natural processes associated with the human activities, or linked to the industrial development. This fact illustrated the seasonal disturbance had involved in the regulation of BOD_5, COD, DO, TSS, NH_3-N and pH, contributing to the overall contamination of the river water. This river water is unsuitable for drinking, irrigation, livestock, recreational and industrial uses.

Table 3. Water classes and uses.

Class	Uses
Class I	Conservation of natural environment. Water Supply I- Practically no treatment necessary. Fishery I- Very sensitive aquatic species
Class II A	Water Supply II- Conventional treatment. Fishery II- Sensitive aquatic species.
Class II B	Recreational use body contact.
Class III	Water Supply III- Extensive treatment required. Fishery III- Common of economic value and tolerant species; livestock drinking.
Class IV	Irrigation
Class V	None of the above.

The dynamic variation of heavy metals (Cu, Cd, Cr, Fe, Ni, Pb and Zn) along the Pahang River was examined. Incidentally, these heavy metals revealed a great amplification, with the concentration level $Fe^{3+}>Zn^{2+}>Cr^{3+}>Pb^{2+}>Ni^{2+}>Cu^{2+}>Cd^{2+}$ in a descending order. These concentrations of Cd, Cr, Fe, Ni and Pb have exceeded the drinking criteria provided by the World Health Organisation (WHO) and U.S. Environmental Protection Agency (USEPA) health-based drinking criteria (Table 4).

The increase in the magnitude of Fe content can be attributed to the erosion from the metal processing industries and water runoffs from the residential areas. The peak concentration of Pb was ascribed to the natural weathering and anthropogenic sources, originated from the petro-chemical effluents and domestic sewage (Aziz et al., 2008). The detected of Ni and Zn were related to estuarine processes, and contaminants from intensive agricultural practice and mining activities, while Cu was deduced mainly from the electro-chemical effluents (DOE, 2011; Scragg, 2006). The excessive presence of these dissolved metals in the water sources might be harmful to the aquatic organisms, to retard the growth rates, and impair the equilibrium of the terrestrial ecosystems.

Table 4. Risk-based drinking water criteria of WHO and USEPA.

Elements	Concentration (mg/L)		Risk-based drinking water criteria (mg/L)	
	Before Flooding	After Flooding	WHO (2011)	USEPA (2009)
Cd	-	0.22	0.003	0.005
Cr	-	0.43	0.050	0.100
Cu	0.03	0.26	2.000	1.300
Ni	-	0.28	0.070	0.100
Pb	0.02	0.36	0.010	0.015
Zn	0.07	0.75	3.000	5.000
Fe	0.59	4.66	35.000	0.300

3.2 Identifications of bacterial pathogens in flood water

The excessive alteration of the water quality during the flood event presents a great possibility of the biological deterioration of the river water that might have serious impact to the public health. The qualitative and quantitative assessment of bacterial pathogens were conducted using the Polymerase Chain Reaction (PCR) analysis, and the images are described in Figure 1.

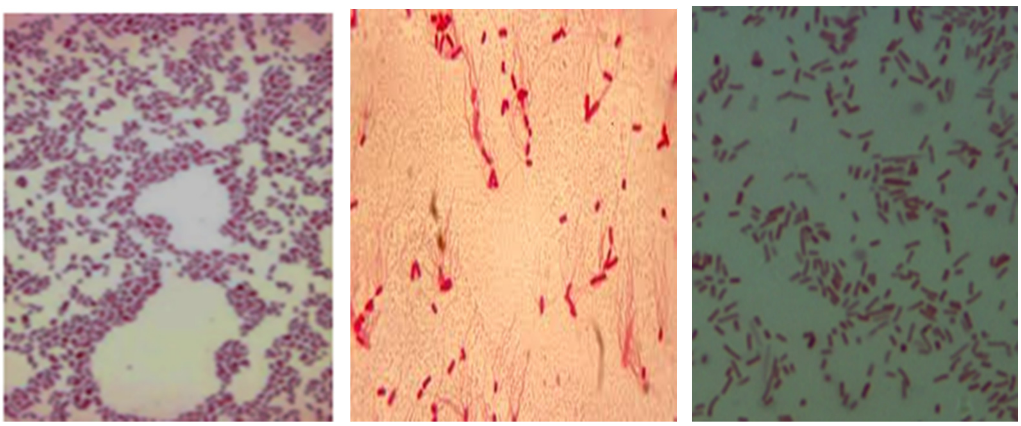

(a) (b) (c)

Figure 1. Detection of (a) *E. coli*, (b) *Salmonella spp*. and (c) *Shigella spp*. in flood water.

Microbial quality is often a source of impairment of the compliance of drinking water supply. The flood water had been found to be contaminated by microbes, with the detection of *Escherichia coli* (*E. coli)* (96 x 10^3 cfu/100 mL), *Salmonella spp.* (≤ 50 cfu/100 mL) and *Shigella flexneri* (125 cfu/ mL). The highest distribution of these microorganisms were expected to be originated from both point and non-point sources of pollution, including the discharges of water treatment plants, non-collective sewage systems or emissions from the hospitals, livestock, farming and industrial activities (Gasim et al., 2005).

A similar phenomenon has been recorded during the 2011 flood in Thailand, with the detection of E. coli, Leptospira spp., Shigella spp., and V. cholera from the water supply system, denoted the total bacterial load of 4.08-6.44 log cfu/ mL (Chaturongkasumrit et al., 2013). The flood water from Malad River and Ciliwung River, India have recorded the distribution of total coliform, fecal coliform and E. coli of 1.1 x 10^3 -1.6 x 10^4, 10^5 -10^6 and 0.2 x 10^3 – 1.1 x 10^3 cfu/100 mL, respectively after a flood event in 2002, that were well above the SW II-waters standards (100/100 mL MPN) (Phanuwan et al., 2006; Sardar et al., 2010), while the presence of E. coli, Shigella, Salmonella and Staphylococcus aureus, with the range of 18 – 96 cfu/ mL was detected in the flood water in River Indus, Pakistan (Baig et al., 2012).

This elevated microbial pathogens caused by the flood waters at the upstream had a deleterious effect on the human health (Hill and Sobsey, 1998). According to the World Health Organization (WHO), the mortality of flood-borne diseases has exceeded 5 million people per year, and with reference to the Environmental Protection Agency (2004) criteria of recreational water, the value of *E. coli* discovered in the flood water has exceeded the limit of 1 cfu/ mL, to cause diarrhoea and gastroenteritis related infections. The discovery of *Salmonella spp.* in the flood water which is a zoonotic pathogens, illustrates a higher health risk for the transmission of salmonellosis and typhoid fever during the flood event. The amount of *Shigella spp.* spotted in the flood water should not be underestimated, due to the ability to grow extensively at warmer temperatures, and reach to a population size of about 10^8-10^9 per gram or millilitre within 6-18 hours (Niyogi, 2005). The high level of *Shigella spp.* would lead to shigellosis and bacillary dysentery to a vulnerable population. In a survey conducted after the Hurricane Floyd in 1998, the microbial-induced illnesses, including diarrhoea, asthma, gastrointestinal and respiratory disease were significantly higher at the flood affected area. Additionally, the widespread of pathogenic microorganisms through the flood water would induce flood-related health problems, including skin rash, joint aches, and transmission of intestinal nematode infections to agricultural workers, and consumers of flood water irrigated crops with faecal bacterial and protozoan diseases; cholera or viral infections, viral gastroenteritis and hepatitis (Centers for Disease Control and Prevention, 2000).

4 CONCLUSIONS

This study established the evaluation of water quality data, and distribution of pathogenic bacteria of the Pahang River basin after the most severe 2014 flood incident during the last 50 years. The biochemical oxygen demand (BOD_5), chemical oxygen demand (COD), ammonical-nitrogen (NH_3-N), total suspended solids (TSS), and heavy metals content after the flood event are significantly increased. During this period, the water supply is unfit for both daily sanitation and consumption. This extreme disaster played a threatening role to the transmission of *Escherichia coli* (*E. coli)*, *Salmonella spp.* and *Shigella spp*. contaminating the water supply system, insinuating the potential of widespread of flood-borne illnesses. Continuously water quality monitoring is crucial to be carried out, and immediate measures should be undertaken by the National Reserves authorities to ensure that the Pahang River is well-protected from further contamination and deterioration.

ACKNOWLEDGMENTS

The authors acknowledge the financial support provided by the Ministry of Higher Education Malaysia under the TRGS 2015 Flood Management research grant scheme (Project No.203/REDAC/6767004).

REFERENCES

Akasah, Z.A. & Doraisamy, S.V. (2015). 2014 Malaysia Flood: Impacts & Factors Contributing towards the Restoration of Damages. *Journal of Scientific Research and Development*, 2, 53-59.

Al-Badaii, F., Gasim, M.B., Mokhtar, M., Toriman, M.E. & Rahim, S.A. (2012). Water-Pollution Study Based on the Physic-Chemical and Microbiological Parameters of the Semenyih River, Selangor, Malaysia. *The Arab World Geographer,* 15, 318-334.

American Public Health Association (APHA). (1998). *Standard Methods for the Examination of Water and Wastewater.* Water Environment Federation. Washington, DC.

Ashbolt, N.J. (2004). Microbial Contamination of Drinking Water and Disease Outcomes in Developing Regions. *Toxicology*, 198, 229-238.

Aziz, H.A., Adlan, M.N. & Ariffin, K.S. (2008). Heavy Metals (Cd, Pb, Zn, Ni, Cu and Cr (III)) Removal from Water in Malaysia: Post Treatment by High Quality Limestone. *Bioresource Technology,* 99(6), 1578-1583.

Baig, S.A., Xu, X. & Khan, R. (2012). Microbial Water Quality Risks to Public Health: Potable Water Assessment for a Flood-Affected Town in Northern Pakistan. *Rural Remote Health*, 12, 2196-2202.

Belhaj, D., Ghrab, S., Medhioub, M. & Kallel, M. (2015). Performance Evaluation of an Industrial Wastewater Treatment Plant in South-Eastern Tunisia. *Desalination and Water Treatment,* 52, 2174-2179.

Centers for Disease Control and Prevention (CDC). (2000). Measuring Healthy Days: Population Assessment of Health-Related Quality of Life. *Atlanta*, 4-6.

Chaturongkasumrit, Y., Techaruvichit, P., Takahashi, H., Kimura, B. & Keeratipibul, S. (2013). Microbiological Evaluation of Water during the 2011 Flood Crisis in Thailand. *Science of the Total Environment,* 463, 959-967.

Department of Environment (DOE). (2011). *Water Quality Index*. Ministry of Science, Technology and Environmental Malaysia, Kuala Lumpur, Malaysia.

Department of Environment (DOE) (1994). *Classification of Malaysian Rivers-Methodology and Classification of Ten Rivers*. Ministry of Science, Technology and Environment, 2, 4.101-4.104.

Diaz, R. J. & Rosenberg, R. (2008). Spreading Dead Zones and Consequences for Marine Ecosystems. *Science,* 321, 926-929.

Dike, N.I., Ezealor, A.U. & Oniye, S.J. (2004). Concentration of Pb, Cu, Fe and Cd during the Dry Season in River Jakara, Kano, Nigeria. *Chemclass Journal,* 1, 78-81.

Eisakhani, M. & Malakahmad, A. (2009). Water Quality Assessment of Bertam River and its Tributaries in Cameron Highlands, Malaysia. *World Applied Sciences Journal*, *7*(6), 769-776.

Environmental Protection Agency (EPA). (2004). *National Recommended Water Quality Criteria*. Office of Science and Technology, Washington, DC.

Eregno, F.E., Tryland, I., Tjomsland, T., Myrmel, M., Robertson, L. & Heistad, A. (2016). Quantitative Microbial Risk Assessment Combined with Hydrodynamic Modelling to Estimate the Public Health Risk Associated with Bathing after Rainfall Events. *Science of the Total Environment,* 548, 270-279.

Foo, K.Y. (2015). A shared View of the Integrated Urban Water Management Practices in Malaysia. *Water Science and Technology: Water Supply*, 15, 456-473.

Gandaseca, S., Rosli, N., Ngayop, J. & Arianto, C.I. (2011). Status of Water Quality Based on the Physico-Chemical Assessment on River Water at Wildlife Sanctuary Sibuti Mangrove Forest, Miri Sarawak. *American Journal of Environmental Sciences*, *7*(3), 269.

Gao, H., Lv, C., Song, Y., Zhang, Y., Zheng, L., Wen, Y., Peng, J. & Yu, H. (2015). Chemometrics Data of Water Quality and Environmental Heterogeneity Analysis in Pu River, China. *Environmental Earth Sciences,* 73, 5119-5129.

Gasim, M.B., Ismail, B.S., Wan, N.A., Muhammad, I.Y. & Marlia, M.H. (2005). Water Quality Assessment of the Semenyih River basin Selangor, Malaysia. *Journal of Chemistry*, 16, 87-95.

Hill, V.R. & Sobsey, M.D. (1998). Microbial Indicator Reductions in Alternative Treatment Systems for Swine Wastewater. *Water Science Technology,* 38, 119-122.

Juahir, H., Zain, S.M., Yusoff, M.K., Hanidza, T.I.T., Armi, A.S.M., Toriman, M.E. & Mokhtar, M. (2011). Spatial Water Quality Assessment of Langat River Basin (Malaysia) using Environmetric Techniques. *Environmental monitoring and assessment,* 173, 625-641.

Kataria, J., Dhekne, P.S. & Sanyal, S. (2006). A Scheme to Control Flooding of Fake Route Requests in Ad-hoc Networks. *In International Conference on Computers and Devices for Communications, CODEC-06*.

Kuo, Y.M., Jang, C.S., Yu, H.L., Chen, S.C. & Chu, H.J. (2013). Identifying Nearshore Groundwater and River Hydrochemical Variables Influencing Water Quality of Kaoping River Estuary using Dynamic Factor Analysis. *Journal of Hydrology,* 486, 39-47.

Liu, J. & Mattiasson, B. (2002). Microbial BOD Sensors for Wastewater Analysis. *Water Res*earch, 36, 3786-3802.

Mallin, M.A., Posey, M.H., McIver, M.R., Parsons, D.C., Ensign, S.H. & Alphin, T.D. (2002). Impacts and Recovery from Multiple Hurricanes in a Piedmont–Coastal Plain River System Human Development of Floodplains Greatly Compounds the Impacts of Hurricanes on Water Quality and Aquatic Life. *Bioscience,* 52, 999-1010.

Mallin, M.A., Williams, K.E., Esham, E.C. & Lowe, R.P. (2000). Effect of Human Development on Bacteriological Water Quality in Coastal Watersheds. *Ecological Applications,* 10, 1047-1056.

McMichael, A.J., Woodruff, R.E. & Hales, S. (2006). Climate Change and Human Health: Present and Future Risks. *The Lancet,* 367, 859-869.

Niyogi, S.K. (2005). Shigellosis. *Journal of Microbiology*, 43, 133-143.

Nyanti, L., Ling, T.Y. & Jongkar, G. (2012). Fish and Crustacean Communities and Fish Length-Weight Relationship of Lutong river, Miri, Sarawak, Malaysia. *World Journal of Fish Marine Science*, 4, 102-110.

Özsoy, T. & Örnektekin, S. (2009). Trace Elements in Urban and Suburban Rainfall, Mersin, Northeastern Mediterranean. *Atmospheric Research,* 94, 203-219.

Pardue, J.H., Moe, W.M., McInnis, D., Thibodeaux, L.J., Valsaraj, K.T., Maciasz, E., Van Heerden, I., Korevec, N. & Yuan, Q.Z. (2005). Chemical and Microbiological Parameters in New Orleans Flood Water following Hurricane Katrina. *Environmental Science & Technology,* 39, 8591-8599.

Patel, K. (2016). Study of Mahisagar River Water by PhysicoChemical Analysis, Taluka Lunawada, Dist: Mahisagar (Gujarat) India. *International Journal of Scientific Research*, 4, 616-618.

Phanuwan, C., Takizawa, S., Oguma, K., Katayama, H., Yunika, A. & Ohgaki, S. (2006). Monitoring of Human Enteric Viruses and Coliform Bacteria in Waters after Urban Flood in Jakarta, Indonesia. *Water Science and Technology*, 54, 203-210.

Rajwa-Kuligiewicz, A., Bialik, R.J. & Rowiński, P.M. (2015). Dissolved Oxygen and Water Temperature Dynamics in Lowland Rivers over Various Timescales. *Journal of Hydrology Hydromechanics*, 63, 353-363.

Rani, S.A., Pitts, B., Beyenal, H., Veluchamy, R.A., Lewandowski, Z., Davison, W.M., Buckingham-Meyer, K. & Stewart, P.S. (2007). Spatial Patterns of DNA Replication, Protein Synthesis, and Oxygen Concentration within Bacterial Biofilms Reveal Diverse Physiological States. *Journal of Bacteriology*, 189, 4223-4233.

Rompré, A., Servais, P., Baudart, J., de-Roubin, M.R. & Laurent, P. (2002). Detection and Enumeration of Coliforms in Drinking Water: Current Methods and Emerging Approaches. *Journal of Microbiological methods*, 49, 31-54.

Sardar, V.K., Vijay, R. & Sohony, R.A. (2010). Water Quality Assessment of Malad Creek, Mumbai, India: An Impact of Sewage and Tidal Water. *Water Science Technology*, 62, 2037-2043.

Sidek, L., Mohiyaden, H.A., Lee, L.K. & Foo, K.Y. (2016a). Potential of Engineered Biomedia for the Innovative Purification of Contaminated River Water. *Desalin. Water Treatment,* 57, 24210-24221.

Sidek, L., Basri, H., Lee, L.K. & Foo, K.Y. (2016b). The Performance of Gross Pollutant Trap for Water Quality Preservation: A Real Practical Application at the Klang Valley, Malaysia. *Desalin. Water Treatment,* 57, 24733-24741.

Scragg, A.H. (2006). The Effect of Phenol on the Growth of Chlorella Vulgaris and Chlorella VT-1. *Enzyme and microbial technology,* 39, 796-799.

Sulaiman, W.N.A., Heshmatpoor, A. & Rosli, M.H. (2010). Identification of Flood Source Areas in Pahang River Basin, Peninsular Malaysia. *Environ. Asia,* 3, 73-78.

United State Environmental Protection Agency (USEPA). (2009). *National Recommended Water Quality Criteria*. Office of Water, Office of Science and Technology, Washington DC, 4304.

William, R.J. & Boorman, D.B. (2012). Modelling In-Stream Temperature and Dissolved Oxygen at Sub-Daily Time Steps: An Application to the River Kennet, UK. *Science of the Total Environment,* 423, 104-110.

World Health Organization (WHO) (2011). *Guidelines for Drinking Water Quality*, World Health Organization: Geneva, Switzerland.

Proceedings of the 37th IAHR World Congress
August 13 – 18, 2017, Kuala Lumpur, Malaysia

MODELING THE IMPACT OF CLIMATE CHANGE ON THE RUNOFF KELANTAN RIVER BASIN

CHEE LOONG WONG(1), JUNENG LIEW(2) & ZULKIFLI YUSOP (3)

(1,3) Faculty of Civil Engineering, Universiti Teknologi Malaysia, 81310 Johor Bahru, Malaysia. wongcl_my@yahoo.com
(1) Department of Irrigation and Drainage, Malaysia, Jalan Sultan Salahuddin 50626 Kuala Lumpur, Malaysia
(2) School of Environment and Natural Resource Sciences, Universiti Kebangsaan Malaysia
(3) Centre for Environmental Sustainability and Water Security, Research Institute for Sustainable Environment, Universiti Teknologi Malaysia, 81310 Johor Bahru, Malaysia

ABSTRACT

Growing evidence of intensifying hydrological cycle due to global climate change leads to increasing interest in understanding large-scale interconnection between the atmospheric and the hydrological variables of land surface processes. However, the assessment and projections of climate change impact on runoff is always highly uncertain due to errors introduced at various modeling stages involved. In current study, five empirically downscaled global climate models (GCMs) outputs which have been bias corrected, were used to assess the hydrological processes, particularly refer to runoff component. The runoff of Kelantan river basin was projected based on the IPCC's RCP4.5 and RCP8.5 emission scenarios. Generally over the studied basin, all five GCMs projected increase in rainfall with a range between 6.4% - 11.6% and 6.7% - 18.3% under RCP4.5 and RCP8.5, respectively. The increase rainfall was found to associate with proportional increase in annual runoff at approximately 11.7% to 22.7% and 11.7% to 36.2% under RCP4.5 and RCP8.5, respectively. This is expected to have major implications for water resources planning and management in Kelantan river basin.

Keywords: Climate change; runoff; Kelantan.

1 INTRODUCTION

Climate change impacts the regional water availability and the assessment of the effects of climate change on catchment runoff has received considerable attention in recent years (Christensen et al., 2004a; Gardner, 2009; Chen et al., 2012; Silberstein et al., 2012; Zulkafli et al., 2013; Roudier et al., 2014; Vetter et al., 2015; Arnell and Gosling, 2016). The climate change impacts assessment is important for informing the policy makers, especially on mitigation efforts. However, climate impacts occur and adaptation policies are usually implemented on the regional or river basin scale, where the projections from global impact models may not be precise enough to provide such information. To ensure that climate impact assessment meets the demand of stakeholders for reliable information, projections of climate impacts should be provided on the regional or river basin scale using validated hydrological models and up-to-date scenarios.

General circulation models (GCMs) and hydrological models are the important tools that have been used in these studies (Oki et al., 1999; Xu et al., 2005; Boé et al., 2007; Chen et al., 2007; Chen et al., 2012). GCMs provide useful climate change scenarios as a basis for simulating the present climate and predict future climate change (Hagemann et al., 2013; Schewe et al., 2014; Gosling and Arnell, 2016; Hattermann et al., 2017). However, to carry out these assessments in regional scale, GCMs do not usually provide sufficient spatial resolution for future water resources management in regional and local applications (Wigley et al., 1990; Solomon et al., 2007; Teutschbein and Seibert, 2010). The inconsistency of spatial scales between GCMs and hydrological models causes the tasks to assess the future rainfall impacts and streamflow in catchment basis to become challenging(Xu, 1999a; Xu et al., 2005).

These mismatch problems can be solved by dynamically or statistically downscaling of GCMs output (Fowler et al., 2007). Dynamical downscaling refers to the use of large-scale lateral boundary conditions from GCMs to simulate higher resolution outputs with a regional climate model (RCM) (Themeßl et al., 2011). The RCM dynamic downscaling technique is often computationally expensive and introduces additional biases due to additional uncertainties in local forcings apart from that inherited from the GCMs output via the lateral boundaries (Déqué et al., 2005; Rowell, 2006). On the other hand, the statistical downscaling techniques (efficient computation) translate large-scale GCM output onto a finer resolution based on empirical relationships between large–scale atmospheric variables (predictors) and local surface variables (predictands) (cf. Wilby et al., 2004).

Hydrological models provide a framework to conceptualize and assess the relationship between effects of climate changes on hydrology and water resources. Various efforts to adopt multiple hydrological models to assess the hydrological response to climate change and project the future state of water resources globally or in basin scales (Xu, 1999a; Christensen et al., 2004b; Gudmundsson et al., 2012; Hagemann et al., 2013).

  / ISSN 1562-6865 (Online) - ISSN 1063-7710 (Print)

However, this approach is still in infant stage, in particular, to Malaysia due to lacking of comprehensive hydrological inputs or data for the certain of hydrological processes in the model.

For this study, we adopted part of methodologies by Xu (1999b; 1999a) in focusing only on using land surface model (LSM) to simulate daily streamflow based on the Representative Concentration Pathways (RCP), i.e. RCP4.5 and RCP8.5 scenarios. The precipitation which is the input to LSM was statistically derived from five GCMs by using quantile mapping (QM) method (Juneng, 2012). The QM downscaling techniques is to link climate models and catchment-scale hydrological model or to provide catchment scale climate scenarios as input to hydrological model and lastly using hydrological model to simulate hydrological impacts of climate change.

This paper focus on the scenarios constructed from the output from several climate models that project hydrological change (particularly focus on streamflow changes) on Kelantan river basin for the period of 2010-2100.

2 STUDY AREA

The Kelantan river basin is located in the northeastern part of Peninsular Malaysia. The main river is some 248 km in length and drains an area of approximately 12,000 km^2 as shown in Figure 1. Elevations range from sea level to some 2000 m in the most inland parts of the basins. The basin is mostly covered by tall natural broadleaf forest, while rubber, oil palm and some paddy are planted in the undulating and lowland parts of the area. Granites and associated soils are found in the mountainous terrains in the west Kelantan, respectively. The lower parts of the basins are characterized by sedimentary covers.

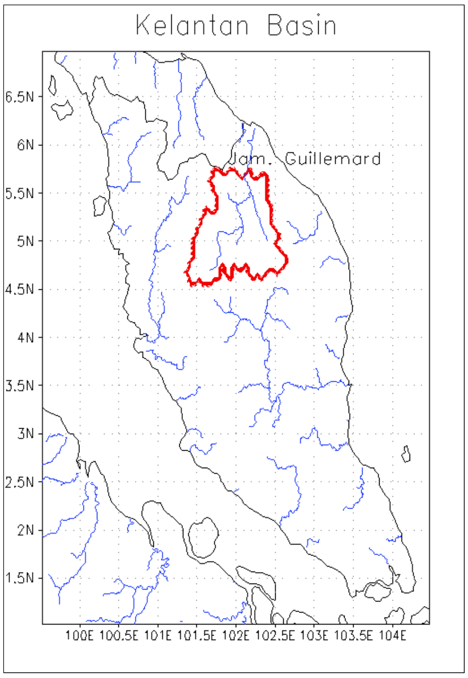

Figure 1. Location of Kelantan basin in Peninsular Malaysia.

Kelantan river basin have an annual rainfall of about 2500 mm/year. A large proportion of the annual rainfall occurs in November and December during the Northeast monsoon. The mean annual temperature and relative humidity is approximately 25^{o}C and 83%.

3 METHODOLOGY

3.1 Rainfall downscaling

The rainfall input for the hydrological model (LSM) was obtained via a statistical downscaling approach using multiple GCMs driven by two emission scenarios, i.e. RCP4.5 and RCP8.5 that were considered to account for the uncertainties of different climate model sensitivity and emission scenarios as shown in Figure 2.

We focused on empirically derived, statistical formulations of the predictor-predict and relationship by adopting quantile mapping (QM) bias correction technique (Widmann et al., 2003). The observed gridded data set (Wong et al., 2011) was used to calibrate a globally available daily reanalysis data set over 14 years (1979 to 1992). The European Centre for Medium-Range Weather Forecast (ECMWF) interim reanalysis (ERA-Interim) (Dee et al., 2011) was used as GCM surrogate for the assessment of the daily rainfall downscaling approaches. The daily precipitation fields from the reanalysis were taken in accordance to the development of

ERA-Interim from 1979 until 2006. The validation of reanalysis data which was projected by the QM, was compared with the observed gridded data set for 1993-2006. The 1.5°×1.5° ERA-Interim daily precipitation field was re-gridded to a regular 0.05° × 0.05° of the observation and the bias correction routine was applied to each pair of the grids of observation and the interpolated ERA-Interim daily precipitation values. Five GCMs (Canadian Centre for Climate Modeling and Analysis, Canada (CanESM), Institute Pierre-Simon Laplace, France (IPSL), Atmosphere and Ocean Research Institute (The University of Tokyo), Japan (MIROC), Max Planck Institute for Meteorology, Germany (MPI) and Norwegian Climate Centre, Norway (NorESM)) from the Program for Climate Model Diagnosis and Intercomparison's (PCMDI) Coupled Model Intercomparison Project Phase 5 (CMIP5) archive were selected to estimate the future rainfall changes driven by the RCP4.5 and RCP8.5 scenarios. The large scale daily prediction fields were downscaled with the calibration carried out in a model output statistics fashion. The changes in rainfall characteristics were examined for three different future epochs – i) 2011-2040, ii) 2041-2070 and iii) 2071-2100, presenting changes in near, mid-term and long term future period.

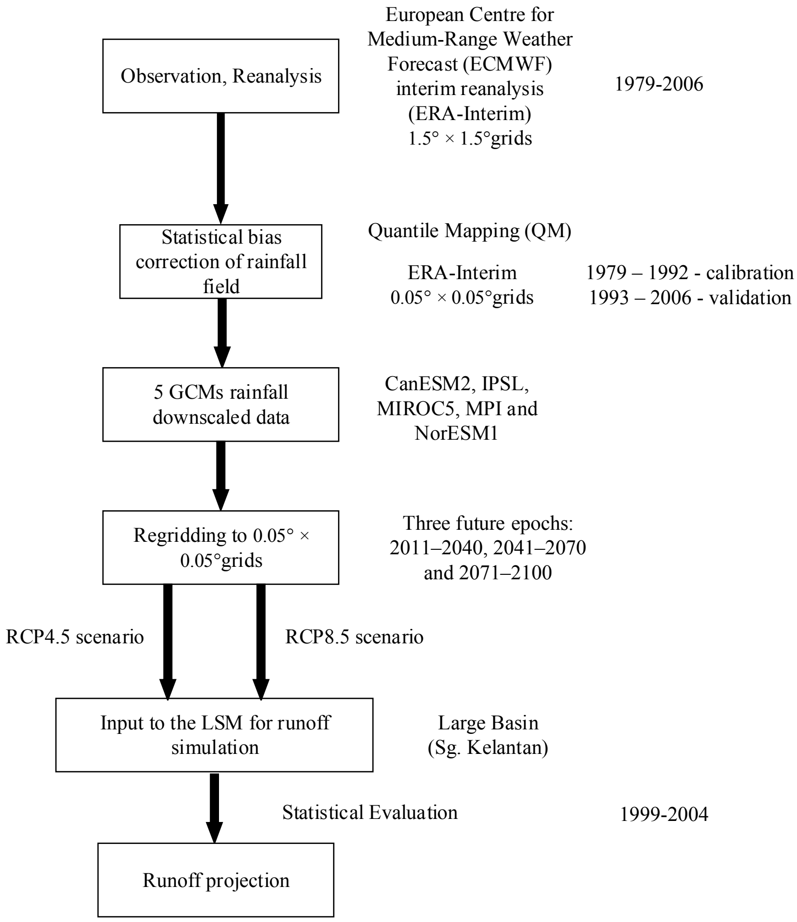

Figure 2. The methodology of the study.

3.2 Hydrological modelling

A new land surface model which is called LSM-A, is a simple computational model to carry out distributed land surface hydrological simulations (Venneker, 2009). The model introduced can be considered as a simple, alternative to existing land surface parameterization schemes applied in GCMs, or land surface hydrological models such as the VIC model (Liang et al., 1994).

A schematic representation of the LSM-A model structure is shown in Figure 3. The land surface is discretized on a regular grid, in which the grid cells are characterized by a biome-related land cover type. The vertical soil profile is subdivided into a discrete number of layers. Spatially variable vegetation and soil physical properties are included on a grid cell basis. Atmospheric forcing data consists of time-varying gridded input fields for downward radiation fluxes, temperature, precipitation, wind speed, pressure and humidity, provided on a daily, or preferably sub-daily, time basis (Wong et al., 2011). The input data are derived from the publicly accessible data sources, satellite imagery products and ground observations. The radiation and energy balance routines compute the upward radiative energy fluxes, the reflection and absorption of radiation by vegetation, snow and soil, and the surface temperature. In this study, some atmospheric forcing data were assumed to remain unchanged, i.e. downward radiation fluxes, wind speed, pressure and humidity due to streamflow production is mainly driven by the precipitation. Precipitation data was obtained from the downscaling processes by five GCMs and temperature data was provided by the GCMs. A single vegetation layer sub-model computes the interception and evaporation of precipitation by the canopy and the water flux towards the ground surface. Soil heat transport computation determines the temperature profile of the sub-soil, including freezing and melting of soil water. The redistribution soil water determines the percolation towards the saturated zone. The surface runoff production originate from the infiltration and saturation excess, the evaporation from the soil surface and the uptake of soil water by vegetation roots which transpired back to the atmosphere. The surface and sub-surface runoff route the water towards the actual river network by a grid box routing processor (GBR) that share a common regular spatial grid of 0.05 degree resolution (approximately 5.5 km).

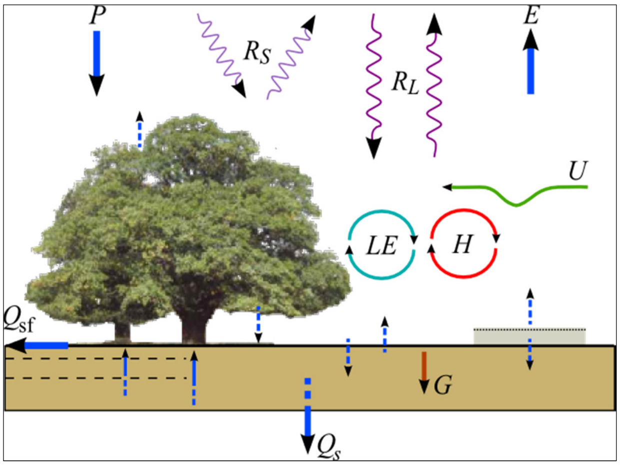

Figure 3. Schematic representation of the LSM-A model showing the major energy and water balance fluxes.

3.3 Evaluation for hydrological model

Three statistical measures were used to assess the simulation error, i.e. the bias, the mean absolute error and the root mean square error, given by

$$\mathrm{Bias} = \frac{1}{N}\sum\left(Q_{\mathrm{sim}} - Q_{\mathrm{obs}}\right) \qquad [1]$$

$$\mathrm{MAE} = \frac{1}{N}\sum\left|Q_{\mathrm{sim}} - Q_{\mathrm{obs}}\right| \qquad [2]$$

$$\mathrm{RMSE} = \sqrt{\frac{1}{N}\sum\left(Q_{\mathrm{sim}} - Q_{\mathrm{obs}}\right)^2} \qquad [3]$$

where the Q_{sim} ($m^3 s^{-1}$) are the simulated discharge values and the Q_{obs} ($m^3 s^{-1}$) are the observed discharge values, and N is the number of observation-simulation pairs. The correlation between observation and simulation is described by the coefficient of determination, i.e.

$$R^2 = \frac{\left[\sum\left(Q_{\mathrm{obs}} - \overline{Q}_{\mathrm{obs}}\right)\left(Q_{\mathrm{sim}} - \overline{Q}_{\mathrm{sim}}\right)\right]^2}{\sum\left(Q_{\mathrm{obs}} - \overline{Q}_{\mathrm{obs}}\right)^2\sum\left(Q_{\mathrm{sim}} - \overline{Q}_{\mathrm{sim}}\right)^2} \qquad [4]$$

where the overbar denotes the mean value. The overall model performance is assessed by the Nash and Sutcliffe (1970) model efficiency, computed by

$$\mathrm{NSE} = 1 - \frac{\frac{1}{N}\sum\left(Q_{\mathrm{obs}} - Q_{\mathrm{sim}}\right)^2}{\frac{1}{N}\sum\left(Q_{\mathrm{obs}} - \overline{Q}_{\mathrm{obs}}\right)^2} \qquad [5]$$

4 RESULTS AND DISCCUSION

4.1 Rainfall projections

For the assessment, the time period 1974–2010 was chosen as the reference period, the changes in rainfall characteristics were examined for three different future epochs – i) 2011-2040, ii) 2041-2070 and iii) 2071-2100, presenting changes in near, mid-term and long term future period. All future rainfall changes were driven by the RCP4.5 and RCP8.5 scenarios. Figure 4 shows the ensemble rainfall projection map under RCP4.5 scenario. The rainfall is unevenly distributed across the whole basin. The upstream or south-west part of basin which is dominant by higher elevation receives relatively lesser annual average rainfall at the range of 2250mm/year and 2750mm/year. Higher annual average rainfall (3250mm/year or more) is generally observed at the east and north-west part of the basin for the three future epochs. For 2011-2040, the annual average rainfall is projected to be at 6.5% higher than the reference period. It increases to 7.7% and 11.6% during the mid-term and long term future period, respectively.

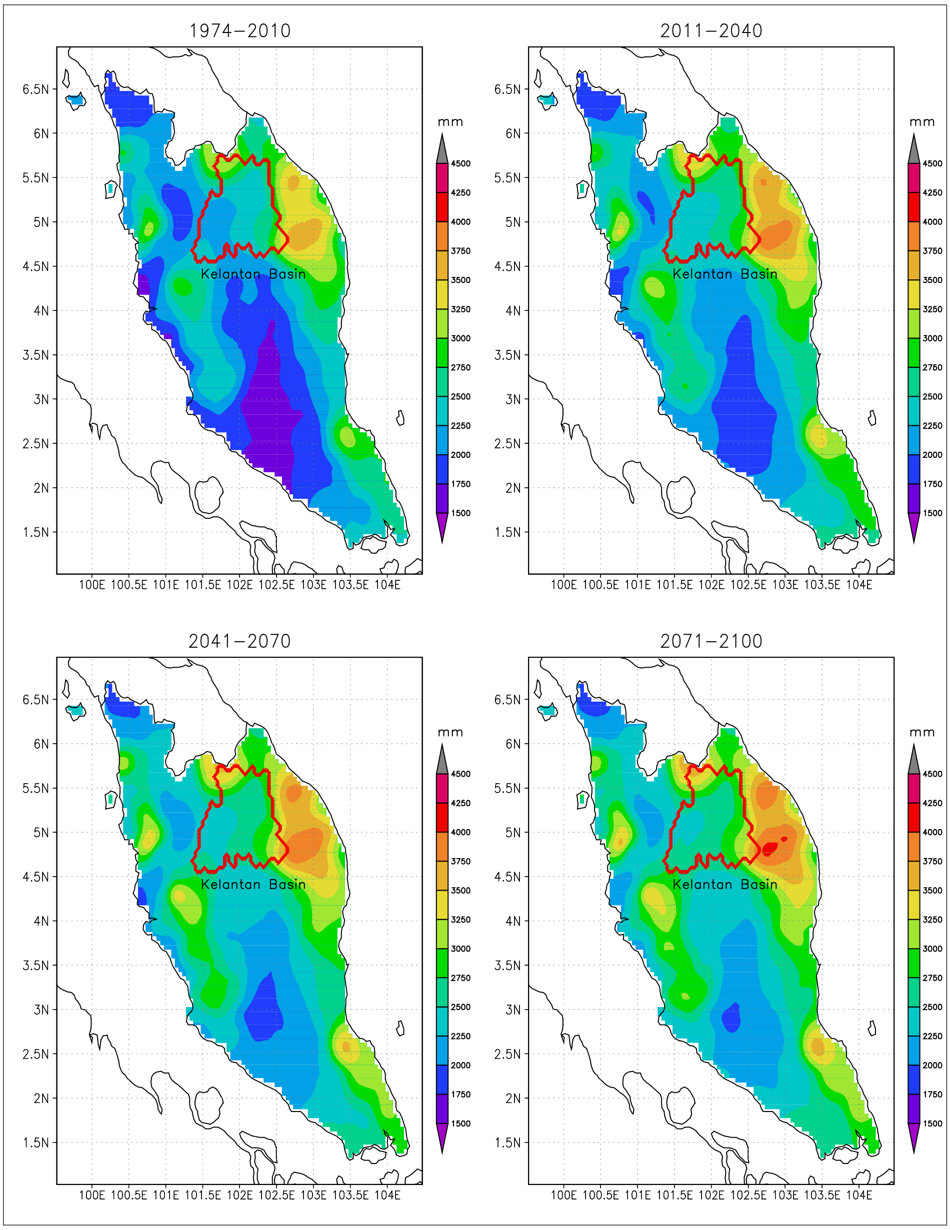

Figure 4. Seasonal rainfall projection map (RCP4.5).

Under the RCP8.5 climate projection scenario, the rainfall projection does not differ much compare to RCP4.5 with an approximately of 6.7% increase of annual average rainfall in the near future (2010-2040) as shown in Figure 5. However, it shows relatively higher annual average rainfall at 10.7% and 18.3% compare to RCP4.5 during the mid-term and long term future period, respectively. The eastern and north-west part of basin shows the annual average rainfall at the range of 2500mm/year to 3500mm/year for the near and mid-term. Meanwhile, the annual average rainfall at the range of 2750mm/year to 4000mm/year is observed during 2070-2100 epoch.

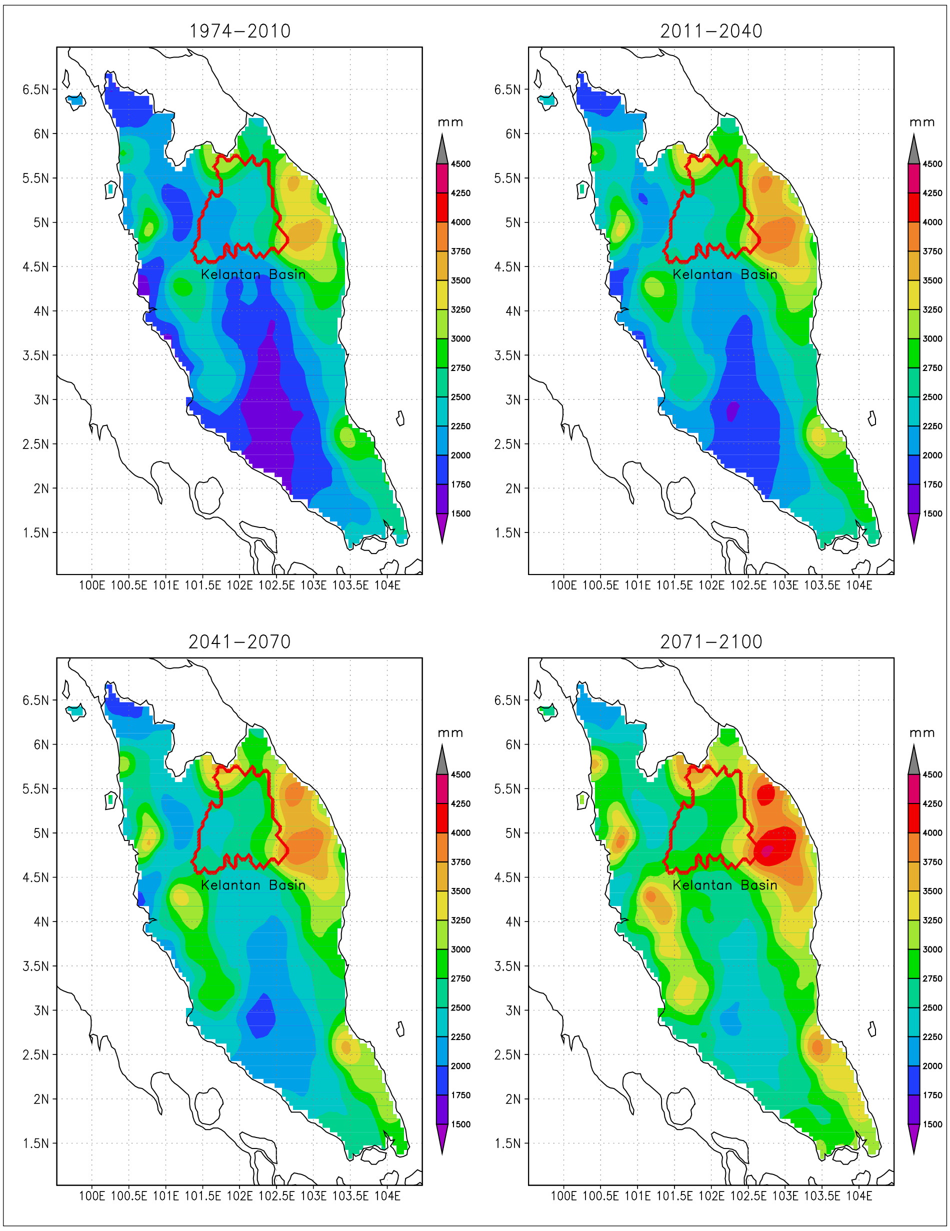

Figure 5. Seasonal rainfall projection map (RCP8.5).

Table 1. Rainfall projections changes on Kelantan river basin.

GCMs	RCP4.5 scenario			RCP8.5 scenario		
	2011-2040	2041-2070	2071-2100	2011-2040	2041-2070	2071-2100
CanESM	–4.6%	–1.1%	1.6%	1.4%	–3.6%	3.1%
IPSL	0.6%	1.3%	1.5%	–2.7%	–5.8%	2.2%
MIROC	20.2%	26.1%	28.4%	8.7%	26.6%	33.1%
MPI	9.3%	4.4%	15.0%	12.4%	14.0%	10.9%
NorESM	7.2%	13.0%	13.9%	13.8%	22.2%	42.4%
Average	*6.4%*	*7.7%*	*11.6%*	*6.7%*	*10.7%*	*18.3%*

The changes in rainfall vary between GCM models as shown in Table 1. Two climate scenarios under CanESM and IPSL show a decrease in rainfall during near and mid-term period. The MIROC scenarios show mostly an increase, which is mostly higher than that simulated by other models, reaching more than 20% of annual average rainfall for all three future epochs (except 2011-2040 under RCP8.5).

4.2 Streamflow simulation under climate scenarios

Observed streamflow data of the period 1999-2004 were used to calibrate and validate the hydrological model. Five downscaled rainfall scenarios simulated by using different GCMs (CanESM, IPSL, MIROC, MPI and NorESM) were used as the input for LSM-A. A comprehensive statistical evaluation was used to test if the models were capable of yielding plausible simulation results. Figure 6 and Table 2 show the streamflow simulation results of different rainfall scenarios and performance statistics for streamflow simulations during the calibration/validation period. Although most of the models projected higher mean monthly streamflow compared to the observed data at the average of 14.2 m^3/s, the difference between them was small. The coefficient of determination (R^2) and NSE of ensemble streamflow simulation by using the rainfall downscaled was at 0.917 and 0.685, respectively. The streamflow driven by the rainfall scenarios from various GCMs have performed relatively well. The results reflect that the rainfall simulations from larger scale predictors by using the adopted statistical downscaling method is able to provide useful rainfall data as input to drive hydrological model.

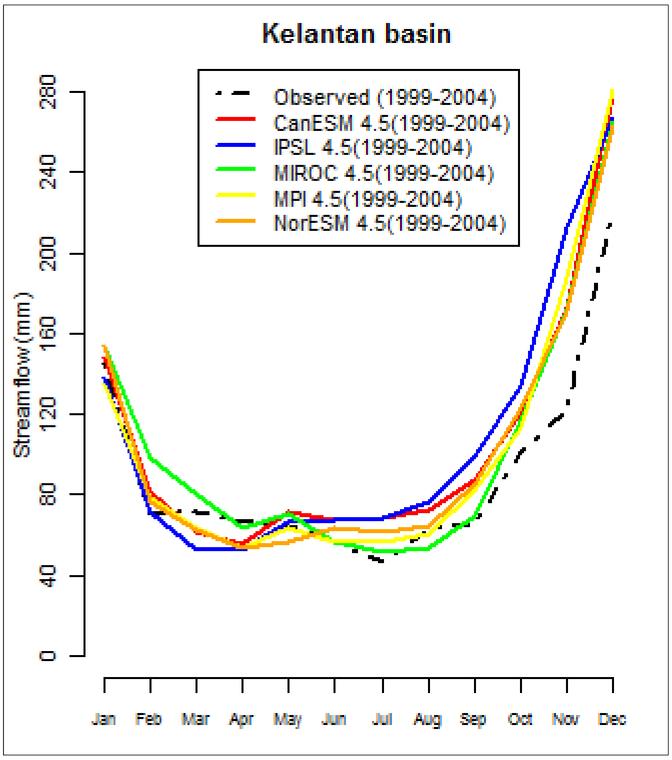

Figure 6. Comparison of mean monthly observed and simulated streamflow during baseline period.

Table 2. Statistical comparison between the observed and ensemble simulated streamflow annual curve.

Validation	Kelantan River Basin
Bias (m^3/s)	14.2
Mean Absolute Error, MAE (m^3/s)	18.7
Root Mean Square Error, RMSE (m^3/s)	7.6
Coefficient of Determination, R^2	0.917
Nash and Sutcliffe Efficiency, NSE	0.685

The hydrological model was applied with quantile mapping (QM) method to simulate streamflow condition under future climate scenarios. The changes of average rainfall projections were generally affecting the changes in streamflow simulations. The increases of annual average rainfall led to the changes in mean

  ISSN 1562-6865 (Online) - ISSN 1063-7710 (Print)

annual streamflow averaged over all GCMs simulations and yielded 11.7% for 2011-2040, 13.6% for 2041-2070 and 22.7% for 2071-2100 (refer to Table 3) under RCP4.5 scenario. It is notable MIROC produced higher changes of streamflow which correlated with higher rainfall projection as shown in Table 1. Most of the models produced positive increase of mean annual streamflow, except CanESM for the near and mid-term future period. For RCP8.5 scenario, the mean annual streamflow during the near future period was found similar to RCP4.5 scenario. The projected changes in streamflow increased drastically to 20.1% for 2041-2070 and 36.2% for 2071-2100. It is noted that each GCMs produced great variation of future rainfall due to coarse resolution and model structure describing related processes and, as a result, impacting the future streamflow productions (Vetter et al., 2015). The changes in total streamflow volume depend on the rainfall prediction (scenario), which depends on the GCM chosen. None of GCMs could provide a single reliable estimate that could be advanced as the deterministic forecast for hydrological planning (Xu, 1999b).

Table 3. Simulated streamflow changes derived by the rainfall projection on Kelantan river basin.

GCMs	RCP4.5 scenario			RCP8.5 scenario		
	2011-2040	2041-2070	2071-2100	2011-2040	2041-2070	2071-2100
Average Rainfall	*6.4%*	*7.7%*	*11.6%*	*6.7%*	*10.7%*	*18.3%*
CanESM	–7.2%	–0.1%	5.2%	2.9%	–4.4%	10.7%
IPSL	2.0%	5.0%	6.1%	–3.5%	-8.0%	8.1%
MIROC	34.3%	46.4%	48.7%	14.7%	47.1%	58.6%
MPI	17.7%	3.0%	30.9%	21.8%	27.6%	29.1%
NorESM	19.3%	27.3%	29.1%	22.7%	38.1%	74.7%
Average	*11.7%*	*13.6%*	*22.7%*	*11.7%*	*20.1%*	*36.2%*

5 CONCLUSIONS

This study focused on the impact of climate change on streamflow productions at Kelantan river basin. We produced future rainfall projections under RCP4.5 and RCP8.5 scenarios. The future rainfall projections were used as input for simulating future streamflow using land surface model, LSM-A.

The main findings of this study are, as follows

a) The future rainfall projections from the statistical downscaling approaches linking with the GCMs could be used directly to drive hydrologic models, which in turn could be used to evaluate the hydrologic and water resource effects of climate change;
b) Similar data were used, but some models predict increases and some decreases in rainfall. It indicates that if single GCM was used to analyze the impact of climate change, the conclusion would not be reliable and robust. More GCMs scenarios should be used in the study of climate change impact on hydrology;
c) The changes of future rainfall projections in Kelantan basin become more pronounced towards the end of the 21st century. It impacts on the mean average streamflow for 2071-2100 results with an increase of 22.7% and 36.2%, under RCP4.5 and RCP8.5, respectively.

Some recommendations for the future research works are as follows:

a) The current study is based on a statistical downscaling method, which assumed that the empirical relationship between the large scale and the local rainfall remain invariant throughout the historical and projection period. It is suggested to have dynamical downscaling as one of the option to simulate higher resolution outputs as this technique can provide realistic physical meaning and may assess the impact of climate change more effectively. Besides, different LSM or hydrological model can be used to evaluate and compare the uncertainty in the simulated runoffs resulting from different statistical downscaling methods and hydrological models.
b) The increase of quantity streamflow to 22.7% and 36.2% under RCP4.5 and RCP8.5, respectively, indicates that flood prone areas within the Kelantan basin is seriously affected and risk is potentially impacting human beings and properties. A better mitigation or measures is necessary to be implemented in the future.

ACKNOWLEDGEMENTS

The authors thank the Department of Irrigation and Drainage Malaysia (DID), Malaysia Meteorological Department (MMD), and NOAA/NCDC for providing the data.

REFERENCES

Arnell, N.W. & Gosling, S.N., (2016). The Impacts of Climate Change on River Flood Risk at the Global Scale. *Climatic Change*, 134(3), 387-401.

Boé, J., Terray, L., Habets, F. & Martin, E., (2007). Statistical and Dynamical Downscaling of the Seine Basin Climate for Hydro-Meteorological Studies. *International Journal of Climatology*, 27(12), 1643-1655.

Chen, H., Guo, S.L., Xu, C.Y. & Singh, V.P., (2007). Historical Temporal Trends of Hydroclimatic Variables and Runoff Response to Climate Variability and their Relevance in Water Resource Management in the Hanjiang Basin. *Journal of Hydrology*, 344(3), 171-184.

Chen, H., Xu, C.-Y. & Guo, S., (2012). Comparison and Evaluation of Multiple Gcms, Statistical Downscaling and Hydrological Models in the Study of Climate Change Impacts on Runoff. *Journal of Hydrology*, 434-435, 36-45.

Christensen, N.S., Wood, A.W., Voisin, N., Lettenmaier, D.P. & Palmer, R.N., (2004a). The Effect of Climate on the Hydrology and Water Resources of the Colorado River Basin. *Climatic Change*, 62(1-3), 337-363.

Christensen, N.S., Wood, A.W., Voisin, N., Lettenmaier, D.P. & Palmer, R.N., (2004b). The Effects of Climate Change on the Hydrology and Water Resources of the Colorado River Basin. *Climatic Change*, 62(1), 337-363.

Dee, D.P., Uppala, S.M., Simmons, A.J., Berrisford, P., Poli, P., Kobayshi, S., Andrae, U., Balmaseda, M.A., Balsamo, G., Bauer, P., Bechtold, P., Beljaars, A.C.M., van de Berg, L., Bidlot, J., Bormann, N., Delsol, C., Dragani, R., Fuentes, M., Geer, A.J., Haimberger, L., Healy, S.B., Hersbach, H., Hólm, E.V., Isaksen, L., Kållberg, P., Köhler, M., Matricardi, M., McNally, A.P., Monge-Sanz, B.M., Morcrette, J.-J., Park, B.-K., Peubey, C., de Rosnay, P., Tavolato, C., Thépaut, J.-N. & Vitart, F., (2011). The ERA-Interim Reanalysis: Configuration and Performance of the Data Assimilation System. *Quarterly Journal of the Royal Meteorological Society*, 137, 553-597.

Déqué, M., Jones, R.G., Wild, F., Christensen, J.H., Hassell, D.C., Vidale, P.L., Rockel, B., Jacob, D., Kjellström, E., de Castro, M. & van den Hurk, B., (2005). Global High Resolution Versus Limited Area Model Climate Change Projections over Europe: Quantifying Confidence Level from PRUDENCE Results. *Climate Dynamics*, 25(6), 653-670.

Fowler, H.J., Blenkinsop, S. & Tebaldi, C., (2007). Linking Climate Change Modelling to Impacts Studies-Recent Advances in Downscaling Techniques for Hydrological Modelling. *International Journal of Climatology*, 27(12), 1547-1578.

Gardner, L.R., (2009). Assessing the Effect of Climate Change on Mean Annual Runoff. *Journal of Hydrology*, 379(3), 351-359.

Gosling, S.N. & Arnell, N.W., (2016). A Global Assessment of the Impact of Climate Change on Water Scarcity. *Climatic Change*, 134(3), 371-385.

Gudmundsson, L., Wagener, T., Tallaksen, L.M. & Engeland, K., (2012). Evaluation of Nine Large-Scale Hydrological Models with Respect to the Seasonal Runoff Climatology In Europe. *Water Resources Research*, 48(11), 1-20.

Hagemann, S., Chen, C., Clark, D.B., Folwell, S., Gosling, S.N., Haddeland, I., Hanasaki, N., Heinke, J., Ludwig, F., Voss, F. & Wiltshire, A.J., (2013). Climate Change Impact on Available Water Resources Obtained using Multiple Global Climate and Hydrology Models. *Earth System Dynamics*, 4(1): 129-144.

Hattermann, F.F., Krysanova, V., Gosling, S.N., Dankers, R., Daggupati, P., Donnelly, C., Flörke, M., Huang, S., Motovilov, Y., Buda, S., Yang, T., Müller, C., Leng, G., Tang, Q., Portmann, F.T., Hagemann, S., Gerten, D., Wada, Y., Masaki, Y., Alemayehu, T., Satoh, Y. & Samaniego, L., (2017). Cross-Scale Intercomparison of Climate Change Impacts Simulated by Regional and Global Hydrological Models in Eleven Large River Basins. *Climatic Change*: 1-16.

Juneng, L., (2012). A Preview of High Resolution Malaysia Daily Rainfall Projection: Bias Correction Downscaling Approaches. *National Conference on Extreme Weather and Climate Change: "Understanding Science and R&D Capacity Needs"*, Auditorium, MMD Office, 1-47.

Liang, X., Lettenmaier, D.P., Wood, E.F. & Burges, S.J., (1994). A Simple Hydrologically based Model of Land Surface Water and Energy Fluxes for General Circulation Models. *Journal of Geophysical Research*, 99(D7), 415-428.

Nash, J.E. & Sutcliffe, J.V., (1970). River Flow Forecasting Through Conceptual Models. Part I - A Discussion of Principles. *Journal of Hydrology*, 10(3), 282-290.

Oki, T., Nishimura, T. & Dirmeyer, P., (1999). Assessment of Annual Runoff from Land Surface Models using Total Runoff Integrating Pathways (TRIP). *Journal of the Meteorological Society of Japan*, 77(1B), 235-255.

Roudier, P., Ducharne, A. & Feyen, L., (2014). Climate Change Impacts on Runoff in West Africa: A Review. *Hydrology Earth System Sciences*, 18, 2789-2801.

Rowell, D.P., (2006). A Demonstration of the Uncertainty in Projections of UK Climate Change Resulting from Regional Model Formulation. *Climatic Change*, 79(3-4), 243-257.

Schewe, J., Heinke, J., Gerten, D., Haddeland, I., Arnell, N.W., Clark, D.B., Dankers, R., Eisner, S., Fekete, B.M., Colón-González, F.J., Gosling, S.N., Kim, H., Liu, X., Masaki, Y., Portmann, F.T., Satoh, Y., Stacke, T., Tang, Q., Wada, Y., Wisser, D., Albrecht, T., Frieler, K., Piontek, F., Warszawski, L. & Kabat, P., (2014). Multimodel Assessment of Water Scarcity under Climate Change. *Proceedings of the National Academy of Sciences*, 111(9), 3245-3250.

Silberstein, R.P., Aryal, S.K., Durrant, J., Pearcey, M., Braccia, M., Charles, S.P., Boniecka, L., Hodgson, G.A., Bari, M.A., Viney, N.R. & McFarlane, D.J., (2012). Climate Change and Runoff in South-Western Australia. *Journal of Hydrology*, 475, 441-455.

Solomon, S., Qin, D., Manning, M., Chen, Z., Marquis, M., Averyt, K., Tignor, M. & Miller, H., (2007). *The Physical Science Basis. Contribution of Working Group I to the Fourth Assessment Report of the Intergovernmental Panel on Climate Change*, Cambridge University Press, Cambridge, United Kingdom and New York, NY, USA.

Teutschbein, C. & Seibert, J., (2010). Regional Climate Models for Hydrological Impact Studies at the Catchment-Scale: A Review of Recent Modeling Strategies. *Geography Compass*, 4(7), 834-860.

Themeßl, M.J., Gobiet, A. & Leuprecht, A., (2011). Empirical-Statistical Downscaling and Error Correction of Daily Precipitation from Regional Climate Models. *International Journal of Climatology*, 31(10), 916-934.

Venneker, R.G.W., (2009). The LSM-A land surface model - *Reference Documentation* (version 1.25), UNESCO-IHE, Delft, the Netherlands.

Vetter, T., Huang, S., Aich, V., Yang, T., Wang, X., Krysanova, V. & Hattermann, F., (2015). Multi-Model Climate Impact Assessment and Intercomparison for Three Large-Scale River Basins on Three Continents. *Earth System Dynamics*, 6(1), 17-43.

Widmann, M., Bretherton, C.S. & Salathé, E., (2003). Statistical Precipitation Downscaling over the Northwestern United States using Numerically Simulated Precipitation as Predictor. *Journal of Climate*, 16(5), 799-816.

Wigley, T.W.L., Jones, P.D., Briffa, K.R. & Smith, G., (1990). Obtaining Sub-Grid Scale Information from Coarse Resolution General Circulation Model Output. *Journal of Geophysical Research*, 95(D2), 1943-1953.

Wilby, R.L., Charles, S.P., Zorita, E., Timbal, B., Whetton, P. & Mearns, L.O., (2004). *Guidelines for Use of Climate Scenarios Developed from Statistical Downscaling Methods*, Data Distribution Centre of the Intergovernmental Panel on Climate Change.

Wong, C.L., Venneker, R., Jamil, A.B.M. & Uhlenbrook, S., (2011). Development of a Gridded Daily Hydrometeorological Data Set for Peninsular Malaysia. *Hydrological Processes*, 25(7), 1009-1020.

Xu, C.-Y., (1999a). Climate Change and Hydrologic Models: A Review of Existing Gaps and Recent Research Developments. *Water Resources Management*, 13(5), 369-382.

Xu, C.-y., (1999b). From Gcms to River Flow: A Review of Downscaling Methods and Hydrologic Modelling Approaches. *Progress in Physical Geography*, 23(2), 229-249.

Xu, C.-Y., Widén, E. & Hall, S., (2005). Modelling Hydrological Consequences of Climate Change - Progress and Challenges. *Advances in Atmospheric Sciences*, 22(6), 789-797.

Zulkafli, Z., Buytaert, W., Onof, C., Lavado, W. & Guyot, J.L., (2013). A Critical Assessment of the JULES Land Surface Model Hydrology for Humid Tropical Environments. *Hydrol. Earth Syst. Sci.*, 17(3), 1113-1132.

Proceedings of the 37th IAHR World Congress
August 13 – 18, 2017, Kuala Lumpur, Malaysia

COMPARISON BETWEEN DETERMINISTIC AND UNCERTAINTY APPROACHES IN SIMULATING DESIGN FLOOD PROFILE ON THE JOHOR RIVER, MALAYSIA

ANUAR MD. ALI [1], GIULIANO DI BALDASSARRE [2] & DIMITRI P. SOLOMATINE [3]

[1, 2, 3] Department of Integrated Water System and Governance, UNESCO-IHE Institute for Water Education, Delft, the Netherlands
a.ali@unesco-ihe.org, d.solomatine@unesco-ihe.org
[1] Department of Irrigation and Drainage, Kuala Lumpur, Malaysia
[2] Department of Earth Sciences, Uppsala University, Sweden
Giuliano.Dibaldassarre@geo.uu.se
[2] Centre for Natural Disaster Science, Uppsala, Sweden
[3] Water Resource Section, Delft University of Technology, the Netherlands

ABSTRACT

Design flood profiles are regarded as important references in the flood management plan. The simulated results of flood modeling are mainly based on deterministic predictions obtained from hydrologic and hydraulic models. This approach of determining flood profiles do not account for various uncertainties that known to influence the simulated results. These uncertainties ranging from input data to modeling equation solver, as well as model parameter and GIS processing tools. In this study, generalized likelihood uncertainty estimation (GLUE) technique is used to represent the uncertainty in model predictions through the Monte Carlo analysis. This study aims to explore and measure the differences arising from the use of deterministic and uncertainty approaches in simulation of design flood profile. The roles of flow and roughness coefficient in uncertainty analysis are explored on the model outputs of one-dimensional HEC-RAS model on Johor River, Malaysia. In general, the results of flood profiles display advantages of uncertainty in design approach are compared with the deterministic single simulation approach.

Keywords: Design flood; GLUE; uncertainty.

1 INTRODUCTION

In hydraulic modelling of floods, estimations of the inundation area (i.e. flood inundation map) and flood profile (i.e. design flood profile) are important for assisting the decision makers in flood relief planning's and operations. The most common representation of simulated results of flood modelling remains a deterministic approach based on a single simulation. Unfortunately, this approach does not account for the uncertainties in the modelling process (Bates et al., 2004) and may lead to an inaccurate hazard assessment (Di Baldassarre et al., 2010). Although the issues of uncertainty in hydraulic modelling of floods have been highlighted in many literatures (e.g. Beven, 2009; Domeneghetti et al., 2013; Dottori et al., 2013), it is difficult to eliminate completely or even quantify these uncertainties due to various constraints such as insufficient computational time or lack of knowledge in the science of floods.

In relation to hydraulic modelling of floods, several uncertainty variables have often been highlighted in scientific literatures such as flow estimation, model parameter (i.e. Manning's *n* roughness coefficient) and source of topography data (i.e. different source of DEMs). In the flow estimation, inflow data is considered one of the most uncertain variables in hydraulic modelling of floods (Pappenberger et al., 2006). Renard et al. (2010) have highlighted that uncertainty from model set up, hydrological data (i.e. number of rain gauges, radar rainfall data) and model parameters give a significant impact when used to generate the design flow in hydrologic modelling. Nevertheless, the uncertainties in inflow data not only arise from the way the observed flow data are estimated but also from the methods used to generate the design flow.

Ample researches related to uncertainty analysis in hydraulic modelling of floods have considered a single model variables and or input datasets as a case study. However, it becomes increasingly important to combine several uncertainties in hydraulic modelling such as in the production of flood inundation map and flood profile.

The objective of this paper is to explore and quantify the difference arising between deterministic approach and uncertainty analysis in simulating design flood profile. This study only considers uncertainty in model parameter and error of 1-in-100 year design inflow, as both uncertainties have shown to be the most influencing variable in the application of 1D hydraulic modelling (Brandimarte and Woldeyes, 2013). The topographic uncertainty was deliberately neglected as this case study is supported with high quality topographic data of Digital Elevation Model (DEM), LiDAR (Light Detection and Ranging).

2 TEST SITE AND DATA AVAILABILITY

The analysis was performed on a 30 km middle reach of the Johor River, Malaysia. The selected river reach flows from northwest towards southeast of the study area (see Figure 1). The river is characterised as a stable main channel with a width ranging from 50 m to 250 m and the average bed slope is about 0.25 m km^{-1}. The study area consists of agricultural land, business centre and residential areas. As reported by DID (2009), the study area has experienced some major floods since 1948. The two latest ones happened in December 2006 and January 2007 to force evacuation of more than 3,000 families.

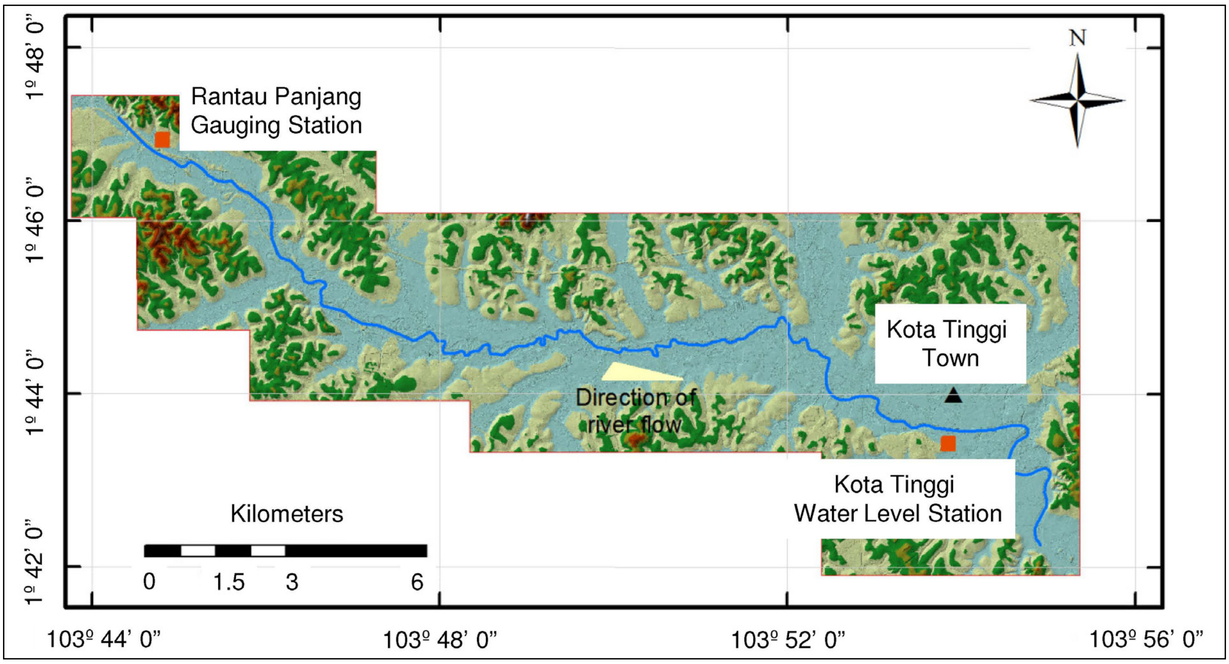

Figure 1. Study area of the Johor River, Malaysia.

Available topographic data for the study were: a 1-m resolution LiDAR (Light Detection and Ranging survey) DEM (Digital Elevation Model) and 32 river cross-sections surveys at approximately 1000 m interval. Both data was made available by the Department of Irrigation and Drainage, Malaysia (DID).

3 HYDRAULIC MODELLING

This study used the 1D code HEC-RAS (US Army Corps of Engineers, Hydrologic Engineering Center 2001) for simulating the hydraulic behaviour of the 30 km reach of the Johor River between Rantau Panjang and 5 km downstream of Kota Tinggi (Figure 1), in unsteady flow conditions. The unsteady numerical code implemented in the HEC-RAS model solves the St Venant equations for a 1D schematization through an algorithm that uses a classical implicit four-point finite difference scheme. Despite the recent development of availability to obtain two-dimensional (2D) hydraulic models in hydraulic modelling of floods, the 1D hydraulic models is still widely used. A friction slope at the downstream cross-section was used as downstream boundary condition, while the observed flow hydrograph at an hourly time step was used as upstream conditions.

4 METHODOLOGY

4.1 Model calibration and validation

Two sets of discharge data from two flood events (i.e. floods of December 2006 and January 2007) were used as inflow data. The measured peak flow of the December 2006 flood, with a peak flow of ~375m^3s^{-1} was used in the calibration. Whereas, the discharge data from the January 2007 flood, with a peak flow of ~595m^3s^{-1} was used for the validation of the calibration model.

The model was calibrated by varying the Manning's n roughness coefficient against the simulated and observed water elevation after the December 2006 flood. To assess the sensitivity of the different models to the model parameters, the Manning's *n* roughness coefficients for all the models were sampled uniformly from 0.02 to 0.08 $m^{-1/3}s$ for the river channel, and between 0.03 to 0.10 $m^{-1/3}s$ for the floodplain. The ranges of Manning's n roughness coefficient in this study were chosen from a variety of documented range of roughness parameters (Chow 1959). The range is sufficiently wide to cover the possible combinations of hydraulic modelling. Further, the performance of the hydraulic model in producing the December 2006 flood profile was assessed by means of the Mean Absolute Error (*MAE*).

4.2 Estimation of design flood profile

The current approach of estimating safety level of the flood protection structure (e.g. dykes, levees) is by considering the freeboard height with the design flood profile. Whereas, the normal approach to determine the design flood profile is by simulating the calibrated hydraulic model with the design flood hydrograph. In Malaysia, DID specified in the manual handbook that the minimum freeboard height to consider when designing the flood protection structure is 1-m above the 1-in-100 year design flood profile.

However, several scientific literatures concern that the use of the 'best fit' model with single design flood estimation in prediction of design flood profiles might misrepresent the existence of any sources of uncertainties in hydraulic modelling simulation (i.e. Beven 2006; Yan et al., 2013). Therefore, to avoid overlooking the existence of any sources of uncertainties which might affect the simulated design flood profile, the use of the probabilistic approach is recommended.

4.2.1 Estimation of design flood profile with uncertainty

As mentioned above, Manning's *n* roughness coefficient was selected as the first variable of uncertainty in hydraulic modelling to be considered in the study. The model was run in a Monte Carlo framework to assess the parameter uncertainty using GLUE. For this scenario, given the accuracy of the used calibration data, all couples of Manning's *n* roughness coefficients (one coefficient each for river channel and floodplain) that gave an *MAE* larger than 1-m were rejected.

This choice of rejection criteria for the *MAE* was made by considering the current policy made by DID that requires any flood defence structure (i.e. dykes, levees) for main river should be at least 1-m above 1-in-100 years flood event. In addition, the Manning's *n* roughness coefficients on the floodplain which were smaller than that on the channel were also eliminated. Adopting the GLUE methodology framework, all the models which passed these rejection criteria were considered as 'behavioural', and were used to simulate 1-in-100 years flood event.

According to the GLUE framework (Beven and Binley 1992), each simulation, *i*, is associated to the (generalized) likelihood weight, W_i, ranging from 0 to 1. The weight, W_i is expressed as a function of the measure fit, ε_i, of the behavioural models.

$$W_i = \frac{\varepsilon_{max} - \varepsilon_i}{\varepsilon_{max} - \varepsilon_{min}} \quad [1]$$

where, ε_{max} and ε_{min} are the maximum and minimum value of *MAE* in behavioural models. Then, the likelihood weights are the cumulative sum of 1 and the weighted 5th, 50th and 95th percentiles. The likelihood weights were calculated as follow:

$$L_i = \frac{W_i}{\sum_{i=1}^{n} W_i} \quad [2]$$

The second variable of uncertainty in this study is the uncertainty in design flood induced by data error. Given that our study aims to evaluate two different approaches of design policies, the analysis was limited to hydraulic modelling only. The detailed analysis of the 1-in-100 year design flood hydrograph was not investigated. This scenario however referred instead to 1-in-100 year design flood hydrograph at Rantau Panjang identified from previous study conducted by DID 2009 (see Figure 2a).

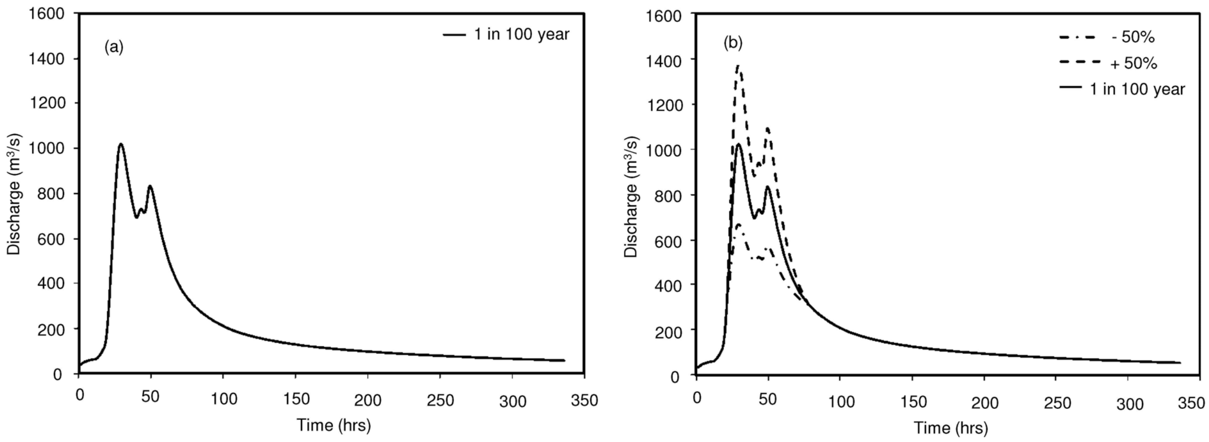

Figure 2. Design flood hydrograph (a) 1-in-100 year design flood hydrograph (b) 1-in-100 year design flood hydrograph by considering of data error.

To evaluate the impact of data error into design flood, we generated 200 values of 1-in-100 years design flood hydrograph, uniformly distributed, by adopting the Eq. [1] and Eq. [2] proposed by Kuczera (1996) and Di Baldassarre et al. (2011). According to Kuczera (1996) the systematic data error can be described as:

$$Q = Q' \text{ If } Q' < Q_a \qquad [3]$$

$$Q = Q_a + \alpha(Q' - Q_a) \text{ If } Q' > Q_a \qquad [4]$$

Where Q indicates the observed value, Q' refers to the true value of river discharge, Q_a represents the river discharge value that overspill in times of high rainfall, and α is a positive value coefficient. Here, the Q_a value is 300 m^3s^{-1} and α = ± 50%. Figure 2b shows the results obtained with α = 0.50 (dash dot line) and α = 1.50 (dash line) and allows an initial interpretation of the practical effects induced by the extrapolation error.

Combining the uncertainties in the Manning's *n* roughness coefficient and estimation of design flood profile, the impact of combined uncertainties was assessed. A total of 4,800 simulations were carried out by feeding all the behavioural models from first scenario (Manning's *n* roughness coefficient) with 200 discharge values from second scenario (estimation of design flood profile).

5 RESULTS AND DISCUSSION

5.1 Calibration and validation

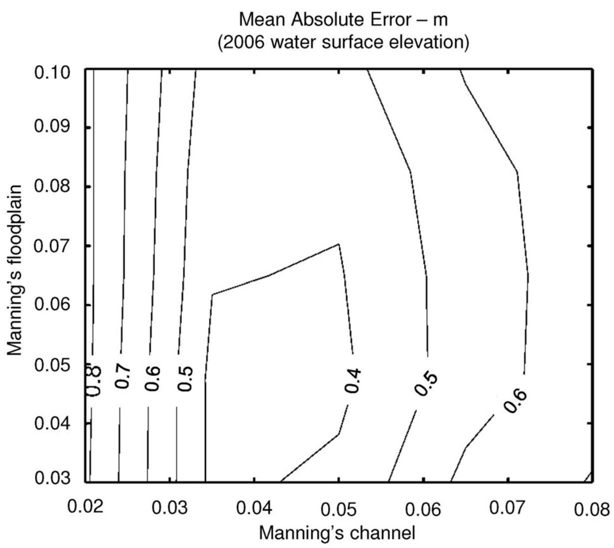

Figure 3. Model responses to variations in Manning's *n* roughness coefficients: (left panel) 2006 flood event; (right panel) 2007 flood event.

Figure 3 shows the model response in terms of *MAE* for the December 2006 flood event. There are different sets of parameters that provide a *MAE* lower than 0.4 m, which was relatively a good performance. The best-fit model performing combination of channel and floodplain coefficients lie inside the hyperbolic shape area by an *MAE* value of 0.38 m. In addition, the model shows to be more sensitive to the Manning's *n* channel roughness coefficient than to the Manning's *n* floodplain roughness coefficient. The optimum Manning's *n* roughness coefficients from the best-fit model above were then used to simulate the January 2007 flood event for model validation. It is found that the *MAE* value for the validation is 0.44 m.

5.2 Estimation of design flood profile

Figure 4a shows the result of simulation in terms of water level of 1-in-100 year flood profile and the profile of water level with a 1-m freeboard. Here, the profile of water level with a 1-m freeboard will be made as a reference height for safety level of any flood protection structure. For the design flood profile, the 1-in-100 year design flood profile for this study was based on the assumption that the hydraulic model calibrated on the 2006 flood event is able to predict the 1-in-100 year flood profile. In addition, a 1-m freeboard height was added to design flood profile with the aims to compensate the many unknown factors that could contribute to flood heights greater than the height calculated for a selected size flood.

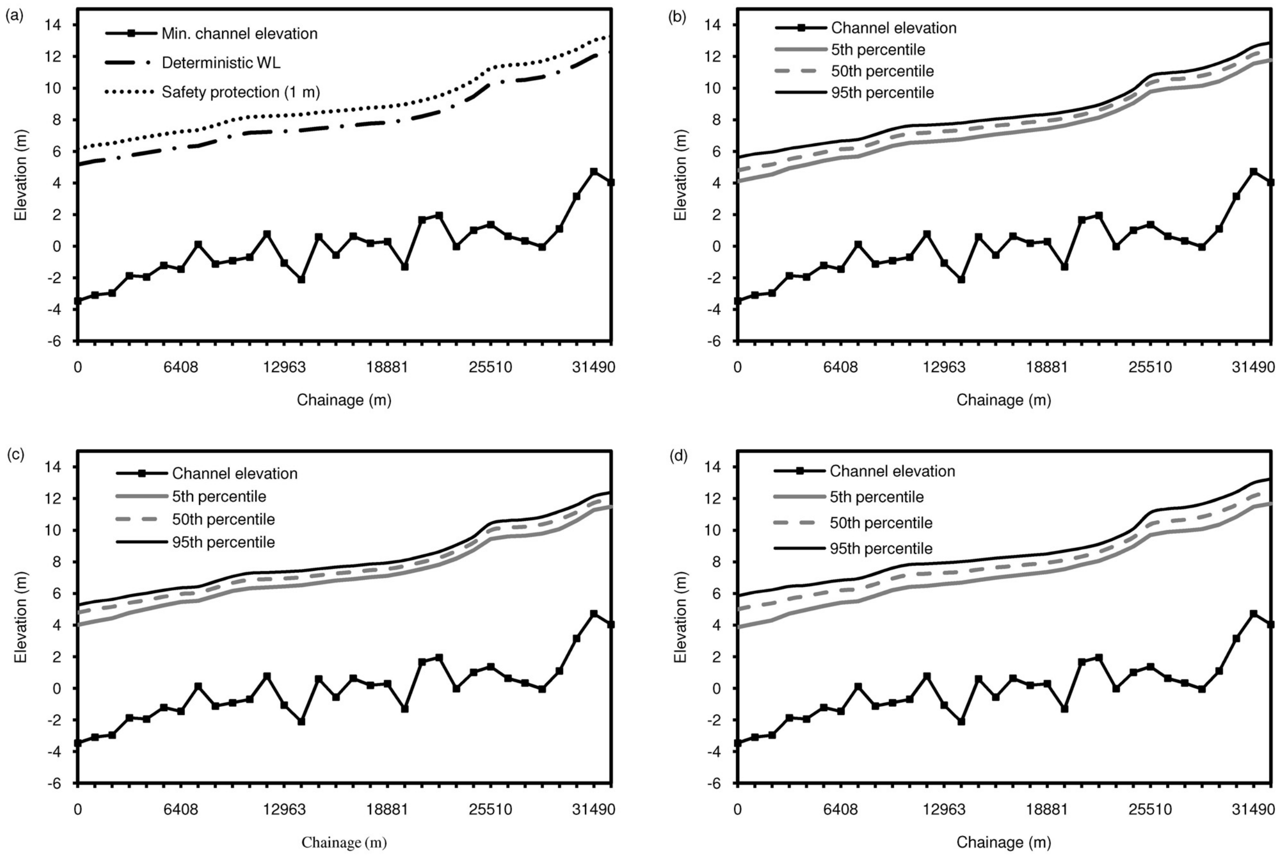

Figure 4. Design flood profiles: panel (a) design flood profile base on single simulation with best fit model and 1-m freeboard; Panels b-d show uncertain design flood profiles by considering the (b) uncertainty in model parameter only; (c) uncertainty in design flow only; and (d) combined uncertainty between model parameter and design flow.

However, the use of freeboard definition in this approach may lead to wrong assumption should the design flood structure (i.e. levee) which is adopting 1-in-100 year design flood profile with 1-m freeboard be assumed as able to protect the flood prone area from extreme flood events of more than 1-in-100 year flood. This assumption have to be corrected by understanding that the freeboard does not provide an additional safety level to the flood prone area but rather to account for the overall uncertainty which may not have been considered during the hydraulic modelling.

Table 1. Results of simulation for estimation of design flood profile.

	Average WSE (m) from change in		
	Roughness	Inflow	Combined
Min	7.41	7.20	7.13
Max	8.67	8.25	9.21
(Max – Min)	1.26	1.05	2.08
5th percentile	7.51	7.26	7.39
50th percentile	8.07	7.80	8.14
95th percentile	8.57	8.21	8.81

Results from Monte Carlo simulations for each uncertainty variables (i.e. Manning's *n* roughness coefficient, flow and combined) when estimating design flood profile are presented in Table 1 and Figure 4b, 4c and 4d. The statistics presented in the Table 1 were computed using the data from all simulations for a particular variable or their combination. For example, a minimum WSE of 7.13 m from combined uncertainty (Table 1 first row, fourth column) represents the minimum WSE among all cross-sections from all 4,800 simulations.

The WSE and uncertainty bounds in Figure 4b, 4c and 4d are also computed using the data at each cross-section from all simulations for specific variable, or the combination of the two variables. Combined uncertainties produced the largest deviation in both minimum and maximum WSE by reducing the minimum WSE by 0.07 m and 0.28 m, while increasing the maximum WSE by 0.24 m and 0.60 m. In this case study, uncertainty in Manning's *n* roughness coefficient creates a wider deviation with uncertainty bound of 1.06 m compared to inflow. Combining the uncertainty in Manning's *n* roughness coefficient and inflow data further enlarges the width of the uncertainty bound to 1.42 m.

However, for this specific case study, it was found that the design flood profile with 1-m freeboard was higher than the 95th percentile uncertainty bound for each uncertainty variables either individual or combined. Hence, the standard freeboard overestimates the overall uncertainty.

6 CONCLUSIONS

The accuracy in prediction of design flood profile is important in flood hazard management. However, the accuracies of the flood profile depend on the uncertainty of the variables used in the flood modelling process. Although a modeller may be aware of the uncertainties involved in data and model parameters during the hydraulic modelling process, understanding and quantifying the role of each uncertain variable in the production of flood inundation map and prediction of design flood profile are still complicated.

The following conclusions are drawn from this study:

a) The use of a 1D hydraulic model and its associated assumptions need additional work. A 1D model such as HEC-RAS provides water surface elevations only along individual cross-sections. Uncertainty can arise in this approach when the water surface elevations at cross-sections are interpolated to create a 2D water surface.
b) Although the finding from this study shows that the design flood profile with 1-m freeboard are higher than the 95^{th} percentile bound for each uncertainty variables, the use of a freeboard should not be considered as an additional safety factor, but rather as a safety margin that allows for uncertainties. Nevertheless, this approach is an attempt to consider the significant sources of uncertainty in design flood profile instead of traditional approach.
c) It was observed that simulating different flooding scenarios with different flow hydrographs and different variables of Manning's *n* roughness coefficient enables accounting for many possible flooding scenarios. This would not be possible with a single flood simulation.

As mentioned above, this study involved in the use of only one particular study area, and therefore similar studies must be carried out for other study areas with different topography, hydrology and sizes. Furthermore, each variable must also be investigated in more detailed with consideration of several other aspects. For instance, the flow data used in this study involved uncertainty arising by the equations. However, in reality when hydrological analyses are carried out to obtain the design flow, uncertainty from input data and hydrologic analysis should also be considered. The overall probability of inundation area within the floodplain area of Johor River could differ if all possible uncertainties from respective scenarios were considered.

ACKNOWLEDGEMENTS

The authors would like to thank to the Department of Irrigation and Drainage, Malaysia (DID) for providing useful input data used in this study. We also acknowledge the Public Service Department, Malaysia for providing a PhD Fellowship funding and study leave for the first author.

REFERENCES

Bates, P.D., Horrit, M.S., Aronica, G. & Beven, K.J. (2004). Bayesian Updating of Flood Inundation Likelihoods Conditioned on Flood Extent Data. *Hydrological Processes,* 18(17), 3347–3370.

Beven, K.J. (2006). A Manifesto for the Equifinality Thesis. *Journal of Hydrology,* 320, 18-36.

Beven, K.J. (2009). *Environmental Modelling: An Uncertain Future?* CRC press: *London*, 328.

Beven, K.J. & Binley, A.M. (1992). The Future of Distributed Models: Model Calibration and Uncertainty Prediction. *Hydrological Process*, 6(3), 279–298.

Brandimarte, L. & Woldeyes, M.K. (2013). Uncertainty in the Estimation of Backwater Effects at Bridge Crossings. *Hydrological Process,* 27, 1292-1300.

Chow, V.T. (1959). *Open-Channel Hydraulics*. McGraw-Hill: New York.

Di Baldassarre, G. & Claps, P. (2011). A Hydraulic Study on the Applicability of Flood Rating Curves. *Hydrology Research,* 42, 10-19.

Di Baldassarre, G., Schumann, G., Bates, P.D., Freer, J.E. & Beven, K.J. (2010). Flood-Plain Mapping: A Critical Discussion of Deterministic and Probabilistic Approaches. *Hydrological Science Journal,* 55, 364-376.

Domeneghetti, A., Vorogushyn, S., Castellarin, A., Merz, B. & Brath, A. (2013). Probabilistic Flood Hazard Mapping: Effects of Uncertain Boundary Conditions. *Hydrology Earth System Science,* 17(8), 3127–3140.

Dottori, F., Di Baldassarre, G. & Todini, E. (2013). Detailed Data is welcome, but with a Pinch of Salt: Accuracy, Precision, and Uncertainty in Flood Inundation Modeling. *Water Resource Research,* 49(9), 6079–6085.

Hydrologic Engineering Center. (2001). *Hydraulic Reference Manual,* US Army Corps of Engineers, Davis, California, USA.

Kuczera, G. (1996). Correlated Rating Curve Error in Flood Frequency Inference. *Water Resource Research,* 32(7), 2119-2127.

Pappenberger, F., Matgen, P., Beven, K., Henry, J., Pfister, L. & Fraipont de, P. (2006). Influence of Uncertain Boundary Conditions and Model Structure on Flood Inundation Predictions. *Advance Water Resource,* 29(10), 1430–1449.

Renard, B., Kavetski, D., Kuczera, G., Thyer, M. &Franks, S.W. (2010). Understanding Predictive Uncertainty in Hydrologic Modeling: The Challenge of Identifying Input and Structural Errors. *Water Resource Research,* 46(5), 1-22.

Yan, K., Di Baldassarre, G. & Solomatine, D.P. (2013). Exploring the Potential of SRTM Topographic Data for Flood Inundation Modelling under Uncertainty. *Journal of Hydroinformatics,* 15(3), 849-861.

ASSESSING FLOOD DYNAMICS IN RIVERS AND RIPARIAN WETLANDS: AN INTEGRATED HYDROLOGICAL APPROACH

MICHAEL BUTTS[(1)], BIRGITTE VON CHRISTIERSON[(2)], CRAIG MACKAY[(3)],TERRY VAN KALKEN[(4)] & SÍLVIA LEIRIÃO[(5)]

[(1,2,5)] DHI Denmark, Agern Alle 5, DK 2970, Hoersholm, Denmark,
mib@dhigroup.com, bvc@dhigroup.com, sls@dhigroup.com
[(3)] DHI Australia, 3A02-0, Suite 8.01, 50 Clarence Street, Sydney, NSW 2000, Australia,
c_craigm@hotmail.com
[(4)] DHI Malaysia, Block G, Pusat Dagangan Phileo, Damansara I, No. 9, Jalan 16/11, Off Jalan Damansara, 46350 Petaling Jaya, Selangor, Malaysia,
tvk@dhigroup.com

ABSTRACT

Floodplain risk management at catchment scale must address flood risk within an integrated water resources management strategy. Flood inundation modelling is important not only for assessing the flood risk to life and property but also for the potential impacts of flood mitigation on riparian wetlands. In this paper, we present an integrated flow modeling tool capable of representing a comprehensive range of flood and catchment processes, including the hydraulic processes in the river, river-floodplain exchanges across the banks, the dynamic surface water-ground water interactions, and the infiltration and evaporation effects. The capabilities of this tool are demonstrated on flood inundation modeling in the Lower Murrumbidgee River, Australia. One of the most important challenges in simulating flood behaviour for catchment management is the need to verify the reliability of model predictions. Traditional observation data are limited to flows or water levels within the river channels. Using satellite imagery and aerial photographs, we investigate the impact of different processes and uncertainties on the flood dynamics and flood extent. The results show that floodwater retention and spilling upstream are very sensitive to local topography and may significantly affect flooding behaviour downstream. This is confirmed when we compare the performance of the integrated hydrological model with high resolution hydraulic modeling. For the longer time scales of wetland flooding, where the hydro period is important for the health and functioning of the riparian wetlands, infiltration and evaporation processes become important.

Keywords: Integrated hydrological-hydraulic modeling; satellite imagery; uncertainty; floodplain inundation; riparian wetlands.

1 INTRODUCTION

Flooding can result in significant social, economic and environmental damage (UNISDR, 2012), and potentially loss of life. Flood risk management has therefore had a narrow focus on managing and minimizing these risks, (Plate, 2002). However, flood management cannot be and should not be considered independently of other river and catchment functions, (Middelkoop et al., 2004). Flood management strategies must become part of a more general integrated water resource strategy that addresses the development and management of the floodplains, surface and groundwater resources, the water quality, the freshwater habitats and ecological conditions.

Hydrodynamic models of river reaches and floodplains are widely used to support flood risk assessment and decision-making. They are used to make scenario predictions of flooding events for different return periods and under future climatic conditions (Hall et al., 2005; Hunter et al., 2007) but most importantly to evaluate different flood mitigation and climate adaptation measures. Such flood mitigation measures range from structural measures such as reservoirs, embankments, detention storages and diversion channels to nonstructural measures such as flood forecasting and flood preparedness as in Table1. These measures are often evaluated by comparing the reduction of flood risk in economic terms of their cost.

The impacts of these measures are however more far reaching, affecting agriculture, navigation, energy production as well as nature and landscape values. Regular flooding, for example, is important to the health and functioning of river wetland ecosystems, (Powell et al., 2008; von Christiersen et al., 2015). There is an increasing recognition of the ecological and economic values and services of wetlands (Duranel et al., 2007; Acreman and Ferguson, 2010). The environmental benefits of riparian wetlands range from improving the recreational value of rivers, biodiversity, water purification, flood protection, shoreline stabilization, groundwater recharge, and streamflow maintenance. While it is more challenging to quantify the economic value to ecosystem services such as recreational value or biodiversity, it is nevertheless important to avoid adverse impacts. Indeed, the restoration of rivers and riparian wetlands is increasingly being used, both in the form of nature-based solutions for flood protection as well as in river basin management strategies across Europe for achieving ‘good ecological status’ of water bodies as required by the EU Water Framework Directive (WFD).

Table 1. Structural and non-structural measures for flood risk mitigation.

STRUCTURAL MEASURES	NON-STRUCTURAL MEASURES
Dikes and Embankments	Zoning controls
Detention storages	Regulation of construction on flood plains
Flood diversion channels	Flood forecasting
Control structures	Flood proofing
Pumps	Control structure and reservoir optimisation
Reservoirs	Public education
Real-time monitoring networks	Flood preparedness
	Flood insurance

A more holistic approach to floodplain and water resource management requires modelling tools capable of modelling a much wider range of processes in the river reaches, floodplains and riparian wetlands than that are currently available. The flood dynamics and inundation extent are controlled by a number of factors, such as the magnitude of the event, vegetation and land use distribution, the floodplain topography, the channel and riverbank geometry. The evaluation of different flood mitigation and climate adaptation measures requires that structural measures such as diversion channels, control structures and etc. which can be represented realistically but more importantly that their impacts on flow regimes and ecological conditions can be reliably predicted. More specifically, within riparian wetlands, processes such as the exchange between surface water and groundwater and losses via infiltration and evapotranspiration can be important both for flood protection and the ecological functioning of wetlands habitats. To address the representation of this wider range of hydrological and ecological processes we present an application of the MIKE SHE integrated hydrological modelling tool that has many of the capabilities needed to assess flooding and flood risk in the larger context of integrated water resource management. We demonstrate, , the capabilities of this tool for simulating flooding in both floodplains and riparian wetlands in the particular case of the Lower Murrumbidgee River, a tributary to the Murray River, Australia.

One of the important challenges in using flood models is to understand the accuracy and reliability of the predictions of future scenarios. Traditionally, river observation data are limited to flows or water levels within the river channels. As a result, there are usually no observations within wetlands or in the floodplain areas of interest, or at most a few point measurements (Butts et al., 2008; von Christiersen et al, 2015). As an alternative to point measurements on the floodplains, satellite imagery and aerial photography of flood extent can be used to understand flooding behavior and to determine the reliability of simulations during flood events (Horritt and Bates, 2002; Butts et al., 2008; Di Baldassarre et al, 2009). This approach is used here to examine the performance of the MIKE SHE model in simulating flooding in the Lower Murrumbidgee River as in Figure 1.

2 LOWER MURRUMBIDGEE STUDY AREA

The study area, the Murrumbidgee River is located in the south east of Australia and is the second largest river in the Murray-Darling Basin. The Murrumbidgee River supports a range of water users including irrigation, drinking-water supply, industry as well as wetland and in-stream ecosystems, and therefore its management and operation is a complicated task. The complex river behaviour, coupled with the need to satisfy diverse water demands from a combination of dam and river storages and natural runoff makes water resources management in the catchment a challenge.

There is a long history of floods in the Murrumbidgee River, with severe flooding in 1852, 1853, 1925, 1950, and 1974 and more recently in December 2010 and March 2012. Within the Murray-Darling Basin, an estimated 90% of floodplain wetlands have been lost as a result of flow regulation, (Wen et al., 2013). However, the Murrumbidgee River supports a large number of wetlands, including two Ramsar sites (Ginini Flats Wetland Complex and Fivebough and Tuckerbil Swamps) and two nationally protected extended wetland complexes (Mid-Murrumbidgee Wetlands and Lower Murrumbidgee Floodplain or Lowbidgee), which are key environmental resources of the Murray-Darling Basin.

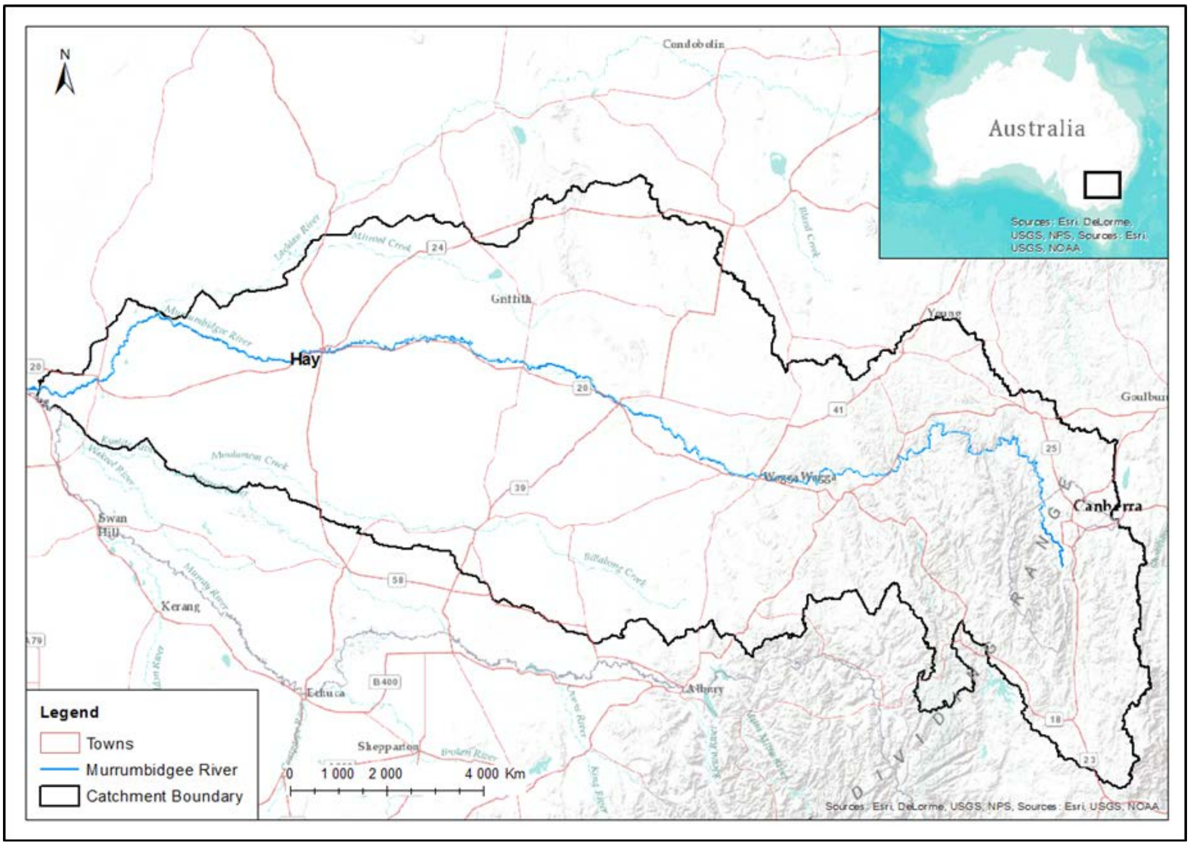

Figure 1. Location map of the Murrumbidgee catchment showing the main river.

3 METHODOLOGY

3.1 Models

The integrated hydrological modelling system MIKE SHE, simulates the major processes of the terrestrial hydrological cycle; snow accumulation and melting, evapotranspiration, river and channel flows, overland flow, and subsurface flow in the unsaturated and saturated zones, (Graham and Butts, 2006). The different flow processes of MIKE SHE were described either by the governing partial differential equations or by empirical relations and these are then solved by discrete grid-based numerical approximations in space and time.

More recently, the process-based formulation of MIKE SHE had been exploited to develop a more flexible modelling tool, where each of the major processes can be modelled using both conceptual and physics-based representations (Butts et al., 2004; Graham and Butts 2006). There are several advantages in this flexibility, the most important being that the mathematical representation of a particular process can be adapted to the modelling goals and the data available. For example, for flood mapping the surface processes may be modelled using one- and two-dimensional hydraulics in great detail but the subsurface processes such as infiltration or groundwater flow can be greatly simplified or even neglected. On the other hand, in cases where infiltration or evaporation losses may be important or where surface water and groundwater interactions control flood behavior, these processes can be directly incorporated.

MIKE SHE uses a coupled 1D-2D approach to model fluvial flooding. The flows in the river channel were simulated using MIKE 11 (1D) model that represents channel flows using a one-dimensional solution to the Saint-Venant equations, (Havnø et al., 1995). The surface flow on the surface and flood plains was modelled using a diffusive wave approximation in two dimensions on a finite difference (raster) grid, (Storm and Refsgaard, 1996).

For comparison, simulations have also been carried out using the comprehensive hydrodynamic flood modelling package, MIKE FLOOD. MIKE FLOOD consists of dynamic links of three independent software packages; MIKE 11 (1D) for rivers and open channels, MIKE URBAN/MOUSE (1D) for urban drainage systems and MIKE21 (2D) for surface flows on floodplains, estuaries and coasts. This combination makes it possible to simulate a wide range of flood problems involving rivers, floodplains, flooding in streets, drainage networks, coastal areas, dam or levee breaches or any combination of these. The 2D domain can be represented either by the widely used finite difference rectilinear grid, referred to as MIKE21 “classic”, (Warren and Bach, 1992) or a finite volume based flexible mesh, MIKE21FM, (Papaioannou et al., 2016). Such hydrodynamic models are being used more frequently in wetland restoration and management and MIKE FLOOD had been used, for example to model wetlands in the Florida Everglades, (Chen et al., 2012) and in the Murray-Darling Basin, Australia (Wen et al., 2011; Wen et al., 2013).

The MIKE SHE and MIKE FLOOD models have been applied to the numerical model domain shown in Figure 2, centered on the town of Hay and covering an area of approximately 2600 km^2.

Figure 2. The simulation model domain used in this study.

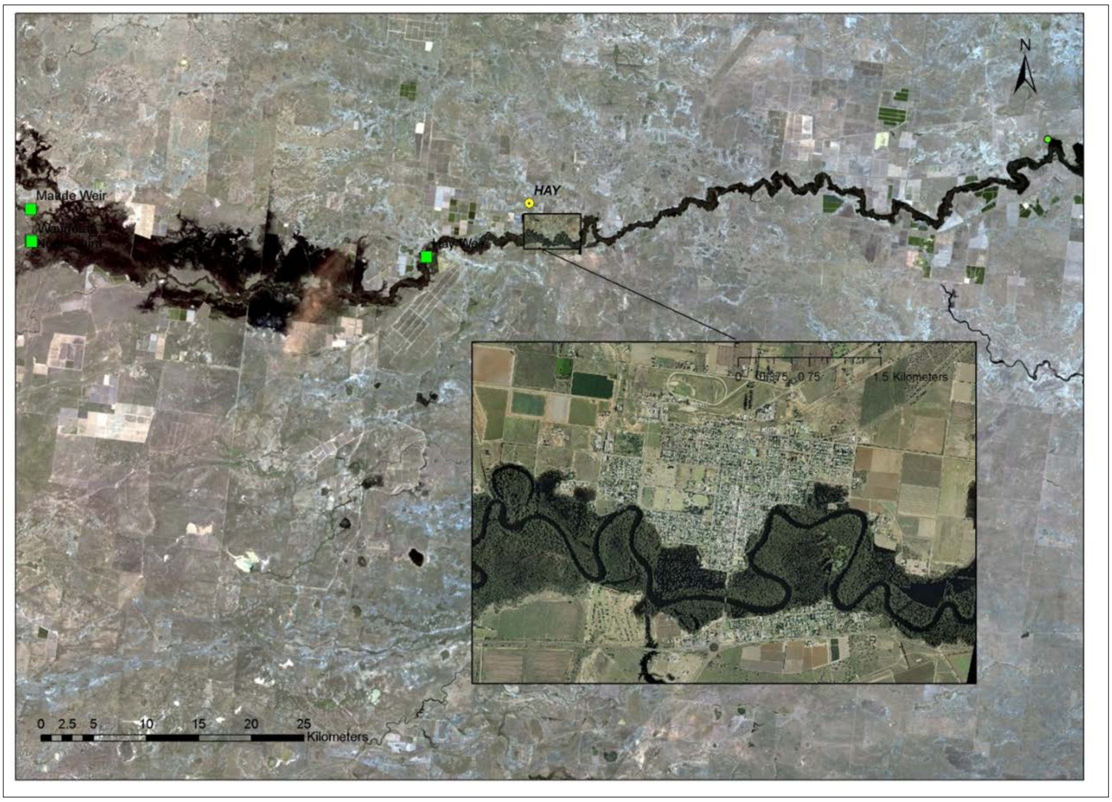

Figure 3. Satellite images of the Lower Murrumbdigee including the upstream end of the Lowbidgee wetlands. The inset is an aerial photograph of the town of Hay.

3.2 Methodology

Both satellite imagery and aerial photographs during flood events have been used to assess the simulations of flood extent. The aerial photographs provide high-resolution flood extent in the urbanized area around the town of Hay while the satellite images show the large scale flooding behavior, particularly for the downstream wetlands. Figure 3 shows examples of these where the dark areas indicate water at or near the surface.

4 INITIAL MODELLING RESULTS

To investigate the importance of different processes that control the flooding behavior and flood extent, we have carried out a number of simulation scenarios. In this paper, we present some of the initial results of this analysis for the MIKE SHE simulations carried out at a surface grid resolution of 100m. In the first set of simulations, a sequence of flood events had been modelled using only the surface processes while direct rainfall on the catchment was neglected. The floodplain therefore acts as an impervious surface in these

  / ISSN 1562-6865 (Online) - ISSN 1063-7710 (Print)

simulations and the flood extent depends mainly on the magnitude of the event, which was determined by the upstream inflows, as well as the hydraulic properties of the river and floodplain and the exchange between these elements. Numerical simulations were carried out for a major flood event which occurred from the middle of November 2010 to the end of January 2011.

The measured and simulated water levels at Hay weir, Figure 4, show reasonable agreement throughout the period of simulation. However, there were differences in both the shape and timing of the discharge hydrograph.

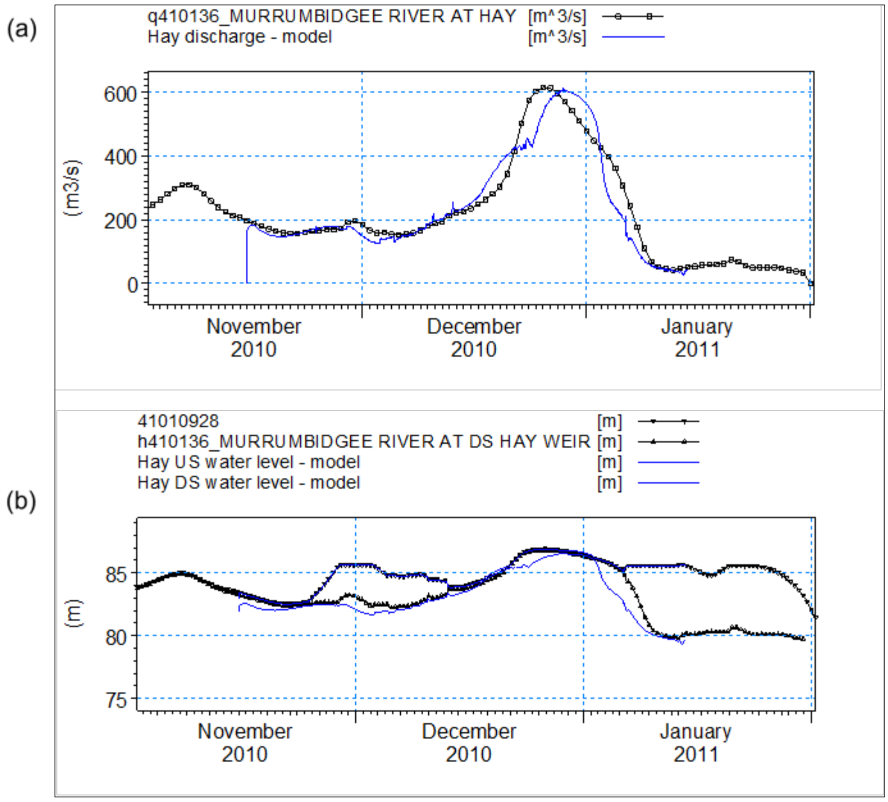

Figure 4. The measured and simulated discharge at the Hay station (a) and the measured and simulated water levels upstream and downstream of the Hay Weir (b).

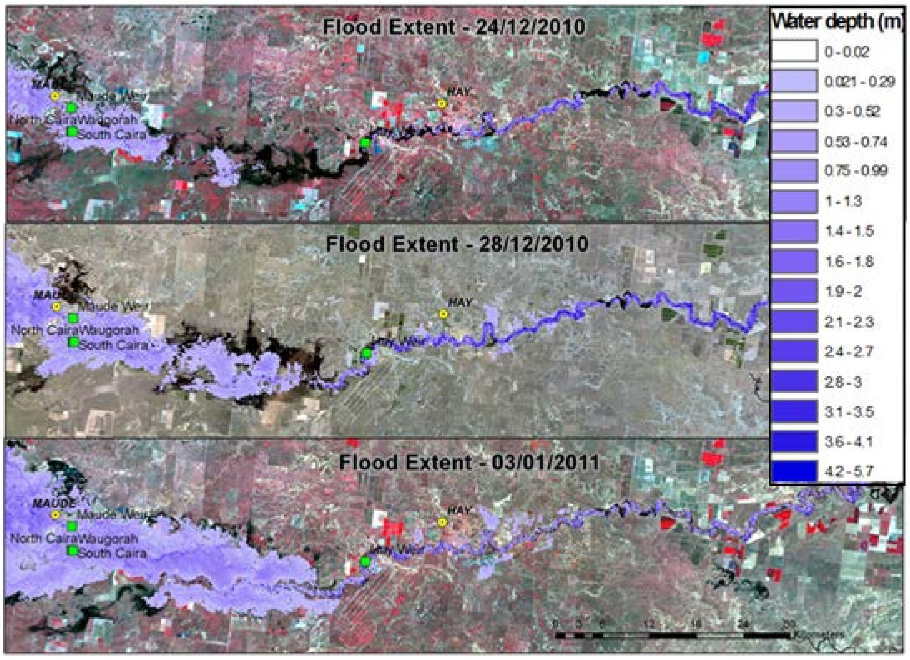

Figure 5. Comparison of the simulated flood extent using mike she with satellite images.

Figure 5 compares the MIKE SHE simulations with satellite images on three different dates when good quality satellite images were available, 24/12/2010, 28/12/2010 and 03/01/2011. The simulated flood extents, generally under-estimate the observed extents captured by the satellite images. This was clearly the case for the upstream part of the Lowbidgee wetlands area in the early part of the flood. However, there were also parts of the river upstream of Hay where the simulation does not reproduce the observed flooding in the main channel. One reason for this may be that the satellite images show wet areas rather than areas with standing water on the surface. The differences in the shape and timing of the observed and simulated flood hydrograph may also account for the discrepancies in flood extent.

A second simulation for the same period was then performed, in which the model was modified to include rainfall falling directly on the model domain and losses from both evapotranspiration and infiltration included. As might be expected, these additional terms appear to reduce the simulated flood extents and the differences are largest towards the end of the flood, (Figure 6). A water balance for the flood event period shows that the effects of rainfall falling directly on the model domain was limited and that flooding was driven by conditions upstream as in Figure 6. The modelled water levels in the wetland area appear to have nearly receded by 15/1/2011, which agrees with the observed extent from a MODIS satellite image (not shown). The net inflow from the river to the wetland indicates that spilling from the river to the floodplains occurs until approximately 4/1/2011 as in Figure 6.

These preliminary results indicate that further investigations are required to determine what is causing the discrepancies between the observed and simulated flood extents. Currently we are carrying out simulations to determine the effects of uncertainties in grid resolution but there are a number of other potential causes including uncertainties in the bank levels, topography, groundwater, rainfall, upstream discharges, hydrometric data error and etc. It should also be noted that flows to the Lowbidgee floodplains are regulated through gate structures that divert water from the Maude Weir pool. Although these were included in the model there were some uncertainties associated with the timing and magnitude of the controlled releases, which may play an important role during flooding.

As a first step in these investigations, we have carried out some initial investigations with the MIKE FLOOD for the same area. Some of the key features of MIKE SHE and MIKE FLOOD are compared in Table 2. Simulations using the two-dimensional finite volume solution (MIKE21 FM) will allow us to take advantage of the high-resolution topography data obtained from LiDAR measurements. Employing high data resolution is expected to achieve a better representation of the spatial pattern of inundation.

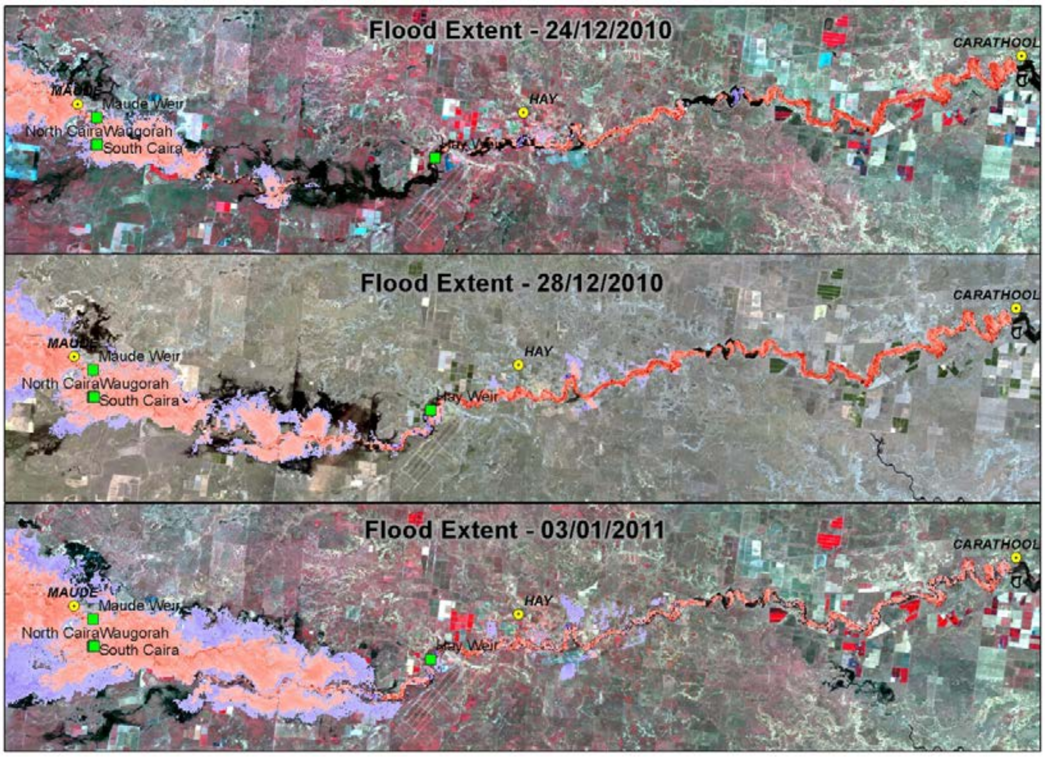

Figure 6. The simulated flood extent using MIKE SHE compared with satellite images. The flood extents shown in blue correspond to the simulations as depicted in Figure 5. The flood extents shown in red, overlaying the blue, show the results when direct rainfall, evapotranspiration and infiltration are included.

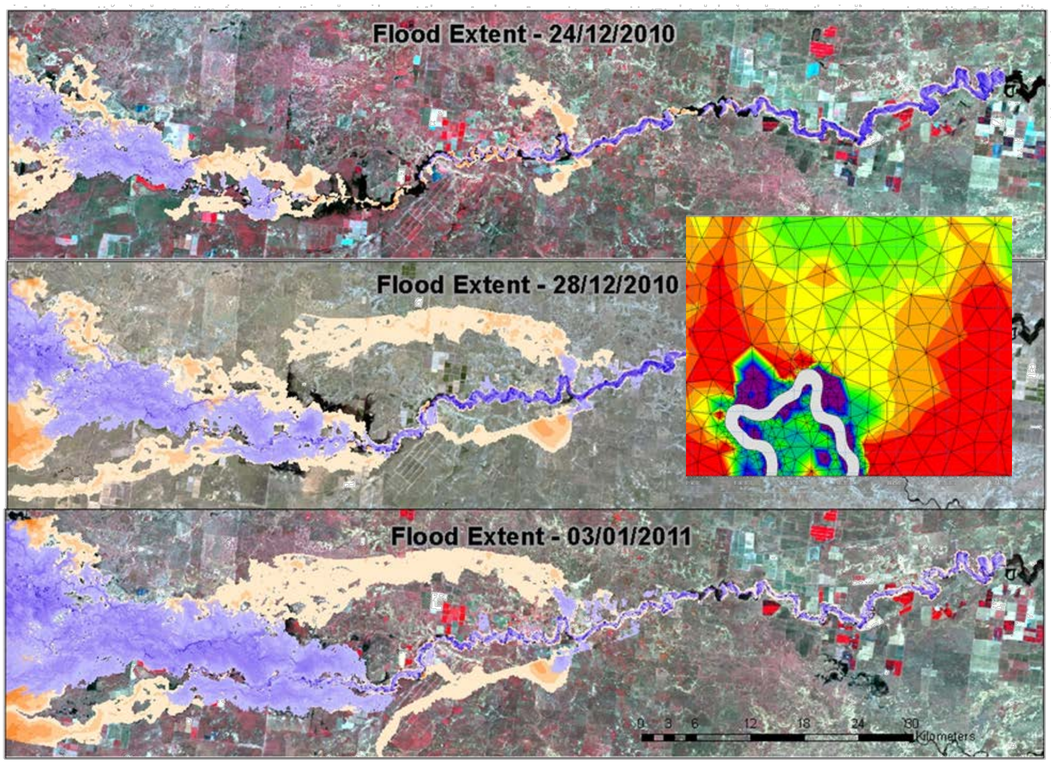

Figure 7. The simulated flood extent using MIKE FLOOD FM compared with satellite images. The flood extents shown in blue correspond to the MIKE SHE simulations as depicted in Figure 5. The flood extents shown in yellow overlaying the blue, show the results obtained from initial simulations using MIKE FLOOD. The inset shows the finite volume mesh and topography near the town of Hay.

The results in Figure 7 show a quite different pattern of inundation with more spilling in the upstream reaches from the flexible mesh description in MIKE FLOOD FM than predicted using the raster based MIKE SHE model. It is not clear whether these discrepancies arise from differences in resolution, errors in the local topography or differences in the numerical description of the spilling process or the floodplain topography. Further simulations are being carried out to investigate these differences further.

Table 2. Key features of the MIKE SHE and MIKE FLOOD models.

MIKE SHE	MIKE FLOOD
Integrated hydrological model for catchments	Hydrodynamic model of rivers, estuaries and floodplains
MIKE 11 (1D) river	MIKE 11 (1D) river
2D diffusive wave approximaton on the flood plain	2D fully dynamic wave approximation on the flood plain
Block centred finite difference approximation (raster)	Both finite difference (raster) and finite voloume flexible mesh proofing
Physics-based modelling of groundwater,evapotranspiration, and infiltration processses	No groundwater, simplified evapotranspiration and infiltration processes

5 CONCLUSIONS

This paper presents the application of the integrated surface water-groundwater model MIKE SHE for modelling flood dynamics and extents in the lower Murrumbidgee River, Australia. The non-linear exchange (spilling) between the river and the floodplain has been represented by detailed hydraulic modelling of the flow over the banks using the cross-sections and LIDAR topography. The simulation results are sensitive to the spilling between the bank and the floodplain, which is controlled by the topographic data and the accuracy of bank elevations in the model. From the comparisons with the satellite images, the model tends to overestimate the flood extent upstream of Hay but underestimate it below Hay. River flood discharges are uncertain and combined with limited groundwater level data; this makes it difficult to determine the exchange flows to the underlying groundwater aquifer during the flood event. The infiltration and evapotranspiration processes clearly affect the flood extent and control the flood recession processes and these are often not represented in purely hydraulic models. Further investigations are required as there are a number of potential causes for these discrepancies such as uncertainties in the topography, bank levels, groundwater, rainfall, upstream discharge and regulation structure operations.

ACKNOWLEDGEMENTS

We would like to thank the Office of Environment and Heritage (OEH), NSW, Australia for making LIDAR data available to this research study. Deimos Imaging provided the DEIMOS satellite data. The U.S. Geological Survey (USGS) supplied the Landsat and MODIS satellite data used.

REFERENCES

Acreman, M.C. & Ferguson, A.J.D. (2010). Environmental Flows and the European Water Framework Directive. *Freshwater Biology*, 55(1), 32-48.

Butts, M.B., Payne, J.T., Kristensen, M. & Madsen H. (2004). An Evaluation of the Impact of Model Structure on Hydrological Modelling Uncertainty for Streamflow Prediction. *Journal of Hydrology*, 298(1-4), 242-266.

Butts, M.B., Fontenot, E., Cavalli, M., Chuah, Y.P, Jensen, T.S., Clausen, T. & Taylor, A. (2008). Development and Evaluation of an Integrated Hydrological Modelling Tool for the Water Framework Directive and Floods Directive. *Proceeding of International Conference Flood Risk*, Oxford, United Kingdom.

Chen, C., Meselhe, E. & Waldon, M. (2012). Assessment of Mineral Concentration Impacts from Pumped Stormwater on an Everglades Wetland, Florida, USA–using a Spatially-Explicit Model. *Journal of Hydrology*, 452, 25-39.

Di Baldassarre, G., Schumann G. & Bates P.D. (2009). A Technique for the Calibration of Hydraulic Models using Uncertain Satellite Observations of Flood Extent. *Journal of Hydrology,* 367(3), 276-282.

Duranel, A.J., Acreman, M.C., Stratford, C.J., Thompson, J.R. & Mould, D.J. (2007). Assessing the Hydrological Suitability of Floodplains for Species-Rich Meadow Restoration: A Case Study of the Thames Floodplain, UK. *Hydrology and Earth System Sciences Discussions*, 11(1), 170-179.

Graham, D.N. & Butts M.B. (2006). *Flexible, Integrated Watershed Modelling with MIKE SHE, Watershed Models*. CRC Press, 245-272.

Hall, J.W., Sayers, P.B. & Dawson, R.J. (2005). National-Scale Assessment of Current and Future Flood Risk in England and Wales. *Natural Hazards*, 36(1-2), 147-164.

Havnø, K., Madsen, M.N. & Dørge, J. (1995). MIKE 11—*A Generalized River Modelling Package. Computer Models of Watershed Hydrology*. Water Resources Publications, Colorado, USA, 733–782.

Horritt, M.S. & Bates, P.D. (2002). Evaluation of 1D and 2D Numerical Models for Predicting River Flood Inundation. *Journal of Hydrology,* 268(1), 87-99.

Hunter, N.M., Bates, P.D., Horritt, M.S. & Wilson, M.D. (2007). Simple Spatially-Distributed Models for Predicting Flood Inundation: A Review. *Geomorphology*, 90(3), 208-225.

Middelkoop, H., Van Asselt, M., Van'T Klooster, S.A., Van Deursen, W., Kwadijk, J.C. & Buiteveld, H. (2004). Perspectives on Flood Management in the Rhine and Meuse Rivers. *River Research and Applications*, 20(3), 327-342.

Plate, E.J. (2002). Flood Risk and Flood Management. *Journal of Hydrology*, 267(1), 2-11.

Papaioannou, G., Loukas, A., Vasiliades, L. & Aronica, G.T. (2016). Flood Inundation Mapping Sensitivity to Riverine Spatial Resolution and Modelling Approach. *Natural Hazards*, 83(1), 117-132.

Powell, S.J., Letcher, R.A. & Croke, B.F.W. (2008). Modelling Floodplain Inundation for Environmental Flows: Gwydir Wetlands, Australia. *Ecological Modelling*, 211(3–4), 350-362.

Storm, B. & Refsgaard, A. (1996). Distributed Physically-Based Modelling of the Entire Land Phase of the Hydrological Cycle. *Distributed Hydrological Modelling*, 22, 55-69.

UNISDR, (2012). *United Nations Office for Disaster Risk Reduction,* UNISDR Annual Report.

Von Christiersen, B., Nieuwenhoven, L.A., Butts, M., Hansen, F.T. Jensen, J.K. & Poulsen J.B. (2015). Modelling Surface Water, Groundwater and Nitrate Processes in a Restored Riparian Wetland. *FEFLOW Conference*.

Warren, I.R. & Bach, H. (1992). MIKE 21: A Modelling System for Estuaries, Coastal Waters and Seas. *Environmental Software*, 7(4), 229-240.

Wen, L., Marsh, N., Mackay, C., Salbe, I., Saintilan, N. & Ling, J. (2011). Linking Wetland Hydrology to Ecological Outcomes in the Lowbidgee Wetlands in Southern New South Wales. *Proceeding of the 19th International Congress on Modelling and Simulation*, Perth, Australia, 2479-2485.

Wen, L., Macdonald, R., Morrison, T., Hameed, T., Saintilan, N. & Ling, J. (2013). From Hydrodynamic to Hydrological Modelling: Investigating Long-Term Hydrological Regimes of Key Wetlands in the Macquarie Marshes, a Semi-Arid Lowland Floodplain in Australia. *Journal of Hydrology*, 500, 45-61.

STUDY ON PARAMETERS ESTIMATION OF THE XAJ MODEL BASED ON UNDERLYING SURFACE CHARACTERISTICS

XING-NAN ZHANG[1], YUAN-HAO FANG[2], BO QU[3], LE-JUN MA[4] & MIAO WU[5],

[1,2,3,4,5]College of Hydrology and Water Resources, Hohai University, Nanjing, China, zxn@hhu.edu.cn
[1] National Cooperative Innovation Center for Water Safety & Hydro-Science, Nanjing, China, zxn@hhu.edu.cn

ABSTRACT

Hydrological models are essential in assessing hydrological processes at both hillslope and watershed scale. The Xin'anjiang (XAJ) Model is a conceptually-based model which was developed on the basis of conception of hillslope hydrology. Although processes like evapotranspiration, runoff yield and routing are represented by generalization rather than physically-based partial differential equations, several parameters of the model have rigid physical definitions which can be estimated by characteristics of the watershed. Due to the lack of measurement and data, these parameters were mainly estimated by calibration which would need high technology and more uncertainties might be introduced into the model. Recently, benefited from Geographic Information System (GIS) and Remote Sensing (RS), data have been significantly improved in both the quantity and the quality. In this paper, the indices of the underlying surface of a watershed were derived firstly (e.g. the slope and aspect of hillside, roughness, soil, vegetation, etc.). These indices were then employed to establish the relationships with the parameters on the basis of the physical definitions or the statistical analysis purely. By the use of this approach, the overall performance of the XAJ model was much more robust than that of the calibration, and more suitable to be used in ungauged catchments.

Keywords: Xin'anjiang model; Parameters estimation; GIS; Underlying surface indices.

1. INTRODUCTION

Hydrological models are useful tools for investigating the hydrological processes at different spatial and temporal scales and for us, to understand the hydrological processes at ungauged catchments where observation of hydrological elements (e.g. discharge, soil moisture, etc.) are not available. Understanding the hydrological processes also serves as the basis for studying other processes (e.g. transport). Recently, a large number of models have been developed, trying to represent main physical processes involved in the rainfall-runoff process (Beven, 2002). Depending on the basis, these models can be identified as physically-based which are mainly based on partial differential equations (e.g. Richards equation, de St. Venant equation, etc.) or conceptual models which usually employ a number of mathematical functions or distributed curves to reproduce hydrological processes (Kampf and Burges, 2007; Niu et al., 2013). Those physically-based models are usually spatial distributed, which are more capable of capturing the complex processes at different scales and representing the interaction with atmosphere. But the applications of physically-based models, especially in watershed scale, are always restricted by input data availability. Conceptual models, on the other hand, despite their relative simple structure, can also achieve high accuracy in terms of stream discharge simulation, which is important in practical real-time forecasting (Yao et al., 2012). For these reasons, conceptual models are sometimes more preferable if internal processes (e.g. soil moisture variation) are not the main concern. Both kinds of models have several parameters which should be estimated before applying to certain catchment. The estimation of parameters, however, is a difficult task even for physically-based models whose parameters can be measured directly. This is partly due to the heterogeneity of catchment and the limitation of our measurement which results in very limited information at hand, so we still need to extrapolate these parameters in order to drive the model. For those conceptual models whose parameters do not have physical definitions, researchers mainly depend on mathematical algorithms to optimize parameters by gradually adjusting the model parameters to match observed data (Ye et al., 2014).

The Xin'anjiang (XAJ) model is a well-known and widely-used distributed conceptual model, it has been applied to many catchments in China. Considering that it is a conceptual-based model, many studies have been focusing on the calibration of its parameters by different kinds of optimization methods. Hapuarachchi (P. et al., 2001) calibrated the XAJ model by SCE-UA and revealed that SCE-UA was capable of finding a global optimum and conceptually realistic parameter set. Li (Zhijia et al., 2011) also employed SCE-UA method to calibrate the model and found that the combined method can increase the calibration speed and reduce the influence of the calibration data period on the results. Ye (Ye et al., 2014) adopted the surrogate modeling approach to study the parameter calibration, such approach could provide valuable information in model calibration and application. Cheng (Cheng et al., 2006) combined Genetic Algorithm with TOPSIS to investigate the parameter calibration of the XAJ model. Wang (Wang et al., 2012) presented a novel hybrid genetic algorithm (GA) combining chaos and simulated annealing (SA) method to calibrate parameters, he found that the hybrid algorithm performed better than GA and CGA.

Although abovementioned approaches are effective and have been proved to ensure good performance of the XAJ model, they still have some defects. First of all, equifinality (i.e. different parameters might have same effects on hydrological flux) might lead to the unrealistic calibration results (Beven and Freer, 2001). Secondly, parameters calibrated by optimization methods are constant over the whole study area, neglecting the spatial variation due to heterogeneity of catchments. Meanwhile, it is still impossible to optimize parameters in ungauged catchments where observed discharge data are unavailable. Moreover, to calibrate parameters in large catchments might be time-consuming. By analyzing the XAJ model, we recognized that some parameters are directly related to underlying surface characteristic but few efforts have been made to investigate the relation between parameters and underlying surface characteristics.

Benefited from the development of remote sensing (RS) and geographic information system (GIS), we now have more information about underlying surface characteristic at high spatial resolution. So it is promising to estimate these parameters based on underlying surface characteristics. In this paper, we selected 20 gauged catchments in SXLY basin with different characteristics for the study. We firstly subdivided the catchment into element area based on DEM and digitalized drainage network then calibrated the parameters with observed discharge. After that, we calculated several indices of underlying surface based on different dataset and investigated the relationship between parameters and underlying surfaces indices, based on which we established the equations for estimating the parameters either by their physical definition or by regression analysis. Finally, we derived the spatial distribution of parameters over whole SXLY basin based on the equations we proposed.

2. MATERIAL AND METHOD

2.1 Study area

Yangtze River, originating in the Qinghai-Tibet Plateau and flowing eastwards to the East China Sea, is the longest river in China. The study area of this paper, namely SXLY, is controlled by Cuntan gauging site (Figure 1). SXLY covers an area of about 333626 km^2, ranging from 24.48N to 32.90 and 101.85E to 109.33E, about 18% of total area of Yangtze River Basin. Average elevation of this area is 1112m, average slope is 17.4°. In this study area, we selected 20 gauged catchments to investigate the relationship between parameters and underlying surface characteristics, among which 18 catchments were used for establishing the equations for parameters estimation and the other 2 catchments were used for validation. To minimize the error, these 20 catchments only have precipitation as their input (i.e. no runoff entering from other catchments).

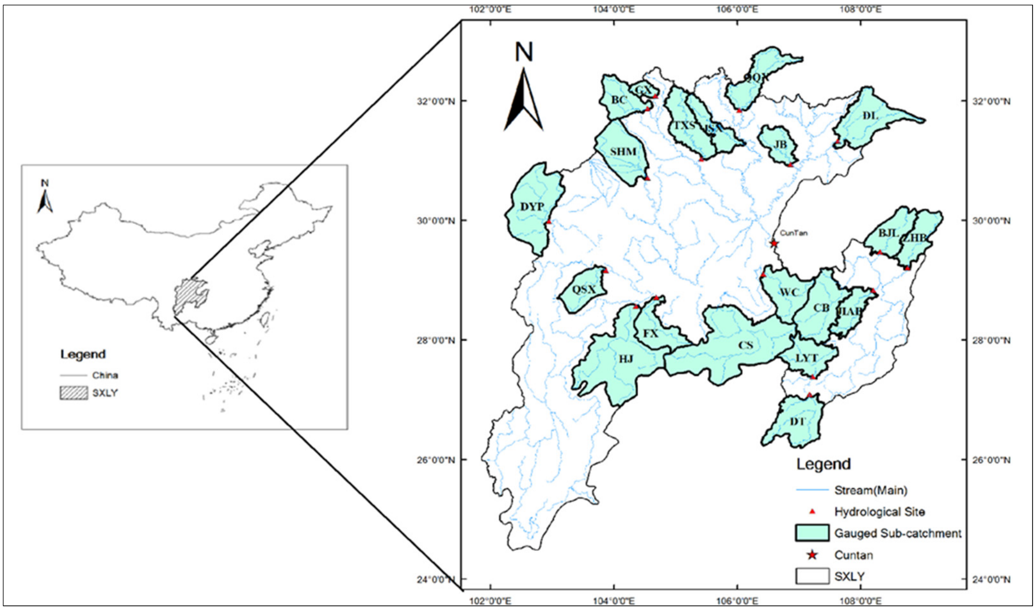

Figure 1. Location of SXLY.

2.2 Description of the XAJ model

The XAJ model was developed by the group led by Zhao (Ren-Jun, 1992). It is based on the concept of runoff formation on repletion of storage, which means for everywhere within the catchment, runoff is not yielded until the volumetric soil moisture content exceeds field capacity. Therefore, the XAJ model is most suitable for humid and semi-humid regions. Considering that it is difficult to measure spatially distributed field capacity when the XAJ model was developed, a statistical tension water capacity curve was introduced to represent the spatial distribution of tension water (difference between field capacity and wilting point), which is regarded as the essence of the XAJ model. The flow chart of the XAJ model is shown in Figure 2. All symbols outside the blocks are parameters, whose physical meanings are shown in Table 1. The inputs to the model are areal mean rainfall (P) and measured pan evaporation (EM). The outputs are the discharge at the outlet of basin (TQ) and the actual evapotranspiration (E).

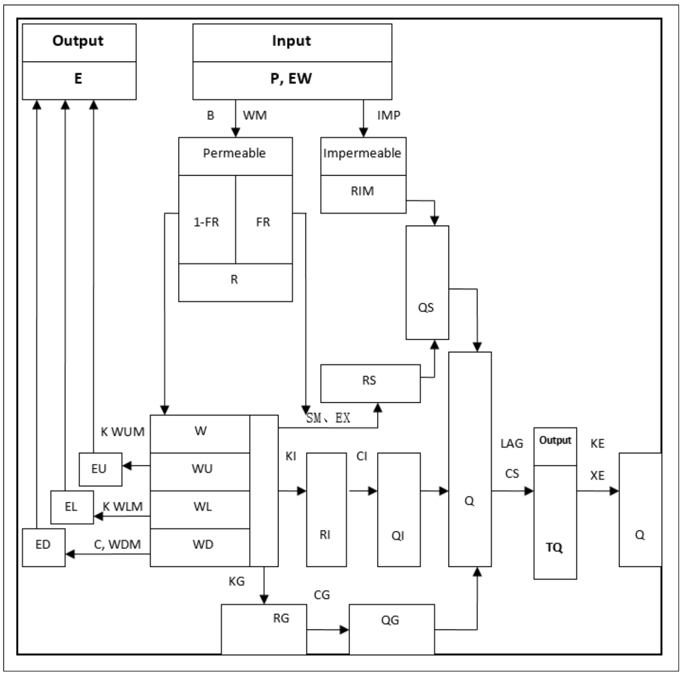

Figure 2. Flow chart of the XAJ model.

Table 1. Parameters of the XAJ Model.

Parameter	Definition
KC	Ratio of potential evapotranspiration to pan evaporation
WUM	Tension water capacity of upper layer
WLM	Tension water capacity of lower layer
C	Deeper evapotranspiration coefficient
WM	Elementary area mean tension water capacity
B	Exponential of the distribution of tension water capacity
IMP	Ratio of impermeable area to the total area in the catchment
SM	Elementary area mean free water capacity
EX	Exponential of the distribution of free water capacity
KG	Outflow coefficient of free water storage to the ground flow
KI	Outflow coefficient of free water storage to the sub-flow
CS	Recession constant of surface water storage
CI	Recession constant of sub-flow storage
CG	Recession constant of groundwater storage

The basic computation unit of the XAJ model is element area, the simulation of outflow from each element area consists of 4 major parts (Qu et al., 2012; Zhijia et al., 2011), more details can be found in (Ren-Jun, 1992):

1. Evapotranspiration, which is simulated by three-layer soil (i.e., upper, lower, and deep) model based on pan evaporation and soil moisture.
2. Runoff yield, which, based on tension water capacity curve, simulates the runoff yield according to the rainfall and soil storage deficit.
3. Runoff separation, which separates the abovementioned runoff into three components, i.e., surface, subsurface, and groundwater;
4. Flow routing, which transfers the local runoff to the outlet of each basin forming the outflow. Several approach including unit hydrograph, liner reservoir, and lag and route can be adopted.

2.3 Underlying surface indices

The hydrology processes are affected by underlying surface and therefore, parameters of the hydrological models have certain relationship, more or less, with those underlying surface indices. Parameters can be calculated directly based on underlying surface indices if they are physically-based, otherwise they can be estimated through the relationship with indices. In this paper, we divided indices into 2 groups, i.e. topography and soil. For each group we calculated several indices based on the data we collected. Considering that most data are grid based, we calculated indices at cell scale and then aggregated (e.g. mean, maximum and minimum value) to sub-catchment scale if necessary.

2.3.1 Topography indices

1. Slope (S): slope represents the maximum rate of change in elevation from one grid to its neighbors. Based on the DEM data, slope of each grid was calculated using the average maximum technique (Burrough, & McDonnell, 1998).

2. Aspect (AS): aspect represents the downslope direction of the maximum rate of change in elevation from one cell to its neighbors. It can be regarded as the slope direction (Burrough, & McDonnell, 1998).

3. Flow direction (FDR): flow direction determines the direction of flow from one cell to its neighbor or neighbors, depending on algorithm applied. In this paper, we employ D8 algorithm(Jenson and Domingue, 1988) to determine the flow direction, which is the direction of steepest descent of each cell.

4. Flow length (FLE): flow length refers to the distance from one cell to the outlet of the catchment. Based on the flow direction, flow length of a given cell can be determined by tracing cells linking it and the outlet of the basin.

5. Relief Amplitude (RA): relief amplitude is the difference between the maximum and minimum elevation of all grids within a certain range (Liu et al., 2013). Here, we calculated Ra for each sub-catchment according to DEM data.

6. Roughness (RS): roughness represents the fluctuation of land surface. Roughness of each cell can be calculated based on slope of the cell:

$$RS = \frac{1}{CosS} \qquad [1]$$

7. Drainage Density (DD): drainage density can be expressed as the total length of all the drainage network in a catchment divided by the total area of the catchment.

2.3.2 Soil indices

1. Wilting water content and field capacity. Wilting water content, field capacity and saturated content are critical to the runoff yield and separation simulation of XAJ model. Theoretically, these abovementioned indices should be determined by laboratory analysis, but it is apparently impractical to collect and analyze soil over whole study area. According to the study of Saxton, soil indices are highly related to the soil texture (Saxton et al., 1986), which is available in soil dataset. In this paper, we calculated grid soil indices based on the equations proposed by Saxton, then, aggregated them to sub-catchment scale for parameter estimation (Figure 3).

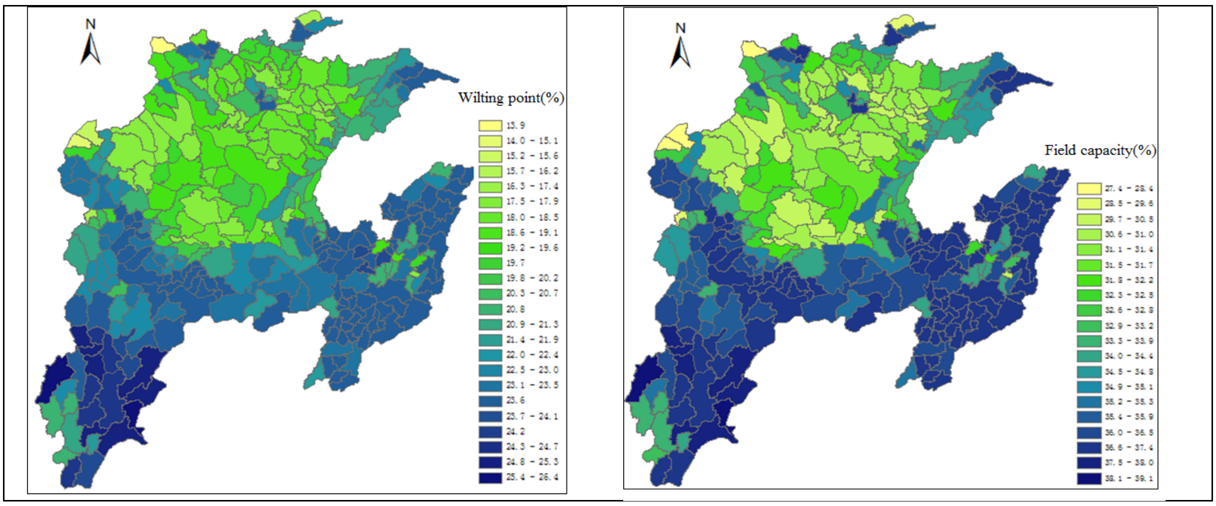

(a) Wilting water content (b) Field capacity

Figure 3. Soil Indices over SXLY.

2. Vadose zone depth. Vadose zone is the part of Earth between the land surface and the top of the ground water. Depth of vadose zone is mainly affected by land cover. At present, there is no vadose zone depth or soil depth data available but study has shown that the depth for natural vegetation is around 0.9m, for shrub and grass is around 0.8m, and for bare soil is around 0.5m. Water body and urban area have vadose

zone depth equal to 0m(Xia, 2008). We estimated the vadose depth of study area by above relationship based on land cover type.

Table 2. Vadose Zone Depth for Different Land Cover.

Land Cover Type	Vadoes Zone Depth (m)	Land Cover Type	Vadoes Zone Depth (m)
Evergreen Needleleaf Forest	0.9	Wooded Grassland	0.8
Evergreen Broadleaf Forest	0.9	Closed Shrubland	0.8
Deciduous Needleleaf Forest	0.9	Open Shrubland	0.8
Deciduous Broadleaf Forest	0.9	Grasslands	0.8
Mixed Forest	0.9	Croplands	0.8
Woodlands	0.9	Bare Ground	0.5
Water	0.0	Urban and Built-up	0.0

2.4 Catchment subdivision

The computation unit of the XAJ model is element area. In order to subdivide the catchment into element area, digitized drainage network and catchment divide should be determined from DEM in advance. Automation of drainage networks extraction from DEM has been well studied and several algorithms have been developed (Lin et al., 2006; Liu and Zhang, 2011; Vogt et al., 2003). The stream threshold, Ts is the minimum accumulation area that can support the drainage network, cells with accumulation area greater than Ts are identified as drainage line. Ts is important because it influences the drainage network generated and further affects the catchment subdivision. Ts can be determined by comparing simulated drainage network with the real one. In this paper, we based on the criterion put forward by Lin(Lin et al., 2006) to evaluate the fitness between simulated and real drainage network.

The error of digitized drainage network includes insufficient, redundant and erroneous part, so the fitness index is calculated as:

$$FI = 1 - \frac{\sum_{s=1}^{ni}(L_i)_s + \sum_{s=1}^{nr}(L_r)_s + \sum_{s=1}^{ne}(L_e)_s}{L_T} \qquad [2]$$

where L_i is insufficient stream length (m), L_r is redundant stream length (m), L_e is erroneous stream length, L_T is total real stream length (m).

The more FI close to 1, the more accurate the digitized drainage network is. Theoretically, total length of digitized drainage network increases when Ts decreases because more cells are identified as channel. For each catchment, we first calculated maximum accumulative area Tsmax and then calculated fitness index for different Ts ranging from 0.001*Tsmax to 0.02* Tsmax to find out the best stream threshold for best-fit drainage network. The catchment was then subdivided according to drainage network generated.

Real drainage network is generally considered as available data which can be retrieved from remote sensing or airborne photo(Lin et al., 2006), but the plotting scale of some dataset is low, leading to overestimate the threshold area. Here, we investigated the relationship between threshold area and topographic indices by backward elimination regression analysis. Backward elimination is one of several computer-based iterative variable-selection procedures. It begins with a model containing all the independent variables of interest. Then, at each step the variable with smallest F-statistic is eliminated. Considering that the drainage network is strongly affected by topographic characters, we chose all topographic indices that we had as independent variables, then, used backward elimination algorithm to identify indices that affects threshold area statistical-significantly.

2.5 Parameters estimation

2.5.1 WM

WM stands for tension water capacity. It, according to the definition, refers to the amount of water between wilting point and field capacity, which can be expressed as:

$$WM = (\theta_f - \theta_r) \times L \qquad [3]$$

Where θ_f is field capacity (-), θ_r is wilting point (-), and L (mm) is vadose zone depth. All the variables were calculated as indices in 2.4.

2.5.2 KI

KI is the outflow coefficient of free water storage to the interflow, which is mainly determined by soil characteristic of the catchment. Unlike WM, there is no physical definition of KI. Instead, we performed multi-factor linear regression analysis of **soil c**haracteristic and calibrated KI in gauged catchments. By analyses, we found KI is highly related to the soil texture and organic content, so we chose these indices as independent variables to establish the regression equation. We selected 18 catchments controlled by gauging sites to establish the regression equation.

2.5.3 CS

CS is recession constant of surface water storage that controls the surface water routing at sub-catchment. It is mainly affected by the topographic indices. Here, we also applied multi-factor linear regression analysis to establish the relationship between CS and topographic indices. We, firstly, performed backward regression analysis to find out the indices that were most related to CS, after that we performed multi-factor linear regression analysis which was the same as what we did to estimate KI.

3. RESULTS AND DISCUSSION

3.1 Catchment subdivision

We calculated the fitness index for all the 18 sub-catchments we selected with threshold area ranging from 0.001*Tsmax to 0.02*Tsmax. Figure 4 is an example of fitness index of DYP catchment. We found that the fitness index increased first with the increase of threshold area then decreased. This indicates that at the very beginning, the digitalized drainage network is redundant than the real drainage network due to low threshold area, the digitalized drainage network became less when threshold area increased and the fitness index increased which means the digitalized drainage network became closer to the real one. The best fitness index was 0.82 when threshold area equaled to 1.68km^2. When threshold area increased further from 1.68 km^2, fitness index started to decrease because the digitalized drainage was more and more insufficient comparing to the real one. Figure 5 demonstrates the comparison of real drainage network and digitalized drainage with different threshold area.

Best Fitness index and its corresponding threshold area is shown in Table 3. Catchment DYP has the highest fitness index of 0.84 while catchment JSX has the lowest fitness index of only 0.44. This may be due to the complex terrain in this catchment and the algorithm for generating drainage network cannot produce correct result.

Table 3. Data for Regression Analysis of FI.

Catchment Name	Ts (km2)	FI	Catchment Name	Ts (km2)	FI
BC	1.80	0.71	JB	2.90	0.65
BJL	6.39	0.50	JIB	2.01	0.76
CB	2.90	0.74	JSX	3.67	0.44
CS	3.21	0.66	LYT	0.92	0.60
DL	2.14	0.71	QQX	2.61	0.77
DT	2.75	0.71	QSX	1.91	0.76
DYP	1.44	0.84	SHM	6.39	0.55
FX	2.32	0.60	TXS	1.80	0.71
GX	3.01	0.53	WC	6.39	0.50
HJ	1.68	0.82	ZHB	2.90	0.74

After backward elimination analysis, we found that mean slope and drainage density are significant variables to threshold area, so the equation that we established is:

$$Ts = 0.0009 * (-87.6 * \mathrm{MS} - 12072.0 * \mathrm{DD} + 10215.2)(\mathrm{P} = 0.00) \quad [4]$$

where Ts is threshold area (km^2), MS is mean slope (Degree), DD is drainage density(km/km^2).

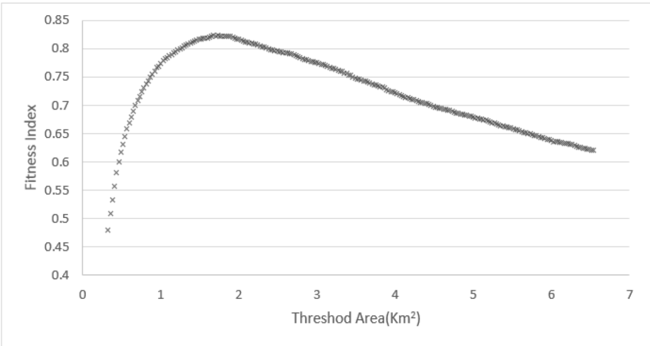

Figure 4. Fitness index distribution of DYP.

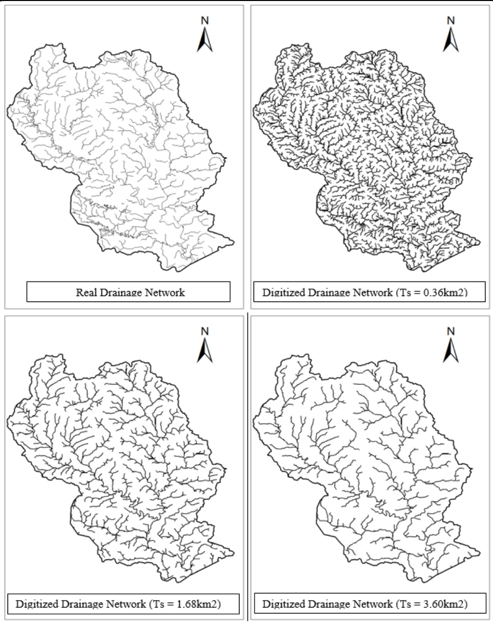

Figure 5. Comparison of real and digitalized drainage network.

R^2 of Eq. [4] is 0.72 and P value of variables MS and GD are 0.31 and 0.00, respectively, which indicates that the independent variables which we selected have significant effects on Ts. In order to validate this equation, we applied it to sub-catchment BJL and DL to calculate their threshold and corresponding fitness index. The result is shown in Table 4. Although relative error of Ts for BJL is -0.35, the corresponding relative error of FI is only 0.04, which can also guarantee the accuracy of digitalized drainage network if there is no real data available to derive the distribution of FI.

Table 4. Validation of Equation for Estimating FI.

Catchment Name	Mean S	GD	Calculated Ts	Estimated Ts	Relative Error	Calculated FI	Estimated FI	Relative Error
BJL	21.46	0.31	4.13	6.39	-0.35	0.50	0.48	0.04
DL	23.28	0.40	3.01	2.90	-0.04	0.74	0.74	0.00

Eq. [4] also indicates that the best threshold area has negative relationship with slope and drainage density, which means that catchment with low slope and drainage density has high threshold area that can supports the channel. This is consistence with the theory of stream formation.

In order to meet the requirement of simulation of the XAJ model, we divided SXLY according digitalized drainage network by two ways (Figure 6). One is to divide SXLY into element areas which are the basic simulation unit of XAJ model and the other way is to divide SXLY into sub-catchments which consist of several element areas. Sub-catchment is usually controlled by gauging site at the outlet so that can be adopted to calibrate or validate model.

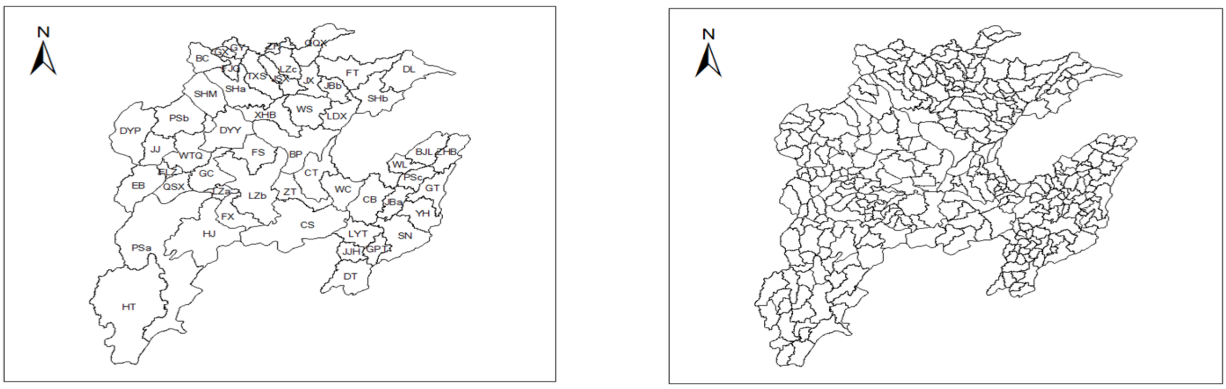

(a)Sub-catchment (b) Element area

Figure 6. Subdivision of SXLY.

3.2 The XAJ model parameters

1. WM. WM was first calculated at grid scale then aggregated to element area by area-weighted method to get the spatial distribution over SXLY (Figure 7).

From the distribution, we found that the value of WM in SXLZ is between 96mm and 128mm depending on the soil properties and vadose depth, which is consistent with the value of suggest WM in humid and semi-humid region.

Table 3 shows the comparison between estimated WM and calibrated WM in 20 gauged sub-catchments and found all the relative error is less than 5.5% which proves the accuracy of our method to estimate WM.

Table 3. Validation of Equation for Estimating WM.

Catchment Name	Calibrated WM	Estimated WM	Relative Error	Catchment Name	Calibrated WM	Estimated WM	Relative Error
BC	120	119	-0.01	JB	110	110	0.00
BJL	110	110	0.00	JIB	110	106	-0.04
CB	110	108	-0.02	JSX	110	107	-0.03
CS	110	114	0.04	LYT	110	109	-0.01
DL	120	116	-0.03	QQX	120	118	-0.02
DT	110	110	0.00	QSX	120	120	0.00
DYP	120	116	-0.03	SHM	120	116	-0.03
FX	110	112	0.02	TXS	110	104	-0.05
GX	120	123	0.03	WC	110	111	0.01
HJ	110	115	0.05	ZHB	110	111	0.01

2. KI. The regression equation for estimating KI was established by estimating coefficient of variables which we selected (i.e. soil indices) with the least square method. The equation we established is:

$$KI = 0.057 * Sa + 0.051 * \mathrm{Cl} + 0.067 * \mathrm{Si} + 0.061 * OM - 5.549 (P = 0.00) \quad [5]$$

where Sa, Cl, Si, OM are sand, clay, silt and organic matter percentage of soil, respectively.

R^2 of Eq. [5] is 0.87 and P value of variables are 0.00, 0.00, 0.01, 0.00 and 0.05, respectively, which indicates that all independent variables we selected have significant effects on KI. In order to validate this equation, we applied it to catchment BJL and DL. The result is shown in Table 4, from which we can see that the relative error of estimated KI is 0.09 for both sub-catchment, which proves the accuracy of regression equation. Based on above analyses, the equation we established can be adopted to estimate KI in other catchments and get the spatial distribution of KI (Figure 8).

Table 4. Validation of Equation for Estimating KI.

Catchment Name	Sand %	Clay %	Silt %	OM *	Calibrated KI	Estimated KI	Relative error
BJL	30	37	33	1.6	0.33	0.36	0.09
DL	30	38	32	1.7	0.32	0.35	0.09

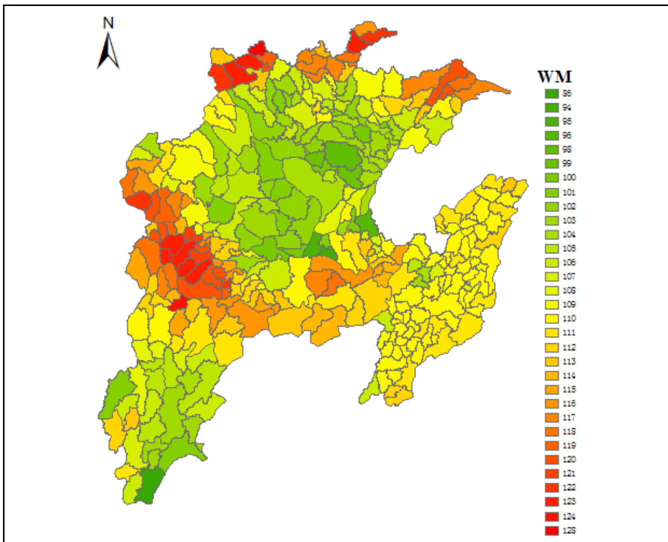

Figure 7. Spatial distribution of WM over SXLY

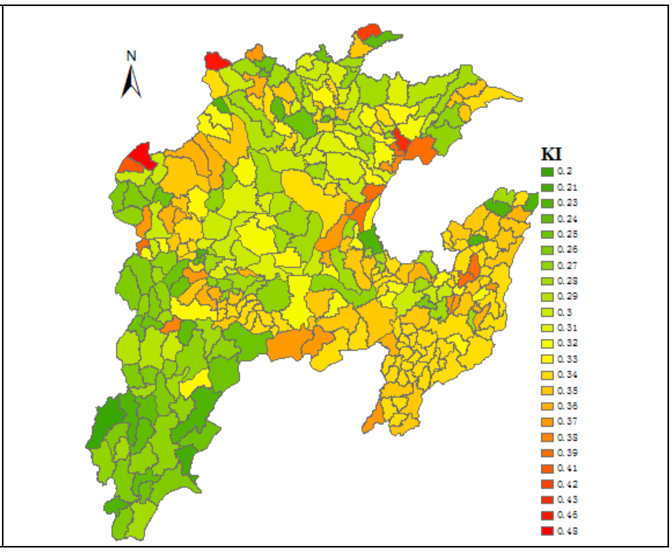

Figure 8. Spatial distribution of KI over SXLY.

3. CS. In order to establish the regression equation for estimating CS, we applied backward regression analysis to find out the indices that affect CS significantly. Results show that mean surface roughness of sub-catchment is highly related to CS. So, the regression equation was determined with mean surface roughness as independent variable and the coefficient were fixed by the least square method too. The equation we established is:

$$CS = -0.384 * \mathrm{MRs} + 1.31 (P = 0.00) \qquad [6]$$

where MRs is mean surface roughness.

R^2 of Eq. [6] is 0.60 and P value of both variables are 0.00, which indicates that the independent variables we selected have significant effects on CS. In order to validate this equation, we again applied it to BJL and DL. The result is shown in Table 3 from which we can see that the relative errors of estimated CS are 0.01 and 0.00 for BJL and DL, respectively, which proves the accuracy of regression equation. Based on the above analyses, the equation we established can be adopted to estimate CS in other catchments based on topographic indices and get the spatial distribution of CS (Figure 8).

Table 3. Validation of Equation for Estimating CS

Catchment Name	Mean Rs	Calibrated CS	Estimated CS	Relative error
BJL	1.10	0.90	0.89	0.01
DL	1.12	0.88	0.88	0.00

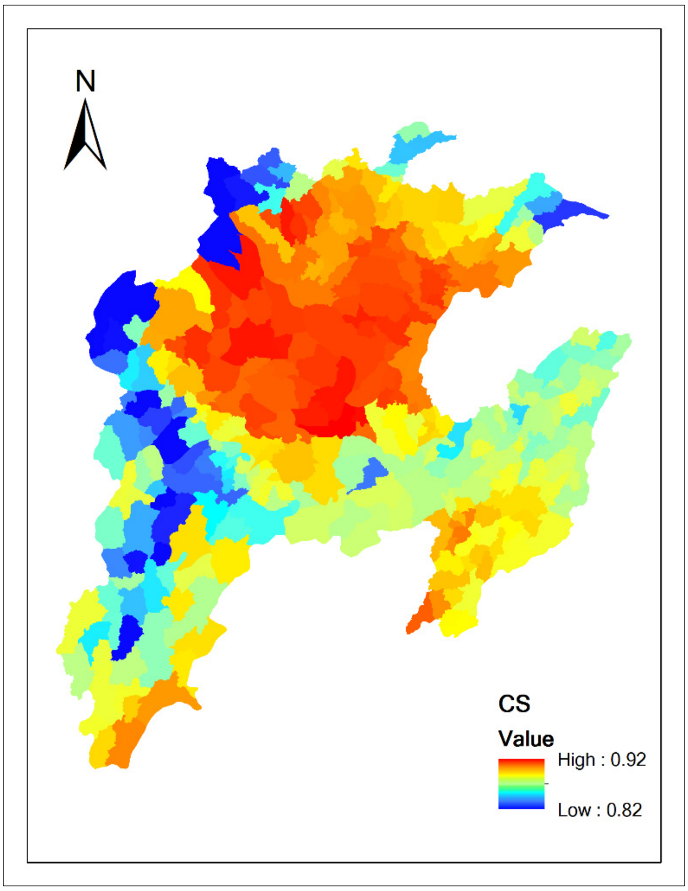

Figure 9. Spatial distribution of CS over SXLY.

4. CONCLUSION

Hydrological models, regardless of physically-based or conceptual models, all have several parameters that need to be determined before models can be applied to investigate hydrological processed at different spatial and temporal scale. For the XAJ model, considering that it is a conceptual model, many studies have been focused on how to calibrate the model by mathematical algorithms. In this paper, we studied the relationship between some parameters and underlying surface characteristics and, based on which, we established the equation for estimating parameters. We calculated several underlying surface indices based on the data we collected in SXLY, which serves as the basis for parameter estimating.

We, firstly, extracted digitalized drainage network from DEM by calculating the fitness index, the best-fit digitalized drainage network was used to subdivide SXLY into sub-catchments and element area. We also chose 18 gauged sub-catchments to study the relationship between best fitness index and topographic indices, the results show that mean slope and drainage density have significant effects on best fitness index and, based on which, we establishing the equation for deriving best-fit digitalized drainage network.

Among the parameters of the XAJ model, WM has physical definition, based on which, we calculated WM by underlying surface indices derived. Other parameters including KI and CS does not have definite definition but still has relationship with underlying surface characteristic, so, we performed backward elimination regression analysis to identify the significant variables and establish the regression equation for estimating KI and CS.

Acknowledgements

This study was funded by grants from National Natural Science Foundation of China (51420105014, 51409090).

REFERENCES

Beven, K., (2002). Towards an Alternative Blueprint for a physically based Digitally Simulated Hydrologic Response Modelling System. *Hydrological Processes*, 16(2), 189-206.

Beven, K. & Freer, J. (2001). Equifinality, Data Assimilation, and Uncertainty Estimation in Mechanistic Modelling of Complex Environmental Systems using the GLUE Methodology. *Journal of Hydrology*, 249(1-4), 11–29.

Burrough, P.A. & McDonnell, R.A. (1998). *Principles of Geographical Information Systems*. Oxford University Press, 1-19.

Cheng, C.-T., Zhao, M.-Y., Chau, K.W. & Wu, X.-Y. (2006). Using Genetic Algorithm and TOPSIS for Xinanjiang Model Calibration with a Single Procedure. *Journal of Hydrology*, 316(1–4), 129-140.

Jenson, S.K. & Domingue, J.O. (1988). Extracting Topographic Structure from Digital Elevation Data for Geographic Information-System Analysis. *Photogrammetric Engineering and Remote Sensing*, 54(11), 1593-1600.

Kampf, S.K. & Burges, S.J. (2007). A Framework for Classifying and Comparing Distributed Hillslope and Catchment Hydrologic Models. *Water Resources Research*, 43(5), 1-24.

Lin, W.-T., Chou, W.-C., Lin, C.-Y., Huang, P.-H. & Tsai, J.-S., (2006). Automated Suitable Drainage Network Extraction from Digital Elevation Models in Taiwan's Upstream Watersheds. *Hydrological Processes*, 20(2), 289-306.

Liu, S., Cui, Y., Lu, F. & Qin, X. (2013). The Analysis of Relief Amplitude in Qinghai Province based on GIS, Geoinformatics (GEOINFORMATICS). *21st International Conference on. IEEE*, 1-5.

Liu, X. & Zhang, Z., (2011). Drainage Network Extraction using Lidar-Derived DEM in Volcanic Plains. *Area*, 43(1), 42-52.

Niu, G.Y., Paniconi, C., Troch, P.A., Scott, R.L., Durcik, M., Zeng, X., Huxman, T. & Goodrich, D.C. (2013). An Integrated Modelling Framework of Catchment-Scale Ecohydrological Processes: 1. Model Description and Tests Over an Energy-Limited Watershed. *Ecohydrology*, 7(2), 427-439.

P., H.H.A., Zhijia, L. & Shouhui, W. (2001). Application of SCE-UA Method for Calibrating the Xinanjiang Watershed Model. *Journal of Lake Science*, 13(4), 304-314.

Qu, S.M., Bao, W.M., Shi, P., Yu, Z.B., Li, P., Zhang, B. & Jiang, P. (2012). Evaluation of Runoff Responses to Land Use Changes and Land Cover Changes in the Upper Huaihe River Basin, China. *Journal of Hydrologic Engineering*, 17(7), 800-806.

Ren-Jun, Z. (1992). The Xinanjiang Model Applied in China. *Journal of Hydrology*, 135(1–4), 371-381.

Saxton, K.E., Rawls, W.J., Romberger, J.S. & Papendick, R.I., (1986). Estimating Generalized Soil-water Characteristics from Texture. *Soil Science Society of America Journal*, 50(4), 1031-1036.

Vogt, J.V., Colombo, R. & Bertolo, F. (2003). Deriving Drainage Networks and Catchment Boundaries: A New Methodology Combining Digital Elevation Data and Environmental Characteristics. *Geomorphology*, 53(3–4), 281-298.

Wang, W.-C., Cheng, C.-T., Chau, K.-W. & Xu, D.-M. (2012). Calibration of Xinanjiang Model Parameters using Hybrid Genetic Algorithm based Fuzzy Optimal Model. *Journal of Hydroinformatics*, 14(3), 784-799.

Xia, X., (2008). *The Study on the Parameters Calculation of Hydrological Model Based on the Geography*, Hohai University, Nanjing.

Yao, C., Li, Z., Yu, Z. & Zhang, K. (2012). A Priori Parameter Estimates for a Distributed, Grid-Based Xinanjiang Model using Geographically Based Information. *Journal of Hydrology*, 468, 47-62.

Ye, Y., Song, X., Zhang, J., Kong, F. & Ma, G. (2014). Parameter Identification and Calibration of the Xin’anjiang Model using the Surrogate Modeling Approach. *Frontiers of Earth Science*, 8(2), 264-281.

Zhijia, L., Penglei, X. & Jiahui, T. (2011). Study of the Xinanjiang Model Parameter Calibration. *Journal of Hydrologic Engineering*, 18(11), 1513-1521.

HYDRODYNAMIC NUMERICAL MODELLING OF DAM FAILURE AND IMPACTS ASSESSMENT OF SUSU DAM WITH MIKE

MOHD RASHID MOHD SHAH(1), LARIYAH MOHD SIDEK(2), MOHD RUZAIMEI YALIT(3), MOHANADOSS PONRAJ(4) & HIDAYAH BASRI(5)

(1,2,3,4,5)Sustainable Technology & Environment Group, Institute for Energy Infrastructure, Universiti Tenaga Nasional, Selangor, Malaysia
rashidshah92@gmail.com

ABSTRACT

Dams are large barriers built across rivers and streams in order to restrain and utilize flow of water for numerous purposes like irrigation, generation of hydroelectricity and controlling the flood. Detention of water by large barriers creates lakes and reservoir. However, huge amount of water stored behind the dam can possess adverse effects to the downstream during the event of dam break. It is very much essential for executing dam break study as to provide possible flood inundation information and impact assessment to the dam. This study is conducted to carry out hydraulic and dam break analysis of Susu Dam for different failure modes. Dam break modelling is performed under two scenarios, Clear Day scenario and Probable Maximum Flood (PMF) scenario. Mike 11 1-D model is used to derive breach outflow hydrograph, whereas Mike 21 2-D model is being used for flood plain modelling and generation of inundations maps downstream of the dam. The routing of flow to the downstream area using Mike Flood model is to obtain the flooded area, flood travel time and maximum flood depth. It was found from the Clear Day scenario, dam breach outflow hydrograph yield the peak value of 45 213 m^3/s and 61 110.8 m^3/s for PMF Failure scenario which showed both has the potential to flood the downstream area of dam. This result helps in identifying the affected location or villages located at the downstream of Susu Dam. Indirectly, it will become a reference for the agencies like Jabatan Pertahanan Awam (JPAM) to take safe precautions during the happening of unwilling disaster.

Keywords: Dam break analysis; inundation map; clear day; probable maximum flood; hydrograph; MIKE.

1 INTRODUCTION

Dams are typical water retaining structure that is constructed for the purpose of irrigation, water supply, power generation, flood mitigation and other needs. Made of various materials, dams fall into the category of soil, rock fill embankment, reinforced concrete and masonry (Chen, 2015). Maintenance and safety of dams are important issue during the period of working. One of the issues is dam break failure resulting after the completion of installation structure. In Malaysia, some of the dams can be rated highly hazardous, which is dam failure that probably results in loss of lives and major damages to property (Ismail, 2004). Meanwhile, most of the dam are constructed at a highly dense population are like traditional villages and developed township. The main reason of risk of dam failure is related to the storage of water behind the dam structure. Breach simulation and breach parameter prediction contains the greatest uncertainty of all the aspects of dam break analysis (Wurb, 1987). Every 10 years, the dam break study must be done due to the changes in several factors such as the population at the downstream of dam and climate in order to mitigate potential hazards (FEMA, 2001). Moreover, existing dam and reservoirs should be reanalysed periodically to ensure that it still meets the test of safety by current standard, seeing that hydrology, seismicity, geological environment accumulates, technology advances and facilities once regarded as safe may need changes (Ros et al., 2007).

It is important to conduct dam break study in order to determine the outflow event to prepare the emergency Response Plan (ERP) and impact to the economy, social and environment at the downstream of dam. Early detection system, improved warning scheme and emergency evacuation routes can be developed by analysing dam break scenarios for downstream. The main reason for dam break study is to minimize the impact of loss of lives and economic damages. Dam break modelling is primarily included with the prediction of outflow hydrograph as a result of dam failure during which it can be used via physical model, laboratory experiment and also numerical modelling technique. Numerical modelling is often taken as a better alternative. In this study, MIKE model is selected to simulate the dam break event at Susu Dam and to determine the outflow hydrograph to be routed to the downstream area and eventually to obtain the flood maps.

2 STUDY AREA

The study area includes the Susu Dam and its construction started in 2011 and was completed by 2015. The dam is located at Mukim Ulu Telom, Cameron Highlands, Malaysia and located 22 km downhill from

Sultan Abu Bakar Dam. The dam was constructed using the advance technology of 750,000 m^3 roller-compacted concrete (RCC). Figure 1 and 2 shows the location of Susu Dam and Typical Dam Section of Susu Dam. The specification of Susu Dam is shown in Table 1.

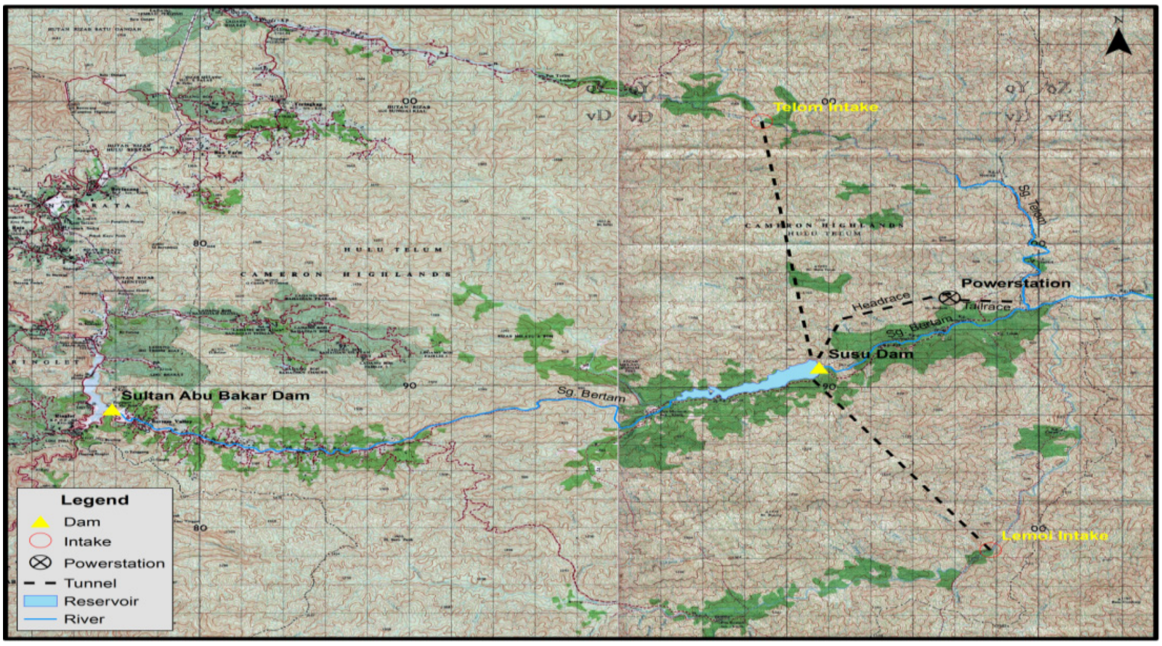

Figure 1: Location of Susu Dam.

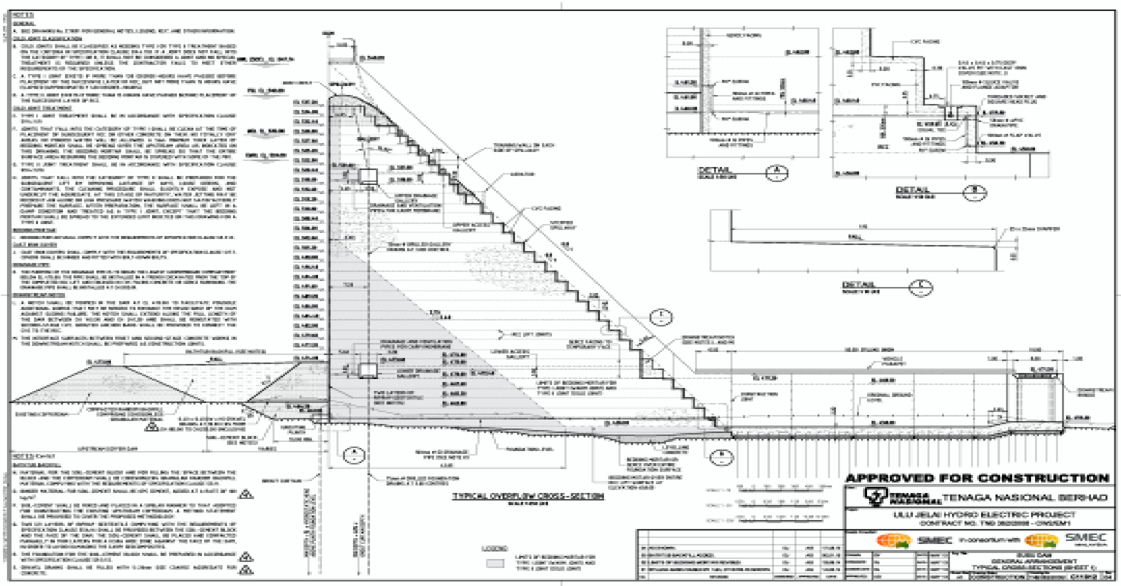

Figure 2: Typical dam section of Susu Dam.

3 METHODOLOGY

3.1 Dam break and flood routing models

MIKE 11 is a 1-D model used to derive breach outflow hydrograph and to simulate river routing. Simple geometry such as platform and cross-sections of the river system is needed. MIKE 11 model requires the x and z coordinate for the geometry input. It is used to represent river routing due to the low flow during flooding caused by dam breach. MIKE 21 is a 2-D modelling tool for the flood plain simulation of free surface flow and sediment transport in lakes, estuaries, bays and coastal areas. The model is able to run simultaneously thus incorporating dynamic feedback from changing hydraulic resistance, bed topography and bank lines to the hydrodynamic behaviour of river. In the dam break study; this tool can actually model the flood map accurately. MIKE 21 2-D hydrodynamic module was chosen for flood plain modelling and generation of inundation maps downstream of the dam. Water level variations and flows in the floodplain were simulated by hydrodynamic module. Figure 3 shows the workflow of Mike 11 and Mike 21.

Table 1: Details of Susu Dam and its reservoir.

Items	Details
Name of Dam	Susu Dam
Type of Dam	Roller-Compacted Concrete
Year Completed	2015
Dam Height (m)	84
Dam Crest Level (m MSL)	548 m MSL
Dam Crest Length (m)	512.5
Dam Crest Width (m)	5.0
Spill Level	540 m MSL
Downstream River	Sg. Bertam
Spillway Crest Level	Ungated Spillway with crest 540 m MSL
Spillway Weir Length (m)	104.2
Surface Area (sq. km)	0.77
Gross Storage (Mm^3)	18.62
Active Storage (Mm^3)	6.354
Max. Water Level (MWL)	EL 547.74 m
Full Supply Level (FSL) /Max. Operating Level	EL 540.00 m
Min. Operating Level (MOL)	EL 530.00 m

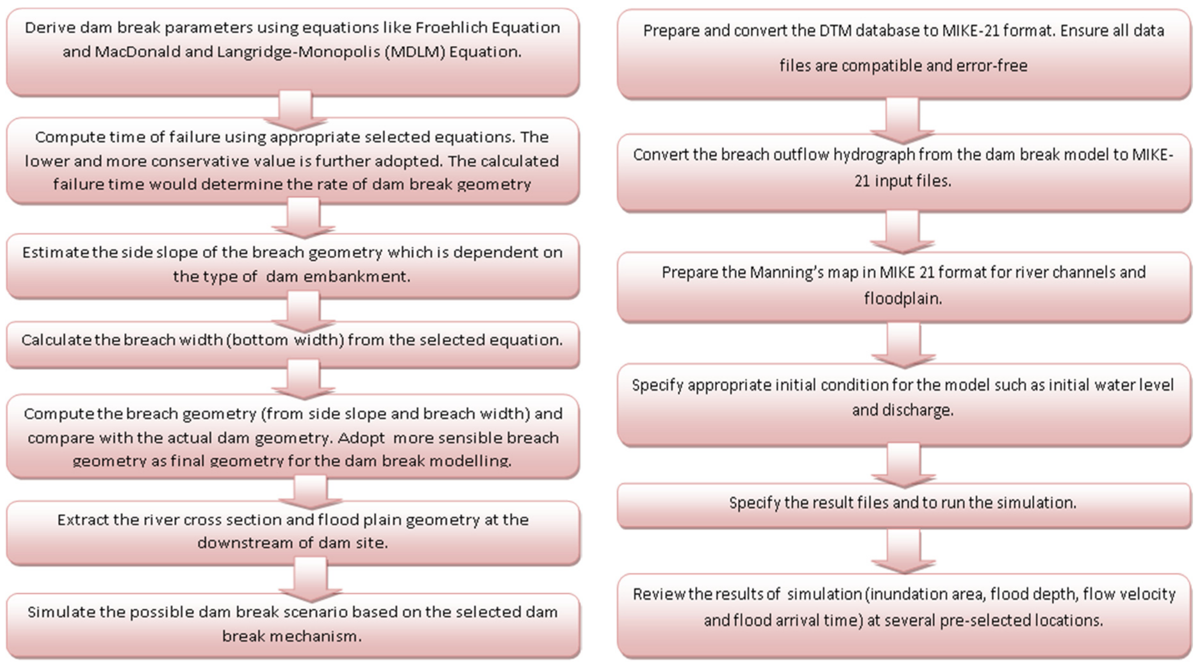

(a) (b)

Figure 3. Workflow of a) MIKE 11 b) MIKE 21.

In MIKE FLOOD model simulation, desired output was extracted out from the results which includes flood arrival time, time of peak, flood depth, subsidence time and flood velocity. From the results, maximum flood depth and flood velocity at selected locations can be extracted. Moreover, flood wave arriving time and time to peak can be determined as well. Flood arrival time is defined as the time calculated for the flood wave to reach a particular location of flood plain during the beginning of dam break event. Meanwhile, the time to peak is described as the duration for reaching maximum flood inundation depth or peak discharge at the specific location.

3.2 Data requirement and assumption

3.2.1 Stage-storage curve:

The curve for Susu Reservoir was obtained from the reports of Reservoir Operation Study prepared by SMEC and it was necessary to observe the water rise in Susu reservoir. Figure 4 shows Susu Reservoir Level – Storage – Area Curves.

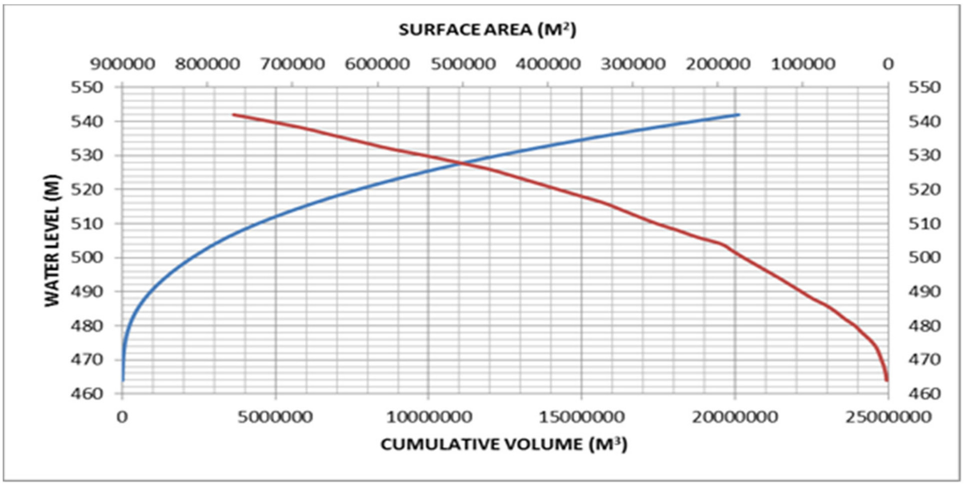

Figure 4: Susu reservoir level – storage – area curves.

3.2.2 Floodplain and topographic information:

The available topographic and floodplain information was used for modelling in MIKE 11 and MIKE 21

- Manning's roughness values 'n' is taken as 0.06 to represent the flood plain surface roughness.
- The existing structure such as culverts, vegetation, weirs, and bridges were not modelled as they would provide insignificant control on the flood caused by dam break.
- Digital Terrain Model (DTM) as the input of ground level data for the floodplains, in this study IFSAR is being used as base map for river and flood routing.

3.3 Dam breach parameters prediction

Breaching mechanism of a dam can be described by dam breach parameters where Froehlich and MacDonald & Langdrige Monopolis (MDLM) are the most suitable relations in predicting the breach parameters (Wahl, 1996). Dam breach parameters are represented by breach width (b), breach height (h), side slope (s) and time of failure (t_f). These parameters could affect the peak flow rate and result in inundation level occurring in the downstream area. Dam breach can be specified by trapezoidal, rectangular, or triangular shape. Linear breaching and erosion-based breaching are both relevant but the latter contains higher degree of uncertainty. Figure 5 shows the Typical Breach Geometry for Concrete Dam.

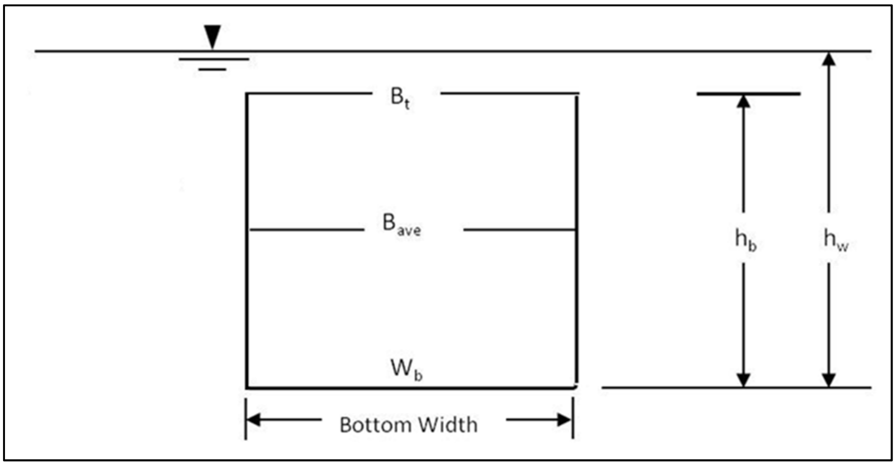

Figure 5: Typical breach geometry for concrete dam.

The published agency guideline which is US National Weather Service (NWS) has been selected as an approach to determine dam breach parameter for this study. Final breached section is assumed to be rectangular with side slope of 1:0. Table 2 and 3 shows the Range of Possible Values for Breach Characteristics and Dam Breach Parameters for Susu Dam.

Table 2: Range of possible values for breach characteristics.

Dam Type	Average Breach Width (B_{avg}) (m)	Horizontal Component of Breach Side Slope (H)	Failure Time, t_f (hours)	Agency
Concrete Gravity	Usually ≤ 0.5L	0	0.1 to 0.5	NWS

L= Dam Crest Length

Table 3: Dam breach parameters for Susu Dam.

Breach Parameters			
Bottom breach width, B (m)	Breach formation time, t_f (hours)	Breach Side Slope (1:*H*)	Breach Depth (m)
256.25	0.2	0	78

The dam break modelling was carried out using MIKE 11 model to derive the breach outflow hydrograph which can be later used as input for MIKE FLOOD 2D flood plain modelling. Parameters that control the magnitude of peak discharge and the shape of the outflow hydrograph includes the breach dimensions, breach formation time, and volume of water stored in the reservoir and the inflow to the reservoir at the time of failure.

3.4 2D flood plain modelling

3.4.1 Digital terrain model (DTM)

The primary component of MIKE 21 model is the elevation data, which is known as the bathymetry. The accurate data of DTM is necessary in order to generate high accuracy of flood inundation map. The MIKE 21 bathymetry file present in grid format was originally converted from IFSAR dataset with horizontal spacing of 5 m. Outside the IFSAR coverage, terrain data was supplemented with topography data from JUPEM which had 20 m contour interval. All projected data had been projected into the Malaysian RSO coordinate system and Kertau Datum. Figure 6 shows the DTM coverage area to the simulated flood plain model for the failure of Susu Dam.

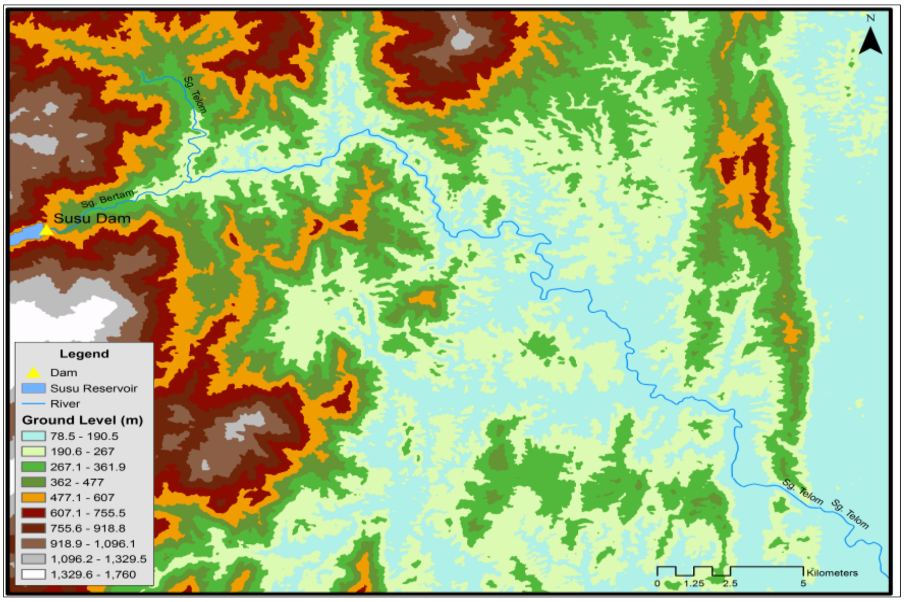

Figure 6: DTM coverage area for floodplain simulation of Susu Dam.

3.4.2 Roughness

Another input for the MIKE 21 model is the manning's roughness. Every grid cell must be assigned with roughness value according to the rough surface condition. Table 4 shows the adopted manning's roughness for MIKE 21 modelling.

Table 4: MIKE-21 adopted manning's roughness values.

Parameter and Criteria	Value
Manning's Roughness for channel n ($m^{(1/3)}/s$)	0.03
Manning's Roughness for flood plain n ($m^{(1/3)}/s$)	0.06

3.4.3 River cross-section

River cross-section data was required for modelling the flood plain. The cross section for Sg. Bertam and Sg. Telom was generated from the data of IFSAR ground. A total of 212 cross-sections of Sg. Bertam and Sg. Telom along 106 km stretching at the downstream of Susu Dam were being modelled as shown in Figure 7.

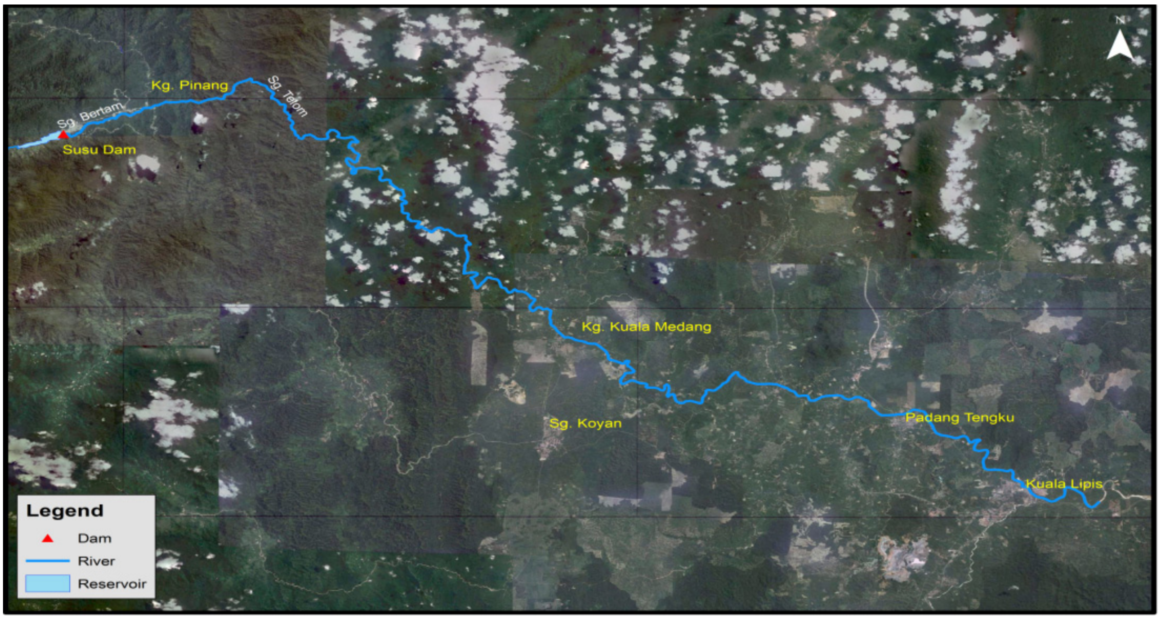

Figure 7: The stretch of Sg Bertam and Sg Telom.

4 RESULTS & DISCUSSION

4.1 Susu Dam clear day failure

The initial Susu reservoir water level was set to the Fully Supply Level (FSL) during a fair weather or a clear day condition which is at EL 540 m with zero inflow entering into the reservoir assuming there was negligible discharge coming to the reservoir. The breach was assumed to occur at FSL and developed linearly over the derived failure time of 0.2 hours until it reached the breach invert level of EL 470 m with the breach side slope of 1V:0H and bottom breach width equal to 256.25 m. The breach outflow hydrograph for this scenario yielded a peak discharge of 45 213 m^3/s and within 50 min the reservoir was found to deplete. Figure 8 shows the Breach Outflow Hydrograph and Reservoir Water Level for Susu Dam Clear Day Failure.

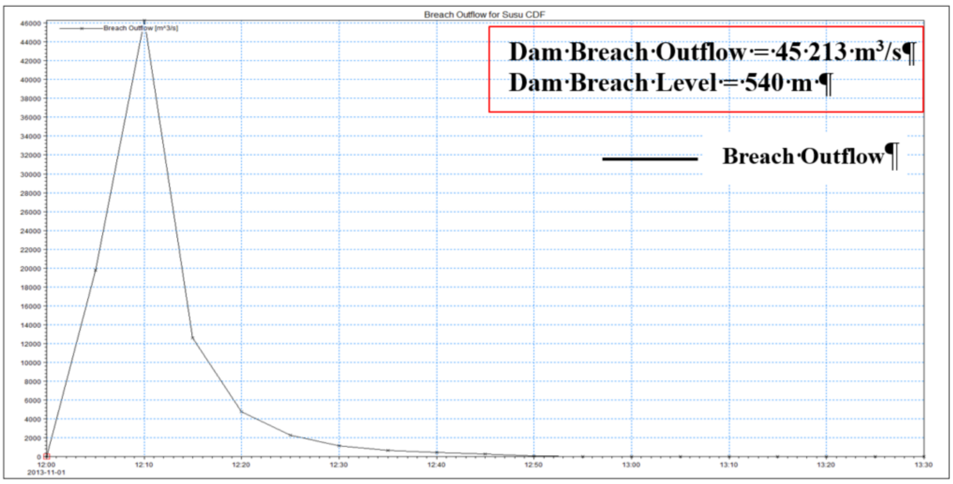

Figure 8: Breach outflow hydrograph and reservoir water level for Susu Dam clear day failure.

4.2 Susu Dam probable maximum flood failure

The PMF inflow with a peak discharge of 3691 m^3/s was routed to the Susu reservoir to determine the flood rise. It was assumed that the initial water level in the Susu reservoir was set at the FSL of EL 540 m and slowly increased to the maximum flood level of EL 547.1 m (1 m below dam crest). The dam was assumed to start to fail at this maximum flood level during PMF event. The time taken for the flood water to increase to maximum flood level is about 6.5 hours. The breach outflow hydrograph for this scenario yielded a peak discharge of 61 110.8 m^3/s and within 3-4 hours the reservoir depletes significantly. PMF inflow required longer time to load up the dam, therefore it provided longer lead time and evacuation time before the formation of breach.

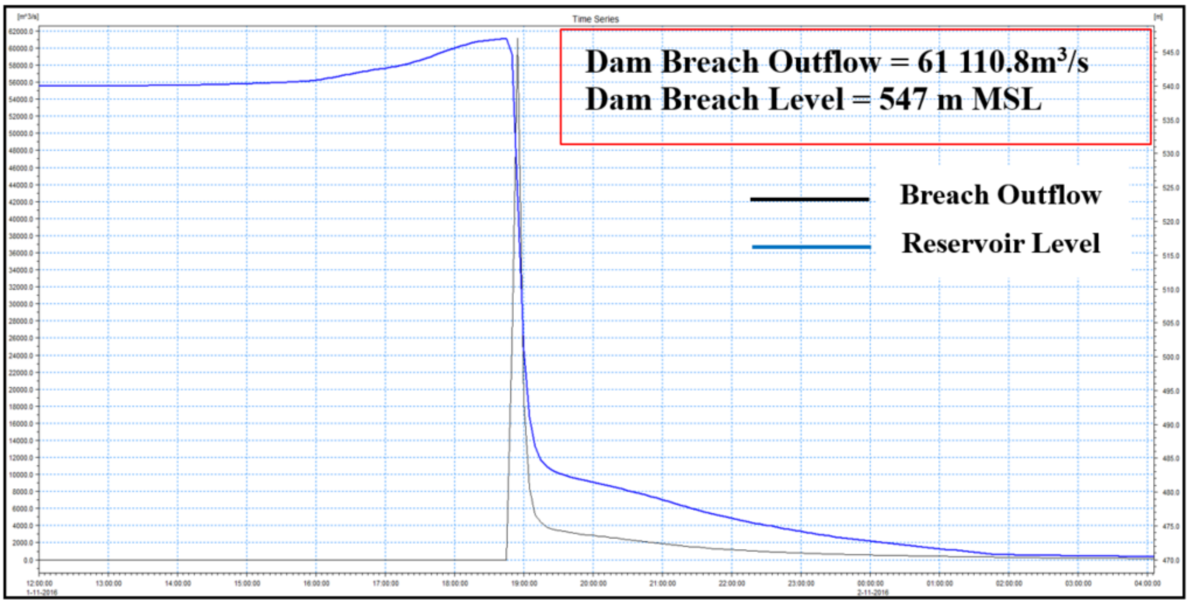

Figure 9: Breach outflow hydrograph and reservoir water level for Susu Dam PMF Failure.

4.3 Affected location

Breach outflow hydrograph for CDF failure and PMF was used to route the flood from Susu dam to downstream. Under both scenarios, flood wave travelled along and within the Sg. Bertam main channel at high velocity, especially in the upper reach. The water level raised rapidly in the channel until it burst its bank to inundate the flood plains. Table 5 and 6 shows the affected locations under CDF Failure and PMF.

Table 5: Affected location under Susu Dam CDF failure.

Location	Distance from Dam (km)	Flood Arrival Time	Time to Peak (min)	Max. Flood Depth (m)	Time to Subside (hour)	Floodplain Velocity (m/s)
Kg Teji	1.94	5.10 (min)	21.67 (min)	3.88	0.94	0.76
Kg. Senangkar	3.10	6.93 (min)	22.67 (min)	14.43	0.67	3.94
Kg. Bako	3.20	14.42 (min)	22.83 (min)	8.41	0.95	3.01
Kg. Susu	3.50	8.37 (min)	23.22 (min)	11.10	0.68	5.02
Pos Telanuk	4.00	12.33 (min)	23.73 (min)	10.39	1.18	3.18
Kg. Renglas	4.50	7.10 (min)	24.57 (min)	14.02	1.10	3.31
Kg. Nyintil	27.90	1.07 (hrs)	1.48 (hrs)	3.71	2.34	0.32
Kg. Medang	30.80	1.50 (hrs)	1.73 (hrs)	0.54	2.07	0.23
Pos Lanai	33.10	1.23 (hrs)	1.95 (hrs)	9.59	4.26	0.79
Kg. Pantos	46.20	2.35 (hrs)	3.54 (hrs)	5.07	6.10	0.18
Kg. Kuala Medang	54.00	3.43 (hrs)	4.93 (hrs)	2.58	7.84	0.40
Kg. Bukit Betong	74.80	6.76 (hrs)	8.44 (hrs)	0.83	10.83	0.14

Table 6: Affected location under Susu Dam PMF.

Location	Distance from Dam (km)	Flood Arrival Time	Time to Peak (min)	Max. Flood Depth (m)	Time to Subside (hour)	Floodplain Velocity (m/s)
Kg Teji	1.94	3.30 (min)	11.48 (min)	8.19	0.78	2.13
Kg. Senangkar	3.10	3.65 (min)	12.75 (min)	18.57	0.54	4.83
Kg. Bako	3.20	5.63 (min)	12.90 (min)	11.81	0.79	3.93
Kg. Susu	3.50	4.57 (min)	13.15(min)	14.40	0.54	5.89
Pos Telanuk	4.00	5.82 (min)	13.77 (min)	13.69	1.03	3.85
Kg. Renglas	4.50	4.80 (min)	14.58 (min)	17.69	5.04	4.02
Kg. Nyintil	27.90	0.94 (hrs)	1.44 (hrs)	5.38	2.56	0.41
Kg. Medang	30.80	1.34 (hrs)	1.68 (hrs)	2.56	2.26	0.72
Pos Lanai	33.10	1.09 (hrs)	1.92 (hrs)	11.60	5.93	0.86
Kg. Pantos	46.20	2.10 (hrs)	3.62 (hrs)	7.57	7.46	0.25
Kg. Kuala Medang	54.00	3.09 (hrs)	5.13 (hrs)	4.42	9.61	0.46
Kg Bukit Betong	74.80	5.84 (hrs)	8.68 (hrs)	2.63	13.87	0.28
Kg. Padang Tengku	83.70	9.78 (hrs)	11.96 (hrs)	1.15	15.84	0.05
Kuala Lipis	97.00	10.08 (hrs)	14.79 (hrs)	4.27	96.00	0.15

The overall flood hazard map in terms of maximum flood depth with the total inundated area of 19.3 km^2 (CDF Failure) and 28.2 km^2 (PMF) is shown in Figure 10 and 11. The distance of the flood extent during the event was found to be approximately more than 100 km. As it move towards the downstream of dam, flood did not spread due to the terrain conditions of floodplain.

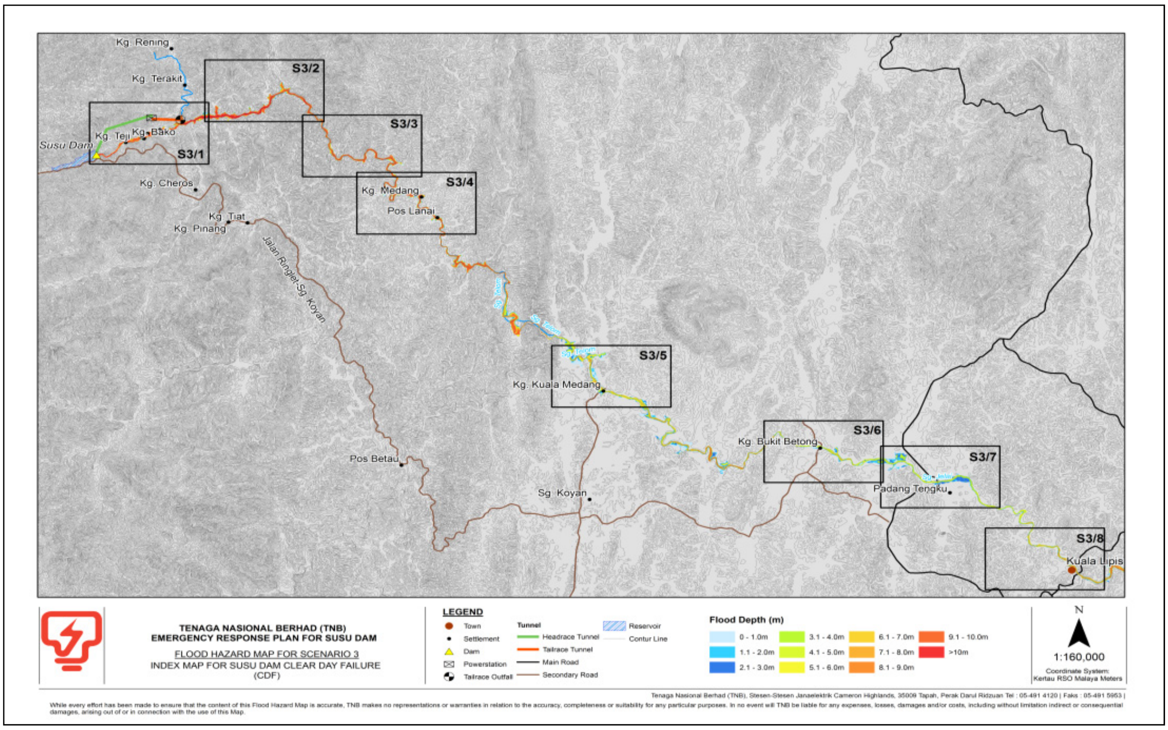

Figure 10: Overall flood hazard map for Susu Dam CDF failure.

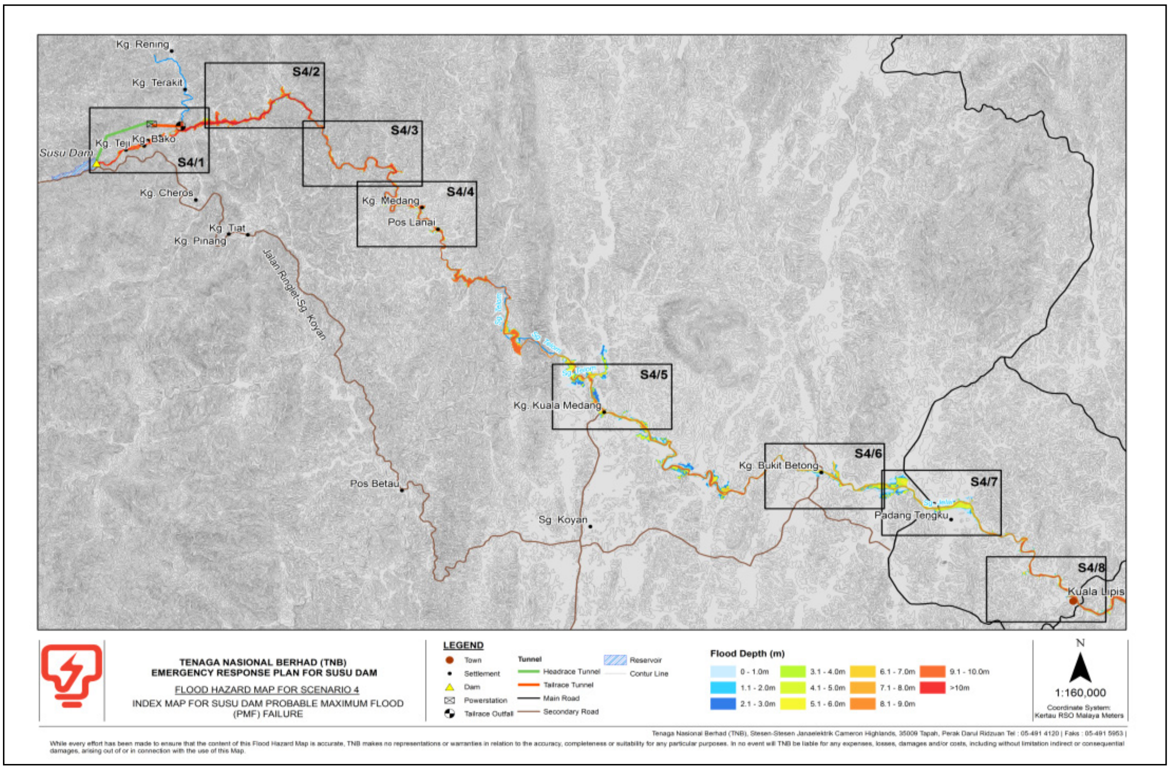

Figure 11: Overall flood hazard map for Susu Dam PMF.

5 CONCLUSION

In general cases like piping, overtopping and foundation results in the failure of dam. So, it is important to predict the breach parameters accurately for dam break modelling. The published agency guideline which is US National Weather Service (NWS) was been selected as an approach to determine dam breach parameter for this study.

It was found that the peak outflow discharge of Susu dam for PMF failure is larger than CDF failure. It happened due to the included PMF inflow with a peak discharge of 3691m^3/s that has been routed to the Susu reservoir. The results show that dam breach outflow hydrograph yielded a peak value of 45 213 m^3/s for CDF Failure and 61 110.8 m^3/s for PMF Failure. Breach outflow hydrograph due to both scenarios have the potential to flood along the downstream area of dam. The time for water in the reservoir to deplete is 50 minutes for CDF Failure and 3 hours for PMF Failure. The conditions where a dam breach on PMF Failure is assumed to cause more damages as the people living downstream does not take precaution and is provided only with ample time for warning and evacuation.

ACKNOWLEDGEMENT

The author would like to acknowledge Tenaga Nasional Berhad Research for the research fund to carry out this project. Author also wishes to acknowledge Centre for Sustainable Technology & Environment from college of Engineering of University Tenaga Nasional Malaysia owing to required assistant for performing of this project.

REFERENCES

Ismail, K. (2004). Dam Break Study, *ME thesis*. Universiti Teknologi Malaysia, Johor Darul Takzim, Malaysia.

Wurbs, R.A. (1987). Dam-Breach Flood Wave Models. *Journal of Hydraulic Engineering*, 113(1), 29-46.

Chen, S.-H., (2015). *Hydraulic Structures*. China: Springer. 1-2.

FEMA. (2001). The National Dam Safety Program: Embankment Dam Failure Analysis. *Proceeding FEMA Workshop*, US Department of Agriculture.

Che Ros, F.M., Sidek, L.N., Ibrahim, N.N.A. & Razad, A.Z. (2007). Probable Maximum Flood (PMF) for the Kenyir Catchment. *International Conference on Construction and Building Technology*, Kuala Lumpur, Malaysia, 325-334.

Wahl, T.L. (1996). *Prediction of Embankment Dam Breach Parameters: Literature Review and Needs Assessment,* USBR, *Water Resources Research Laboratory*, PAP-735.

Proceedings of the 37th IAHR World Congress
August 13 – 18, 2017, Kuala Lumpur, Malaysia

IMPROVING HYDROLOGICAL PREDICTION WITH GLOBAL DATASETS: EXPERIENCES WITH BRAHMAPUTRA, UPPER AWASH AND KAAP CATCHMENTS

BISWA BHATTACHARYA[1], MD. TOHIDUL ISLAM[2], MD. SOHEL MASUD[3], SURAFEL MAMO[4], MJAWA SHENDULI[5], PRABIN ROKAYA[6], SCHALK JAN VAN ANDEL[7] & ILYAS MASIH[8]

[1,5,6,7,8]UNESCO-IHE Institute for Water Education, Delft, The Netherlands
[2,3]Institute of Water Modelling, Dhaka, Bangladesh
[4]Ministry of Water and Energy, Addis Ababa, Ethiopia
B.Bhattacharya@unesco-ihe.org: mtm@iwmbd.org: msm@iwmbd.org; surafel.m2@gmail.com; shenduli80@yahoo.co.uk; prabinrokaya@gmail.com; S.vanandel@unesco-ihe.org; I.Masih@unesco-ihe.org

ABSTRACT

The lack of hydro-meteorological data for a large number of catchments around the world is a major constraint to implementing efficient water resources management. One of the possible solutions to the scarcity of rainfall data or transboundary data issues seems to be in making use of the variety of satellite based estimates and meteorological model products for rainfall. The abundance of a variety of rainfall products such as TRMM, WATCH, ERA-Interim, etc. provide a good basis of hydrological modeling in data-scarce catchments. The usefulness of the satellite based rainfall data needs further validation with hydrological modeling, by comparing simulated hydrodynamic/hydrological response with the measured ones. In this respect, the spatio-temporal scale is an important aspect to reckon as refining the temporal/ spatial scale may increase uncertainty due to the inherent incompatibility between the different spatio-temporal scales of different meteorological products and hydrological simulation. The following three catchments ware chosen for the research: Brahmaputra (India), Upper Awash (Ethiopia) and Kaap (Swaziland, South Africa). Rainfall estimates from TRMM and atmospheric models (ECMWF) are compared with gauge rainfall at different spatial and temporal scales. The comparison shows that the satellite based rainfall products are comparable to gauge rainfall at fortnightly or monthly temporal scales. The accuracy drops for shorter temporal scales (~weekly) but for the daily scale the error level is substantial. The spatial scale also plays an important role. With larger spatial scales, the accuracy increases. Lumped conceptual hydrological models are built for the three catchments. Hydrological simulation of the catchments using gauge and satellite based rainfall estimates shows promising results. It is concluded that the satellite based rainfall estimates, together with the gauge rainfall, can be used in the optimal use of the catchments.

Keywords: Rainfall; TRMM; ERA-Interim; Brahmaputra; Upper Awash; Kaap.

1 INTRODUCTION

Knowledge about spatial and temporal variation of rainfall is absolutely important in hydrological studies for analysing catchment characteristics. Such studies may be required for flood or drought management, water allocation or assessing climate change impact. Carrying out these studies in data-scarce catchments is difficult as the estimation of water availability requires an understanding of the spatial and temporal variability of the rainfall (Wilk et al., 2006). Unfortunately, a large part of the globe is characterized by scarce gauge network. The quality, availability and coverage of rain gauge data are considered the biggest obstacles to effective water resource planning in most developing countries (Thorne et al., 2001). Conversely, these are also countries where improved estimates of water resources availability are required (Hughes, 2006). Another hindrance is sharing of data in trans-boundary catchments as competing interests make sharing data among nations more difficult (Thinh, 2010). Often data sharing protocols are not adequately in place, and rainfall-runoff computation becomes difficult.

One of the possible solutions to the scarcity of rainfall data or transboundary data issues seemed to be in making use of the variety of alternative data sources. Broadly there are four categories of rainfall data sources: gauge, weather radar, satellite remote sensing and numerical weather models (Beck et al., 2016). Among them, rain gauges are the most trusted source of rainfall information. The errors rain gauges make are generally understood and to a considerable extent quantifiable (Bell and Kundu, 2003).

The advancement in reasonably dense network of weather radar stations has greatly improved the capability to routinely monitor local, regional, and continental scale rainfall patterns over the industrially developed countries of the world. However, they are expensive and usage requires calibration with gauges, and as a result cannot be used everywhere.

Satellite remote sensing can potentially close some of the gaps in data availability (Stisen et al., 2008). An increasing number of rainfall estimates from satellite remote sensing are now available in near–real time over the Internet to help meet the needs of weather forecasters and climate scientists, as well as a wide range of decision makers, including hydrologists, agriculturalists, emergency managers, and industrialists (Ebert et al., 2007). The abundance of a variety of rainfall products from satellite remote sensing such as the widely used one from the Tropical Rainfall Measuring Mission (TRMM) provides a good basis of hydrological modelling of data-scarce catchments. Sampling frequency of these rainfall products vary from hourly to monthly.

Rainfall estimates from atmospheric retrospective analysis models such as ERA-Interim from the European Centre for Medium Range Weather Forecasts (ECMWF) also can be used in hydrological studies.

In this research, we have considered TRMM (3B42, version 7) as the rainfall data from satellite remote sensing and ERA-Interim as the rainfall data from atmospheric models. No weather radar data was available. TRMM is a joint project by National Aeronautics and Space Administration (NASA) of the United States and the Japan Aerospace Exploration Agency (JAXA) launched on November 27, 1997. It is designed to monitor and study tropical rainfall. TRMM data covers areas between latitudes of 50^{o}N and 50^{o}S at a spatial scale of 0.25^o (about 27kmx27km) and provides access to near real time 3-hourly rainfall data.

The ERA-Interim data is a global atmospheric reanalysis data, which is produced by simulating atmospheric models (together with the associated data assimilation system). This data is available since 1979 with a spatial resolution of 0.75^{0}x0.75^0 (about 80 km x 80km) at every 6 hours.

Before using the TRMM or ERA-Interim data, their accuracy needs to be compared with the gauge data. Differences in rainfall estimate may origin partly due to the measurement technique and partly due to the spatial and temporal sampling frequency employed in gathering data. Rain gauges measure continuous rainfall in a fairly straightforward way of what is falling on a tiny area of 150 cm^2. Contrary to that, TRMM rainfall estimates are based on the indirect measurement of the volume integrated microwave emission within the satellite instrument's (TMI) field of view (FOV). When TRMM satellite is viewing a given area, rain rates within the area must be inferred indirectly with remote sensing methods and are therefore subject to retrieval errors. Associated with its indirect measurement, there are various factors contributing to the uncertainty in rainfall estimation by TRMM. These factors include mechanical and electronic problems, geo-location and data transmission problems and inherent uncertainties of computer software. A gauge records rainfall continuously whereas in case of TRMM a snap shot is made at 3-hourly interval.

The availability of new rainfall products has influenced research on their accuracy and usefulness. It has been generally observed that with a large spatial scale and temporal scale, the rainfall data from all sources are largely comparable. At monthly temporal scales, the coefficient of determination between gauge and TRMM is often greater than 0.9 whereas for daily values it drops to less than 0.5 (Arias-Hidalgo et al., 2013; Bell and Kundu, 2003). The comparability also varies from catchment to catchment also due to the differences of physical properties. Therefore, there is a need to investigate the accuracy of these alternative data sources for catchments where they are planned to be used. In such investigations, often an alternative approach is employed where a hydrological model of the catchment is developed and simulated with different rainfall products. Simulated hydrographs with different rainfall products are compared with the measured hydrograph to infer about the accuracy of different datasets.

In this paper, we have compared TRMM and ERA-Interim rainfall estimates with gauge data firstly by directly comparing them and secondly, by simulating runoff with the built hydrological model using the three rainfall datasets and comparing the simulated runoffs with the measured one.

2 STUDY AREA

Three study areas were chosen: one very large, one medium and one small. Rainfall data from satellite remote sensing and reanalysis models work well when the catchment size is rather large. Accordingly, we chose three catchments to see the usefulness of the different datasets. The catchments are described below.

2.1 Brahmaputra

Brahmaputra River originates from the great glacier mass of Chema-Yung-Dung in the Kailas range of southern Tibet at an elevation of 5300 m and traverses 3410 km flowing through China (1995 km.), India (983 km.) and Bangladesh (432 km.) before emptying into the Bay of Bengal. The basin has an area of around 556365 km^2 spreading over China (~50%), Bhutan (~8%), India (~34%) and Bangladesh (~8%) (Figure. 1). The basin comprises quite diverse environments such as the cold dry plateau of Tibet, rain-drenched Himalayan slopes, landlocked alluvial plains of Assam and vast deltaic lowlands of Bangladesh. The Brahmaputra basin, excluding the Tibetan portion, forms an integral part of the southeast Asian monsoon regime with a mean annual rainfall of 2300 mm. Distribution of rainfall over the basin varies ranging from 1200 mm in parts of Nagaland to over 6000 mm on the southern slopes of the Himalaya. Monsoon rains from June to September account for 60-70% of the annual rainfall in the basin, while the pre-monsoon season from March through May produces 20-25% of the annual rainfall. Snowfall is experienced in the basin in areas with elevations of 1500 m above sea level (ASL) and above.

2.2 Upper Awash

The Upper Awash basin which is one of the susceptible flood-prone areas in Ethiopia is affected by flooding during each flood season. This study area is geographically located 50 km south-west of Addis Ababa and lies between 8°8' and 9°23' latitudes and 37°57' and 39° longitudes having an area of about 12931 km^2 (Figure 2). The altitude of this catchment varies from 2200 - 3000 m ASL. This basin is also the main source of Awash River. Most of the catchment is affected by flooding and inundated both by rainwater and river water. The rainfall begins in June and reaches its peak in July and August. The climate of Upper Awash basin is under the influence of Inter Tropical Convergence Zone. The low pressure zone marks the convergence of dry tropical zone, and the seasonal rainfall distribution within the basin results from the annual migration of the ITCZ. In March, it advances towards the north (from the south) across the basin, bringing small rain (or spring rains). In June and July, it reaches beyond the basin which experiences heavy rain (or summer rains). It returns southward during August to October and restoring the drier easterly air stream which prevails until the cycle repeats itself in March. The distribution of the rainfall over the high-land areas has orographic effects and is significantly correlated with altitude. The mean annual rainfall of this sub-catchment is about 1100 mm and its mean annual temperature varies from 13 to 20°C (Yitbarek et al., 2012) during dry and wet seasons, respectively.

2.3 Kaap catchment

This case study was on the Kaapbasin, which is a part of the larger Incomati basin. The Kaap River is a major contributor of flow to the Crocodile River which then flows to the transboundary Incomati River (Suarez, 2014). Because of its transboundary nature shared among South Africa, Swaziland and Mozambique, several water-sharing agreements have been carried out among these countries (Slinger et al., 2010). The area of the catchment is about 1640 km^2. The elevation ranges from 300 to 1800 m ASL. Bushvelds and grasslands are the predominant land cover. The area is characterized by semi-arid climate with cool dry winters and hot wet summers. The catchment receives most of the rainfall in its rainfall during October to March. Average annual rainfall varies inside the catchment from 583 (lower valley) to 1243 mm (high altitudes). The average monthly rainfall is highest in January (160 mm) and the average monthly discharge at the Kaap outlet is highest in February (9 m^3/s). The lowest monthly average discharge occurs at the end of the dry period and is about 0.8 m^3/s (in September).

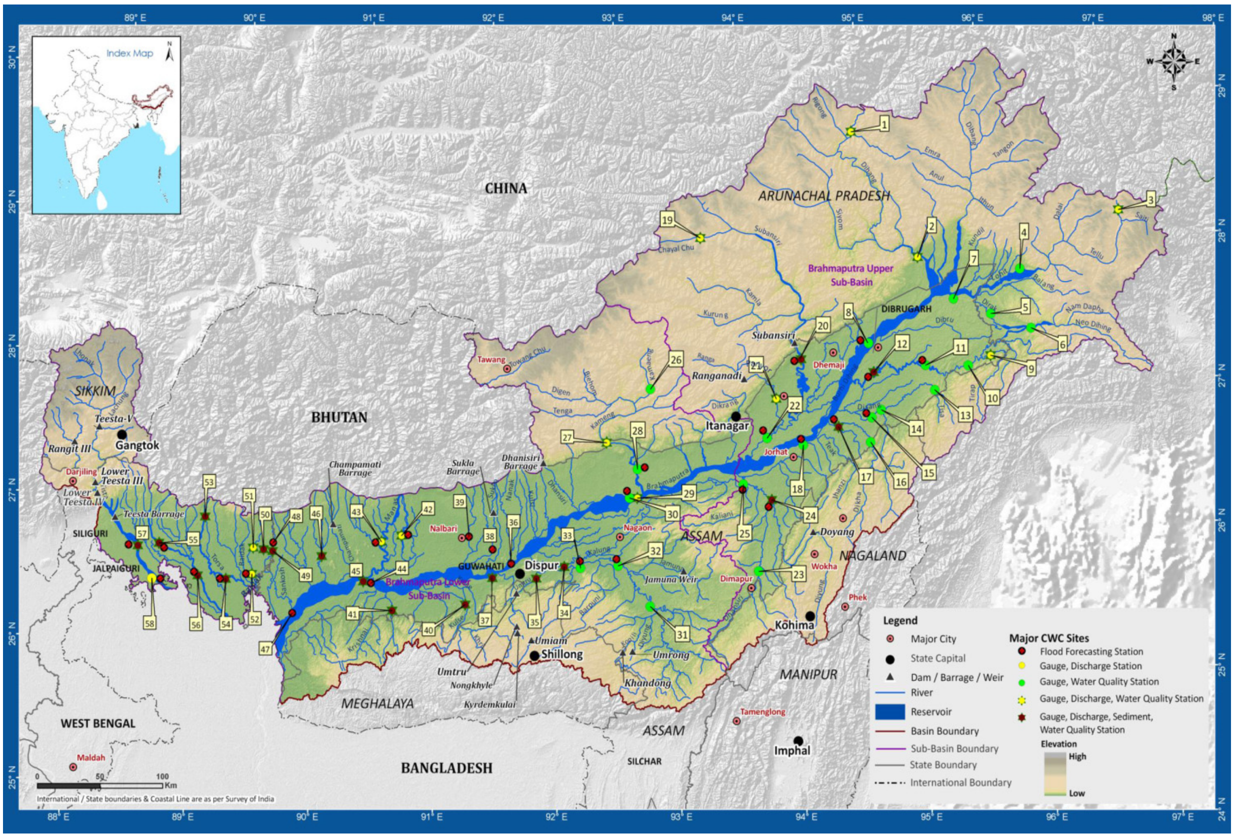

Figure 1. Map showing the Indian part of the Brahmaputra basin (Sharma and Paithankar, 2014).

 ©2017, IAHR. Used with permission / ISSN 1562-6865 (Online) - ISSN 1063-7710 (Print)

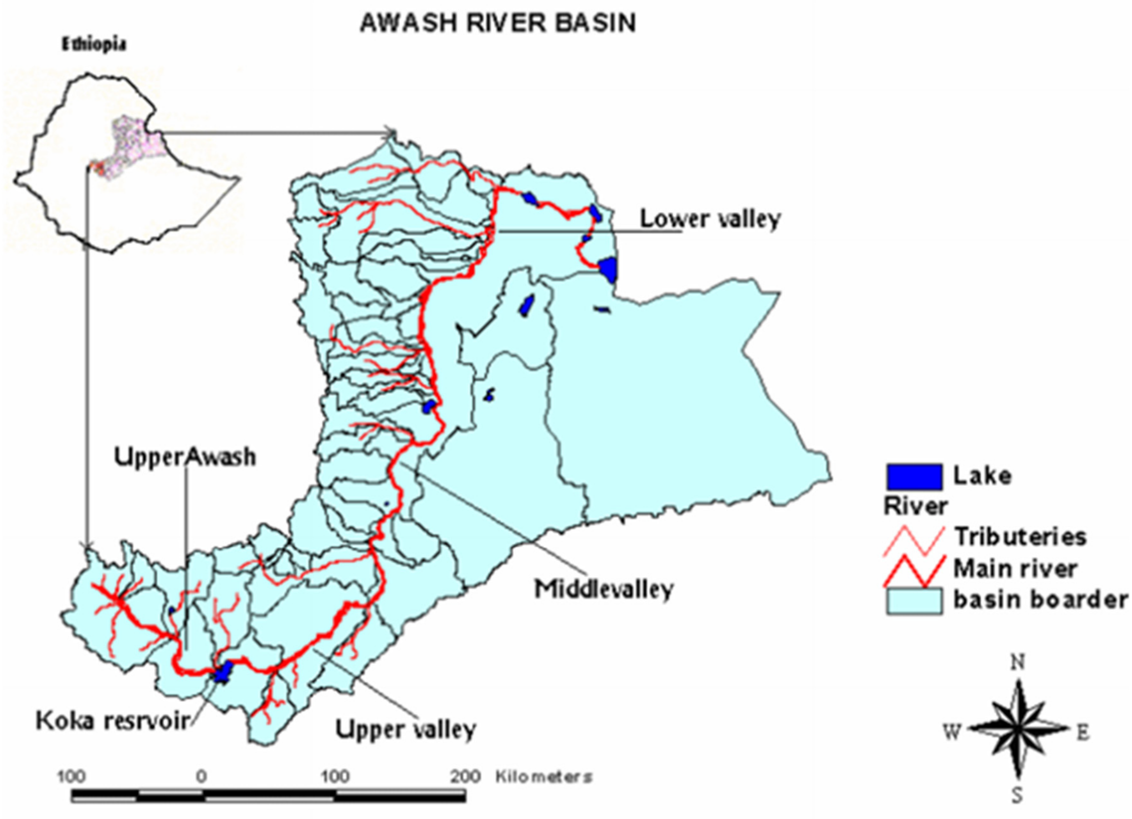

Figure 2. Upper Awash basin map along with the hydro-meteorological stations of the basin (Shenduli, 2014).

Figure 3. Location of the Kaap catchment (Suarez, 2014).

3 DATA AND METHODS

3.1 Rainfall data

Rainfall data was naturally the most important data for carrying out this study. We considered three categories of rainfall data: gauge, TRMM (3B42, version 7) and ERA-Interim. For the Brahmaputra case study, the gauge rainfall data was available only from 10 rain gauges. Compared to the size of the catchment, the availability of gauge rainfall data was really limited. For the Upper Awash catchment, the rainfall data was available for 23 gauges and the data was collected from the National Meteorological Agency of Ethiopia (NMA). For the Kaap catchment, the rainfall data from 19 rain gauges were used in the study (Table 1).

Table 1. Data availability and time period of study.

Catchment	Gauge	TRMM	ERA-Interim	Period of study
Brahmaputra	2002-2013	1998-2015	1979-2015	2002-2013
Upper Awash	1998-2008	1998-2015	1979-2015	1998-2008
Kaap	1998-2000	1998-2015	1979-2015	1998-2008

3.2 Methodology

Gauge rainfall is measured almost everywhere using comparable tipping buckets. However, their density varies. As a result, areal rainfall, which is normally required in hydrological studies and is computed using any geostatistical techniques, bears uncertainties. Uncertainties in areal rainfall computation depends not only upon the gauge density but also on the type of rainfall (e.g. orographic or convective), meteorological factors (e.g. wind speed) and physical characteristics of the catchment (e.g. altitude). In this research, areal rainfall was not compared. Rather, we compared the rainfall data from TRMM and ERA-Interim with the gauge rainfall at different temporal scales. Such comparison provides knowledge about the accuracy of different data products.

The different rainfall data were compared further by using them in hydrological modelling and then comparing the runoffs generated. Lumped conceptual hydrological models were developed for the three case study areas. Among the widely available modelling tools, Hydrological Modelling System (HMS) was used for the Upper Awash and Kaap catchments. Due to an additional requirement of soil erosion estimates (not reported in this paper), the Soil and Water Assessment Tool (SWAT) was used for the Brahmaputra catchment.

Digital elevation models (DEM) of catchments were developed using data from Shuttle Radar Topography Mission (SRTM), which has got a resolution of 90m by 90m. Brahmaputra and Upper Awash are sufficiently large and the rivers and floodplains are wide enough for the resolution of this data. The data is not error free, particularly for elevations. However, SRTM data was used due to the unavailability of a better quality data. Moreover, many publications have reported its adequacy in hydrological studies for a number of catchments (Arias Hidalgo et al., 2013). The physical representation of the catchment in the model additionally requires river networks (including cross-sections), land cover and soil data. River networks were extracted from the SRTM data. The land cover and soil data from the Food and Agriculture Organization (FAO) was used. Based on the availability of data, the time period of study was chosen (Table 1).

4 HYDROLOGICAL MODELLING

Lumped conceptual models were developed and used to simulate runoff using different rainfall data. The simulated runoff was compared with the measured one. In addition to the visual comparison of the simulated and measured hydrographs, the root mean square error (RMSE) and coefficient of determination (R^2) were computed.

For the Brahmaputra basin, a model was developed using SWAT. SWAT is designed to predict the impact of land management practices on water, sediment and agricultural chemical yields in large complex catchments with varying soils, land use and management conditions over long periods of time. The model was calibrated with the data from the period 2002-2008 and was validated with the data from the period 2009-2013.

For the Upper Awash basin, a HEC-HMS model was developed. HEC-HMS is a widely used tool from the Hydrological Engineering Center of United States Army Corps of Engineers. HMS is designed to simulate rainfall-runoff processes. The model was calibrated using data from the period 1998 to 2004 and validated using data from the period 2005 to 2008. The model parameters were optimized using the automatic optimization procedure of HEC-HMS. The model was run with a daily time step.

For the Kaap catchment, a HEC-HMS model was developed. The adopted methodology was similar to the one used for the Upper Awash catchment. The calibration period was 1998-2003 and the validation period was 2004-2008.

5 RESULTS AND DISCUSSION

5.1 Data analysis in temporal and spatial scales

Comparison of the TRMM and ERA-Interim rainfall estimates with the gauge rainfall at different temporal scales was carried out. Results are presented for a representative gauge location (Table 2 and Figure 4). Comparable results were obtained for other locations. Due to the varying gauge density and the associated uncertainty in computed areal rainfall, the comparison of areal rainfall was not carried out. Four temporal scales were considered: daily, weekly, fort-nightly and monthly.

  / ISSN 1562-6865 (Online) - ISSN 1063-7710 (Print)

It is discernible from Figure 4 and Table 2 that the daily rainfall estimates from TRMM and ERA-Interim at the daily time step had very high errors. For the TRMM data, the daily rainfall averaged over 6 years (2002-2007) had RMSE=5.5 mm with average gauge rainfall = 1.3 mm leading to normalized RMSE = 4.2. Also, the coefficient of determination (R^2) was barely 0.1. For the ERA-Interim data, the error was even more. Also, the scatters (Figure 2) suggested that the differences are too high. As the time scale of comparison increased, the error level decreased gradually. At the monthly time scale for the TRMM data, the R^2 value increased to 0.91. The error was still high (normalized RMSE = 0.65). For the ERA-Interim, a similar trend was observed although the error level was even more (normalized RMSE=1.8).

The level of errors suggests that for small areas, the TRMM and ERA-Interim rainfall estimates may have very high level of errors. If the rainfall over a relatively large catchment is considered then the error drops. In several studies, it is reported that when a catchment area is relatively large then the R^2 values are often observed to be about 0.5 for daily time scale and it increases further to ~0.75 at weekly time scales (Bell and Kundu, 2003).

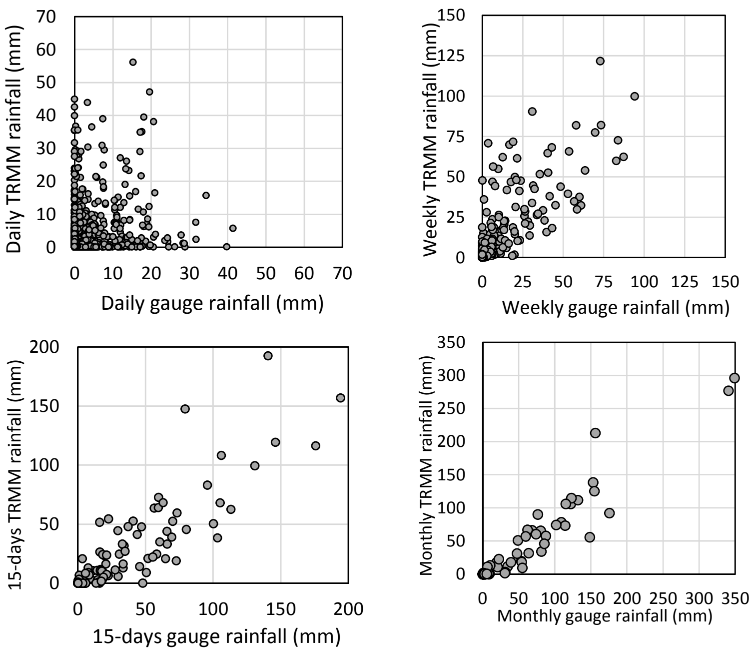

Figure 4. Comparison of rainfall estimates from TRMM with gauge data at varying temporal scales inside the Brahmaputra Basin (location: 29.30^0 N, 90.98^0 E).

Table 2. Comparison of TRMM and ERA-Interim rainfall estimates with gauge rainfall at different temporal scales inside the Brahmaputra Basin (location: 29.30^0 N, 90.98^0 E).

	Average gauge rainfall	TRMM			ERA-Interim		
		RMSE	Relative bias	R^2	RMSE	Relative bias	R^2
	mm	mm	[-]	[-]	mm	[-]	[-]
Daily	1.3	5.5	-33.7	0.10	6.7	-53.3	0.08
Weekly	8.8	12.7	-33.7	0.63	17.3	-53.3	0.53
Fortnightly	18.8	18.6	-33.7	0.78	31.3	-53.3	0.69
Monthly	38.9	25.4	-33.7	0.91	72.7	-53.3	0.83

Figure 5 and Table 3 present similar results for the Upper Awash basin. The data was considered for 7 years (1998 to 2004). The error of TRMM and ERA-Interim data was observed to be very high. With the TRMM data at the daily scale, the RMSE was 7.5 mm with average gauge rainfall 3.2 mm (normalized RMSE = 2.2). The error dropped with increasing time scales and at the monthly level, the error was the lowest (normalized RMSE=0.39). With the ERA-Interim data, a similar trend was observed. Compared to the Brahmaputra catchment, the two datasets were more comparable for the Upper Awash catchment.

Figure 6 and Table 4 show the comparison of rainfall for the Kaap catchment. It may be noticed that compared to the other two basins, the level of errors was higher for the Kaap catchment. Further details at other time scales can be observed in Table 4.

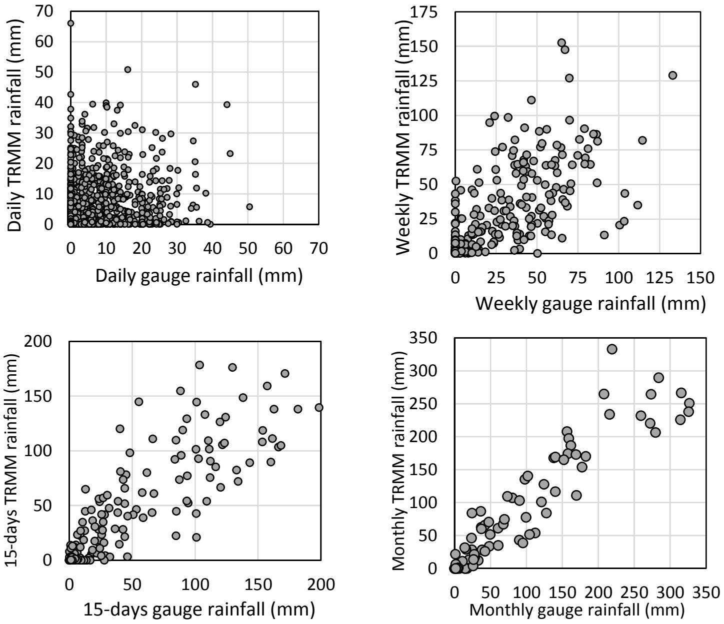

Figure 5. Comparison of TRMM rainfall estimates with gauge rainfall at different temporal scales inside the Upper Awash basin (location: 9.03^0 N, 38.24^0 E).

Table 3. Comparison of TRMM and ERA-Interim rainfall estimates with gauge rainfall at different temporal scales inside the Upper Awash basin (location: 9.03^0 N, 38.24^0 E).

	Average gauge rainfall	TRMM			ERA-Interim		
		RMSE	Relative bias	R^2	RMSE	Relative bias	R^2
	mm	mm	[-]	[-]	mm	[-]	[-]
Daily	3.2	7.1	-5.7	0.11	7.5	-47.2	0.12
Weekly	22.2	21.6	-5.7	0.51	27.9	-47.2	0.51
Fortnightly	47.5	31.6	-5.7	0.70	49.0	-47.2	0.66
Monthly	96.7	37.0	-5.7	0.88	83.1	-47.2	0.82

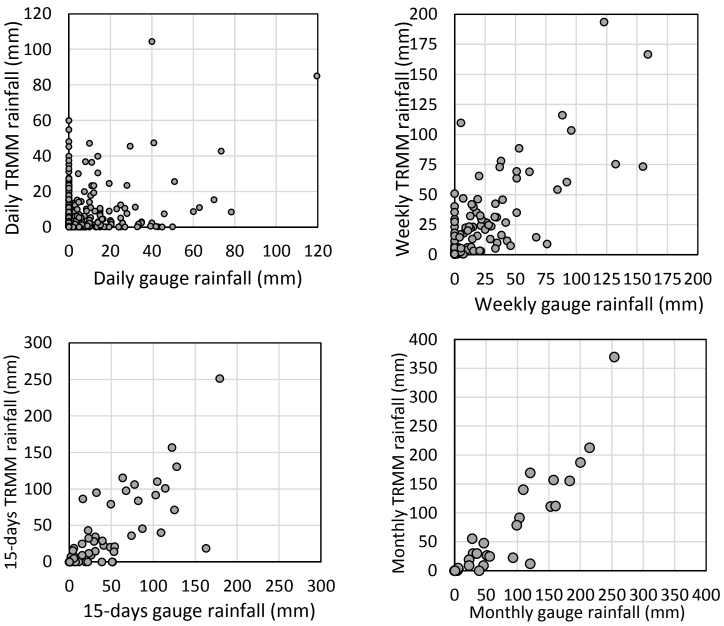

Figure 6. Comparison of TRMM rainfall estimates with gauge rainfall at different temporal scales inside the Kaap basin (location: Oorschot).

Table 4. Comparison of TRMM and ERA-Interim rainfall estimates with gauge rainfall at different temporal scales inside the Kaap catchment (location Oorschot).

	Average gauge rainfall	TRMM RMSE	TRMM Relative bias	TRMM R2	ERA-Interim RMSE	ERA-Interim Relative bias	ERA-Interim R2
	mm	mm	[-]	[-]	mm	[-]	[-]
Daily	2.4	9.7	-16.7	0.14	11.8	-41.2	0.01
Weekly	17.1	21.4	-16.7	0.58	48.0	-41.2	0.12
Fortnightly	36.6	33.3	-16.7	0.71	56.1	-41.2	0.19
Monthly	76.8	42.7	-16.7	0.81	169.9	-41.2	0.41

5.2 Hydrological simulation results and discussion

The SWAT model of the Brahmaputra basin was simulated using TRMM and ERA-Interim data and the model outputs had been compared with the observed (rated) discharge at Bahadurabad of Bangladesh (Figure 7). Unfortunately, there was not enough gauge data available to simulate the model just with the gauge rainfall. The validation results in Figure 7 show that the simulated discharge with the TRMM generally followed the trend of the measured discharge although the error was substantial. The RMSE was 17654 m^3/s whereas the average discharge was 24000 m^3/s. The R^2 was 0.5. Out of the five hydrological years, the flood peaks were reproduced well for 3 years. For 2010, the peak was under-estimated whereas for 2011 the peak was over-estimated. The dry period flow was more or less correctly estimated. The spring discharge was always under-estimated. This could be due to higher levels of errors in TRMM data for snow-covered regions or due to inaccuracies in the snow melt component of the model. The simulation with the ERA-Interim data was much worse. It has always under-estimated the discharge. The R^2 was 0.5 and the RMSE was 20125 m^3/s.

Figure 8 shows the simulation results of the Upper Awash basin for the time period 1998 to 2004. In the calibration period (1998-2004), the daily observed and simulated discharge with the gauge rainfall did not correlate well for peak flows, mainly due to uneven distribution of rain gauges within the catchment. On the other hand, the hydrographs agreed for the low flows. R^2 obtained was 0.83 and RMSE was 148m^3/s using the mean monthly flows. The mean monthly flow was 39.5 m^3/s and therefore, the RMSE was very high. In the validation period (2005 - 2008), the daily observed and simulated curves (not shown here) were also not correlated well for peak flows. The simulated hydrograph slightly underestimated peaks and overestimated low flows. The R^2 was 0.85 and RMSE was 144m^3/s to measure the model performance on monthly basis.

Figure 8 also shows the simulated hydrograph using TRMM rainfall data. The result shows overall agreement with the observed runoff but not for the peak flows. The R^2 and RMSE values were obtained on monthly basis: 0.71 and 292m^3/s, respectively. Simulation using ERA-Interim rainfall data (Figure 8) shows that peak flows were underestimated, except for two events in 2003. The monthly R^2 value for this analysis was 0.50 and RMSE was 383m^3/s. In this rainfall comparison, the ERA-Interim data (on August 21 and 22, 2003) showed very high rainfall, leading to very high simulated runoff. This needs to be further analyzed for errors/outliers.

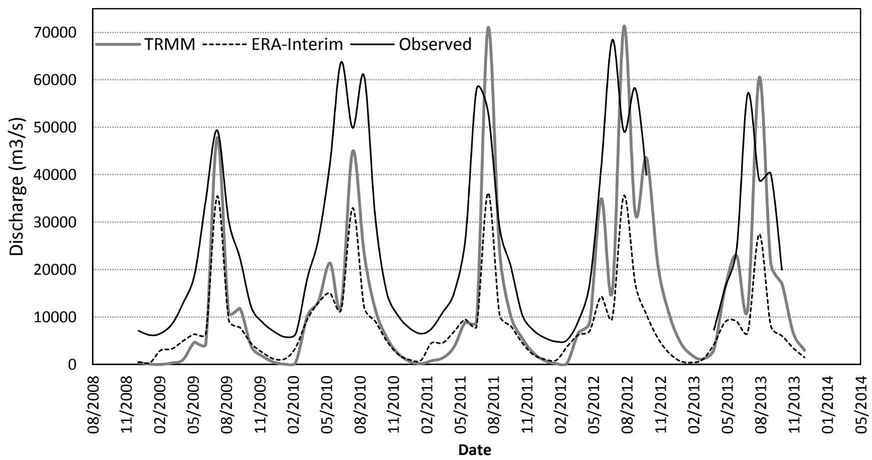

Figure 7. Comparison of simulated discharge of TRMM and ERA-Interim data with the measured discharge at Bahadurabad for the Brahmaputra basin.

Simulation results for the Kaap catchment showed much higher errors. The RMSE of the simulated discharge with the gauge rainfall was 3.9 m^3/s whereas the average discharge was 1.9 m^3/s. The corresponding RMSE with the TRMM data was 32.7 m^3/s. Because of the high errors, the simulation results are not presented here. The simulation with the ERA-Interim estimates was not carried out as this rainfall dataset showed even larger errors compared to the TRMM data. We anticipate that the smaller catchment size may be one of the main reasons for much larger errors for the Kaap catchment. Also, the representation of the narrow rivers of the catchment in the digital elevation model built with the SRTM data of 90mx90m resolution might have brought additional uncertainties.

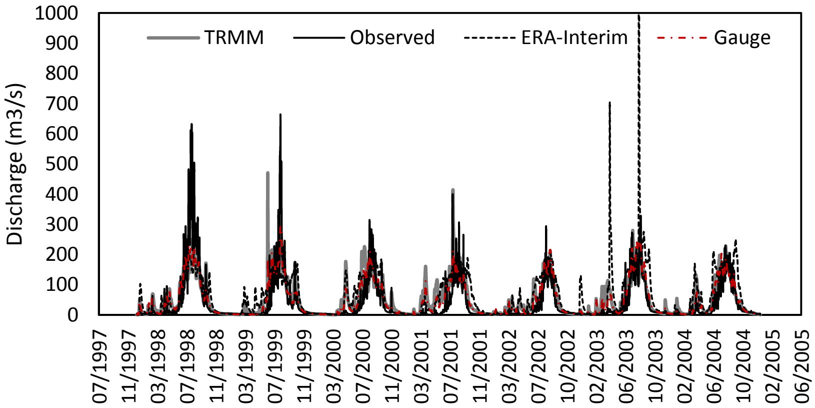

Figure 8. Comparison of simulated discharge with gauge, TRMM and ERA-Interim data with the measured discharge for the Upper Awash basin.

6 CONCLUSIONS

Rainfall estimates from TRMM and ERA-Interim have been compared with the gauge rainfall at different temporal scales for three catchments: Brahmaputra, Upper Awash and Kaap. It has been observed, that the accuracy of the TRMM data increases with increasing temporal scales. It is noted that the TRMM data at a temporal scale of 15 days to one month shows relatively good accuracy, whereas, at a daily scale the error level is observed to be very high. Between the TRMM and ERA-Interim data, the former shows higher accuracy over the later.

A hydrological model using SWAT is developed for the Brahmaputra basin and hydrological models using HEC-HMS are developed for the Upper Awash and Kaap catchments. Three rainfall products namely, gauge, TRMM and ERA-Interim are used to estimate the basin discharge. Based on the comparison of the simulated discharge with the observed discharge, it can be concluded that the simulated runoff with TRMM and ERA-Interim rainfall estimates closely follows the trend of the measured discharge both for the Brahmaputra and Upper Awash catchments. However, substantial errors are observed. More investigation is needed before this data can be used in more specific purposes. For the Kaap catchment, the errors are very high, which might be due to the smaller catchment size. For this catchment, based on this experiment, the possibility of applying rainfall estimates from satellite remote sensing and atmospheric models has more limited possibilities compared to the other two catchments.

ACKNOWLEDGEMENT

We acknowledge the financial support of the project Rain PRED funded by DGIS, The Netherlands and UNESCO-IHE Programmatic Cooperation (DUPC).

REFERENCES

Arias-Hidalgo, M., Bhattacharya, B., Mynett, A.E. & van Griensven, A. (2013). Experiences in using the TMPA-3B42R Satellite Data to Complement Rain Gauge Measurements in the Ecuadorian Coastal Foothills. *Hydrology and Earth Systems Sciences*, 17(7), 2905- 2915.

Beck, H.E., van Dijk, A.I.J.M., Levizzani, V., Schellekens, J., Miralles, D.G., Martens, B. & de Roo, A. (2016). MSWEP: 3-hourly 0.25 Global Gridded Precipitation (1979–2015) by Merging Gauge, Satellite and Reanalysis Data. *Hydrology and Earth System Science Discuss*ion, 21(1), 589.

Bell, T.L. & Kundu, P.K. (2003). Comparing Satellite Rainfall Estimates with Rain Gauge Data: Optimal Strategies Suggested by a Spectral Model. *Journal of Geophysical Research,* 108, 1-15.

Ebert, E.E., Janowiak, J.E. & Kidd, C. (2007). Comparison of Near-Real-Time Precipitation Estimates from Satellite Observations and Numerical Models. *Bulletin of the American Meteorological Society*, 88(1), 47-64.

Hughes, D.A. (2006). Comparison of Satellite Rainfall Data with Observations from Gauging Station Networks. *Journal of Hydrology*, 327(3–4), 399-410.

Sharma, J.R. & Paithankar, Y. (2014). *Brahmaputra Basin Report*, Ministry of Water Resources, Government of India.

Shenduli, M.M. (2014). *On Combining Satellite Rainfall Data with Rain Gauge Data for Improved Flood Prediction in Upper Awash Basin-Ethiopia*, *MSc Thesis.* UNESCO-IHE, Delft, The Netherlands.

Slinger, J.H., Hilders, M. & Juizo, D. (2010). The Practice of Transboundary Decision-Making on the Incomati River: Elucidating Underlying Factors and their Implications for Institutional Design. *Ecology and Society,* 15(1), 1.

Stisen, S., Jensen, K.H., Sandholt, I. & Grimes, D.I.F. (2008). A Remote Sensing Driven Distributed Hydrological Model of the Senegal River Basin. *Journal of Hydrology*, 354(1–4), 131-148.

Suarez, V.V.C. (2014). Identification and Quantification of Runoff Components in the Kaap Catchment, South Africa, MSc Thesis. UNESCO-IHE Institute for Water Education, Delft, Netherlands.

Thinh, D.Q. (2010). Hydrological Simulation of a Transboundary River Basin using TRMM and Gauge Rainfall Data, *MSc Thesis*. UNESCO-IHE Institute for Water Education, Delft, Netherlands.

Thorne, V., Coakeley, P., Grimes, D. & Dugdale, G. (2001). Comparison of TAMSAT and CPC Rainfall Estimates with Rain Gauges, for Southern Africa. *International Journal of Remote Sensing*, 22(10), 1951-1974.

Wilk, J., Kniveton, D., Andersson, L., Layberry, R., Todd, M.C., Hughes, D. & Vanderpost, C. (2006). Estimating Rainfall and Water Balance over the Okavango River Basin for Hydrological Applications. *Journal of Hydrology*, 331(1–2), 18-29.

Yitbarek, A., Razack, M., Ayenew, T., Zemedagegnehu, E. & Azagegn, T. (2012). Hydrogeological and Hydrochemical Framework of Upper Awash River Basin, Ethiopia: With Special Emphasis on Inter-Basins Groundwater Transfer between Blue Nile and Awash Rivers. *Journal of African Earth Sciences,* 65(0), 46-60.

DEVELOPMENT OF CLIMATE HAZARDS INDICATORS BASED ON DRIVERS–PRESSURES–STATE–IMPACTS–RESPONSES (DPSIR) FRAMEWORK: CASE STUDY IN CAMERON HIGHLANDS, MALAYSIA

KOK WENG TAN[(1)] & PHUI NYING LOH [(2)]

[(1,2)]Faculty of Engineering and Green Technology, Universiti Tunku Abdul Rahman Perak Campus, Malaysia
tankokweng@utar.edu.my, phuinying17@gmail.com

ABSTRACT

An important part of the natural hazard's risk management is a decision support system. This study aims to propose a set of indicators for decision support system that suits the local climate hazard situation in Cameron Highlands. The climate hazard Decision support system (DSS) development is based on Driver–Pressure–State–Impact-Response(DPSIR) conceptual framework which includes the following elements: populations, waste, land use, flood disaster, development/investment opportunities, climate change indicators, health and sanitation, soil quality, disasters/mass movements, socio-economic, environmental quality, private and public sectors and individuals. In this study, focus group interview session is carried out on 85 local respondents in major townships of Cameron Highlands. Principal Component Analysis (PCA) is applied in order to synthesise the outcome of the interview session. Total 25 DSS indicators are extracted based on PCA outcomes. The pre-defined indicators are then given a weightage and rating by 11 experts in Malaysia. The changing climate is threatening the livelihood of local community and the environment sustainability. The local community seems to be struggling to cope with such changes. Without strategic planning in Cameron Highlands, all of these changes can affect negatively the two main industries in the highlands which are agriculture and tourism. Hence, the climate hazards DSS is recognized as an integral part in decision-making for the future local plan.

Keywords: Cameron Highlands; climate hazards; indicators; DPSIR framework.

1 INTRODUCTION

Our earth's climate system has changed since the last century. Scientific evidences show that climate change increases the frequency and intensity of extreme events e.g. floods, droughts and storms that threaten human health and safety (EPA, 2017). It may exacerbate the problem of desertification, drought and soil degradation (Brevik, 2013). Besides, climate change may expose more people to tropical diseases such as dengue and malaria. It due to a warmer climate is probably increasing the risk of illnesses and death from extreme heat and poor air quality. Flood and landslide are common in Malaysia due to a combination of geographical, climatic, hydrological and human systems (Chan, 2002). Landslide has been the second natural disaster threat for Malaysia after the flood (Matori et al., 2011). The series of massive flood events occurred between year 2014 and 2015 has seriously affected several states in Peninsular Malaysia, evacuating over 200,000 people in Kelantan, Terengganu, Pahang, Perak and Perlis, mostly in the northern and eastern regions (ASEAN, 2015). What is happening currently strongly indicate that it is not one-off events but part of a national, regional and global pattern linked to climate change and extreme weather events. Al-Zaquan (2014) stated that the flood events that devastated have been described as the worst in decades in Malaysian History.

According to a paper published by Malaysian Meteorological Department (MetMalaysia) in 2012 titled "Malaysia Climate Change Scenarios", the northeast monsoon has become more intense. There were drier months corresponding with heavier rainfall in the past 10 years (Khor, 2015). Azlee (2015) stated the National Security Council (NSC) identified two major reasons for this bizarre disaster. One is the changing climatic patterns and the adverse weather effects. Others could be the result of uncontrolled land management and the swelling number of trees and exploitation of land resources.

Cameron Highlands is chosen as the case study area. It is the smallest district of Pahang State and is located within the Main Range of Peninsular Malaysia. Figure 1 shows the location of Cameron Highlands in Peninsular Malaysia. The average elevation of the catchment area is between 1000 and 1830 m above sea level with Mount Brinchang peaks at 2031 m above sea level (Clarkson, 1968). It covers an area of 712 km^2 (Fortuin, 2006). The three sub-districts of the highlands are Hulu Telom (89.44%), Tanah Rata (3.08%) and Ringlet (7.48%) (JPS, 2012). The cool temperature climate of Cameron Highlands ideally suits the production of temperate vegetables, with maximum mean monthly temperature ranging from 21.3 to 23.4 °C and minimum from 14.8 to 15.9 °C for the year 1984 – 2015 (MetMalaysia, 2016). Annual rainfall for the past 32 years averaged 2840 mm/yr (MetMalaysia, 2016). Local perception on temperature rises and rainfall variation

  / ISSN 1562-6865 (Online) - ISSN 1063-7710 (Print)

over the past three decades were in line with the observation data from the Malaysian Meteorological Department. Cameron Highlands is drained by eight rivers with Bertam River, Telom River and Lemoi River, being the major ones. Cameron Highlands forms the headwater catchment areas for many rivers in Pahang. However, the water quality of the rivers has been deteriorating over the years, mainly due to siltation from land clearing for developments, road construction and agriculture.

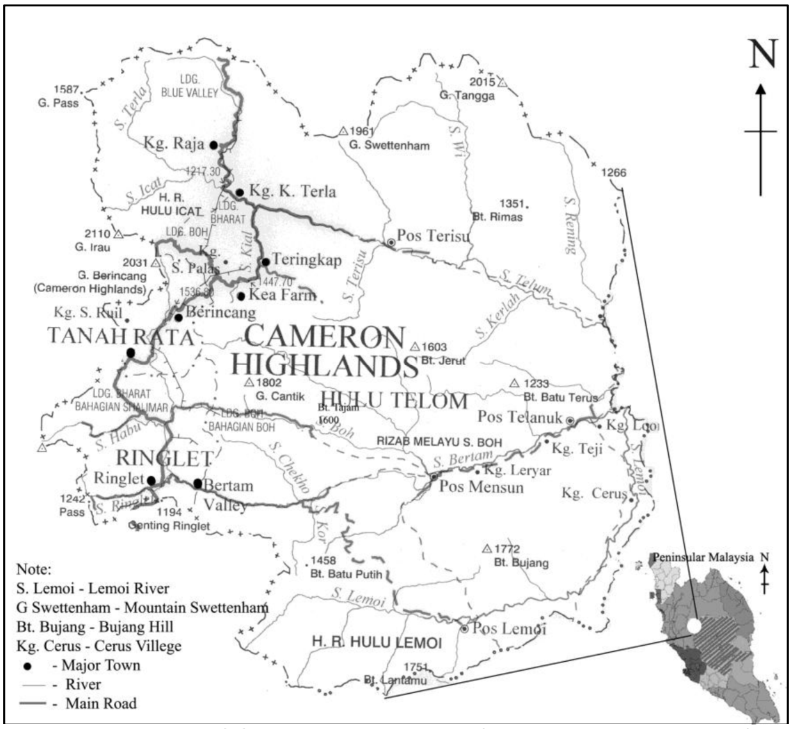

Figure 1. Map of Cameron Highlands (source: JUPEM, 2008).

Cameron Highlands is known for the Lake Ringlet flood disaster of 2013. In October that year, flash flooding in the catchment of the Lake Ringlet reservoir, coupled with existing siltation resulted in a rapid rise in the water level of the reservoir. Authorities believed a controlled release of water was necessary. This resulted in the flooding of 100 houses as the water ripped through Bertam Valley which is situated downstream of the dam. Four people were killed (Davies, 2014). The release of water was implemented according to standard operation procedure, yet it still causes such calamity. Hill (2013) identified a number of contributing factors. These include a more rapid rise in water level than usual, owing to deforestation, increasingly intensive agricultural activities and in some cases poorly managed agricultural practices in the dam's catchment area. This is coupled with poor land use practices and the encroachment of urban development on the flood plain area downstream of the dam.

In year 2014, Cameron Highlands had again experienced a deadly flooding, just over a year after four people died in floods in the same region (Davies, 2014). Three people died and five were injured after flash floods and mudslides swept through the area after a period of heavy rainfall. This recent heavy rainfall meant that water also had to be released from the Sultan Abu Bakar Dam. This time around things ran more smoothly compared to 2013 disaster. Residents were evacuated and it is not thought that the water release was the cause of any of the fatalities. However, the floods have damaged at least 20 houses in Ringlet new village and Bertam Valley and forced around 150 people to evacuate their homes in Tanah Rata, the main town in the highlands. Since then, minor landslides and flash floods occurred whenever continuous and sometimes heavy rainfalls in between year 2015 and 2016 (Loh, 2015; Avineshwaran, 2016).

The problem that Cameron Highlands is facing is due to the opening of land for construction purposes that had disrupted the hydrological cycle and altered the amount of energy absorbed by the land area which in turn increased the surface temperature and local air temperature. Barrow et al. (2005) stated that poor planning control will lead to speculative building, excessive farming, tourism-related pollution, track and forest damage and littering. The threat of future landslides will be a fact in Cameron Highlands if lacks of stringent measures are drawn upon control of opening up of farm land and uncontrolled development.

Hence, well-defined climate hazard indicators could assist decision-makers to modify the operation policies based on future climate (Tayebiyan et al., 2014) e.g. a local plan for development. The local plan provides direction to future growth and identifies some of the environmental constraints to development. Decision-making in conservation and natural resource management is substantial. Similarly, Nikolova and Gikov (2013) assessed vulnerability to climate hazards at municipality level in Bulgaria.

2 METHODOLOGY

This study focused on identifying the climate change vulnerable domains and indicators for Cameron Highlands based on drivers–pressure–state–impacts–response (DPSIR) framework. This study adopted a qualitative approach in order to develop the climate hazards decision support system. Apart from literature review, local community opinion survey and expertise interview were the main research activities. The questionnaire was designed in two main parts: Part A will obtain information on the demographic profile of respondents, whilst Part B will collect information pertaining to the respondents' perception on the climate hazard indicators for Cameron Highlands. The questionnaire that was set for this research consisted of "close-ended" questions. The close-ended questions were in the form of multiple choice answers to give a selection. The opinion survey was conducted in April, May and June 2016 in major townships, Cameron Highlands namely Tanah Rata, Brinchang, Ringlet, Tringkap and Bertam Valley.

Questionnaires were distributed to 85 individuals from vulnerable populations comprising local authorities, local farmers, hotel operators and NGOs. The number of responses to be collected was determined by the study of UCLA (2016), who suggested that five to 12 people per group are acceptable. However, Morgan (1996) may accept smaller or slightly larger groups. According to the situation in Cameron Highlands, different focus groups were conducted in different townships on similar types of people. The analysis for this study was computed using Statistical Package for Social Science (SPSS). The reliability test was run on survey results to measure the overall consistency. The statistical index used is referred to as Cronbach's alpha. Cronbach's alpha ranges from 0 to 1.00, with values close to 1.00 indicating high consistency. A reliability coefficient of 0.70 or higher is considered "acceptable" in most literature (Cronbach, 1951; Bland & Altman, 1997; DeVellis, 2003; Nunnally & Bernstien, 1994). Principal Component Analysis (PCA) was applied to extract the climate hazard indicators for Cameron Highlands. Hair et al. (1998) recommended a sample size of 85 respondents and factor loading of 0.60 is considered significant.

The climate hazard decision support system was constructed based on three activities. Firstly, selecting indicators based on the DPSIR framework by adopting PCA outcomes. Secondly, 25 indicators were grouped into 13 sub-components (domains) which were population, waste, land use, flood disaster, developments/investment opportunities, climate change indicators, health and sanitation, soil quality, disasters/mass movements, socioeconomic, environmental quality, private and public sectors and individuals; each of which formed a sub-component. Indicators that were extracted with loadings of similar subspaces were categorised into the sub-components with similar characteristics. Each indicator was then given weightage based on expertise input to form a composite index. The pre-defined indicators were given a weightage and rating by 11 experts from different institutions i.e. Universiti Kebangsaan Malaysia (UKM), Universiti Malaya (UM), Universiti Putra Malaysia (UPM), Universiti Sains Malaysia (USM) and Universiti Teknologi Petronas (UTP). Based on this method, weightage was given to show the applicability of the indicators. Experts may add or remove desired indicators. After the experts' adjustment, several indicators were omitted and some indicators were reworded and simplified.

Figure 2 shows the pyramid model in selecting indicators with the largest component on the bottom and narrowing up. The first tier of the pyramid model comprises a whole set of indicators suggested by the local community. After screening and conditional filtering, the numbers of indicators are narrowing up along the pyramid, leaving the final outcomes to be only 25 indicators.

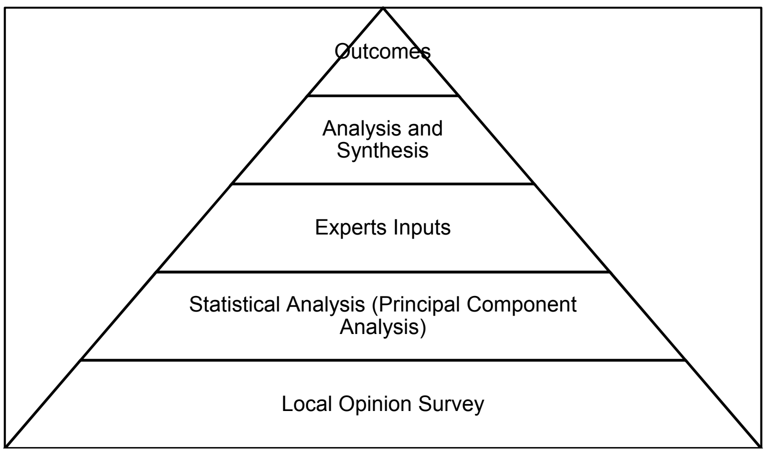

Figure 2. Pyramid model in selecting indicators

3 RESULTS

This study identified the climate change vulnerable domains (sub-components) and indicators for Cameron Highlands based upon the DPSIR framework as shown in Table 1. Within the context of DPSIR framework, the task of decision makers is to analyse the territorial system and assessing the acting drivers, their pressures, the consequences on state variables and their ultimate impact. The reliability test based on Cronbach's alpha was computed in SPSS and obtained an overall value of 0.952 (where $\alpha > 0.70$). It indicated a high level of internal consistency of the questionnaire. This finding shows that the responses from the local community is reliable and contains a high level of internal consistency. Thus, the opinion survey is valid for further analysis and synthesis.

Table 1. Proposed climate hazard indicators for Cameron Highlands of the DPSIR framework.

Components	Sub-components	Indicator description	Unit
Driving forces	Population	• Changes in population	%
	Waste	• Individual waste generation	%
	Land Use	• Land use percentage for recreational	%
		• Land use percentage for transportation	%
		• Land use percentage for agriculture	%
		• Land use percentage for residential	%
		• Land use percentage for commercial	%
Pressures	Flood Disaster	• Total populations affected by flood per year	No.
		• Total loss of properties	RM (million)
	Developments/ Investment Opportunities	• Gross domestic product in primary sector	%
		• Gross domestic product in secondary sector	%
		• Gross domestic product in tertiary sector	%
States	Climate Change Indicators	• Daily maximum rainfall intensity	mm/yr
		• Annual minimum temperature	°C
		• Annual maximum temperature	°C
	Health and Sanitation	• Number of health facilities (hospital/clinic)	No.
		• Drinking water supply by PAIP	m^3
	Soil Quality	• Sediment deposition rate in Ringlet reservoir per year	kg/yr
Impacts	Disasters/Mass Movements	• Number of floods event	No.
		• Cost of repairing landslide-prone slopes	RM (million)
	Socioeconomic	• Number of touristsvisit Cameron Highlands	No.
	Environmental quality	• Water quality index	Q-Value
Responses	Private and Public Sectors	• Law enforcement performance	%
		• Number of trees replanting	No.
	Individuals	• Recycling rate	metric ton

4 DISCUSSION

The driving forces are represented by natural and social processes which can lead to environmental problems, e.g. energy, agriculture, industry and waste management. Examples are the human demands for agricultural land, energy, industry, transport and housing. The pressure indicators are outcomes of the driving forces, which influence the current environmental state. A common expression of this is the use of resources (land, water, minerals, fuels, etc.): representing an input for a variety of natural processes and leads to the changes of the environmental condition. State indicators describe physical, chemical or biological phenomena in the given reference area. They may describe the land uses or their current condition (forest health). Impact indicators refer to the consequence of an environment state change. The result of an impact, such as air pollution, is followed by many effects (global warming, loss of biodiversity) at various temporal and spatial scales (extinction of some animal species). Impact may be expressed in terms of the level of environmental harm. The responses demonstrate the efforts by society (e.g. politicians, decision makers) to solve the problems identified by the assessed impacts, e.g. policy measure or planning actions.

Principal component analysis (PCA) was run separately on the base of DPSIR framework. It is a causal framework for describing the interactions between society and the environment. Appropriate SPSS outputs were interpreted. For each component of the model, two to three components were extracted and contained a certain percentage of the variation from the original variables, respectively. Variables loaded in the same component means they have interrelationship for each other. A smaller number of uncorrelated variables that are easier to interpret and analyse can be formed.

Local communities believed that population, waste and land uses belong to the driver category. Cameron Highlands has an average annual population growth rate of 2.75% for the period 2000–2010 (DRTCH, 2015). This rapid population growth in Cameron Highlands has put pressure on the demand of land for development as well as additional requirements for the basic amenities. This in turn impacts on the environmental quality in Cameron Highlands. Population growth causes environmental degradation (Ray & Ray, 2011). The growing population leads to increasing amount of solid waste and this increase poses serious threats to the environment including the underground water (Dahiya, 2015). Apart from agricultural organic and physical wastes, fertilisers which cause biological contamination and chemical contamination from pesticides are also common. In addition to climate and population changes, changes in land use patterns can have alterations in surface features with different impacts on surface fluxes of radiation, heat, moisture and momentum (Betts, 2005). Development control and land use management are necessary to maintain the quality of the environment as well as to prevent and minimise the impact of disasters.

Flood disaster and development/investment opportunities are included in the pressures category. The major risk disasters in Cameron Highlands are landslides and flash floods. These are closely related to topography, geology and climate effects, and changes in land use associated with development activities. Flash floods tragedy in Bertam Valley on 21 November 2014 which resulted in the loss of lives and properties showed that Cameron Highlands is experiencing extreme environmental exploitation and degradation (Baharuddin, 2014). The improper practice of agricultural activities has led to shallower riverbank due to sediments. This in turn led to more frequent flooding in the area. Cameron Highlands depends on two main economies which are agriculture and tourism. These two sectors are profitable and because of that, rapid and insensitive development is widespread in the highlands.

Climate change indicators such as health,sanitation, and soil quality are identified as state. The principle parameters of climate change are temperature and precipitation which can significantly affect hydrological cycle as a result of climate change. The observed mean temperature over the past 30 years has revealed significant changes. Climate change is not only characterized by the mean values, but also by the frequency of occurrence of extreme events and by their intensity (Tomozeiu et al., 2002). Tayebitan et al. (2014) found that the temperature will rise around 0.3 to 0.8 °C at the Ringlet reservoir and this was validated based on observation data obtained from Malaysia Meteorological Department (2016). Trends in extremes of maximum and minimum temperature were derived from observed station data for the period 1984 to 2015. The lowest temperature at Cameron Highlands was recorded to be 14.8 °C and highest temperature recorded was 23.4 °C. Based on Tan and Loh (2017), the maximum, minimum and mean temperatures are projected to rise 3.8°, 1.8° and 2.8 °C, respectively in 100 years' time.

Disasters/mass movements, socioeconomic, environmental quality are considered as impacts. Clearing of forest will have a significant impact which is increased flow rate of the top surface (run-off peak flows) that causes flash floods during continuous rainfalls. Cameron Highlands' locals were threatened by two major mud flood events that happened near the end of year 2013 and 2014. Both tragedies had been largely attributed to illegal land clearing. The amount of sediment and waste must be minimized to prevent further soil erosion, sedimentation and flash floods. Tourists have been staying away from Cameron Highlands even though the incidents happened in the agricultural and the local housing areas which are located far away from the tourist areas. Year 2014 recorded the lowest number of tourists accounting for almost 140,000 people only due to the natural disasters i.e. floods and landslides that happened last year (DRTCH, 2015). Mass tourism has contributed to an improvement in the employment opportunities and the demand for food and domestic goods. However, it also raises side effects if it is not controlled, such as the increasing amount of traffic on the road, increasing risk of irresponsible use of resources and damage to the natural environment which had already exceeded its carrying capacity. Same goes to the water quality. The water quality of rivers in Cameron Highlands has deteriorated significantly due to land clearing for agriculture, excessive usage of pesticides and fertilisers as well as construction activities in rapidly developing urban areas (Eisakhani et al., 2011).

Based on the predictions, appropriate management responses from private and public sectors and individuals can be implemented. The government has to thoroughly relook at the local plan for Cameron Highlands to ensure the highlands' sustainability is not affected in the long run (The Sun, 2015). The government has to bear an estimated RM2.2 billion for Cameron Highlands' rehabilitation program due to the actions of some irresponsible quarters (Kannan, 2016). Deepening rivers to mitigate flood will only serve as a short-term measure if forest clearing at the upstream of rivers continues (Srinivasan, 2014). Non-governmental organisations can carry out more awareness campaigns such as tree-planting and discourage rubbish littering by engaging the local to maintain Cameron Highlands. Local community established a partnership with NGOs to raise awareness on development and environmental issues in the highlands as water catchments (WWF, 2005).

The PCA identifies patterns in the whole set of data. The higher the component loadings, the more important that variable is to the component. Combinations of positive and negative loadings are interpreted as "mixed", such a way as negative correlation. As one variable increases/positive, the other variable decreases/negative, and vice versa. Partial variables were extracted from PCA and weightage were given by expert after that, finishing with minor adjustments that suit the Cameron Highlands' condition. The whole set of parameters were narrowed down as climate change indicators are too general . In the study, the climate hazards were defined as floods and mudslides which matched the situations in Cameron Highlands . The pre-defined indicators are classified under suitable domains. For instance, new sub-components had been added namely socioeconomic and environmental qualities . The confusing existing terms used for the pre-defined indicators were added with descriptions. Several terms had been changed and explained . After screening and conditional filtering, the proposed climate hazard indicators for Cameron Highlands of the DPSIR framework came into Table 1.

5 CONCLUSIONS

Overall, the changing climate is threatening the socio-economic welfare of farmers, the environment, ecology and sustainable agriculture in Cameron Highlands. The communities in the area seem to be struggling to cope with such changes. All of these changes have negatively affected the two main industries in the highlands which are agriculture and tourism. A decision support system needs to be included as an integral part in decision-making for the future local plan. The climate hazards indicators should consider 13 key domains, namely: populations, waste, land use, flood disaster, development/investment opportunities, climate change indicators, health and sanitation, soil quality, disasters/mass movements, socio-economic, environmental quality, private and public sectors and individuals.

ACKNOWLEDGEMENTS

We would like to thank the UTAR Education foundation for providing research funding – IPSR/RMC/UTARRF/2015-C2/T01. We also appreciate the cooperation and efforts of all authors in producing the Proceedings. This will be a great congress following the tradition of our sponsoring organizations.

REFERENCES

Al-Zaquan, A. H. (2014). Record Numbers Evacuated in Malaysia's Worst Floods in Decades. Investing.com. Retrieved 12 January 2017 from http://www.investing.com/news/world-news/record-numbers-evacuated-in-malaysia's-worst-floods-in-decades-321473.

Association of Southeast Asian Nations (ASEAN) (2015). Malaysia: Flood Situation Update No.1. Retrieved 12 January 2017 from http://reliefweb.int/sites/reliefweb.int/files/resources/SituationUpdate_1_AHA_MAL_FL2015.pdf. [Accessed: 20 December 2016]

Avineshwaran, T. (2016). Minor Landslide on Cameron-Tanah Rata Road. The Star Online. Retrieved 19 January 2017 from http://www.thestar.com.my/news/nation/2016/12/25/landslide-on-cameron-tanah-rata-road/

Azlee, A. (2015). Worst Floods in Kelantan, Confirms NSC. The Malay Mail Online. Retrieved 12 January 2017 from http://www.themalaymailonline.com/malaysia/article/worst-floods-in-kelantan-confirms-nsc

Baharuddin, A. (2014). Lessons from Cameron Highlands. The Star Online. Retrieved 20 January 2017 from http://www.thestar.com.my/opinion/columnists/ikim-views/2014/12/02/lessons-from-cameron-highlands/

Barrow, C.J., Clifton, J., Chan, N.W. & Tan, Y.L. (2005). Sustainable Development in the Cameron Highlands, Malaysia. *Malaysian Journal of Environmental Management,* 6, 41 – 57.

Betts, R.A. (2005). Integrated Approaches to Climate–Crop Modelling: Needs and Challenges. *Philosophical Transactions of the Royal Society B Biological Sciences*, 360, 2049 – 2065.

Bland, J. & Altman, D. (1997). *Statistics Notes,* Cronbach's Alpha. BMJ, 572.

Brevik, E.C. (2013). Climate Change, Soils, and Human Health. *In Soils and Human Health*. CRC Press: Boca Raton, FL, USA, 15, 7-12.

Chan, N.W. (2002). Floods Hazards and Disasters in Malaysia: Causes, Impacts and Solutions With Respect to River Floods. *Rivers: Towards Sustainable Development.* Universiti Sains Malaysia Publisher, Penang, 114-127.

Clarkson, J.D. (1968). *The Cultural Ecology of a Chinese Village: Cameron Highlands, Malaysia,* (Research Paper no. 114). Chicago: Department of Geography, University of Chicago.

Cronbach, L.F. (1951). Coefficient Alpha and the Internal Structure of Tests. *Psychometrika,* 16, 297 – 334.

Dahiya, R. (2015). Projections for the Population Growth and Its Impact on Solid Waste Generation of a Medium Sized North Indian City. *International Journal of Technical Research and Application,* 3(6), 57 – 61.

Davies, R. (2014).Three Dead after More Floods in Cameron Highlands, Malaysia. Flood List. Retrieved 12 January 2017 from http://floodlist.com/asia/3-dead-floods-cameron-highlands

Department of Irrigation and Drainage Cameron Highlands, (JPS). (2012). Profil Daerah jps@komuniti. Jun 2012.

Department of Survey and Mapping Malaysia, (JUPEM). (2002). *Map of Pahang State,* Scale 1:250,000. Kuantan.

DeVellis, R. (2003). *Scale Development: Theory and Applications.* Thousand Oaks, CA: Sage.

Eisakhani, M., Pauzi, A., Karim, O. & Malakahmad, A. (2011). Investigation and Management of Water Pollution Sources in Cameron Highlands, Malaysia. *WIT Transactions on Ecology and the Environment,* 148, 231 – 241.

Environmental Protection Agency, (EPA). (2017). Climate Impacts on Human Health. Retrieved 20 January 2017 from https://www.epa.gov/climate-impacts/climate-impacts-human-health.

Fortuin, R. (2006). Soil Erosion in Cameron Highlands, an Erosion Rate Study of a Highland Area. *Saxion University Deventer.*

Hair, J. F., Tatham, R.L., Anderson, R.E. & Black, W. (1998). *Multivariate Data Analysis.* (Fifth Ed.) Prentice-Hall: London.

Hill, E. (2013). What Went Wrong at Lake Ringlet? Flood List. Retrieved 12 January 2017 from http://floodlist.com/asia/floods-lake-ringlet-Malaysia.

Kannan, H. K. (2016). Saving Cameron Highlands: RM2.2 Billion Needed for Rehabilitation. New Straits Times. Retrieved 22 January 2017 from http://www.nst.com.my/news/2016/04/140168/saving-cameron-highlands-rm22-billion-needed-rehabilitation.

Khor, M. (2015. Lessons from the Great Floods. The Star Online. Retrieved 12 January 2017 from http://www.thestar.com.my/Opinion/Columnists/Global-Trends/Profile/Articles/2015/01/19/Lessons-from-the-great-floods/

Loh, I. (2015). Small Landslide Causes Cameron Highlands Traffic Jam. The Star Online. Retrieved 19 January 2017 from http://www.thestar.com.my/news/nation/2015/11/09/cameron-highlands-landslide/

Malaysian Meteorological Department, (MetMalaysia). (2016). *Temperature and Rainfall Observation data 1981-2016 Kuala Lumpur.*

Matori, A.N., Basith, A. & Harahap, I.S.H. (2011). Study of Regional Monsoonal Effects on Landslide Hazard Zonation in Cameron Highlands, Malaysia. *Arabian Journal of Geosciences,* 5, 1069 – 1084.

Morgan, D.L. (1996). Focus Groups. *Annual Review of Sociology,* 22, 129-52.

Nikolova, M. & Gikov, A. (2013). Assessment of Vulnerability to Climate Hazards in Municipality of Lom, Bulgaria. *International Conference "Natural Hazards – Links between Science and Practice".*

Nunnally, J.C. & Bernstein, I.H. (1994). *Psychometric Theory 3.* New York: McGraw-Hill, INC.

Ray, S. & Ray, I.A. 2011. Impact of Population Growth on Environmental Degradation: Case of India. *Journal of Economics and Sustainable Development,* 2(8), 72 – 77.

Regional Environmental Awareness Cameron Highland. (REACH). (2015). *The Blueprint of Cameron Highlands 2030 (Replacement) / Draf Rancangan Tempatan Daerah Cameron Highlands 2030, (Penggantian),* Cameron Highlands District Council, Pahang Town and Country Planning Department, Federal Department of Town and Country Planning Peninsular Malaysia.

Srinivasan, S. (2014). Call for Immediate Moratorium on Forest Clearing in Cameron Highlands. *WWF – Malaysia.* Retrieved 22 January 2017 from http://www.wwf.org.my/?18305/Call-for-Immediate-Moratorium-on-Forest-Clearing-in-Cameron-Highlands

Tan, K.W. & Loh, P.N. (2017). Climate Change Assessment on Rainfall and Temperature in Cameron Highlands, Malaysia Using Regional Climate Downscaling Method. *Carpathian Journal of Earth and Environmental Sciences,* 12(2), 413-421.

Tayebiyan, A., Ali, T.A.M., Ghazali, A.H. & Malek, M.A. (2014). Future Consequences of Global Warming on Temperature and Precipitation at Ringlet Reservoir, Malaysia. *International Conference on Advances in Environment, Agriculture & Medical Sciences (ICAEAM-14).* November 16-17, 2014. Kuala Lumpur (Malaysia).

Tayebiyan, A., Ali, T.A.M., Ghazali, A.H. & Malek, M.A. (2014). Future Consequences of Global Warming on Temperature and Precipitation at Ringlet Reservoir, Malaysia. *International Conference on Advances in Environment, Agriculture & Medical Science (ICAEAM`14).* November 16-17, 2014 Kuala Lumpur.

The Sun. (2015). Government to Relook Cameron Highlands Local Plan, Says Muhyiddin. The Sun Daily. Retrieved 22 January 2017 from http://www.thesundaily.my/news/1307975

Tomozeiu, R., Pavan, V. & Cacciamani, C. (2002). *Changes in Extreme Minimum and Maximum Temperature in Emilia-Romagna as Derived from Observed Data during 1960 – 2000 Period,* Servizio Meteorological Regionale – ARPA.

UCLA Center for Health Policy Research (2016). Section 2: Focus Groups. Retrieved 12 January 2017 from http://healthpolicy.ucla.edu/programs/health-data/trainings/Documents/tw_cba21.pdf

World Wide Fund for Nature, WWF-Malaysia (2005). *Community and Non-governmental Organisation (NGO) Partnership in Highland Catchment Management in Malaysia.*

METHODOLOGY FOR FLOOD RISK MAP DEVELOPMENT. APPLICATION TO VU GIA THU BON CATCHMENT, VIETNAM

NGOC DUONG VO[1] & PHILIPPE GOURBESVILLE[2]

[1] Faculty of Water Resource Engineering, University of Science and Technology, the University of Da Nang, Viet Nam.
vo.ngoc.duong@dut.udn.vn
[1,2] Innovative City lab URE 005, Polytech'Nice Sophia, Nice Sophia Antipolis University, France
philippe.gourbesville@unice.fr

ABSTRACT

Vietnam is located in the region of the Southeast Asia monsoon. Most of the population work in agriculture and inhabitants essentially concentrate at the coastal plain. Vietnam is one of the countries which are most heavily affected by the consequences of climate change. For these reasons, predicting the potential damages due to extreme flood events, especially under climate change impact is mighty necessary for the coastal area in this country. This paper present the potential risk maps in Vu Gia Thu Bon catchment, a largest river system in Viet Nam central. These flood risk maps were built with tree GCMs under A2 scenario in the end of 21st century by overlapping the flood hazard and land use map in 30m resolution. The result is hoped to provide adequate scientific evidences to help the local authority to make suitable strategies for adapting with the variation of climate in the future.

Keywords: Flood modeling; flood risk maps; climate change; Vu Gia Thu Bon catchment.

1 INTRODUCTION

The natural environment is obviously the human living space. All components of natural environment such as climate, weather, and natural resource, have an influence on human survival and economic activity (Johnson et al., 1997). However, besides positive effects, the natural environment includes natural hazards, which frequently bring undesirable impacts to human society. In the last decade (2003-2013), there were annually 383 natural disaster events globally, which killed a significant number of people (98,923) and made more than 205.13 million victims. Like other indicators, natural disaster claimed 153.24 billion US$ from worldwide economy (Guha-sapir et al., 2013). In the context of climate change, natural disasters are predicted to occur more frequently and with more complexity. The consequence relating to natural disaster is expected to be more severe in the future. Unfortunately, the occurrence of natural factor is inevitable. It is requested that the people has to look for the way to confront nature. Prevention is seen as the best method for mitigating the impact of natural disaster to human beings.

Vietnam is located in the region of the south East Asia monsoon. Most of the population work in agriculture and inhabitants essentially concentrate at the coastal plain. Vietnam is among the countries which are most heavily affected by the consequences of climate change. According to the assessment of Vietnam government, in the late 21st century, Vietnam's yearly mean temperature will increase 2-3°C, the total yearly and seasonal rainfall will increase while the rainfall in dry seasons will decrease, the sea level could rise 0.75 to 1m compared to the 1980-1999 period. About 10-12% of Vietnam's population are directly impacted and country could lose around 10% of GDP (Nguyen, 2011). These challenges urge Vietnam to have a plan and suitable policies and measures to improve public awareness, as well as capacity to respond to climate change.

This study is realized to provide generally the impact of natural disaster towards the coastal area of central Vietnam, where has sustained the natural hazard catastrophic consequences. Based on assessment of variation in hydrological regime of Vo et al. (2015) and of flood propagation of Vo & Gourbesville (2015), the study's result is hoped to provide valuable input for decision makers about the flood risk at Vu Gia Thu Bon catchment in the end of 21st century to establish better adaptation strategies with climate change.

2 METHODOLOGY

According to the definition of the EU Floods Directive - European Commission (European Commission, 2007), flood risk is the combination of the probability of a flood event and of the potential adverse consequences for human health, the environment, cultural heritage and economic activity associated with a flood event. The quality of flood risk assessments depends deeply on the accurate estimation of the flood hazard and of the potential impact on human activities (Alfieri et al., 2015). In this study, the flood hazard is simulated via a 1D/2D coupling model (Mike Flood from DHI). This hydraulic model has a high performance to demonstrate, spatially, the impact of future Vu Gia Thu Bon river flooding with the catchment (Vo & Gourbesville, 2015). The future flow is obtained from the study of Vo et al. (2015) which used a deterministic hydrological model - MIKE SHE – to estimate the impact of climate change over 10,350 km2 of Vu Gia Thu Bon river system. Flood risk map is constructed by overlaying the flood hazard map with land use map. This work, realized in the resolution of 30m, is hoped to provide overall view about the serious consequences of climate change for local population and authority.

3 STUDY AREA

The Vu Gia - Thu Bon river system, which originates from the eastern side of the Truong Son mountain range and drains to the Vietnamese East Sea near the cities of Da Nang and Hoi An. It is the biggest coastal river system in the central region of Vietnam. There are two main rivers in this system, the Vu Gia and the Thu Bon. The topography over this region is complex with the relatively narrow mountainous area on the upstream and the flat coastal zone at the downstream. Located at a tropical monsoon climate region with influence of the ocean to the east, rain and storm in this region behave complicatedly. The average annual rainfall of this area is from 2000mm to 4000mm with 65% to 80% annual rainfall from September to December. This region is also attacked by two to four typhoons annually (RETA 6470, 2011; TO, 2005). Consequently, inundation related to typhoon is very serious. On the contrary, drought frequently occurs in the remaining months. Despite these complicated climate conditions, the hydrological infrastructure in the basin is still underdeveloped. The density of meteorological and hydrological stations is sparse. The area is 10350 km2 and there are about 15 rainfall stations (Figure 1). The fact of lacking of data and poor data quality causes many difficulties in managing natural phenomenon.

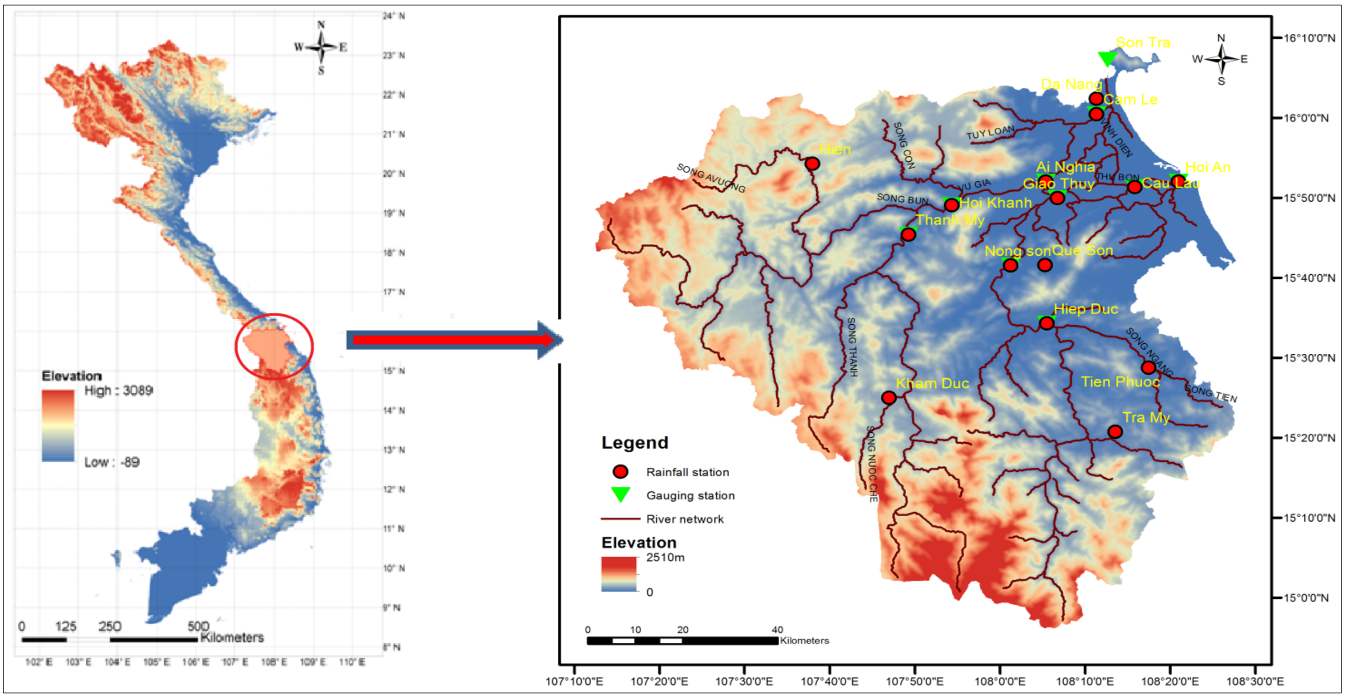

Figure 1. Vu Gia - Thu Bon catchment in central Vietnam, and hydro-meteorological network.

Due to the violence of climatological events, the fragile economic condition and the underdeveloped infrastructure, the natural disasters related to river flow deeply affect the socio-economy. The lost caused by flood and storm disaster annually in Quang Nam province is estimated with the average up to 6.26% of the GDP (Nguyen, 2011). According to the prediction of IPCC's scenario, under the impact of global warming, sea level increase, the change in hydrological cycle, flood and drought disaster, abnormal phenomena, e.g. phenomena El Nino and La Nina in Vu Gia Thu Bon basin will happen more frequently and more seriously. It makes the consequences of natural disasters to people, livelihood, social economic development becomes more severe. Vietnamese government assessed, in the late 21st century, the mean temperature of this region will increase from 2°C to 3°C, the total yearly and seasonal rainfall will increase while the rainfall in dry seasons will decrease, the sea level may rise 0.75 m to 1 m compared to that of 1980-1999 period. (Viet Nam Government, 2011). These challenges urge the local authority to have suitable policies and measures in order to improve both of public awareness and its capacity to respond to climate change.

4 RESULT AND DISCUSSION

4.1 Scale variability of inundation area

The result of Vo et al. (2015) presents that the stream flow would change significantly in the whole Vu Gia Thu Bon catchment. During rainy season, mean flow could be increased from 25% to 125% in comparison with the present time in all analyzed locations. The increase of flood flow demonstrated certainly implies the enlargement of flood plain. The difference between the future and today is shown via the change of water level at downstream and the change of inundation area. The comparison is realized on the simulated result of the extreme flood event in November 1999 and its projecting scenarios in 2099 corresponding with CCSM, ECHAM, MIROC scenarios. The second comparison is on the 100 year return period flood event in the future and present. The peak water level variation is expressed via the number at Table 2. Scale variability of inundation area under the impact of climate change at the downstream area of Vu Gia Thu Bon is explicitly shown in Figure 2 and the figures in Table 3, 4 demonstrate the serious increase of flood area at Vu Gia Thu Bon downstream region under the impact of flood flow increase due to global warming.

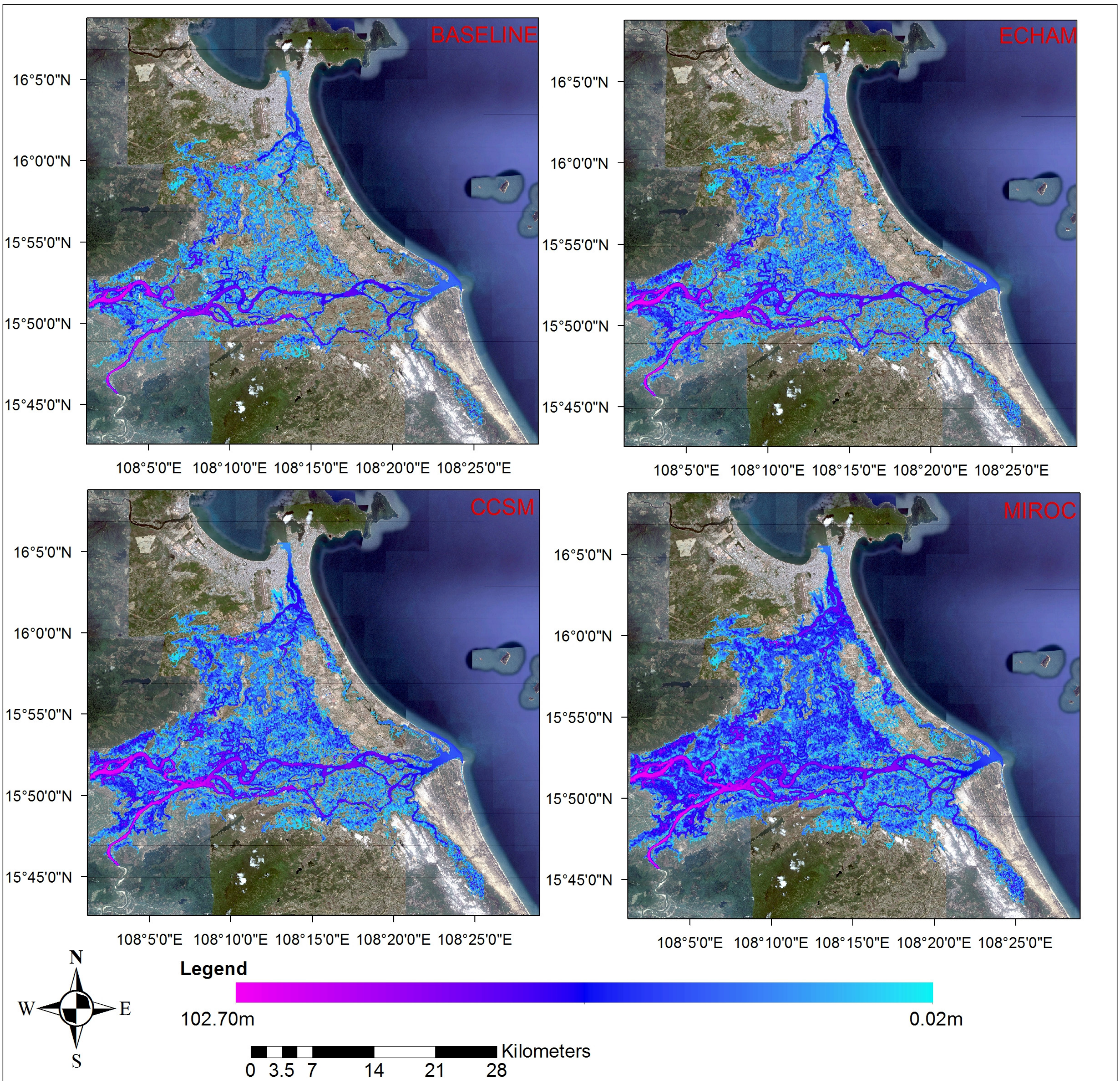

Figure 2 a. Scale variability of inundation area under the impact of climate change – Scenario of 1999 historical flood event and projected ones, 100 year return period event and corresponding projected ones).

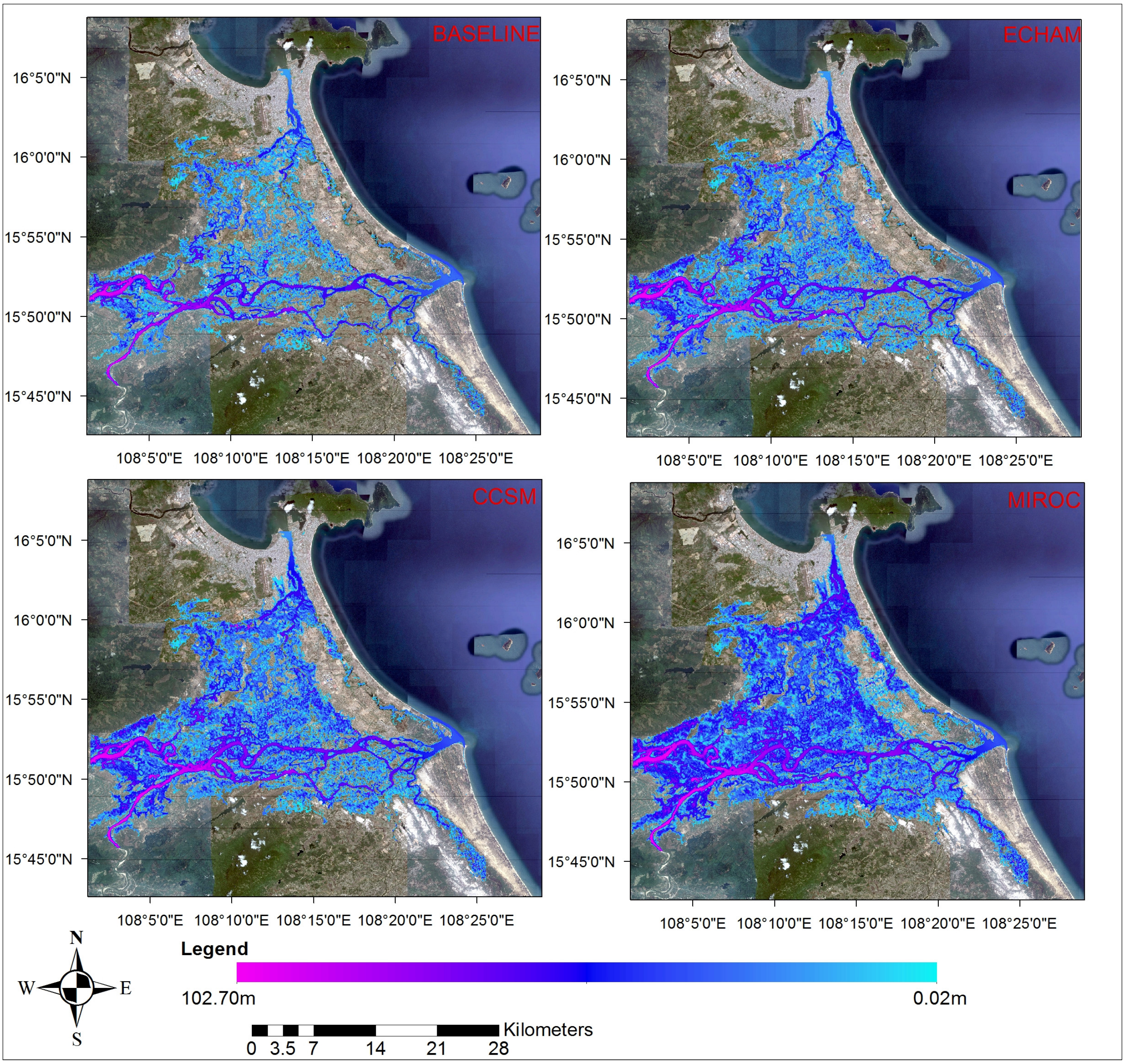

Figure 2 b. Scale variability of inundation area under the impact of climate change – Scenario of 100 year return period event and corresponding projected ones.

Table 2. Peak water level comparison between future and baseline scenario (m).

Station	**Historical flood event**				**100 year return period event**			
	1999	*ECHAM*	*CCSM*	*MIROC*	*Baseline*	*ECHAM*	*CCSM*	*MIROC*
Ai Nghia	11.773	12.94	13.61	14.616	12.364	13.187	14.014	14.95
Giao Thuy	10.967	12.433	13.326	14.935	11.945	12.957	13.983	15.188
Cau Lau	6.117	7.218	7.974	8.756	6.856	7.65	8.58	9.402

Table 3. Scale variability of inundation area due to climate scenario in the case of 1999 flood event base line scenario. (hectare).

Area (ha)	**< 0.5**	**0.5-1.0**	**1.0-2.0**	**2.0-4.0**	**4.0-8.0**	**>=8.0**	**total>0.5**
1999	4,124.43	3,911.13	5,910.75	6,534.45	2,548.80	31.86	18,936.99
CCSM	3,679.38	4,179.96	8,898.84	13,518.45	7,083.63	617.76	34,298.64
ECHAM	3,839.22	4,198.50	7,986.78	10,207.26	5,080.95	232.56	27,706.05
MIROC	2,846.25	3,190.41	7,161.84	17,264.70	15,932.43	2114.37	45,663.75

The maps and numbers describe the serious impact of climate change to this area. It is predicted to have an extremely increasing trend of flood disaster in this region. The increase trend of discharge in hydrological model leads to raise almost water level at the downstream. The future water level at several cases can be roughly over 3 m than the actual value (Table 2). Thus, it is not surprising when the inundation area in the end of 21st augments is great in comparison with current ones at Vu Gia Thu Bon catchment. Total inundation area (corresponding flood depth >=0.5m) is minimum, 46.31 % higher than 1999 flood event. Especially, the difference is really catastrophic with MIROC scenario when the future inundation area might be 141% higher than the 1999 flood event (Table 4). The increasing trend is similar with 100 year return period event (Figure 2), however, the variation is not so great with the real scenario (Table 3, 4). The maximum difference between future and present is MIROC. The flood area due to 100 year return period of MIROC just increases 56.72%.

Table 4. Scale variability of inundation area due to climate scenario in case of 100 year return periods (hectare).

Area (ha)	< 0.5	0.5-1.0	1.0-2.0	2.0-4.0	4.0-8.0	>=8.0	total>0.5
Baseline	3,884.85	4,381.2	8,808.3	11,853.36	5,977.44	405.81	31,426.11
CCSM	2,974.32	3,334.68	7,450.2	17,171.82	13,752.36	1,674.54	43,383.6
ECHAM	3,412.26	3,888	8,825.67	14,985.9	8,457.03	907.02	37,063.62
MIROC	2,535.84	2,937.15	6,560.82	16,661.34	20,034.36	3,057.3	49,250.97

4.2. Future flood risk increase

The water level considered here is higher than the flood depth of 0.5m. The uncertainty in the impact of climate change is also shown via different impacts of climate scenario. The results are described at Figure 3 for the risks of 1999 historical event and its projected scenarios. By looking at these figures, the largest damages are from MIROC scenario. The statistic demonstrates that if this MIROC climate scenario happens in future, this region will be devastated catastrophically.

Table 5. Potential risk area at Vu Gia Thu Bon against 0.5m flood depth of 1999 flood event and its corresponding future scenarios.

	Potential risk area (hectare)							
	Historical flood event				100 year return period event			
	1999	*CCSM*	*ECHAM*	*MIROC*	*Base line*	*CCSM*	*ECHAM*	*MIROC*
Cemetery	64.44	172.89	134.01	346.05	162.18	283.95	192.15	532.53
Industrial zone	2.88	3.6	3.24	74.7	3.33	25.11	4.14	106.56
Military	4.41	6.84	5.13	17.46	5.94	11.61	7.11	25.2
Other annual crops	3,725.0	5,877.3	5,113.8	7,106.6	5,468.4	6,861.1	6,179.2	7,401.2
Other perennial crops	0	0.09	0	0.27	0	0.27	0.18	0.45
Other rice fields	76.86	167.49	112.86	299.07	144.72	285.12	204.3	336.06
Other upland annual crops	180.63	408.24	327.69	595.35	394.38	527.22	436.86	665.73
Perennial cash crops	2.07	5.13	4.14	6.57	4.5	6.57	5.94	6.57
Planted production forest	105.39	205.38	165.24	269.46	192.15	257.49	221.31	292.14
Planted protection forest	76.23	122.13	98.91	244.35	112.5	174.87	123.12	298.08
Protection forest	40.32	122.4	72.9	169.11	111.51	162.9	137.61	184.41
Religion	0	0.09	0	0.18	0	0.18	0.09	0.18
Rural settlement	6,848.2	13,604.7	10,437.1	19,041.7	12,108.8	18,058.0	14,997.3	20,713.2
Special use water surface	66.6	103.5	88.74	129.24	94.77	122.49	108.54	132.84
Specialized rice field	4,425.5	8,766.6	7,070.0	11,269.6	8,110.1	10,809.4	9,444.2	12,033.5
Unused flat land	523.26	697.41	622.98	866.7	669.78	821.16	730.8	937.08
Unused mountain land	171.09	253.89	186.21	310.23	251.73	301.32	271.53	334.98
Urban settlement	663.57	1,472.0	1,089.1	2,300.67	1,323.7	2,114.9	1,623.3	2,526.1

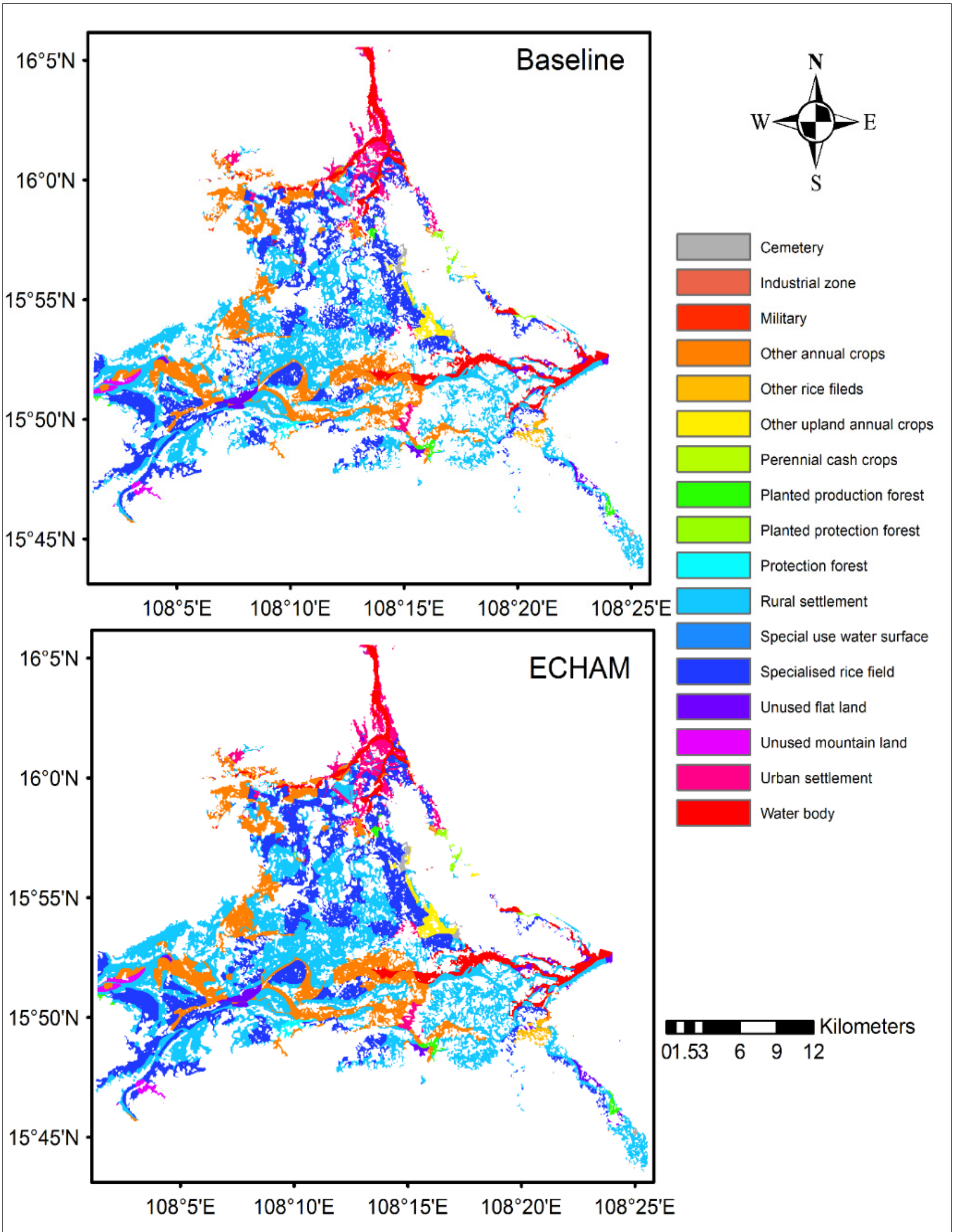

Figure 3a. Flood risk map for 1999 historical event and its corresponding future scenarios.

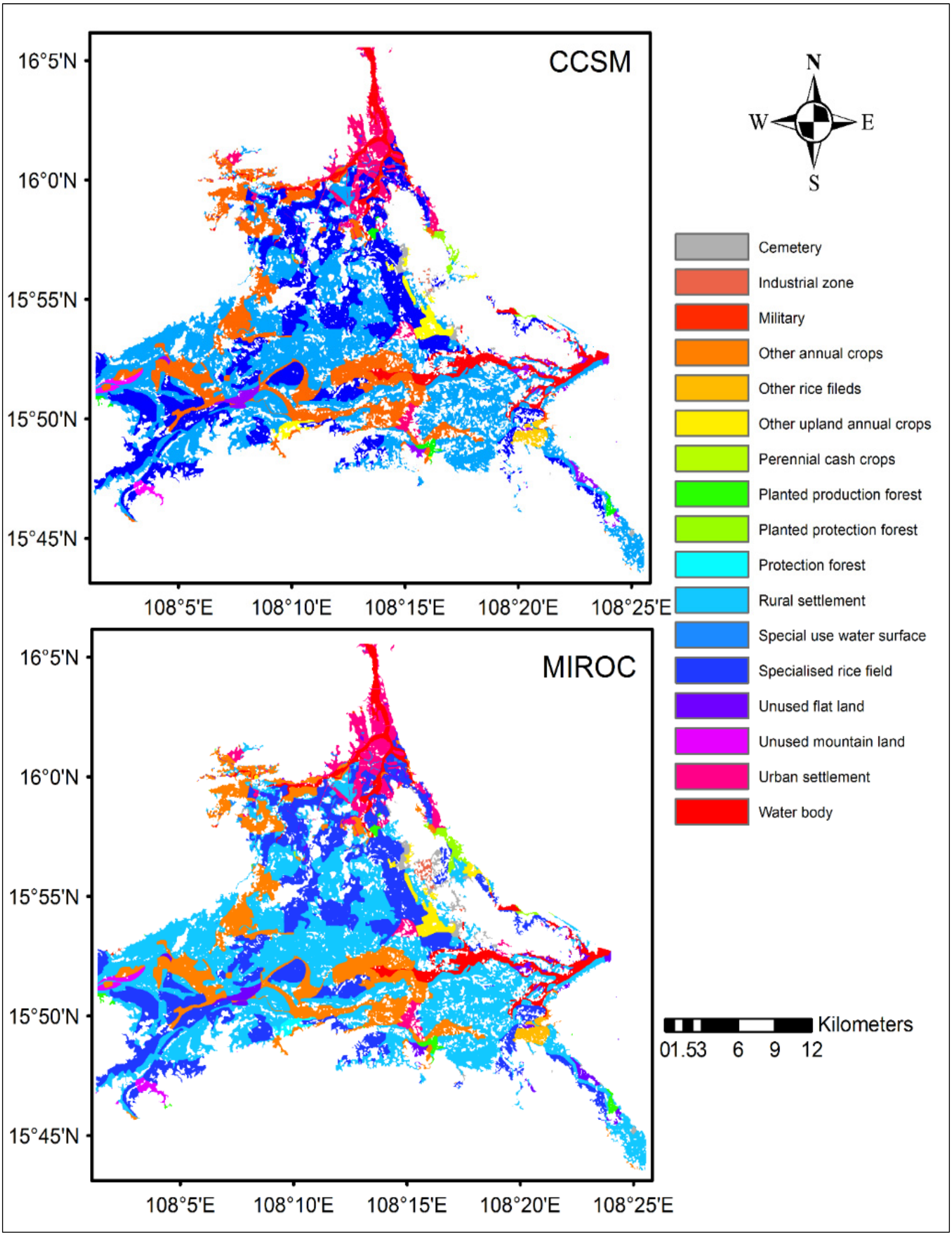

Figure 3b. Flood risk map for 1999 historical event and its corresponding future scenarios.

Moreover, the damages are concreted for each type of land use at the Figure 3 and by the numbers at Table 5. The considered area situates at the downstream, so there is no surprise when damages from flood disaster mostly concentrate on the domain of rural settlement, annual crops, and specialized rice field. In 1999, three of the above land use types occupy roughly 88% of total flood area. This rate is not changed in the case of 100 year return period flood event at present and future scenarios. In the biggest varied scenario, MIROC, inundated settlement area in the end of 21st century is predicted higher than three times in comparison with 1999 event. The increase of this kind of land use is around 12,193.51 hectare. With the remaining scenarios, the consequences for this domain are lower but the seriousness does not change.

5 CONCLUSIONS

The consequence of river flow change due to global warming is expected to significantly damage local socio economic development and people at Vu Gia Thu Bon Catchment in the end of this century. In the face of the context, this study is aiming to provide realistically scientific evidences about these impacts to the catchment, especially the scale variability of inundation area and potential risk of this catchment faced to the climate change. The variation of flood flow is utilized in hydraulic modelling to project the change of future inundation area. The methodology by combining distributed hydrological and hydraulic models is hoped to reduce the uncertainty and save the time to reflect, most accurately, the change in stream flow and flood area in Vu Gia Thu Bon catchment. The inundated area results are overlapped with land use map to demonstrate the flood potential risks of this river system.

Total inundation area is roughly 46.31 % higher than 1999 flood event. More seriously, the inundation area deeper than 2m could expand around 70% in comparison with present scenario. It might cause the inundation over catchment. It is sure that this flood hazard increase will put Vu Gia Thu Bon catchment downstream area to face huge catastrophes and unforeseen consequences. The risk maps demonstrate the serious consequences due to natural catastrophes towards agricultural productions, especially rice production and rural settlement in Vu Gia Thu Bon. Counting with flood level higher 0.5 m, rural settlement, annual crops, and specialized rice field are three domains which will be influenced greatly by the consequence of global warming. In the last years of 21st century, flood rural settlement area might be 19,041 hectare, increasing 178% versus 1999 flood event. This trend is similar to annual crops and specialized rice field, when their flood area are 7,106 hectare, 91% and 11269 hectare, 156% respectively. The above results are considered as a basis for local authorities to make strategies in order to mitigate the effect of climate change to this area and to help the population in Vu Gia Thu Bon Catchment to prevent actively and adapt better with natural disasters in the end of this century. It is also useful to water resource agencies, irrigated management, and agricultural departments to get an insight on this phenomenon. From that, they will reorganize the product scheme, harvest plan, as well as suitable structure of crop plans.

ACKNOWLEDGMENTS

Thanks to the Hydro meteorological Center in mid central Vietnam, the Central Vietnam Division of Water Resources Planning and Investigation, LUCCI project, P1-08 VIE project where provided the data for this study, National University of Singapore.

REFERENCES

Alfieri, L., Feyen, L., Dottori, F. & Bianchi, A. (2015). Ensemble Flood Risk Assessment in Europe under High End Climate Scenarios. *Global Environmental Change, 35, 199–212.*

European Commission. (2007). *Directive 2007/60/EC of the European Parliament and of the Council of 23 October 2007 on the Assessment and Management of Flood Risks*. The European Parliament and the Council of the European Union, Civil Protection and Disaster Management.

Guha-sapir, D., Hoyois, P. & Below, R. (2013). *Annual Disaster Statistical Review 2013 the numbers and Trends*, Centre for Research on the Epidemiology of Disasters (CRED) Institute of Health and Society (IRSS) Université catholique de Louvain – Brussels, Belgium.

Johnson, D. L., Ambrose, S. H., Bassett, T. J., Bowen, M. L., Crummey, D. E., Isaacson, J. S. & Winter-Nelson, A. E. (1997). Meanings of Environmental Terms. *Journal of Environmental Quality,* 26(3), 581–589.

Nguyen, B.Q. (2011). *Assessing Impacts of Climate Change on Disasters Related to Stream Flow (Flood and Drought) in Quang Nam, Viet Nam*, Sub-project 5, Project P1-08VIE. Institute of Geography, Vietnam Academy of Science and Technology.

RETA 6470. (2011). *Investment, Managing Water in Asia's River Basins: Charting Progress and Facilitating - The Vu Gia-Thu Bon Basin*, Department of Natural Resources and Environment, Quang Nam Province.

TO, T. N. (2005). *Strategic Plan for Integrated Water Resources Management of the Vu Gia Thu Bon Basin*, Organization. Economic and Social Commission for Asia and the Pacific, United Nations.

Viet Nam Government. (2011). *National Strategy on Climate Change*, Director-General: Vi Quang Dao.

Vo, N. D. & Gourbesville, P. (2015). Establishing the Flood Map for the Downstream of Vu Gia-Thu Bon Catchment – A Coastal Region of Viet Nam Central. Scale Variability of Inundation Area under the Impact of Climate Change. *In 36th IAHR World Congress* - The Hague, Netherlands.

Vo, N. D., Gourbesville, P., Vu, M. T., Raghavan, S. V. & Liong, S.-Y. (2015). A Deterministic Hydrological Approach to Estimate Climate Change Impact on River Flow: Vu Gia–Thu Bon Catchment, Vietnam. *Journal of Hydro-Environment Research.* 11, 59-74.

NUMERICAL SIMULATION OF FLOOD INUNDATION AND SEDIMENTATION CONSIDERING THE EFFECTS OF PADDY FIELDS

KENJI KAWAIKE[1], MASAKAZU HASHIMOTO[2] & HAJIME NAKAGAWA[3]

[1,2,3] Disaster Prevention Research Institute, Kyoto University, Kyoto, Japan,
e-mail kawaike.kenji.5n@kyoto-u.ac.jp

ABSTRACT

We numerically simulated the Kinu River flood inundation at Joso City in 2015. In the inundated areas, sedimentation in the paddy fields and their irrigation channels was a serious problem. In our simulation, we tried to reproduce the flood inundation flow and its attendant sedimentation in the study area. In order to consider the ridges and irrigation channels of the paddy fields, models of the vertical walls and one-dimensional network of the channels were incorporated in the two-dimensional inundation flow model. The maximum water level in the simulation agreed well with the measured value, and approximately 50 cm thick sedimentation deposits were observed on the overland and irrigation channels around the overflow and dike breach points, which might have caused severe damage to rice crops in the paddy fields and the drainage function of the irrigation channel.

Keywords: Flood inundation; sedimentation; paddy field; ridge; irrigation channel.

1 INTRODUCTION

On September 9–10, 2015, an overflow and river dike breach occurred at the 25.23 k and 21.0 k points, respectively, on the left-hand side of the Kinu River. This caused a flood inundation disaster and resulted in severe damage to Joso City of Ibaraki Prefecture, Japan.

We focused on the sedimentation with the inundation flow during this flood disaster. In our field survey, we found that large amounts of sediment were deposited on paddy fields, irrigation channels, and gutters near the overflow and dike breach points. Such sediment deposits led to severe direct damage of rice crops in the paddy fields and disorder of the drainage function of the channels. The Ministry of Land, Infrastructure, Transport, and Tourism (MLIT) of Japan reported that large amounts of sediment were removed from the channels after the inundation water was drained. The remaining sediment in the paddy fields was difficult to remove and became a serious problem for the farmers.

In this study, we numerically simulated the flood inundation in Joso City by considering sediment deposition as well as inundation flow. For the simulation methodology, we considered the effects of two structural factors of the paddy fields that occupied a large part of the inundated area: how the ridges separating each rice paddy delayed the propagation of inundation water as linear high mound structures, and how the irrigation channels facilitated the quick propagation of inundation water and sediment deposition.

2 OUTLINE OF THE SIMULATION MODEL

The colored area in Figure 1 shows the target area for the simulation: it contains Joso City, Shimotsuma City, and Tsukubamirai City in Ibaraki Prefecture, Japan. This area is situated between the Kinu River and Kokai River, and its topography is mostly flat. Houses are located on relatively high places along the two rivers, and most of the remaining area is used as paddy fields. The Hakkembori River runs through the middle part of the area from north to south, and a sluice gate and pumping station are located at its confluence with the Kinu River. The Kinu River channel's part from 31.8 k to 10.95 k (Mitsukaido water level observatory) was also included in the simulation area. We carried out two-dimensional simulations to reproduce the inundation water flow and sediment deposition during the disaster.

2.1 Inundation flow model

This study employed a two-dimensional inundation flow model with unstructured grids considering sediment deposition that we developed (Kawaike et al., 2002). The governing equations are given below:

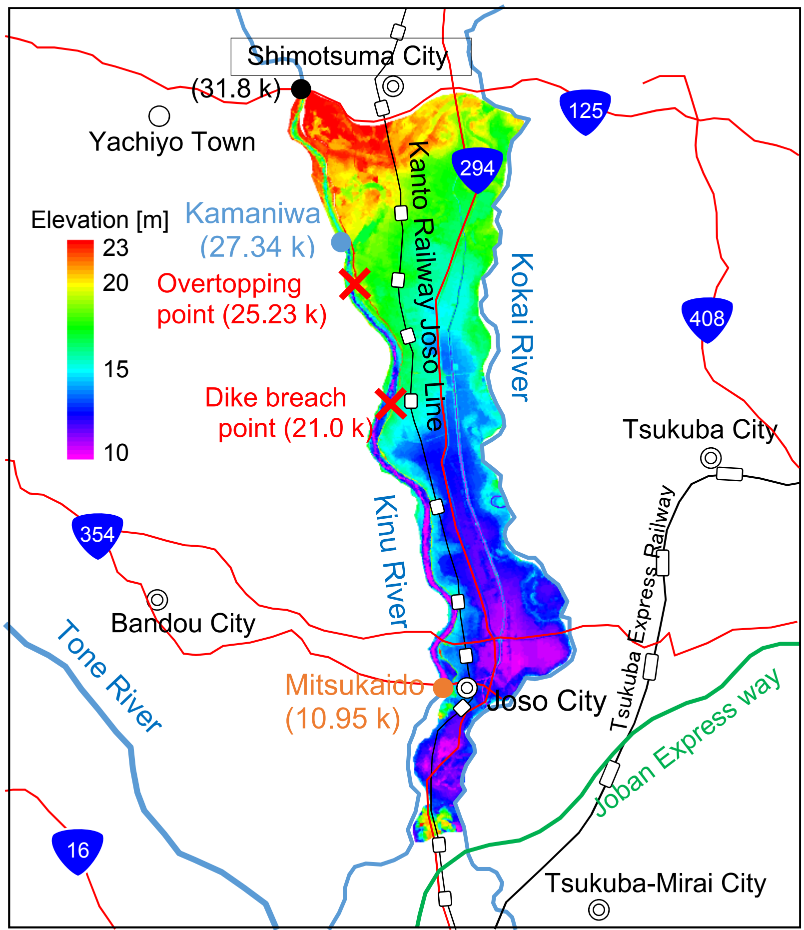

Figure 1. Study area.

$$\frac{\partial h}{\partial t}+\frac{\partial (uh)}{\partial x}+\frac{\partial (vh)}{\partial y}=r_e-q_g+i \quad [1]$$

$$\frac{\partial (uh)}{\partial t}+\frac{\partial (u^2h)}{\partial x}+\frac{\partial (uvh)}{\partial y}=-gh\frac{\partial (z_b+h)}{\partial x}-\frac{\tau_{bx}}{\rho_T} \quad [2]$$

$$\frac{\partial (vh)}{\partial t}+\frac{\partial (uvh)}{\partial x}+\frac{\partial (v^2h)}{\partial y}=-gh\frac{\partial (z_b+h)}{\partial y}-\frac{\tau_{by}}{\rho_T} \quad [3]$$

$$\frac{\partial (Ch)}{\partial t}+\frac{\partial (Cuh)}{\partial x}+\frac{\partial (Cvh)}{\partial y}=-q_gC+iC_* \quad [4]$$

$$\frac{\partial z_b}{\partial t}+i=0 \quad [5]$$

where h is the flow depth, u and v are the flow velocities in the x and y directions, respectively, r_e is the effective rainfall intensity, q_g is the interaction flow discharge per unit area between the ground surface and irrigation channel, z_b is the ground surface elevation, C is the volumetric sediment concentration, C_* is the volumetric sediment concentration deposited on the bottom, and g is the acceleration of gravity. τ_{bx} and τ_{by} are the bottom shear stresses in the x and y directions, respectively; they employ different equations depending on the sediment concentration (Nakagawa et al., 2003). The volumetric sediment concentration in the first term on the right-hand side of Eq. [4] is taken from the upstream side of the interaction flow. ρ_T is the mixture density of sediment and water and is expressed as $\rho_T = \sigma C + (1-C)\,\rho_m$, where σ is the sediment particle density and ρ_m is the fluid density. i is the erosion or deposition velocity of the sediment and is expressed as follows.

In the case of erosion:

$$i=\delta\frac{C_\infty-C}{C_*-C_\infty}\sqrt{u^2+v^2} \quad [6]$$

In the case of deposition:

$$i = \delta' \frac{C_\infty - C}{C_*} \sqrt{u^2 + v^2} \qquad [7]$$

Here, C_∞ is the equilibrium sediment concentration that yields neither erosion nor deposition. δ and δ' are the coefficients of the erosion and deposition velocity equations, respectively, where δ is fixed as 0.0007, and δ' is described in the section 4.1. For details of the model, refer to Kawaike et al. (2002).

2.2 Paddy field model

We considered two factors in the simulation model for the effect of the paddy field structures on the inundation flow: the ridges and irrigation channels.

2.2.1 Ridge model

The ridges were set as roads with higher elevation. We selected roads with an elevation high enough to be recognized as ridges dividing each paddy field in digital elevation map with 5 m resolution (hereinafter "5mDEM") issued by the Geospatial Information Authority of Japan. These roads were used as a grid border in the grid generation. We assumed a vertical wall along this grid border with Δh greater than the lower elevation of grids on both sides. Based on the field survey and 5mDEM, Δh was set to be uniformly 0.5 m. The flow discharge over the ridge was calculated according to the following overflow equations:

$$q = \mu_1 h_1 \sqrt{2gh_1} \qquad \text{if } h_2/h_1 \geq 2/3 \qquad [8]$$

$$q = \mu_2 h_1 \sqrt{2g(h_1 - h_2)} \qquad \text{if } h_2/h_1 < 2/3 \qquad [9]$$

where q is the discharge per unit length over the ridge. This was divided into the x and y directions and used as the flow fluxes (uh and vh) instead of the ones derived in Eqs. [2] and [3]. h_1 and h_2 are the higher and lower water levels extracted by the ridge elevation (the value of h_1 or h_2 becomes zero if negative). μ_1 and μ_2 are the discharge coefficients, which are set as 0.35 and 0.91, respectively.

2.2.2 Irrigation channel model

The irrigation channels appeared to have had a significant influence on the inundation flow propagation. In this study, these channels were modeled as a one-dimensional network composed of nodes and links. All of the channel links were recognized as linear structures regardless of the overland grids. These links were divided into small discretized reaches of approximately 20 m length to carry out a one-dimensional unsteady flow simulation.

$$\frac{\partial h}{\partial t} + \frac{\partial (uh)}{\partial x} = \frac{q_c}{B} + i \qquad [10]$$

$$\frac{\partial (uh)}{\partial t} + \frac{\partial (u^2 h)}{\partial x} = -gh \frac{\partial (z_b + h)}{\partial x} - \frac{\tau_b}{\rho_T} \qquad [11]$$

$$\frac{\partial (Ch)}{\partial t} + \frac{\partial (Cuh)}{\partial x} = \frac{q_c C}{B} + iC_* \qquad [12]$$

$$\frac{\partial z_b}{\partial t} + i = 0 \qquad [13]$$

Here, q_c is the interaction discharge per unit length between the ground surface and irrigation channel, and B is the channel width. The cross-section of the channel was set as rectangular with no embankment based on the field survey. The section size was categorized as large channels (5.0 m wide and 2.5 m deep) or small channels (2.0 m wide and 1.0 m deep). The elevation of the channel bed was lower by the above-mentioned depth from the elevation of the corresponding ground surface grid where the centroid point of each discretized reach was located. The interaction discharge q_c was calculated from Eqs. [8] and [9] and the following Eq. [14] by comparing the water levels of the channel and corresponding ground surface grid.

$$q_c = \mu h \sqrt{gh} \qquad [14]$$

If sediment is deposited on a channel bed with a height larger than the depth of the channel, the inflow from the ground surface into the channel cannot happen. The sediment concentration of the first term on the right-hand side of Eq. [12] is for the upstream side of the interaction flow.

There are always nodes at both the upstream and downstream ends of a link. The bottom area of a node was set to 10 m^2 for numerical stability or 25 m^2 if connected to a 5.0 m wide link. The bottom elevation of the node was set to be the same as the lowest among the connected link elevations. The downstream end of the channel network is connected to the Kinu River, Kokai River, Hakkembori River. A connection with the Kinu River or Kokai River was not considered here under the assumption of gate closure at the connection points. At the connection points with the Hakkembori River, the water level of the node was replaced with that of the Hakkembori River if the water level was continuous (i.e., if the water level of the Hakkembori River was higher than the node elevation).

3 APPLICATION TO THE STUDY AREA

3.1 Computational conditions

In this study, a 48 h simulation was carried out from 6:00 pm on September 9 to 6:00 pm on September 11. The study area was divided into about 35,000 triangular unstructured grids that were categorized as the Kinu River channel, Hakkembori River channel, river embankment, densely populated areas, streets, and paddy fields. Figure 2 shows how the grids were categorized.

The grid size was approximately 50 m for the Kinu River channel, Hakkembori River channel, river embankment, and streets and approximately 100 m for the other categories. For the grid generation and recognition of the ridges and irrigation channels, we used national geographical information issued by the Geospatial Information Authority of Japan to determine the precise horizontal location. The 5mDEM data were used to determine the ground surface elevation, as shown in Figure 1. The ridges and irrigation channels considered in this study are shown in Figure 2. The roughness coefficient was 0.030 $m^{-1/3}$ s for the Kinu River channel, 0.035 $m^{-1/3}$ s for the Hakkembori River channel, 0.04 or 0.08 $m^{-1/3}$ s for the paddy fields, river embankment, and streets, and 0.06 or 0.10 $m^{-1/3}$ s for the densely populated areas, which was determined from the previous studies (e.g. Nakagawa et al., 2003).

At the upstream and downstream ends of the Kinu River channel, we used the water level observation data at Kamaniwa (27.34 k) and Mitsukaido (10.95 k), as shown in Figure 3. At the downstream end (10.95 k), the water level data at Mitsukaido were used as the boundary condition. At the upstream end (31.8 k), a time series of the assumed water level was used so that the calculated water level at Kamaniwa (27.34 k) agreed with the observed value through trial and error.

The other boundaries were assumed to be surrounded by high walls or high elevation areas; hence, there was no water exchange there. In order to express the water level rise of the Hakkembori River and irrigation channels because of the forerunning rainfall before overtopping or a dike breach occurred, the rainfall observed at the Shimotsuma rain gauge station every 10-min was uniformly applied to the entire target area. The operation of the sluice gate and pumping station (maximum pump capacity of 30 m^3/s) was considered in the simulation during the time indicated in Figure 3.

The sediment concentration was assumed to be constant within the Kinu River channel. Flood-water with that constant sediment concentration flowed into the protected area from the overtopping or dike breach points. However, no sediment erosion or deposition was assumed to happen within the river channels of the Kinu River and Hakkembori River.

3.2 Modeling of overflow and dike breach

At the 25.35 k point on the left-side bank of the Kinu River, the flood flow overtopped the river embankment at 6:30 am, on September 10. According to the MLIT, the elevation of the river embankment around this point decreased around 2014; hence the elevation data of the 5mDEM do not reflect the decreased elevation. Therefore, in this simulation, the elevation data around the overtopping point were adjusted so that the overtopping flow would happen around 6:30 am on September 10.

At the 21.0 k point on the left-side bank, the river embankment was breached, and a large amount of flood-water flowed into the residential area. The breach length was reported to be 20 m at 12:50 pm, 80 m at 13:36 pm, and finally ended up as 200 m. In the simulation, at 12:50 pm on September 10, the elevation of the grid corresponding to the initial breach point instantaneously decreased to the elevation measured after the dike breach. After that, the breach length was calculated at each computational time interval; it was assumed to expand at the same speed to the final length. The elevation of the corresponding grids decreased as the breach expanded, and the inflow discharge was adjusted by multiplying the ratio of the breach length and the grid side length. Thus, the inflow discharge from the breach point was calculated.

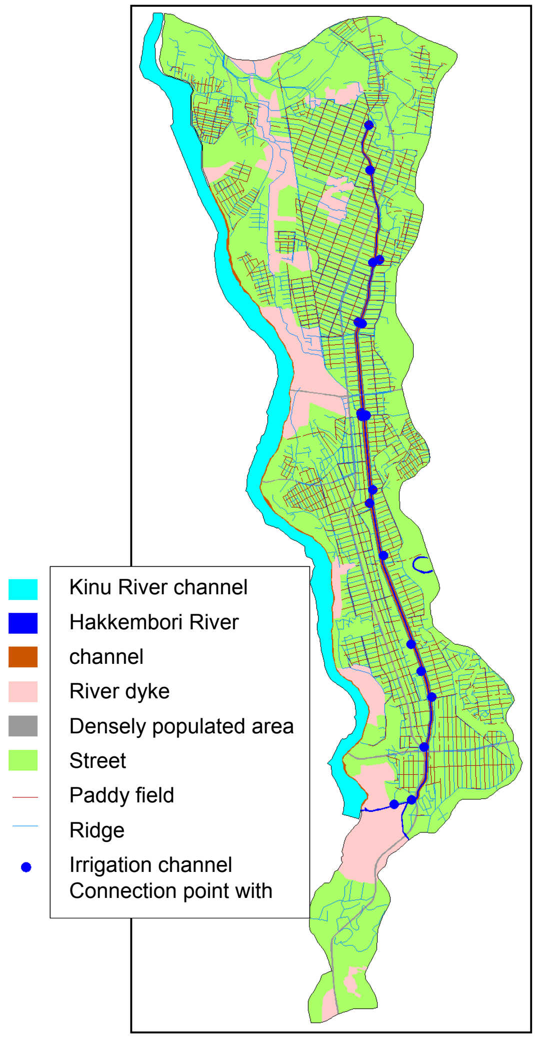

Figure 2. Categories of the computational grids and the ridges and irrigation channels.

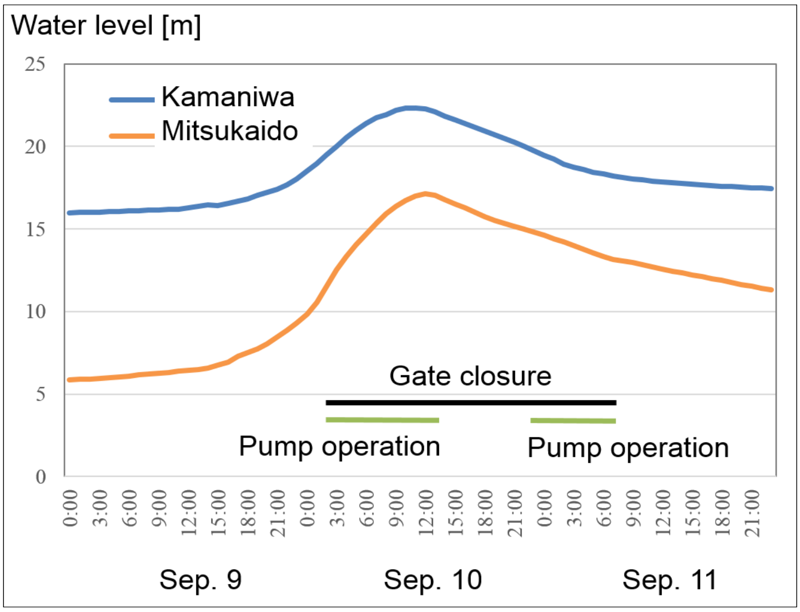

Figure 3. Observed water levels at Kamaniwa and Mitsukaido and the gate closure and pump operation.

4 RESULTS AND DISCUSSION

4.1 Comparison with the measured water level and the parameter determination

In the simulation, the values of several parameters with a significant influence on the inundation depth, thickness of the sediment deposition, and inflow discharge from the Kinu River had to be determined. In this study, we selected the roughness coefficient of the paddy fields (0.08 m $^{-1/3}$ s or 0.04 m $^{-1/3}$ s), coefficient of the deposition velocity δ' (0.0001 or 0.0005), mean diameter of the sediment particles (0.1 or 1.0 mm), and constant sediment concentration within the Kinu River (0.05 or 0.10) as parameters to be determined. In total, 16 simulation cases were carried out for different combinations of these parameters, and the simulation results were compared with the water level measured by Sayama & Takara (2016). The results were compared according to the residual sum of the square. The best combination of those parameters was 0.08 m $^{-1/3}$ s for the roughness

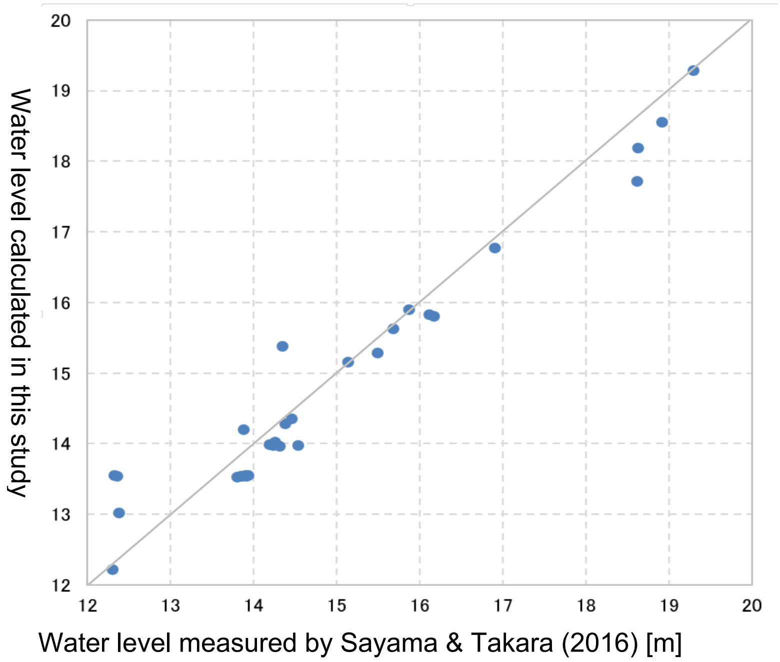

Figure 4. Comparison between the measured and calculated maximum water levels.

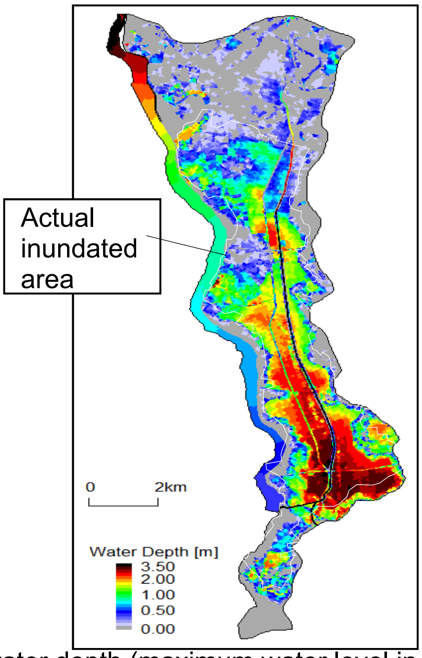

Figure 5. Maximum water depth (maximum water level in the Kinu River channel).

coefficient of the paddy fields, 0.0001 for the coefficient of the deposition velocity, 0.1 mm for the mean diameter of the sediment particles, and 0.05 for the constant sediment concentration within the Kinu River.

Figure 4 compares the water levels calculated in this study and measured by Sayama et al. (2015; 2016). The calculated water levels at most of the measurement points agreed well with the measured values, although a difference of more than 1 m was found at several points. However, the propagation velocity of the inundation water in this study was rather faster than the simulation results of the other researchers or the image data from the Geospatial Information Authority of Japan. Figure 5 shows the maximum water depth obtained from the simulation. Although the water depth was overestimated in the north part because of the forerunning rainfall, the inundated area in most of the target area was reproduced well.

4.2 Sediment deposition in the paddy fields and the irrigation channels

Figure 6 shows the sediment deposition results at the end of the simulation (6:00 pm on September 11). Areas with thick deposition can be seen around the dike breach point, along the inundation flow directions from the overtopping point to the south-east, and from the dike breach point to the south. In many places, the sediment deposit was approximately 50 cm thick, which reproduced the paddy field situation where rice crops just before harvest were partially buried around the dike breach point. In areas with the inundation flow to the south, stripes of sediment deposition were formed, which represents the effect of the ridges on the inundation water flow and sediment deposition.

Figure 7 shows the sediment deposition results along the irrigation channels at the end of the simulation. The results along the irrigation channels also showed a similar tendency to that of overland sediment deposition. In many channels, deposits approximately 50 cm thick were observed around the overtopping and dike breach points, and a 1 m thick deposit was observed along some channels. These sediment deposits must have decreased the cross-sectional area of the channels, which prevented the inundation water from flowing into the channel and delayed its drainage.

5 CONCLUSIONS

In this study, the inundation flow in Joso City was simulated by considering the sediment deposition and effects of ridges and irrigation channels of paddy fields. The computed maximum water level corresponded well to that measured for the actual inundated area by Sayama & Takara (2016), and approximately 50 cm thick sediment deposits were calculated for the paddy fields and irrigation channels near the overtopping and dike breach points. Although the accuracy and validation of the thickness of the sediment deposits were not enough in this study, it is more important to predict and develop countermeasures against sediment deposition, considering the quick drainage of the inundation water and prompt recovery from inundation damage.

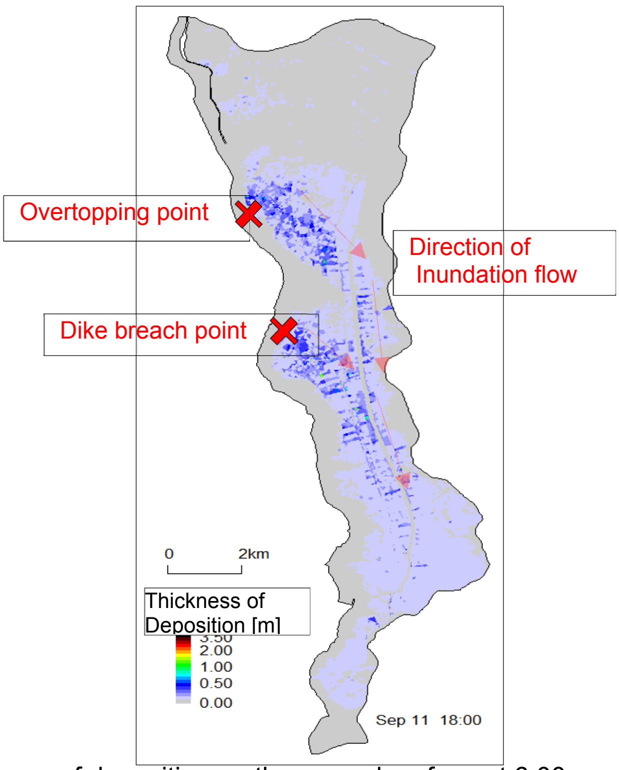

Figure 6. Thickness of deposition on the ground surface at 6:00 pm September 11.

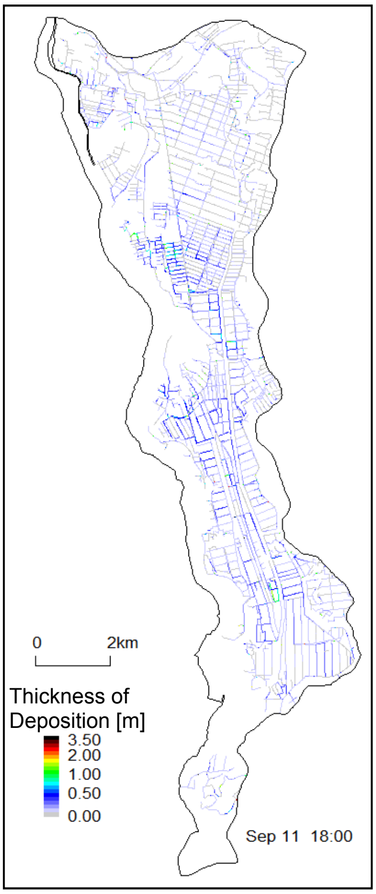

Figure 7. Thickness of deposition on the irrigation channels at 6:00 pm September 11.

ACKNOWLEDGMENTS

This work was supported by a JSPS Grant-in-Aid for Special Purposes (No. 15H06923).

REFERENCES

Kawaike K., Inoue K., Toda K. & Nakai T. (2002). Effects of Sediment Yield on Inundation Flow in a Hillside City. *Journal of Hydroscience and Hydraulic Engineering*, JSCE, 20(1), 151-166.

Nakagawa, H., Takahashi, T., Satofuka, Y. & Kawaike, K. (2003). Numerical Simulation of Sediment Disasters Caused by Heavy Rainfall in Camuri Grande Basin, Venezuela 1999. *In Proceedings of the Third Conference on Debris-Flow Hazards Mitigation: Mechanics, Prediction, and Assessment*, Switzerland, Rotterdam, 671-682.

Sayama, T. (2015): *Field Survey on Inundation Depth Distribution around the Joso City Caused by the Kinu River Flooding by 2015.09* Kanto-Tohoku Heavy Rainfall Report, Kyoto.

Sayama, T. & Takara, K. (2016). Estimation of Inundation Depth Distribution for the Kinu River Flooding by 2015.09 Kanto-Tohoku Heary Rainfall. *Journal of Japan Society of Civil Engineers*, *Ser. B1 (Hydraulic Engineering),* 72(4), 1171-1176. (In Japanese).

ROBUSTNESS OF RISK-BASED OPTIMIZATION METHODOLOGY FOR FLOOD PROTECTION DECISIONS

BALQIS MOHAMED REHAN[(1)]

[(1)] Department of Civil Engineering, Faculty of Civil Engineering, Universiti Putra Malaysia
balqis@upm.edu.my

ABSTRACT

Historically, flood events have caused disastrous impacts to human life. Severe damages to properties and infrastructures, environmental damage and even loss of lives have been experienced in many countries due to the natural disaster. Recognizing the importance of protecting vulnerable society from the adverse consequences of extreme flood events and managing long-term flood risk has become a salient adaptation response. Engineered structural flood protection is one of the many measures that significantly reduce the impacts of flooding. In deciding upon an optimal flood protection design of a structural protection, there is now a shift from the traditional standard fixed return period to a more holistic approach of risk-based decision making. A risk-based optimization methodology is one of the decision tools in flood risk management that prioritize public expenditure whilst providing protection against disastrous flood impacts. This study aims to investigate the robustness of the methodology against uncertainty caused by the natural variability. A modeling approach comprises simulations of annual maxima flow series and of decision makers' behavior in applying the risk-based optimization methodology is adopted. 128 annual maxima flow discharges from Thames at Kingston gauging records in London were processed and used for a realistic representation of an extreme distribution. The performance of decisions from the risk-based optimization methodology is captured in economic terms. It is found that the risk-based optimization methodology is robust to uncertainty caused by the natural variability and that decisions are performing well economically for a service period of 100 years. These findings provide evidence that the methodology is suitable to be adopted in deciding upon the optimal flood protection designs of structural measures.

Keywords: Risk-based decision making; flood risk management; optimization; decision making.

1 INTRODUCTION

Floods have been regarded as one of the most damaging natural disasters in the world (IPCC, 2012). Compared to other natural disasters, floods have caused more damages over the last 100 years with approximately 359 Billion US dollar economic losses estimated from 1900 to 2013 (Konrad, 2013). Severe damages to properties and infrastructures, environmental damage and loss of lives have been experienced in many countries due to the extreme events. Asian regions, for example, have faced disastrous flood consequences with many displaced and losses mounting (Irandoust and Biswas, 2012). The alarming consequences emphasize that long-term risk of flooding should be appropriately managed and that decisions of long-term protection should be robust.

Engineered hydraulic structures can tremendously reduce the consequences of flood events. Dams, flood defense and other flood control structures are designed to suffice a targeted discharge capacity or so-called protection design. There has been much emphasize on the importance of appropriate designs for flood mitigation structures (Hall, 2014). The traditional way is to select a specific return period as a targeted level of protection. The return period selected may reflect a disastrous flood event that once occurred (Rasekh et al., 2010). The identified level of protection is then combined with a freeboard in aiming to accommodate uncertainty (Subramanya, 2008). Whilst the traditional approach is able to protect the community at risk from the impacts of floods, the cost-effectiveness of the decisions is less highlighted. Since public money may be limited and prioritization can become a national issue, the investment allocation should be decided carefully as it can be very expensive for such irreversible structure that meant to be functional for decades (Harvey et al., 2009).

Over the past decades, there has been a shift in the way protection design is decided in many developed countries (Great Britain, 2010). The traditional approach has been transformed into a more comprehensive approach of risk-based flood management, where among all the societal aspect is accounted for more explicitly when establishing the protection design (Sayers et al., 2013). Possible damages of flood events are considered in the decision making and protection design is no longer based on the probabilistic characteristic of flood hazard, i.e. the return period, backed by the past experience of flood events alone. Decisions on flood protection design has now been guided by the assessment of flood risk in which the probabilistic components of flood hazard and the possible economic consequences are integrated (Merz et al., 2010). Furthermore, the decision making is based on a cost-benefit framework that emphasize on the cost-effectiveness of the structural measures. Thus, an optimal protection design is sought whilst acknowledging the need for prioritization of public money elsewhere. This so-called risk-based optimization methodology is one of the many decision tools that could enhance the way protection design is decided.

Despite the advantage of the methodology as a decision tool in managing flood risk, the estimated protection design may not be robust to uncertainties. Uncertainties due to the natural variability, i.e. aleatory uncertainty, or due to the imprecision of model formulation, parameterization and input data, i.e. epistemic uncertainty (Apel et al., 2004) influence the estimated level of protection. Concerning on the robustness of the decisions made through the risk-based optimization methodology, this study aims to investigate the uncertainty range and sensitivity caused by the natural variability of extreme flows. An effective way to capture the uncertainty range is through simulations of multiple possible worlds (Serinaldi and Kilsby, 2015; Hall, 2014), where the effects of natural variability is implicitly transmitted through a modelling chain to the final results (Mkhandi et al., 1996; Apel et al., 2004; Merz and Thieken, 2009). Different sample size is also used in the study to capture the effect of the natural variability. This is reflected by two scenarios of investment strategies; proactive or reactive decision making.

The study presented in the paper is based on real dataset of extreme flows (Section 2). A modelling approach in the context of flood protection decision analysis is established for the simulation study (Section 3). The results are presented and discussed (Section 4) and conclusion is given together with identified limitations and improvements (Section 5).

2 DATA

The dataset of annual maxima flows was extracted from the mean daily flows of Thames at Kingston gauging station available from the Centre for Ecology and Hydrology website (2014). The gauging area is located in the western area outskirt from London. The dataset extracted comprises 128 annual maxima flow records of water, years ranging from year 1883 to 2011. The long real dataset used for the simulation study allows a realistic parameterization of the underlying stochastic properties of flood hazard. Studies have shown that the dataset exhibit a stationary stochastic property (Marsh and Harvey, 2012), hence suitable to be used for simulation of independent identically distributed flow series.

3 METHODOLOGY

3.1 Modelling approach

Figure 1 shows the modelling approach used in the study. It is represented by a structured workflow that is divided into three main steps: the first step is the simulation of n set of long time series of annual maxima flows (First row in Figure 1). The simulation was undertaken through the Monte Carlo simulation methodology, where a parameterized GEV distribution from the real dataset of extreme flows was used. Each series of annual maxima flows simulated will be taken forward into the second step (second row in Figure 1) comprising simulations of decision makers' behavior in deciding upon a cost-effective protection design. The third step is to use the simulated flow series in quantifying the decision performance (the third and fourth row of Figure 1). The quantification of the decision performance will be the basis for the uncertainty and sensitivity analysis.

In the exploration study, it was assumed that the decision makers are to invest on a structural flood defense in attempt to reduce flood risk. Using the risk-based optimization methodology as the decision tool, it was assumed that the decision makers are being rational in deciding upon the design flood. Furthermore, it was assumed that the decision makers have a risk-neutral attitude. The simulation of decision makers' behavior uses simulated 'historical records' in the risk estimates. In the risk-based optimization methodology, investment costs and benefits of risk reduction associated with a range of considered design floods were compared to identify the optimum design discharge. Section 3.3 further explains the algorithm behind the risk-based optimization methodology.

The simulation of decision makers' behavior was repeated for each simulated series of extreme flows to capture the uncertainty range due to the natural variability. Each decision made in the second step of the modelling approach was brought forward into the third step to assess the performance. The performance here refers to the net present value (NPV) and benefit cost ratio (BCR), which were quantified using the simulated extreme flows of appraisal period. The number of simulation set of the flow series governs the number of decisions and associated performance indices. Hence, the uncertainty was captured across n number of possible worlds.

In order to test the sensitivity of the risk-based decisions to the different timings of intervention, two scenarios of investment strategies were used; a proactive (PRO) strategy and a reactive (RCT) strategy. The 'proactive' (PRO) strategy is defined as an adaptation action at a present time to effectively decide upon a flood defense protection design in alleviating potential consequences. The 'reactive' (RCT) strategy refers to the same intervention action but at a postponed time when the status-quo threshold is being exceeded. The considered strategies are of practical examples that are often surfaced in discussions among flood risk managers, stakeholders or decision makers alike predominantly due to conflicting interests on whether to secure societal safety from unforeseen flood consequences proactively or whether to prioritize limited resources when more information is at hand.

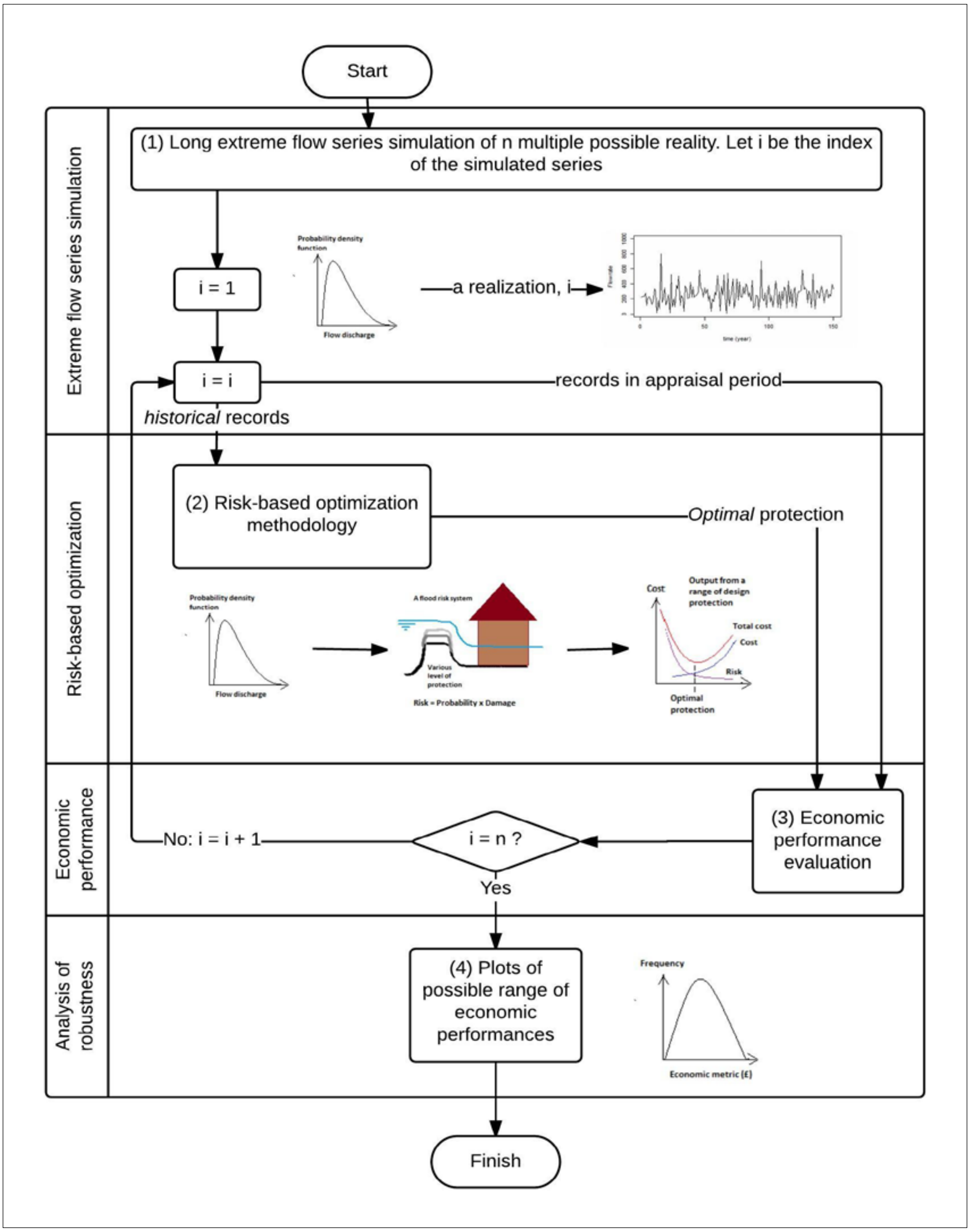

Figure 1. Modelling approach for the simulation study.

In general, both alternatives have their advantages and downsides. In terms of societal benefit, PRO strategy allows the protected community to be resistant from early on by securing them with flood protection. However, one of the downsides of PRO intervention is the possibility of significant under or over estimation due to relatively smaller sample of extreme flows. PRO strategy also requires investment to be allocated at a present time, which might result in serious repercussion of overspending due to possible severe sampling error. With the downsides of the PRO strategy, the RCT strategy might be more attractive as it potentially increases the reliability of risk estimation hence promote a good investment decision. Furthermore, it relatively reduces present value spending of public funds with the delay in investment. However, RCT strategy also brings a negative effect of possible significant consequences due to unforeseen flood events within the waiting time. Perhaps these are among the reasons why in practice, proactive intervention usually was applied for cities that are of greatest importance to the national economy, with a more reactive approach taken elsewhere (O'Connell and O'Donnell, 2014).

The formulation of the modelling approach considers 50 years for the historical records and a subsequent 100 years for the appraisal period for the case of PRO strategy. For RCT strategy, the historical record of 50 years was added with the waiting period before the first flood occurs, whilst appraisal period was still considered to be 100 years similar to the PRO strategy. This means that in the decision making process, the historical records for PRO and RCT strategies differ but not the appraisal period. Also because of the discounting, RCT strategy was only considered when the first flood happens to be within 75 years records.

3.2 GEV distribution

The GEV distribution function is by far the most comprehensive extreme value distribution that combines Frechet, reverse Weibull and Gumbell distributions. It is also the asymptotic distribution for 'block-maxima' dataset (Coles, 2002). The GEV can be expressed in different forms, as shown in Table 1 (El Adlouni et al., 2007). u is the location parameter, α is the scale parameter and κ is the shape parameter. x represents the magnitude of variable of concern, in this case the extreme flows in cubic meter per second unit (m^3/s). $F(x)$ is the cumulative distribution function (CDF), $x(F)$ is the quantile function of extreme flows, and $F(x)$ is the probability distribution function (PDF). The quantile function is the inverse of the CDF.

The GEV distribution is used in this study to represent the underlying stochastic properties of the extreme flows both in the first and second step of the modelling approach (i.e. of the generation of multiple possible series of extreme flows and of the simulation of the decision makers' behavior). Also in both steps, the parameter of the GEV distribution was estimated using the L-moments (Hosking, 1990).

For the simulation of multiple possible series of extreme flows, the quantile function $x(F)$ was used with F ranging from [0,1] from the uniform distribution. This study simulates 1000 series of extreme flows of the same size, which was deemed sufficient for convergence. Whereas for the simulation of the decision makers' behavior, the PDF of the GEV distribution was used to estimate the risk associated with flooding. The GEV distribution parameters estimated for the risk estimation was governed by the variability of the 'historical data' used.

Table 1. Generalized extreme value (GEV) distribution functions.

Cumulative density function (CDF)	$F(x) = exp\left[-\left(1-\kappa\frac{(x-u)}{\alpha}\right)^{\frac{1}{\kappa}}\right]$
Quantile function	$x(F) = \begin{cases} u + \frac{\alpha}{\kappa}(1-(-\log(1-F))^{\kappa}), & \kappa \neq 0 \\ u - \alpha \log(-\log(1-F)), & \kappa = 0 \end{cases}$
Probability density function (PDF)	$y = \begin{cases} (1-\frac{\kappa(x-u)}{\alpha})^{\frac{1}{\kappa}}, & \kappa \neq 0 \\ e^{-\frac{x-u}{\alpha}}, & \kappa = 0 \end{cases}$ $f(x\|u,\alpha,\kappa) = \frac{1}{\alpha}y^{1-\kappa}e^{-y}$

3.3 Risk-based optimization methodology

The risk-based optimization methodology adopted in the decision making process search for the optimal design of long-term flood investment. It trades off the cost of an intervention (C_t) and the estimated risks (R_t) associated with the intervention to obtain the most cost-effective solution. Risk as the product of probability and consequences can be denoted as:

$$R_t = \int_{q_o or\ \hat{q}}^{q_L} \rho_t(q) D_t(q) dq \qquad [1]$$

Where $\rho_t(q)$ represents the PDF of extreme flows and $D_t(q)$ as a flood damage function. The risk function is associated with a particular year (t) where the function acknowledges the possible variation of risk across the temporal scale. For this study, risk was considered as an average annual damage, where it was considered to be equally the same every year over the appraisal period (Dawson et al., 2011). The integrations' lower limit represents a discharge threshold of no damage either from the base case (q_o) or from a considered design discharge ($\hat{q}$)

The optimum design discharge in Eq. [2] is represented by the minimum total present value costs (TPVC) over the project lifetime period (n_{str}) (Jonkman et al., 2009). To solve for the optimum value, recursive computations was undertaken where the minimum TPVC across the range of possible protection design discharge was identified. Where appropriate, a social time preference rate (r) is used to transform investment cost and flood damages to present values. The optimization procedure requires an input of a unimodal function constructed based on the TPVC of a range of appropriate protection design ($\hat{q}$) and is undertaken numerically. The $t = 0$ in the equation represents the initial year the flood defense was constructed. For an exploration purpose, r can be of any reasonable value that may be recommended by experts. Because the use of dataset of the UK, the standard social preference rate of 3.5% suggested by HM Treasury of Great Britain (2015) is used in this study.

$$\min_{\hat{q}} TPVC = \sum_{t=0}^{n_{str}} \frac{1}{(1+r)^t} \left(R_t(\hat{q}) + C_t(\hat{q})\right) \qquad [2]$$

The structural forms of the cost and damage functions were taken as square root and quadratic functions, respectively. The relationship between the two functions has been derived based on manning equation and a hypothetical flood prone area. Flow discharge had been selected as the connecting variable (i.e. the decision variable), which was consistent with the structure of the proposed risk-based optimization methodology in Eq. [1]. The derivations of the functions can be referred to in Balqis and Hall (2014).

3.4 Uncertainty of economic performance

The net present value (NPV) and benefit cost ratio (BCR) to quantify the economic performance of decisions are denoted in Eq. [3] and Eq. [4], respectively. Notations used in the equations have the same descriptions as the ones used in Section 3.3. In order to solve the formulae, benefits and costs associated with a particular decision made from the decision making process should first be calculated. The extreme flow discharges simulated over the appraisal period and its relative value to the design discharge dictate the conditions of damaging flood event. For the RCT scenario, the calculation of benefit across the 100 years appraisal period will differ for years without intervention and for years with intervention. The former refers to the period before and when the first flood occurs whilst the latter refers to the period after the first flood occurs.

The values of benefit and costs at a discrete time t with respect to each strategy were then transformed into present values (PV) using the same assigned discount rate for the risk-based optimization methodology. The NPV and BCR can subsequently be solved using the PV benefit and the PV costs associated with the estimated optimal design discharge from the decision making process. Repeating the above process for the *n* number of simulations allows the range of outcomes from the competing time-dependent interventions to be graphically captured and the effects of sampling error to be visually compared.

$$NPV = \sum_{t=0}^{n_{str}} \frac{1}{(1+r)^t} \left(\mathrm{D}_t(q > \hat{q}) - \mathrm{D}_t(q > q_o)\right) - \sum_{t=0}^{n_{str}} \frac{1}{(1+r)^t} \left(\mathrm{C}_t(\hat{q})\right) \qquad [3]$$

$$BCR = \frac{\sum_{t=0}^{n_{str}} \frac{1}{(1+r)^t} \left(\mathrm{D}_t(q > \hat{q}) - \mathrm{D}_t(q > q_o)\right)}{\sum_{t=0}^{n_{str}} \frac{1}{(1+r)^t} \left(\mathrm{C}_t(\hat{q})\right)} \qquad [4]$$

where,

$\mathrm{D}_t(q > \hat{q})$ is the damage that occurs when the extreme flow exceeds the design discharge
$\mathrm{D}_t(q > q_o)$ is the damage that occurs when the extreme flow exceeds the do-nothing no damage threshold.

A detail workflow that distinguishes the process of obtaining the economic performance of decisions associated with the differing strategies is illustrated in Figure 2. Some boxes in this figure are numbered to attribute them to the numbered boxes in Figure 1.

4 RESULTS AND DISCUSSIONS

Figure 3 tabulates 1000 outcomes of the investment costs of intervention associated with the timings of when the interventions take place. The investment costs of PRO strategy can be tabulated in the first year of the appraisal period, whilst the RCT strategy was tabulated from the second year onwards. The intervention timings following the RCT strategy can be seen fade out after the first 10 years into the appraisal period, indicating a vulnerable condition of the do-nothing scenario. Furthermore, approximately ten years difference of the far end RCT intervention and the PRO intervention suggests that the size of historical records used in the statistical model was fitting of the two competing strategies and they were not much different.

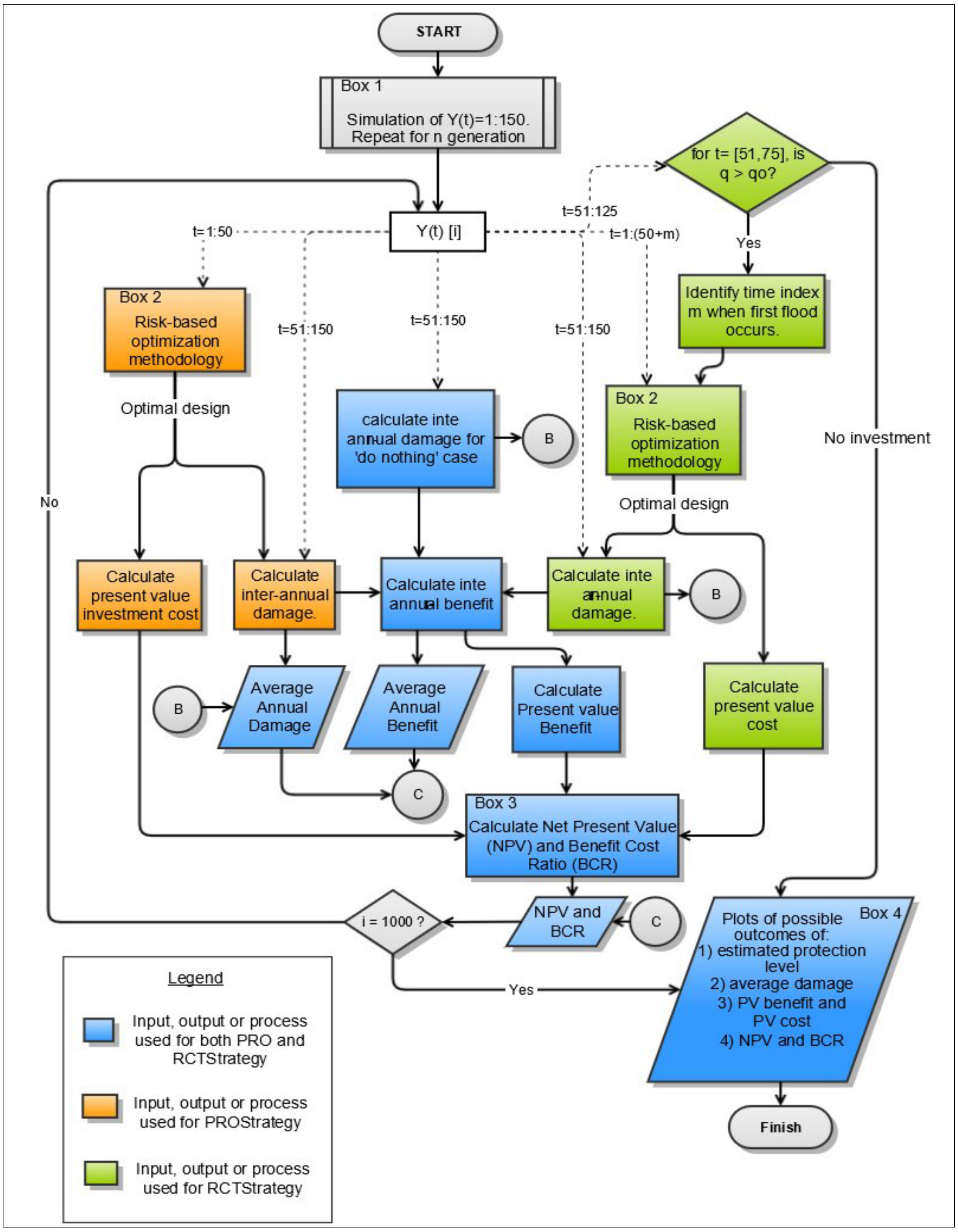

Figure 2. Flow diagram to capture the uncertainty range of decisions performance.

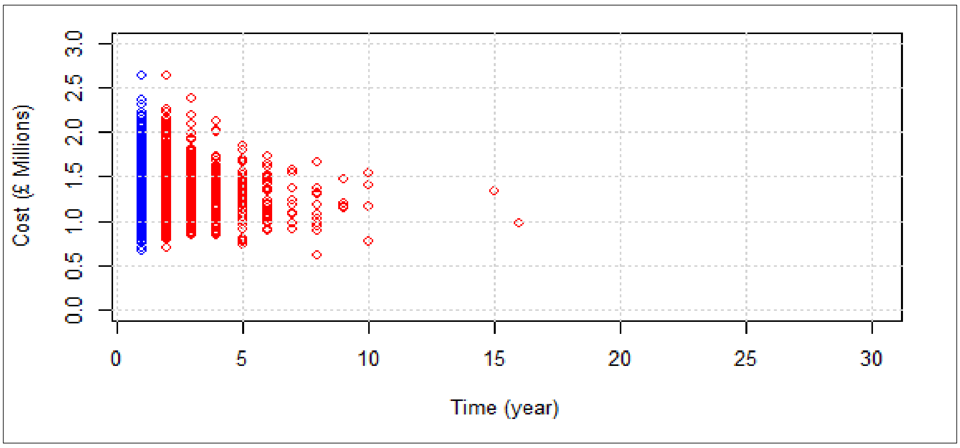

Figure 3. Box and whisker plots of NPV and BCR of PRO and RCT strategies across 1000 simulations of different scenarios.

The modelling outcomes tabulated in Figure 4 and Figure 5 are shown in terms of uncertainty range from the effect of the natural variability of the extreme flows. The investment costs associated with the two strategies are tabulated in Figure 4 (a). Due to the generally small difference of sample size used between the two strategies, the uncertainty of the design discharge was found to be in a similar range. The minor difference in the sample size used also reflected in the mean annual damage between the two strategies, as depicted in Figure 4 (b). Nevertheless, PRO strategy can be seen to reduce flood damage slightly more than the RCT strategy.

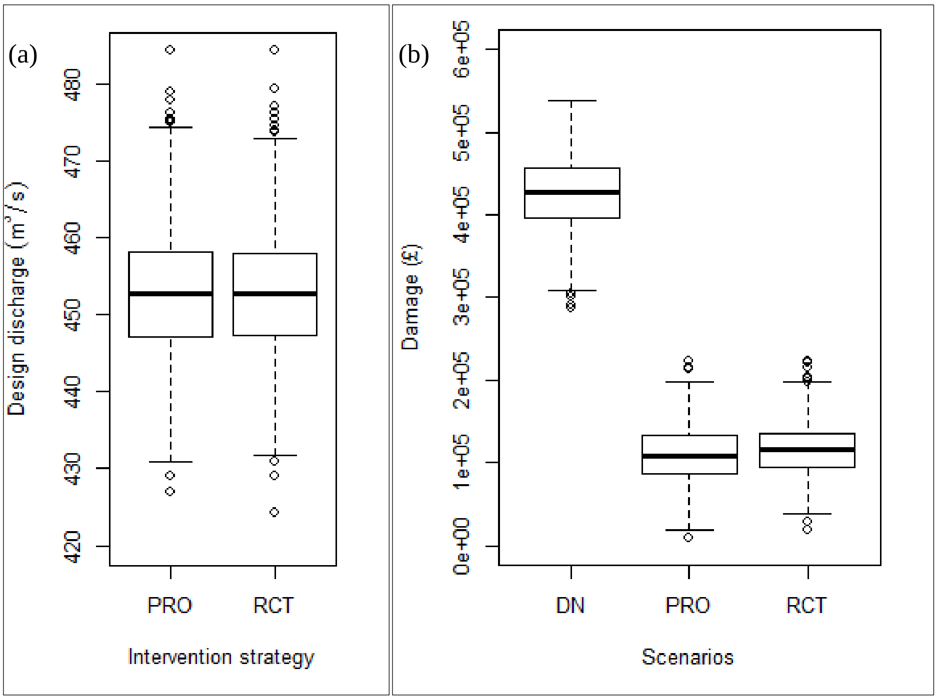

Figure 4. Box and whiskers plots representing uncertainty range of investment costs of PRO and RCT strategies (a) and mean annual damage of do-nothing, PRO and RCT scenarios (b).

Figure 5 (a) and (b) explicitly shows the intermediate results of uncertainty range of investment costs and benefits in present values that govern the economic performance of decisions, i.e. the NPV and BCR. The median of the present value investment costs of PRO strategy can be seen in Figure 5 (a) to be relatively higher than the investment costs of RCT strategy. This reflects the higher commitment of public spending when investment was proactively taken. Whilst this might be a defending reason supporting the RCT strategy, the median present value benefits shown in Figure 5 (b) are proven to be higher for the PRO strategy as compared to the RCT strategy. Furthermore, the resulting NPV in Figure 5 (c) shows that the PRO strategy outperforms the RCT strategy with a higher median NPV. The preference of the PRO strategy over the RCT strategy in terms of the NPV indicates that the marginal PV benefit of having the PRO strategy as compared to the RCT strategy which was much greater than the savings from the lower PV investment costs of the RCT strategy as compared to the PRO strategy. In terms of the BCR, Figure 5 (d) shows that the median values were generally the same for both PRO and RCT strategies.

Overall, the results of the uncertainty range of decisions performance respective to the PRO and RCT strategies shows only minor discrepancies. There is also agreement on the expected values from both strategies that can be seen from the BCR. Furthermore, both NPV and BCR of the possible risk-based decisions promise positive returns of investments regardless of strategy adopted. The results suggest that the risk-based optimization methodology was robust to the timing of intervention. Nevertheless, it should be stressed that a risk-based proactive intervention to combat flood risk should always remain a default national strategy despite the relatively higher sampling error and the expected higher investment costs.

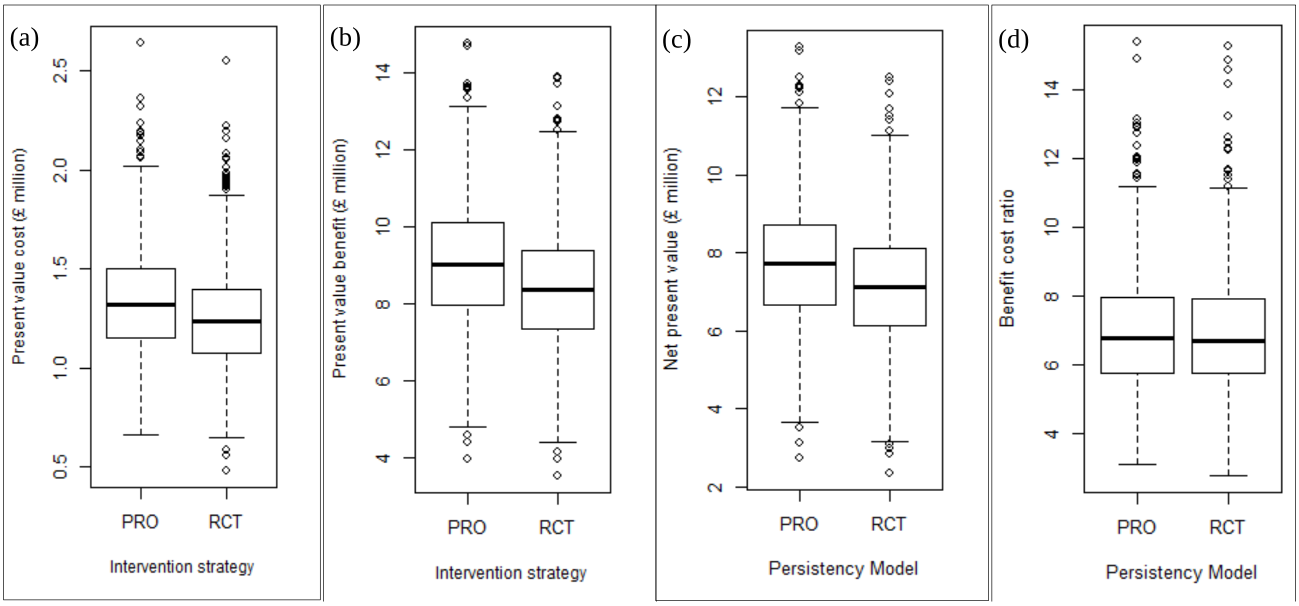

Figure 5. Box and whisker plots representing uncertainty range of PV costs (a), PV benefits (b), NPV (c) and BCR (d) of PRO and RCT strategies.

5 CONCLUSIONS

The study demonstrates a modelling approach in capturing the uncertainty range and sensitivity of risk-based decisions of flood protection investment strategies. A decision analysis is conducted based on real dataset of extreme river flows and incorporating simulations of decision making process. The aim is to explore the robustness of risk-based optimization methodology in flood protection decision making against the natural variability.

The findings prove that the risk-based optimization methodology is robust, which suggest that the approach is suitable to be used in the real world cost-benefit analysis of engineering flood protection structure. This supports the adoptability of the methodology such that presented in many studies (Jonkman et al., 2009; Rosner et al., 2014). The direct use of the probability distribution for the risk estimation further extended the applicability of the approach to a wide range of probabilistic model and future scenarios.

Further study to improve the reliability of the methodology can be made by taking into account the real flood risk system for the cost and damage function. These variables greatly influence the protection design estimated from the risk-based optimization methodology. The robustness of decisions against aleatory uncertainty can also be tested using different dataset of extreme flows that represent different hydrological regime. Investigation on the robustness of the decisions performance can also be explored for epistemic uncertainty, for example by testing the sensitivity against a number of possible cost and damage formulations. Moreover, the robustness against different climate scenarios may also be explored.

ACKNOWLEDGEMENTS

This work is part of the author's PhD work that was supported by the Malaysian Government scholarship. The author would like to thank Professor Jim Hall from the University of Oxford who supervised her throughout the PhD study.

REFERENCES

Apel, H., Thieken, A.H., Merz, B. & Blöschl, G. (2004). Flood Risk Assessment and Associated Uncertainty. *Natural Hazards and Earth System Sciences,* 4(2), 295-308.

Balqis, M.R. & Hall, J.W. (2014). Flood Risk Management Decision Analysis with Finite Historical Records and Highly Variable Climate Effects. *Second International Conference on Vulnerability and Risk Analysis and Management (ICVRAM) and the Sixth International Symposium on Uncertainty, Modeling, and Analysis (ISUMA),* 2867-2879.

Centre for Ecology and Hydrology (2014). *National River Flow Archive: 39001 - Thames at Kingston,* [Online] Available from: http://www.ceh.ac.uk/data/nrfa/data/peakflow.html?39001 [Accessed 2012].

Coles, S. (2001). *An Introduction to Statistical Modeling of Extreme Values.* Springer, London.

Dawson, R.J., Ball, T., Werritty, A., Hall, J.W. & Roche, N. (2011). Assessing the Effectiveness of Non-Structural Flood Management Measures in the Thames Estuary Under Conditions of Socio-Economic and Environmental Change. *Global Environmental Change,* 21(2), 628-646.

El Adlouni, S., Ourda, T.B.M.J., Zhang, X., Roy, R. & Bobee, B. (2007). Generalized Maximum Likelihood Estimators for the Nonstationary Generalized Extreme Value Model. *Water Resources Research,* 43(3).

Environment Agency (2010). *Flood and Coastal Erosion Risk Management Appraisal Guidance,* [Online]. Available from: https://www.gov.uk/government/publications/flood-and-coastal-erosion-risk-management-appraisal-guidance [Accessed 2013].

HM Treasury (2011). *The Green Book: Appraisal and Evaluation in Central Government,* [Online]. Available from: https://www.gov.uk/government/uploads/system/uploads/attachment_data/file/220541/green_book_complete.pdf [Accessed 2012].

Hall, J.W. (2014). *Applied Uncertainty Analysis for Flood Risk Management*. Imperial College Press, London, Book, Chapter C1.

Harvey, H., Hall, J.W. & Peppe, R. (2012). Computational Decision Analysis for Flood Risk Management in An Uncertain Future. *Journal of Hydroinformatics,* 14(3), 537-561.

Hosking, J.R.M. (1997). *Regional Frequency Analysis: An Approach Based on L-Moments.* Cambridge University Press, Cambridge, UK.

Intergovernmental Panel on Climate Change (IPCC). (2012). *Managing the Risks of Extreme Events and Disasters to Advance Climate Change Adaptation. A Special Report of Working Groups I and II of the [Field, C.B., V. Barros, T.F. Stocker, D. Qin, D.J. Dokken, K.L. Ebi, M.D. Mastrandrea, K.J. Mach, G.-K. Plattner, S.K. Allen, M. Tignor, & P.M. Midgley (eds.)].* Cambridge University Press, Cambridge, UK, and New York, NY, USA.

Irandoust, S. & Biswas, A.K. (2012). *Floods in Asia: Lessons to be Learned from Thailand,* Available from: http://www.nationmultimedia.com/opinion/Floods-in-Asia-Lessons-to-be-learned-from-Thailand-30174413.html [Accessed 2015].

Jonkman, S.N., Kok, M., Van Ledden, M. & Vrijling, J.K. (2009). Risk-Based Design of Flood Defence Systems: A Preliminary Analysis of the Optimal Protection Level for the New Orleans Metropolitan Area. *Journal of Flood Risk Management,* 2(3), 170-181.

Konrad A. S. (2013). *Climate Change in Asia,* [Online]. Available from: http://ejap.org/environmental-issues-in-asia/natural-disasters-asia.html [Accessed in 2014].

Marsh, T. & Harvey, C.L. (2012). The Thames Flood Series: A Lack of Trend in Flood Magnitude and a Decline in Maximum Levels. *Hydrology Research,* 43(3), 203-214.

Merz, B. & Thieken, A. (2009). Flood Risk Curves and Uncertainty Bounds. *Natural Hazards,* 51(3), 437-458.

Merz, S.B., Hall, J., Disse, M. & Schumann, A. (2010). Fluvial Flood Risk Management in a Changing World. *Natural Hazards and Earth System Sciences,* 10(3), 509.

Mkhandi, S.H., Kachroo, R.K. & Guo, S.L. (1996). Uncertainty Analysis of Flood Quantile Estimates with Reference to Tanzania. *Journal of Hydrology,* 185(1-4), 317-333.

O'Connell, P.E. & O'Donnell, G. (2014). Towards Modelling Flood Protection Investment as a Coupled Human and Natural System. *Hydrology and Earth System Sciences,* 18(1), 155-171.

Rasekh, A., Afshar, A. & Afshar, M.H. (2010). Risk-Cost Optimization of Hydraulic Structures: Methodology and Case Study. *Water Resources Management,* 24(11), 2833-2851.

Rosner, A., Vogel, R.M. & Kirshen, P.H. (2014). A Risk-Based Approach to Flood Management Decisions in a Nonstationary World. *Water Resources Research,* 50(3), 1928-1942.

Sayers, P., Yuanyuan, L., Galloway, G., Penning-Rowsell, E., Fuxin, S., Kang, W., Yiwei, C. & Le Qusne, T. (2013). *Flood Risk Management: A Strategic Approach.* UNESCO, Paris.

Serinaldi, F. & Kilsby, C.G. (2015). Stationarity is Undead: Uncertainty Dominates the Distribution of Extremes. *Advances in Water Resources,* 77, 17-36.

Subramanya, K. (2008). *Engineering Hydrology*. 3rd Ed. McGraw-Hill International, Singapore.

Proceedings of the 37th IAHR World Congress
August 13 – 18, 2017, Kuala Lumpur, Malaysia

FLASH FLOOD INUNDATION ANALYSIS CONSIDERING THE AGGRADATION OF RIVERBED IN GOWAIN RIVER, BANGLADESH

MASAKAZU HASHIMOTO(1), KENJI KAWAIKE(2), YUJI HASEGAWA(3), TOMONORI DEGUCHI(4), SHAMMI HAQUE(5), ARPAN PAUL(6), MASHFIQUS SALEHIN(7) & HAJIME NAKAGAWA(8)

hashimoto.masakazu.5e@kyoto-u.ac.jp
(4) Nittetsu Mining Consultants Co., Ltd., Tokyo, Japan,
(5,6,7) Institute of Water and Flood Management, Bangladesh University of Engineering and Technology, Dhaka, Japan

ABSTRACT

This study focuses on the effect of riverbed aggradations on the scale of flood inundation. Using a distributed runoff model, one-dimensional riverbed variation calculations and a two-dimensional flood inundation models, a flooding analysis for a flash flood in an un-gauged basin were performed. Due to the limitations of the available datasets, we first performed riverbed variation calculations by using daily discharge and water level data that were collected during April–Sept 2000. Next, we performed a runoff analysis by using 3-hourly satellite rainfall data that were observed during April–May 2006. Finally, riverbed data and discharge data are considered in the flash flood inundation analysis. The results show that after the riverbed aggradations was considered, the flood area becomes 2 times larger than that for the case where riverbed aggradation was not considered. Thus, we recommend considering riverbed aggradations in flash flood risk assessments.

Keywords: Un-gauged basin; riverbed aggradations; flash flood; flooding analysis; runoff analysis.

1 INTRODUCTION

Flash flooding following intense rainfall is a typical type of flooding hazard in Bangladesh, especially in hilly areas such as Sylhet and Chittagong. These types of floods occur frequently. In contrast to the long time scale of monsoon floods, which take place over several months, flash floods usually transpire rapidly over a time course of several hours. In addition, because flash flooding is mainly caused by strong rainfall events, the flood flows tend to contain abundant sediment, which in turn can trigger sediment-related disasters.

In the hilly area of Sylhet district, flash floods originate from the mountainous area of the Meghalaya plateau. Even though some hydrological data are available for this mountainous area, obtaining the observed data in a timely manner can be difficult, and thus, modeling approaches are needed to assess flood hazards. Here, we regard the study of catchment as an un-gauged basin.

Currently, satellite data such as topographic data and rainfall data can be obtained easily from satellite products; however, bathymetry data are not included in the elevation, and rainfall datasets need to be calibrated by using observed data. Furthermore, in many cases, the time resolution of the observed water level data is only at daily interval and short-term floods are rarely recorded in such datasets. Thus, additional observational hydrological and topographical data are necessary to depict hydrological phenomena accurately.

In part, the above mentioned constraints, targeted flooding analyses within un-gauged basins are difficult to perform, and simulations of actual phenomena can easily lead to underestimations or overestimations of the flooding risk. In order to evaluate the flood risk in an un-gauged basin accurately, we need to combine several types of analytical methods. In particular, rainfall-runoff models, riverbed variation calculations and flood inundation analyses are valuable techniques to employ.

To simulate short-term rainfall-runoff, such as that during a flash flood, daily hydrological data are not sufficient for the modeling work. For example, in many cases the daily data do not include the peak value and the short-term variation of the water level is not recorded. Thus, runoff modeling is needed to generate a fine-time resolution discharge dataset. These days, 3-hourly satellite rainfall data are available for many locations, and this has enabled model simulations of the hourly discharge in various catchments.

The objectives of this study were as follows: 1) to reproduce a fine-time resolution discharge dataset for an area in Bangladesh that is prone to flooding, and this was accomplished by using a cell-based distribution runoff model with 3-hourly satellite rainfall data; 2) to estimate the riverbed aggradations by using a one-dimensional (1-D) riverbed variation calculation model; and 3) to evaluate the effect of riverbed aggradations on the scale of the flooding.

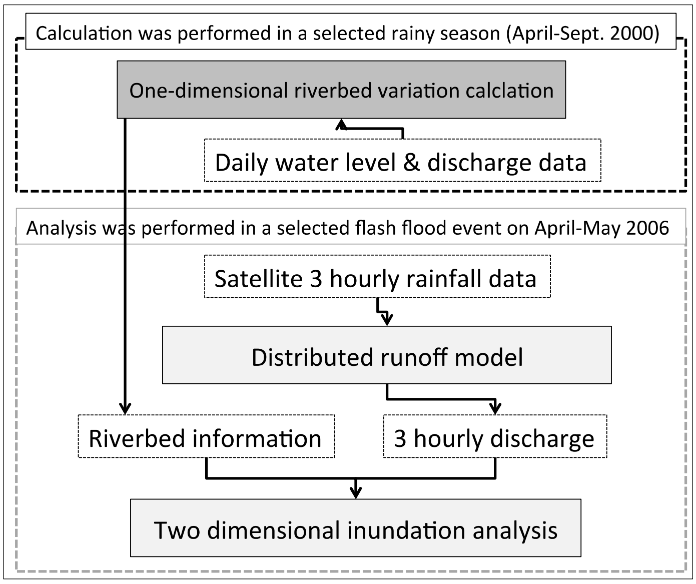

Figure 1. Flow chart of the analysis procedure.

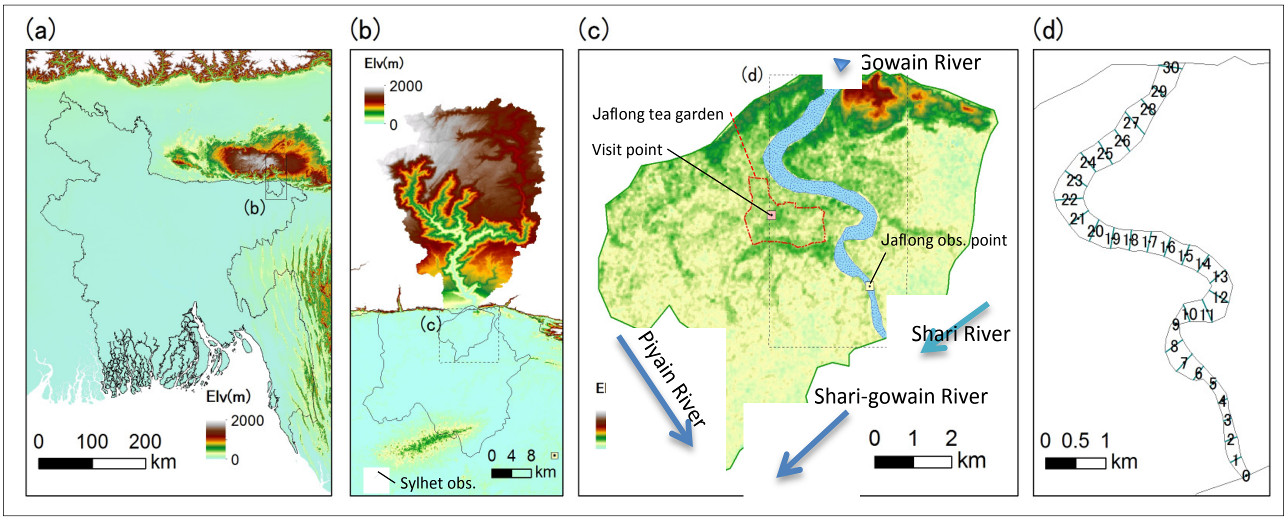

Figure 2. Study area. (a) Location of the Gaibandha Upazila in Bangladesh (the background shows the SRTM3 data), (b) Enlarged view of the Gaibandha Upazila and Gowain River catchment (the rainfall observation site is shown in the bottom-left portion of the image, and the background shows the SRTM3 data), (c) Jaflong area (selected area for the flood inundation analysis, the centre river is the Gowain River, and the background shows the SRTM1 data), (d) Cross sections used for the riverbed variation calculations (numbers indicate the positions of the cross sections from the confluence of the Sari–Gowain River).

2 METHODOLOGY

We used three different numerical models in this work, namely, a flood inundation model, a cell-based runoff model and a 1-D riverbed variation calculation model. Each model will be explained in detail in the following sections. Firstly, we performed a runoff analysis considering the 3-hourly satellite rainfall data. Secondly, we performed riverbed variation calculations considering daily water depth and discharge data from April–September 2000. Finally, we performed a flood inundation analysis using the discharge data with the initial riverbed condition (case 1: smooth riverbed, and slope was the same as the surrounding terrain), end riverbed condition (case 2: approximately 1.0-2.0m aggradations and 0.5m degradation from initial condition) and peak aggradations riverbed condition (case 3: approximately 1.0-3.0m aggradations and 1.0m degradation from initial condition). A flow chart of the analysis procedure is presented in Figure 1.

2.1 Study area

The study area is in Jaflong, Gowainghat Upazila, Sylhet Division, Bangladesh (Figure 2a, 2b, 2c). In Bangladesh, the rainy season is from April to September, and flash flooding occurs in hilly areas such as Sylhet and Chittagong during this time. Because the catchment of the Gowain River is in the Meghalaya plateau within India's territory (Figure 2a), data sharing is important for river basin management efforts.

Human fatalities were relatively rare in these flash flooding events, but serious damage to agricultural resource was common. The study area was in the rice-producing district, and residents tend to experience damage to their crops just before the rice was harvested because of the timing of the rainy season. According to the hearing survey in the Jaflong area, the flash flood that occurred on 25 April 2016 caused flood inundation for 4-5h with a 1.5-2.0m water depth (Figure 2c).

Sylhet is famous for its haor area, which consists of bowl-shaped wetland depressions. Therefore, earlier flooding research focused on the entire haor area and several catchments during the entire rainy season (Oka and Salehin, 1997). However, to focus on the risk caused by the flash flooding, we selected a small catchment of the Gowain River for the analysis in this study.

2.2 Cell-based distributed runoff model

The rainfall-runoff model used in this study represents the hill slope as a set of slope units and its routes of water flow by using a kinematic wave model that accounts for the field capacity of the soil layer. The kinematic wave equations that consider the field capacity are as follows (Ichikawa et al., 2001):

$$\frac{\partial h}{\partial t}+\frac{\partial q}{\partial x}=r \qquad [1]$$

$$q=\begin{cases} ah & (0\le h<d) \\ \alpha(h-d)^m+ah & (h\ge d) \end{cases} \qquad [2]$$

where, h is the water depth (m), q is the unit discharge (m^2/s), r is the rainfall intensity (m/s), a is the flow velocity in the soil layer (m/s) (=$k\ sin\theta/\gamma$), k is the permeability (m/s), γ is the effective porosity of the soil layer, α, m are constant values, and when using the hill slope θ_s and Manning's formula, m=5/3, α= $\sqrt{\sin\theta_s}\,/\,N$ and N is the equivalent of roughness coefficient; d is the depth of effective pore contained in a soil layer and D is the depth of a soil layer.

The selected area for the analysis in the Gowain River catchment is shown in detail in Figure 2b. On the Meghalaya plateau, the soil layer varies in depth from 0.5-2 m (Government of Meghalaya, 2016). Hence, we set the depth of the soil layer to be 1.0m during the model development and verification procedure. Additionally, the texture of soils varies from sandy-loam to silty-clay. Hence, the effective porosity and permeability were set to small values because the diameter of the soil was small, i.e., tentative values of γ = 0.15 and k = 0.002 were used in the model. In regards to the land use, the area is occupied by dense forest. Thus, we set the N = 0.7s/$m^{1/3}$ (Government of India, 2012).

Topographic data were obtained from the United States Geological Survey (USGS), and Shuttle Radar Topographic Mission (SRTM) 3 (90m grids) products were applied in the model. For the selected catchment, which covers an area of about 900km^2, 111,738 grid cells were applied. Rainfall data were obtained from PERCIANN-CSS, which supplies data at a 3-hourly time resolution and on a 4 km spatial resolution. This product covers South Asia, and the provided period was 2006-2010. Because discharge data were also available for 2006, we selected this year for the runoff analysis. We used the satellite rainfall data and had to multiply it by 2 times to calibrate it with the observed rainfall data, i.e., the satellite data were underestimated compared to observed rainfall data at Sylhet (Figure 2b). The spatial resolution of the rainfall and topography datasets was different. Thus, the nearest rainfall data were used for the grid cells. The discharge used to validate the model results was obtained from the Jaflong observation point (Figure 2c) by Bangladesh Water Development Board (BWDB).

2.3 Riverbed variation calculations

In order to understand the extent of the riverbed variation, we performed 1-D riverbed calculations during the entire rainy season. Parallel simulations with the runoff model were possible if the calculation period was set to 2006. However, we obtained discharge and water level data that were considered as boundary conditions in 1996, 1998, 1999 and 2000, and within these data, we found a high peak discharge event on August 2000. Thus, the year of 2000 was used for the riverbed variation calculations and the calculations were performed from 1 April to 30 September (183 days of calculations).

We performed 1-D riverbed variation calculations with a uniform sediment diameter. Specifically, this method employed the Ashida–Michiue empirical equation with a uniform sediment diameter (Ashida and Michiue, 1972):

$$\frac{q_{Bo}}{\sqrt{sgd^3}}=17\tau_*^{\frac{3}{2}}(1-\frac{\tau_{*c0}}{\tau_*})(1-\sqrt{\frac{\tau_{*c}}{\tau_*}}) \qquad [3]$$

where q_{B0} is the unit of bed load, s is the specific gravity of sediment in water (= σ/ρ-1, where σ is the density of soil particles (1.65g/cm^3) and ρ is the density of water (1.00 g/cm^3)), g is the acceleration of gravity, d is the diameter of sediment particles (0.1mm) and τ_* is the dimensionless tractive force (= u_*^2/sgd). The amount of flow up of sediment was estimated by using Itakura and Kishi's equation (Itakura and Kishi, 1980).

Cross sections for the calculations were set at every 300m from the confluence of the Sari River and Gowain River, and 31 cross sections were analyzed along the 9km length of the river (Figure 2d). The diameter of the soil particles was set as 0.1mm uniformly, and Manning roughness coefficient was set as 0.025s/m$^{1/3}$. Daily discharge and daily water level data, which were observed by the BWDB at the Jaflong observation site, were applied for boundary conditions (Figure 2c). Discharge was set at the upstream area of the river, and the water level was set at the downstream area of the river (Figure 3). The inflow sediment concentration was assumed as the equilibrium sediment concentration, and we also assumed river flows over the whole river width.

In regard to the initial condition of the riverbed, first, the lowest riverbed height was set to a uniform flow depth. Second, we checked the slope of the surrounding river terrain, and we set the values to 0.0013 for cross section Nos. 0-9, 0.007 for Nos.9-22 and 0.0019 for Nos.22-30.

2.4 Two-dimensional flood inundation model

The flood model used in this study was a two-dimensional (2-D) unsteady flow model based on the following shallow-water equations:

$$\frac{\partial h}{\partial t}+\frac{\partial M}{\partial x}+\frac{\partial N}{\partial y}=0 \quad [4]$$

$$\frac{\partial M}{\partial t}+\frac{\partial (uM)}{\partial x}+\frac{\partial (vM)}{\partial y}=-gh\frac{\partial H}{\partial x}-\frac{gn^2u\sqrt{u^2+v^2}}{h^{1/3}} \quad [5a]$$

$$\frac{\partial N}{\partial t}+\frac{\partial (uN)}{\partial x}+\frac{\partial (vN)}{\partial y}=-gh\frac{\partial H}{\partial y}-\frac{gn^2v\sqrt{u^2+v^2}}{h^{1/3}} \quad [5b]$$

where h is the water depth (m), M and N are the x- and y-direction fluxes (m^2/s), respectively, u and v are velocities in the x- and y-directions (m/s), respectively, H is the water level (m) and g is the acceleration due to gravity (m/s^2). To solve the equations, this method employed a leap-frog difference scheme with unstructured grids (Kawaike et al., 2000).

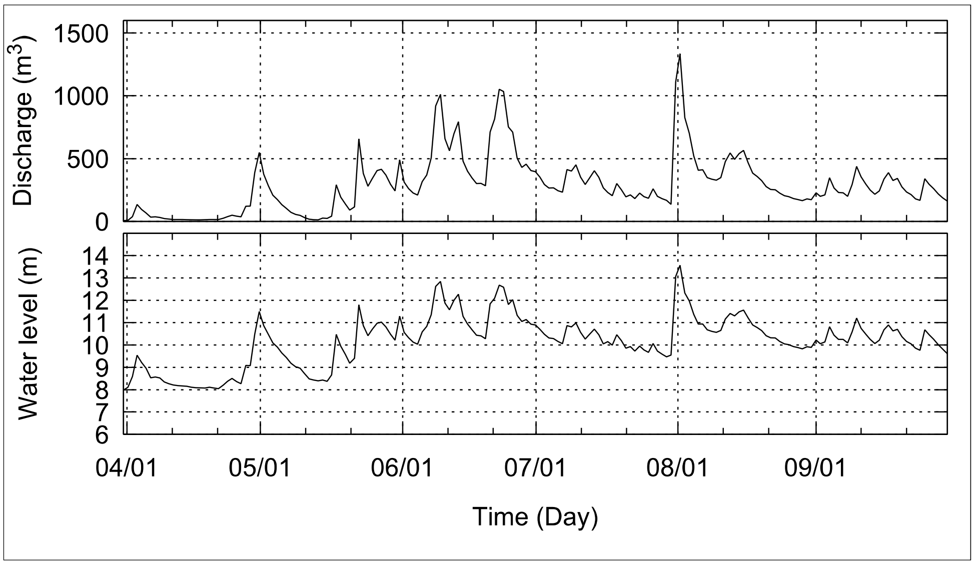

Figure 3. Observed discharge and water level.

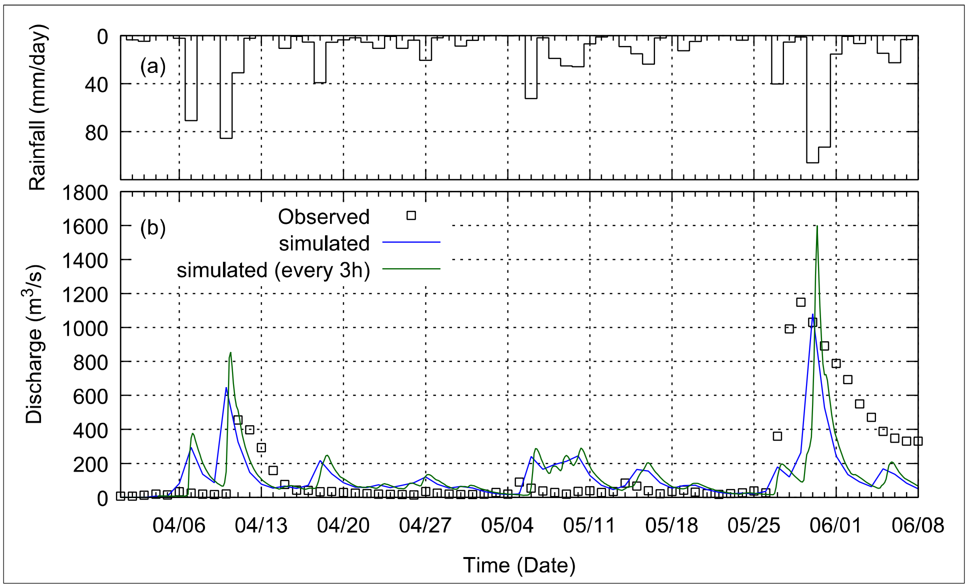

Figure 4. (a) Comparison of catchment accumulated rainfall (black line indicates daily observed rainfall that was considered uniformly, blue line indicates satellite rainfall that was considered and blue dash line indicates double satellite rainfall that was considered), (b) comparison of the satellite rainfall data from PERCIANN-CSS with the observed data collected at the Sylhet observation point (April–September 2006).

The 3-hourly discharge that was calculated by the runoff model was considered as the boundary condition of the upstream area. Outflow was calculated with Manning's equation. In regard to the Manning roughness coefficient, a value of 0.025s/m$^{1/3}$ was used in the river area and a value of 0.030s/m$^{1/3}$ was used in the other areas, which mainly consisted of tea gardens, residential areas and paddy fields.

In the selected study area, the Piyain River flows through the northwestern part of the region and the Sari–Gowain River flows through the southern part of the region. In this study, we did not consider flows from these rivers, and flood water that reached the surrounding rivers flowed out in a uniform flow.

The elevation was set by using SRTM1 data (30m grids). For the fitting of grid and elevation data, first, the topographic data were interpolated by using the inverse distance weighting (IDW) method into a 5m spatial resolution dataset. Then, each point that was located inside of the unstructured mesh was considered as an average value. In regards to the elevation in the river area, first, the elevation data that were calculated by the riverbed variation calculations were set at the centre of each cross section. Then, the elevation of each mesh was interpolated by using the nearest two points according to the IDW method.

3 RESULTS AND DISCUSSIONS

3.1 Validation of the runoff discharge

Figure 4 shows the validation results that were obtained by comparing the simulated daily discharge to the observed daily discharge. Simulation outputs were also generated every 3hours. In regards to the mean daily discharge, the simulation and observation results showed reasonably good agreement for high values of discharge. In general, the simulated data tended to underestimate the measured data. In terms of the overestimation, around 6 April 2006 and from mid-April to mid-May, the method used for the rainfall seemed to have played a role in the overestimation. In addition, at times, the simulated runoff was quicker than that of the observed runoff. Hence, in future research, we will need to adjust the parameters used for the soil layer to improve the accuracy of the results.

In regard to the discharge results that were put out every 3 hours, these data were fairly similar to the simulated daily discharge, but variations were detected around the time of peak discharge at the end of May. To simulate the variation of discharge during flash flooding, data with a higher time resolution would be better to use. While there are several observations sites within the study area (e.g., private sites within the tea gardens) that allow for high spatial resolution datasets, obtaining high temporal resolution datasets would be difficult.

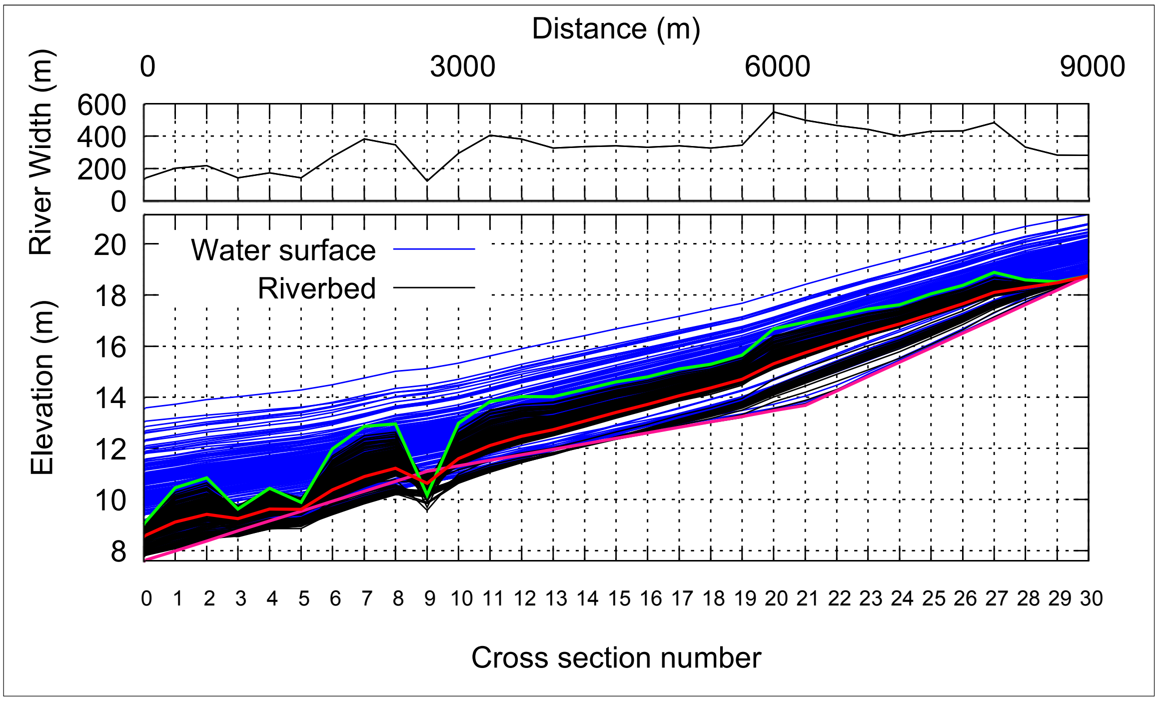

Figure 5. Results of the riverbed variation calculations. Green line indicates the peak aggradations, red line indicates the riverbed after the calculations and pink line indicates the initial riverbed condition.

3.2 Riverbed variation calculations

Figure 5 shows the simulation results for the riverbed variation during the entire rainy season in 2000. By comparing the initial riverbed condition to the riverbed condition at the end of the study period, a 1 m riverbed aggradations tendency was confirmed. This aggradations tendency was most pronounced when the river width was broad, and a degradation tendency was detected when the river width was narrow. In addition, the riverbed was lower at cross section 9 compared with the initial condition. The peak timing of the aggradations was observed at the same time as the peak discharge (1 August 2000). Maximum aggradation was observed at cross section 21, and the deposition depth was 3.02m compared to the initial condition. In reality, bank erosion along the river and slope failures in the mountainous area occurred, and these events contributed to the riverbed aggradations. For further research, we need to apply a distributed sediment runoff model to calculate the runoff sediment discharge due to slope failures. In addition, 2-D riverbed variation calculations need to be performed to consider the effects of bank erosion.

3.3 Flood inundation analysis

Figure 6 shows the validation results of the water level of the downstream boundary. In cases 2 and 3, the over-estimation due to riverbed aggradations was considered. However, the peak water level was reasonably simulated in all the cases.

Figure 7 shows the results of the flooding analysis. Inundated area was confirmed in each case, and the area amounted to 4.77km^2 for the case 1 (initial riverbed condition), 7.05km^2 for case 2 (riverbed after the calculations ended), and 12.41km^2 for case 3 (peak aggradations). Thus, these data suggested that riverbed aggradations had a substantial effect on the scale of the flood inundation. Furthermore, these results also highlighted the importance of sediment management within the river basin. In particular, to reduce the flood inundation risk, proactive counter measures need to be taken such as the dredging.

If additional parallel calculations of flood inundation and riverbed variation performed, the effects of riverbed changes on flood flows could be evaluated in more detail, and sediment diffusion to agricultural lands could also can be simulated.

Discerning the effect of riverbed aggradations was the first step of our research, and we will continue to collect data to validate the analyzed results. Furthermore, we would like to optimize the methods to evaluate the flood risk in future work.

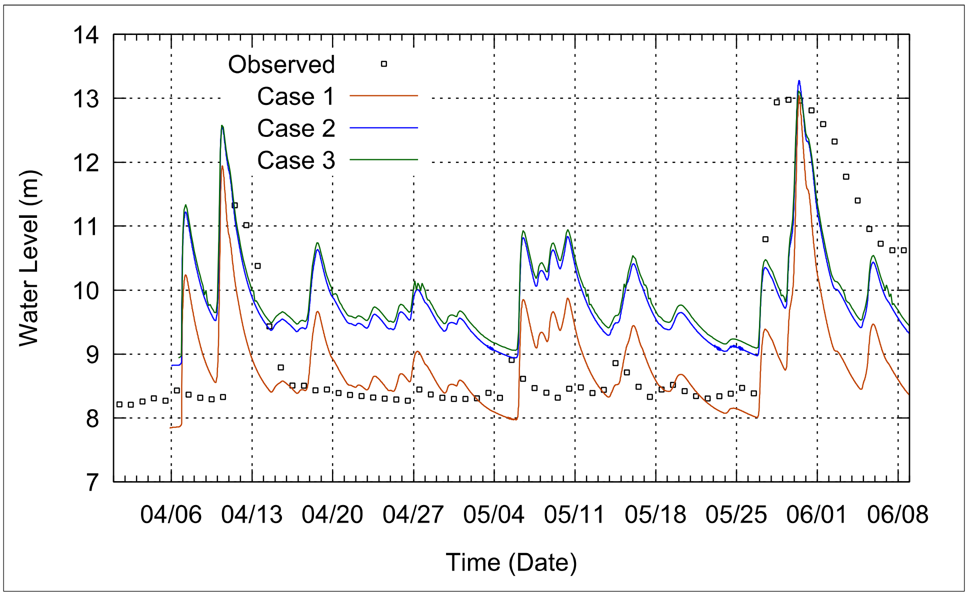

Figure 6. Validation results of the water level of the downstream boundary (simulated water levels were delineated from 6 April when the flood flow reached the downstream boundary).

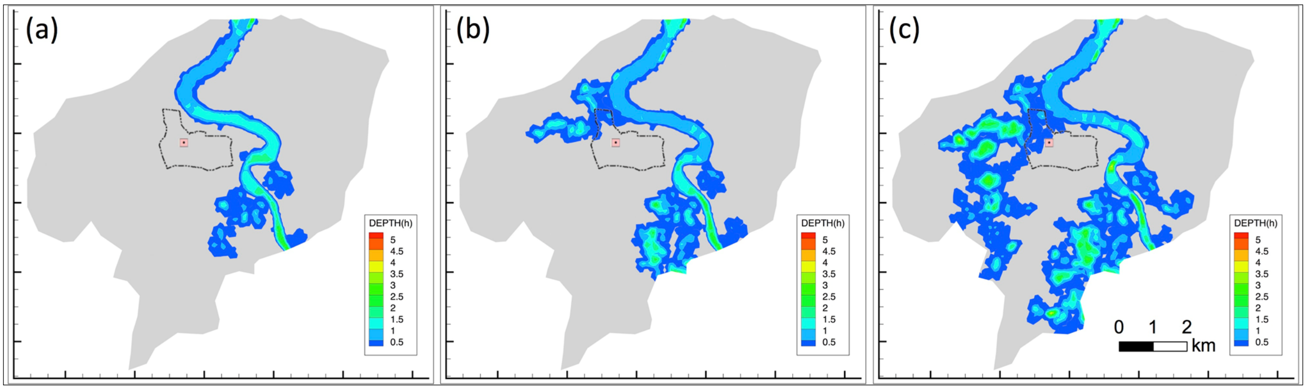

Figure 7. Results of the two-dimensional flood inundation analysis. (a) Case 1: initial riverbed condition, (b) case 2: riverbed after the calculations ended and (c) case 3: peak aggradations.

4 CONCLUSIONS

By using a 1-D riverbed variation calculation model, distributed runoff model, and a 2-D flood inundation model, we evaluated the effects of the riverbed aggradations on the scale of flooding in the Jaflong area of Bangladesh. Results showed that the condition of the riverbed has a pronounced effect on the scale of flooding, and these findings imply that sediment management may help to mitigate the flood risk. In this study, we encountered limitations in regards to the available datasets. Hence, the riverbed variation calculations and the flood analysis are performed with different terms and by different models. In order to perform a parallel analysis for the inundation and the riverbed variation, we will continue to collect data and conduct field measurements. For future research, conducting work on the following topics would be useful: 1) calibrate parameters of the runoff model in consideration of the land cover, land use and geology; 2) conduct field measurements to obtain the exact concentrations of sediment; 3) compile additional datasets of cross sectional data; and 4) produce hazard maps that can be used to protect the residents.

ACKNOWLEDGEMENTS

This study is funded by the JST/JICA SATREPS Program on Disaster Prevention/Mitigation Measures against Floods and Storm Surges in Bangladesh (PI: Dr. H. Nakagawa). In addition, this research project received much valued support from researchers at the Bangladesh University of Engineering and Technology (BUET) in terms of research assistance and field trip logistics. Datasets relating to infrastructure are provided by the Centre for Environment and Geographic Information Services (CEGIS).

REFERENCES

Ashida, K. & Michiue, M. (1972). Study on Hydraulic Resistance and Bed-Load Transport Rate in Alluvial Streams. *Proceedings of the Japan Society of Civil Engineers,* 1972(206), 59-69.

Central Ground Water Board, Ministry of Water Resources, Government of India (2012). *Aquifer Systems of Meghalaya*. Retrieved 2017/02/10, from http://cgwb.gov.in/AQM/Meghal aya.pdf.

Department of Agriculture, Government of Meghalaya (2016). *Soil*. Retrieved 2017/02/10, from http://www.megagriculture.gov.in/.

Ichikawa, Y., Murakami, M., Tachikawa, Y. & Shiiba, M. (2001). Development of a Basin Runoff Simulation System Based on a New Digital Topographic Model. *Journal of Japan Society of Civil Engineers,* 2001(691), 43-52.

Itakura, T. & Kishi, T. (1980). Open Channel Flow with Suspended Sediments. *Journal of the Hydraulics Division,* 106(8), 1325-1343.

Kawaike, K., Inoue, K. & Toda, K. (2000). Application of Unstructured Meshes to Inundation Flow Analysis in Urban Area. *Proceedings of Hydraulic Engineering*, 44, 461-466.

Oka, T. & Salehin, M. (1997). Numerical Simulation of Flood in Northeast Region of Bangladesh. *Proceedings of International Symposium of Natural Disaster Prediction and Mitigation*, 267-272.

Proceedings of the 37th IAHR World Congress
August 13 – 18, 2017, Kuala Lumpur, Malaysia

ADAPTING TO CLIMATE CHANGE THROUGH HOLISTIC RISK ASSESSMENT - THE PEARL APPROACH

ZORAN VOJINOVIC(1), ARLEX SANCHEZ(2), ALIDA ALVES(3), YARED ABEBE(4), NEILER MEDINA(5), OLE MARK(6), NINA STO. DOMINGO(7), SLOBODAN DJORDJEVIC(8), ALBERT CHEN(9), KATYA PYATKOVA(10), MARK PELLING(11), ARABELLA FRASER(12), JOERN BIRKMANN(13), LINDA SORG(14), JAUME AMOROS(15), NATASA MANOJLOVIC(16), PETER FROHLE(17), AMINEH GHORBANI(18), IGOR NIKOLIC(19), DONG-JIING DOONG(20)

(1,2,3,4,5) UNESCO-IHE, Westvest 7, 2611 AX Delft, The Netherlands,
z.vojinovic@unesco-ihe.org
(6,7) DHI, Horsolom, Denmark,
(8,9,10) University of Exeter, Exeter, UK,
(11,12) King's College London, London, UK,
(13,14) University of Stuttgart, Stuttgart, Germany,
(15) CETAQUA, Barcelona, Spain,
(16,17) TUHH, Hamburg, Germany,
(18,19) TUD, Delft, The Netherlands,
(20) National Cheng Kung University, Tainan, Taiwan

ABSTRACT

Coastal floods are one of the most dangerous and harmful natural hazards affecting urban areas adjacent to shorelines. The present paper discusses the FP7-ENV-2013 EU funded PEARL (Preparing for Extreme And Rare events in coastal regions) project which brings together world leading expertise in both the domain of hydro-engineering and risk reduction and management services to pull knowledge and practical experience in order to develop more sustainable risk management solutions for coastal communities focusing on present and projected extreme hydro-meteorological events. The main goal of PEARL is to develop adaptive, socio technical risk management measures and strategies for coastal communities against extreme hydro-meteorological events minimizing social, economic and environmental impacts and increasing the resilience of Coastal Regions in Europe. PEARL adopts a holistic risk management approach, and uses different tools which range from complex adaptive system (CAS) models to numerical 1D/2D models and 3D animations. The results obtained suggest that a variety of data and methods is needed to reveal different insights of risk and its root causes. The risk assessment framework developed is holistic as it attempts to take into consideration a variety of root causes of vulnerabilities and risk as well as multiple impacts (e.g., direct and indirect damages, public health, traffic and other urban infrastructure disruption).

Keywords: Flood risk; flood management; hazards; vulnerability; holistic approach.

1 INTRODUCTION

Out of all natural disasters, floods are regarded as one of the most dangerous and harmful. Climate change combined with rapid urbanization and poor governance is likely to make the current situation even more disastrous (Price and Vojinovic, 2008; Mynett and Vojinovic, 2009; Vojinovic and van Teeffelen, 2009).

As discussed in Vojinovic (2015), the purpose of the flood risk assessment is to undertake a systematic investigation of root causes and define a set of appropriate intervention measures that can minimize (if not completely eliminate) its negative impacts. Traditionally, the use of physically-based computational modelling coupled with GIS mapping has been very valuable in this regard (Vojinovic et al., 2006a; Vojinovic et al., 2006b; Vojinovic et al., 2008; Vojinovc and Abbott, 2012; Vojinovic et al., 2014; Alves et al., 2016). However, there are numerous issues associated with data processing, selection of models, modelling and GIS mapping techniques that can affect accuracy and quality of flood modelling results (Abbott et al., 2006; Vojinovic et al., 2006a; Abdullah et. al., 2009; Vojinovic and Tutulic, 2009; Abdullah et. al., 2011a; Abdullah et. al., 2011b; Vojinovic et al., 2011; Vojinovic et al., 2012; Meesuk et. al., 2015).

The purpose of the present paper is to describe the framework and its supporting tools which have been developed within the FP7-ENV-2013 EU funded PEARL (Preparing for Extreme And Rare events in coastal regions, www.pearl-fp7.eu) project to support assessment of flood risk. The framework developed can be regarded as holistic as it attempts to take into consideration multiple root causes of vulnerabilities and impacts (e.g., direct and indirect damages, public health, traffic and other urban infrastructure disruption, emergency services and institutional behavior). To achieve its objectives, PEARL project has been structured around eight work packages over a period of four years (2014 - 2018). Forming the basis of the work are six European case studies covering different coastal regions and several International case studies.

2 FLOOD RISK ASSESSMENT

The literature to date indicates that risk assessment frameworks differ from one application to another, and depending on the background of researchers, some place they emphasis either on estimation of hazards or on vulnerabilities. Also, some of them attempt to involve stakeholders in their risk analysis work while some other researchers base their analysis only on estimation of direct damages.

Some authors performed multi-risk assessment at a single location (Greiving, 2006; Grünthal et al., 2006; Marzocchi et al., 2009). A national-scale flood risk assessment methodology for England and Wales has been presented in Hall et al. (2003). In Koks et al. (2015), a flood risk assessment methodology at the household level has been presented. Meyer et al. (2009) designed a multi criteria risk mapping approach which encompasses economic, social and environmental flood risk factors at the river basin scale. Kubal et al. (2009) also used the multi criteria risk mapping approach at a city scale.

In the present paper, we discuss the holistic risk assessment framework which has been developed within the PEARL project (www.pearl-fp7.eu).

3 PEARL RISK ASSESSMENT FRAMEWORK

3.1 Introduction

One of the key assumptions in the PEARL holistic risk assessment framework is that disasters related to hydro-meteorological events (e.g. extreme winds, storm surges, coastal and estuarine floods) were interconnected and interrelated with both human activities and natural processes (Figure 1). This assumption in turn requires holistic approaches to help us understand complexity of interrelated processes in order to design and develop adaptive risk management approaches that minimize social and economic losses and environmental impacts plus increases resilience to such events. Therefore, the holistic risk assessment framework was based on the following three premises:

- First, risk management is a sociotechnical process, which cannot be studied by separating social and technical processes (i.e., parts) and designing them in isolation;
- Second, the relationships between the parts are mutual, emergent, dynamic and nonlinear and are guided by the self-organizing capacities of each part and the (unpredictable) dynamics of their coevolution;
- Third, the process of strengthening any kind of flood risk mitigation measure (such as forecasting, prediction and early warning capabilities) should be understood and studied within the context of the larger flood management process which depends on interactions with other sub-processes at different levels.

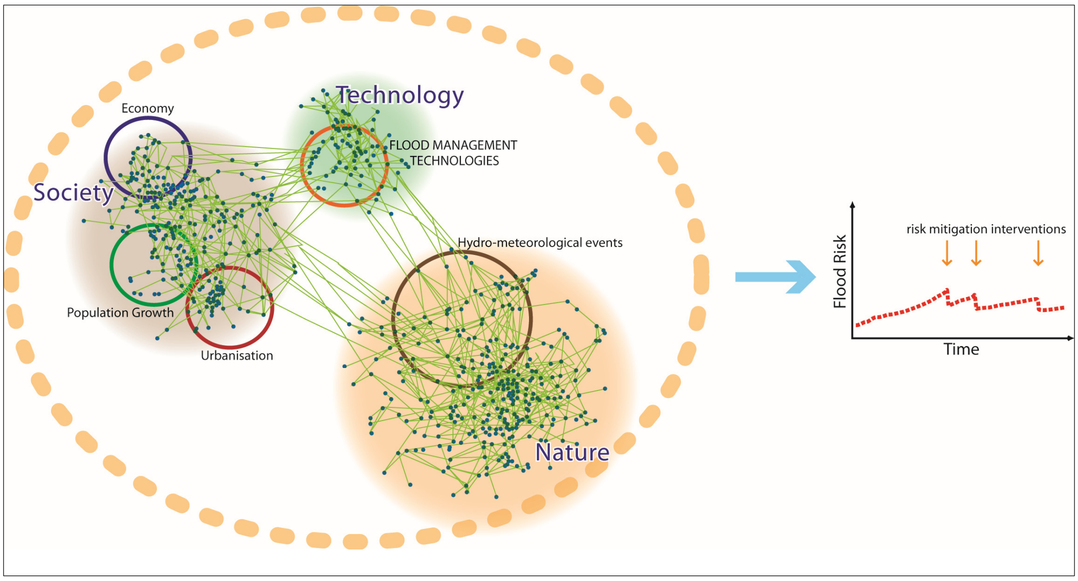

Figure 1. Formation and propagation of risk is a result from the co-evolutionary nonlinear process between the ever changing social, technical and natural processes. Dots represent sub-processes and activities and lines represent their interactions (Source: Vojinovic 2015).

In what follows, we describe the key aspects of the PEARL holistic risk assessment framework.

3.2 Root cause analysis

The root cause analysis is based on FORIN approach which is in essence a qualitative method that incorporates systematic, probing and dispassionate investigations to address how and why decisions were made and management options were chosen. The main aspects of concern were disaster risk research and understanding of the reasons for growth in public vulnerability and wider exposure, integrated and participatory research involving wide range of disciplines and specialists, precise identification and structuring of responsibilities in the creation and/or the prevention of the growth of vulnerability and exposure and new and better ways of communicating scientific understanding about disaster risk reduction. The data used for this kind of investigation was collected through desk studies and interviews. The desk study includes review of documents relating to the disaster such as newspapers, academic papers, study reports and government publications (Fraser et. al., 2016). The work undertaken leads to identification of potential actors whose regulations, policies or actions (i.e., "behaviors") have an influence on the creation and propagation of vulnerabilities. These actors were then considered as agents in the Agent Based Modelling (ABM) work.

3.3 Vulnerability assessment

Vulnerability usually refers to the conditions and capacities that make a system or an individual susceptible to harm as a result of a hazard. In PEARL, vulnerability assessments is to investigate four dimensions which are physical, social, economic and cultural (Vojinovic et. al., 2016a; 2016b) as in Figure 2.

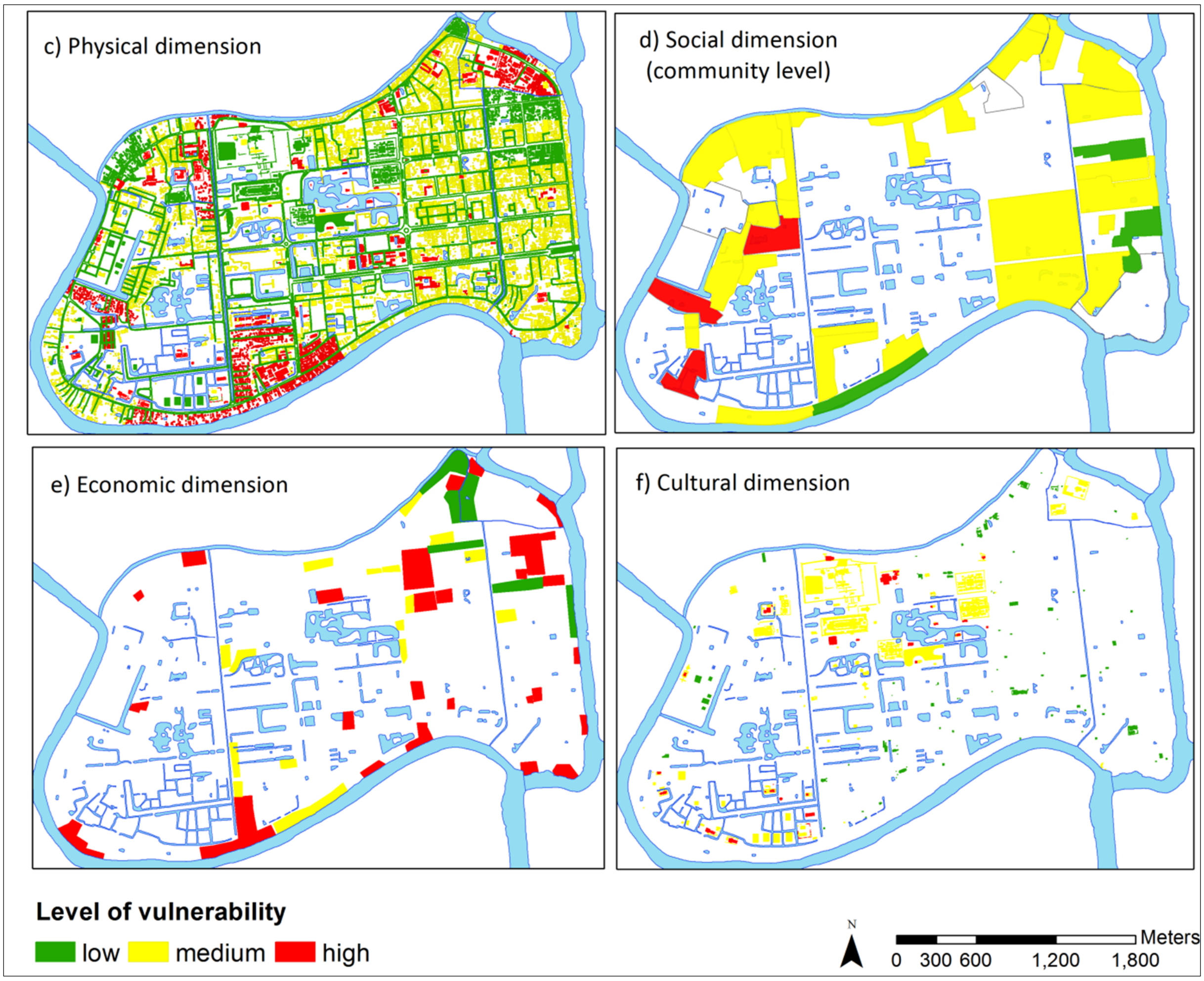

Figure 2. Example of vulnerability maps developed for Ayutthaya Island (Thailand), see also Vojinovic (2015) and Vojinovic et al. (2016a; 2016b).

3.4 Assessment of hazards

In PEARL, hazards were assessed from the numerical modelling work. The numerical modelling framework for hazard assessment is given in Figure 3.

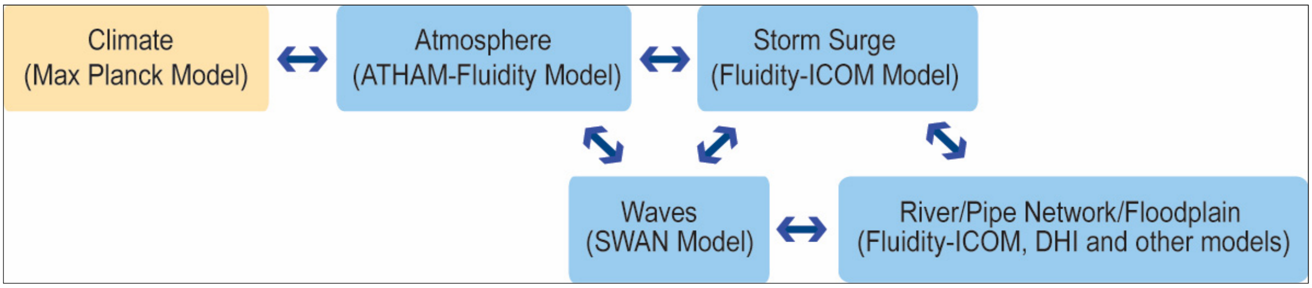

Figure 3. The numerical modelling framework for hazard assessment.

The numerical modelling framework starts with climate models which provide forcing into the atmospheric, coastal and catchment processes to define characteristics of potential hazards and to plan improvement measures accordingly. Typical hazard parameters were flood depths, velocities and flood durations as in Figure 4.

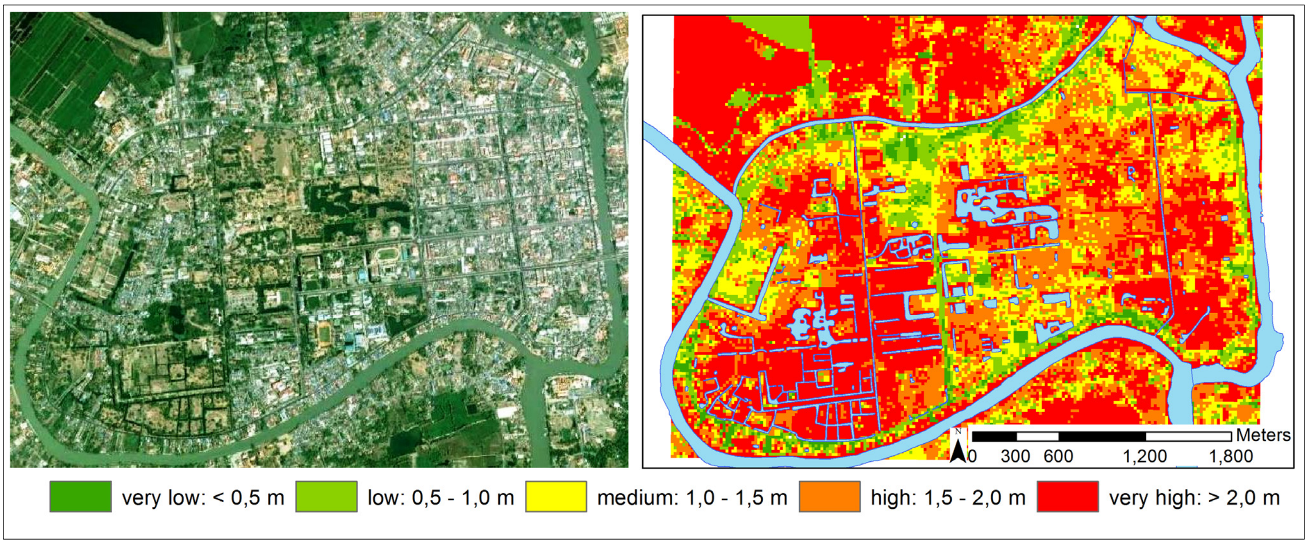

Figure 4. Example of a flood hazard map developed for Ayutthaya Island (Thailand): (left) satellite image of the study area, (right) flood hazard map of the study area (see also Vojinovic et al., 2016a; 2016b; Vojinovic 2015).

4 ASSESSMENT OF IMPACTS

The following key impacts are considered which were assessment of damages, public health impacts, impacts on cultural properties and impacts on other urban infrastructures. Assessment of direct tangible damages had been computed on the basis of depth-damage curves derived from local surveys. In addition to direct tangible damages, PEARL project also addresses the so-called indirect tangible damages. These damages were related to capital and goods, in contrast of the assets and stocks that were considered as direct tangible damages. In terms of the public health impacts, quantitative assessment of the health impacts of urban flooding was performed using a combination of hydrodynamic and water quality flood modelling (with advection-dispersion process computation module) and Quantitative Microbial Risk Assessment (QMRA) methodology. Furthermore, PEARL project also addresses impacts on other urban infrastructure through the so-called cascading effects. A simple example of a cascading effect due to a flood event is the situation where at certain locations of the flood water depth reaches certain depth, the low laying installations of the electricity network (e.g., transformers) which are below this level will be affected and cause outages in the areas connected to these substations. The cascading impacts on electricity, telecommunication, transportation (Pyatkova et al., 2015) and water/wastewater services have been taken into consideration. The final results were presented with different means. An example of presentation of combined results is the spider chart given in Figure 5. The framework also includes estimation of the Flood Resilience Index (Batica et al., 2013).

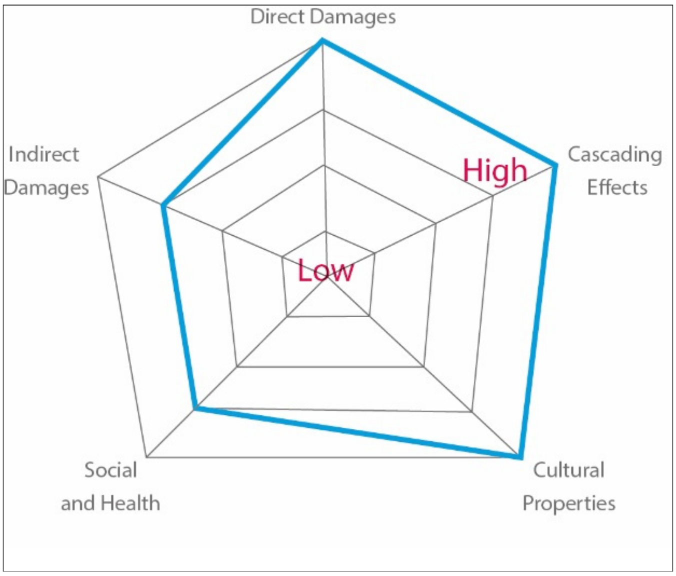

Figure 5. Example of a spider chart which combine assessment of different impacts and vulnerabilities.

5 CONCLUSIONS

This paper presents a holistic risk assessment framework developed within the FP7-ENV-2013 EU funded PEARL (Preparing for Extreme and Rare events in coastaL regions, www.pearl-fp7.eu) project which aims to address various aspects of flood risk. The framework includes a comprehensive assessment of root causes of vulnerabilities and risk. It also addresses multiple impacts such as direct and indirect damages, public health, traffic and impacts to urban infrastructure services. The work performed highlights the need for addressing the risk from a holistic perspective through combination of quantitative and qualitative data and methods which can range from observations, measurements, model simulations, and economic analysis to signs, statements, experiences, feelings, and perceptions. It also promotes a combination of analytical thinking with sharp analysis of social, ethical, and wider ecological considerations, while utilizing a variety of means to express risk from different perspectives. Different aspects of the risk assessment work have been demonstrated on six European and three International case study areas (www.pearl-fp7.eu).

ACKNOWLEDGEMENTS

The research work presented here has received funding from the European Union Seventh Framework Programme (FP7/2007-2013) under Grant agreement n° 603663 for the research project PEARL (Preparing for Extreme And Rare events in coastaL regions). The research and its conclusions reflect only the views of the authors and the European Union is not liable for any use that may be made of the information contained herein.

REFERENCES

Abbott, M.B., Tumwesigye, B.M. & Vojinovic, Z. (2006). The Fifth Generation of Modelling in Hydroinformatics, *In Proc. of 7th International Conference on Hydroinformatics*, Acropolis, Nice, France, 2091-2098.

Abdullah, A.F., Vojinovic, Z. & Price, R.K. (2011a). Improved Methodology for Processing Raw LIDAR Data to Support Urban Flood Modelling—Accounting for Elevated Roads and Bridges. *Journal of Hydroinformatics*, 14(2), 253-269.

Abdullah, A.F., Vojinovic, Z. & Price, R.K. (2011b). A Methodology for Processing Raw LIDAR Data to Support 1D/2D Urban Flood Modelling Framework. *Journal of Hydroinformatics*, 14(1), 75-92.

Abdullah, A., Rahman, A. & Vojinovic, Z. (2009). Lidar Filtering Algorithms for Urban Flood Application: Review on Current Algorithms and Filters Test. *Laserscanning*, 38, 30–36.

Alves, A., Sanchez, A., Vojinovic, Z., Seyoum, S., Babel, M. & Brdjanovic, D. (2016). Evolutionary and Holistic Assessment of Green-Grey Infrastructure for CSO Reduction, *Water*, 8(9), 402.

Batica, J., Gourbesville, P. & Hu, F. (2013). Methodology for Flood Resilience Index, *International Conference on Flood Resilience: Experiences in Asia and Europe*, Exeter, United Kingdom.

Fraser, A., Paterson, S. & Pelling, M. (2016). Developing Frameworks to Understand Disaster Causation: from Forensic Disaster Investigation to Risk Root Cause Analysis. *Journal of Extreme Events*, 3(2), 1-21.

Greiving, S. (2006). *Measuring Vulnerability to Natural Hazards: Towards Disaster Resilient Societies.* United Nations University Press, Tokyo, Japan, Chapter C11, 210–226

Grünthal, G., Thieken, A.H., Schwarz, J., Radtke, K.S., Smolka, A. & Merz, B. (2006). Comparative Risk Assessments for the City of Cologne – Storms, Floods, Earthquakes. *Natural Hazards*, 38(1-2), 21–44.

Hall, J.W., Dawson, R.J., Sayers, P.B., Rosu, C., Chatterton, J.B. & Deakin, R. (2003). A Methodology for National-Scale Flood Risk Assessment, *Proceedings of the ICE - Water and Maritime Engineering*, 156(3), 235–248.
Koks, E.E., Jongman, B., Husby, T.G. & Botzen, W.J.W. (2015). Combining Hazard, Exposure and Social Vulnerability to Provide Lessons for Flood Risk Management. *Environmental Science & Policy*, 47, 42–52.
Kubal, C., Haase, D., Meyer, V. & Scheuer, S. (2009). Integrated Urban Flood Risk Assessment - Adapting a Multicriteria Approach to a City. *Natural Hazards and Earth System Sciences*, 9(6), 1881–1895.
Marzocchi, W., Mastellone, M.L., Ruocco, A.D., Novelli, P., Romeo, E. & Gasparini, P. (2009). *Principles of Multi-Risk Assessment: Interaction amongst Natural and Man-Induced Risks*. Office for Official Publications of the European Communities, Luxembourg.
Meesuk, V., Vojinovic, Z., Mynett, A. & Abdullah, A.F. (2015). Urban Flood Modelling Combining Top-View Lidar Data with Ground-View SfM Observations. *Advances in Water Resources*, 75, 105–117.
Meyer, V., Haase, D. & Scheuer, S. (2009). Flood Risk Assessment in European River Basins—Concept, Methods, and Challenges Exemplified at the Mulde River. *Integrated Environmental Assessment and Management*, 5(1), 17–26.
Mynett, A. & Vojinovic, Z. (2009). Hydroinformatics in Multi-Colours—Part Red: Urban Flood and Disaster Management. *Journal of Hydroinformatics*. 2009, 11(3-4), 166–180.
Price, R.K. & Vojinovic, Z. (2008). Urban Flood Disaster Management. *Urban Water J*ournal, 5(3), 259–276.
Pyatkova, K., Chen, A.S., Djordjević, S., Butler, D., Vojinović, Z., Abebe, Y.A. & Hammond, M.J. (2015). Flood Impacts on Road Transportation using Microscopic Traffic Modelling Technique, *SUMO User Conference 2015*.
Vojinovic, Z., Bonillo, B., Chitranjan, K. & Price, R.K. (2006a). Modelling Flow Transitions at Street Junctions with 1D and 2D Models. *In Proceedings of 7th International Conference on Hydroinformatics*, Nice, France, (1), 377-384.
Vojinovic, Z., Solomatine, D.P. & Price, R.K. (2006b). Dynamic Least-Cost Optimisation of Wastewater System Remedial Works Requirements. *Water Science and Technology*, 54(6-7), 467–475.
Vojinovic, Z. & Van Teeffelen, J. (2007). An Integrated Stormwater Management Approach for Small Islands in Tropical Climates. *Urban Water*, 4(3), 211–231.
Vojinovic, Z., Sanchez, A. & Barreto, W.J. (2008). Optimising Sewer System Rehabilitation Strategies between Flooding, Overflow Emissions and Investment Costs. *In Proceedings of 11th International Conference on Urban Drainag*e, 31.
Vojinovic, Z. & Tutulic, D. (2009). On the Use of 1D and Coupled 1D-2D Approaches for Assessment of Flood Damages in Urban Areas. *Urban Water*, 6(3), 183–199.
Vojinovic, Z., Seyoum, S.D., Mwalwaka, J.M. & Price, R.K. (2011). Effects of Model Schematization, Geometry and Parameter Values on Urban Flood Modelling. *Water Science and Technology*, 63(3), 462–467.
Vojinovic, Z., Seyoum, S., Salum, M.H., Price, R.K., Fikri, A.F. & Abebe, Y. (2012). Modelling Floods in Urban Areas and Representation of Buildings with a Method based on Adjusted Conveyance and Storage Characteristics. *Journal of Hydroinformatics*, 15(4), 1150–1168.
Vojinovic, Z. & Abbott, M.B. (2012). *Flood Risk and Social Justice: From Quantitative to Qualitative Flood Risk Assessment and Mitigation*. International Water Association, London, UK.
Vojinovic, Z., Sahlu, S., Seyoum, S., Sanchez, A., Matungulu, H., Kapelan, Z. & Savic, D. (2014). Multi-Objective Rehabilitation of Urban Drainage Systems under Uncertainties. *Journal of Hydroinformatics*, 16(5), 1044–1061.
Vojinovic, Z. (2015). *Flood Risk: The Holistic Perspective - From Integrated to Interactive Planning for Flood Resilience*. International Water Association, London, UK.
Vojinovic, Z., Hammond, M., Golub, D., Hirunsalee, S., Weesakul, S., Meesuk, V., Medina, N., Sanchez, A., Kumara, S. & Abbott, M. (2016a). Holistic Approach to Flood Risk Assessment in Areas with Cultural Heritage: A Practical Application in Ayutthaya, Thailand. *Natural Hazards*, 81(1), 589–616.
Vojinovic, Z., Keerakamolchai, W., Weesakul, S., Pudar, R.S., Medina, N.P. & Alves, A. (2016b). Combining Ecosystem Services with Cost-Benefit Analysis for Selection of Green and Grey Infrastructure for Flood Protection in a Cultural Setting, *Environments*, 4(3), 1-16.

Proceedings of the 37th IAHR World Congress
August 13 – 18, 2017, Kuala Lumpur, Malaysia

SIMPLIFIED PHYSICALLY-BASED MODELING OF LEVEE BREACH ON SUTTER BYPASS CHANNEL

WEIMING WU[1]

[1] Department of Civil and Environmental Engineering, Clarkson University, Potsdam, NY 13699, USA
wwu@clarkson.edu

ABSTRACT

A series of storms caused record flows throughout the California Central Valley in early January 1997. High flows on the Sacramento River activated overflow weirs, diverting water into the Sutter Bypass Channel. The southwest levee of Sutter Bypass failed due to piping or seepage, shortly after the peak flow passed on January 4, 1997. The final breach was about 274 m wide, and approximately 130 km^2 of the Meridian Basin was inundated. A simplified physically-based dam and levee breach model, DLBreach, is used in this study to simulate the Sutter Bypass levee breaching process. The time series of water levels in the Sutter Bypass Channel at the breach location calculated using HEC-RAS are imposed as the headwater condition for the present breach modeling. The volume-elevation curve of the Meridian Basin is obtained by using the 1-foot contour lines generated from a Lidar data collection in 2008. In order to account for the effect of the roads, the basin volume-elevation curve is modified by considering that the flood water filled in the zone below the breach first and then overtopped the roads and entered the remaining zones. The representative soil in the levee body was silty sand (SM) or clayey sand (SC), and the soil erodibility k_d is estimated at 14.5 cm^3/N·s. The model reproduces well the levee breach widening process. The calculated final breach width is 270.4 m, which agrees well with the measured value.

Keywords: Levee breach; simplified physically-based model; piping; flood; sutter bypass channel.

1 INTRODUCTION

A series of storms dumped warm, heavy rains into a nearly double than average snow pack in the Sierra Nevada Mountains in late December 1996, and caused record flows throughout the California Central Valley in early January 1997. High flows on the Sacramento River activated overflow weirs, diverting water into the Sutter Bypass channel (Figure 1). Shortly after the peak flow passed on January 4, 1997, the southwest levee of Sutter Bypass failed suddenly, inundating approximately 130 km^2 of the Meridian Basin. Virtually every facility in the basin was destroyed or damaged, including nearly 100 homes and a school standing in 1.2 m of water (Sutter County, CA, 2015).

The Sutter Bypass Channel levee breach was one of the many similar events occurred all over the world. Mitigation and control of such flood disasters has been a challenging but important task for all related agencies, engineers and scientists. Numerical modeling of earthen embankment breaches is one key component of the flood mitigation strategies and technologies. A number of earthen embankment breach models have been reported in the last decades. ASCE/EWRI task committee (2011) classifies the earthen embankment breach models into parametric, simplified, and detailed physically-based models. The detailed models include one-, two- and three-dimensional numerical models. However, because of data limits, most of the earthen embankment breach models have been developed for dam breach or tested only using dam breach data. Levee is one type of the earthen embankments, but has different characteristics from others such as dam. Dam breach is usually controlled by only the upstream reservoir water, but levee breach is controlled by both the upstream river flow and the downstream receiving water body. Levee breach has been studied much less than dam breach. It is not confident to apply a tested dam breach model to simulate a levee breach. Thus, it is sorely needed to collect experimental and field data of levee breach and test the levee breach models.

After the Sutter Bypass Channel levee breach, USACE (US Army Corps of Engineers) Sacramento District (1997), California Flood Emergency Action Team (1997) and Sutter County, among other agencies and institutions, repaired the broken levee. They collected data for the breach geometry, levee structure, soil characteristics, and so on. Risher and Gibson (2016) used the hydrodynamic model HEC-RAS to simulate the January 1997 flood event in the Sacramento River system. All these efforts have led to a comprehensive data set for a field case study of levee breach. The present study aims to apply and test a simplified physically-based earthen embankment breach model DLBreach (Wu, 2013, 2016) in the simulation of the Sutter Bypass Channel levee breach process.

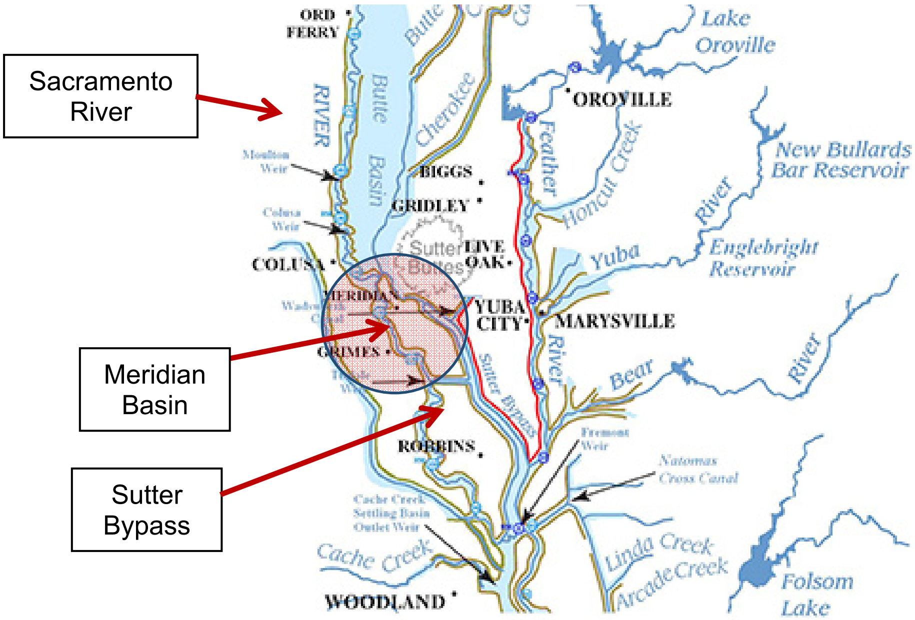

Figure 1. Map of study area (http://www.spk.usace.army.mil/Missions/Civil-Works/Sutter/).

2 BREACH MODEL USED

DLBreach is a simplified physically-based Dam/Levee Breach model developed by Wu (2013, 2016). It can simulate the breaching processes of homogenous and composite earthen embankments due to overtopping and piping in inland and coastal contexts. The model considers the one-way breach of inland dam and levee by unidirectional flows, and the two-way breach of coastal and estuarine levee and barrier, in which flow may reverse. The piping breach model was used in the present study.

DLBreach approximates the piping breach as a flat pipe with rectangular cross-section shown in Figure 2, until the pipe top collapses, and then overtopping takes place. The piping flow was calculated using the orifice flow equation:

$$Q = A\sqrt{\frac{2g\left(z_s - \max(z_{bp}, z_t)\right)}{K_u + K_d + fL/(4R)}} \qquad [1]$$

where Q = breach flow discharge, A = cross-sectional area of the breach flow, g= gravitational acceleration rate, z_{bp} = elevation of pipe centerline referring to the embankment bottom, L = breach length, z_s = headwater level, z_t = tailwater level, K_u and K_d = local head loss coefficient due to contraction at the pipe entrance and outlet, R = hydraulic radius of the breach cross-section, and f = Darcy-Weisbach friction factor.

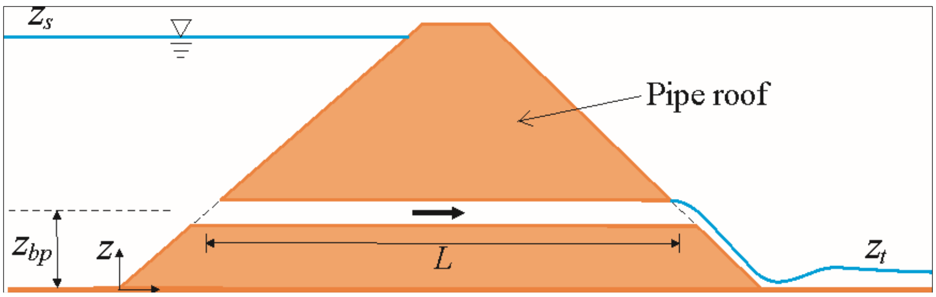

Figure 2. Longitudinal section of piping breach.

The model approximates the overtopping breach cross-section as a trapezoid, and the breach longitudinal section as a flat top connected with a head cut (vertical drop) or a straight slope for cohesive and non-cohesive homogeneous embankments, respectively. For composite embankment with a clay core, the downstream becomes two straight slopes along the core and shoulder after the core was exposed. After the piping phase is finished, the overtopping phase was divided into two stages. The first stage was the intensive breaching or erosion stage, in which the breach flow was supercritical, controlled by upstream. The second stage was the general breach evolution stage, in which the flow was subcritical, controlled by downstream or both upstream and downstream. In the first stage, the breach flow was calculated using the weir flow equation:

$$Q = k_{sm}\left(c_1 bH^{1.5} + c_2 mH^{2.5}\right) \quad [2]$$

where $H = z_s - z_b$, z_b = elevation of breach bottom, b = bottom width of the breach, m = side slope of the breach, $c_1 = 1.7$, $c_2 = 1.3$, and k_{sm} = submergence correction for tailwater effects.

In the second stage, the overtopping breach flow was calculated using the Keulegan equation:

$$z_s - z_t = \left(\frac{2gn^2L}{R^{4/3}} + \lambda_{en} + \lambda_{ex}\right)\frac{Q|Q|}{2gA^2} \quad [3]$$

where λ_{en} and λ_{ex} = local head loss at the breach entrance and exit, and n = Manning's roughness coefficient.

A non-equilibrium total-load transport model and a cohesive sediment erosion model were adopted for non-cohesive and cohesive embankment erosion, respectively. The time-averaged head cut migration rate was determined using the energy-based formula of Temple (1992). In the present study, the cohesive sediment erosion model was used, and the erosion rate, $d\varepsilon/dt$, was determined using the following equation:

$$\frac{d\varepsilon}{dt} = k_d\left(\tau_b - \tau_c\right) \quad [4]$$

where τ_b = boundary shear stress, τ_c = critical shear stress, and k_d = erodibility coefficient. The boundary shear stress was calculated with

$$\tau_b = \frac{\rho g n^2 Q^2}{A^2 R^{1/3}} \quad [5]$$

where ρ = water density.

Stabilities of the side slope, pipe top, head cut and clay core were analyzed by comparing the driving and resistance forces. A planar slope stability analysis model was developed to find the steepest stable slope and its corresponding failure slope, and then set the breach side slope as the average of these two. The model allows subbase erosion and incomplete breach. It can consider breaching at one side or in the middle of embankment length.

DLBreach was able to handle dam and levee breaches by adopting various routing algorithms for head and tail water levels. For dam breach, the reservoir water level was determined by using the water balance equation. For levee breach, the upstream water level can be set as the measured time series or calculated using another hydrodynamic model. The downstream water level was given as measured time series, or determined by assuming a uniform channel flow or solving the water balance equation for the receiving water body such as bay or lake. In the present study, the water level in the Meridian Basin was determined using the water balance equation:

$$\frac{dV}{dt} = A_s\frac{dz_t}{dt} = Q_{\text{in}} + Q \quad [6]$$

where V = volume of water in the basin, A_s is the surface area of the basin water, and Q_{in} is the inflow from other sources to the basin.

DLBreach considers surge overflow and wave overtopping discharge, wave setup, wind setup, and longshore sediment transport in cases of coastal levee and barrier breaches.

DLBreach has been extensively tested by using 50 sets of dam breach data and 4 sets of levee/barrier breach data from laboratory experiments and field case studies (Wu, 2016). The calculated peak breach discharges, breach widths, and breach characteristic times agree generally well with the measured data. It had been also compared with other embankment breach models, such as NWS BREACH and HR BREACH, and demonstrated to have more capabilities (Zhong et al., 2016).

3 THE 1997 SUTTER BYPASS LEVEE BREACH PROCESS

The Sutter Bypass Channel levee breach occurred shortly after the peak flow passed on January 4, 1997. No problems or seepage were noted at 5:00pm, but the breach was observed and reported by 6:30 pm (Risher and Gibson, 2016). The breach grew rapidly, reaching 30 m in an hour and 150 m by 1:00 am (USACE Sacramento District, 1997; Risher and Gibson, 2016). Aerial photos in the next morning show a breach over 200 m wide and still growing (California Flood Emergency Action Team, 1997), see Figure 3. The levee crest was a few meters higher than the river water at the time of breach, indicating the failure was due to piping or seepage. In the following day (Jan 5, 12:00 pm), the levee at the south end of the basin was cut to allow the water to return to the Bypass. This engineered relief breach eventually grew into a full breach (Figure 4). On the evening of 6 January large rip rap stones were dumped on both sides of the levee breach to prevent further erosion (Risher and Gibson, 2016). The final breach was about 274 m. The breach bottom reached about 4 m below the levee base.

Figure 3. Photo of Sutter Bypass levee breach (http://ww3.hdnux.com/photos).

Figure 4. Relief cut of the levee at the south end of the Meridian Basin developed to a full breach (Photo taken three weeks after the breach) (http://www.water.ca.gov/historicaldocs/irwm/feat-1997/jand1.html).

4 LEVEE, SOIL AND BASIN CONDITIONS

The levee was built from dredge spoils in the early 1900s (Risher and Gibson, 2016). It was placed wet of optimum and received little compaction. In 1940 the basin was flooded and the landside of the levee was damaged by extensive erosion. The levee was raised and landside repaired using borrow material from the Sutter Bypass. The levee surface material is mostly clay while deeper materials include more silt and sand. This likely left the original levee more pervious than the repair. In 1955 and 1958 boils, ground heaving, and excessive seepage were observed nearby prompting more than 3 km of repairs. The 1997 breach site was just upstream of the 1958 repair work. The soil layer structures were estimated using boring information, as shown in Figure 5 (Paul Risher, 2016, personal communication). The representative soil in the levee body was silty sand (SM) or clayey sand (SC), considering piping as the breach mode.

The levee embankment height was 6.96 m, and crest width was 6.098 m. The riverside (upstream) slope was 0.303:1 (V/H), and the landside (downstream) slope was 0.357:1. The simulation using DLBreach here assumes an initial pipe of 0.15 m high and wide, located at 0.46 m above the levee toe. The orifice flow equation [1] was used to compute the piping flow discharge at the piping stage. The broad-crested weir equation [2] was used for the intensive formation period where supercritical flow is expected. The Keulegan equation [3] was used for the general evolution period, in which the flow may be subcritical and tailwater effect exists. The entrance head loss coefficient was set as 1.0 in the Keulegan equation.

Cohesive sediment erosion model was used in this test case. The soil was assumed to have a diameter of 0.1 mm, porosity of 0.4, clay content of 5%, cohesion of 10 kPa, and internal friction angle of 18°. The critical shear stress for erosion was set as 0.15 Pa. The soil erodibility k_d was calibrated as 14.5 $cm^3/N\cdot s$ by comparing the calculated and measured breach widths. This k_d value is larger than the value 10.3 $cm^3/N\cdot s$ measured by Hanson et al. (2005) for SM soil. A Manning's n of 0.016 was used. A maximum subbase erosion of about 4 m was observed. Because DLBreach approximates the breach cross-section as a trapezoid, the subbase erosion limit was set as 2 m in the simulation to represent the average bottom elevation.

The volume versus elevation, V(z), curve of the Meridian Basin is shown in Figure 6. The curve was obtained by using the 1-foot contour lines generated from a Lidar data collection in 2008 provided by Jarvis Jones, Sutter County Development Services, CA. It was found that the Meridian Basin has several roads (Highway 20, Progress Road, etc.), which are about 12.2-12.8 m above the reference datum (The levee base was 11 m (36 ft) above the U.S. reference datum). These roads are a few feet higher than the farm lands in the basin, particularly in the south parts of the basin. In order to account for the effect of the roads on the flood propagation, the basin was divided into four zones, as shown in Figure 7. The V(z) relation was calculated for each zone using the 1-foot contours. The breach was located in zone 1. The flood water could reach zones 2, 3, and 4 only after the water level in zone 1 rose above the top of the roads. Therefore, the basin V(z) curve is modified by considering the road effect. The modified basin V(z) curve uses only the curve of zone 1 when the elevation is below 12.5 m (i.e., 1.5 m above the levee base), and then uses the sum of all the four zones' volumes when the elevation is above 12.5 m. The modified basin V(z) curve is also shown in Figure 6 using the red solid line. The regular and modified V(z) curves are tabulated in Table 1.

The levee at the south end of the basin was cut in Jan. 5 to allow the water to return to the Bypass. The final geometry of the relief breach is given in Table 2. The relief breach is considered in the simulation as weirs with different crest elevations. The weir flow discharge coefficient is set as 1.7.

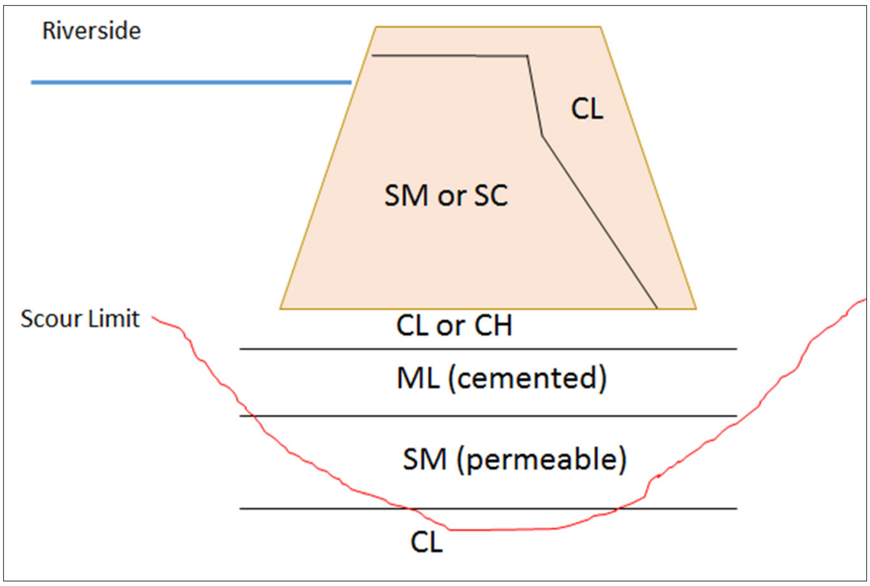

Figure 5. Estimate of embankment and foundation soils (CL – clay, >70% fines; SM – silty sand, 12%-70% fines; SC – clayey sand, 12%-70% fines; ML – silt, >70% fines) (Risher, 2016, personal communication).

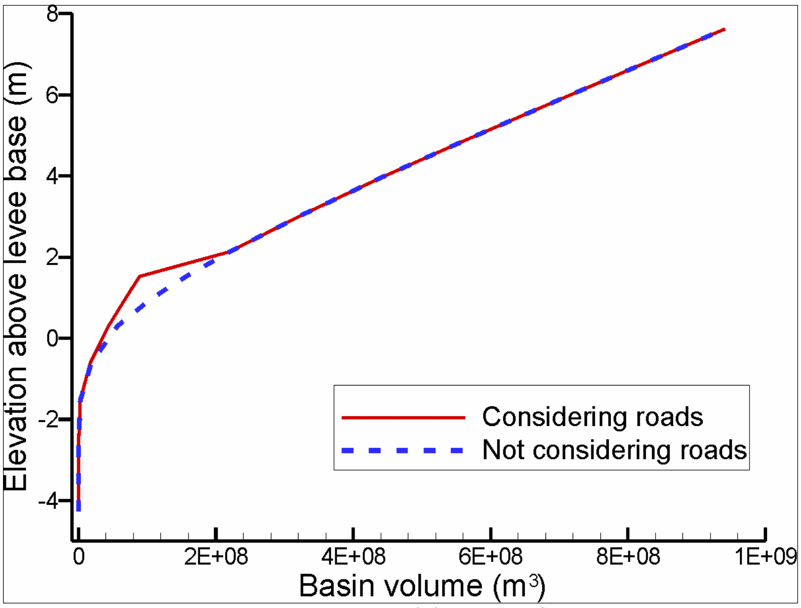

Figure 6. Volume and level V(z) curve of Meridian Basin.

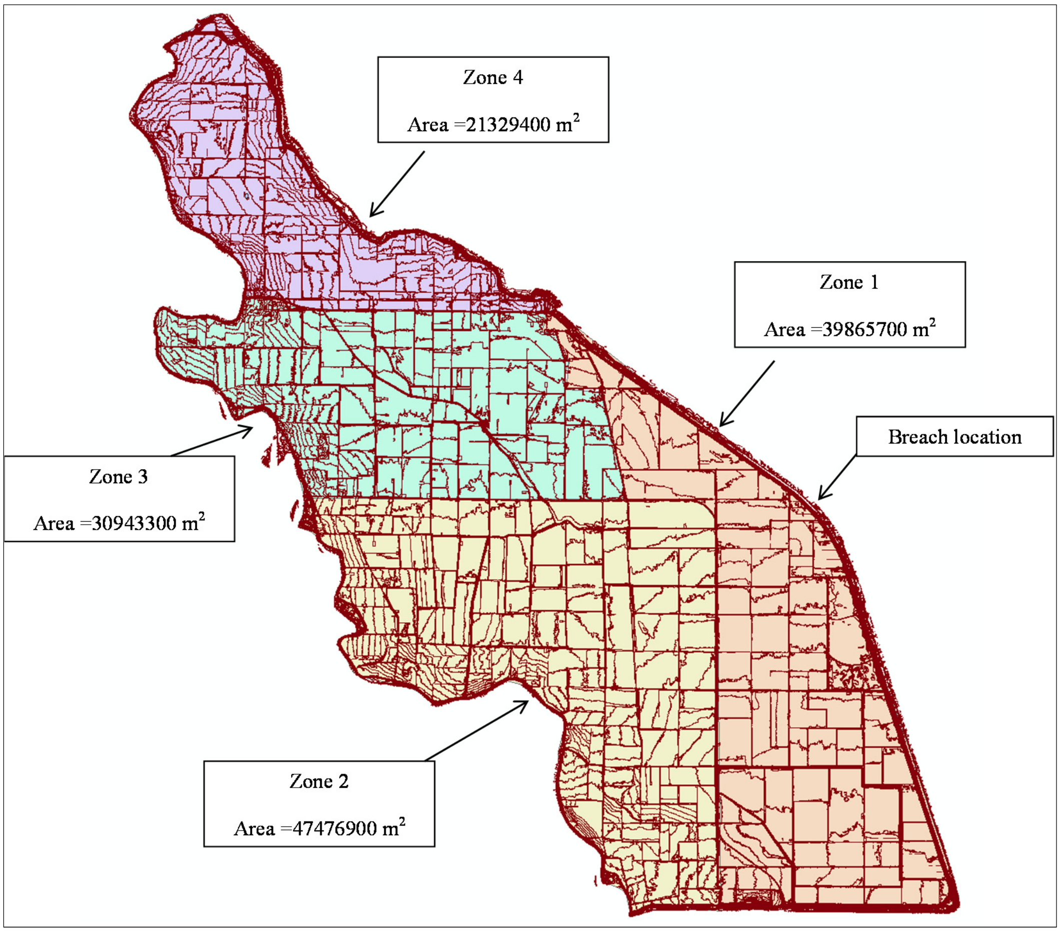

Figure 7. Meridian Basin divided to four zones by roads which are a few feet above the lower farm lands.

Table 1. Meridian Basin volume vs. elevation.

Elevation above levee base* (m)	Basin volume (m^3)	
	without considering roads	with considering roads
-4.27	584.9	584.9
-3.35	69532.4	69532.4
-2.44	399900.7	395979.3
-1.52	2580678.7	2509458.1
-0.61	18491462.0	16953334.5
0.30	56799763.7	43731798.4
0.91	101294758.3	65832330.4
1.22	127935098.3	77311638.4
1.52	156838861.9	88937960.1
2.13	220403963.5	220403963.5
3.05	326397223.4	326397223.4
3.96	441057989.5	441057989.5
4.88	562807858.0	562807858.0
5.79	687969826.1	687969826.1
6.71	814327405.6	814327405.6
7.62	941119965.6	941119965.6

*: Levee base was 11 m (36 ft) above the U.S. reference datum

Table 2. Downstream relief breach geometry (Risher, 2016, personal communication).

Distance (m)	Elevation above levee base (m)
0.00	6.49
32.41	6.58
63.44	6.68
93.92	3.94
95.14	0.91
118.08	0.91
119.61	3.96
142.54	2.44
165.48	3.96
200.64	3.96
202.17	3.05
244.99	3.05
246.51	3.96
285.66	3.96
287.19	1.52
333.06	1.52
334.58	3.90
365.24	6.53
385.68	6.37

5 SIMULATION RESULTS

The time series of water level in the Sutter Bypass Channel at the breach location was calculated by Risher and Gibson (2016) using HEC-RAS. The riverside water level was falling after the flood peak on the Sacramento River and Sutter Bypass Channel, as shown in Figure 8. Figure 8 also shows the times of relief cut of downstream (D/S) levee and dumping of the rip rap stones. The time series of riverside water level was used as the headwater condition for the breach process, while the water level in the Meridian Basin was determined using the water balance equation [6].

Two simulations were conducted using the regular and modified basin V(z) curves, while the other parameters are the same. Figure 9 compares the calculated and measured breach widths. Both simulations reproduce generally well the measured breach width development, although the simulation using the modified V(z) curve gives somehow better results than using the regular V(z) curve without effect of roads. Each simulation started from 18:00 pm of Jan. 4. In about 10 minutes, the pipe roof failed. This indicates the piping process was not actually simulated. This is normally done by assuming a relatively large initial pipe. On the other hand, the soil does not have strong cohesion. After the pipe failed, overtopping breach mode took over. Then the breach widened quickly in the first 24 hours, and then the widening died out due to rising of the water level in the basin and falling of the riverside water level. The measured final breach width at the time of rip rap stones dumped is 274 m. The calculated breach widths using the regular and modified V(z) curves in the corresponding time are 277.9 and 270.4 m, respectively. The errors are quite small.

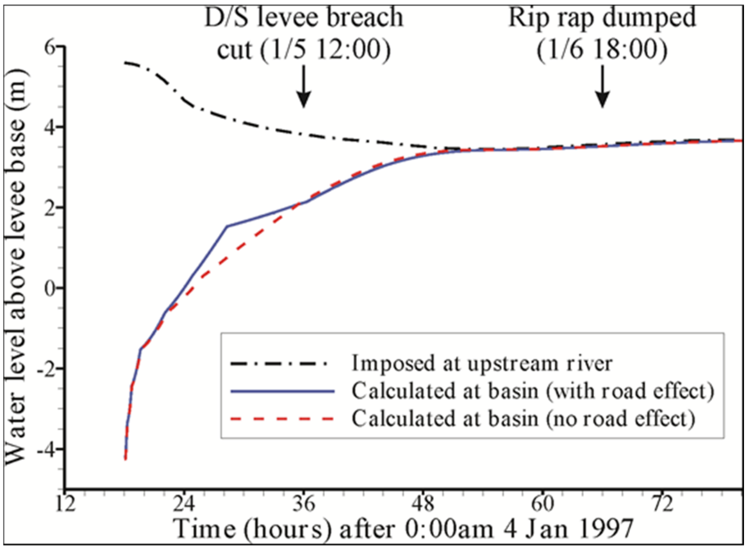

Figure 8. Imposed riverside water level and calculated basin water levels, with timing of downstream (D/S) levee cut and rip rap dumping

Figure 8 shows the calculated basin water levels. The water started to fill the basin when the simulation started. The simulation using the modified V(z) curve gives a faster rising in the basin water level, due to that only zone 1 was used to store the water in the early filling stage. In Jan. 5, 12:00 pm when the south levee was cut for relief, the basin water level calculated using the modified V(z) curve was 2.11 m above the levee base, which is equivalent to 13.11 m above the reference datum. The ground level of the Meridian Elementary School is about 13.41 m. This explains well why the south basin levee was cut to relieve the flood pressure to the town of Meridian. After the relief cut, the basin water level still continued to rise until about 12 hours later when the riverside and basin water levels became close. The final basin water level calculated using the modified basin V(z) curve is about 3.66 m above the levee base, i.e. 14.66 above the reference datum. This gives a 1.25 m water depth on the Meridian Elementary School ground. This result agrees very well the reported water depth of 1.2 m there. This excellent agreement is attributed to the predictions of riverside water level by HEC-RAS as well as the breaching process and basin water filling calculated by the present levee breach model.

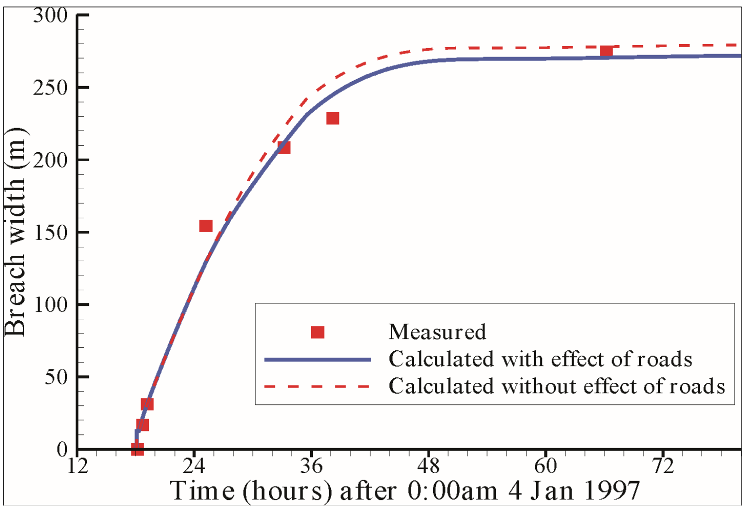

Figure 9. Comparison of measured and calculated breach widths

6 CONCLUSIONS

The simplified physically-based dam and levee breach model, DLBreach, has been used in this study to simulate the Sutter Bypass Channel levee breaching process due to piping or seepage occurred on Jan. 4, 1997. The breach model simulation is driven by the time series of water level in the Sutter Bypass Channel at the breach location calculated using HEC-RAS. The volume-elevation curve of the inundated Meridian Basin is obtained by using the 1-foot contour lines generated from a Lidar data collection in 2008.The curve is modified to account for the effect of the roads by considering that the flood water filled the zone below the breach first and then overtopped the roads and entered the remaining zones. The model reproduces well the levee breach widening process. The calculated final breach width was 270.4 m, compared well with the measured 274 m. The calculated peak water level was about 1.25 m above the school ground level, which agrees well the reported value of 1.2 m. The soil erodibility k_d is calibrated as 14.5 cm^3/N·s by comparing the calculated and measured breach widths. This value agree generally well to the literature erodibility value 10.3 cm^3/N·s for silty sand (SM), which is the representative soil in the studied levee. The difference may be attributed to differences in soil structures, compaction, moisture, etc. This test demonstrates that DLBreach is able to simulate the levee breach process due to piping or seepage flow.

ACKNOWLEDGEMENTS

This study was partially supported by the Coastal Inlets Research Program, ERDC, US Army Corps of Engineers, Vicksburg, MS, through the Project W912HZ-15-P-0058 under ERDC Broad Agency Announcement BAA Category CHL-11: Coastal Processes, Coastal Inlets, and Navigation Channels. The Program Manager was Dr. Julie D. Rosati.

The author thanks Mr. Paul Risher at HEC, US Army Corps of Engineers for providing the water level value in the Sutter Bypass Channel calculated using HEC-RAS, and other data and information on the breach. Thanks also go to Mr. Jarvis Jones, Sutter County Development Services, CA, for providing the 1-foot contour lines generated from a Lidar data collection in 2008.

REFERENCES

ASCE/EWRI Task Committee on Dam/Levee Breaching. (2011). Earthen Embankment Breaching. *J. Hydraulic Eng.*, ASCE, 137(12), 1549–1564.

California Flood Emergency Action Team (1997). Governor's Task Force on 1997 Flooding in California. *Final Report.*

Risher, P. & Gibson, S. (2016). Applying Mechanistic Dam Breach Models to Historic Levee Breaches. *FLOODrisk 2016 - 3rd European Conference on Flood Risk Management*, Lyon, France.

Sutter County, California (2015). Sutter County Operational Area Emergency Operations Plan, ANNEX 5 – *Floods and Dam Failure*.

Temple, D.M. (1992). Estimating Flood Damage to Vegetated Deep Soil Spillways. *Applied Engineering in Agriculture*, 8(2), 237–242.

Sacramento District, USACE. (1997). Collection of Emergency Situation Reports and Emergency Repair Design Documents.

Wu, W. (2013). Simplified Physically-Based Model of Earthen Embankment Breaching. *Journal of Hydraulic Engineering*, ASCE, 139(8), 837–851.

Wu, W. (2016). Introduction to DLBreach — A Simplified Physically-Based Dam/Levee Breach Model (version 2016.4). *Technical Report*, Clarkson University, NY.

Zhong, Q., Wu, W., Chen, S. & Wang, M. (2016). Comparison of Simplified Physically-Based Dam Breach Models. *Natural Hazards*, 84,1385–1418.

ISSUES CONCERNING SPATIAL DATA COLLECTION AND PROCESSING FOR URBAN FLOOD MODELLING

AHMAD FIKRI ABDULLAH(1), ZORAN VOJINOVIC(2) & VORAWIT MEESUK(3)

(1) Department of Biological and Agricultural Engineering, Faculty of Engineering,
Universiti Putra Malaysia, 43400 Serdang, Selangor, Malaysia
ahmadfikri@upm.edu.my
(2,3) UNESCO-IHE, Westvest 7, 2611 AX Delft, The Netherlands,

ABSTRACT

The flows in drainage networks are typically modelled with one-dimensional (1D) models. With the need to model overland flows, which may be confined to street flows, 1D pipe network models are combined with another 1D network of streets and ponds (major system). Such model is commonly referred to as 1D/1D model. Furthermore, coupling between channel/pipe network flow models can be also done with 2D flood flow models that treat the overland surface as a two-dimensional flow domain. However, there are numerous issues related to the collection and processing of surface data for urban flood modelling. The present paper discusses some of the issues related to terrain data processing and collection which can either improve or deteriorate predictive capability of numerical models. These are related to terrain data resolution and ability to detect and capture some of the typical urban features.

Keywords: Flood models; one-dimensional models; two-dimensional models; terrain data; urban features.

1 INTRODUCTION

Over the past twenty years, urban flood managers have been increasingly investing in collection of data that can be used for urban flood modelling applications (Price and Vojinovic, 2008; Mynett and Vojinovic, 2009). The use of numerical models for urban flood modelling has been invaluable (e.g., Abbott et al., 2006; Abbott and Vojinovic, 2009; Seyoum et al., 2012; Vojinovic and Abbott, 2017). With the use of such models, urban flood managers are able to explore the processes that lead to floods and flood-related disasters (urbanization, population growth or climate change). Furthermore, such models have been very effective in the assessment of flood protection measures and in this regards, they have been coupled with other kinds of models, e.g., optimization models (see for example Barreto et al., 2006; Vojinovic et al., 2006a; Barreto et al., 2008; Vojinovic et al., 2008; Barreto et al., 2009; Kumar et al., 2013; Sanchez et al., 2014; Vojinovic et al., 2014; Alves et al., 2016; Singh et al., 2016; Vojinovic, 2015; Vojinovic et al., 2016; Vojinovic et al., 2017).

Depending on the desired level of details and complexity of processes, the 1D pipe (or open channel) flow models are typically developed on a skeletal (or simplified) or a more detailed level (Vojinovic et al., 2006b; Vojinovic and Abbott, 2012), Figure 1a. This depends on the modelling objectives, availability of data and financial possibilities. Model simplification requires certain assumptions. This is usually done by incorporating additional storages and head-losses (i.e., storages and head-losses that are omitted from the larger network) to the simplified network. For 1D/1D models, the system is modelled with sets of 1D equations for each of the two systems (i.e., urban surface and pipe, or channel, network), Figure 1b. The case of coupled 1D/2D models is more complex and it is often computationally expensive, Figure 1c. The 2D model simulates vertically-integrated two-dimensional unsteady flow given the relevant boundary conditions and terrain configuration (Vojinovic and Tutulic, 2009; Vojinovic et al., 2011; Vojinovic et al., 2012). The interactions between the domains of two models (1D and 2D) are determined according to the type of link. For discharges generated by pumping stations, weirs or orifices are treated as the lateral inflows to the 2D model. In the case of the surcharges from 1D model, the discharge is computed by the weir (or orifice) discharge equation and it represents a lateral inflow to the 2D model. The 2D flow simulation can be done on a structured or unstructured (or flexible) mesh – regular or irregular grid. For model instantiation purposes, the structured regular grid is more convenient as it can directly use LiDAR data, whereas the other approach may need more data processing time. The present paper concerns the use of 2D models with regular grids and explores the difference between results obtained from 1D-2D models based on different data resolution and data processing techniques.

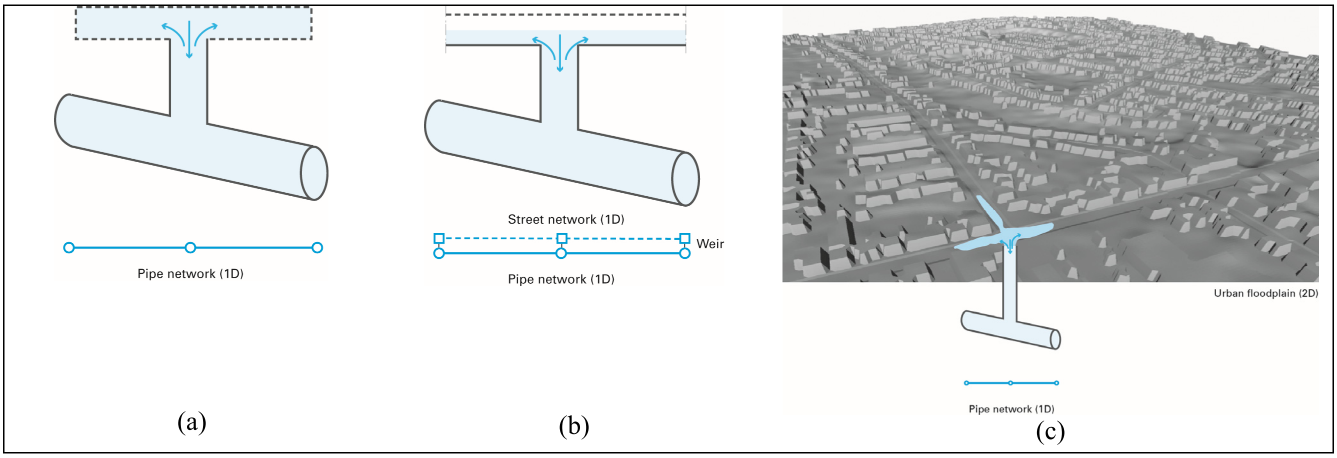

Figure 1. Urban Flood modelling approaches: (a) 1D, (b) 1D/1D, (c) 1D/2D (After: Vojinovic and Abbott, 2012).

2 PROCESSING TERRAIN DATA FOR URBAN FLOOD MODELLING

2.1 Data resolution

It is a well-accepted fact that different resolution will determine a level of details that can be reproduced. With 2D numerical models, increasing the grid size can improve computational efficiency, but it will at the same time reduce the level of details. For instance, elevations of buildings represented in fine-grid (or high resolution) models will be smeared or completely removed when the grid is coarsened. Therefore, depending on the topography, the terrain data resolution will have an impact on whether the 2D model will properly reflect the local flow phenomena or not, Figure 2.

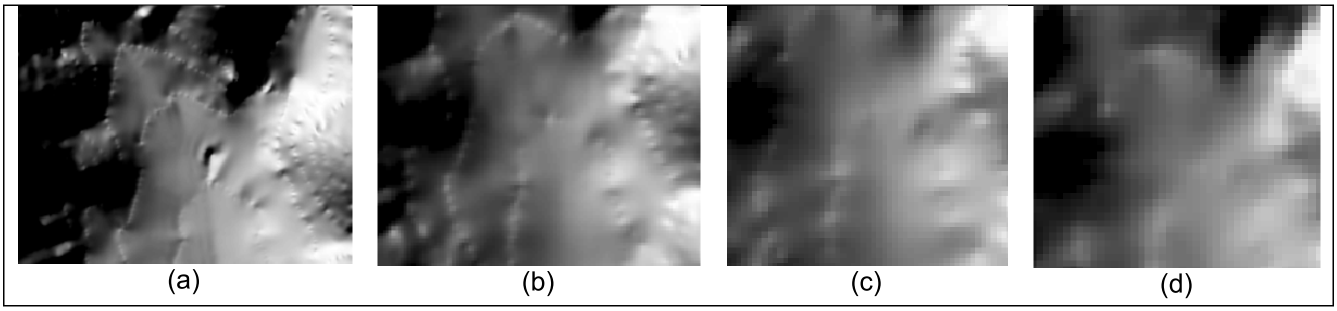

Figure 2. Variation of terrain discontinuity with DTM resolution: a) for DTM 5m b) for DTM 10m c) for DTM 15m d) for DTM 20m.

2.2 Representation of urban features

A digital terrain model (DTM) is commonly referred to as a model of terrain elevations, whereas, the term DEM (or digital elevation model) refers to elevations of a surface of almost any kind. There are various structures of DEMs and some of them are: line model, triangulated irregular network (TIN) and grid network. There are several methods that can be used to obtain DEM data and some typical ones are: ground surveys, aerial stereo photography, satellite stereo imagery and airborne laser scanning.

Airborne Laser Scanning (ALS) or Light Detection and Ranging (LiDAR) has become very popular (and cost-effective) in the recent time. It is an optical remote sensing technology which measures properties of scattered light in order to detect information related to surface elevation. This technique is capable of collecting highly accurate and dense points from the surface or terrain to a desired resolution. The point cloud data collected from LiDAR is used to construct a DEM data set. However, construction of a DEM data set is not a trivial task. Several pre- and post-processing techniques need to be applied in order to obtain reliable data. One of the most challenging tasks is the task associated with filtering of urban features (see also, Abdullah et al., 2009; Abdullah et al., 2011a and Abdullah, et al., 2011b; Holopainen et al., 2013).

Since urban environments can contain many different features (i.e., geometric 'discontinuities') such as roads, stairs, pavement curbs, fences, and other objects, which play an important role in diverting flood water flows that can be generated and propagated along urban surfaces, the question concerning terrain data processing is an important one. In cases where those features are not adequately represented, it is highly likely that the model will not be able to produce satisfactory results. For this purpose, selecting an appropriate LiDAR filtering algorithm can be a crucial factor for determining the quality of results from numerical models.

Furthermore, a new technique, Structure from Motion technique (SfM), offers some additional capabilities in detecting urban features to support urban flood modelling work.

Structure from Motion (SfM) technique is a modern stereo-photogrammetry technique which can be used to create a digital topographic map (a.k.a. 3D reconstructions) by combining LiDAR data with the low-cost acquisition tools (consumer-grade digital cameras, camcorders, or even mobile phone cameras which can be used for 3D reconstructions to provide a more accurate quality of topographic data). The LiDAR data provides details of the terrain and land cover from a top-view, which is suitable to represent a larger surface area. However, such data may not be able to represent some hidden structures in a dense urban setting, Figure 3. Therefore, an approach that combines multidimensional views obtained from LiDAR and photographs taken from the ground, i.e., structure from Motion technique (SfM), has shown promising results.

Figure 3. Example of a narrow opening between buildings which cannot be detected from the point cloud top-view LiDAR survey but which can play an important role in propagation of a flood wave.

In the following section we illustrate some of the points related to different terrain resolutions and different data processing techniques which can create substantial differences in 1D-2D model results.

3 ILLUSTRATION OF RESULTS

3.1 Data resolution

To address the effects of terrain data resolution, the case study area from St Maarten was used, Figure 4. St Maarten is located in the Caribbean region and it is part of the Netherlands Antilles, see also Vojinovic and van Teeffelen, 2007; Vojinovic and Tutulic, 2009. St Maarten has hilly topography where elevations range from near sea level at the southern end to 380 m above mean sea level at the northern hilly part. Overland flows converge towards the low lying areas and the stormwater runoff is discharged at many locations.

The land use is predominantly residential with some scattered commercial parts. Since large areas of the island are steep, with relatively little vegetation coverage, almost any rainfall can cause a high level of runoff (e.g., flash floods) and erosion which carries large volumes of silt and debris. In this paper, four DTMs with different resolutions (5m, 10m, 15m and 20m DTM resolutions) were used to build four 2D models which were then coupled with the 1D model comprised of watercourses and streams.

The software used is DHI MikeFlood® software. The results presented in Figure 4 concern one part on the Dutch side of the Island, known as Cul De Sac, and they are generated by running 100 year ARI storm event through the 1D-2D model.

The results presented in Figure 4 show that differences in terrain resolution can have substantial effects on flood model results. For example, flood water depths in the model result with 5m resolution were found to be almost 50% larger than the results with 20m resolution. Also, in terms of the flood extents, the difference between the models with 5m and 20m resolutions were found to be around 35% different (i.e., the model with 5m resolution produced smaller flood extent area).

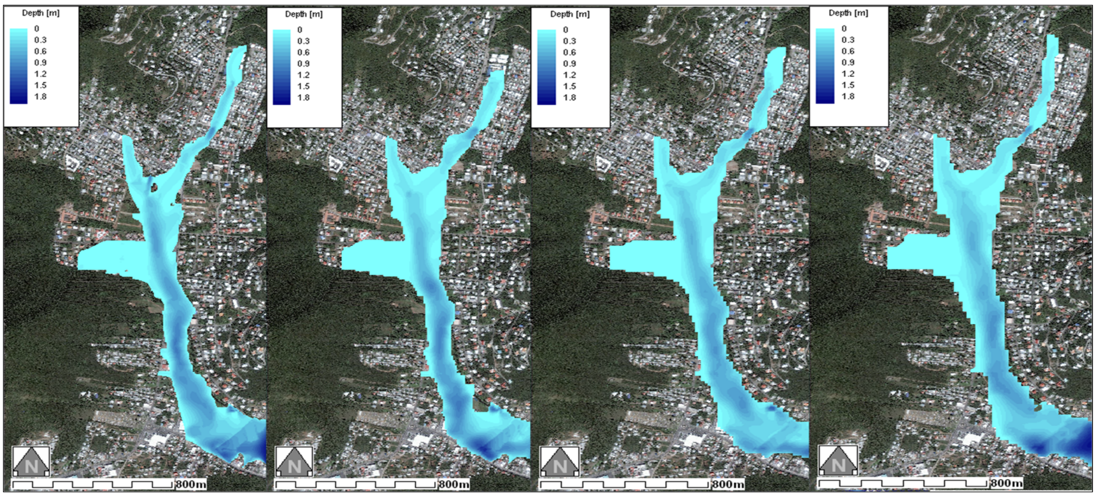

Figure 4. Impacts of different DTM resolutions on model results (5m, 10m, 15m and 20m DTM resolutions).

3.2 Filtering algorithms

Filtering is a process of detecting features on land. A number of algorithms are available for this purpose. Typically, there are four key filtering algorithms used in the practice (Figure 5):

1. Morphological filtering algorithm;
2. Progressive filtering algorithm;
3. Algorithms that progressively increase the density of the DTM; and
4. Filtering algorithm based on segments.

The main difference between the above mentioned algorithms is the procedure that they use to estimate differences in heights between objects and surface points (see for example Glira et al., 2014, Muhadi et al., 2016). It should be noted that most of these algorithms are developed for rural environments and they have limited capabilities for separating urban features (see for example Abdullah et al., (2011a) and Abdullah et al., (2011b)).

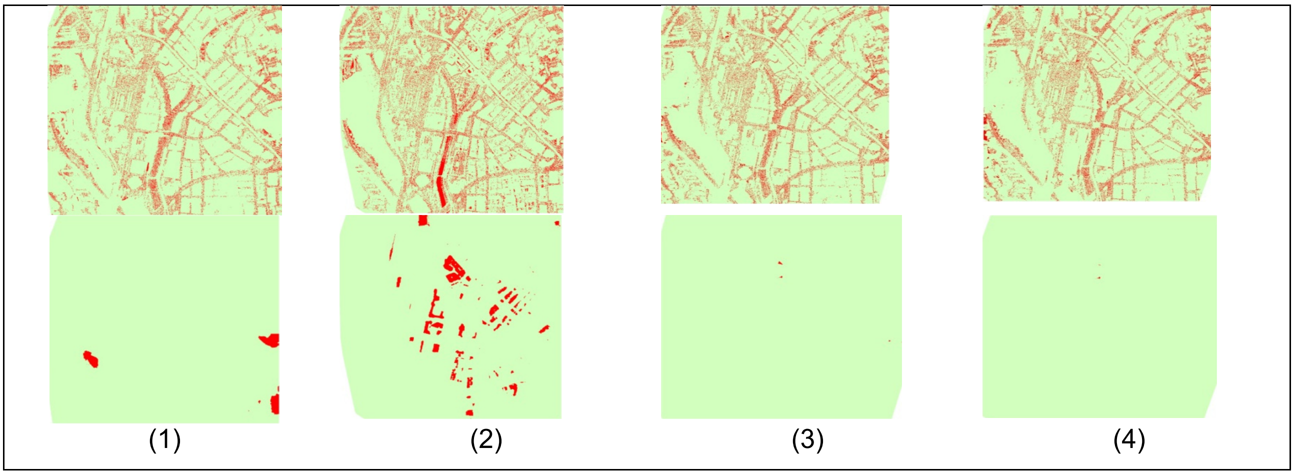

Figure 5. Different LiDAR filtering algorithms: first raw depicts DEMs produced from four different algorithms (morphological filtering algorithm; progressive filtering algorithm; an algorithm that progressively increases the density of the DTM; and filtering algorithm based on segments) and second row depicts incorrectly filtered points. The DEMs concern the case study area of the Klang River basin in Kuala Lumpur, Malaysia.

In terms of the analysis concerning different LiDAR filtering algorithms, the work presented in this paper concerns a small part of the Klang River basin in Malaysia. Four filtering algorithms, which are often used in the practice, were applied in the present work (morphological filtering algorithm; progressive filtering algorithm; algorithms that progressively increase the density of the DTM; and filtering algorithm based on segments) to produce four DTMs (Figure 5) which are then used to set up four 2D models. These models are then coupled with the 1D river model.

A set of measurement data from a major flood event that took place on 10th June in 2003 was made available for the present work. This dataset was used to calibrate the 1D model of the Klang River flowing from the Northeast, and the Gombak River flowing from the Northwest. The 1D model was coupled with the 2D model (using DHI MikeFlood® software) in order to investigate the propagation of excess floodwater from

  / ISSN 1562-6865 (Online) - ISSN 1063-7710 (Print)

the two main rivers (the Klang and Gombak Rivers) into the 2D urban area. The time-series recorded were: discharge at Jalan Tun Rasak and Jambatan Sulaiman stations, water levels at Lorong Yap Kwan Seng station, and rainfall at Jambatan Sulaiman station and these data sets were used as boundary conditions for the 1D model. Manning friction coefficient (n) of 0.020 was applied uniformly for the constructed 1D channels following the criteria defined by Chow (1959). In terms of the 2D urban surface area, the Manning friction coefficient (n) value of 0.033 was applied. The data from six measurement locations (which contained floodwater records from streets) was sourced from the Department of Irrigation and Drainage (DID), Figure 6.

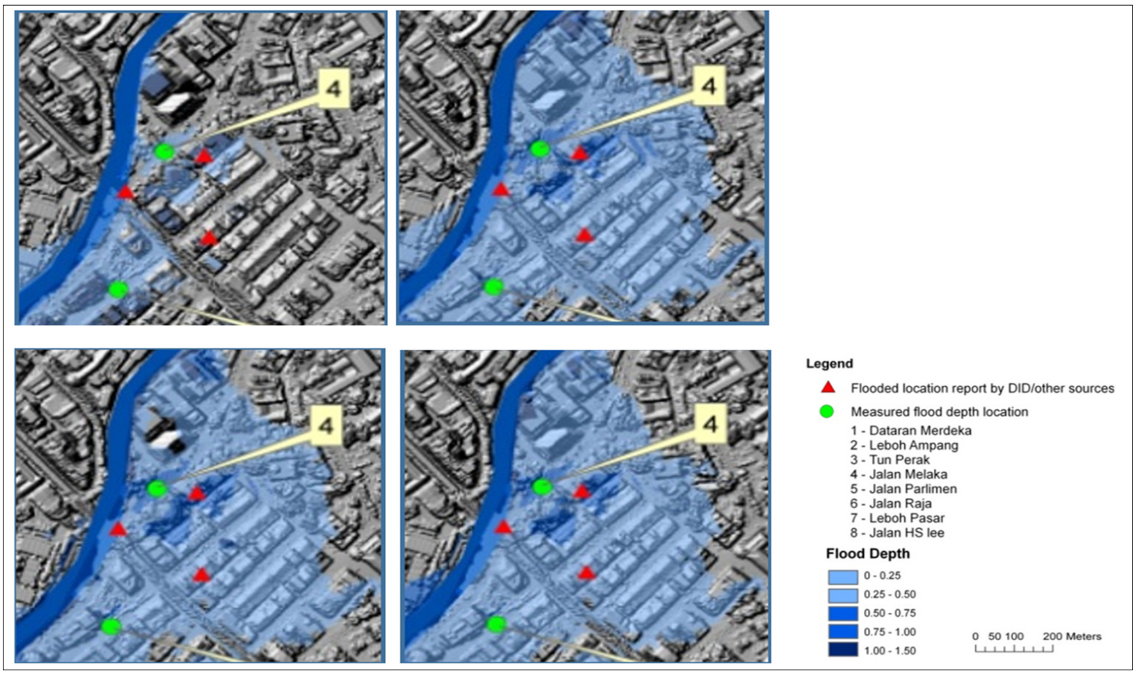

Figure 6. 1D/2D model results with four different filtering algorithms (up-left: morphological filtering algorithm; up-right: progressive filtering algorithm; below-left: algorithms that progressively increase the density of the DTM; and below-right: filtering algorithm based on segments).

The results presented in Figure 6 show that the difference in flood results obtained from the models that used different filtering algorithms can be substantial. The computed flood depths and flood extents were found to vary significantly between different locations. For example, flood results in the area of Jalan Melaka (marked as 4 in Figure 6) vary by almost 100% between different models.

3.3 Fusion of top-view LiDAR and ground-view data through SfM technique

The presence of hidden structures in a dense urban setting can cause large discrepancies in terrain data and as such it can produce different 2D model domains and corresponding flood results. As introduced earlier, the use of SfM technique (also referred to as Multidimensional Fusion of Views MFV-DTM technique) can enable the authors to perform fusion between top-view LiDAR and ground-view data. This can account for small urban features such as small openings between buildings and under the buildings. As a result, 2D model predictions of floodwater can be closer to reality, see Figure 7 (see also Meesuk et al., 2015).

In the case study work carried out in the same part of the Klang River basin in Malaysia, the differences were found to be significant between the two models (and against street measurements) where the 2D model based on SfM-LiDAR DTM produced more realistic results. The results based on the model with raw LiDAR data were generally underpredicted. For example, the differences in computed water depths taken at location A (Jalan Melaka) were found to be around 30 cm lower from the actual measurements (and also from the model based on SfM data set), whereas computed water depths taken at location B (Leboh Ampang) were found to be around 20cm lower. Also, the inundation extent was found to be around 130,000 m2 in the results of the model based on the raw LiDAR data, whereas the inundation extent of 160,000 m2 was found in the results of the model based on the SfM-LiDAR DTM.

Furthermore, the model based on raw LiDAR data shows that the simulated floodwaters (Figure 7a) were confined to roads. Inundations were located in the North-Eastern and South-Western areas and they were separated by the sky train track. However, the 2D model based on SfM-LiDAR DTM (i.e., MSV-DTM) produced more realistic results which fit much better with street measurements. The floodwaters were not only accumulated along the riverbanks but they were also propagated further in the North-Eastern and South-Eastern directions along the roads, which were found to be hidden underneath under the sky train track. Such hidden inundation areas can be revealed only by employing the SfM technique.

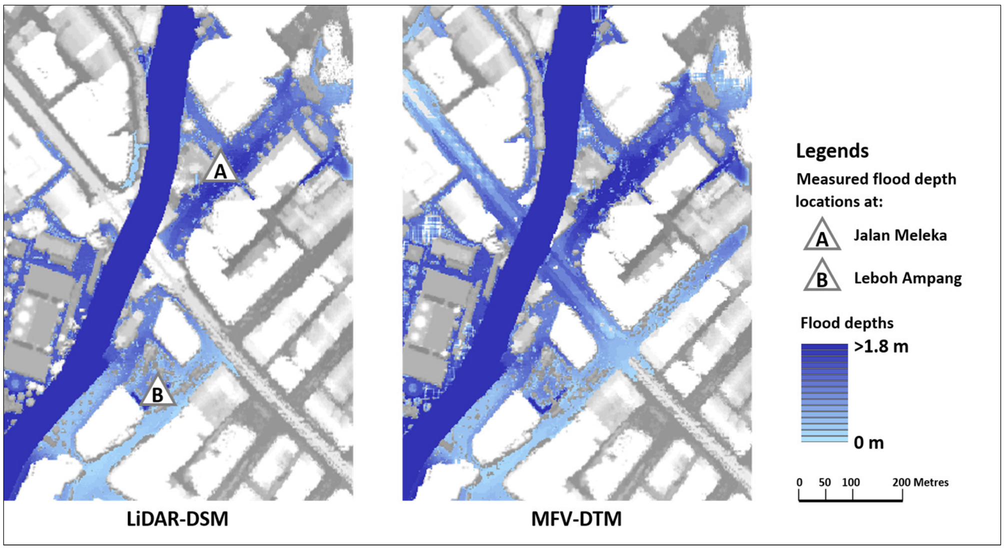

(a) (b)

Figure 7. Flood simulation results with LiDAR DSM (or DTM) (a) and SfM-LiDAR DTM or MFV-DTM (b).

4 CONCLUSIONS

The present paper discusses some of the terrain data processing issues which can have an influence on the results of flood models. Issues that are discussed here are related to terrain data resolution and detection of urban features. In the case study work presented, the 1D-2D numerical modelling approach was used to simulate flood events that occurred in St Maarten and Kula Lumpur (Malaysia). In the case of St Maarten, we demonstrate the effects of different DEM resolutions on 1D-2D model results. In the case of Kuala Lumpur (Malaysia), several standard LiDAR filtering algorithms were compared and it was found that none of them is fully suitable to support urban flood modelling work. Therefore, further improvements of LiDAR filtering techniques is necessary.

In addition, this paper also presents the Structure from Motion (SfM) technique which proved to be useful in detecting some of the important hidden urban features that may exist between and around buildings. From the analysis, it was found that a standard LiDAR-DTM technique is not fully suitable for instantiation of 2D models which in turn can cause the resulting flow patterns and water depths to be not correctly represented due to the presence of urban features (which are impossible to be detected by top-down LiDAR survey).

The overall analysis suggest that straightforward application of LiDAR data may introduce significant shortcomings in the 2D model results. Therefore, a great care should be given to terrain data processing and their subsequent application in the numerical modelling work. Hence, novel LiDAR filtering algorithms as well as the use of SfM technique can lead to generation of better results.

REFERENCES

Abbott, M.B., Tumwesigye, B.M. & Vojinovic, Z. (2006). The Fifth Generation of Modelling in Hydroinformatics. *7th International Conference on Hydroinformatics*, Acropolis - Nice, France, September.

Abbott, M.B. & Vojinovic, Z. (2009). Applications of Numerical Modelling in Hydroinformatics. *Journal of Hydroinformatics,* 11(3-4), 308-319.

Abdullah, A., Rahman, A. & Vojinovic, Z. (2009). LiDAR Filtering Algorithms for Urban Flood Application: Review on Current Algorithms and Filters Test. *Laserscanning09* 38, 30-36.

Abdullah, A.F., Vojinovic, Z. & Price, R.K. (2011a). Improved Methodology for Processing Raw LIDAR Data to Support Urban Flood Modelling - Accounting for Elevated Roads and Bridges. *Journal of Hydroinformatics,* 14.2, 253-269.

Abdullah, A.F., Vojinovic, Z. & Price, R.K. (2011b). A Methodology for Processing Raw LIDAR Data to Support 1D/2D Urban Flood Modelling Framework. *Journal of Hydroinformatics,* 14(1), 75-92.

Alves, A., Sanchez, A., Vojinovic, Z., Seyoum, S., Babel, M. & Brdjanovic, D. (2016). Evolutionary and Holistic Assessment of Green-Grey Infrastructure for CSO Reduction. *Water,* 8(9), 402.

Barreto, W.J., Vojinovic, Z., Price, R.K. & Solomatine, D. (2006). Approaches to multi-objective multi-tier Optimisation in Urban Drainage Planning. *7th International Conference on Hydroinformatics*, Nice, France, 1-8.

Barreto W., Vojinovic Z., Price R.K. & Solomatine D.P. (2008). Multi-tier Modelling of Urban Drainage Systems: Muti-objective Optimization and Parallel Computing. *11th International Conference on Urban Drainage*, Edinburgh, Scotland, 1-10.

Barreto W., Vojinovic, Z., Price, R.K. & Solomatine, D. (2009). Multiobjective Evolutionary Approach to Rehabilitation of Urban Drainage Systems. *ASCE Journal of Water Resources Planning and Management,* 136(5), 547-554.

Chow, V.T. (1959). *Open-channel Hydraulics*. McGraw-Hill Book Company, Inc; New York, 1-700.

Glira, P., Briese, C., Pfeifer, N., Dusik, J., Hilger, L. & Neugirg, F. (2014). Accuracy Analysis of Height Difference Models Derived from Terrestrial Laser Scanning Point Clouds. *EGU General Assembly Conference Abstracts,* 16, 15987.

Holopainen, M., Kankare, V., Vastaranta, M., Liang, X., Lin, Y., Vaaja, M. & Alho P. (2013). Tree Mapping using Airborne, Terrestrial and Mobile Laser Scanning - A Case Study in a Heterogeneous Urban Forest. *Urban For Urban Green,* 12(4), 546–553.

Kumar, D.S., Arya, D.S & Vojinovic Z. (2013). Modeling of Urban Growth Dynamics and its Impact on Surface Runoff Characteristics. *Computers, Environment and Urban Systems, Elsevier,* 41, 124-135.

Meesuk, V., Vojinovic, Z., Mynett, A & Abdullah, A.F. (2015). Urban Flood Modelling Combining Top-View Lidar Data with Ground-View Sfm Observations. *Advances in Water Resources,* 75, 105-117.

Muhadi, N.A., Abdullah A.F. & Kassim M.S.M. (2016). Quantification of Terrestrial Laser Scanner (TLS) Elevation Accuracy in Oil Palm Plantation for IFSAR Improvement. *IOP Conference Series: Earth and Environmental Science,* 37 (1), 1-9.

Mynett, A. & Vojinovic Z. (2009). Hydroinformatics in multi-colours – part red: Urban Flood and Disaster Management. *Journal of Hydroinformatics,* 11(3-4), 166-180.

Price, R.K. & Vojinovic, Z. (2008). Urban Flood Disaster Management. *Urban Water Journal,* 5(3), 259-276.

Sanchez, A., Medina, N., Vojinovic, Z. & Price R. (2014). An Integrated Cellular Automata Evolutionary-based Approach for Evaluating Future Scenarios and the Expansion of Urban Drainage Networks. *Journal of Hydroinformatics,* 16(2), 319-340.

Seyoum, S.D., Vojinovic, Z., Price, R.K. & Weesakul, S. (2012). A Coupled 1d and non-Inertia 2d Flood Inundation Model for Simulation of Urban Pluvial Flooding. *ASCE Journal of Hydraulic Engineering, ASCE,* 138(1), 23-34.

Singh, R., Arya, D.S., Taxak, A. & Vojinovic, Z. (2016). Impact of Climate Change on Rainfall Intensity-Duration-Frequency (IDF) Curves in Roorkee. *Water Resources Management,* 1-14.

Vojinovic, Z., Solomatine, D.P. & Price R.K. (2006a). Dynamic Least-Cost Optimisation of Wastewater System Remedial Works Requirements. *Water Science and Technology,* 54(6-7), 467-475.

Vojinovic, Z., Bonillo, B., Chitranjan, K. & Price, R. (2006b). Modelling Flow Transitions at Street Junctions with 1D and 2D Models. *7th International Conference on Hydroinformatics, Acropolis* - Nice, France, September, 4-8.

Vojinovic, Z. & van Teeffelen J. (2007). An Integrated Stormwater Management Approach for Small Islands in Tropical Climates. *Urban Water Journal,* 4(3), 211-231.

Vojinovic, Z., Sanchez, A. & Barreto W.J. (2008). Optimising Sewer System Rehabilitation Strategies between Flooding, Overflow Emissions and Investment Costs. *11th International Conference on Urban Drainage,* Edinburgh, Scotland, 31, 1-10.

Vojinovic, Z., & Tutulic, D. (2009). On the Use of 1D and Coupled 1D-2D Approaches for Assessment of Flood Damages in Urban Areas. *Urban Water Journal, 6*(3), 183–199.

Vojinovic, Z., Seyoum, S.D., Mwalwaka J.M. & Price R.K. (2011). Effects of Model Schematization, Geometry and Parameter Values on Urban Flood Modelling. *Water Science and Technology,* 63(3), 462-467, IWA Publishing.

Vojinovic, Z., Seyoum, S., Salum, M.H., Price, R.K., Abdullah, A.F. & Abebe, Y. (2012). Modelling Floods in Urban Areas and Representation of Buildings with a Method based on Adjusted Conveyance and Storage Characteristics. *Journal of Hydroinformatics,* 15(4), 1150–1168.

Vojinovic, Z. & Abbott, M.B. (2012). Flood Risk and Social Justice: *From Quantitative to Qualitative Flood Risk Assessment and Mitigation*. IWA Publishing, 1-600.

Vojinovic, Z., Sahlu, S., Seyoum, S., Sanchez, A., Matungulu, H., Kapelan, Z. & Savic, D. (2014). Multi-Objective Rehabilitation of Urban Drainage Systems under Uncertainties. *Journal of Hydroinformatics,* 16(5), 1044-1061.

Vojinovic, Z. (2015). Flood Risk: *The Holistic Perspective, From Integrated to Interactive Planning for Flood Resilience*. IWA Publishing, 1-296.

Vojinovic, Z., Hammond, M., Golub, D., Hirunsalee, S., Weesakul, S., Meesuk, V., Medina, N.P., Abbott, M., Sanchez, A. & Kumara, S. (2016). Holistic Approach to Flood Risk Assessment in Urban Areas with Cultural Heritage: A Practical Application in Ayutthaya, Thailand. *Natural Hazards, Springer,* 81(1), 589-616.

Vojinovic, Z., Keerakamolcha,i W., Weesakul, S., Pudar, R.S., Medina, N.P. & Alves, A. (2017). Combining Ecosystem Services with Cost-Benefit Analysis for Selection of Green and Grey Infrastructure for Flood Protection in a Cultural Setting. *Environments 2017,* 4(1), 3.

Vojinovic, Z. & Abbott, M.B. (2017). Twenty-Five Years of Hydroinformatics. *Water 2017,* 9(1), 59.

Proceedings of the 37th IAHR World Congress
August 13 – 18, 2017, Kuala Lumpur, Malaysia

IMPLEMENTATION OF A METHODOLOGY TO REVIEW HIGH HAZARD DAMS

FERNANDO J. GONZÁLEZ VILLARREAL[1], JONATHAN BOLAÑOS CASTILLO[2], MIGUEL ANGEL BRIBIESCA RODRÍGUEZ[3] & IRVING GARCÍA REYES[4]

[12,3,4] Institute of Engineering, National Autonomous University of Mexico, Mexico City, Mexico.
fgonzalezv@iingen.unam.mx; jbolanosc@iingen.unam.mx; mbribiescar@iingen.unam.mx; igarciar@iingen.unam.mx

ABSTRACT

Dams play an extremely important role in the development of countries. They are allowed to be a water storage facility for further use, as protection against extreme rainfalls and in some cases, for electric energy generation. In Mexico, there are 5,000 inventoried dams, of which 572 are classified as large dams. Some of them date back to the 16th century, but mostly the dams were built in Mexico at the period of the early 20th century to date. Many of these structures have passed beyond their span of useful life. In addition, dams have changed their operating conditions due to multiple factors, including reduced capacity storage, modification of the spillways, development of human settlements, changes in operating policies, reconstruction of structures and etc. Therefore, it is important that a periodic review and assessment of these structures related to the safety of these dams are carried out.

Keywords: High risk dams; methodology; dam spillway; sudden discharge; hazard zones.

1 INTRODUCTION

The Institute of Engineering of the National Autonomous University of Mexico (UNAM for Spanish language) has been developing a methodology for the review of dam safety. The methodology involves different kind of analysis, such as hydrological, hydraulic, geotechnical, structural and electromechanical, which led to the detection of types of hazard that are not mentioned in the inspection visit reports of level type I. This work began back in 2013 and continues until today.

During that time 21 dams are classified as high hazard (Figure 1), 7 of which are rigid type and 14 are flexible type with all of them distributed in different states of the Mexican Republic. It has been observed in this research that Level 1 inspections provide an idea of the type of hazard it has in the structures, however, a complete analysis is needed to obtain a clearer, type of hazard than the one they show. The main goal of making specialized studies is to give solid support to the recommendations and thus to improve the structural, functional or operational conditions, in order to reduce the level of hazard of the studied dams.

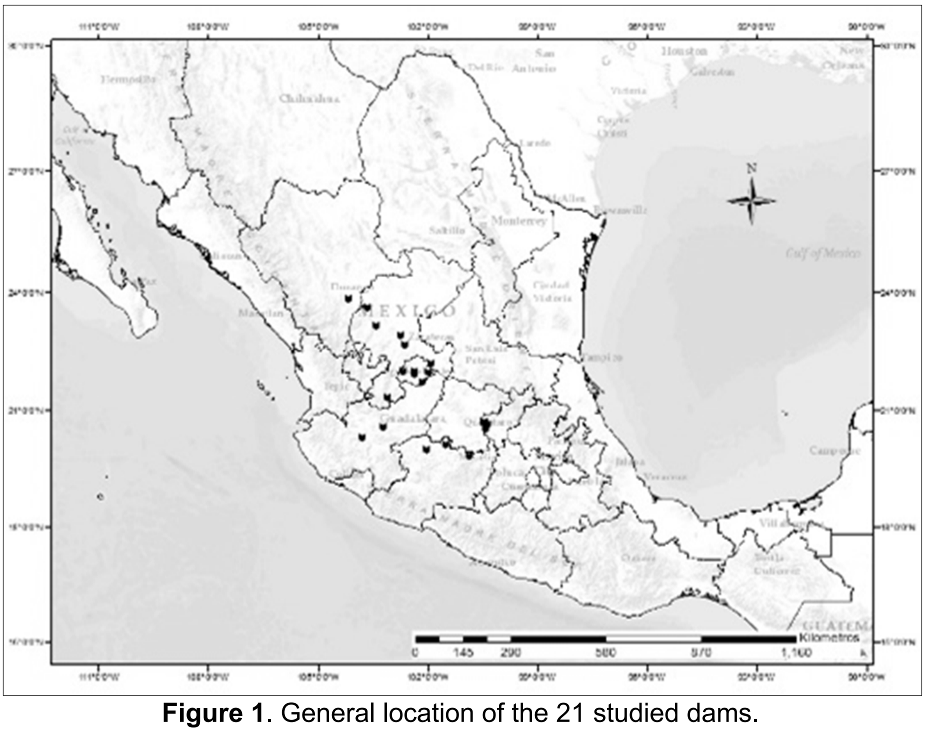

Figure 1. General location of the 21 studied dams.

2 METHODOLOGY DEVELOPMENT

The proposed methodology in this paper was used to review high hazard dams, and it features four main stages: Data analysis and generation, Hazard assessment and diagnosis, Dictum (Structure hazard) and Hazard mitigation conceptual design. Next, a description of each of these stages and their elements is described.

2.1 First stage: Data analysis and generation.

This first stage basically features of three activities: Data collection, Inspection visits and Exploration work (scouting).

The Data collection was carried out in three different government entities: the first one is the National Water Historical Archives, which had the very first collected and recorded data ever in matters of dam projects and construction from the year of 1985 to date. The second one is the CONAGUA´s Dam Safety System (Comisión Nacional del Agua, 1998), which had records from 1990 to date, and the third one is the local managements of the Mexican states in which the studied dams are located and have work tracing records.

Once the data had been collected, it was analyzed to elaborate a timeline with the most important activities carried on the dam such as previous inspection visits, structure modifications, working spillway dates, maintenance and replacement of electro mechanic equipment (valves, sluices, etc.), topography, and etc., in order to get a clear outlook of the dam and its behavior as times goes by.

The second activity was the inspection visit. It was about a Level II inspection visit (based on the USBR standards), in which the following determinations were made based on direct measurements of the elements of the dam. Through the inspection visit, the dam location was obtained using a manual Global Positioning System (GPS), and all of the dimensions of the structures that composed the dam were measured by using measuring tape, a clinometer, levelling rod, laser measurement device (with a range of 200m and a resolution of 1mm), leveling instrument with tripod and one hand compass.

The main dimensions of the dam´s curtain were measured, in other words: length, height, crown´s width, upstream and downstream slope leanings, and if it is required, rift´s length and openings up, such as the characteristics of the materials of the curtain. As sighting refers, there were binocularsused for the analysis and manual and visual classification of soils and rocks. Moreover, a magnifying glass, a geologist´s hammer and a Brunton compass, so as the classification tests recommended by the United Soil Classification System (USCS) were also used. The leaks on the dam were estimated through visual methods and, if possible, with a calibrated volume flask or a bucket and its turbidity will be observed with the aid of a transparent glass vessel.

Through the hole inspection, the state of the dam´s structures, such as the reservoir and the upstream and downstream riverbed were analyzed. The intake´s geometry and present elements dimensions were obtained through the direct measurement of its elements, such as: valves and pipes diameters, spillways geometry for gauging, energy-breaker box sections, irrigation channels and etc. Also, the spillway´s geometry and dimensions were obtained and some of its main characteristics and previous spill records and historical flood records were obtained as well. Instant pictures were taken by using high definition cameras with filming and audio capacity.

Finally, the third activity to do in this first stage is the scouting works which consist of three main points: bathymetrical and topographical surveys, geotechnical scouting and lab tests. In the first point, the curtain and auxiliary structures surveys were made (intake structure, spillway structure, etc.), as well as the reservoir´s bathymetry (which is used to get the elevations-capacities curve) and the topography of one dam´s downstream section were also obtained. The survey was carried out by using the RTK type equipment (TOPCON brand), furthermore, several level banks for horizontal and vertical control are placed in. With this survey the necessary data was obtained in order to perform the geotechnical and/or structural safety studies within the dam´s curtain and as well as to elaborate hydrological studies, hydrological and hydraulics safety studies of the dam and its auxiliary structures.

On the other hand, the geotechnical exploration aims the characterization of materials in flexible dams (embankment dams), through open pit´s scouting campaigns and/or mixed probes and/or Lafranc tests by extracting altered and unaltered samples. Lab tests were carried out on the extracted soil samples, mainly the index tests (water content, density of solids, volumetric weight, both liquid and plastic limits, finer material content, granulometry and soil classification), as well as mechanical tests (triaxial UU test, triaxial CU test, one-dimensional consolidation, etc.), in order to determine their main mechanical properties.

If necessary, geophysical explorations are carried out, in order to construct stratigraphic profiles of the reservoir´s slopes and the curtain´s foundation of ground both longitudinally and transversal way of the curtain´s axis. This was including seismic refraction tests up to at least three times the curtain´s height or embankment, as well as vertical electric probes to get to know the geological base and to define the groundwater runoff.

Once the data had been generated and analyzed, it can be proceeded to use all the collected data for the stage two analyses. Figure 2 shows must do activities scheme for the first stage of the proposed methodology.

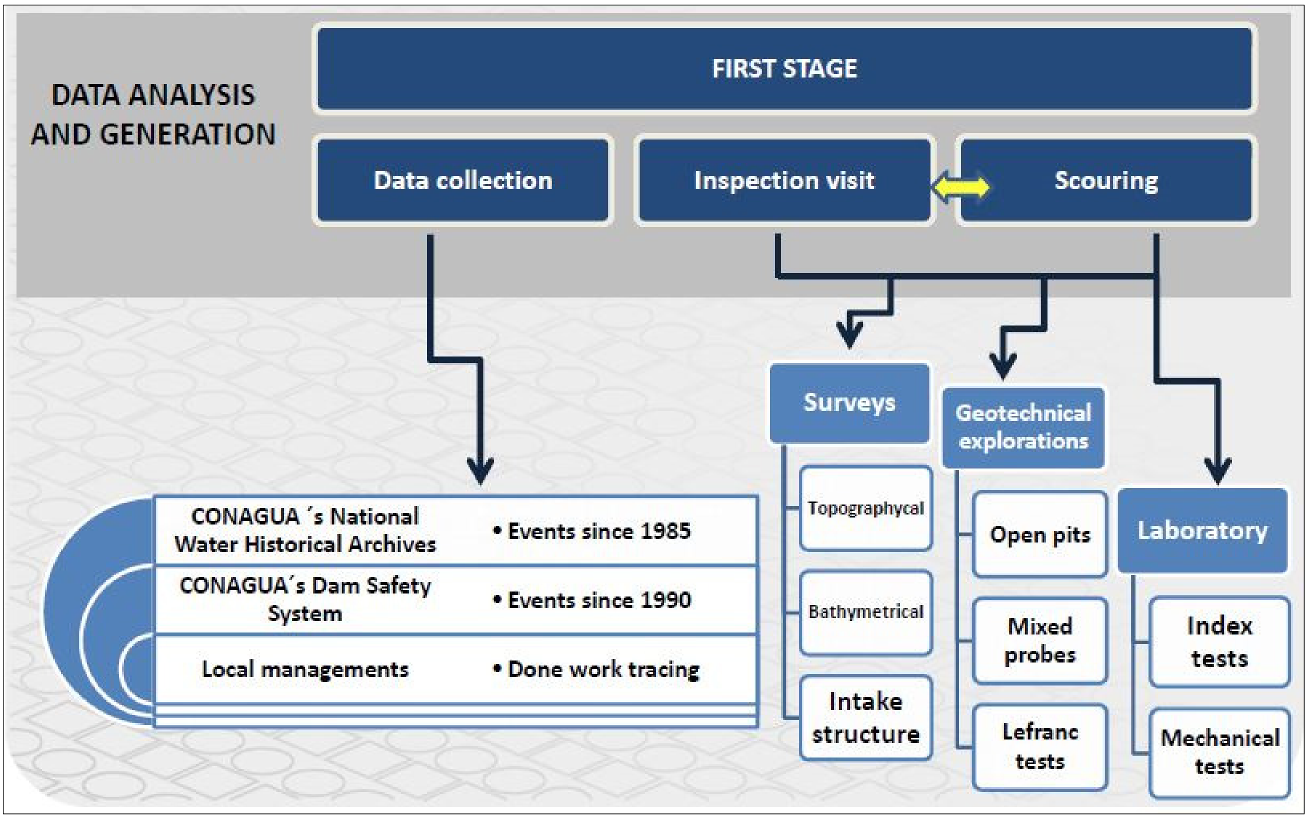

Figure 2. Activities to be performed at the first stage of the proposed methodology. (Comisión Nacional del Agua, 1998).

2.2 Second stage: Hazard diagnosis and assessment

This stage features four main activities: Hydrological assessment, Hazard zones delimitation, Curtain´s stability analysis and Functional and operational review of the dam.

The hydrological assessment features the physiographical description of the input basin (location, main stream´s length, time of concentration, area of the basin, etc.), dam´s input of hydrographs calculation (which features the space-time analysis of the rainfalls with influence on the input basin, design hydrograph, runoff coefficient, etc.), transit of avenues within the reservoir, as well as the free surface water levels assessment (United States Corp of Engineers, 2003).

The maximum level reached by the water as the flood was transited through the reservoir needs to be compared. It was compared by using the different return periods with the dam´s characteristic levels (The ordinary maximum water level, the extraordinary maximum water level and the dam´s crown). The required data to get the flood transit completed are the hydrographs for different return periods, as well as the elevations-capacities curve and the intake structure´s elevations-discharges curve. Both were obtained from the topographical and bathymetrical surveys from the first stage of the proposed methodology. The water initial level within the reservoir, which in all cases the Ordinary Maximum Water Level (OMWL) is the one used, because it provides the most unfavorable operation condition.

In this stage, the first two activities were related to each other, due to the Hazard Zones delimitations which totally depend on the flood transit within the reservoir. This is because, to get the Hazard Zones delimitation done, two main stages are analyzed, which they use some of the flood transit obtained hydrographs: the first of the two scenarios consist of a controlled discharge where the induced damages caused by a 100-year of return period rainfall, were assessed. This rainfall gets controlled and transited through the intake structure, whereby although the dam spill by the spillways, the dam will have no harm at all.

The second scenario corresponds to a non-controlled discharge, being that the dam´s rupture gets simulated, where simulation on which a 10,000-year returns period of hydrograph was used. The assumptions taken into account in this second scenario were: the water level at the beginning of this stage would be the Extraordinary Maximum Water Level (EMWL) and in that instant (with the EMWL) a 10,000-year of return period hydrograph (United States Corp of Engineers, 2001) gets into the reservoir; and from that on the dam´s rupture will be obtained as well as the results of that condition.

In order to get the Hazard Zones delimitation, a bi-dimensional model called Iber was used, which is a mathematic model which discretizes the Saint Venant equations in 2D by using a finite volumes scheme. The

  / ISSN 1562-6865 (Online) - ISSN 1063-7710 (Print)

Iber´s hydrodynamic module solves the 2D Shallow Water Equations (2D-SWE) as well as the Saint Venat equations[1].

By using the above equations, the assumption on both uniform hydrostatic and velocities distribution was made. In order to feed the mathematical model, a Digital Elevation Model (DEM) is required to study the zone (it is commonly used a model for every 15 m, or a Lidar model, if applies). The topography and bathymetry of the studied dam were also required, as well as the dam´s downstream topography, which can include culverts and roads if they cross the river (Instituto Nacional de Estadística Geografía e Informática, 2016).

The obtained results for both scenarios (controlled and non-controlled discharges) were presented in geo-referenced blueprints which had the following informations: flooded area, maximum velocities, maximum depths and dam´s rupture hazard, which can be obtained as the multiplication of the depth and the speed. This hazard could be a high one if that multiplication equals to a number higher or equal to 1.25, a medium hazard features numbers smaller than 1.25 and higher than 0.025, and finally a lower hazard features numbers lesser or equals to 0.025.

By obtaining the flooded area and the population density from the studied area, the most likely affected population was estimated for each scenario, and the most likely damaged infrastructure gets analyzed. (Bridges, ports, streets, houses, etc.)

Figure 3 shows the procedure to be carried out within the first two activities of this second stage, as well as the relationship among them. It is presented as an example, a geo-referenced blueprint in which the red color features a high hazard (Hazard value ≥1.25), the yellow color features a medium hazard (1.25>Hazard value >0.025) and the green color features low hazard (Hazard value≤1.25).

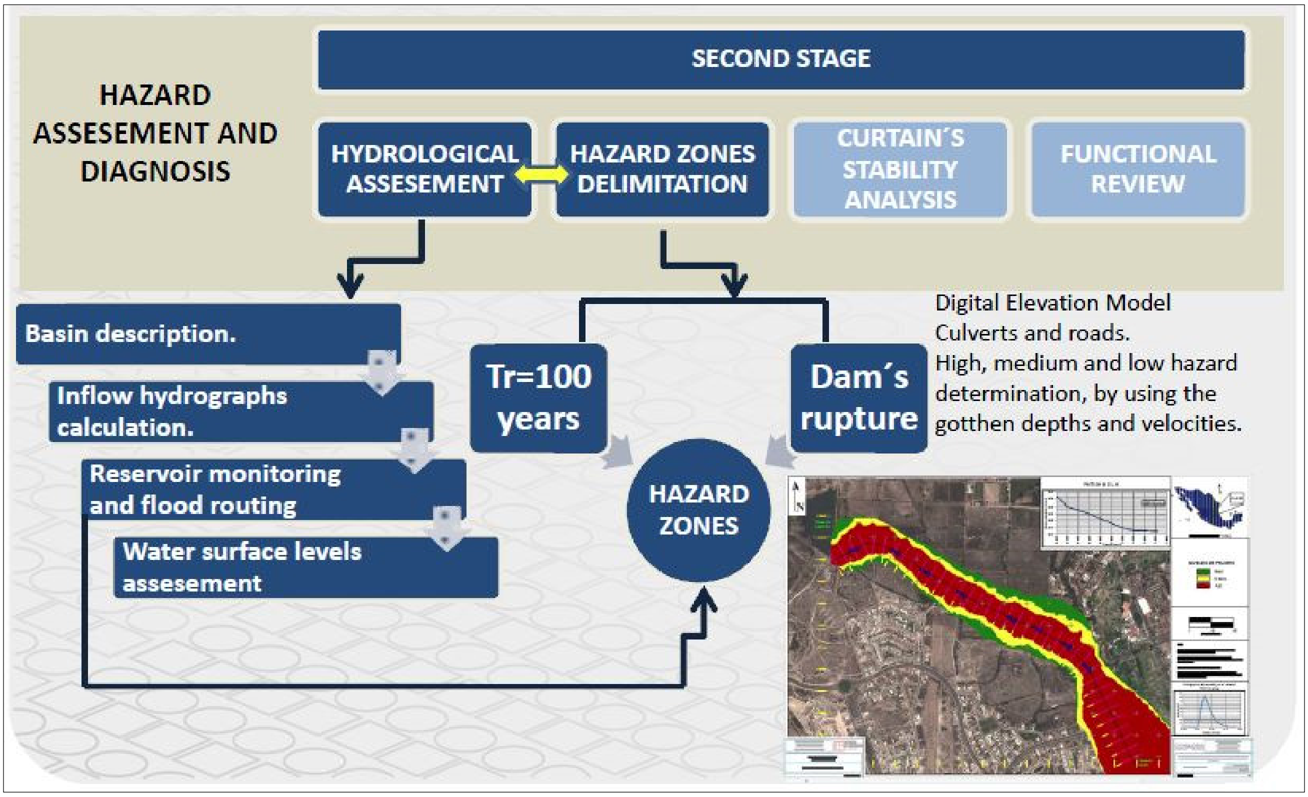

Figure 3. First two activities to be carried out within the second stage of the proposed methodology (Iber, 2012).

The curtain´s stability analysis was carried out according to the curtain´s type. This could be according to the materials it is made of (embankment dams) or if it is a flexible or rigid dam (masonry or cyclopean concrete).

In the case of the flexible dams (embankment dams), dam´s topographical and bathymetrical data was used, in particular as the dam´s geometry. This data gets numerically analyzed by using two procedures: the first one is the *balance to the limit.* In this procedure the slope´s stability calculation was obtained by using the voussoir´s method. Considering the mechanical properties, the materials, properties were obtained by using the geotechnical explorations and the lab tests of the first stage (Comisión Nacional del Agua, 1998).

The calculation method was applied to the slope´s analysis in terms of effective or total forces in cohesive, friction-cohesive and friction soils by considering circular or composed failure surfaces in which the

[b] For further information, please chcek the Iber´s referenced manual

leak forces among voussoirs and the seismic forces could be related for a pseudo-static analysis. The safety factor gets calculated with two different methods in order to verify congruence in the results, and thus, to specify if the force balance, moment balance or both of them get satisfied.

The second procedure was the *finite elements* in this procedure, where a water flow analysis wascarried out. With this calculation, the dam´s force status could be determined for different load conditions. In order to verify the dam´s stability, three analysis conditions were considered which are established flow, quick drawdown and seismic conditions. To guarantee the dam´s safety, the fulfillment of the safety factor was verified as follow:

- For the established flow condition, the minimum required safety factor is 1.5 for the dam´s downstream slope, and the analysis was carried out considering the water level within the reservoir is the EMWL;
- For the quick drawdown condition, the minimum required safety factor is 1.2 for the dam´s upstream slope, and the analysis was carried out by considering the water level in the EMWL and, the final level is the one where the intake structure is located;
- For the seismic condition, the minimum required safety factor is 1.0 for both of the dam´s slopes, and the analysis was carried out by considering the water level within the dam in the OMWL.

For rigid dams, the three main analyzed conditions are overturning, dam´s glide and excessive forces. In order to verify curtain´s stability for overturning, the total amount of opposing overturning moments must be greater than the total amount of the overturning inducing moments. For the glide condition, the total amount of the opposing glide forces must be greater than the glide inducing forces.

This kind of curtains (the rigid ones) also gets analyzed by using the finite elements method (in 2D or 3D, according to the case). In both cases, the topographical and bathymetrical data collected at the first stage is extremely important due to the dam´s geometry, and can be represented in the mathematic model (SAP 2000 for example).

The mechanical properties of the curtain´s material were taken from specialized bibliography, in case there are no samples of the dam´s curtain. In case there are, the mechanical tests to get those mechanical properties are carried out.

For concrete curtains, a sclerometer was used to get an estimation of the simple compression strength for four previously collected cores, from duly selected sites, in such a way the perforations do not generate any further weak or leak sensitive zones. As the perforations get done, they get plugged with a concrete injected special mixture, which guarantees the suitable functioning of the structure. The simple compression of the concrete gets estimated in the four collected cores through destructive tests.

For the masonry curtains case, by using a signed form from the person responsible for the dam, a suitable zone is picked out, on which a squared section of the wall could be extracted, which involves at least three 0.7 m long rock pieces, in all directions (x, y and z). This sample gets tested by using a diagonal tension test in the lab.

After the piece extraction; the masonry wall will get recovered by using cement mortar, Portland lime and hydrated sand with an adhesive additive to get the fresh mortar glued over hard mortar and rock.

The gotten strength parameters in the above tests are used to get the curtain´s stability analysis and, thus, the axial forces of the curtain´s base are gotten, as well as the curtain´s body forces and the maximum pulling and shearing forces. At the finite elements model, it must be checked that forces on the structure´s important points will be lesser than the specified maximum permissible forces for different load unfavorable conditions, and that is how the structure was checked to not to be working by tension forces.

This calculation was carried out for three functioning conditions:

- The water level within the dam is at the OMWL;
- The water level within the dam is at the EMWL;
- The water level within the dam is at the OMWL and it gets a seism.

To get the third condition, the necessary studies were carried out to determine the seismic hazard in the zone.

In the operational and functional assessment, the actual functioning of the different dam´s components get described, as well as their physical condition and any other existing anomaly, for example, in the valves, sluices, the spillway structure, etc. Likewise, the dam´s operational protocols (if there are any) must be reviewed, and if it is the case, operational measures to get suitable dam´s water levels were proposed. It is also analyzed if the dam´s freeboard was suitable enough.

Figure 4 shows the procedure to be carried out at the two last activities of the second stage of the proposed methodology.

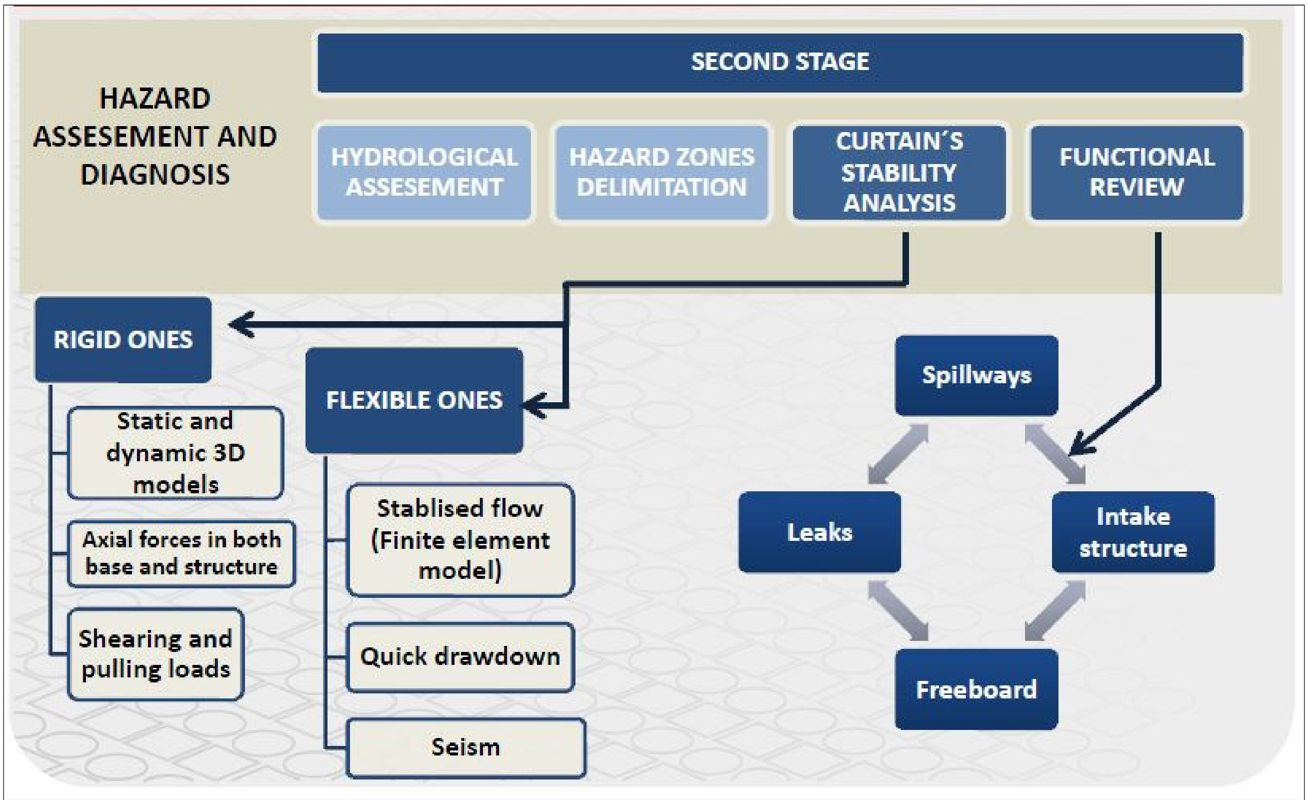

Figure 4. The last two activities to be carried out in the last stage within the proposed methodology.

2.3 Third stage: Resolution (Structure hazard)

In this third stage, a resolution based results were obtained for the four previous scenarios of the second stageto determine if there is any hazard within the dam and what type of hazard. The most probable hazard a dam could have are:

- Hydrological hazard: It will be a hydrological hazard within a dam if the maximum water level within the reservoir is greater than its EMWL by performing the flood transit within the reservoir;
- Geotechnical hazard (flexible curtains): If the previously obtained safety factors (within the second stage) are lesser than recommended, then the dam will get a geotechnical hazard;
- Structural hazard (for rigid dams): If the curtain´s stability analysis obtained results in pulling and shearing loads, there will be a structural hazard;
- Functional hazard: The structure will have a functional hazard if its spillways get eroded, their structure gets an irregular crown level, non-functional electro mechanic mechanisms and a non-sufficient freeboard;
- Land management hazard: This kind of hazard is about a possible invasion at the federal zone of the dam´s reservoir, at the federal zone of the downstream riverbed and generally at the dam´s influence zone. If one of the previous situations comes true, then it will be a land management hazard.

If it is the case which the dam does not get any hazard at all, then general recommendations will be issued, for example, a curtain´s general cleaning, maintenance of the dam´s electro mechanic devices, reservoir´s monitoring, leak repair and etc.

Figure 5 show the procedure to be carried out within the third stage of the proposed methodology.

2.4 Fourth stage: Conceptual design for hazard mitigation

In this stage, once the type of dam´s hazard had been detected (third stage), some measures to eliminate (or in some cases to diminish) the hazard are proposed. Among the probable actions to follow, there will be the hydrological and hydraulics ones, geotechnical and/or structural ones, or in case the dam is in very poor conditions, it is proposed to put it out of service.

Particularly some of the actions proposed are suitable construction for spillways, building or re-building shock-absorber tanks, building suitable level for the dam´s crest, dam´s downstream riverbeds and channels rectification, berms and filters construction, as well as, the replacement of old electro mechanic equipment. From these actions, a conceptual design was carried out in order to be supporting for the corresponding authorities to help them out for decision making in hazard elimination and/or diminution.

Finally, general recommendations within this stage were also formulated, in order to increase the structure´s safety. Figure 6 shows the carried-out procedure for the fourth stage of the proposed methodology.

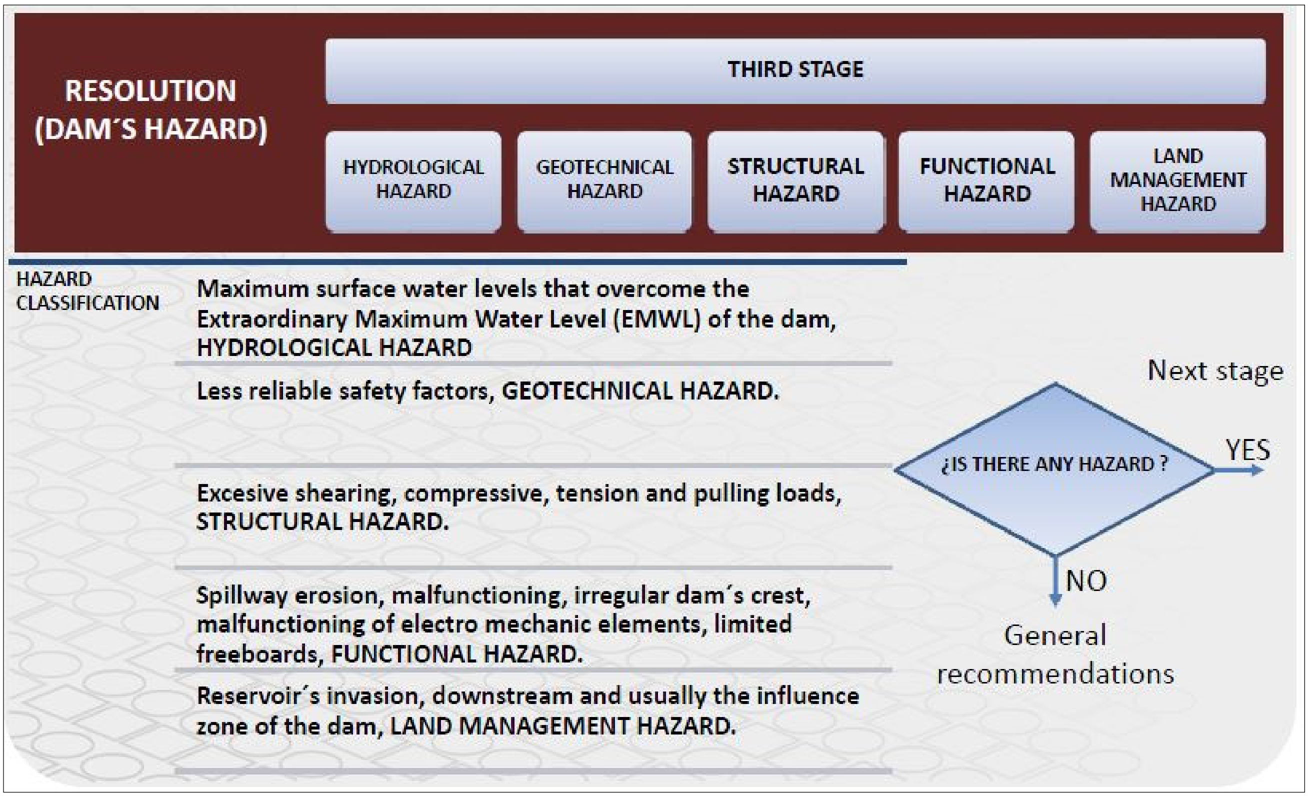

Figure 5. Activities to be carried out within the third stage of the proposed methodology.

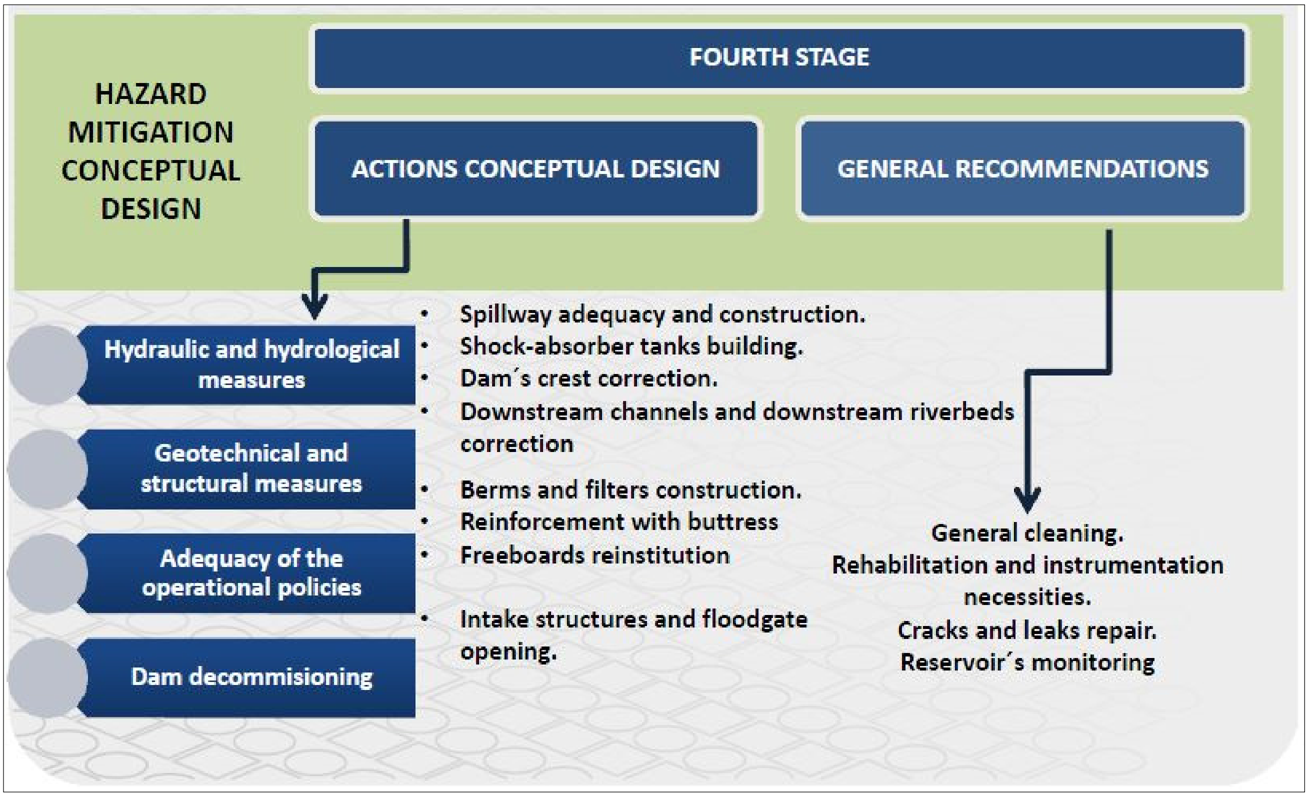

Figure 6. Activities to be carried out within the fourth stage of the proposed methodology.

3 CONCLUSIONS

The proposed methodology has been carried out at the review of 28 Mexican dams and it has been useful for the detection of other type of structure hazard which the Level I inspection visit cannot determine. It has been observed that 71% of the studied dams have a high hydrological hazard which when the Level I inspection visit was made, it was not detected. It has also been observed that several of the studied dams has high structural and geotechnical hazard reports, nonetheless, by carrying out the analysis of these structures, it was concluded that there was no hazard at all.

The carried-out activities have let the current information to be updated and in some cases, having new information which did not exist back when it was collected to be added. The influence area of determination in downstream of the dam has helped to get some clues of the hazard magnitude that dams could get if the spillway gets an extreme event or in case of a dam break and thus a sudden discharge.

REFERENCES

Comisión Nacional del Agua (1998). *Inspección de presas de tierra. Manual de capacitación en seguridad de presas*. Mexico, 95.

Comisión Nacional del Agua (1998). *Preparativos para efectuar una inspección de seguridad de una presa. Manual de capacitación en seguridad de presas.* Mexico, 104.

Iber Software (2012). *Manual de Referencia Hidráulico*. España, 59.

Instituto Nacional de Estadística Geografía e Informática (2016). Tecnología Lidar. *Geodesia*, viewed 15 August 2016, http://www.inegi.org.mx/geo/contenidos/geodesia/lidar.aspx.

Hydrologic Engineering Center (HEC). (2000). *Hydrologic Modeling System: Technical Reference Manual,* United States Army Corps of Engineers.

Hydrologic Engineering Center (HEC). (2003). *Geospatial Hydrologic Modeling Extension*: *User´s Manual,* United States Army Corps of Engineers.

Proceedings of the 37th IAHR World Congress
August 13 – 18, 2017, Kuala Lumpur, Malaysia

IDENTIFYING URBAN FLOODING VULNERABILITY USING MCDM APPROACH

GYUMIN LEE[1], JINWON CHOI[2] & KYUNG SOO JUN[3]

[1] Construction and Environmental Research Center, Sungkyunkwan University, Suwon, Korea
greenbeing@skku.edu.
[2,3] Graduate School of Water Resources, Sungkyunkwan University, Suwon, Korea
cjw0314@skku.edu; ksjun@skku.edu

ABSTRACT

This study provides an approach for assessing flood vulnerability at the urban catchment scale. Influencing factors for urban flood vulnerability assessment include urban structure, buildings, and critical objects. The procedure for the urban flood vulnerability assessment is divided into four stages in this research. In the first stage, the influencing factors are selected and weight values are calculated, which are applied to the flood vulnerability assessment. In the second stage, the input data for the selected assessment factors are collected and standardized according to the measurement units and categories of data. For the third stage, the spatial information of the region for the assessment is established using ArcGIS, based on the standardized data. Lastly, the vulnerability is assessed using the Multi-criteria Decision Making (MCDM) methods as TOPSIS, and the priority control regions in the vulnerable area are determined. The approach is applied to the Dorimcheon basin in Seoul, South Korea. Data are collected from the object regions according to the selected assessment index, and organized spatially. Since the collected data have different spatial distributions and units, 0.1 × 0.1 km grids are set up to assess the vulnerability, and the applicable values are recalculated in each grid depending on the index. All weights on criteria are derived from an objective procedure. This study uses Delphi technique to select all criteria and quantify all weights. The assessment results provide information on the regions that are relatively more vulnerable to urban floods in the object area, and can be used as useful data to select the priority control region when floods occur in the area.

Keywords: Urban flood vulnerability; Delphi; MCDM; TOPSIS.

1 INTRODUCTION

Recent cities are becoming increasingly vulnerable to flooding because of rapid urbanization and installation of complex infrastructure. Furthermore, changes in the precipitation patterns which cause global climate change also increases the flood risk. Urban floods have also become a repeated occurrence in Seoul, capital city of South Korea. It has been suggested that the poor rainfall runoff, which is caused by faulty sewage pipes, and the influence of backwater from the nearby streams are key factors associated with these floods.

Kim et al. (2006) suggested that the factors affecting the urban flood risk are (1) the rainfall as an inducing factor, (2) the sociocultural and economic aspects as a weight factor, and (3) the inundated area as a damage factor. These items were related to the urban flood damage, through both correlation analysis for the amount of urban flood damage and factorial analysis. A multivariate statistical analysis considering factors such as the liberal culture; facilities; and societal, economic, and meteorological aspects was conducted. However, urban floods cause damage not only to human life and property but also to overall urban function; thus, urban floods hamper productivity and stability. Barroca et al. (2006) classified the factors for the assessment of the vulnerability to urban floods according to the subjects of the damage. These include the residential, commercial and industrial regions; response capabilities to urban disaster; and previous damage history. Chakraborty et al. (2005) contributed to the development of an emergency evacuation strategy on the basis of the spatial vulnerability assessment in view of the social vulnerability index. They emphasized that the characteristics of the indigenous people should be carefully considered.

The diversity and complexity of the damage caused by floods to the community should be taken into account when assessing the vulnerability to floods. Therefore, it is necessary to more precisely investigate the vulnerability factors so as to prepare for urban floods. Notably, factors other than those that have been used for the existing flood vulnerability assessment should be applied because of the damages to both human lives and property due to the underground inundation in the recent domestic cases of urban floods. In this research, considering the cases of recent domestic urban flood damage as well as the related domestic and foreign research, the social vulnerability to urban floods in the Dorimcheon stream basin, which was damaged by inland inundation in 2011, is assessed. This is carried out by selecting assessment factors for the vulnerability to urban floods based on the composition of the social vulnerability factors.

2 THEORETICAL BACKGROUND

2.1 Procedures for flood vulnerability assessment

The procedure for the urban flood vulnerability assessment was divided into four stages in this research.

- The influencing factors were selected and weight values were calculated, which were applied to the flood vulnerability assessment.
- The input data for the selected assessment factors were collected and standardized according to the measurement units and categories of data.
- The spatial information of the region for the assessment was established using ArcGIS, based on the standardized data.
- Lastly, the vulnerability was assessed using the TOPSIS technique, and the priority control regions in the vulnerable area were determined.

2.2 TOPSIS assessment technique

TOPSIS is a technique that allows humans to induce rational choice by considering the best and worst alternatives simultaneously, i.e., this is a concept for choosing an alternative that is closest to the positive ideal solution (PIS) and/or choosing an alternative that is farthest from the negative ideal solution (NIS), preferentially (Jun et al., 2007; Chu, 2002).

Therefore, it is a method that provides the assessment priority using a range scale. Furthermore, the assessment results of all the alternatives are easily calculated and presented in the form of multiple criteria (Chung and Lee, 2009; Kim et al., 1997; Lee et al., 2013; Lee and Chung, 2007):

$$v_{ij} = x_{ij} \times w_i, \qquad [1]$$

where x_{ij}j is built by alternatives $A_j, (j = 1, \cdots, n)$ which are to be evaluated against $C_i, (i = 1, \cdots, m)$. The performance matrix is composed of rows of unit area with columns of criteria.

The positive ideal solution (FPIS) and negative ideal solution (FNIS) of unit area are computed as follow in Eq. [2]. The weighted normalized values for each criterion are sorted in descending order.

$$\begin{aligned} A^+ &= v_1^+, v_2^+, \cdots, v_n^+ \\ A^- &= v_1^-, v_2^-, \cdots, v_n^- \end{aligned} \qquad [2]$$

The distance from the positive ideal and the negative ideal solution for each alternative is calculated as:

$$d_i^+ = \left(\sum_{j=1}^{n} (v_{ij} - v_j^+)^2\right)^{1/2}, \qquad (i = 1, \cdots, m) \qquad [3]$$

$$d_i^- = \left(\sum_{j=1}^{n} (v_{ij} - v_j^-)^2\right)^{1/2}, \qquad (i = 1, \cdots, m) \qquad [4]$$

The optimum membership degree of each alternative is calculated as follows:

$$C^+ = \frac{d_i^-}{d_i^+ + d_i^-}, \qquad (i = 1, \cdots, m) \qquad [5]$$

Priority is determined by ranking, using the values obtained from Eq. [5].

2.3 Delphi procedure

This study used Delphi technique to select all criteria and quantify all weights. The Delphi technique consists of several steps and repeated surveys. The procedure of the Delphi technique is as follows. The first step is to select a panel. The selected panel answers the questions through sequential Delphi rounds. It also enables the panel to exchange views.

According to Dalkey, (1962), the reliability of the survey increases with the number of panelists. However, more recent research shows that useful results can be obtained from panels with 10 or less expert members. The second step is for the panelists to directly quantify the relative importance of and to assess the priority of the factors.

It can be said that the stability of the research is secured to some extent, if the opinions of the experts reach a consensus through multiple steps of repetition and re-evaluation of the questionnaire. Finally, after comparing the progress made so far, we integrated the results and created the comprehensive report.

3 APPLICATIONS

3.1 Study area

The Dorimcheon stream basin was selected as the object of assessment in this research. The Dorimcheon stream, the first branch of the Anyangcheon stream, rises from the valley of Gwanak and the Samsung Mountains and joins the Anyangcheon stream. Its length is 14.20 km, and the area of basin is 42.50 km². It flows through a total of five administrative districts, which are the Guro, Geumcheon, Yeongdeungpo, Dongjak, and Gwanak districts. More than 90% of Gwanak and Yeongdeungpo, approximately 40% of Dongjak and Guro, and 10% of the total area of Geumchun were included in the area of the assessment object.

3.2 Establishment of assessment matrix

This study used Delphi technique to select all criteria and quantify all weights. Panels of experts in urban flood vulnerability and water resources were selected and consulted. A total of 11 vulnerability assessment experts were surveyed: 7 (64%) in research institutes, 2 (18%) in the engineering field, and 2 (18%) civil servants in other administrative agencies. The length of time that respondents spent in their current professions was less than 10 years for 6 respondents (55%), accounting for more than half. In this section, it was expected that these experienced professionals could provide opinions based on practical experience. Given that in addition to having a Master's degree, more than half of the respondents held a PhD degree, we expected that our panelists possessed a high level of expertise in their fields. Therefore, we expected the results of the Delphi technique to be able to reflect the opinions of experts.

As shown in Table 1, the selected assessment index was classified by the vulnerability factors, such as land cover and resident, the critical points specific to urban floods, and the response capabilities. Data were collected from the object regions according to the selected assessment index, and organized spatially. Figure 1 shows examples of collected data such as the density of the population and the rate of land use.

Table 1. Criteria and weights for urban flood vulnerability.

Criteria and sub-criteria		weight	Classification
Land cover	Residential area	0.358	Single residence facility
			Co-residence facility
	Industrial area	0.182	Industrial facility
	Commercial area	0.140	Commercial facilities
			Integrated Facility
	Traffic area	0.172	Airport
			Harbour
			Railroad
			Road
			Other traffic communication facilities
	Public utility area	0.148	Basic environmental facility
			Education/Administrative facilities
			Other public facilities
Resident	Population density	0.618	Population density
	Resident characteristics	0.382	Percentage of people in vulnerable age groups
			Percentage of disabled and/or immobile persons among residents
Critical points	Transportation facilities	0.418	Maximum road utilization per hour
			Roads with more than four lanes
	Underground facilities	0.582	Subway
			Underground commercial facility
			Underpass
Response capabilities	Rescue organization	0.600	119 Rescue center, fire department
			Police office
	Response organization	0.400	Administrative agency

The selected indicators are defined as single indicators constructed by aggregating variables with different units and properties. Indicators with such individual characteristics need to be standardized. Based on the obtained data, a standardization method called scale rebalancing was used. We standardized the indices so that the maximum value was 1. Since the collected data have different spatial distributions and

  / ISSN 1562-6865 (Online) - ISSN 1063-7710 (Print)

units, 0.1 × 0.1 km grids were set up to assess the vulnerability, and the applicable values were recalculated in each grid depending on the index.

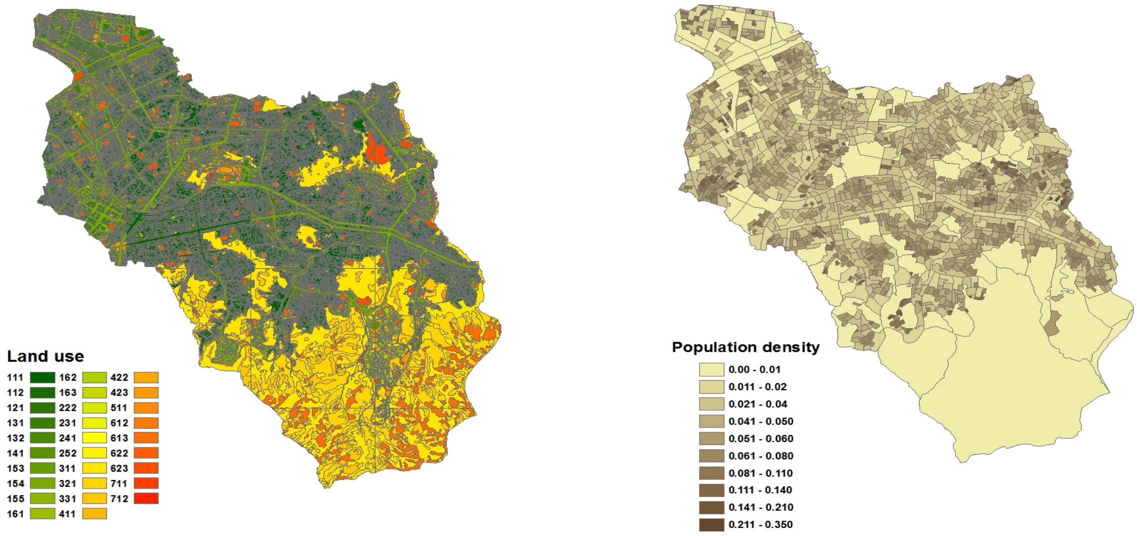

Figure 1. Collected data of criteria.

Recently, GIS is widely used for simulating and analyzing the spatial distribution in area units. GIS can be defined as a system that helps to utilize geographic information through construction, management and computerization of a diverse array of geographical information.In this study, various social, economic, and geographical characteristics (slope, land cover, land usage) in the administrative sections of Dorimcheon area were constructed by GIS. Each element was overlapped and rankings were constructed for each cell unit for the evaluation of vulnerability of Dorimcheon. The form of the data is a raster, and the structure of the data is made simpler and easier to simulate by using a grid network, a discrete type of graphic element, with the smallest unit being a uniform 100 m cell. The slope of Dorimcheon basin was calculated by converting the numerical map into a GIS shape file. After constructing the shape file of the same unit for each indicator factor, the geographical characteristics were constructed for the corresponding spatial locations.

In order to construct a single map, the data from the grid made of 100 m cells was averaged by applying the average value of each spatial position or corresponding unit. The data construction using GIS is effective in that it can easily apply the weights to perform the superimposition and spatially display the results when calculating the final result (Figure 2).

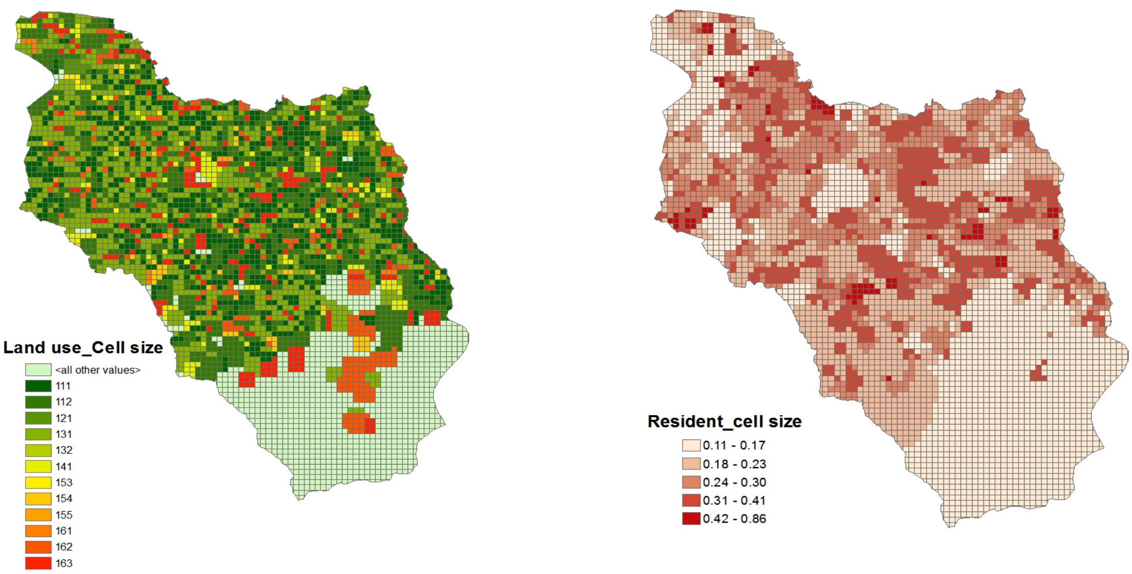

Figure 2. Constructed data with grid.

3.3 Results of assessment

Figure 3 shows the results of the flood vulnerability assessment using the TOPSIS technique for each 100 m x 100 m cell-area. When we look at the vulnerability evaluation results calculated for each grid, it can be seen that the difference in vulnerability was significantly different even in adjacent cells. The large difference between cell units seemed to be due to the influence of residents and vulnerable areas. This appears to be due to the impact of areas with inadequate traffic conditions as well as characteristics of each space, such as population density and land cover. In addition, in the case of rescue response, there was little difference between neighboring cells, therefore having little influence on evaluation results. Traffic jamming and land cover, in that order, showed the greatest differences in data values. Also, the values for the two indices had a large impact, depending on the spatial characteristics. The assessment results provide information on the regions that are relatively more vulnerable to urban floods in the object area, and can be used as useful data to select the priority control region when floods occur in the area.

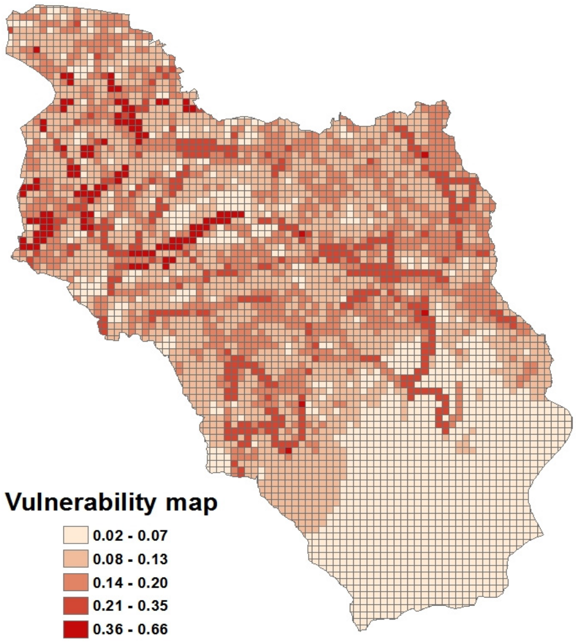

Figure 3. Assessment result.

4 CONCLUSIONS

The study presents an approach that uses indicators derived from geodata and census data to analyze the vulnerability to floods in urban area. We derive social indicators which take into account social characteristics of urban areas, to be used in flood vulnerability assessments, and to construct the evaluation model by applying the multi-standard flood vulnerability assessment technique to Dorimcheon area in Seoul. Social vulnerability indicators consist of land cover, residents, vulnerable areas, and disaster response, which are calculated by standardization of different variables and assignment of weights.

The study shows that a vulnerability assessment considering social characteristics can reveal that there is a large difference in vulnerability to flood even within the same administrative district. The results of this study present countermeasures and defensive measures against flooding in the form of cell units for the sites selected as areas vulnerable to urban flooding. This representation of vulnerability characteristics of each site according to the abovementioned vulnerability assessment may be used as a countermeasure against urban flooding.

ACKNOWLEDGEMENTS

This study is financially supported by a grant (13AWMP-B066744-01) from Advanced Water Management Research Program by Ministry of Land, Infrastructure and Transport and the Basic Science Research Program of the National Research Foundation of Korea (NRF), which is funded by the Ministry of Education (NRF-2016R1A6A3A11932509).

REFERENCES

Barroca, B., Bernardara, P., Mouchel, J.-M. & Hubert, G. (2006). Indicators for Identification of Urban Flooding Vulnerability. *Natural Hazards and Earth System Science*, 6(4), 553–561.

Chakraborty, J., Tobin, G.A. & Montz, B.E. (2005). Population Evacuation: Assessing Spatial Variability in Geophysical Risk and Social Vulnerability to Natural Hazards. *Natural Hazards Review*, 6(1), 23–33.
Chu, T.C. (2002). Selecting Plant Location via a Fuzzy TOPSIS Approach. *International Journal of Advanced Manufacturing Technology,* 20, 859–864.
Chung, E.S. & Lee, K.S. (2009). Prioritization of Water Management for Sustainability using Hydrologic Simulation Model and Multi Criteria Decision Making Techniques. *Journal Environmental Management*, 90, 1502–1511.
Dalkey, N. & Helmer, O. (1962). Experimental Application of the Delphi Method to the Use of Experts, The RAND Corporation. *Management Science,* 9(3), 458-467.
Jun, K.S., Chung, E.S., Sung, J.Y. & Lee, K.S. (2011). Development of Spatial Water Resources Vulnerability Index Considering Climate Change Impacts. *Science of Total Environment,* 409, 5228–5242.
Kim, B.K., Jang, D.W., Jang, N. & Yang, D.M. (2006). The Deduction of Urban Flood Risk Factor Considering Climate Change. *Crisisonomy,* 7(1), 125–142.
Kim, G., Park, C.S. & Yoon, K.P. (1997). Identifying Investment Opportunities for Advanced Manufacturing Systems with Comparative Integrated Performance Measurement. *International of Journal Production Economics*, 50, 23–33.
Lee, G., Jun, K.S. & Chung, E.S. (2013). Integrated Multi-Criteria Flood Vulnerability Approach using Fuzzy TOPSIS and Delphi Technique. *Natural Hazards and Earth System Science,* 13, 1293–1312.
Lee, K.S. & Chung, E.S. (2007). Development of Integrated Watershed Management Schemes for an Intensively Urbanized Region in Korea. *Journal of Hydro-Environment Research,* 1, 95–109.

FLOODSS: CALL FOR COMMUNITY ACTION

MARIAN MUSTE(1)

(1) IIHR-Hydroscience & Engineering, The University of Iowa, Iowa City, U.S.A.,
marian-muste@uiowa.edu

ABSTRACT

Flood mitigation has considerably evolved with the adoption of a flood-risk centered decision-making approach that integrates methodologies pertaining to three different domains: hydro-meteorological & hydraulic data, modelling of the physical processes, and decision support analyses. The approach has been successfully incorporated in early warning systems and planning tools for flood prevention. In parallel, a large number of flood-focused decision-support systems (DSS) have emerged for solving specific flood mitigation objectives (i.e., to assist before, during or after the floods). Most of these systems were developed through place- and project-based efforts, hence, not serving all levels of decision making nor being readily transferable to other flood-affected communities. The increased socio-economic threat posed by floods globally would considerably benefit from widely-accessible generalized flood DSS (FLOODSS) that can be quickly deployed in any flood-prone areas irrespective of their size and geo-political location. The FLOODSS envisioned in this paper strives to fulfill this goal by assembling hydro-meteorological data, results of flood process simulations, and actionable information and syntheses for supporting decision-making in one web-platform through customized flood-related services and machine-to-machine communication. FLOODSS is essentially a customized cyberinfrastructure[1] that integrate multiple resources (data, information, and knowledge) that are subsequently made available to stakeholders in flood-prone areas to mitigate risk and enhance community resilience. The paper describes the overall architecture of the FLOODSS, reviews its components, and highlights the impacts of this new platform on enhancing the collaborative planning process for flood mitigation and resilience. The benefits brought by FLOODSS to flood science and research are also identified and briefly discussed. As efficient and fast-paced translation of the FLOODSS from concept to practice can only be attained through a wide collaborative effort that transcend disciplines, institutions, and countries, the papers launches a call for community action and offer a road map for guiding the FLOODSS implementation.

Keywords: Flood risk mitigation; flood resilience; flood management; decision-support systems; hydroinformatics.

1 INTRODUCTION

Flood mitigation has considerably evolved with the adoption of a flood-risk centered decision-making approach that integrates methodologies pertaining to three different domains: hydro-meteorological & hydraulic (H&H) data, H&H modelling, and decision support analyses. The connections among the three domains and their components are illustrated in Figure 1. The flood-risk centered approach has been successfully incorporated in early warning systems (e.g., FLOODSite, 2016; FEMA, 2016, WMO, 2006) and planning tools for flood prevention (e.g., Zorzi et al., 2016; Flood-CBA, 2016). In parallel, a large number of flood-focused decision-support systems (DSS) have emerged for solving specific flood mitigation objectives (Giupponi et. al., 2011; Laine, 2012). Most of these systems were developed through place- and project-based efforts (i.e., for assisting activities before, during or after the floods), hence, not serving all levels of decision making nor being readily transferable to other flood-affected communities. The accelerated pace of anthropogenic impacts on the landscape and ongoing climate change are collectively exacerbating the flood threats at the global scale posing new challenges for risk assessment and planning. These threats calls for widely-accessible generalized flood DSS (FLOODSS) that can be quickly deployed in any flood-prone areas irrespective of their size and geo-political location.

Attaining operational FLOODSS is not actually challenged by the lack of knowledge on hydrologic/hydraulic processes or on risk management (Giordano et al., 2008; Cutter et al., 2008; Levy, 2005). The perceived challenges are rather related to the lack of a framework for integrating multi-scale, multi-domain data provided by measurements and numerical simulations originating from heterogeneous sources in an operational platform easily accessible by stakeholders engaged in co-production of actionable knowledge for decision making (King & Thornton, 2016). Currently, there is no unified vision on the architecture, components, and the needed computer and communications technologies for attaining generic FLOODSS for

[1] Cyberinfrastructure (CI) is an active area of academic research and industrial development jointly carried out by domain and computer area specialists for handing "big data" cases.

flood mitigation and resilience. Moreover, there is no guidance of what components should be developed first and how to build human-computer interfaces to ensure efficient stakeholder engagement and consensus in actions. Fortunately, contemporary computing environments developed in other areas of activities (i.e., commerce, business) have demonstrated considerable progress (Watson et al., 2002; Muste, 2014; Mackay et al., 2015; NOAA, 2009; Sayers et al., 2002), giving hopes that our community can benefit by similar advantages if the more generic FLOODSS are becoming available.

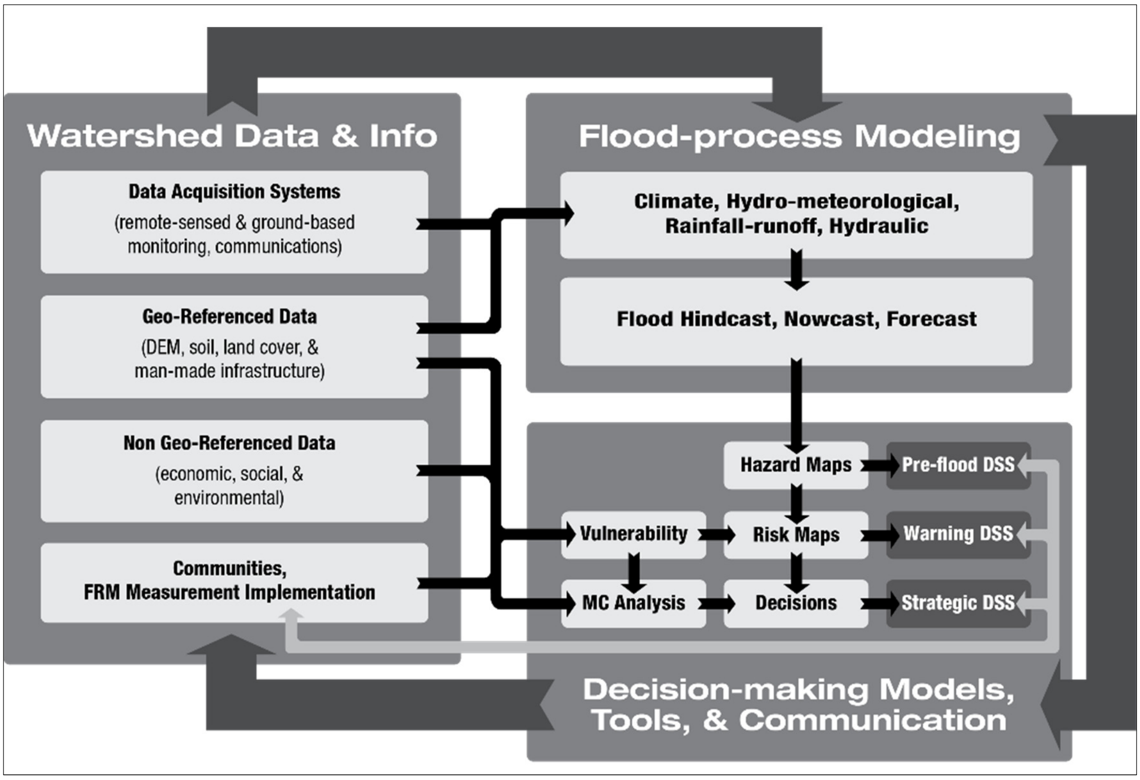

Figure 1. Flow diagram of an end-to-end DSS for multi-purpose flood risk management. Side arrows indicate the necessary connections between domains and that the connections are iterative and continuously evolving in time commensurate with the changes within the domains (Muste & Firoozfar, 2016).

The FLOODSS envisioned in this paper might fill this technological gap as it strives to assemble hydro-meteorological data, results of simulations of the flood physical processes, and actionable information and syntheses for supporting decision-making in one web-platform through customized flood-related services and machine-to-machine communication. The main challenges associated with the creation of generalized flood DSS are to design and develop the needed information and communication infrastructure (i.e., cyberinfrastructure or hydroinformatics) for handling and ingest the massive amount of data and observations into flood and socio-economic collaborative models to obtain in real time operational flood hazard and risk maps. Overcoming these challenges requires coherent and systematic community efforts for deep and wide integration of flood-risk management knowledge with the relevant aspects of information and communication technologies within a flexible framework.

The overarching goal of this paper is to create a strategic partnership to gradually build a web-GIS computational environment enabling the integration of the data and information generated by surveys and monitoring with multi-domain modeling over a range of spatio-temporal scales for timely supporting collaborative decision-making on flood risk and resilience. The paper describes the overall architecture of the FLOODSS, reviews its main cyberinfrastructure aspects, and highlights the impacts of this new platform on enhancing the collaborative planning process for flood mitigation and resilience. The benefits brought by FLOODSS to flood science and research are also identified and briefly discussed. Efficient and fast-paced translation of the FLOODSS from concept to practice can only be attained through a wide collaborative effort that transcend disciplines, institutions, and countries. The papers closes with a call for the strengthening the current flood DSS effort and gather the relevant communities to action. A road map for guiding the FLOODSS development and implementation is also suggested.

2 WHAT IS FLOODSS?

The overall role of FLOODSS is to provide decision-makers with resources (data, information, domain knowledge) and procedures to formulate alternative outcomes, assess trade-offs and identify solutions that meet the priority objectives. Besides supporting the modeling leading to flood hazard mapping, the FLOODSS-supported activities more closely related to decision-making include:

a) assisting in planning for flood prevention and recovery (i.e., “build back better” approach)
b) assisting during flood crises
c) engaging communities in the planning process to reduce risk exposure
d) educating communities on the capabilities and limitations of structural and non-structural mitigation measures
e) shedding new insights in flood science for learned practitioners, and
f) informing stakeholders on how prevention and response capabilities enhance resilience (by reducing overall risk exposure and having responses in place when design levels are exceeded).

FLOODSS is an interactive web-based platform providing customized flood-related services by assembling in real time hydro-meteorological data, simulations of flood processes, conduct of analyses to support decision-making (from prevention, mitigation, preparedness, response, and recovery from the impacts of flooding) using an inclusive stakeholder participatory approach (Muste & Firoozfar, 2016). The development of FLOODSS is a typical “Big data” use case whereby tasks such as curation, storage, information privacy protection, search, transfer, visualization, and sharing of the large amount of data produced from observation and modeling as well as their analysis and updating with fast speed need to be seamlessly accomplished through machine-to-machine interaction (Muste, 2014). Consequently, the methodological aspects for managing flood risk illustrated in Figure 1 require a DSS making extensive use of:

- Standardized and scalable inter-domain services for connecting on demand the data and information required for flood hazard, risk, and resilience assessment irrespective of the geographical location, watershed size, and data status (i.e., data-rich or ungagged basins);
- High-performance computing for execution of hydro-meteorological simulations using open data services operating on a library of models simulating rainfall-runoff (lump, distributed) and river hydraulics (1-D, 2D and 3-D) processes in near-real time over a wide range of spatio-temporal resolutions;
- Grid and cloud infrastructure for handling the voluminous multi-domain data required by the collaborative models and tools used for assessing the hazard, risk, and resilience before, during and after floods with consideration of climate and socio-economic evolution, as well as the preferences of the flood-affected citizens;
- Software and service infrastructure for enabling open (or selective) access to the decision-making process during emergencies (short-term protection) and strategic decisions (long-term planning and policy) irrespective of the spatial extent of the river and the temporal resolutions of the solution space;
- Globally interoperable, open and trusted cyberinfrastructure sources for enabling multi-jurisdictional collaboration and dissemination through user-friendly interfaces and a format and language understood by all stakeholders.

A generic layout of the FLOODSS components, workflows, and the ancillary cyberinfrastructure is illustrated in Figure 2. The cyberinfrastructure ensures that hazard forecasts and risk management options are generated through data and information exchanges between local and distributed interoperable web servers customized to carry out the functions illustrated in Figure 1, i.e., acquisition and management of data/observations, coupling data with models, and integrating simulation models in a collaborative decision-making modeling platform. Web technologies (e.g., servers, databases, web-programming languages), specialized processing tools (e.g., enterprise or open source GIS applications), and protocols (for interfacing databases with models and models among themselves) are selected to comply with specifications required by a service-oriented system (Mysiak et al, 2005; Power & Sharda, 2007).

The main challenge associated with the creation of generalized DSS for flood stems in the fact that the information and communication system is strongly dependent on the specific application domain for which it is developed. The conceptualization and design of a decision-support system for flood risk have to solve intricate interdependencies among engineered systems and the natural world, with some of them not fully understood, hence, assuming open areas of the architecture. Some of the information embedded n FLOODSS (especially the one related to decision making) is not strongly structured leading to obstacles in the machine-to machine communication. Additional challenges are related to design the DSS with a user-centered, interactive approach whereby users, their characteristics, and contexts are incorporated in system architecture (Kramer et al., 2000). Intrinsic variability across the human population is associated with variable responses to environmental stressors. Understanding both the sources and the magnitude of the variability is a key challenge not only for scientists and for decision makers but for the FLOODSS platform designer.

Progressing from vision to practical implementation requires, firstly, the conceptualization of the FLOODSS architecture. This effort can be phased over several steps: a) formulating the workflows for linking the multi-disciplinary processes; b) choosing the resources needed to inform the processes; c) designing the specifications for the hardware-software package that convey the information between the process components; d) choosing the web technology to execute the modeling architecture of the system; e) developing the interfaces for access, retrieve, visualize the workflow outcomes. Steps a), b), and c) mostly involve domain specialists. Steps d) and e) are typically tackled by cyberinfrastructure specialists working in close collaboration with the domain specialists.

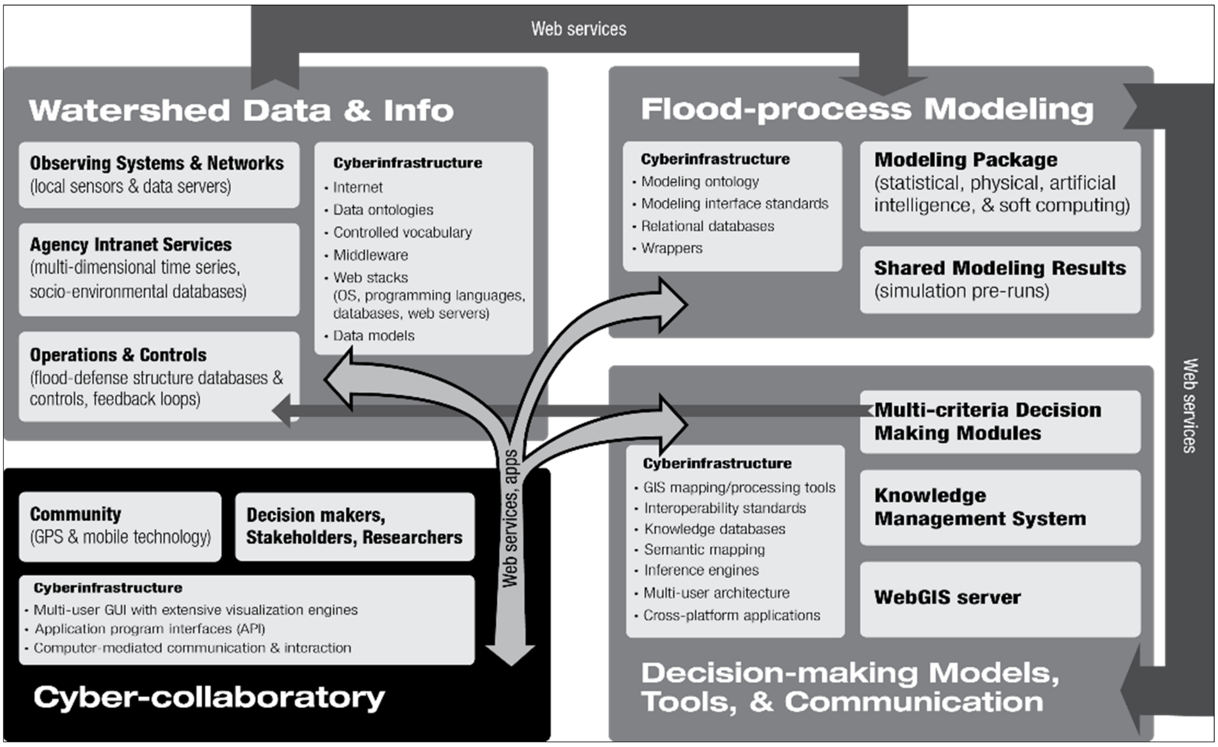

Figure 2. Flow diagram of the FLOODSS components and ancillary cyberinfrastructure). Some of the cyberinfrastructure elements (e.g., databases) are shared by multiple FLOODSS domains and components.

3 WHAT ARE THE BENEFITS OF FLOODSS?

The initial discussions on the necessity to construct FLOODSS were triggered by its relevance for supporting decision- and policy-making in the area of flood risk management. However, by bringing together multi-disciplinary data from historical records and current measurements in a centralized computational environment where the data can be easily accessed and processed, the operational FLOODSS can equally attract practitioners and scientists. The main FLOODSS users are regional and local flood risk managers, flood-focused mitigation groups, and communities with high flood-risk exposure. The integration of the multi-domain data and information into a “one-stop shop” accessible via the Internet creates a new paradigm not only for managers and communities with high flood-risk exposure, but also for scientists and researchers who are continuously seeking for new research opportunities. The availability of such a system will enable interdisciplinary flood research teams to uncover and investigate together the subtler aspects of flood risk management science that are currently rendered invisible by our limited capability to access, visualize, and analyze massive amounts of data and information describing flood-related processes from disparate sources. Therefore, the benefits of FLOODSS will be discussed separately having in mind of the management and scientific communities.

3.1 Co-production of decision-making

Web-based, platform independent system*.* Development of web-based, client–server systems DSS introduces an increased layer of complexity compared with conventional server-based DSS through the consideration of concurrent session management, human–machine interaction, and server performance. However, placing the platform on a cloud computing environment allows to handle multitude of data and information type in real-time and facilitate interactive, multi-user decision-making. Successful deployments of web-DSS in other domain areas (e.g., banking, manufacturing) have demonstrated that they can revolutionize the decision-making process by seamlessly integrating in one virtual hub data, models, knowledge, and business processes (Power & Sharda, 2007). Among the distinct advantages of the web-based DSS delivered as a service are (adapted from Zhang et al., 2011):

i. Centralized control over models and data (leading to lower costs for hardware, software, distribution, maintenance, and training, as well as greater efficiency in real-time modeling and data update)
ii. Global and easy accessibility (no need for modeling or GIS knowledge, training, or other specific software)

iii. Platform independence (encourage stakeholders and public to participate in planning and decision-making)
iv. Scalable and transferable to watersheds of various sizes
v. Modular data model construction (model components can be quickly changed as soon as more efficient versions of the simulation models are available)
vi. Improved communication and coordination [web-based DSS has become a de-facto standard of collaborative decision-making enabling user to participate during various planning stages that are directly affecting them; facilitating consensus among decision makers, stakeholders, and the public (Sun, 2013)];

Seamless integration of physical and socio-economic data and information. The generalized nature of the FLOODSS is referring to both methodological and operational capabilities of the system. The FLOODSS decision-making methodology operates on multi-disciplinary data, information, and models applicable to both strategic and operational decision making irrespective of the size of the catchment or basin. The type of data and information, models, decision-making tools, actions, and their connections within FLOODSS are visualized in Figure 1. Inclusion of the communities in the data and information block of the figure is intended to emphasize that the community input (i.e., concerns, goals, perceptions as well as any relevant data, information and knowledge that it might provide) is an integral part of the decision-making process, hence, the co-production nature of the process. The connections between various resources visualized in Figure 1 are not exhaustive nor universally valid and they can run in series or parallel. For example, the climate change impacts are both the drivers of the flood extent and frequency but in the same time they influence the vulnerability of the infrastructure exposed to risk, as illustrated in Figure 1.

Transparency and privacy of the data. The FLOODSS decision-making operational features seamlessly integrate the data management systems, flood-related models, and the tools for flood-risk decision support in a web-based environment accessible by all stakeholders. A point of careful evaluation in the implementation of an open system such as FLODSS is to not convey publicly sensitive information protected by private property rights or competitive data pertaining to competitive institutions involved in flood mitigation (e.g., insurance companies). These issues have to be considered in strict agreement with the legal frameworks and institutional regulations possibly though aggregation of the confidential data at larger scale without losing their relevance to flood risk evaluation. This aggregation of data has been already successfully tested in other domains (Ilyas et al., 2011).

The development of FLOODSS will also address behavioral issues (i.e., attitudes of the users vs. the functional features and outcomes of the DSS). The behavioral aspects are ultimately as important as the technical ones as many failures of DSS implementation are associated with the flexibility, ease of use, openness, and extensibility of the decision-making platforms (Giuponni et al., 2011). The FLOODSS interfaces should hide the complexity of the technical aspects of the decision-making while providing the needed information in an understandable formulation that is adapted to the technical skills of the local watershed stakeholders.

Local stakeholder engagement. Decisions formulated by conventional means are only understood by experts, and are, therefore, not accessible to a wider audience, which limits the public participation in the decision-making processes. The widely-accessible nature (including general public) and appropriate representation of the FLOODSS can efficiently support stakeholder engagement in a timely manner. Engaging and co-producing decisions using participatory approaches with involvement of the local stakeholders can be fully attained through the customization of the FLOODSS interfaces. This feature of the platform will address one of the critical needs of contemporary management that currently there is a general perception that by simply combining advances in flood science, information technologies, and communication technologies is not sufficient to fulfill comprehensive and stringent flood-related national and international regulations. FLOODSS can not only facilitate the participatory approach to the decision-making but can also assist with education and training of various stakeholder segments.

Decisions formulated by FLOODSS are accessible via the Internet, making it an efficient for stakeholder engagement involved in traditional forms of communication (joining local watershed groups, donating time or money to a local project, voting or commenting on plans, implementing a conservation practice, attending training courses or public meetings) and also through more contemporary ones (web collaboratory, mobile devices, and online social networking tools). Collectively, these forms of involvement inject the local (public) knowledge into the decision-making process. This engagement results in bringing important human dimensions such as health and economic well-being, vulnerability, cultural vitality, spiritual well-being, and ownership rights to the techno-scientific considerations. More importantly, given the online communication means available today, FLOODSS can act as central hubs for spontaneous community participation through swarm intelligence (Herzog, 2011). Swarm intelligence is defined as the coordinated action of individuals in a group without direct leadership (e.g., gathering information acquired by citizen science and precision agriculture systems attached to farm equipment); it has the potential to solve extremely complex problems efficiently through collective thinking. According to Herzog (2011), among the key components for implementation of swarm intelligence are: taxonomy, knowledge distillation, content management system, mobility, visualization, online simulations and analyses. All these features are necessary attributes of the IFLOODSS described herein. Consequently, FLOODSS has a realistic potential for organizing and directing users to action through online communication and collaboration with the aim of resolving flood-related problems table issues in the watersheds.

Democratization of the decision-making process. The envisioned FLOODSS does not require any particular process or decision support software on the client computer. The ideal operational environment for FLOODSS is a web-based, platform-independent system. Using the web browser, multiple users can change remotely the models' spatial and temporal inputs. This is in stark contrast with the practice of the conventional desktop-based modeling environment whereby a single user was accommodated at one time. The web-based approach allows simultaneous intervention from, for example, researchers and policy makers as both are interested in problem solving. The FLOODSS framework should allow for models to evolve around the "access – refine – re-run" pathway envisioned by Loucks et al. (1985) whereby a single model for a particular geographic location can be manipulated and analyzed differently by various type of users.

The collaborative aspects of the modeling are essential today as watershed management and science are increasingly collaborating in solving practical water problems. This collaboration is already mature for natural-scale observations and data (e.g., in situ observations, geospatial data sets, and remote sensing products) whereby data collected and freely disseminated by numerous federal, state, and local agencies are complemented by data acquired by academic scientists. Connecting science and management through FLOODSS can be far reaching as described below.

3.2 Flood-related sciences

Before highlighting the potential benefits of the implemented FLOODSS, it is appropriate to make note of two realizations that have been emerging in the water-related scientific communities in the last several decades. The first one is related to the scientific investigations focused on watershed processes. Specific observation has resulted in an understanding that water-related issues in natural scales cannot be separated from water resources management as they are both drivers and sources of perturbation of the natural water systems. Consequently, the scientific studies, aiming at understanding and predicting the interactions between water systems and climate change, land use, the built environment, and ecosystem function and services, should be made through placed-based research that relies on a comprehensive and integrative systems approach (NSF, 2010). These type of studies cannot be conducted without the observations collected by management agencies with the mission to monitor and preserve the sustainability of water resources, hence, the need for interaction and collaboration.

The second relevant realization is referring to the pillars of the scientific investigations of natural systems. The traditional pillars have been observation (plus experiments), theory, and analysis (plus computation). Arguably, the on-going digital revolution has not only radically changed many facets of society but it has also dramatically changed the way we conduct scientific studies. In addition to that, the capabilities of the modern information and communication technologies, grouped here under the broader term of hydroinformatics, have become the fourth pillar of scientific research by allowing us to address a new class of problems around the organization of data and information and extraction of knowledge stemming from them. Hydroinformatics is the water-related science and engineering that occupies the gap between information and communication technology systems by delivering relevant and valuable service to a wide range of users such as researchers, decision makers and the public.

Fostering multi-disciplinary synergy. A brief historical survey of the integrative approaches used in science and management reveals that their rise has emerged from a bottom-up pressure to understand and manage complex water related problems. Nevertheless, science and management integrative approaches have been developed in parallel with little connection. Currently, the need for integration of science and management is critical and it appears that the advancements in watershed science and management themselves depend, to a large extent, on the degree of their integration. Today, many data collection agencies are increasingly making their information available through web-based systems. The provision of the systems to store metadata ensures that new users know when, where and how the datasets were collected. Efforts are made to address the challenges related to adapting data collected for other purposes in a water specific ontological framework and for representing secondary data such as socio-economic variables in a usable format. The FLOODSS described in this paper is a prototype of meaningful integration between science and management for mitigating the most socio-economic natural hazard: floods.

Discovery of scientific hypothesis. The capabilities of the new generation of field instruments to acquire data from space, close-range and submersed in the waterscapes can increasingly describe phenomena through direct high spatial and temporal resolution observations, and are becoming, at times, more reliable than those obtained through our modeling, due to sheer density of measured variables. While simulation modeling will continue to be used for predictive assessments, mining of large multivariate databases may reveal hidden, and perhaps subtle yet essential dependencies on the physical processes, but more importantly on the coupled natural-human systems that are less understood. Consequently, analyses applied by scientists to FLOODSS datasets are likely to reveal hypotheses that can then be tested through experiments, reversing the usual method of hypothesis-driven observational design. Time series of multiple datasets stored in the FLOODSS represent a “gold mine” for data driven modeling as alternative frameworks for predictive explorations (Kumar, 2011).

Improvement of the information services. Information services are the prerequisite for providing basic data and information that allow an understanding of the environmental, economic, social, and cultural interactions over a range of various spatial and temporal scales. They involve technical aspects of the water resources information systems such as system interoperability and data exchanges, eGIS and geo-Intelligence, integrated information delivery, the acquisition and management of observations and surveillance, and technological research and development associated with the creation of these services (NOAA, 2009). Most current flood mitigation efforts are local, fragmentary, and expensive and are not readily transferable over scales or between communities. The modular and flexible construct of FLOODSS allows to continuously update the platform in order to take advantage of novel solutions for flood mitigation, resilience, and adaptation as soon as they occur. The use of mature FLOODSS is not only relevant for scientists and managers but also for training and educating the new generations, in more efficiently educate future scientists and managers on their role for enhancing society’s ability to mitigate floods as an increased threat to the global community.

The capability of FLOODSS to interoperate and exchange data services are vital mechanisms for enabling seamless communication, coordination and collaboration of products obtained with enterprise solutions (consisting of systems, models, data, products and services) used at multiple individual water resource agencies. These mechanisms enable highly efficient, transparent and automated data exchanges as well as sharing across agency boundaries. Enterprise GIS services manage common, comprehensive sets of key baseline GIS data layers that are shared by all watershed stakeholders. Geo-Intelligence services are high performance tools and procedures that visualize, interpret, model consequences of, create derived products for, generate reports for, and invoke actions or changes in behavior based on forecasted water resources events in a geospatial and temporal context. Integrated delivery services bring together existing and anticipated hardware, software, telecommunications systems, and protocols that facilitate the automated delivery of products and services to external stakeholders (the internal stakeholder needs are met by the system’s interoperability and database synchronization focal area). The observations and surveillance focal area involves the acquisition and management of observational data and metadata, data usage coordination, and data distribution mechanisms. All the above mechanisms and associated services are in actuality necessary components and functions for a robust web-based FLOODSS.

4 ROAD MAP FOR FLOODSS DEVELOPMENT

A wide collaborative effort is required to translate the FLOODSS ambitious vision from concept to practice. Most of the challenging efforts are related to the assemblage of the cyberinfrastructure laid out in Figure 2. The breadth and depth of FLOODSS vision extends well beyond the capabilities of a single research development group, or even one nation (as flooding is tied to local conditions). Thus, it requires the integration of capabilities and efforts of flood and information science experts globally and for a longer term commitment.

We call for a multi-institutional and international alliance of core partners that builds on the existing scientific and technologic advancements, selects the necessary flood science and cyberinfrastructure, and ensures long-term continuity through upgrades of the FLOODSS as new technologies occur. The FLOODSS core partners would:

i. Identify and engage strategic partners for FLOODSS development and implementation. The long-term intention is to develop a partnership to include water-focused professional communities (e.g., IAHR, IAHS, IWA), international scientific and applied sciences governmental agencies (e.g., WMO, UNESCO), specialized research centers (e.g., National Water Center, IFC – USA; CIMA – Italy; IWHR – China, UNESCO/IHE – The Netherlands, Wallingford -UK, ICHARM - Japan), industrial software developers (e.g., DELTARES, DHI) are all essential for a robust development of the conceptual architecture, production process, and formulating a business model of FLOODSS. However, the first steps would be more modest and will include significantly less partners such as to ensure continue capacity building progress.
ii. Set short-term and long-term development schedules backed up by formal collaborative agreements (for ensuring the sustainability of the FLOODSS initiative wide participation from governmental agencies, flood practitioners, universities, and industry is critical)
iii. Formulate the strategy for securing FLOODSS governance and development funding [among the main targets are international non-governmental organizations (e.g., World Bank, GWP), international scientific agencies, applied sciences agencies (e.g., WMO, UNESCO), flood consulting and insurance companies, and private donors concerned with the flood-related disasters].
iv. Elaborate an evaluation matrix for FLOODSS development (for ensuring a measure of a sustainable progress of the product development)
v. Identify early-stage FLOODSS-relevant research testbeds that can facilitate transparent integration of research components suggested by the alliance and subsequent assessments for identification of

further research needs. Launch proof-of-concept studies (using coherent methodology and global scale models and data sets) followed by evaluations to continuously improve individual components of the model cascade. Potential testbed candidates so far: Iowa Flood Center (USA) and China Institute for Water Resources and Hydropower Research (China).

vi. Develop the conceptual architecture and the production process leading to an operational FLOODSS. Identification of existing components, producers, and early prototypes that are readily usable in the generic platform for accelerating the overall FLOODSS development.

vii. Consult with relevant stakeholders (governmental agencies, local communities, industry, and flood insurance agencies are expected to engage in formulating the operational requirements, supporting the implementation of the proof-of concepts to specific testbeds and acting as reviewers for specific platform developments).

viii. Develop a business model for sustained economic development of the FLOODSS [specifications on the governance model, attraction of industrial partners for attaining industrial grade performance, and solving the intellectual property issues. For a start, check similar efforts carried out through various EC-funded projects [DRIHM (http://www.drihm.eu); OpenMI (http://www.openmi.org); FLOODSite (http://www.floodsite.net), and FLOODIS (http://floodis.eu)].

ix. Foster synergistic collaboration with mission agencies that has potential to accelerate FLOODSS maturation, demonstration, and transition to practice.

ACKNOWLEDGMENTS

The support provided to the author by The University of Iowa's Office of Research & Economic Development and IIHR-Hydroscience & Engineering's Iowa Flood Center made the preparation of this paper possible.

REFERENCES

Cutter, S.L., L. Barnes, M. Berry, C.G. Burton, E. Evans, E.C. Tate & J. Webb (2008). A Place-Based Model for Understanding Community Resilience to Natural Disasters, *Global Environmental Change*, 18(4), 598-606.

DRIHM (2016). Distributed Research Infrastructure for Hydro-Meteorology. [http://www.drihm.eu - last accessed 06/10/2016]

FEMA (2016). National Flood Insurance Program: Flood Hazard Mapping, Department of Homeland Security, [http://www.fema.gov/national-flood-insurance-program-flood-hazard-mapping - last accessed 06/10/2016].

Flood-CBA (2016). A Common Framework of Flood Risk Management Cost Benefit Analysis Features, Support Tools no 1 and 2, Middlesex University Flood Hazard Research Centre [www.floodcba.eu - last accessed 06/10/2016].

FLOODIS (2016). European Community Project FP7-SPACE-2013-1. [www.floodis.eu - last accessed 06/10/2016].

Firoozfar, A. R. (2016). *Literature on Dss for Flood Mitigation*. *IIHR Internal document*. Personal communication.

Giordano, R., Uricchio, V. F. & Vurro, M. (2008). *Monitoring Information Systems to Support Integrated Decision-Making*. Timmerman, J. G., Pahl-Wostl, C. and Moltgen, J. (eds.). IWA Publishing, London (UK), 113–129.

Giupponi, C., Mysiak, J., Depietri, Y. & Tamaro, M. (2011). *Decision Support Systems for Water Resources Management: Current State and Guidelines for Tool Development, Vanrolleghem, P.A. (Ed.).* IWA Publishing, London (UK), 107-202.

Herzog, M.T. & Labadie, J.W. (2011). Building Public Knowledge for Mobilizing Action in IWRM. *AWRA Summer Specialty Conference*, Snowbird, UT, 1-6.

Ilyas, M.U., Shafiq, M.Z., Liu, A.X. & Radha, H. (2011). A Distributed and Privacy-Preserving Algorithm for Identifying Information Hubs in Social Networks, *IEEE International Conference on Computer Communications (INFOCOM)*, Shanghai China, 561-565.

King, A.B., & Thortnton, M. (2016), Staying the Course: Collaborative Modeling to Support Adaptive and Resilient Water Resources Governance in The Inlamd Norwest. *Water*, 8(6), 232.

Laine, R., Cook, C., & Lemass, B. (2012). Decision Support: Informing Flood Management. *52nd Floodplain Management Association*, 1-10.

Levy J.K. (2005). Multiple Criteria Decision Making and Decision Support Systems for Flood Risk Management. *Stochastic Environmental Research and Risk Assessment*, 19(6), 438-447.

Loucks D. P., Kindler J. & Fedra K. (1985). Interactive Water Resources Modeling and Model Use: An Overview. *Water Resources Research*, 21(2), 95–102.

Kramer J., Noronha S., & Vergo J. (2000). A User-Centered Design Approach to Personalization. *Communications of the ACM*, 43(8), 44-48.

Kumar, P. (2011). Topology of Hydrologic Predictability. *Water Resources Research*, 47(3), 1-9.

Mackay, E.B., Wilkinson, M.E., MacLeod, C.J.A., Beven, K., Percy, B.J., Macklin, M.G., Quinn, P.F., Stutter, M. & Haygarth, P.M. (2015). Digital Catchment Observatories: A Platform for Engagement and Knowledge Exchange between Catchment Scientists, Policy Makers, and Local Communities. *Water Resources Research*, 51(6), 4815-4822.

Muste, M. (2014). *Information-Centric Systems for Underpinning Sustainable Watershed Resource Management*. Chapter 13 in “Comprehensive Water Quality and Purification,” Ahuja S. (Ed), vol 4, Elsevier, 270-298.

Muste, M. & Firoozfar, A.R. (2016). Toward Generalized Decision Support Systems for Flood Risk Management. *Proceedings the 3rd European Conference on Flood Risk Management*, Lyon, France, 1-12.

Mysiak, J., Giupponi, C. & Rosato, P. (2005). Towards the Development of a Decision Support System for Water Resources Management. *Environmental Modelling & Software*, 20(2), 203-214.

NOAA (2009). *Integrated Water Resources Science and Services (IWRSS),* An integrated and adaptive roadmap for operational implementation, IWRSS NOAA/ USACE/USGS Consortium.

NSF (2010). “Water Sustainability and Climate” Program Solicitation 10-524, National Science Foundation, Arlington, VA – available on line at: [http://www.nsf.gov/pubs/2010/nsf10524].

Power, D.J. & Sharda, R. (2007). Model-Driven Decision Support Systems: Concepts and Research Directions. *Decision Support Systems*, 43(3) 1044-1061.

Sayers, P., Hall, J. & Meadowcroft, I. (2002). Towards Risk-Based Flood Hazard Management in the UK. *Civil Engineering*, 150(5), 36-42.

Watson, L.T., Lohani, V.K., Kibler, D.F., Dymond, R.L., Ramakrishnan, N. & Shaffer, C. A. (2002). Integrated Computing Environments for Watershed Management. *Journal of Computing in Civil Engineering*, 16(4), 259-268.

WMO (2006). *Integrated Flood Management Concept Paper,* Associated Program for Flood Management, Technical Document No.1, second edition, World Meteorological Organization, Geneva, Switzerland.

Zhang, Y., Sugumaran, R., McBroom, M., DeGroote, J., Kauten, R.L. & Barten P.K. (2011). Web-Based Spatial Decision Support System and Watershed Management with a Case Study. *International Journal of Geosciences*, 2(3), 195-203.

Zorzi, N., Rosatti, G., Zugliani, D., Rizzi, A. & Piffer, S. (2016). New Technology in Debris-Flow Modelling: A Web-GIS Integrated Solution for TRENT2D. *Proceedings River Flow Conference*, St Louis, U.S.A, 1924-1931.

PROPOSITION OF FLASH FLOOD FRAMEWORK USING OBJECT ORIENTED BAYESIAN APPROACH

QUAN LIU[(1)], BRAHIM BOUTKHAMOUINE[(2)], AYELEY TCHANGANI[(3)], HELENE ROUX[(4)] & FRANÇOIS PERES[(5)]

[(1,2,3,5)]Université Fédérale Toulouse Midi-Pyrénées
Laboratoire Génie de Production,INP-ENIT
quan.liu, bboutkha,ayeley.tchangani, francois.peres @ enit.fr
[(4)] Institut de Mécanique des Fluides de Toulouse (IMFT) - Université de Toulouse, CNRS-INPT-UPS, Toulouse FRANCE,
helene.roux@imft.fr

ABSTRACT

A flood forecasting approach based on Bayesian Networks (BN) is presented. In order to represent the behavior of an extended geographical zone like a basin for instance, two modelling levels are considered. In a first step, a Bayesian network later referred to as the elementary model is proposed to characterize the influence of the main variables controlling the physical processes (precipitations, runoff, infiltration, discharge) involved in a flood generation at local scale. The processes corresponding to forcing production (rainfall or snow), runoff production and runoff transfer are described through causal relations and the most relevant causal relations among variables are identified. In a second step, based on the observation that the use of BN techniques for risk assessment becomes increasingly complex when the size of the system increases, Object Oriented Bayesian Networks (OOBN) are introduced. Indeed, when the system to be characterized exhibits a repetitive structure or a generic pattern representative of the various dimensions of a problem, OOBN appears to be a good alternative. With this in mind, individual elementary models are combined in a large network connecting a set of variables according to the catchment topology. The use of OOBN as modelling tools makes it possible not only as the representation of the spatial dimension of the flood phenomenon but enables also the introduction of dynamic variables characterizing the time evolution. These techniques are applied and give rise to a first tentative of modelling of natural disasters and in particular, flash flooding events.

Keywords: Flash flood; flood risk; Bayesian techniques; object oriented approach; large scale models.

1 INTRODUCTION

In many parts of the world, the melt of snowpack phenomena are considered as the most important events of the year. The snowmelt supplies dams, lakes, rivers and groundwater aquifers through infiltration processes. A record snowfall followed by a rapid thaw may cause flash flooding especially when combined with heavy rains. The consequences of these floods can be devastating in regions where this type of risk is not very well known or not taken into account in urbanization policies. Such is the case, for instance, for low-lying areas where the snowfall is an unusual phenomenon. In that way, on the 12th September 2014, the coast city of Cherbourg (northwest of France) was the scene of a severe flood caused by its river, Divette, overflowed. This overflowing was generated by important snowmelts in the hills upstream combined with heavy rains. A similar case was produced on 17th Jun 2013 at the base of Pyrenees in southwest of France, when heavy rains combined with exceptional snow melts have led to historical floods in the region causing two victims and remarkable property damages amounting to dozens of millions of euros. Mindful of this reality, hydrological forecasting and warning systems should integrate snow melting as a key component of their forcing data alongside liquid precipitations.

Many flood-forecasting systems have been developed to prevent floods and their potential damage. These systems are intended to provide assistance to catchment managers in identifying the best hydraulic control actions to take during flood threats and inform civil protection staff about the situation, in order to take the right strategy for emergency responses minimizing damage on life and properties. Most of the time, flood forecasting systems rely on deterministic precipitations-runoff models as first solution to meet these needs. These deterministic models can vary from relatively simple to specific and highly complex. The use of detailed models improves the efficiency of flood warning systems, but it brings additional complexities into decision process. Decision makers usually have difficulties interpreting the results, especially since these results are clouded by uncertainties. Such uncertainties are mostly tied to model structure (equations, approximations), to the model parametrization or to the model forcing data (spatio–temporal rainfall, initial conditions). These uncertainties can be estimated and taken into account by expert hydrologists, but have to be explained to the decision makers, possibly under great stress as the flood is quickly arising.

Our aim in the work presented here is to make a real-time probabilistic forecasts that could be simply used by decision makers. The idea is to encode knowledge of deterministic models in a computational framework able to provide decision makers with the occurrence probability of some future flood risks scenarios relevant to decision making. To address this challenge, the potential of graphical models (GMs) and, more precisely, Bayesian Networks (BNs) is explored in this study. These networks are Directed Acyclic Graphs (DAGs) in which relationships of variables describing knowledge of a certain phenomenon are represented. Each node of the graph corresponds to a variable and arcs represent the probabilistic dependencies between these variables. BNs provide a complete suite of algorithms for the probabilistic and decisional aspects of a problem at hand. Furthermore, they are easy to visualize, inspect and enhance modeling transparency. In order to use BNs for the assessment of the flooding risks, this study is divided into two parts. First, identifying all the variables controlling the flood generation on the scale of small geographic zone considered relatively homogenous. The qualitative explanation of this issue is then reached by establishing the cause and effect relationships between these variables that correspond to the structure of the so-called BN. These underlying relationships will further be evaluated by their strength through Conditional Probabilities Tables (CPTs). These CPTs will be estimated using information coming from databases, deterministic models and hydrologic expertise. At the end of this stage, this study will have a cognitive structure, called Basic Model (BM), able to estimate the flood risk on a small zone. The second part of this work is to estimate this risk at the catchment scale by aggregating these BMs into a spatiotemporal framework based on Object Oriented Bayesian Network (OOBN).

2 BASIC MODEL FOR FLOOD RISK ASSESSMENT

The most important question in hydrology is to estimate the stream flow that occurs in a river in response to a given amount of precipitation (rainfall and snow melt). Answering this question requires partitioning water inputs at earth's surface into components that flow over land and directly enter streams, called surface flow, and components that infiltrate (Figure 1). Infiltrated water can follow lateral pathways beneath the ground surface and move back slowly to the streams, in which case it is called subsurface flow. Infiltrated water can also percolate deeply into the ground and recharge groundwater aquifers. It can also remain in the soil surface and return later to the atmosphere by evapotranspiration. The produced runoff (surface flow and subsurface flow) is afterward transferred, though hillslopes and streams network, to the outlet of the considered area.

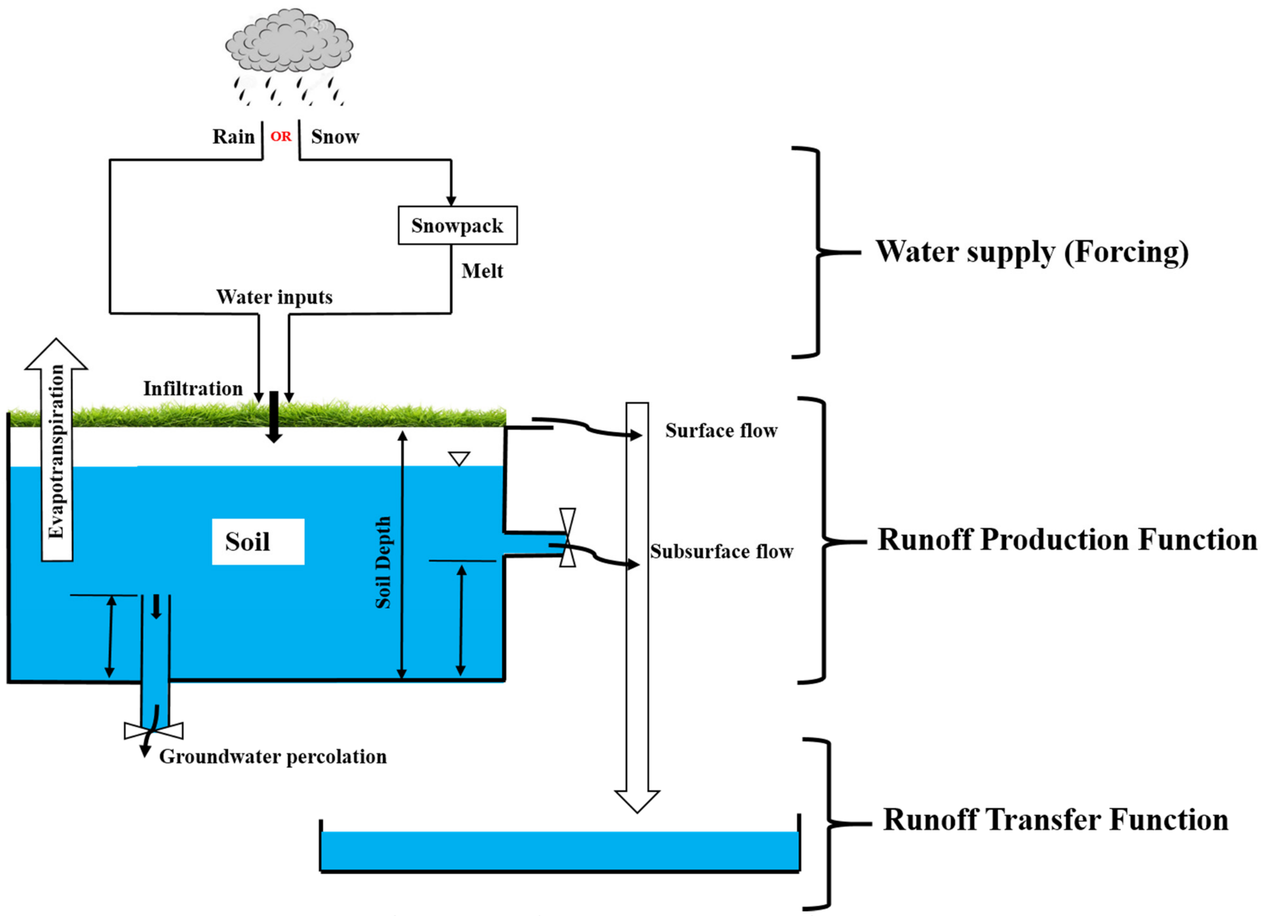

Figure 1. Schematic of processes controlling flood generation.

In the following paragraphs, this study will describe the different phenomena that contribute to flash flood process in order to derive influence relationships between variables upon which the model will be built.

2.1 Water supply

Flood forecasting requires the separation of total precipitations P_t into snow (P_s) or rain(P_l). This separation is critical to determine whether water is available for direct runoff and soil infiltration, or if it is stored as snowpack (S_p) and melted later (S_m). Figure 2 shows dominant variables involved in both separation rain/snow and evolution of snowpack.

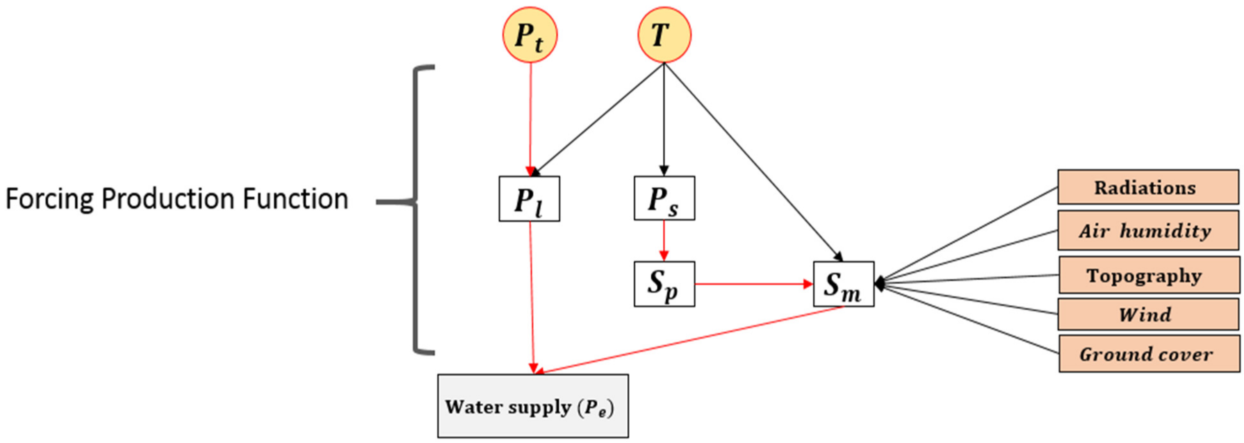

Figure 2. Main variables controlling the separation rain/snow and snowpack evolution.

The nature of precipitation reaching the soil surface is closely related to the temperature profile between the ground and the base of clouds. Many scenarios are possible but the most common are:

a) If the temperature (T) is negative all the way down from the clouds to the ground, the precipitations fall in the form of snow (P_s).
b) When the temperature becomes more and more positive towards the ground, the precipitations become liquid (P_l) as they reach the ground.

However, other meteorological conditions may also play a role, such as type of clouds, air mass movement, humidity, altitude and latitudes (US Army Corps of Engineers, 1956). It depends on many factors, not all measurable even though it is appropriate to consider the temperature as a dominate factor.

The accumulation of snow precipitations over a given period of time forms the snowpack **(S_p).** Understanding the evolution of this snowpack requires understanding of the physical processes controlling snow melting. Snowmelt is a result of many heat transfers between snowpack and its ambient environment (surface soil and atmosphere). The processes underlying these transfers are variable in place (forest/ clearing, low-altitude/ high-altitude zones, etc.) and time (starting/ending of melt, day/night, etc). According to Kuusisto, (1986), the radiations (short and long wave radiations) and the convective exchanges (due to the **air** humidity) are the two main factors controlling the snowpack melt: radiations are important in protected sites (forests) on clear days, while convective exchanges are preponderant in non-protected sites on cloudy or rainy days.

At the catchment scale, heterogeneity of catchment conditions induces the variation of snowpack. These conditions could be divided into two parts: meteorological conditions and physiographic characteristics. The first one combined with topography influences the repartition of snowpack; the altitudinal gradients of temperature and precipitations enable important accumulation of snow in high-altitudes zones. The wind, for its part, transports mass of snow and allow its redistribution. On the other hand, heterogeneity of catchment physiographic characteristics, accentuates the snow cover disparities inside the catchment. One can likely find important and stable accumulation of snow in depressions. The area exposure **(**topography) influences the snow melting (faster in south facing than north-facing aspects). Steep aspects promote snow avalanches and accumulation of snow downstream. Finally, the vegetation (ground cover) protects the snowpack from the wind and likely has an effect of snow cover distribution.

2.2 Runoff production function

The infiltration process is particularly important in hydrology. It controls the portion of water infiltrated vertically through the top layers of the soil and consequently impacts the direct runoff (surface flow). In order to estimate the surface flow resulting from some precipitations (water supply(P_e)), many factors strongly affecting infiltration have to be considered (Figure 3).

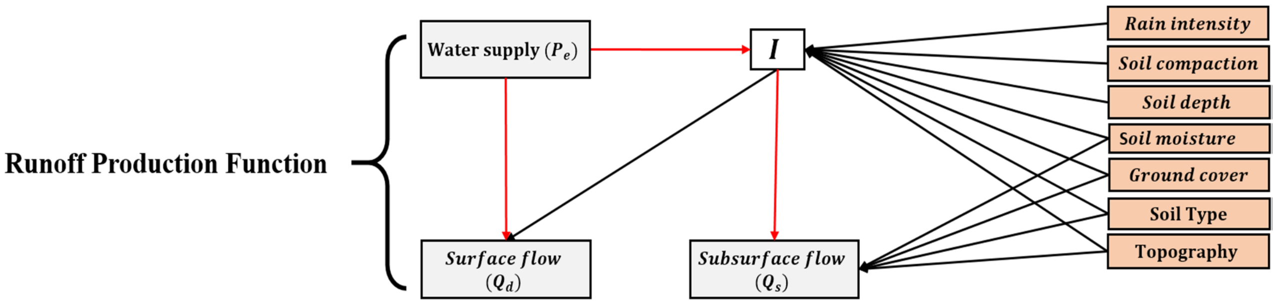

Figure 3. Mean variables controlling infiltration process (*I*).

a) Rain intensity: raindrops can induce soil crusting and consequently reduce soil infiltration ability.
b) Soil compaction**:** raindrops (soil crusting) and other anthropic factors (soil tillage, compaction of soil by machines) can lead to degradation of soil structure and formation of an impermeable and dense layer at the top surface of soil. Such layer prevents water from infiltrating and accelerates direct runoff.
c) Soil depth: soil depth controls the water-holding capacity of the soil. Obviously, for the same type of soil, important soil depths hold a lot of water contrary to low ones.
d) Soil moisture: soil moisture level is a dominating factor controlling infiltration process. The infiltration rate profile depends strongly on soil initial conditions (dry or saturated).
e) Ground cover: the vegetation accelerates infiltration by slowing down the flow water at soil surface and giving it much time to penetrate down through the soil. It also protects the soil from crusting. In addition, by its root system, the soil infiltrability can be increased.
f) Soil type: (structure, texture, porosity), the characteristics of the soil matrix affect directly the capillarity and therefore its ability to absorb water which in turn govern in part infiltration process.
g) Topography: steep slopes for its part reduce infiltrations and promote runoff flows.

Part of the infiltrated water flows laterally in the top soil layer and exfiltrate through drain channels. This flow is called subsurface flow. The presence of a relatively impermeable shallow layer favors this flow. According to (Bachmair, 2012), the most important factors controlling subsurface flows can be classified into static factors (surface, bedrock topography) and dynamic ones (soil properties, soil moisture, vegetation (ground cover)).

2.3 Evapotranspiration

Evaporation and transpiration occur simultaneously and there is no easy way of distinguishing between the two processes. The two processes when combined are called evapotranspiration. The evaporation from a cropped soil is mainly determined by the evaporative demand and the water and energy supplies. When the crop (vegetation) is small, water is predominately lost by soil evaporation, but once the crop is well developed and completely covers the soil, transpiration becomes the main process.

2.4 Runoff transfer function

At a local scale (homogenous small zone), the produced runoff flow (surface flow and subsurface flow) is transferred to the outlet of considered zone and thus to the inlet of downstream zones. This transfer can be done through river streams and hillslopes. Direction, velocity and amount of this flow depend on many factors. One can see clearly that the topography is a dominant factor. Steep slopes accelerate flow speed and water transfers. On the other hand, ground cover (vegetation for example) increases the sol friction and reduces the flow speed. Geometric characteristics of the streams (river streams or hillslope, depth, width, etc.) also have an impact on the transfer of surface flows. The transfer of water through subsurface layers (subsurface flows) is controlled by soil properties, vegetation (through its root system), soil moisture conditions and of course, topography. Figure 4 summarizes dominant factors controlling runoff transfer of both surface and subsurface flows from one zone to another.

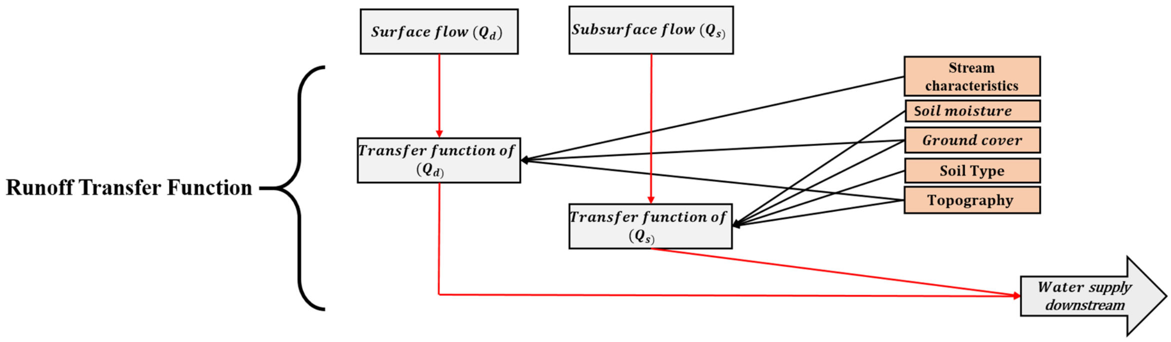

Figure 4. Main variables controlling runoff transfer function.

In the following paragraph, this study will combine variables and relationships identified in the previous paragraphs to obtain a rainfall-runoff model in terms of a Bayesian network for a limited zone that this study referred to as the Basic Model and which will constitute the fragment or object of the global model to be built using object oriented approach.

2.5 Basic model (BM)

As described above, this study identified the main variables affecting physical processes involved in flash-flood production at the scale of a small area. A Basic Modeling terms of a Bayesian Network was designed as depicted in Figure 5.

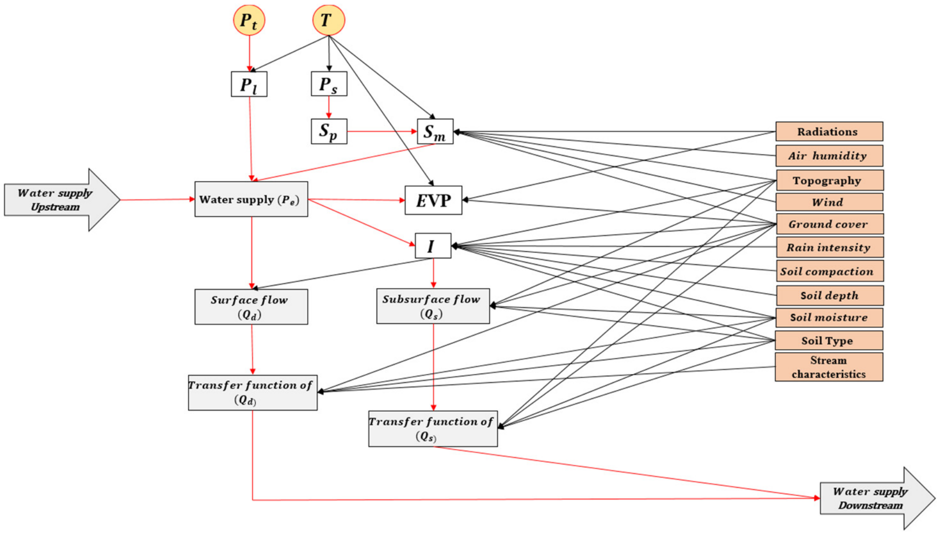

Figure 5. Bayesian Network (Basic Model) representing the flood generation at a local scale.

Next section will be devoted to presenting the extended object oriented Bayesian network (EOOBN) as a candidate tool for modeling flood phenomenon over a large area. Indeed, in terms of modeling, a large area can be divided into small pieces having near homogeneous conditions so to obtain a basic model that constitutes an object in an EOOBN; then by connecting these objects, one can obtain the model at the large area scale.

3 EXTENDED OBJECT ORIENTED BAYESIAN NETWORKS IN FLASH FLOOD SIMULATION

A flash flood is a phenomenon that changes very fast in time. Due to the complexity of this phenomenon (physical processes under which this phenomenon takes places, different variables and relationships connecting these variables, inherent uncertainty of these relationships, etc.), Bayesian network approach is a suitable candidate to obtain a sound and reliable model of flash flood phenomenon. As it has been shown that the spatial distribution of rainfall and catchment characteristics have an important impact on flash-flood generation (Garambois et al., 2014), the catchment was divided into some homogenous zones to take these distributions into account. Each of these small zones is a BN as shown in Figure 5 and then they were put together at last. In that way, the dimension of the BN model becomes a problem. Especially when there is a dynamic behavior, the dimension will be too large for modelling. Based on these special requirements, a new efficient modelling tool should be developed. In this section, this study presented an Extended Object Oriented Bayesian Networks (EOOBN) to deal with the flash flood simulation. The basic definitions of EOOBN are given followed with a general construction method based on EOOBN eventually applied to flash flood event representation.

3.1 Extended Object Oriented Bayesian Networks (EOOBN)

Though there exists some research about the classical Object Oriented Bayesian Networks like (Bangsø et al., 2000; Koller et al., 1997), their propositions treat the construction problems. Koller et al. (1997) used the class and objects on the hierarchy level to simplify the global model. Langseth et al. (2001) supposed the object may inherit all from the class that includes the graph and the CPTs based on OO assumption.

All of them benefited from the "object oriented" concept to simplify the design task but they were not suitable in this situation as one need to consider possible non-homogeneous conditions from one small zone to another. Indeed, as stated in previous sections, some rainfall-runoff models (e.g. (Arnold et al., 2012, 1998)) discretize the catchment into some homogenous areas often called Hydrologic Response Unit (HRU), using land use and ground cover considerations and these homogenous areas generally have the same structures but their numerical features are different. These small pieces also need to communicate with each other, at the same time one zone should have its dynamic behavior. Under these circumstances, this study needs to develop a new modelling tool, which deals with the repeatable structure, large scale and variable parameters. The Extended Object Oriented Bayesian Networks developed in (Liu et al., 2016a, 2016) inherits all the advantages from the classic OOBN and have much more flexibility in varying parameter and introducing the dynamic evolution. This study will present in the following sections the construction guide, which gives the designer a simple and standard procedure to build such a large and dynamic model.

Extended Object Oriented Bayesian Networks (EOOBN): An EOOBN is a large-scale Bayesian network, which is built by connecting small independent networks. The independent network is called object who is an instantiation of a defined class.

There are two main parts in EOOBN, namely the class and the object. To have the possibility of varying the parameters, this study distinguished strictly between the class and object.

Class: A class (C) is the structure part (S) which corresponds to the graph in a BN regardless of the parameters. It has three kinds of nodes, namely: input nodes, output nodes and internal nodes. Only the input and output nodes are visible from outside the class.

Object***:*** An object (O{S, P}) in the EOOBN is an instantiation of the corresponding class. The structure (S) inherits from the class and parameters (P) are defined by experts or learning processes. This study referred to input and output nodes as communication channels for the class/object entity because they are in charge of exchanging information. Here below are the conditions to be satisfied (Liu et al., 2016) when defining an EOOBN:

- Input nodes cannot have parents inside the class;
- Input node is a reference node which is the projection of an output or an internal upstream node;
- Internal nodes cannot have neither parents nor children outside the class;
- Output nodes cannot have children inside the class.

These conditions help the designer to build the class and improve the readability of the model. Meanwhile, they keep the independence of the object, which will turn out to be an advantage when treating the inference technique issues. In order to consider the system dynamic behavior, the concept of virtual nodes can be used for communication between time-slices.

Virtual node: A virtual node is a communication channel for the class/object; it usually stands for an internal dynamic node:

- The virtual node is either an input node or an output node in the class/object;
- It is added for dynamic node in the class/object as a communication channel with other time-slices;
- The transition model represents the parameters between the virtual input and dynamic node. Conditional probabilities between a dynamic node and its virtual output are equaled to 1 meaning that a dynamic node is similar to the corresponding virtual node for communication purpose.

The virtual node encapsulates the dynamic evolution information into the class/object keeping so the independency between objects. The virtual nodes introduce not only the dynamic evolution into the system, but also the other benefits into the system (Liu et al., 2016) such as introducing multi-dimensions into the system and reducing the higher degree system to a first degree system.

3.2 Construction method

The construction of a dynamic EOOBN can be done by carrying out the following steps:

i. Formalize the structure S of the system by splitting the system into different classes C;
ii. Design the structure of each class (C) with respect to S and without considering the dynamic part;
iii. Identify the dynamic node in the class and add the corresponding virtual input and output node around the dynamic node;
iv. Instantiate the class by introducing the parameters to obtain the corresponding object;
v. Connect the object through their communication channels.

By introducing the virtual nodes, designer could build a static model at the first time (step 2) and identify the dynamic variable in the network afterwards (step 3). Using the virtual nodes in the EOOBN not only simplifies the construction work during the design process, but also allows the designer to add the extra dynamic information into the model whenever he finds the dynamic evolution without modifying the structure of the class.

3.3 Illustration

In flash flood simulation, the experts may divide a catchment into HRU in order to have much more precise results. The division depends on the characteristics of the piece. Normally, the small pieces have the same structure but they may have different numerical features. Following steps are necessary to obtain the model at the catchment scale.

3.3.1 Formalize the structure of the system by splitting the system into different class

In this step, the designer analyses the target catchment and divides it into several homogeneous zones. Because generally these zones have the same structure, only one class is to be considered and the whole catchment is a combination of these zones in geography dimension as shown in Figure 6

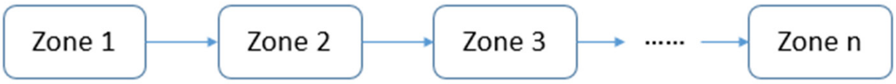

Figure 6. EOOBN for a flash flood.

To simplify the model, here this study considered a one-dimensional catchment as the target. This means that a zone is only supplied with water by its upstream neighbour. Figure 6 shows the global structure of the target catchment. Each zone communicates through its communication channel with its neighbor zones. In this simulation, this study had only one class to design and each zone was an instantiation of class whose basic structure had been developed in last section (Figure 5).

3.3.2 Design the structure of each class with respect to structure (S) without considering the dynamic part.

The basic structure was done in the last section (Figure 5). In this step, the basic BN was transferred into a class. The input nodes, output nodes and internal nodes were identified. The main role of input/output nodes is communicating the water level in each zone, which is the water supply level. Therefore, the input variable for a class is the Upstream Water Supply and the output variable is the Downstream Water Supply. The other variables in Figure 5 are the internal nodes for a class. The structure of class is shown in Figure 7 and Table 1 shows the variables description.

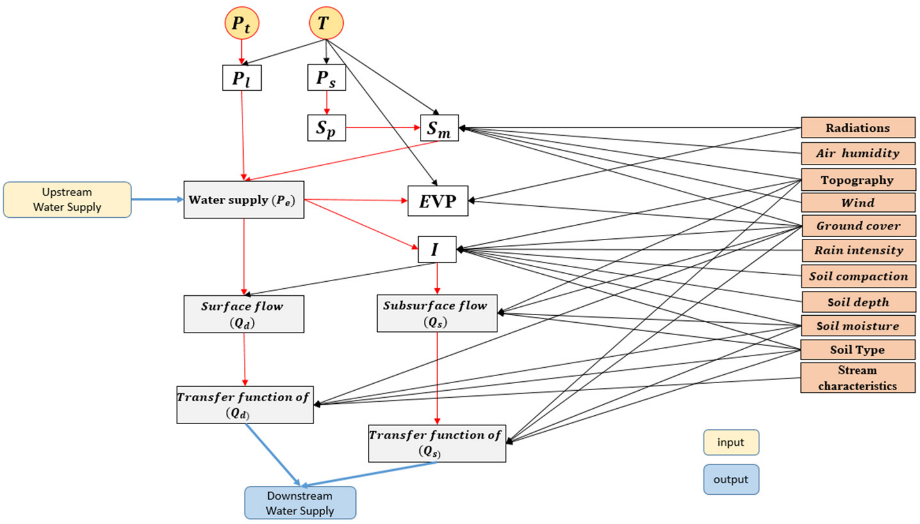

Figure 7. Class for the basic model.

In this framework, all continuous variables involved in flood generation were described in a discrete domain. A simple discretization based on uniform intervals was selected.

Table 1. The variables' information of class for flood analyzing.

Input variable	Output variable	Internal variables			
		Name	Modality	Name	Modality
Upstream Water supply (in mm)	Downstream Water supply (in mm)	Total precipitation (P_t)	Continuous in mm equivalent of water	Air humidity	Discrete (low, moderate, high)
		Liquid precipitation (P_l)	Continuous in mm	Topography	Continuous in mm / mm (%)
		Snow precipitation (P_s)	Continuous in mm equivalent of water	Wind	Continuous in m/s
		Temperature (T)	Continuous in °C	Ground Cover	Discrete: vegetation heights (low, medium , high)
		Snowpack (S_p)	Continuous in mm snow water equivalent	Rain intensity	Discrete (light, moderate, strong)
		Snow melt (S_m)	Continuous in mm	Soil compaction	Discrete (low, moderate, high)
		Infiltration (I)	Continuous in mm	Soil depth	Discrete (low, moderate, high)
		Evapotranspiration (EVP)	Continuous in mm	Soil moisture	Discrete (low, medium, high)
		Surface flow (Q_d)	Continuous in mm/h	Soil type	Discrete (Gravel, Sand, Silt, Clay)
		Subsurface flow (Q_s)	Continuous in mm/h	Stream characteristics	Discrete: (river streams, hillsides)

3.3.3 Identify the dynamic nodes in the class and add the corresponding virtual input/output nodes around it

Based on the class in Figure 7, using expert's opinion and the consideration of the simplified model, the Snowpack, Evapotranspiration and Infiltration were chosen as the dynamic nodes. So the virtual nodes should be added around them (Table 2) and the final class structure as shown in Figure 8.

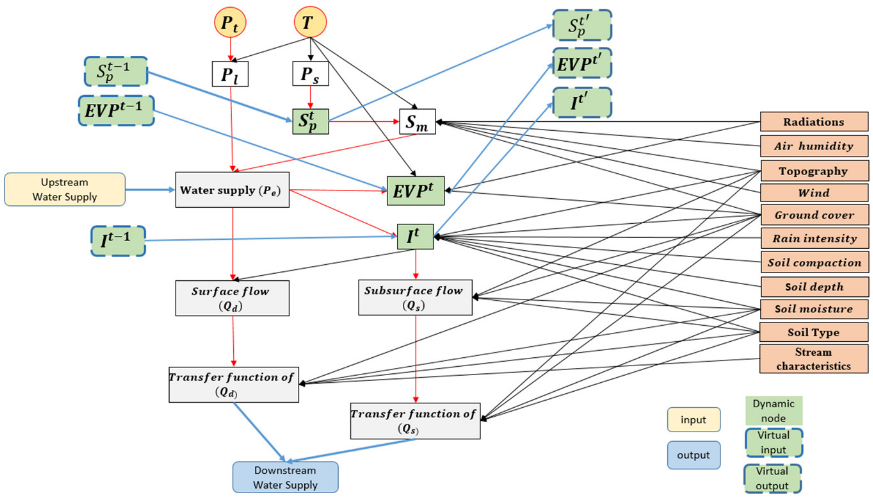

Figure 8. Dynamic class for the basic model.

Table 2. Dynamic information in the class.

Dynamic variable	**Virtual input**	**Virtual output**
Snowpack (S_p^t)	Snowpack at t-1(S_p^{t-1})	Snowpack for t+1 ($S_p^{t'}$)
Evapotranspiration (EVP^t)	Evapotranspiration at t-1 (EVP^{t-1})	Evapotranspiration for t+1 ($EVP^{t'}$)
Infiltration (I^t)	Infiltration at t-1 (I^{t-1})	Infiltration for t+1 ($I^{t'}$)

3.3.4 Instantiate the class by introducing the parameters to obtain the corresponding object

In these steps, the conditional probability tables (CPTs) were assigned for each variable in every object. The CPTs may come from the expert's opinion or by a learning process if one disposes of sufficient experimental data. All of these CPTs were saved in a database.

3.3.5 Connect the object through their communication channel

After instantiating the class, this study had all the objects, which represented models of $zone_i$ with $i = 1,2,\ldots,n$ in Figure 8. Then, they were connected through their communication channels to have the basic structure of the target catchment in Figure 6. Meanwhile, there were dynamic evolutions in each object and the final global EOOBN was presented in Figure 9.

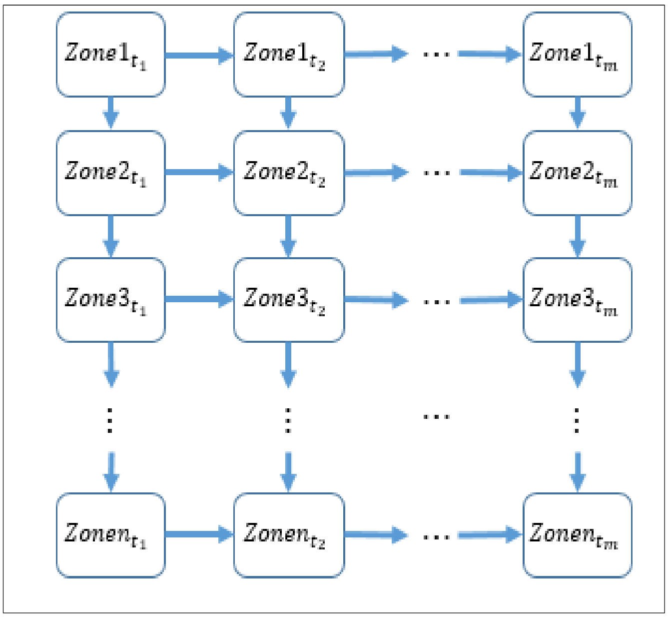

Figure 9. EOOBN for a flash flood process of a catchment.

Figure 9 presents the global dynamic evolution in the target catchment. The evolution of such a large network may necessitate massive calculation for inference purpose, but building on the communication channels mechanisms less demanding computation algorithm has been developed for the inference for EOOBN by Liu et al. (2016). With the help of EOOBN specificities, a lot of time can be saved not only in the building process but also during the inference. The developed algorithm for inference, permits to do the simulation for a local object and also to have the possibility of doing inference simultaneously, allowing by therefore the parallelization of this algorithm.

4 CONCLUSIONS

In this paper, a methodology is proposed to assess the risk of flash flooding in mountainous areas. The modeling work is divided into 2 parts. As a first step, an elementary time-independent Bayesian network is established for the characterization of the influence of variables on a small geographical area, homogeneous in terms of topology. It consists of first identifying the influential parameters in the generation of the flood phenomenon, which attempts to determine the cognitive structure in retrieving the corresponding information. This leads to the representation of a basic model, subsequently considered as an object characteristic of the evolution of all of the variables that may be brought into play. The second part aims to create a spatio-temporal causal model for the explanation and the probabilization of the feared events for diagnostic and prognostic purposes. In order to characterize the spatiality of the phenomenon, the idea is then to exploit the basic model as a generic block of modeling and then to associate the different bricks instantiated with respect to the considered area and sequenced temporally according to the phenomenon timeline. Objects Oriented Bayesian Networks appears to be appropriate to characterize this chronology characterized by similar variables instantiated according to the corresponding spot. Future works will consider the way to feed the conditional probability tables through learning techniques based on transfer.

ACKNOWLEDGEMENTS

This work could not have been realized without the support of the Occitanie Midi-Pyrénées Region, the University of Toulouse as well as the Grand Tarbes urban community. We would like to express our warm thanks to all these institutions.

REFERENCES

Arnold, J.G., Moriasi, D.N., Gassman, P.W., Abbaspour, K.C., White, M.J., Srinivasan, R., Santhi, C., Harmel, R.D., Van Griensven, A. & Van Liew, M.W. (2012). SWAT: Model Use, Calibration and Validation. *Transactions of the ASABE 55,* 1491–1508.

Arnold, J.G., Srinivasan, R., Muttiah, R.S. & Williams, J.R. (1998). Large Area Hydrologic Modeling and Assessment. I. Model Development. *Journal of American Water Resources Association,* 34, 73–89.

Bachmair, S. & Weiler M. (2012). Hillslope Characteristics as Controls of Subsurface Flow Variability. *Hydrology and Earth System Sciences,* 16(10), 3699-3715.

Bangsø, O. & Wuillemin, P.H. (2000). *Object Oriented Bayesian Networks: A Framework for Top-Down Specification of Large Bayesian Networks with Repetitive Structures.* Aalborg Universitetsforlag.

Garambois, P.-A., Larnier K., Roux, H, Labat, D. & Dartus, D. (2014). Analysis of Flash Flood-Triggering Rainfall for a Process-Oriented Hydrological Model. *Atmospheric Research,* 137, 14-24.

Koller, D. & Pfeffer, A. (1997). Object-Oriented Bayesian Networks. *Proceedings of the Thirteenth Conference on Uncertainty in Artificial Intelligence*, 302-313.

Kuusisto, E. (1986). *The Energy Balance of a Melting Snow in Different Environments.* IAHS-AISH Publication 155, IAHS, Budapest, 37-45.

Langseth, H. & Bangsø, O. (2001). Parameter Learning in Object-Oriented Bayesian Networks. *Annals of Mathematics and Artificial Intelligence*, 32(1), 221-243.

Liu, Q., Pérès, F. & Tchangani, A. (2016a). Object Oriented Bayesian Network for Complex System Risk Assessment. *IFAC-Papers Online*, 49(28), 31-36.

Liu, Q., Tchangani, A. & Pérès, F. (2016). Modelling Complex Large Scale Systems using Object Oriented Bayesian Networks (OOBN). *IFAC-Papers Online*, 49(12), 127-132.

US Army Corps of Engineers, (1956). *Snow Hydrology,* USACE North Pacific Division, Portland, Oregon, 437.

EVALUATION OF DIFFERENCE MESH SIZE FOR OVERLAND ROUTING MODEL

WAN HAZDY AZAD WAN ABDUL MAJID[(1)], LARIYAH MOHD SIDEK[(2)], HIDAYAH BASRI[(3)], SUHANI SAIDIN[(4)], & ABD. JALIL HASSAN[(5)]

[(1,2,3,4)] Sustainable Technology & Environment Group, Institute for Energy Infrastructure,
Universiti Tenaga Nasional, Selangor, Malaysia
wanhazdyazad@gmail.com; Lariyah@uniten.edu.my; BHidayah@uniten.edu.my; suhanisaidin@gmail.com;
[(1)]Department of Irrigation and Drainage, Jalan Sultan Salahuddin, Kuala Lumpur, Malaysia
[(5)]HR Wallingford Asia Sdn Bhd, Kuala Lumpur, Malaysia
abdjalil.hassan@gmail.com

ABSTRACT

Two dimensional flow modelling are widely used for flood plain analysis and considered to be a viable tool for evaluating flood propagation. The accuracy of open channel hydraulic and flood plain model is dependent on the refinement of model mesh or grid in representing ground model topography using high resolution Light Detection and Ranging (LiDAR). This paper investigates the sensitivity of unstructured mesh size of two dimensional (2D) shallow water models. The accuracy of presenting overland flood propagation is carried out using Delaunay refinement method. The study is performed by connecting to the 2D hydrodynamic modelling platform Info Works Integrated Catchment Modelling (ICM) using two different methodologies. The first method is based on the generation Baseline of mesh model from the digital terrain model (DTM), whereas the second method is based on the coarser of base mesh. The results of flood propagation are analysed using distinctive mesh resolutions as a part of term of surge degree and run time. The flood overland flow results as provided by the mesh techniques demonstrate all the changes when contrasted to their identical standard situations. However, further study is necessary to understand the entire performance of the two suggested methods.

Keywords: 2 dimensional modelling; shallow water models; unstructured mesh; hydrodynamic modelling.

1 INTRODUCTION

Flooding is a chronic natural hazard with potentially devastating consequences, giving rise to a third of all losses due to natural events. Extreme weather events over the last decade have fuelled the perception that, whether due to anthropogenic global warming or otherwise, flooding is becoming more extreme, more widespread and more frequent (WMO, 2011). Two dimensional (2D) flow models have been progressively utilized as a part of flood modelling and are giving an important device in the appraisal of stream ways and along these lines the receptors of flooding.

Light Detection and Ranging (LiDAR) innovation has permitted the fast accumulation of itemized ground models for the most part at 0.5 to 1.0 m flat determination on which hydrodynamic flood model can be based on. In any case, 2D hydrodynamic flood modelling is impressively more PC concentrated than the 1D models generally utilized and subsequently frequently comes about as a part of essentially expanded keep running times. This, therefore, prompts a trade-off between the runtime of the 2D model and accuracy of the model at addressing the 2D surface. The greater size of mesh components allow models to run more quickly, however, may not precisely address each one of the components of the surface.

Generally, 2D hydrodynamic flood models contain either a structured grid or an unstructured mesh to represent the ground topography. Unstructured meshes have the favourable position that triangle sizes can differ within the mesh, permitting the modeller to create a better work in territories obliging point-by-point examination and a coarse mesh in general to accomplish sensible keep running times. The ideal 2D mesh will represent the 2D topography with adequate precision to give trust in model results while keeping up a sensible run time.

The objective of this study is to evaluate the response and performance of the shallow water model when using different mesh sizes to flood plains, subjected to the river flooding. Basically, attention is given to the relationship between mesh size and model run times. Apart from that, analysis also consider the flood depth and flooded area extension in the flood plain. Shallow water models, associated to finite element and finite volume resolving schemes, allow adopting a varying degree of spatial resolution through the use of unstructured meshes, from a coarse deep-water discretization to localized refinements in the area at risk of flooding (Blanton, 2008). Moreover, the coupling of 1D-2D hydrodynamic models requires that the resolutions of each model grid/mesh in the overlapping regions are similar, to avoid the loss of information (Zundel, 2002).

2 STUDY SITE DESCRIPTION

Kelantan covers an area of 15,099 km^2 and is located on the north eastern region of Peninsular Malaysia, bordered by parts of southern Thailand to the north, Perak to the west, Pahang to the south and Terengganu to the southeast. Hilly terrains are found on the southern parts of the State, separated by the Titiwangsa Mountain Range, with fertile coastal plains downstream defining the geography of the region. Figure 1 shows the Kelantan main river sub-catchment.

The river originates in the southern rugged and steep region of the state where the elevation ranges between 1,000 m to 2,000 m LSD. Meandering through the hilly areas in the upper catchment, River Nenggiri at the south-west flows in a north easterly direction to join River Galas at Bertam. From there, River Galas flows north to capture River Pergau, which flows south easterly from Jeli, at Dabong. From Dabong, River Galas flows in northeast direction and meets River Lebir, which flows in northwest direction from Gunung Gagau, at Kuala Krai. From Kuala Krai, the river is called River Kelantan and flows towards north to the river mouth. The river length from Kuala Krai to the river mouth is approximately 100 km. The river mouth is situated about 15 km north Kota Bharu. About 760 km² of the lower river catchment has a low-lying flat terrain prone to annual flooding. Kota Bharu, Kelantan has been selected for the case study area.

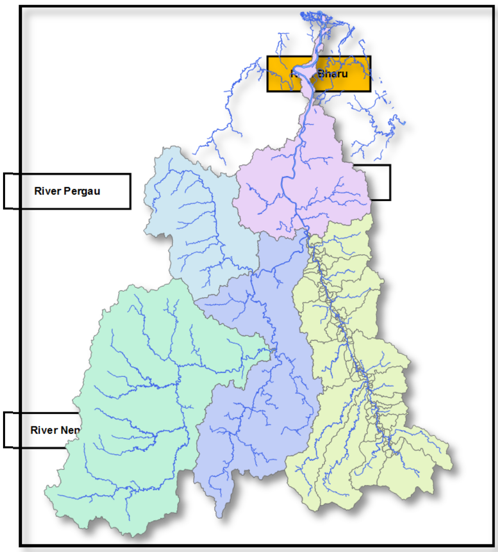

Figure 1. Kelantan River Main Sub catchment.

3 MODEL DESCRIPTION

The basic equations used in most of the one dimensional (1D) Hydrodynamic Models are based on the 1D unsteady state gradually varied flow equations (Garcia-Navarro, and Brufau, 2006), which are termed as the Saint Venant equations can be written as Eq. [1] and Eq. [2]:

- the mass conservation / continuity equation:

$$\frac{\partial Q}{\partial x}+\frac{\partial A}{\partial t}=c \qquad [1]$$

- the momentum conservation or dynamic equation:

$$\underbrace{\frac{\partial Q}{\partial t}}_{(I)}+\underbrace{\frac{\partial}{\partial x}\left[\frac{\beta Q^2}{A}\right]}_{(II)}+\underbrace{gA\left[\frac{\partial h}{\partial x}-S_0\right]}_{(III)}+\underbrace{g\frac{AQ|Q|}{K^2}}_{(IV)}=0 \qquad [2]$$

where:

$Q(x, t)$ = discharge (m^3/s)
t = time (s)
x = stream wise direction (m)
c = lateral inflow per unit length of flow
$A(x, t)$ = cross-sectional area (m^2)
g = gravitational acceleration (m/s^2)
h = water level (m)
S_o = bed slope (m/m)
K = conveyance (m^3/s)
β = Boussinesq coefficient

and

i. local acceleration term
ii. convective term (responsible for non-linearity of equation)
iii. pressure term due to change in depth over reach – if So is neglected, then dh/dx approximates the friction slope based on the change in water level
iv. source/gravity term causes water to flow

In some instances, Equation 1 is set equal to c(x, t) m^2/s, which is equivalent to specifying lateral inflows from small rivers. Underground sources and ground water can influence the lateral inflow and this directly influences the calculation.

The assumptions inherent in the application of Equation 1 and Equation 2 are:

i. the flow is one-dimensional, i.e. a single velocity and elevation can be used to describe the state of the water body in a cross-section;
ii. the water is incompressible with a constant density (=1000 kg/m^3) uniformly distributed;
iii. the bed slope is small;
iv. the streamline curvature is small and vertical accelerations are negligible, hence the pressure is hydrostatic;
v. the effects of boundary friction and turbulence can be accounted for by representations of channel conveyance derived for steady state flow; and
vi. all functions and variables are continuous and differentiable;

Flows in flood modelling often take short cuts through flood plains where the 1D description may become quite inaccurate. This is even more the case for dam or embankment failures, where the flow may leave the flood plain completely and inundate natural terrains. For this reason, the 2D shallow water equations are introduced. Following the same principles as for 1D flow, the mass conservation / continuity equation reads as below in Eq. [3]:

$$\frac{\partial h}{\partial t}+\frac{\partial (uh)}{\partial x}+\frac{\partial (vh)}{\partial y}=0 \qquad [3]$$

where, the y axis, orthogonal to the x axis, is introduced with its flow velocity *v* (m/s) associated to it. The convective momentum terms are subjected to the same principles as discussed for the 1D approximation.

In terms of the Manning's roughness coefficient, *ŋ*, this was considered to be spatially variable according to the Earth surface cover types obtained from available aerial photos of study area. Table 2 shows the used values for *ŋ*, referred from Chow, 1981 and Bunya, et al. 2010.

Table 2. Manning's roughness coefficient (ŋ) associated to the surface of the flood plain

Land cover type	*ŋ*
Open waters	0.02
Estuarine waters	0.025
Agriculture crop/grass	0.04
Natural streams, with some shoals	0.033

4 METHODOLOGY

The selection criteria of focused area were based on complex topography that will require a more refined mesh to correctly represent flow paths. Topographically complex areas were characterised by rapid changes in slope and included features such as embankments and cuttings for roadway, railways and drainage in urban environments. The InfoWorks Integrated Catchment Modelling (ICM) hydrodynamic model was used by utilizing different mesh sizes. ICM uses an unstructured triangular mesh using Delaunay refinement method and possesses a range of features for mesh editing, import/export from GIS tools and a powerful visualisation engine, which make it ideal for running these meshes in a case study catchment.

4.1 Model calibration

Calibration of the 2D model will be carried out using observed water levels at Jeti Kastam, Kota Bharu during the December 2014 flood event. This flood was the largest event recorded in 50 years (DID, 2015) and very useful to accurately calibrate storage volumes in Kota Bharu floodplains. The set of fit statistics which was Pearson Correlation Coefficient and Nash-Sutcliffe Efficiency will be used for hydrodynamic model calibration.

4.2 Baseline model

An initial mesh, called baseline had been created using a standard meshing algorithm. Standard mesh size with resolution of $1m^2$ was generated as baseline case to replicate the 2014 flood event. This baseline model will be used as reference to other scenario simulated for this study. The $1m^2$ size of mesh uniform resolution was extended in flood plain with area of 757.39ha in Kota Bharu Town. The Baseline Mesh Model (Figure 2) had 2,344,842 numbers of vertices, 4,681,410 numbers of triangles and 3,994,185 numbers of 2D elements.

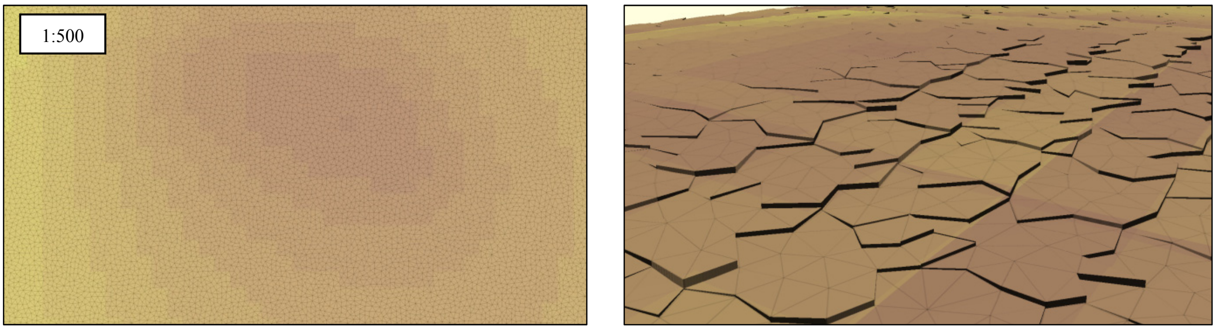

(a) **(b)**

Figure 2. Baseline Mesh Model (a) in 2D view and (b) in 3D view. Both views were overlaid with DTM generated from LiDAR.

4.3 Model convergence scenario

In order to evaluate the relationship between mesh size and model simulation time, 8 different scenarios were created with different mesh size. This methodology was based on the refinement of a basemesh generated from baseline mesh model. The eight scenarios for this study are tabulated as Table 3 below.

Table3. Mesh properties for the 8 scenarios in this study.

Model	maximum mesh zone triangle size	numbers of vertices	numbers of triangles	numbers of 2D elements	total time for mesh generation
Baseline	1m^2	2,344842	4,681,410	3,994,185	0:04:24
Model 1	5m^2	941,493	1,877,435	1,856,542	0:01:38
Model 2	10m^2	471,621	939,200	797,499	0:00:48
Model 3	20m^2	236,384	469,641	398,812	0:00:23
Model 4	50m^2	94,866	187,473	185,501	0:00:08
Model 5	100m^2	47,802	93,820	79,952	0:00:04
Model 6	200m^2	24,201	46,909	39,978	0:00:02
Model 7	500m^2	9,982	18,772	18562	0:00:01
Model 8	1000m^2	5,200	9,340	7,998	0:00:01

4.4 Fit statistic for model calibration

The calibration process of the 2D hydrodynamic model is a trial and error iterative process, during which a set of modelling parameters are adjusted until the simulated water level are in a good agreement with the observed data at the selected gauging station. The selected station was a water level station named Jeti Kastam which was located at Kota Bharu. The model was calibrated for duration from December 17, 2017 to January 1, 2015 flood event and analysed using fit statistics, which were Pearson Correlation Coefficient, Correlation Coefficient and Nash-Sutcliffe Efficiency (NSE), defined in Eq. [4], Eq. [5] and Eq. [6].

$$r = \frac{N\sum xy - (\sum x)(\sum y)}{\sqrt{[N\sum x^2 - (\sum x)^2][N\sum y^2 - (\sum y)^2\,]}} \quad [4]$$

$$r = \frac{1}{n-1}\sum \left(\frac{x-\bar{x}}{S_x}\right)\left(\frac{y-\bar{y}}{S_y}\right) \quad [5]$$

$$NSE = 1 - \frac{\sum_{i=1}^{n}\left(Q_{sim_i} - Q_{obs_i}\right)^2}{\sum_{i=1}^{n}\left(Q_{obs_i} - \bar{Q}_{obs}\right)^2} \quad [6]$$

4.5 Model performance indices for model convergence scenario

In order to quantify the discrepancy between the baseline model and other mesh sizes, and assessing the model sensitivity to mesh configurations, a set of statistical indices frequently used in the optimization of hydrodynamics (French, 2010) model was used. The Nash-Sutcliffe Efficiency (NSE), Mean Absolute Error (MAE) and Root Mean Square Error (RMSE), are defined in Eq. [7], Eq. [8] and Eq. [9].

$$MAE = \frac{\sum_{i=1}^{n} \left| \left(Q_{sim_i} - Q_{obs_i} \right) \right|}{n} \quad [7]$$

$$RMSE = \left[\frac{\sum_{i=1}^{n} \left(Q_{sim_i} - Q_{obs_i} \right)^2}{n} \right]^{1/2} \quad [8]$$

$$NSE = 1 - \frac{\sum_{i=1}^{n} \left(Q_{sim_i} - Q_{obs_i} \right)^2}{\sum_{i=1}^{n} \left(Q_{obs_i} - \bar{Q}_{obs} \right)^2} \quad [9]$$

Both MAE and RMSE provide statistical error estimation in the variable unit, while NSE is a normalized performance index, with efficiency of one perfect reproduction of an event.

5 MODEL EVALUATION

5.1 Model calibration

Calibration of the 2D hydrodynamic model was carried out using observed water levels at Jeti Kastam, Kota Bharu during the December 2014 flood event. This flood was the largest event recorded in 50 years and so was useful to accurately calibrate storage volumes in Kota Bharu floodplains. Based on the analysis, calibration curves at Jeti Kastam, Kota Bharu are shown in Figure 3. The calibration curves showed good agreement between observed and simulated water levels, both in terms of peak water levels and time to the peak. Statistics, as well as correlation factors, are summarised in Table 4.

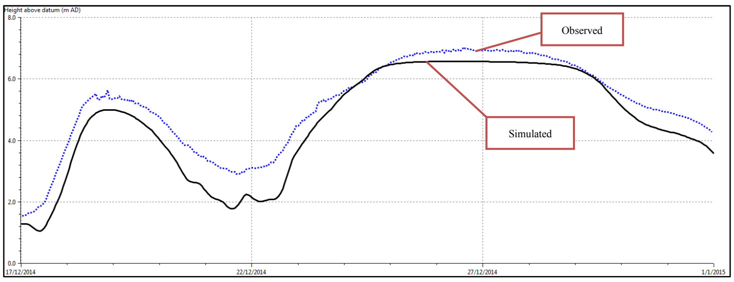

Figure 3. Calibration curves for the December 2014 flood event at Jeti Kastam, Kota Bharu.

Table 4. Fit Statistics for December 2014 calibration run.

JPS Water Level Gauge Station: Jeti Kastam			
Time of record available: From December 17, 2014 to January 1, 2015			
Event	Pearson Correlation Coefficient	Correlation Coefficient	NSE
Dec 2014	0.90	0.63	0.86

6 RESULTS

Here a series of meshes, generated for Kota Bharu according to different meshing sizes were tested in eight scenarios. The chosen meshing sizes represent the possible discretization approaches on which modeller relies when dealing with shallow water finite element and volume models. In order to understand which meshing sizes guarantee an acceptable performance, the accuracy in reproducing the free water surface elevation, the flood depth, the depth average speed, flood extent, and total 2D simulation time were assessed. The evaluation of the proposed discretization on a quantitative basis, the performance indices MAE, RMSE and NSE were evaluated at Sites A, B, and C (Table 5 and Figure 4).

Analysis on water surface elevation, flood depth and depth averaged speed did not show significant relationship with mesh sizes. Even though Sites A, B and C had the same catchment characteristics, the performance indices for different mesh size varied, and did not show specific trend with respect to increasing mesh sizes. Figure 4 shows the performance plots 8 models for meshes at Sites A, B and C

It can be assumed that satisfactory resolution for Site A is attributed to the flat area of the slope at the selected area compared to Sites B and C, and therefore contributes to better model behaviour with respect to other meshes size. This result is giving another perspective with the logical perception of the 2D hydrodynamic modeller, who introduces more refinement where more accuracy is desired. This result also shows there is a need to give very careful consideration when selecting and introducing different mesh sizes at any particular area.

Table 5. Performance indices for meshes at Sites A, B and C.

	Water Surface Elevation (m AD)			Flood Depth (m)			Depth Averaged speed (m/s)		
	MAE	RMSE	NSE	MAE	RMSE	NSE	MAE	RMSE	NSE
Site A									
Baseline	-	-	-	-	-	-	-	-	-
Model 1	0.00	0.01	1.00	0.00	0.01	1.00	0.00	0.00	1.00
Model 2	0.00	0.01	1.00	0.00	0.01	1.00	0.00	0.00	1.00
Model 3	0.02	0.02	1.00	0.02	0.03	1.00	0.01	0.01	0.99
Model 4	0.02	0.03	1.00	0.02	0.03	1.00	0.01	0.02	0.99
Model 5	0.04	0.23	0.98	0.02	0.04	0.99	0.02	0.03	0.96
Model 6	0.06	0.33	0.95	0.02	0.05	0.99	0.02	0.03	0.96
Model 7	0.09	0.41	0.92	0.06	0.08	0.97	0.03	0.05	0.89
Model 8	0.11	0.41	0.92	0.08	0.11	0.94	0.04	0.06	0.84
Site B									
Baseline	-	-	-	-	-	-	-	-	-
Model 1	0.00	0.01	1.00	0.01	0.01	1.00	0.00	0.00	1.00
Model 2	0.01	0.01	1.00	0.01	0.01	1.00	0.00	0.01	0.99
Model 3	0.04	0.23	0.98	0.02	0.04	0.99	0.01	0.01	0.97
Model 4	0.28	0.70	0.77	0.10	0.15	0.89	0.12	0.15	-0.08
Model 5	0.04	0.23	0.98	0.03	0.04	0.99	0.01	0.02	0.82
Model 6	0.02	0.03	1.00	0.03	0.03	0.99	0.01	0.02	0.89
Model 7	0.15	0.58	0.88	0.07	0.10	0.95	0.01	0.02	0.84
Model 8	1.61	2.67	-0.11	0.12	0.17	0.88	0.02	0.02	0.62
Site C									
Baseline	-	-	-	-	-	-	-	-	-
Model 1	0.00	0.01	1.00	0.00	0.01	1.00	0.00	0.00	1.00
Model 2	0.04	0.47	0.98	0.01	0.02	0.97	0.01	0.01	0.98
Model 3	0.06	0.58	0.97	0.01	0.01	0.99	0.00	0.01	0.99
Model 4	0.11	0.75	0.95	0.02	0.04	0.89	0.02	0.03	0.85
Model 5	3.20	4.51	0.78	0.03	0.05	0.80	0.02	0.03	0.84
Model 6	0.17	0.89	0.92	0.04	0.07	0.22	0.03	0.05	0.57
Model 7	0.23	1.06	0.89	0.05	0.09	-0.48	0.03	0.05	0.31
Model 8	0.18	0.89	0.92	0.06	0.11	-2.73	0.04	0.07	-0.78

Table 6. Results comparison using different meshes at the study area.

Model	Effective Area (ha)	Maximum flooded area (ha)	Total 2D simulation time (s)
Baseline	603.60 (100%)	531.09 (87.99%)	848,902.06
Model 1		529.19 (87.67%)	232,387.07
Model 2		527.82 (87.44%)	75,190.48
Model 3		529.63 (87.75%)	20,339.89
Model 4		526.91 (87.29%)	7,346.30
Model 5		524.64 (86.92%)	2,229.65
Model 6		519.71 (86.10%)	939.99
Model 7		516.50 (85.57%)	435.67
Model 8		518.76 (85.94%)	229.59

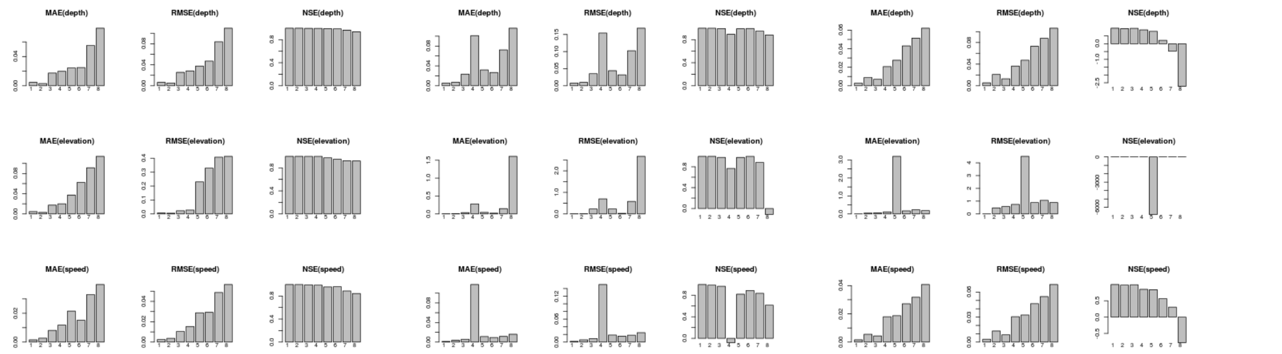

(a) Site A **(b) Site B** **(c) Site C**

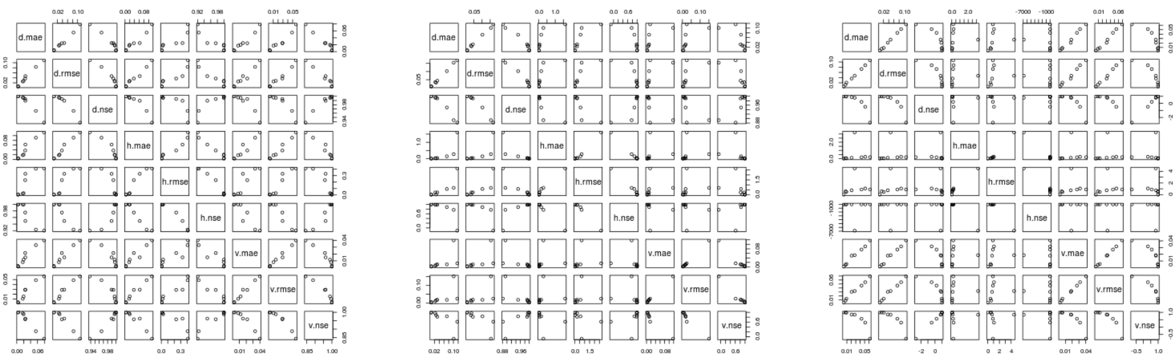

(d) Site A **(e) Site B** **(f) Site C**

Figure 4. Performance plots 8 models for meshes at Sites A, B and C. (a), (b), and (c) are the bar charts, while (d), (e), and (f) are the scatter plot matrices for performance indices.

Analysis of model performance using different mesh sizes was also conducted with respect to flood coverage and 2D simulation time. Table 6 showed trend of decreasing flood coverage with increasing mesh size. This happens because the volume-depth and flow-area-depth relationship in each of the mesh triangle is derived from a DEM. Heights at the vertices of the generated mesh elements calculated by interpolation from a DEM, resulted in different impact of flow path at the specified area with respective mesh. Figure 5 to Figure 13 show the extent of flood coverage with different mesh sizes. Some particular sites and models also showed significant difference in flood depth and flood coverage, depending on mesh sizes (Figure 7 and Figure 8 for Site A).

Result also showed finer mesh size will result in longer simulation period. The simulation time is not favourable for very fine mesh. This is because the meshing algorithm generates very small triangles, which have the effect of decreasing the time step of the 2D hydrodynamic model, leading to an increased run time. It appears that, with the small difference between baseline and model 8 of only 2.05%, clearly shows that for similar level of accuracy, it produces faster run time magnitude.

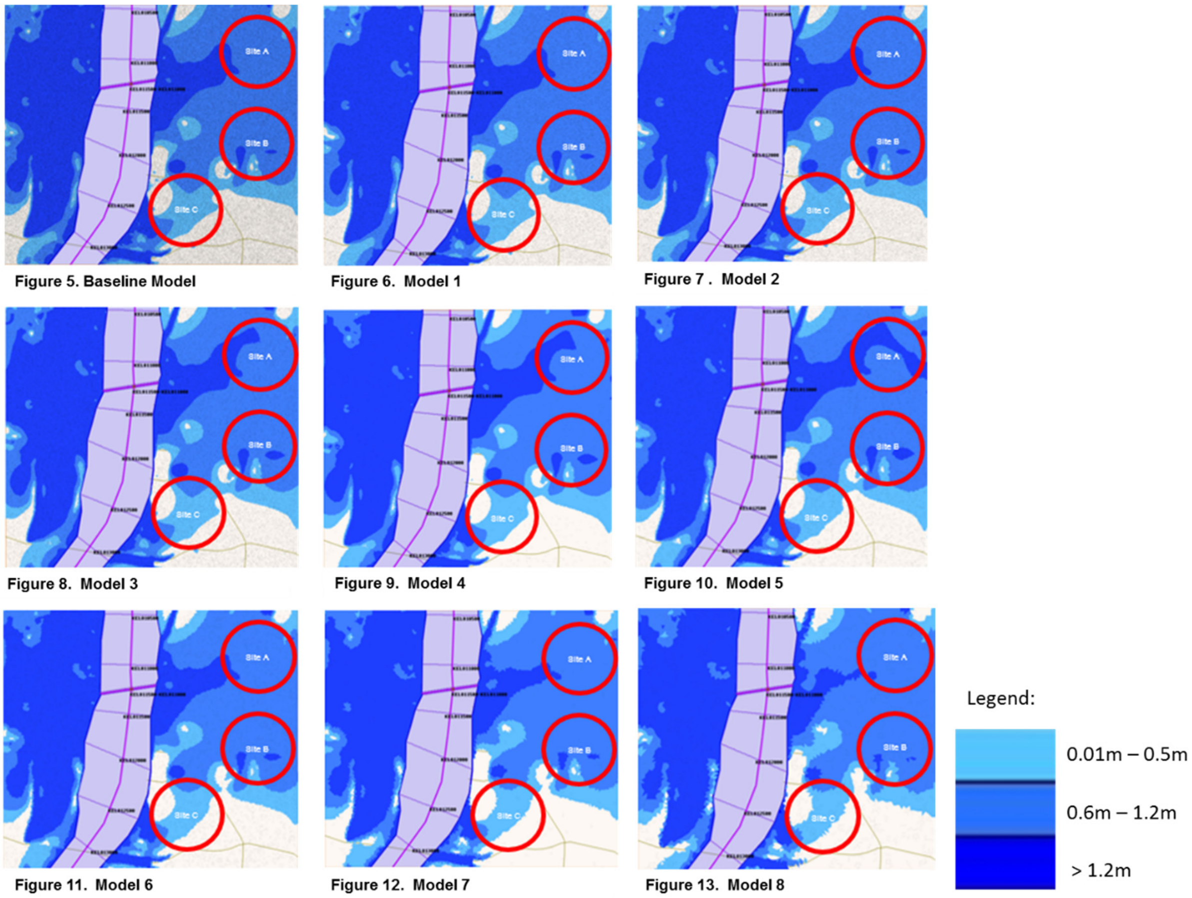

Figure 5 to Figure 13. Extent of flood coverage with different mesh sizes.

7 CONCLUSIONS

Utilizations of flexible mesh technique give flexibility for modelling 2D overland flows in a complex urban environment. However, complex geometries can be challenging for many modellers to deal with. This paper presents the results of several meshing sizes for two dimensional shallow water models, tested for the discretization of the meshing sizes. Further research is still required on this topic to better understand the sensitivity of the meshing sizes as well as the DEM and infrastructure in the flood plain.

ACKNOWLEDGEMENTS

The authors would like to acknowledge the Department of Irrigation and Drainage, Malaysia (DID) for providing data to be used for this study. Special thanks also go to HR Wallingford Asia for the support using InfoWorks ICM 7.5.4 software.

REFERENCES

Blanton, B.O. & Luettich, R.A. (2009). *North Carolina Coastal Flood Analysis System Model Grid Generation,* RENCI Technical Report, TR-08-05.

Bunya, S., Dietrich, J.C., Westerink, J.J., Ebersole, B.A., Smith, J.M. & Atkinson, J.H. (2010). A High-Resolution Couple Riverine Flow, Tide, Wind, Wind Wave and Storm Surge Model for Southern Louisiana and Mississippi. Part I: Model Development and Validation. *Monthly Weather Review,* 138, 345–77.

Chow, V.T. (1981). *Open Channel Hydraulics,* Development of Uniform Flow and its Formulas, 88–123.

Department of Irrigation and Drainage. (DID). (2015). *Laporan Banjir Tahunan,* Jabatan Pengairan dan Saliran, Malaysia.

French, J.R. (2010). Critical Perspectives on the Evaluation and Optimization of Complex Numerical Models of Estuary Hydrodynamics and Sediment Dynamics. *Earth Surface Process Land*, 35, 174–89.

Garcia-Navarro, P. & Brufau, P. (2006). *Numerical Methods for the Shallow Water Equations: 2D approach, River Basin Modeling for Flood Risk Mitigation.* Taylor & Francis, 409-428.

Zundel, A.K., Cialaone, M.A. & Moreland, T.J. (2002). *SMS Steering Module for Coupling Wave Sand Currents, 1: ADCIRC and STWAVE,* Coastal and Hydraulics Engineering Technical Note ERDC/CHLCHETN-IV-41. Vicksburg, MS: U.S. Army Engineer Research and Development Centre.

Proceedings of the 37th IAHR World Congress
August 13 – 18, 2017, Kuala Lumpur, Malaysia

FLOOD FREQUENCY ANALYSIS AND CURVES OF EQUAL PREDICTED PEAK DISCHARGE

DRISSIA THOTTUNGAL[1], VINAYAKAM JOTHIPRAKASH[2] & ALAYIL BAHULEYAN ANITHA[3]

[1,2] Indian Institute of Technology, Bombay, Powai, India
drissia13@gmail.com; vprakash@iitb.ac.in
[3] Centre for Water Resources Development and Management, Kozhikode, Kerala, India
aba@cwrdm.org

ABSTRACT

Flood frequency analysis is a prerequisite for designing flood control structures. It is also used in flood management, design floods and flood investigation works. Gumbel method is commonly used for predicting peak discharge for a given return period. Nevertheless, this method gives at site flood frequency for a given return period. In this study, probability weighted moments and L moments were used for estimating the at site flood frequency. Probability weighted moments was used for estimating the parameters for Gumbel Extreme Value distribution and Log Pearson Type III distribution at a given site. The study area taken is the west flowing rivers in Kerala, India. The whole area is 40849 km^2 with 41 small rivers originating from Western Ghats and reaches Arabian Sea. L moments were used for the parameter estimation of Generalised Extreme Value (GEV), Generalised Pareto (GPA) and Generalised Logistic (GLO) distribution. The best fit distribution was found using statistical indices. Using the best fit distribution, flood frequency was calculated for all the gauging stations like isohyets and isopluvial lines, an attempt was made to create contour of equal peak discharge for return periods 20, 50 and 100 years. This was achieved using ArcGIS 10, GIS software. These curves give information about the magnitude of flood frequency in each location.

Keywords: L moments; Generalised Logistic; Generalised Pareto; Geographic Information System.

1 INTRODUCTION

Extreme events like floods and droughts are occurring worldwide. Floods are high stages in discharge which brings overflowing of river banks. Knowledge of the magnitude and probable frequency of recurrence of floods is necessary to the proper design and location of structures such as dams, bridges, culverts, levees, highways, waterworks, sewage- disposal plants, and industrial buildings (Darymple, 1960). For understanding of the probability of occurrence of floods, flood frequency analysis is carried out. Methods like Gumbel extreme value distribution, Index flood method, multiple correlations, logarithmic normal distribution, log pearson type III distribution and gamma distributions are used for flood frequency analysis. (Cruff and Rantz, 1965). Gumbel method is widely used for plotting flood frequency. For these methods, probability weighted moments are used for the estimation of parameters. Moni and Husain (2014) applied Gumbel method, Log Pearson method and log normal methods to find the flood frequency analysis in Jiya Dhol river of Brahmaputra river, India. Log Pearson type III method was found to be the best method for flood frequency, though Gumbel method can also be effectively used.

Regional flood frequency analysis was carried out to find the design flood over an ungauged site (Burn and Kowalchuk, 1997; Kumar and Chatterjee, 2005). L moments developed by Hosking (1990) has been used for regional flood frequency. L moments are more robust than probability weighted moments (Hoiskings, 1990). In a study conducted by Izinyon and Ehiorobo (2015), L moments were used for at site flood frequency analysis in Nigeria. In this study, generalized extreme value distribution (GEV), generalized logistic distribution (GLO) and generalized Pareto distribution (GPA) were taken and the parameters were estimated by L moments. Statistical indices are used to find the best fit distribution. Vivekanandan (2015) used method of moments and L moments were used for the parameter estimation of Exponential, Extreme value type I, Extreme value type II, Generalised Extreme Value, Generalised Pareto and normal distribution. Extreme value type I distribution was found to be the best fit distribution for Malakkara and Neeleswaram gauging stations in Kerala, India. Predicting flood accurately at different frequencies is required for all flood management measures. For this, selection of appropriate distribution is crucial and hence in this study, statistical indicators are used to evaluate the result. In addition to this, a comparison between probability weighted moments and L moments were attempted.

In hydrology, many curves of equal values are in use, such as isohytel and isopluvial lines. An isohyte is a curve of equal rainfall and isopluvial line is a curve of equal pluvial index. For regional rainfall mapping, isohytes are commonly referred as isopluvials (Ponce, 1989). Although many curves were available for rainfall, the same were not available for discharge. This is because unlike rainfall, discharge depends on many factors like area, slope, rainfall and other topographical parameters. Nevertheless, an attempt was made in this study to create curves of peak discharge curves using Geographic Information System. This will give a spatial representation of the peak discharge at different frequencies in various locations of the study area.

2 STUDY AREA

The study area taken is the west flowing rivers in Western Ghats of Kerala, India (between the global Coordinates 8º18' and 12º48' N latitude and 74º52' and 77º22' E longitude). The area is 40,849 km^2 with 41 small rivers originating from Western Ghats and reaches Arabian Sea. As such a streamlet with more than 15km is taken as a river that gives a 41 number with basin area ranging from 52 km^2 to 6,186 km^2. There are only four medium rivers in Kerala, Periyar, Bharathapuzha, Pamba and Chaliyar. Based on the size of catchment area, the medium rivers are defined as the river basins with catchment area between 2000-20,000 km^2 and minor rivers are basins with catchment area below 2000 km^2. The average annual rainfall in Kerala is 3000 mm. This southern State of India has a unique physiography which affects hydrology, landuse and other related environmental factors. There are three physiographic zones; the highland (above 76 m from the mean sea level), the midland (between 7.6 and 76m above mean sea level), and the lowland (below 7.6m from the mean sea level). The location of medium and minor rivers along with the discharge locations are given in Figure 1.

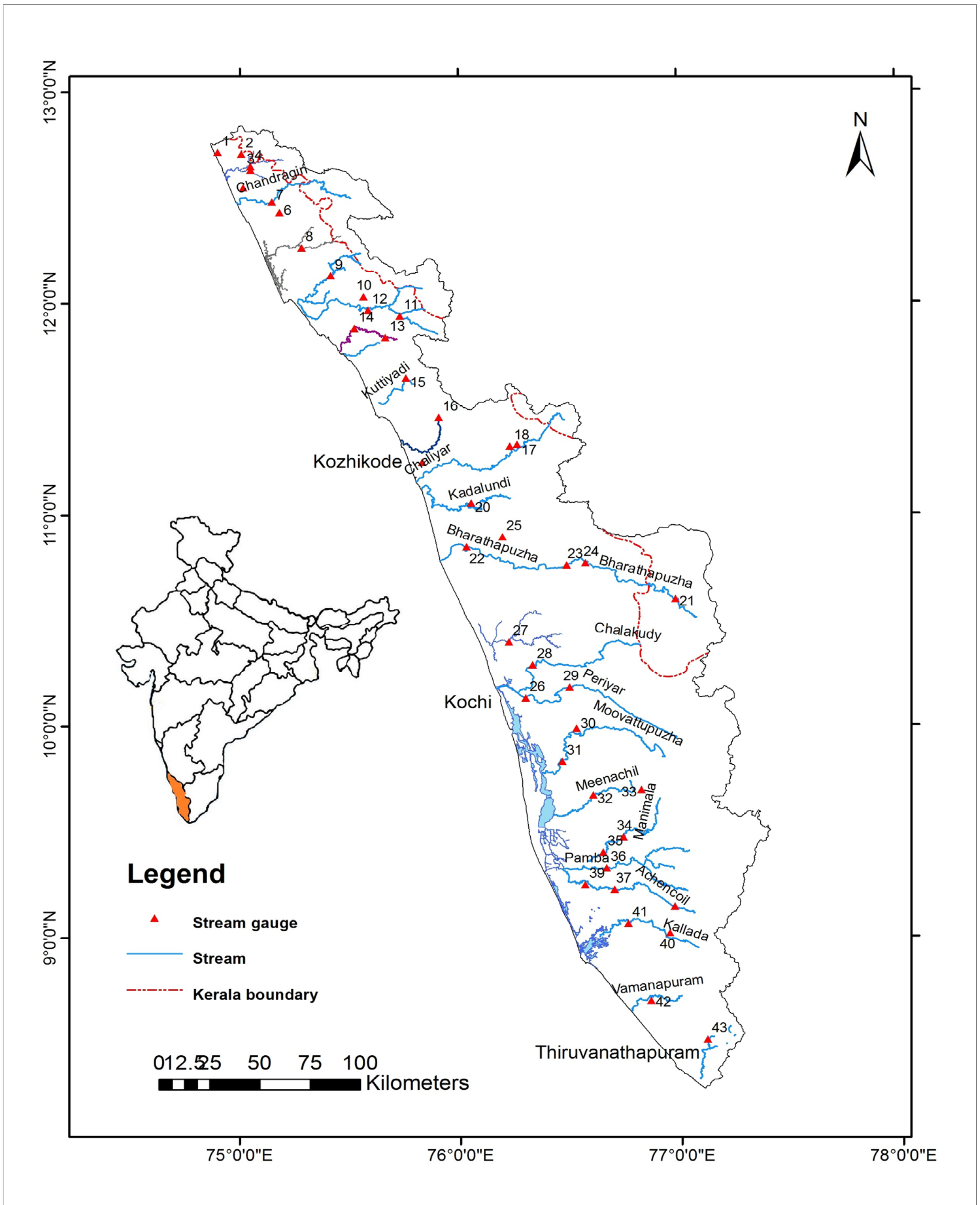

Figure 1. The location of stream gauge stations.

3 MATERIALS AND METHODS

The observed discharge data of 20 stream gauge stations maintained by Central Water Commission, Government of India and 23 gauging stations maintained by Water Resources Department, Kerala were used in this study. The annual peak discharge was extracted from 43 gauging sites whose data availability ranges from 13 to 47 years. These data were used to predict peak discharge for various return periods and flood frequency curves were developed for each station. The first four moments were calculated for all the 43 Gauging stations. This probability weighted moments (PWM) was used to estimate the parameters of Gumbel Extreme Value distribution (GM) and Log Pearson Type III (LP3) distribution.

3.1 L moments and distributions

L moments introduced by Hosking (1990) are defined as linear combination of probability weighted moments (Hosking and Wallis, 1993). The benefits of L moment ratios over product moment ratios are that the L moments are more robust in the presence of extreme values and do not bound the sample size related bounds. It is also pointed out that L moments are more easily interpretable as measures of distributional shape.
The first four moments are related to probability weighted moments as (Kumar and Chatterjee, 2005)

$$\begin{gathered} \lambda_1 = \beta_0 \\ \lambda_2 = 2\beta_1 - \beta_0 \\ \lambda_3 = 6\beta_2 - 6\beta_1 - \beta_0 \\ \lambda_4 = 20\beta_3 - 30\beta_2 - 12\beta_1 - \beta_0 \end{gathered} \qquad [1]$$

L moment ratios are quantities as given below:

L-coefficient of variation, L-CV (τ_2) = λ_2/λ_1, L-coefficient of skewness, L-skew (τ_3) = λ_3/λ_2 and L-coefficient of kurtosis, L-kurtosis (τ_4) = λ_4/λ_2, where λ_1=mean of distribution, λ_2=measure of scale, τ_3 =skewness and τ_4 =kurtosis

The Generalized Extreme Value distribution (GEV), Generalized Pareto (GPA) and Generalized Logistic (GLO) were used to estimate the flood frequency using L moments. For estimating the parameters of respective distributions, L moments were used. The quantile functions and equations are used for parameter estimation using L moments (Ahmad and Zakaria, 2011).

3.2 Statistical Evaluation

The evaluation of the predicted peak flood for each distribution with the observed data was carried out using Statistical indices. The flood frequency from observed data was estimated for return periods 2, 5, 10 and 20 years using Weibull method. These values were used for estimating the statistical indicators for evaluation of the predicted value. D index was used to evaluate the result between Gumbel extreme value distribution and Log Pearson Type III distribution (Das and Qureshi, 2014).

$$D = \frac{\sum_{i=1}^{N}|x_i - y_i|}{\bar{x}} \qquad [2]$$

where $\bar{x}$ = mean of the annual peak discharge series, x_i = ith highest recorded discharge and y_i = ith highest estimated discharge.

GEV, GLO and GPA were evaluated using Mean Absolute Deviation Index (MADI), Root Mean Square Error (RMSE), Relative Root Mean Square Error (RRMSE) and Probability Plot Correlation Coefficient (PPCC). The equations are as follows

$$\mathrm{MADI} = \frac{1}{N}\sum_{i=1}^{N}\left|\frac{x_i - y_i}{x_i}\right| \qquad [3]$$

$$\mathrm{RMSE} = \left(\frac{\sum x_i - y_i^{\,2}}{N-m}\right)^{1/2} \qquad [4]$$

$$\mathrm{RRMSE} = \left(\frac{\sum\left(\frac{x_i - y_i}{x_i}\right)^2}{N-m}\right)^{1/2} \qquad [5]$$

$$\mathrm{PPCC} = \frac{\sum[(x_i-\bar{x})(y_i-\bar{y})]}{[\sum(x_i-\bar{x})^2\sum(y_i-\bar{y})^2]^{1/2}} \qquad [6]$$

where x_i are the observed peak discharge for a given return period, y_i are the predicted peak discharge, N is the number of data points and m is the number of parameter estimated. $\bar{x}$ and $\bar{y}$ are the average value of observed and predicted flood quantiles, respectively. In the case of MADI, RMSE and RRMSE the lower value indicates the best fit distribution while a value nearer to 1 is taken as the best for PPCC. Since it is difficult to visually compare the result of all the test, a ranking method was adopted for identifying the best fit distribution for each station. The lowest value for each test was given 4 and the next lowest value was given 3 and so on for MADI, RMSE and RRMSE. In the same manner, higher value of PPCC was given the rank 4. For each distribution, the ranks are summed up and the highest value gives the best fit distribution (Izinyon and Ehiorobo, 2015).

3.3 Spatial Variation

In order to understand the spatial variations of the peak value, ArcGIS was used to plot the peak discharge contours for various return periods. The peak discharge was calculated for 2, 5, 20, 50 and 100 return periods for all stations. This was used for plotting flood frequency curves for each station. The magnitude of high discharge for return periods 20, 50 and 100 years for each station were taken to create the curves of equal peak discharge using ArcGIS. In spatial analyst tool box, interpolation tool was used to create a raster image for predicted peak discharge of 20, 50 and 100 return period. Inverse Distance Weighted (IDW) interpolation tool was used to find the spatial variation with an interval of 500 m^3/s. In this way, curves of equal peak discharge were created for each return period of 20, 50 and 100 years.

4 RESULTS AND DISCUSSION

The flood frequency analyses of 43 gauging stations of Kerala Rivers (west flowing rivers) were analysed using probability weighted moments (PWM) and L moments (LM). Based on the best fit distribution in two methods spatial variation was plotted in GIS. The values of mean (βo), Standard deviation ($\beta 1$), L coefficient of variation (L cv), L coefficient of skewness (L skew) and L kurtosis (L kurt) were given in Table 1.

4.1 Probability Weighted Moments

Probability weighted moments (PWM) was used for estimating parameters for Gumbel extreme value distribution and Log Pearson Type III distribution. The peak discharge was calculated for return periods 2, 5, 10, 20, 50, 90 and 100. D index was calculated for each station using the predicted and observed flood frequency. The lowest value of D index gives the best fit distribution. The D index values for both distributions were shown in Figure 2. From the figure, it was found that Log Pearson Type III distribution was the best fit distribution at 26 gauging stations and for the remaining it was Gumbel extreme value distribution (Table 1). The flood frequency curve for each station was plotted using the best fit distribution among the GM and LP3 and is shown in Figure 3. Based on this, it was clear that the maximum peak discharge prediction was found at Neeleswaram gauging site of Periyar river basin followed by Kumbidi on Bharathapuzha river basin and Kuniyil on Chaliyar river basin. The lowest prediction is at Ambarampalayam site in upstream side of Bharathapuzha river basin.

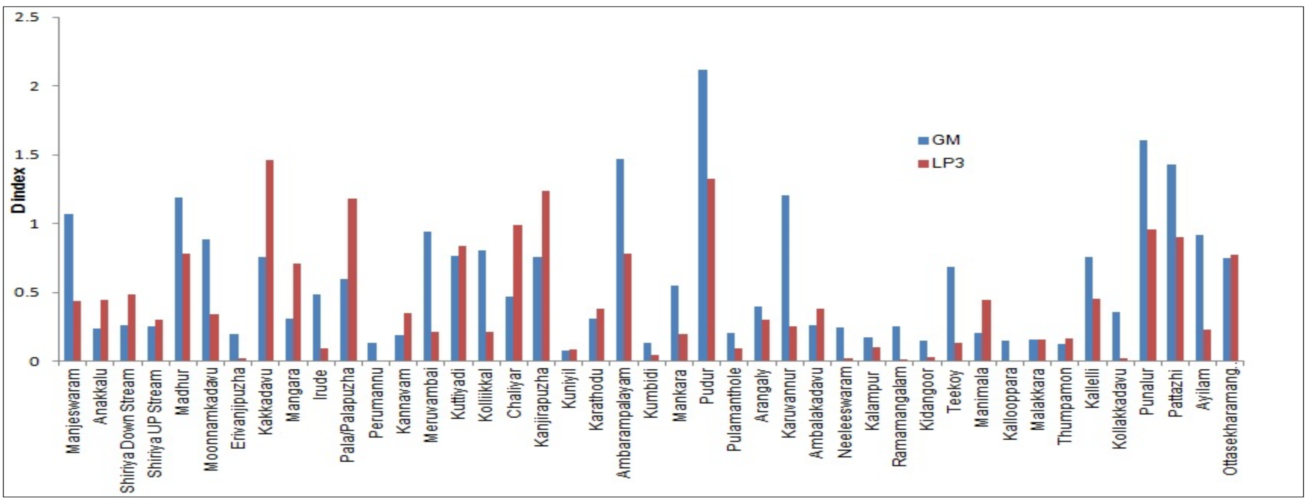

Figure 2. D index values for GM and LP3 distribution.

Table 1. L moment ratios and Best fit distribution

Sl no	Stream gauge	A (km2)	N	β0	β1	Lcv	Lskew	Lkurt	Best fit distribution	
									PWM	L moments
1	Manjeswaram	25.44	27	25.71	17.50	0.32	0.55	0.00	LP3	GPA
2	Anakkalu	166.25	30	119.58	48.69	0.22	0.17	0.19	GM	GLO
3	Shiriya Down Stream	322.56	29	499.32	288.45	0.29	0.36	0.21	GM	GPA
4	Shiriya UP Stream	348	44	390.05	221.27	0.32	0.25	0.05	GM	GPA
5	Madhur	66.04	27	63.17	43.33	0.31	0.56	0.05	LP3	GPA
6	Moonnamkadavu	216.8	47	546.25	352.23	0.32	0.24	0.22	LP4	GLO
7	Erivanjipuzha	957	28	818.10	265.85	0.19	0.08	0.14	LP5	GPA
8	Kakkadavu	276.5	44	561.33	373.51	0.34	0.33	0.25	GM	GPA
9	Mangara	109.6	32	595.64	457.16	0.39	0.31	0.05	GM	GPA
10	Irude	189.63	44	734.02	348.26	0.30	0.15	0.04	LP3	GPA
11	Pala/Palapuzha	237.25	42	297.01	178.56	0.30	0.30	0.21	GM	GPA
12	Perumannu	1070	28	1516.68	447.71	0.17	0.06	0.06	LP3	GLO
13	Kannavam	60.75	40	94.13	36.20	0.21	-0.01	0.15	GM	GLO
14	Meruvambai	180	47	188.06	91.05	0.26	0.23	0.20	LP3	GLO
15	Kuttiyadi	34.82	38	401.84	225.45	0.32	0.33	0.13	GM	GPA
16	Kolliikkal	343	13	90.34	66.05	0.26	0.36	0.20	LP3	GPA
17	Chaliyar	386	42	408.05	270.04	0.35	0.30	0.16	GM	GPA
18	Kanjirapuzha	64	45	112.75	99.61	0.42	0.39	0.24	GM	GPA
19	Kuniyil	1876	32	1719.50	635.02	0.21	0.13	0.17	GM	GPA
20	Karathodu	1345	27	420.72	233.28	0.28	0.35	0.27	GM	GPA
21	Ambarampalayam	950	34	111.43	120.22	0.53	0.48	0.17	LP3	GEV
22	Kumbidi	5755	33	1601.83	701.74	0.24	0.16	0.18	LP3	GPA
23	Mankara	2775	28	378.68	248.26	0.35	0.26	0.22	LP3	GLO
24	Pudur	1313	27	190.64	227.34	0.52	0.58	0.35	LP3	GPA
25	Pulamanthole	940	27	664.03	320.40	0.27	0.22	0.19	LP3	GPA
26	Arangaly	1342	35	652.52	239.49	0.20	0.18	0.16	LP3	GLO
27	Karuvannur	725	46	269.50	178.11	0.34	0.17	0.18	LP3	GLO
28	Ambalakadavu	1160	25	498.57	282.22	0.28	0.26	0.19	GM	GPA
29	Neeleeswaram	4234	42	2100.81	744.74	0.20	0.12	0.10	LP3	GLO
30	Kalampur	405	27	429.55	145.85	0.19	0.17	0.12	LP3	GPA
31	Ramamangalam	1208	35	958.46	222.85	0.13	0.03	0.04	LP3	GEV
32	Kidangoor	615	27	530.39	117.29	0.13	0.04	0.20	LP3	GPA
33	Teekoy	57	30	116.50	51.28	0.25	0.16	0.07	LP3	GPA
34	Manimala	490	39	411.46	263.42	0.36	0.18	0.15	GM	GPA
35	Kallooppara	731	27	572.91	154.85	0.16	0.03	0.10	LP3	GLO
36	Malakkara	1713	27	1007.88	332.49	0.18	0.18	0.13	GM	GPA
37	Thumpamon	810	35	401.46	176.19	0.25	0.18	0.04	GM	GPA
38	Kallelli	419	24	264.86	168.19	0.33	0.34	0.18	LP3	GPA
39	Kollakkadavu	952.71	42	314.87	130.93	0.23	0.19	0.07	LP3	GPA
40	Punalur	870	46	312.47	328.29	0.49	0.47	0.27	LP3	GPA
41	Pattazhi	1210	35	415.13	401.53	0.39	0.49	0.40	LP3	GPA
42	Ayilam	540	34	284.84	163.46	0.28	0.28	0.28	LP3	GPA
43	Ottasekharamangalam	247.35	42	150.11	119.64	0.40	0.31	0.05	GM	GLO

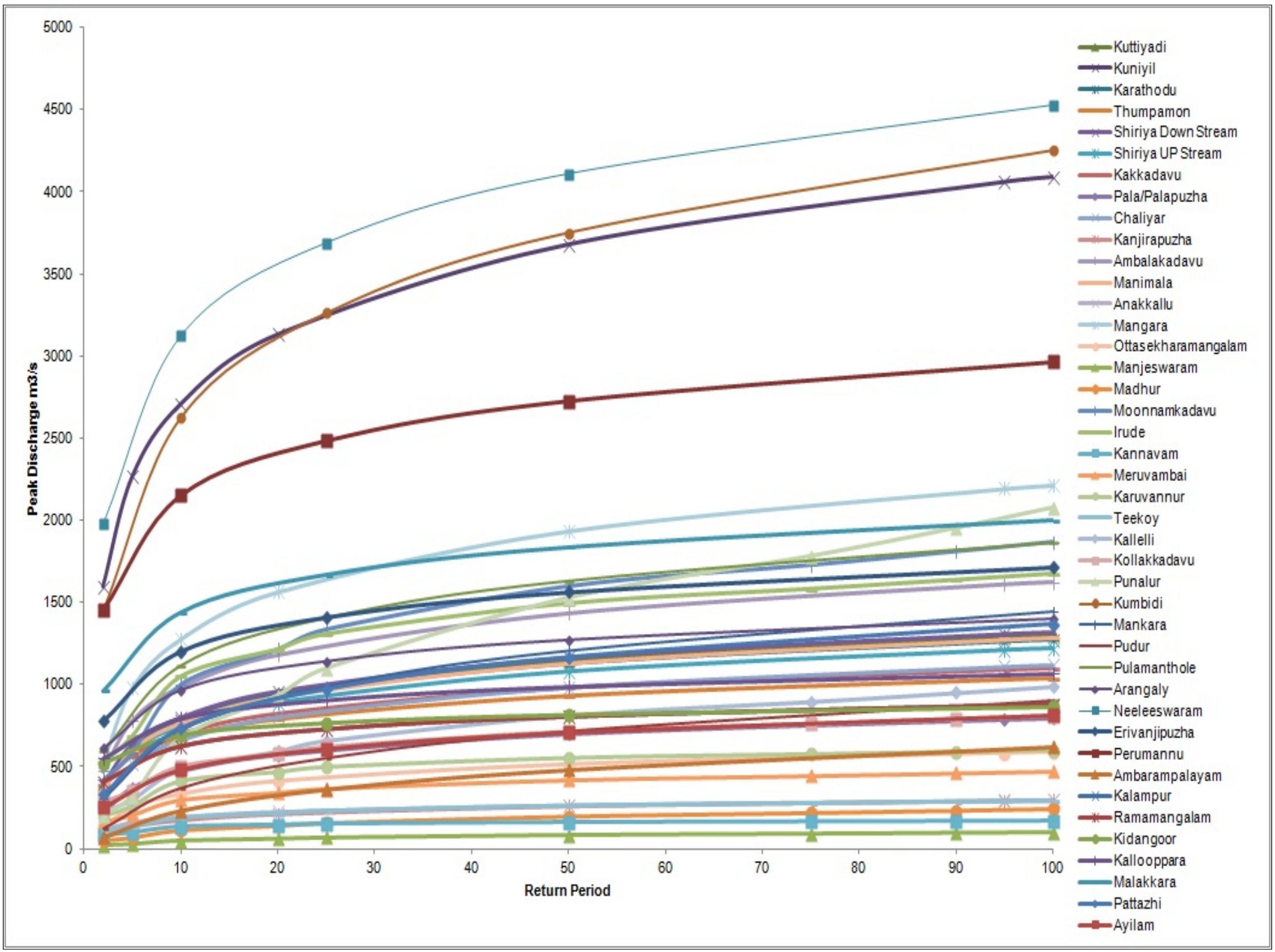

Figure 3. Flood frequency curves using PWM.

4.2 L Moments

The L moments were calculated for each gauging station and were used for the parameter estimation of the distributions, GEV, GLO and GPA. The goodness of fit test using four statistical indicators Mean Absolute Deviation Index (MADI), Root Mean Square Error (RMSE), Relative Root Mean Square Error (RRMSE) and Probability Plot Correlation Coefficient (PPCC) were analysed. According to indictor value, ranks were given for each distribution and are given in Table 2. The distribution with highest rank is taken as the best fit distribution for the stream gauge station. From the table, it was clear that GPA was the best fit distribution for most of the stations (30 stream gauge stations). Eleven stations showed GLO as the best fit distribution. GEV was found to be the best fit distribution for only two stations. The best fit distributions for each station are given in Table 2. The QT vs T graph was plotted using the quantile function of the best fit distribution (Figure 4). Likewise, in this graph, Neeleswaram gauging station has highest peak discharge followed by Kumbidi on Bharathapuzha river basin and Kuniyil on Chaliyar river basin.

4.3 Evaluation of the result

An evaluation was carried out between the predicted peak discharge and observed peak discharge for 20years return period. The observed flood frequency was calculated using Weibull method. Scatter plot between the observed peak discharge and predicted peak discharge using probability weighted moments and L moments were shown in Figure 5. A linear positive correlation was obtained between predicted and observed values. A comparison of peak discharge that were calculated using probability weighted moments (PWM) and L moments were plotted using the scatter plot (Figure 6). The scatter plot of 2 years return period shows that in both the methods the peak discharge was almost similar. As the return period increases, some variation were found in the values of the peak discharge.

  / ISSN 1562-6865 (Online) - ISSN 1063-7710 (Print)

Table 2. Rank given for each distribution

Sl. No	Rivergauging	GEV	GLO	GPA	Best fit Distribution	Sl. No.	Rivergauging	GEV	GLO	GPA	Best fit Distribution
1	Manjeswaram	4	8	12	GPA	22	Kumbidi	6	8	10	GPA
2	Anakkalu	5	12	7	GLO	23	Mankara	5	10	9	GLO
3	Shiriya DS	5	7	12	GPA	24	Pudur	7	6	11	GPA
4	Shiriya US	4	8	12	GPA	25	Pulamanthole	6	8	10	GPA
5	Madhur	4	8	12	GPA	26	Arangaly	4	10	10	GLO
6	Moonnamkadavu	5	10	9	GLO	27	Karuvannur	2	1	3	GLO
7	Erivanjipuzha	4	8	12	GPA	28	Ambalakadavu	5	9	10	GPA
8	Kakkadavu	5	9	10	GPA	29	Neeleeswaram	5	12	7	GLO
9	Mangara	5	7	12	GPA	30	Kalampur	5	7	12	GPA
10	Irude	5	7	12	GPA	31	Ramamangalam	10	8	6	GEV
11	Pala/Palapuzha	5	9	10	GPA	32	Kidangoor	9	5	10	GPA
12	Perumannu	6	11	7	GLO	33	Teekoy	6	8	10	GPA
13	Kannavam	5	12	7	GLO	34	Manimala	5	9	10	GPA
14	Meruvambai	5	12	7	GLO	35	Kallooppara	6	10	8	GLO
15	Kollikkal	5	7	12	GPA	36	Malakkara	6	8	10	GPA
16	Kuttiyadi	6	7	11	GPA	37	Thumpamon	4	8	12	GPA
17	Chaliyar	4	8	12	GPA	38	Kallelli	5	9	10	GPA
18	Kanjirapuzha	5	9	10	GPA	39	Kollakkadavu	5	7	12	GPA
19	Kuniyil	5	9	10	GPA	40	Punalur	5	9	10	GPA
20	Karathodu	4	9	11	GPA	41	Pattazhi	5	9	10	GPA
21	Ambarampalayam	10	5	9	GEV	42	Ayilam	5	11	8	GPA
						43	Ottasekharamangalam	5	8	11	GLO

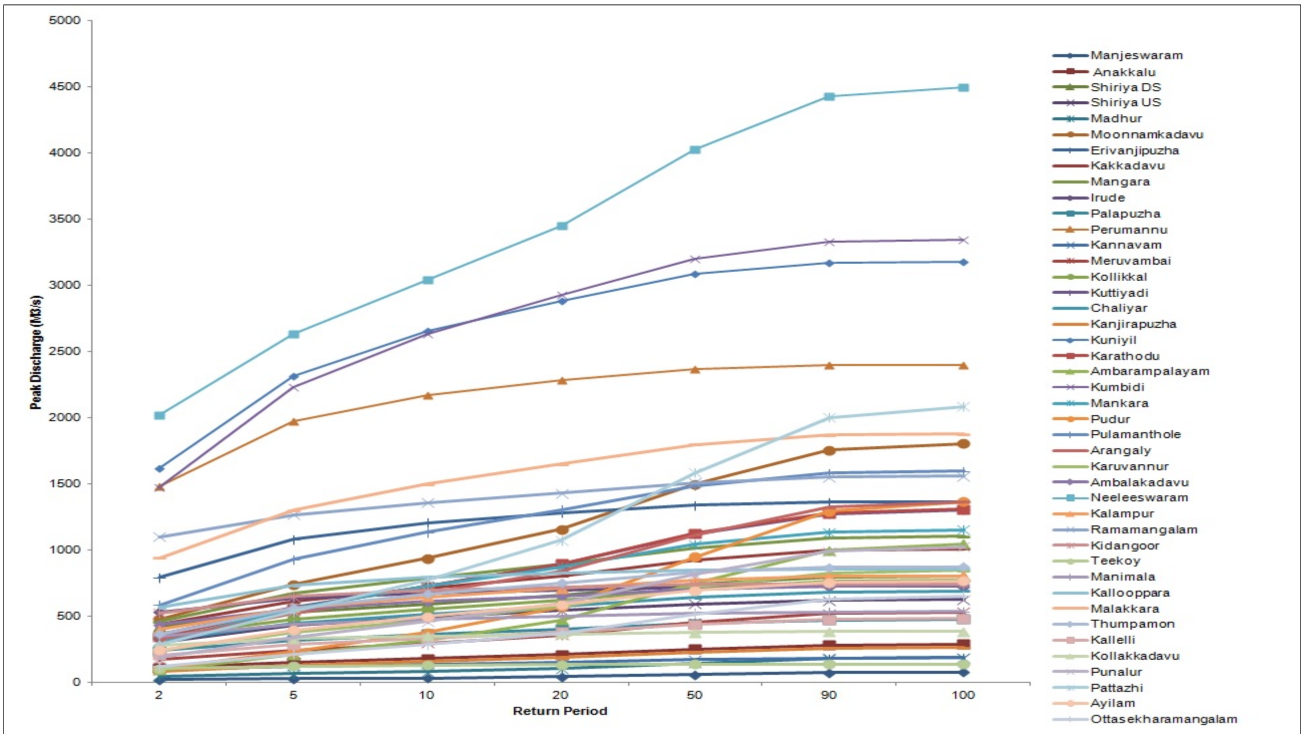

Figure 4. Flood frequency curves using L moments.

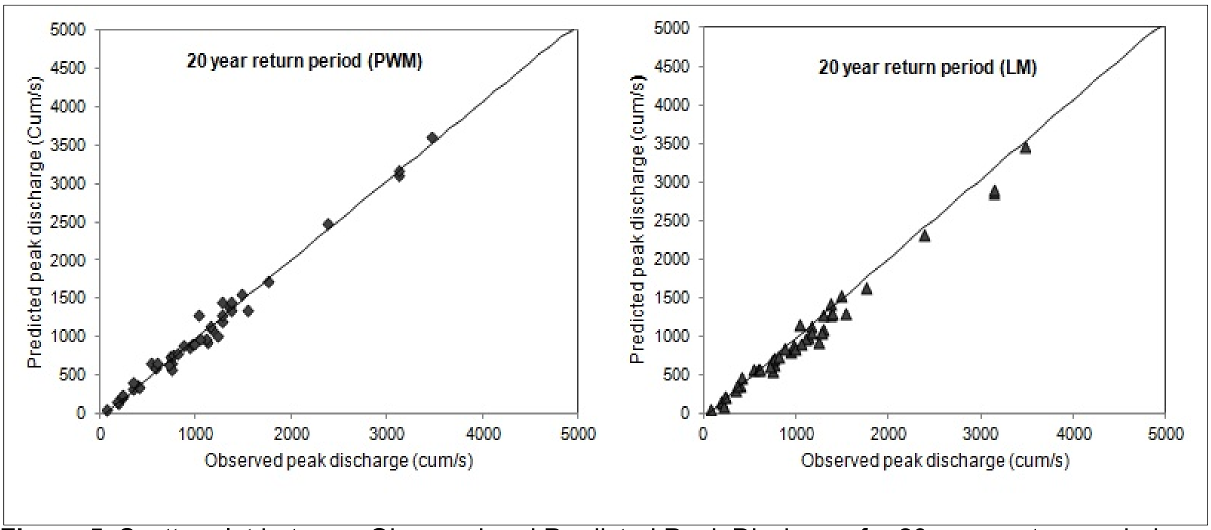

Figure 5. Scatter plot between Observed and Predicted Peak Discharge for 20 years return periods.

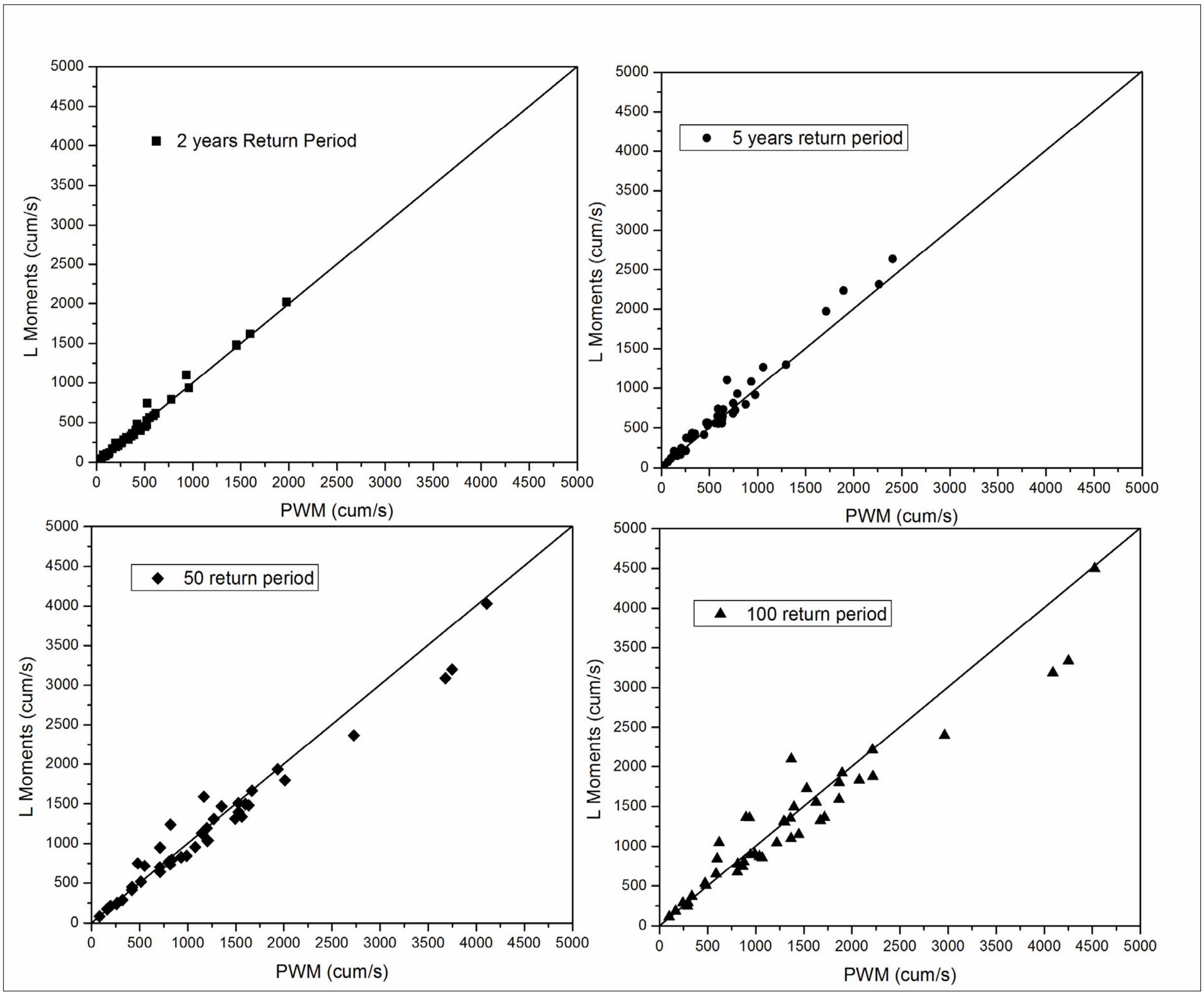

Figure 6. Scatter plot between PWM and L moments.

4.4 Spatial Variation of flood frequency

The curves of equal predicted peak discharge for 20, 50 and 100 years return period by PWM and L moments are given in Figure 5a and 5b respectively. The curves are plotted at an interval of 500 m^3/s. Just like storm eye in isohyet maps, three concentric circles of high discharge are visible in Figure 7a and 7b. These are the downstream stations of Periyar, Bharathapuzha and Chaliyar, the three medium rivers in Kerala. In most of the other areas, the peak discharge comes to about 1000-1500 m^3/s.

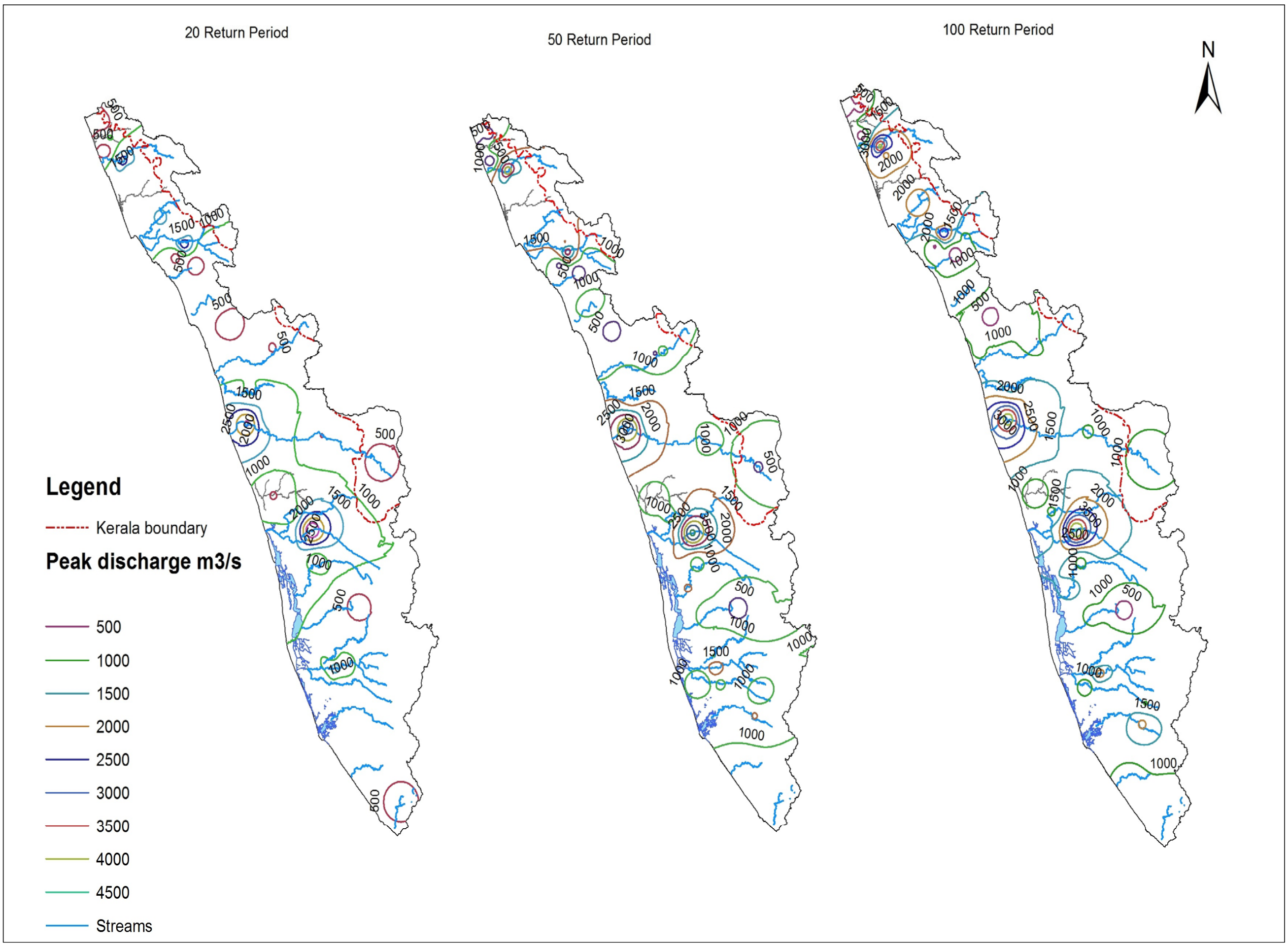

Figure 7a. Curves of equal peak discharge using probability weighted moments.

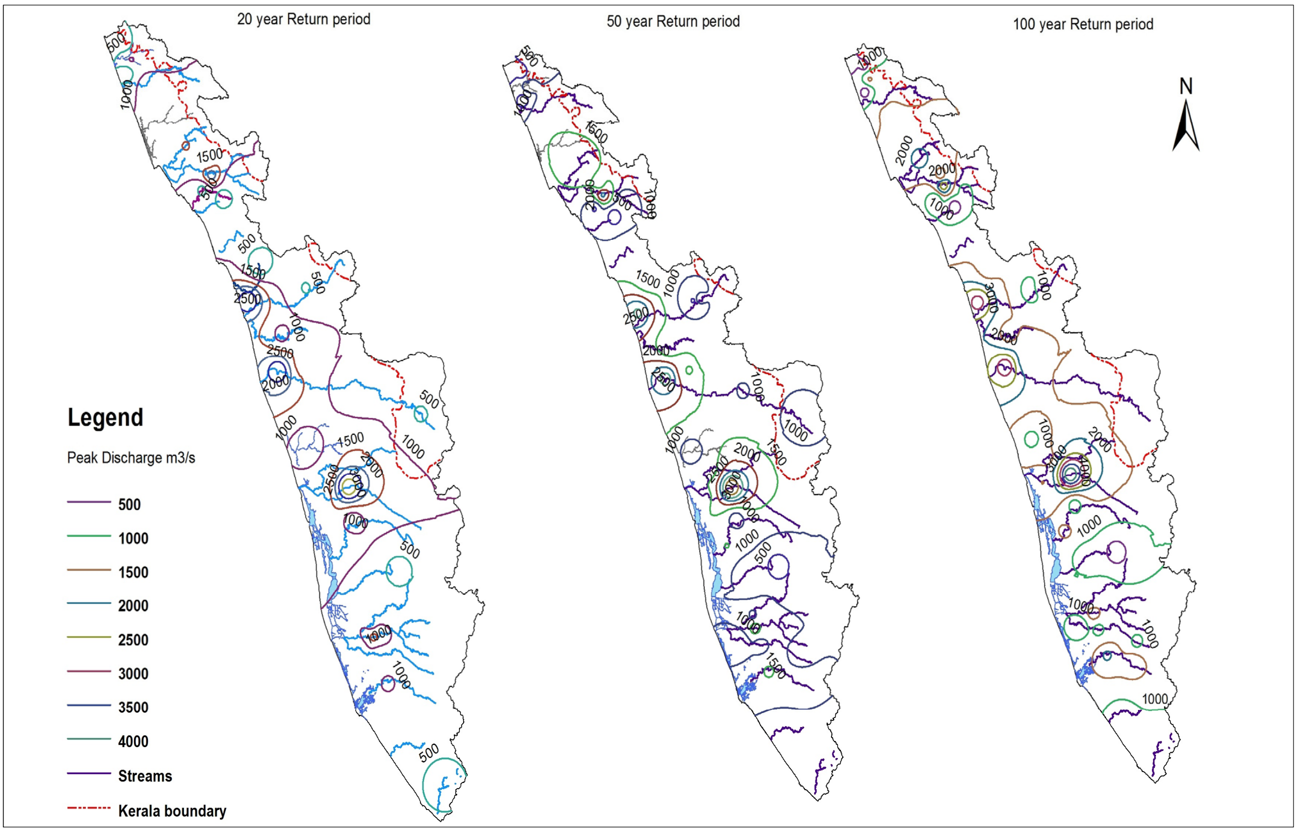

Figure 7b. Curves of equal peak discharge using L moments.

5 CONCLUSIONS

Flood frequency analysis was carried out for west flowing rivers in Kerala using Gumbel extreme value distribution, Log Pearson Type III distribution, GEV, GLO and GPA. About 63% of the gauging stations show Log Pearson Type III distribution based on probability weighted moments as the best fit distribution. In L moments based parameter estimation GPA was the best fit distribution for about 70 % of the stations. It is found that for lower return periods, both PWM and L moments predicted same flood magnitude, but for higher return periods, there are large differences in the magnitudes. The curves for equal peak discharge for return periods 20, 50 and 100 years were plotted for both PWM based distributions and L moments based distributions. These curves gave an implication of spatial variation of the peak discharge for each return period.

ACKNOWLEDGEMENTS

The authors are grateful to the Head, Department of Civil Engineering, IIT Bombay and Executive Director, Centre for Water Resources Development and Management, Kozhikode, India for the support given for this study.

REFERENCES

Ahmad UN., Shabri A. & Zakaria ZA. (2011). Flood Frequency Analysis of Annual Maximum Stream Flows using L-Moments and TL-Moments Approach. *Applied Mathematical Sciences*, 5(5), 243–253.

Burn DH. Zrinji Z. & Kowalchuk M. (1997). Regionalization of Catchments for Regional Flood Frequency Analysis. *Journal of Hydrologic Engineering*, 2(2), 76–82.

Cruff RW. & Rantz SE. (1965). *A Comparison of Methods Used in Flood-Frequency Studies for Coastal Basins in California*, Flood Hydrology Survey, Water supply Paper. 1580-E, California Department of Water Resources, Washington.

Das L M. & Qureshi ZH. (2014). Flood Frequency Analysis for Jiya Dhol River of Brahmaputra Valley, Basic and Applied Research. *International Journal of Sciences: Basic and Applied Research*, 14(2), 14-24.

Hosking J RM (1990). L moments : Analysis and Estimation of Distributions using Linear Combination of Order Statistics. *Journal of Royal Statistical Society*, 52(1), 105–24.

Hosking JRM. & Wallis JR. (1993). Some statistics useful in regional flood frequency. *Water Resources Research*, 29(92), 271-281.

Izinyon OC. & Ehiorobo, JO. (2015). L-moments Method for Flood Frequency Analysis of River Owan at Owan in Benin Owena River Basin in Nigeria. *Current Advances in Civil Engineering*, 3(1), 1–10.

Kumar R. & Chatterjee, C., (2005). Regional Flood Frequency Analysis using L Moments for North Brahmaputra Region of India. *Journal of Hydrologic Engineering,* 10(1), 293–300.

Moni L. & Husain Z. (2014). Flood Frequency Analysis for Jiya Dhol River of Brahmaputra Valley. *International Journal Science Basic Applied Research*, 4531, 14–24.

Ponce VM. (1989). *Engineering Hydrology Principles and Practices*, Prentice Hall, New Jersy.

Vivekanandan N. (2015). Flood Frequency Analysis using Method of Moments and L-Moments of Probability Distributions. *Cogent Engineering,* 2(1), 1-10.

A NEW APPROACH FOR IMPROVING FLOOD MODEL PREDICTIONS BASED ON THE SEQUENTIAL ASSIMILATION OF SAR-DERIVED FLOOD EXTENT MAPS

RENAUD HOSTACHE(1), MARCO CHINI(2), LAURA GIUSTARINI(3), MELISSA WOOD(4), GIOVANNI CORATO(5) AND PATRICK MATGEN(6)

(1,2,3,4,5,6) Luxembourg Institute of Science and Technology, Esch sur Alzette, Luxembourg
renaud.hostache@list.lu
(4) University of Bristol, Bristol, United Kingdom

ABSTRACT

Hydrodynamic models represent an important component in flood prediction systems. However, providing reliable model predictions and reducing the associated uncertainties remain challenging, especially in poorly gauged river basins. As Synthetic Aperture Radar-derived flood image databases are significant (and expected to grow rapidly with contributions from new satellites such as Sentinel-1), there are emerging opportunities for using these data collections to improve model predictions. In this context, our aim is to contribute to the development of a global and near real-time remote sensing-based service that delivers flood predictions to support flood management. The study takes advantage of recently developed efficient, rapid and automatic algorithms for the delineation of flood extent using SAR images. The main objective of the study is to show how near real-time sequential assimilation of SAR derived flood extents can improve model predictions. As a test case, we use several flood events of the river Severn (UK). We use the Lisflood-FP hydraulic model coupled with the Superflex hydrological model and adopted a particle filter-based assimilation scheme. An important issue in the framework of the assimilation of remote sensing-derived information is to quantify observation uncertainty. To do so, an image processing approach that assigns to each pixel a 'probability to be flooded' based on its backscatter values was introduced for the first time. The sequential assimilation of SAR-derived flood extent maps shows a significant improvement in the hydraulic model predictions. The main achievement of the study is that model predictions are clearly improved by the assimilation of SAR-derived flood extent not only in terms of predicted flooded areas but also in terms of predicted discharge and water level surface elevation hydrographs.

Keywords: Flood prediction; Hydrological modeling; hydraulic modeling; Synthetic Aperture Radar remote sensing; and assimilation.

1 INTRODUCTION

Central to mitigating the impact of floods are globally consistent and accurate short- to medium-range flood forecasts that allow stakeholders in flood management to better anticipate critical needs such as: search and rescue, medical assistance, managing displacement of people and goods, reducing the individual risk of being exposed to water-borne diseases, maintaining food security conditions, as well as avoiding the interruption of critical supply chains that are known to cause extreme financial losses to industry. However, optimal decision making in emergency situations is hampered by uncertainties inherent to numerical modelling-based flood forecasting. A well-established way for reducing these uncertainties is to periodically control and correct the models via external observations. In forecasting model, such data assimilation applications allow keeping the predictions on track. Ideally, this is achieved via the assimilation of streamflow measurements from distributed hydrometric stations. However, gauging stations are relatively sparse and irregular in space and their number is in decline (Mason et al., 2012). An inviting alternative that has obtained increased attention over the last years is to improve the predictions of runoff by assimilating hydrology-related data derived from globally and freely available Earth Observation data. The purpose of this study is to improve water elevation and flood extent simulations by correcting a coupled hydrologic-hydraulic model using microwave remote sensing-derived flood inundation information.

2 METHODOLOGY

The objective of the proposed method is to improve flood forecasts of a model cascade by assimilating SAR derived flood maps. This section first focuses on the set up of the modeling cascade. Next, the probabilistic flood mapping algorithm and the particle filter based assimilation framework are presented.

2.1 Flood forecasting model cascade set up

The flood forecasting model cascade is based on the loose coupling of a conceptual hydrological model (Superflex) and a 2-dimensional hydraulic model (Lisflood-FP).

Superflex (Fenicia et al, 2011) is a modeling framework that has been designed for hypothesis testing in hydrological modeling. It is a conceptual model based on reservoirs, lag functions and connection elements. Various reservoirs have been introduced to reproduce different hydrological concepts such as rainfall interception, upper soil root zone storage, riparian zone storage, fast and slow runoff components generation etc. Each type of reservoir can be easily switched on or switched off so that many model structures can be easily set up. The functions describing the storage/discharge relationships and the shape of lag functions are taken from a function library allowing a lot of flexibility. Superflex uses time series of rainfall as inputs and potential evapotranspiration and produces time series of simulated storage and runoff as outputs. In this study, the rainfall and ETP (Hamon formula, based on 2m air temperature) time series are derived from ERA-Interim public dataset (Dee et al., 2011).

Lisflood-FP (Bates and De Roo, 2000) is a grid based 2-dimensional hydraulic model. In the floodplain, this solves a simplified inertial version (neglecting convective acceleration) of the 1-dimensional momentum conservation equation over the two horizontal dimensions x and y using a finite difference method. *A posteriori* developments of the model integrate a subgrid channel routine (Neal and Bates, 2012) for simulating the flow within the channel using the 1-Dimensional de Saint Venant equation. As usual in hydraulic modeling, Lisflood-FP requires the downstream boundary conditions, the inlets for all river streams within the area of interest, the ground elevations in the floodplain and the geometry of river streams. The main hydraulic parameter is the Manning friction coefficients that can be spatially distributed.

For the loose coupling of Superflex and Lisflood-FP, the runoff time series simulated by the hydrological model are used as inlet inputs of the hydraulic model. The model cascade outputs time series of water depth and water fluxes for each model grid cell. As a matter of fact, the model provides for any time step a water depth map that can be converted into a simulated flood extent map by considering as flooded pixels with positive water depth, the remaining pixels corresponding to no-water. Binary simulated flood extent maps are therefore obtained.

2.1.1 The ensemble forecast generation

For generating the ensemble forecast, we assumed that the main source of uncertainty is the predicted amounts of rainfall. Therefore, we perturb the rainfall deterministic predictions provided by the ERA-Interim dataset using a random lognormal multiplicative noise and we propagated it to the complete forecasting chain.

2.2 Probabilistic flood mapping from SAR image

With an objective of assimilating flood extent maps into a hydrodynamic model, it is of primary concern to estimate the uncertainty associated to the flood extent map. To do so, a method recently developed by Giustarini et al. (2016) allows for estimating the probability of a pixel being water based on its backscatter values. The method has its origins in the previous studies of Matgen et al. (2011), Hostache et al. (2012) and Giustarini et al. (2013) and is based on Bayesian theory. As defined in Giustarini et al. (2016), the probability of a pixel being open water given its recorded backscatter value is given by Bayes theorem as follows:

$$p(w|\sigma^0) = \frac{p(\sigma^0|w)p(w)}{p(\sigma^0|w)p(w) + p(\sigma^0|nw)p(nw)} = \frac{p(\sigma^0|w)p(w)}{p(\sigma^0)} \qquad [1]$$

In Eq. 1, $\mathrm{p}(\sigma^0|\mathrm{w})$ is the probability of recording the backscatter σ^0 if the pixel corresponds to water, $\mathrm{p}(\sigma^0|\mathrm{nw})$ is probability of recording the backscatter σ^0 if the pixel does not correspond to water, *p(w)* and *p(nw)* are the prior probabilities of a pixel being water and non-water, respectively. The solution of the equation requires two sets of probabilities: conditional probabilities and prior probabilities. As there is no information about the prior probabilities, we set *p(w)=p(nw)=.5* as suggested in Giustarini et al. (2016). Our key assumption is that the unknown quantities $\mathrm{p}(\sigma^0|\mathrm{w})$ and $\mathrm{p}(\sigma^0|\mathrm{nw})$ can be estimated from an empirical distribution of backscatter values derived from the flood image. We therefore assume that the image histogram is a mixture of two curves, where the first one corresponds to flooded pixels and can be approximated by a gaussian curve and the second one corresponds to non-flooded pixels and can be estimated as the difference between the total histogram and the estimated Gaussian curve component (Giustarini et al., 2013). This procedure allows attributing a flood probability to every pixel included in the considered area of interest. A recent further development of this method allows to calibrate the theoretical curve based on a Hierarchical split based approach (Chini et al., submitted). This allows to calibrate the theoretical PDF of water backscatter over large images regardless of the area covered by water in the images. The flood probability map that is therefore obtained indicates on each pixel the probability (ranging between 0 and 1) of this to be water (i.e. flooded) based on the backscatter observation.

2.3 Assimilation of flood probability maps into a 2D hydrodynamic model

A second task is to define a data assimilation framework for assimilating flood extent data into a 2D hydraulic model. The output of the model cascade is a time series of binary maps where each pixel is either flooded or non-flooded. Therefore, the probability of each pixel being flooded/non-flooded can be seen as a success/failure experiment, which can be described by a binomial distribution. To optimally combine observations and simulations we adopt a Particle Filter (PF) approach as this has been shown efficient for improving hydrodynamic model predictions (*e.g.* Matgen et al., 2010; Giustarini et al., 2011; Hostache et al., 2015). In a PF, the prior (before the assimilation) and posterior (after the assimilation) model probabilities are approximated by a set of models with various equations, forcings, and/or parameters. In this study, the main source of uncertainty is assumed to be the predicted amounts of rainfall. As a matter of fact, all particles (i.e. all members of the model ensemble) share the same properties except for the forcing data (rainfall amounts). The PF is then used to periodically correct the model cascade predictions based on a series of satellite flood extent observations. The PF does not necessarily assume a Gaussian distribution of the observation errors and thus can be adapted to any other probability density function. The SAR-derived flood probability map that is to be assimilated into the model is a map where each pixel has a value in the continuous range 0-1. Hence, based on the binomial PDF, the weight that is related to the generic ith observation, kth pixel and jth model (particle), can be calculated as follows:

$$w_{k,j}^{i} = \begin{cases} \theta_k^i & if\ pixel\ k\ is\ simulated\ as\ flooded \\ 1-\theta_k^i & if\ pixel\ k\ is\ simulated\ as\ dry \end{cases} \quad [2]$$

In Eq. 2, $wf_{k,j}^{i}$ is the particle weight and θ_k^i is the value given by the ith flood probability map. In a particle filter, the individual weights are spatially aggregated in order to obtain one single so called global weight for each particle. Based on these global weights, an expectation (weighted mean) can be computed for any state variable of the modeling cascade.

3 Study area, data processing and model set up

The study area is a 30.5 km by 52.4 km domain around the city of Tewkesbury (UK), located at the confluence of Rivers Severn and Avon. Figure 1 shows the model domain and the river network. In figure 1, the red squares indicate the model upstream boundaries while the yellow stars indicate internal gauging station available for results evaluation. Hence, two evaluation stations are located downstream the confluence between rivers Avon and Severn, and the two others are located in the downstream part of river Avon and river Severn, respectively.

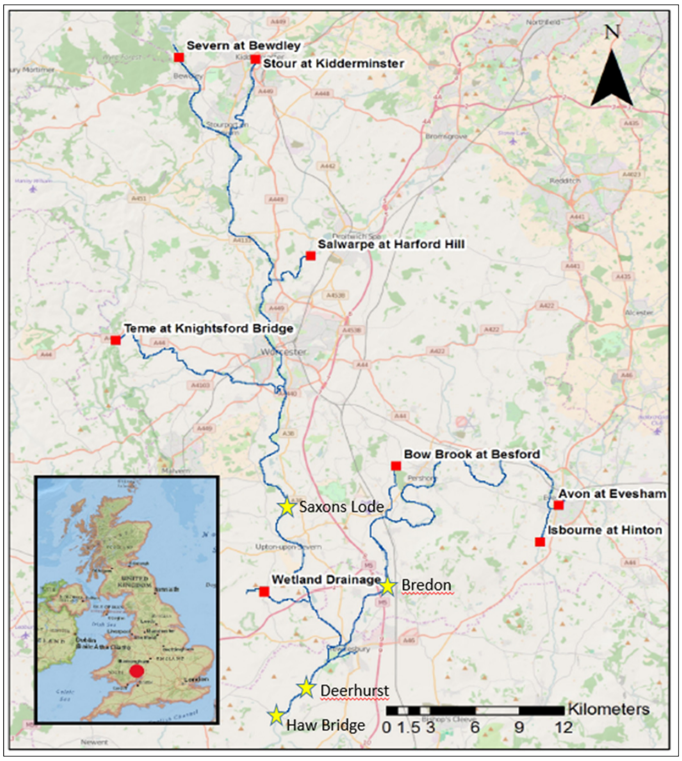

Figure 1. Extent of the River Severn model (after Wood et al. 2016) illustrates the model domain, showing the two main rivers and their tributaries.

Two Superflex hydrological models were calibrated for the two main rivers in order to predict discharge hydrographs at Eversham (river Avon, see Figure 1) and at Bewdley (river Severn, see Figure 1). The calibration of these two models was based on the Nash-Sutcliffe Efficiency, comparing simulated and observed discharge time series. The friction and river geometry parameters of the 2D hydraulic model LISFLOOD-FP were previously calibrated using *in situ* measured water levels (Neal and Bates, 2012). By randomly perturbing the rainfall prediction provided by ERA-Interim, we simulated 128 discharge hydrographs at Bewdley and Eversham respectively for the four considered flood events. Next, an ensemble of 128 simulated flood extent time series was generated by routing the ensemble of discharge hydrographs generated by the Superflex hydrological model in the Lisflood-FP model.

From the whole archive of Envisat Wide Swath Mode images, we selected 11 flood images covering four moderate to large magnitude flood event respectively in March and July 2007, January 2008, and January 2010. The satellite database is described in detail in Wood et al. (2016). Figure 2 below shows two flood probability maps derived from SAR images as an example.

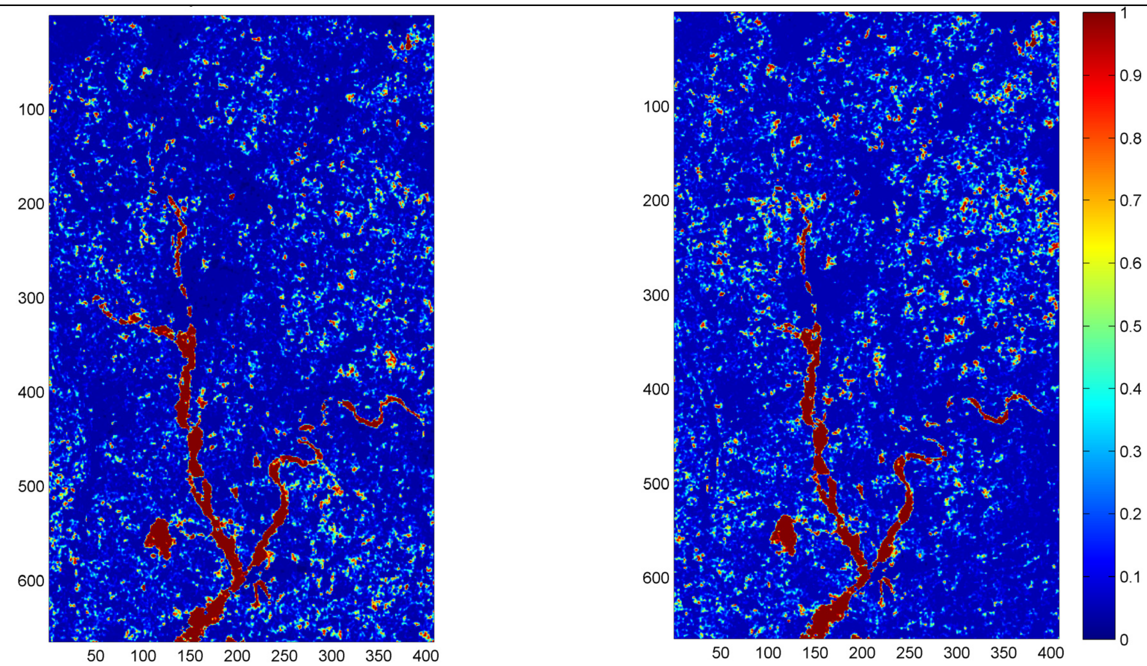

Figure 2. Flood probability maps obtained from ENVISAT ASAR data acquired on July 23 2007 morning (left) and evening (right).

4 RESULTS AND DISCUSSION

The method proposed for assimilating the SAR derived flood probability maps was applied to the four flood events that occurred in March 2007, July 2007, January 2008 and January 2010. In this context, an ensemble of 128 perturbed rainfall amounts was used as forcings of the two calibrated Superflex models for rivers Severn and Avon. The ensemble of simulated hydrographs therefore obtained for the two rivers is routed in the Lisflood-FP hydraulic model. These 128 particle simulations were stopped each time a SAR image is available and the corresponding flood probability map was then assimilated.

The posterior probability of each particle was computed, the particle weights were updated and the hydraulic simulations were continued until the next time a SAR image is available. The efficiency and the robustness of the sequential assimilation was assessed based on model expectation using as a reference the Water Surface Elevation (WSE) measurements at Saxons Lode, Bredon, Hawbridge and Deerhurst gauging stations (see Figure 1). To carry out this efficiency and robustness assessment, two cases were considered: an open loop simulation where no image is assimilated (all particle are supposed to be equally weighted at any time step) and a sequentially updated simulation (particle weights are updated each time an image is available). Figures 3 to 6 show the results obtained for the four considered flood events, respectively March 2007, July 2007, January 2008 and January 2010.

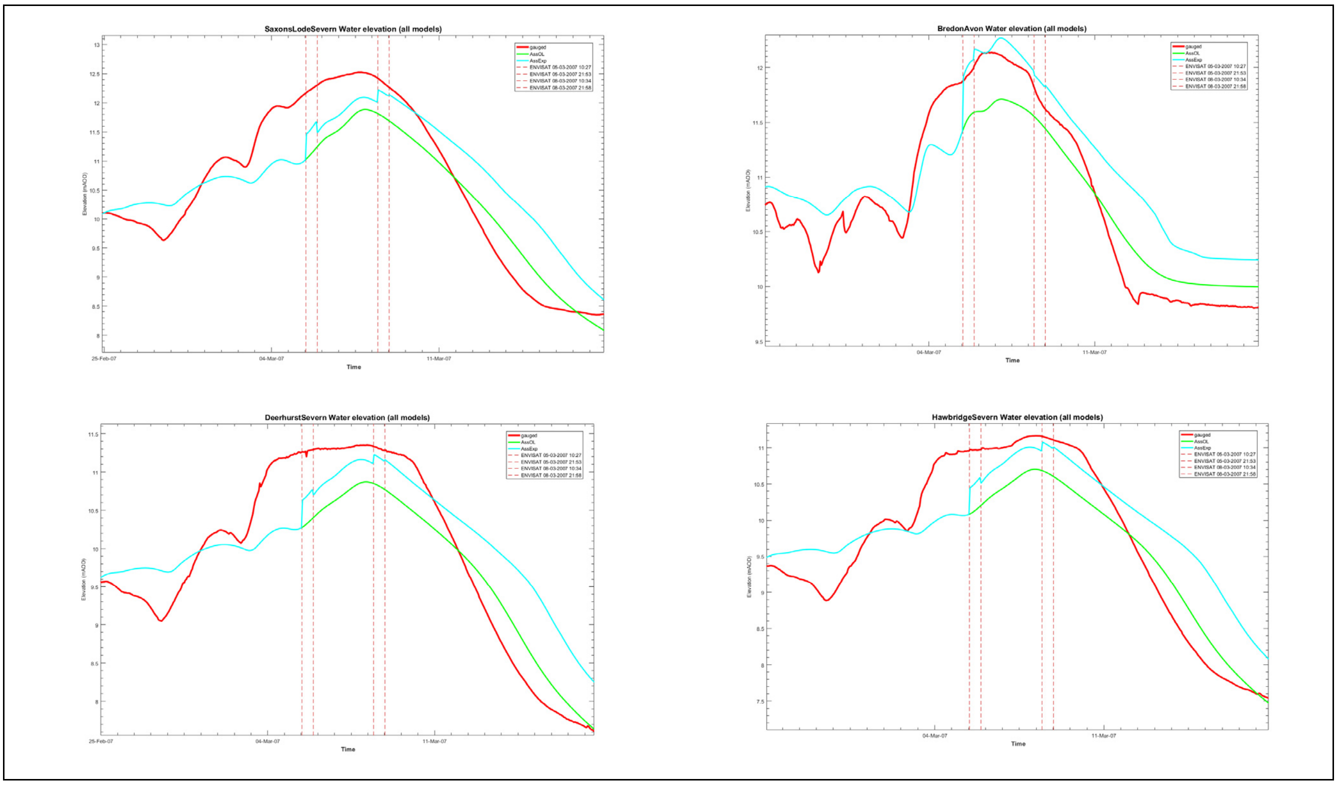

Figure 3. Simulated WSE time series: open loop (green), simulated with assimilation (cyan) and observed (red) water surface elevation time series for the March 2007 flood events at (from top left to bottom right) Saxons Lode, Bredon, Deerhurst and Hawbridge gauging stations.

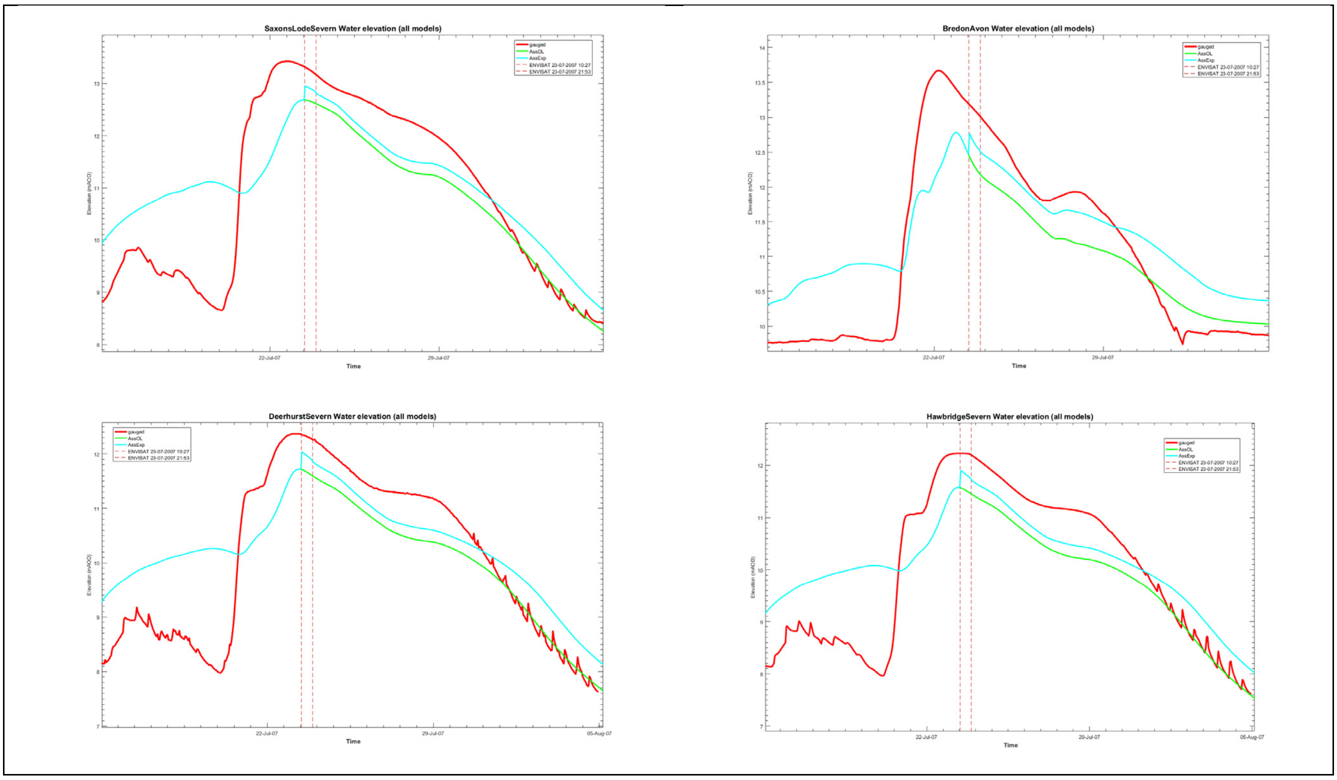

Figure 4. Simulated WSE time series: open loop (green), simulated with assimilation (cyan) and observed (red) water surface elevation time series for the July 2007 flood events at (from top left to bottom right) Saxons Lode, Bredon, Deerhurst and Hawbridge gauging stations.

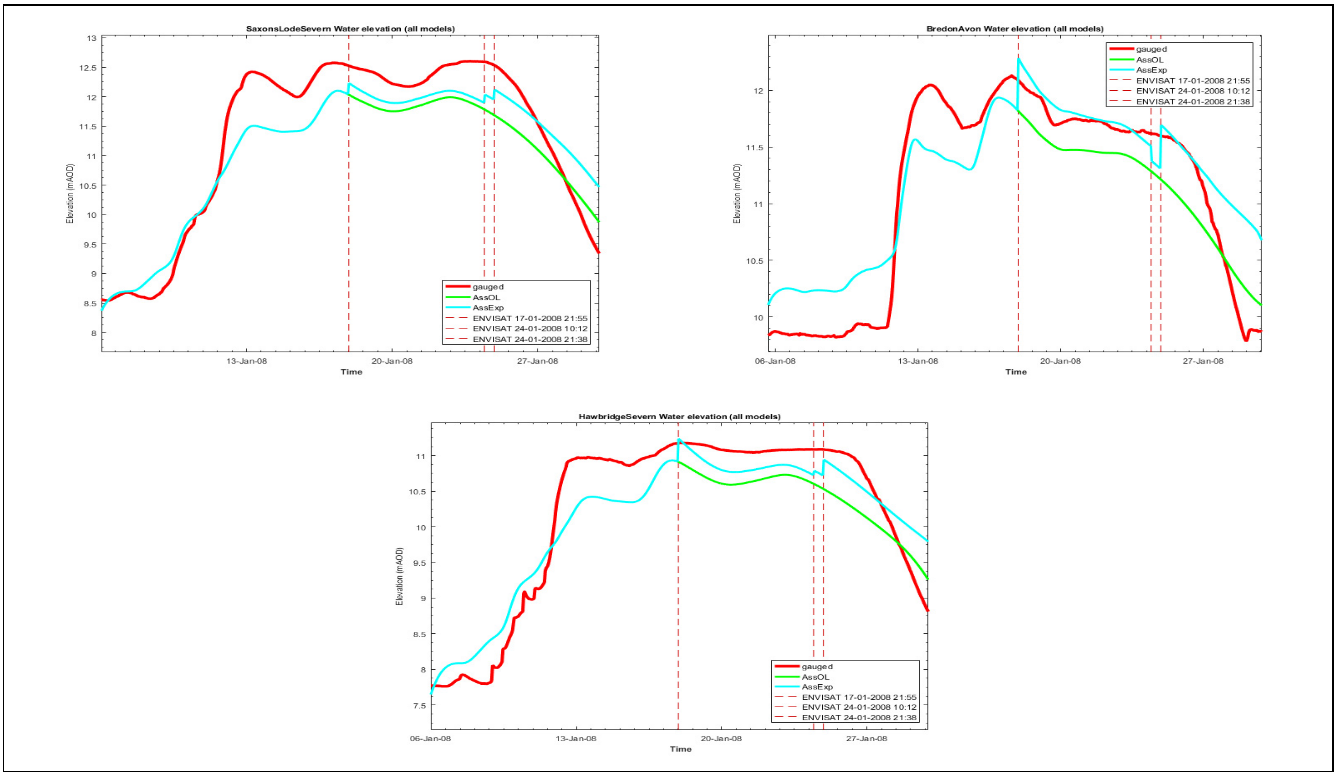

Figure 5. Simulated WSE time series: open loop (green), simulated with assimilation (cyan) and observed (red) water surface elevation time series for the January 2008 flood events at (from top left to bottom right) Saxons Lode, Bredon and Hawbridge gauging stations.

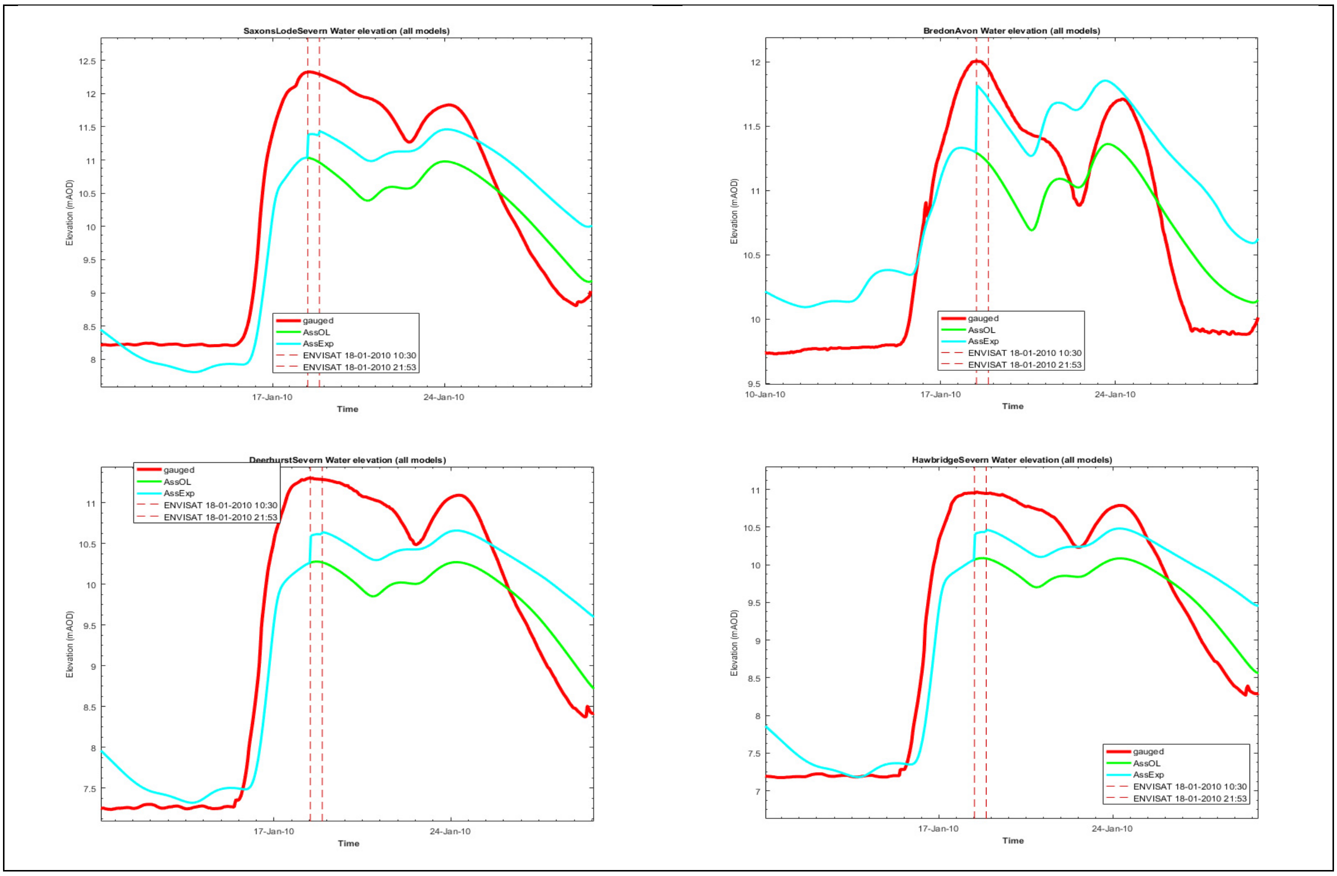

Figure 6. Simulated WSE time series: open loop (green), simulated with assimilation (cyan) and observed (red) water surface elevation time series for the January 2010 flood events at (from top left to bottom right) Saxons Lode, Bredon, Deerhurst and Hawbridge gauging stations.

One can notice that the results for Deerhurst are not showed in figure 5 as there was no WSE records at this gauging station during the January 2008 flood event. In figures 3 to 6, the red lines correspond to the observed WSEs at the four gauging stations, the green lines correspond to the open loop simulated WSEs (ensemble expectation) at the same locations and the cyan lines correspond to the simulated WSEs with sequential assimilation of SAR derived flood probability maps (ensemble expectation) at the same locations. The vertical dashed lines indicate the acquisition time of the SAR images. It is worth noting that, for each flood event the open loop and sequentially updated simulations are identical before a satellite image has been acquired as particle prior probabilities are assumed uniform before the first assimilation step.

Looking at these figures undoubtly leads to the conclusion that the sequential assimilation of the satellite observations improves model results and significantly reduces model errors as the cyan lines move closer to the observation than the green line at any assimilation step. Errors between model results and ground observations are reduced most of the time by at least two levels of magnitude regardless of the considered flood event, gauging station or SAR image.

Another encouraging result is that the improvement is not only visible at the assimilation time but also for a significant number of subsequent time steps. As a matter of fact, the improvement due to the assimilation is positively persisting over time for a few hours to a few days depending on the station and the flood event that is considered. Unfortunately, a longer time after the assimilation, the update starts to have a negative effect since the models that were best performing at the time step of the assimilation are not necessarily well performing anymore especially in the event where hydrological condition significantly changed (*e.g.* strong water recession) in the meantime. Figure 6 shows a good example of this effect. In this figure where the two satellite images were acquired at the flood peak, the improvement due to the assimilation persist for a few days until the recession has become significant. This shows one limitation of the method due to too long revisit time of the satellite. Indeed, if other images are available later on, a new assimilation would have been possible and the expectation would have likely moved toward the observation. Results shown in figure 3 for Bredon gauging station confirm this hypothesis as the recession is better reproduced by the expectation when images are assimilated at the beginning of the recession.

It has to be mentioned that very similar results are obtained when comparing simulated and observed discharge. For the sake of conciseness, these results are not shown in this paper.

As a matter of fact, the overall picture provided by figures 3 to 6 show that the assimilation is most beneficial during the time steps following the data assimilation but still contributes to an increase of the model performance for longer periods as long as hydrological condition do not change too rapidly.

5 CONCLUSIONS

We propose a particle filter based method for assimilating SAR derived flood maps in a model cascade composed of a conceptual hydrological model coupled with a hydraulic model. Four flood events and a set of 11 related SAR derived flood maps over rivers Severn and Avon were used as a test case. The sequential assimilation of the 11 flood maps show a significant and systematic improvement of the model cascade simulations. Model errors on simulated water levels were reduced by an order of magnitude of 2 on average at the time steps of the assimilation. Moreover, the improvement of model results is not limited to the time step of the assimilation, but also persist a few hours to a few days after the assimilation time step, depending on the hydrological conditions. These results provide some strong evidence that the assimilation of flood extent data improves the model results.

ACKNOWLEDGEMENTS

The research reported herein was funded by the National Research fund of Luxembourg (Paparazzi C11/SR/1277979 and Mosquito C15/SR/10380137) projects). The authors would like to thank Dmitri Kavetski and Jeffrey Neal for their help in setting up the experiment.

REFERENCES

Bates, P. & De Roo, A. (2000). A Simple Raster-Based Model for Flood Inundation Simulation. *Journal of Hydrology*, 236(1), 54-77.

Chini, M., Hostache, R., Giustarini, L. & Matgen, P. (submitted). A Hierarchical Split-Based Approach (HSBA) for parametric thresholding of SAR images: flood inundation as a test case. *IEEE Transactions on Geoscience and Remote Sensing*.

Dee, D., Uppala, S., Simmons, A., Berrisford, P., Poli, P., Kobayashi, S., Andrae, U., Balmaseda, M., Balsamo, G., Bauer, P., Bechtold, P., Beljaars, A., van de Berg, L. Bidlot, J., Bormann, N., Delsol, C., Dragani, R., Fuentes, M., Geer, A., Haimberger, L., Healy, S., Hersbach, H., Hólm, E. , Isaksen, L., Kållberg, P., Köhler, M., Matricardi, M., McNally, A., Monge-Sanz, B., Morcrette, J.-J., Park, B.-K., Peubey, C., de Rosnay, P., Tavolato, C., Thiepaut, J.-N. & Vitart, F. (2011). The Era-Interim Reanalysis: Configuration and Performance of the Data Assimilation System. *Quaterly Journal of the Royal Meteorological Society*, 137(656), 553-597.

Fenicia, F., Kavetski, D. & Savenije, H.H.G. (2011). Elements of a Flexible Approach for Conceptual Hydrological Modeling: 1. Motivation and Theoretical Development. *Water Resources Research*, 47(11), 1-13.

Giustarini, L., Matgen, P., Hostache, R., Montanari, M., Plaza, D., Pauwels, V. R. N., De Lannoy, G. J. M., De Keyser, R., Pfister, L., Hoffmann, L. & Savenije, H. H. G. (2011). Assimilating SAR-Derived Water Level Data into a Hydraulic Model: A Case Study. *Hydrology and Earth System Sciences*, 15(7), 2349-2365.

Giustarini, L., Hostache, R., Matgen, P., Schumann, G. J.-P. , Bates, P. D. & Mason, D. C. (2013). A Change Detection Approach to Flood Mapping in Urban Areas Using TerraSAR-X. *IEEE Transactions on Geoscience and Remote Sensing*, 51(4), 2417-2430.

Giustarini, L., Hostache, R., Kavetski, D., Chini, M., Corato, G., Schlaffer, S. & Matgen, P. (2016). Probabilistic Flood Mapping using Synthetic Aperture Radar Data. *IEEE Transactions on Geoscience and Remote Sensing*, 54(12), 6958-6969.

Hostache, R., Matgen, P. & Wagner W. (2012). Change Detection Approaches for Flood Extent Mapping: How to Select the Most Adequate Reference Image from Online Archives? *International Journal of Applied Earth Observation and Geoinformation*, 19, 205-213.

Hostache, R., Matgen, P., Giustarini, L., Teferle, F.N., Tailliez, C., Iffly, J.-F. & Corato, G. (2015). A Drifting GPS Buoy for Retrieving Effective Riverbed Bathymetry. *Journal of Hydrology*, 520, 397-406.

Mason, D.C., Schumann, G., Neal, J., Garcia-Pintado, J. & Bates, P.D (2012). Automatic Near Real-Time Selection of Flood Water Levels from High Resolution Synthetic Aperture Radar Images for Assimilation into Hydraulic Models: A Case Study. *Remote Sensing of Environment*, 124, 705-716.

Matgen, P., Montanari, M., Hostache, R., Pfister, L., Hoffmann, L., Plaza, D., Pauwels, V. R. N., De Lannoy, G. J. M., De Keyser, R. & Savenije, H. H. G. (2010). Towards the Sequential Assimilation of SAR-Derived Water Stages into Hydraulic Models using the Particle Filter: Proof of Concept. *Hydrology and Earth System Sciences*, 7(2), 1785-1819.

Matgen, P., Hostache, R., Schumann, G., Pfister, L., Hoffmann, L. & Savenije, H.H.G. (2011). Towards an Automated SAR-Based Flood Monitoring System: Lessons Learned from Two Case Studies. *Physics and Chemistry of the Earth*, 36(7-8), 241-252.

Neal, J., Schumann, G. & Bates, P. (2012). A Subgrid Channel Model for Simulating River Hydraulics and Floodplain Inundation over Large and Data Sparse Areas. *Water Resources Research*, 48(11), 1-16.

Wood, M., Hostache, R., Neal, J., Wagener, T., Giustarini, L., Chini, M., Corato, G., Matgen, P. & Bates, P. (2016). Calibration of Channel Depth and Friction Parameters in the LISFLOOD-FP Hydraulic Model using Medium-Resolution SAR Data and Identifiability Techniques. *Hydrology and Earth System Sciences*, 20(12), 4983-4997.

NUMERICAL ANALYSIS OF INUNDATION FLOW DUE TO HEAVY RAINFALL IN THE SHIRAKAWA RIVER ON JULY 2012

XIANG CHEN (1), RYUICHI HIRAKAWA (2) & TERUNORI OHMOTO (3)

(1, 2) Dept. of Civil and Environmental Engineering, Maebashi Institute of Technology, Maebashi City, Japan,
m1646502@maebashi-it.ac.jp,hirakawa@maebashi-it.ac.jp
(3) Dr. Eng., Graduate School of Science and Technology, Kumamoto University, Kumamoto City, Japan,
ohmoto@kumamoto-u.ac.jp

ABSTRACT

In July, 2012, local heavy rainfall caused severe flooding in the Kyushu area, Kumamoto prefecture, mainly within Shirakawa River. This study considers behavior through numerical simulations of a runoff model and a 2-D inundation flow model is proposed to undergo this study. The surveys show that the flood was caused by the heavy rainfall in a short period. The mathematical model could express the inundation process. To calculate numerical simulation, the fine mesh ground date is modeled by using the LP data and the house map. The simulation results are showing good agreement with the field survey data and some interviews. According to numerical analysis distributions of water depth, flow velocity and momentum flux was revealed.

Keywords: Flood disaster; inundation analysis; numerical simulation; Shirakawa River; flood on July 2012 in Kumamoto prefecture.

1 INTRODUCTION

Recently, the frequency of flood disasters caused by local heavy rain has increased. In particular, flooding in downstream areas caused by torrential rainfall in the mountainous upstream areas has become more frequent. Examples include the flood in Matsue City, caused by torrential rainfall in July, 2006 or the flood in 2010 in Atsusa, Sanyo-Onoda City, Yamaguchi Prefecture. Moreover, because of rapid urbanization, many houses are built in poorly drained areas, such as swamps, back swamps, river traces, and floodplains. Land in these areas is cheap because of the high risk of floods. As a result, many houses were built, and the number of houses damaged by floods has increased. The target area in this research was Tatsudajinnai 4-chome, Kumamoto City, which is located beside the Shirakawa River (a class-A river). This area is located on a floodplain and was seriously damaged by the flood on July, 2012. The river is steep, and the floodplain is urbanized and crowded with many houses. The frequency of flood disasters caused by local heavy rainfall in residential areas is considered to be on increase. Research on the mechanism of overflow and inundation in the Tatsudajinnai area is becoming increasingly important for taking measures against flooding in urban areas.

The arrival time behavior of floodwater flow is affected by the positions of houses and streets. In order to investigate the inundation water depth, flow velocity distribution, flow vector in the river channel, and force distribution of a flood, a numerical simulation of the inundation from the flood of July 2012 in Kyushu was performed.

2 ABOUT TARGET AREA AND FLOOD

2.1 Target area

The Shirakawa River is located in the central part of Kyushu. Because this river is levelled at its upper and lower reaches and steep at its middle reach, floodwater has difficulty flowing out to the Ariake Sea when flood occurs. Tatsudajinnai 4-chome, Kumamoto City, is located on the floodplain at the bend in the middle reach of Shirakawa River. This area was once used for agricultural purposes, such as rice paddies or farms. However, since the "Riverside New Town Project" was proposed in 1973, this area has been drastically urbanized. Most of the houses in this area are on mounds that are 0.5–1.0m high. According to the landform classification map for flood control shown in Figure 1, this area is located on a "floodplain" and was hit many times by floods. Figure 2 shows the topographic map based on digital elevation model (DEM) data. Tatsudajinnai 4-chome is located on the bend of the Shirakawa River. This area protrudes into the river and stretches to the south. As shown in figure 3, the elevation in this area gradually decreases from the northwest toward the southeast side, and the elevation difference in this 500m section is 15m.

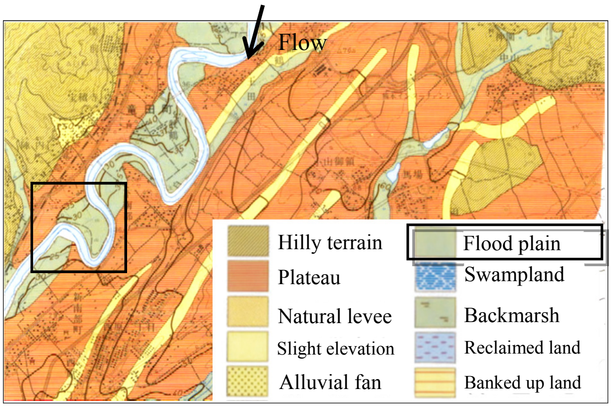

Figure 1. Classification map of flood control topography.

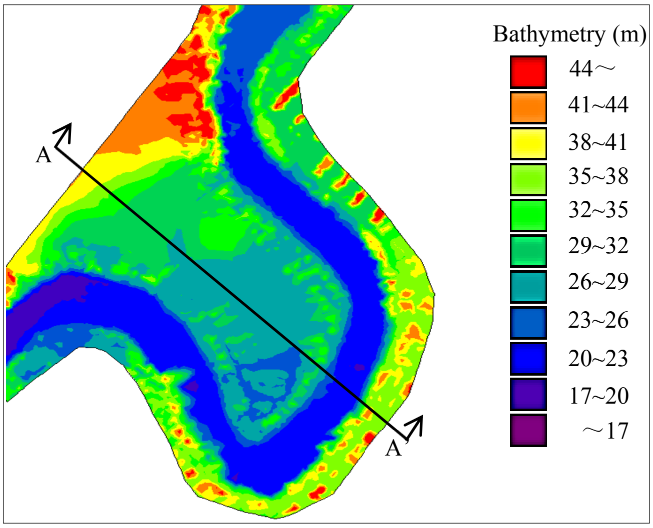

Figure 2. Ground elevation.

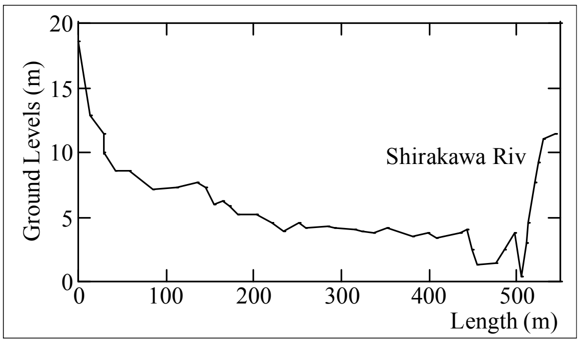

Figure 3. Section view A-A'.

2.2 Flood damage situation

From July 11 to 13, 2012, humid air moved in from the south to the baiu front, causing heavy rain from western to eastern Japan. In the Kumamoto-Aso area, there was record breaking heavy rain in the early morning of July 12th. On the same day, the Meteorological Agency announced, "Please be cautious about this never-before-seen heavy rainfall." Six hours of torrential rainfall struck the Aso-otsuhime area, which is located in the Shirakawa River valley. The 10-min precipitation was recorded as more than 200mm. The maximum precipitation in an hour was 106mm, and the total precipitation was 500mm. On the other hand, in Kumamoto City, the 10-min precipitation was 14mm, the maximum 1-h precipitation was 30.5mm, and the total precipitation was 179.5mm, as shown in figure 4. The total precipitation at Kumamoto was about 40% compared to that of the Aso-otsuhime area. However, the flood caused by violent torrential rainfall in Aso-otsuhime, which is located in the upstream areas of the Shirakawa River, brought serious damage to Tatsudajinnai, which is located in the downstream area. Approximately 2300m^3/s of floodwater flowed, although the capacity of the channel in this area is only 1500m^3/s. During interviews with residents of Tatsudajinnai, one of them said, "There was no flooding before 8:00, but at 8:15, when I finished watching TV and went out of the house, it had begun. And after I moved my car to a hill and came back, the water depth increased, and I could not go back to my house." The water overflowed in the floodplain area in a very short period. The prefectural police, fire department, and Self-Defense Force rescued 32 and 50 stranded people by helicopter and rubber boat, respectively.

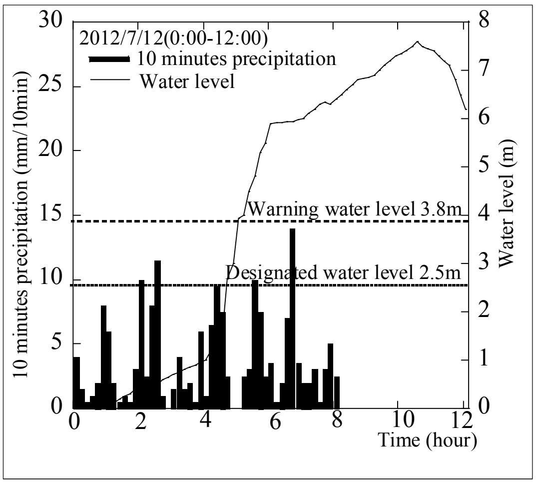

Figure 4. Change in 10-minute rainfall amount and river water level at the substitute bridge, the reference point of the Shirakawa system.

3 FLOOD INUNDATION FLOW SIMULATION

3.1 Mathematical model

In this study, the flow of floodwater was assumed to be two-dimensional planar flow, and a two-dimensional flood simulation was conducted. The following equations were applied for the simulation:

$$\frac{\partial h}{\partial t}+\frac{\partial M}{\partial x}+\frac{\partial N}{\partial y}=0 \qquad [1]$$

$$\frac{\partial M}{\partial t}+\frac{\partial (uM)}{\partial x}+\frac{\partial (vM)}{\partial y}=-gh\frac{\partial H}{\partial x}-\frac{\tau_x}{\rho}+\frac{\partial}{\partial x}\left(\varepsilon\frac{\partial M}{\partial x}\right)+\frac{\partial}{\partial y}\left(\varepsilon\frac{\partial M}{\partial y}\right) \qquad [2]$$

$$\frac{\partial N}{\partial t}+\frac{\partial (uN)}{\partial x}+\frac{\partial (vN)}{\partial y}=-gh\frac{\partial H}{\partial y}-\frac{\tau_y}{\rho}+\frac{\partial}{\partial x}\left(\varepsilon\frac{\partial N}{\partial x}\right)+\frac{\partial}{\partial y}\left(\varepsilon\frac{\partial N}{\partial y}\right) \qquad [3]$$

where x, y are rectangular coordinates, u, y are depth-averaged velocities, τ_x, τ_y are bottom face shearing forces in the x- and y-directions, ε is the eddy viscosity coefficient, t is time, ρ is density, h is depth, H is water level, and M, N are discharge fluxes ($M = uh,\ N = vh$).

3.2 Calculation of conditions

The target area for the simulation was Tatsudajinnai 4-chome, as shown in Figure 5. In a previous simulation, the roughness length according to land use or the synthesized roughness length, which has building occupancy or water depth as parameters, were applied to the meshes. However, the spatial resolution was not sufficient to simulate the flow behavior in narrow roads or between buildings, which were smaller than the meshes. In this study, in order to investigate the flow behavior in a residential area, geographic data with a 5m spatial resolution was used, and the studied area was divided into unstructured meshes based on streets or spaces between buildings. The shapes or positions of buildings, districts, and streets were defined according to maps of the Geospatial Information Authority of Japan or aerial photographs. Twenty-meter by ten-meter (flow direction x flow crossing direction) rectangular meshes and cross-sectional survey data of the riverbed obtained by real-time kinematic (RTK) GPS were used to define the plane rectangular coordinates of each inflection point. This was done to define the normal vector position and shape of the riverbed. The boundary conditions at the junction of the river channel and floodplain were defined so that outflow–inflow could be calculated according to the height of the right bank using the Honma function. Because the height of the left bank was high enough to prevent overflow, the boundary condition of the left bank was set to the closed state. The flow discharge at the edge of the upstream areas was set according to the Shirakawa River Improvement Plan and previous floods: 2000m^3/s (probability of once in 20–30 years), 2300m^3/s (the peak in the flood of July 12, 2012), and 3000m^3/s (probability of once in 150 years). The flow discharge was controlled at the Tatsuno Dam, and its value at peak time was measured at the Yotsugi Bridge. In the downstream areas, the boundary condition was set to the open state, and the buildings in the floodplain were set to the closed state. The roughness lengths of the river channel and floodplain were determined as 0.050m$^{-1/3}$ s and 0.033m$^{-1/3}$ s, respectively. The time duration was determined as 0.02s.

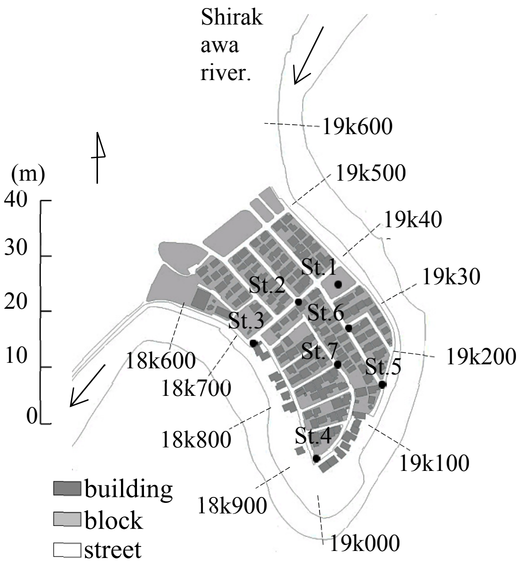

Figure 5. Structural of analysis target area.

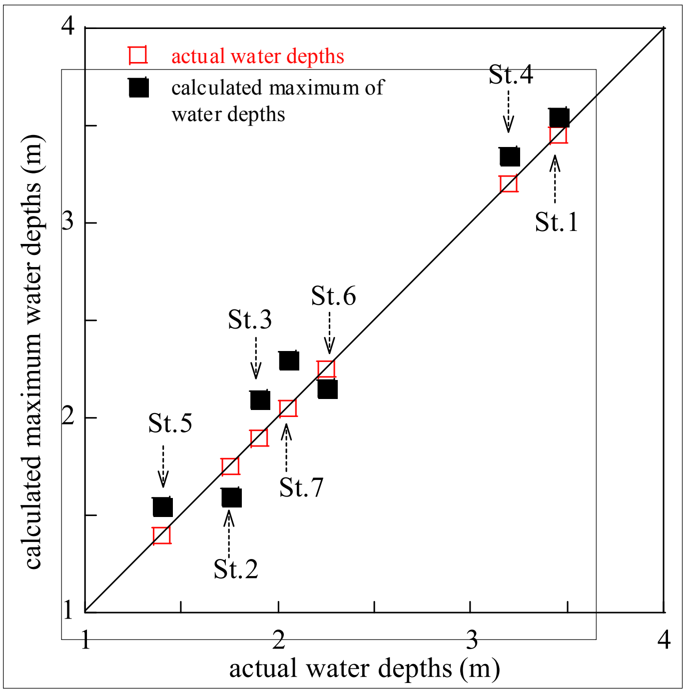

Figure 6. Comparison of calculation results (maximum depth) and trace depth of flooding analysis.

4 RESULTS AND DISCUSSIONS

4.1 Simulation accuracy

In this research, the inundation situation of Tatsudajinnai 4-chome, a populated area seriously damaged by the flood, was discussed. Figure 6 shows a comparison between the calculated maximum and actual inundated water depths. The simulated and actual water depths of areas St. 1–7 shown in Figure 5 are in approximate agreement.

4.2 Flood depth

The floodwater flowed from area 19k400, and the inundation area of the floodplain increased. Figure 7 shows the river depth and distribution of the inundation depth of the floodplain. When the flow discharge was

2000 m^3/s, 2300 m^3/s, and 3000m^3/s, the maximum flood depth in the park near 19k400 was 3.6m, 4.7m, and 5.3m, whereas the maximum flood depth in the floodplain near 19k000 was 2.7m, 4.5m, and 4.9m, respectively. The water depth increased because the park area is close to the overflow point, and 19k000 has a low elevation.

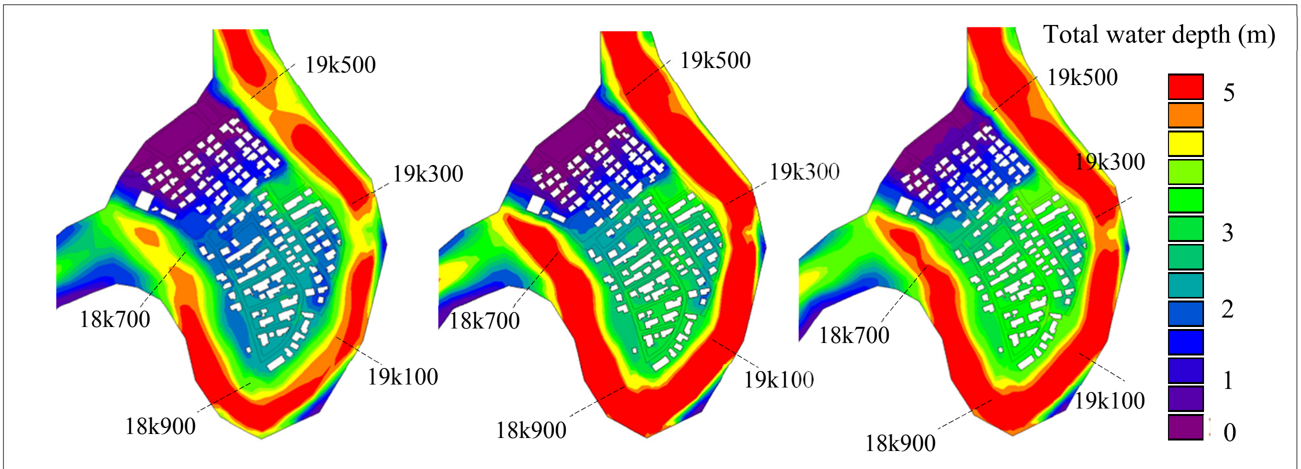

Figure 7. Water depth of river way and flood depth distribution inside the dam.

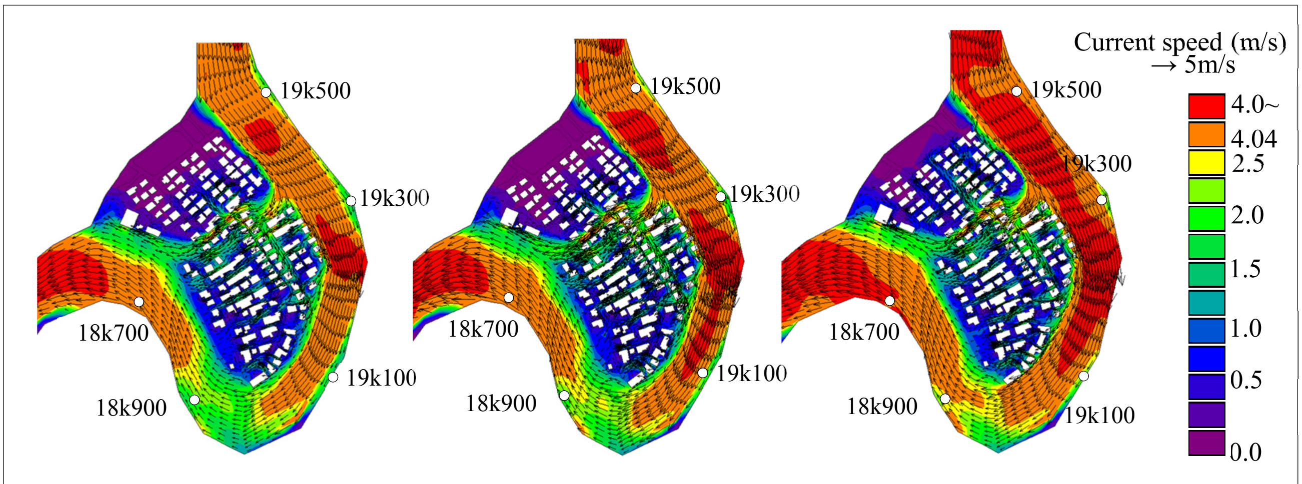

Figure 8. Flow velocity distribution and flow velocity vector in river way and urban area.

4.3 Flood flow velocity

Figure 8 shows the flow velocity distribution and flow velocity vector of the flood flow in the river and floodplain. The flow velocity distribution in the river is faster than that in 19k500. In addition, the flow velocity increased in the narrow section of 19k200.

In the floodplain, water overflowed in the area of the river bank from 19k500 to 19k200. Floodwater flowed into the residential area and streets, across the central part of the floodplain, past area 18k700, and joined the main stream. The velocity of the flow was very fast: 2.3m/s at 2000m^3/s, 3.0m/s at 2300m^3/s, and 4.3m/s at 3000m^3/s. Both the water depth and flow velocity increased at the bank of the floodplain. Floodwater overflowed from the section between 19k000 and 18k800. It is thought that the water level increased because of a decrease in the flow velocity.

The time from the water overflow and flow through the landside area to join the main stream is one minute for each flow discharge. When the flow discharge is 3000m^3/s, the flow velocity at St. 5 is very fast. This is because the river becomes narrow in 19k200 with flow discharge that is twice the capacity (1500m^3/s) flowing through the channel.

4.4 Flood force

Flooding in an urban area causes serious damage, such as the mass destruction of buildings and loss of lives. On the other hand, the only information about inundation depths is available from conventional flood hazard maps. Additional information such as flow velocity, direction, and forces is necessary for reducing the damage caused by flooding. Figure 9 shows the maximum flux momentum distribution in a building cluster, according to the research by Takahashi and Tanaka on the risk of losing houses by flooding. In their simulation, the flow behavior changes, caused by floating debris stacks such as driftwoods or debris from flushed houses was not considered. The relationship between the flux momentum U^2h and flow force F_d are expressed by

$$F_d = \frac{1}{2}\rho_s C_d B(U^2h) \qquad [4]$$

where ρ_s is the fluid density, C_d is the resistance coefficient, B is the building width, U^2h is the momentum flux, and h is water depth. Equation [4] shows the relationship between the square of the average flow velocity and the building width in a direction across the flow. As shown in figure 9:

(1) The maximum momentum flux in areas 19k500, 19k400, and 18k800 of the floodplain is increased;
(2) There is a park in area 19k400, and the momentum flux increased because water overflowed from the special bank continued through the roads beside the bank and then entered the park;
(3) In the case of a house on the side of the river, negative pressure and flow force in the opposite direction were thought to be generated;
(4) The area that is away from the road in 18k800 but beside the river is dangerous because of the crowded and parallel arrangement of the houses, which caused a strong flood force.

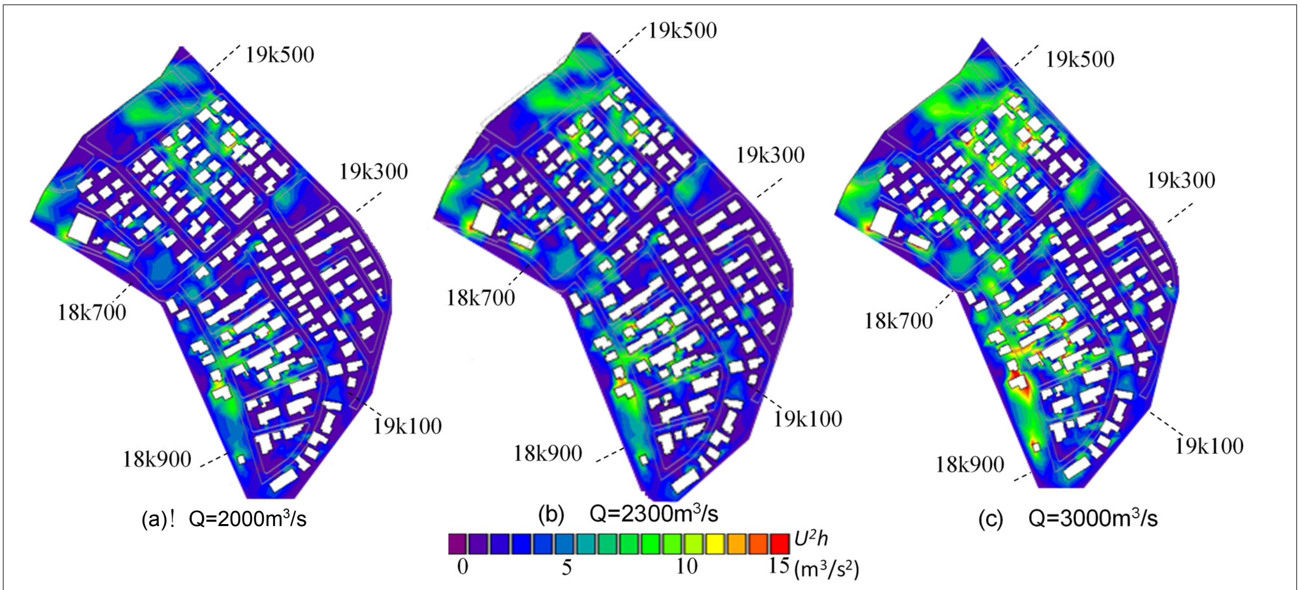

Figure 9. Distribution of maximum flux momentum.

5 CONCLUSIONS

In this research, we considered the effect of buildings on the inundation water flow and used numerical simulation to clarify the behavior of the floodwater flow when the flow discharge was 2300m^3/s. We also calculated the water depth and flow velocity distribution in the cases of 2000m^3/s and 3000m^3/s. As a result, we found the following facts:

(1) The maximum inundation water depth in the floodplain is recorded in the park near the overflow point for each flow discharge;
(2) According to the water depth and flow velocity distributions, the narrow section of channel in area 19k200 hadsa greater depth and faster flow velocity compared with the upstream areas. The flow velocity decreased, and the water level increased in area 18k800. In fact, the water overflowed between 19k000 and 18k800;
(3) When the flow discharge was 2300m^3/s, the floodwater that overflowed from the park in 19k400 flowed across the floodplain from the northeast to southwest direction. The maximum flow velocity was 3.0m/s.

ACKNOWLEDGEMENTS

The authors are grateful to Ministry of Land, Infrastructure, Transport and Tourism Kumamoto Office of Rivers and National Highways, River Division of Kumamoto Prefecture Civil Engineering Office, and Kumamoto Civil Engineering Office, for much valuable information.

